

The background of the cover features a stylized brain composed of various colored segments (yellow, orange, red, purple, blue, green) arranged in a circular pattern. A network of white lines connects nodes, resembling a neural network or a complex graph, overlaid on the brain segments. The top half of the cover has a blue background, while the bottom half is white.

FROM CELL PHYSIOLOGY TO EMERGING BRAIN FUNCTIONS

EDITED BY: Philippe Isope, Lisa Mapelli, Marylka Yoe Uusisaari and
Alexander Tang

PUBLISHED IN: Frontiers in Cellular Neuroscience



frontiers

Frontiers eBook Copyright Statement

The copyright in the text of individual articles in this eBook is the property of their respective authors or their respective institutions or funders. The copyright in graphics and images within each article may be subject to copyright of other parties. In both cases this is subject to a license granted to Frontiers.

The compilation of articles constituting this eBook is the property of Frontiers.

Each article within this eBook, and the eBook itself, are published under the most recent version of the Creative Commons CC-BY licence.

The version current at the date of publication of this eBook is CC-BY 4.0. If the CC-BY licence is updated, the licence granted by Frontiers is automatically updated to the new version.

When exercising any right under the CC-BY licence, Frontiers must be attributed as the original publisher of the article or eBook, as applicable.

Authors have the responsibility of ensuring that any graphics or other materials which are the property of others may be included in the CC-BY licence, but this should be checked before relying on the CC-BY licence to reproduce those materials. Any copyright notices relating to those materials must be complied with.

Copyright and source acknowledgement notices may not be removed and must be displayed in any copy, derivative work or partial copy which includes the elements in question.

All copyright, and all rights therein, are protected by national and international copyright laws. The above represents a summary only. For further information please read Frontiers' Conditions for Website Use and Copyright Statement, and the applicable CC-BY licence.

ISSN 1664-8714

ISBN 978-2-88966-000-1

DOI 10.3389/978-2-88966-000-1

About Frontiers

Frontiers is more than just an open-access publisher of scholarly articles: it is a pioneering approach to the world of academia, radically improving the way scholarly research is managed. The grand vision of Frontiers is a world where all people have an equal opportunity to seek, share and generate knowledge. Frontiers provides immediate and permanent online open access to all its publications, but this alone is not enough to realize our grand goals.

Frontiers Journal Series

The Frontiers Journal Series is a multi-tier and interdisciplinary set of open-access, online journals, promising a paradigm shift from the current review, selection and dissemination processes in academic publishing. All Frontiers journals are driven by researchers for researchers; therefore, they constitute a service to the scholarly community. At the same time, the Frontiers Journal Series operates on a revolutionary invention, the tiered publishing system, initially addressing specific communities of scholars, and gradually climbing up to broader public understanding, thus serving the interests of the lay society, too.

Dedication to Quality

Each Frontiers article is a landmark of the highest quality, thanks to genuinely collaborative interactions between authors and review editors, who include some of the world's best academicians. Research must be certified by peers before entering a stream of knowledge that may eventually reach the public - and shape society; therefore, Frontiers only applies the most rigorous and unbiased reviews. Frontiers revolutionizes research publishing by freely delivering the most outstanding research, evaluated with no bias from both the academic and social point of view. By applying the most advanced information technologies, Frontiers is catapulting scholarly publishing into a new generation.

What are Frontiers Research Topics?

Frontiers Research Topics are very popular trademarks of the Frontiers Journals Series: they are collections of at least ten articles, all centered on a particular subject. With their unique mix of varied contributions from Original Research to Review Articles, Frontiers Research Topics unify the most influential researchers, the latest key findings and historical advances in a hot research area! Find out more on how to host your own Frontiers Research Topic or contribute to one as an author by contacting the Frontiers Editorial Office: researchtopics@frontiersin.org

FROM CELL PHYSIOLOGY TO EMERGING BRAIN FUNCTIONS

Topic Editors:

Philippe Isope, Centre National de la Recherche Scientifique (CNRS), France

Lisa Mapelli, University of Pavia, Italy

Marylka Yoe Uusisaari, Okinawa Institute of Science and Technology Graduate University, Japan

Alexander Tang, University of Western Australia, Australia

Citation: Isope, P., Mapelli, L., Uusisaari, M. Y., Tang, A., eds. (2020). From Cell Physiology to Emerging Brain Functions. Lausanne: Frontiers Media SA.
doi: 10.3389/978-2-88966-000-1

Table of Contents

- 05** ***Maturation of GABAergic Transmission in Cerebellar Purkinje Cells is Sex Dependent and Altered in the Valproate Model of Autism***
Sébastien Roux, Ann Lohof, Yehezkel Ben-Ari, Bernard Poulain and Jean-Louis Bossu
- 19** ***Intracellular Dynamics in Cuneate Nucleus Neurons Support Self-Stabilizing Learning of Generalizable Tactile Representations***
Udaya B. Rongala, Anton Spanne, Alberto Mazzoni, Fredrik Bengtsson, Calogero M. Oddo and Henrik Jörntell
- 44** ***Decreased Number and Expression of nNOS-Positive Interneurons in Basolateral Amygdala in Two Mouse Models of Autism***
Xiaona Wang, Jisheng Guo, Yinsen Song, Qi Wang, Shunan Hu, Lingshan Gou and Yinbo Gao
- 51** ***Color Processing in Zebrafish Retina***
April Meier, Ralph Nelson and Victoria P. Connaughton
- 70** ***Modulation of Hyperpolarization-Activated Inward Current and Thalamic Activity Modes by Different Cyclic Nucleotides***
Maia Datunashvili, Rahul Chaudhary, Mehrnoush Zobeiri, Annika Lüttjohann, Evanthia Mergia, Arnd Baumann, Sabine Balfanz, Björn Budde, Gilles van Luijtelaa, Hans-Christian Pape, Doris Koesling and Thomas Budde
- 89** ***Oscillatory Cortical Activity in an Animal Model of Dystonia Caused by Cerebellar Dysfunction***
Elena Laura Georgescu, Ioana Antoaneta Georgescu, Carmen Denise Mihaela Zahiu, Alexandru Răzvan Șteopoaie, Vlad Petru Morozan, Adrian Ștefan Pană, Ana-Maria Zăgrean and Daniela Popa
- 112** ***How Do Cells of the Oligodendrocyte Lineage Affect Neuronal Circuits to Influence Motor Function, Memory and Mood?***
Renee E. Pepper, Kimberley A. Pitman, Carlie L. Cullen and Kaylene M. Young
- 126** ***PDI Knockdown Inhibits Seizure Activity in Acute Seizure and Chronic Epilepsy Rat Models via S-Nitrosylation-Independent Thiolation on NMDA Receptor***
A. Ran Jeon and Ji-Eun Kim
- 144** ***Morphine Binds Creatine Kinase B and Inhibits Its Activity***
Ivan Weinsanto, Jinane Mouheiche, Alexis Laux-Biehlmann, François Delalande, Arnaud Marquette, Virginie Chavant, Florian Gabel, Sarah Cianferani, Alexandre Charlet, Marie-Odile Parat and Yannick Goumon
- 154** ***Corrigendum: Morphine Binds Creatine Kinase B and Inhibits Its Activity***
Ivan Weinsanto, Jinane Mouheiche, Alexis Laux-Biehlmann, François Delalande, Arnaud Marquette, Virginie Chavant, Florian Gabel, Sarah Cianferani, Alexandre Charlet, Marie-Odile Parat and Yannick Goumon

- 155** *Long-Lasting Response Changes in Deep Cerebellar Nuclei in vivo Correlate With Low-Frequency Oscillations*
Letizia Moscato, Ileana Montagna, Licia De Propriis, Simona Tritto, Lisa Mapelli and Egidio D'Angelo
- 171** *Corrigendum: Long-Lasting Response Changes in Deep Cerebellar Nuclei in vivo Correlate With Low-Frequency Oscillations*
Letizia Moscato, Ileana Montagna, Licia De Propriis, Simona Tritto, Lisa Mapelli and Egidio D'Angelo
- 172** *S1 Employs Feature-Dependent Differential Selectivity of Single Cells and Distributed Patterns of Populations to Encode Mechanosensations*
Yoo Rim Kim, Chang-Eop Kim, Heera Yoon, Sun Kwang Kim and Sang Jeong Kim
- 183** *Circuit Investigations With Open-Source Miniaturized Microscopes: Past, Present and Future*
Daniel Aharoni and Tycho M. Hoogland
- 195** *Spontaneous and Acetylcholine Evoked Calcium Transients in the Developing Mouse Utricle*
Holly A. Holman, Lauren A. Poppi, Micah Frerck and Richard D. Rabbitt
- 213** *Enriched Environment Shortens the Duration of Action Potentials in Cerebellar Granule Cells*
Abdelmoneim Eshra, Petra Hirrlinger and Stefan Hallermann



Maturation of GABAergic Transmission in Cerebellar Purkinje Cells Is Sex Dependent and Altered in the Valproate Model of Autism

Sébastien Roux¹, Ann Lohof², Yehezkel Ben-Ari³, Bernard Poulain¹
and Jean-Louis Bossu^{1*}

¹Institut des Neurosciences Cellulaires et Intégratives (INCI)—CNRS, UPR 3212, Strasbourg, France, ²Sorbonne Université, CNRS UMR 8256, Biological Adaptation and Ageing, Paris, France, ³Neurochlore, Ben-Ari Institute of Neuroarcheology, Campus Scientifique de Luminy, Aix Marseille Université, Marseille, France

OPEN ACCESS

Edited by:

Enrico Cherubini,
Scuola Internazionale Superiore di
Studi Avanzati (SISSA), Italy

Reviewed by:

Tommaso Pizzorusso,
Consiglio Nazionale delle Ricerche
(CNR), Italy
Andrea Barberis,
Fondazione Istituto Italiano di
Tecnologia, Italy

*Correspondence:

Jean-Louis Bossu
jlbossu@inci-cnrs.unistra.fr

Received: 04 May 2018

Accepted: 16 July 2018

Published: 30 July 2018

Citation:

Roux S, Lohof A, Ben-Ari Y, Poulain B
and Bossu J-L (2018) Maturation of
GABAergic Transmission in
Cerebellar Purkinje Cells Is Sex
Dependent and Altered in the
Valproate Model of Autism.
Front. Cell. Neurosci. 12:232.
doi: 10.3389/fncel.2018.00232

Brain development is accompanied by a shift in gamma-aminobutyric acid (GABA) response from depolarizing-excitatory to hyperpolarizing-inhibitory, due to a reduction of intracellular chloride concentration. This sequence is delayed in Autism Spectrum Disorders (ASD). We now report a similar alteration of this shift in the cerebellum, a structure implicated in ASD. Using single GABA_A receptor channel recordings in cerebellar Purkinje cells (PCs), we found two conductance levels (18 and 10 pS), the former being dominant in newborns and the latter in young-adults. This conductance shift and the depolarizing/excitatory to hyperpolarizing/inhibitory GABA shift occurred 4 days later in females than males. Our data support a sex-dependent developmental shift of GABA conductance and chloride gradient, leading to different developmental timing in males and females. Because these developmental sequences are altered in ASD, this study further stresses the importance of developmental timing in pathological neurodevelopment.

Keywords: cerebellum, Purkinje neuron, chloride gradient, autism, sexual dimorphism, GABA_A channels

INTRODUCTION

Gamma-aminobutyric acid (GABA) is the main inhibitory neurotransmitter in the central nervous system. By opening GABA_A receptor channels and via chloride flow down its electrochemical gradient, GABA hyperpolarizes the membrane potential and thus reduces neuronal excitability in the mature nervous system. Intracellular chloride concentration ($[\text{Cl}^-]_i$) is regulated by cation-chloride co-transporters that determine the strength of GABAergic inhibition (Rivera et al., 1999; Watanabe and Fukuda, 2015; Raimondo et al., 2017). If the intracellular chloride concentration is high enough that the equilibrium potential for chloride is positive compared to the resting membrane potential, GABA_A receptor activation can depolarize the cell above the action potential threshold, acting like an excitatory neurotransmitter (Ben-Ari et al., 1989; Ben-Ari, 2014). This regulation of ($[\text{Cl}^-]_i$) has been reported in a wide range of animal species and brain structures; it is affected by many factors including sex steroids, BDNF and IGF-1 signaling (Galanopoulou, 2008; Tsutsui et al., 2011; Waddell and McCarthy, 2012; Ben-Ari, 2014; Watanabe and Fukuda, 2015). Immature neurons have lower ($[\text{Cl}^-]_i$) than neurons of young adults, leading to depolarizing GABA actions which both activate voltage-gated calcium currents and allow NMDA receptor activation, underlying the well-known trophic actions of GABA in development (Ben-Ari, 2002, 2014; Witte et al., 2014; Raimondo et al., 2017). GABAergic signals also generate action potentials

in many immature neurons, and the switch between excitatory and inhibitory GABA effects occurs at specific developmental time-points, depending on the neural structure and animal species. For example, the GABA “switch” occurs between E15.5 and E 17.5 in mouse spinal motoneurons (Allain et al., 2011), around P5 in the ventral horn of the rat spinal cord (Stein et al., 2004) and in ganglion and amacrine cells of the retina (Zhang et al., 2006), and from P8–P10 in mouse hippocampal pyramidal cells (Ben-Ari et al., 1989; Tyzio et al., 2007). Changes in the timing of the GABA switch, due to genetic mutations and/or environmental insults, are thought to contribute to neurodevelopmental disorders including autism (Ben-Ari et al., 1989; Ben-Ari, 2017).

GABA_A receptors are composed of 2 α subunits, 2 β subunits and 1 γ subunit, which together form a central ion pore. Excluding splice variants and point mutations, 6 α isoforms, 3 β isoforms and 3 γ isoforms have been characterized, as well as some minor subunits (δ , ρ , ϵ , θ , π and ϕ). In theory, therefore, a very large number of GABA_A receptor types may be found even in a single cell. The major adult isoform is generally accepted to be composed of $\alpha 1$, $\beta 2$ and $\gamma 2$ subunits. Whereas some subunits have a broad expression throughout the central nervous system, other subunits show a restricted cellular and subcellular localization (Sigel and Steinmann, 2012). The expression of GABA_A receptor subunits is developmentally regulated, notably with a developmental switch in α subunit expression associated with a slow-to-fast shift in the kinetics of GABA-mediated inhibitory postsynaptic potentials (Laurie et al., 1992; Fritschy et al., 1994). Thus, in thalamic reticular neurons, a postnatal switch in GABA_A receptor subunits from $\alpha 5$ to $\alpha 3$ is believed to play a role in the early development of the circuit (Pangratz-Fuehrer et al., 2016). Experiments using subunit expression in HEK cells or mouse fibroblasts show that single GABA channels currents have distinct opening conductance levels depending upon subunit composition (Mortensen and Smart, 2006).

Studies on developmental GABA shifts during normal development and in relation to autism spectrum disorders (ASD) have been done primarily in cortical structures. Yet abnormalities of the cerebellum and of cerebellar Purkinje cells (PCs) are frequently described in post mortem studies of humans with autism (Fatemi et al., 2012) as well as in the rodent valproate model of autism (Ingram et al., 2000). In addition, PCs undergo considerable post-natal development, including regression of climbing fiber multi-innervation and dramatic dendritic arbor expansion (Dusart and Flamant, 2012), allowing investigation of these important developmental processes after birth.

We have now measured the changes in somatic GABA_A channel properties and chloride gradient in PCs, comparing these changes in male and female mice, since sex differences in the GABA shift have been reported (Galanopoulou, 2008). We report that in normal and valproate-model male and female mice, the dominant GABA_A receptor channel shifts from high-conductance in the newborn to low-conductance in juvenile and adult mice. This shift in conductance parallels the GABA switch from depolarizing to hyperpolarizing, as it is sex dependent, being delayed in naïve females compared to

males. Furthermore, the GABA switch is delayed in mice of both sexes after prenatal exposure to valproate, supporting a role of cerebellar dysfunction in the pathology of autism.

MATERIALS AND METHODS

Mice

Pregnant C57 mice were injected intraperitoneally with 600 mg valproate sodium salt ($n = 18$) or saline ($n = 15$) at embryonic day 12.5 (Roulet et al., 2013). Either control pups or pups from valproate-treated dams were used to prepare acute cerebellar slices for patch-clamp experiments at ages between postnatal days 5 (P5) and 45 (P45). For the study of climbing fiber synapse elimination, either C57 or Swiss pups (because of large number of pups per litter) were used; no differences were found in synapse elimination between the two strains of mice. All procedures followed guidelines established by le Comité National d'éthique pour les Sciences de la Vie et de la Santé (EU Council Directive 2010/63/EU) and were approved by Institutional Animal Care and Use Committees (CREMAS, Comité Régional d'Éthique en experimentation animale de Strasbourg).

Slice Preparation

Standard procedures were used to prepare 250- μ m or 300- μ m parasagittal slices from control or valproate-treated mice at P5–P45 following a protocol approved by the European and French guidelines on animal experimentation established by le Comité National d'éthique pour les Sciences de la Vie et de la Santé (EU Council Directive 2010/63/EU) and were approved by Institutional Animal Care and Use Committees (CREMAS, Comité Régional d'Éthique en experimentation animale de Strasbourg). Briefly, mice were killed by decapitation under isoflurane anesthesia. Brains were dissected in ice-cold artificial cerebrospinal fluid (ACSF) and sliced with a vibratome (Leica VT1200S) at 4°C. Slices were maintained for 30 min at 32°C in an interface chamber containing ACSF equilibrated with 95% O₂, 5% CO₂ and containing (in mM): NaCl 124, KCl 2.7, CaCl₂ 2, MgCl₂ 1.3, NaHCO₃ 26, NaH₂PO₄ 0.4, glucose 10, ascorbate 4, then for at least 1 h at room temperature before being transferred to a superfusing recording chamber.

Electrophysiological Recordings

Slices were transferred to a recording chamber on an upright microscope. The recording chamber was continuously perfused at room temperature with bath solution containing: (mM) NaCl 124, KCl 2.7, CaCl₂ 2, MgCl₂ 1.3, NaHCO₃ 26, NaH₂PO₄ 0.4, glucose 10, pH 7.4, equilibrated with 95% O₂, 5% CO₂. For cell-attached recordings (in order to stabilize the resting membrane potential) the bath solution contained tetrodotoxin (TTX) 10^{−5} M and NBQX 10^{−5} M. In some experiments isoguvacine or NBQX were applied to the bathing fluid at a concentration of 10^{−5} M. For experiments recording climbing fiber currents, the ACSF contained 10^{−4} M picrotoxin.

Most electrophysiological experiments were performed on visually identified PCs using the patch-clamp technique in the cell-attached configuration. Electrodes were filled for single channels recordings with the following solution (mM): KCl 110, NaCl 2, MgCl₂ 2, CaCl₂ 2, HEPES 10, tetra-ethyl-ammonium-chloride (TEA) 20, TTX 10⁻³, CsCl₂, 4-aminopyridine (4AP) 1, BaCl₂ 1, Isoguvacine or Muscimol 10⁻⁵, pH 7.4; and for spiking activity with the following solution (mM): NaCl 124, KCl 2.7, CaCl₂ 2, MgCl₂ 1.3, NaHCO₃ 26, NaH₂PO₄ 0.4, glucose 10, equilibrated at pH 7.4 with 95% O₂, 5% CO₂.

For experiments recording climbing fiber currents, patch pipettes were filled with a solution containing (mM): Cs-D-gluconate 120, biocytin 13, 10 HEPES, BAPTA 10, TEACl 3, Na₂ATP 2, MgATP 2, NaGTP 0.2, pH 7.3, 290–300 mOsm. Climbing fiber currents were elicited by stimulation in the internal granular layer with a saline-filled glass pipette.

Signals were recorded and filtered at 5 kHz using an Axopatch 200A amplifier (Axon Instrument). Current and voltage signal were digitized at 50 kHz using a Digidata 1322A (Axon Instruments) prior to being recorded directly using Clampex (10.2) software. Analysis was performed off-line using Clampfit (10.2) software. Data were filtered before analysis with a cut off frequency of 1.5 or 1 kHz.

Graphs, Fitting Procedures and Statistics

Sigma plot 12.5 software was used for graphic representations of the data, fitting procedures and statistical analysis. For channels conductance analysis the normality Shapiro-Wilk test, and equal variance test were used before running an un-paired Student's *t*-test. Data were considered statistically significant when $P < 0.05$. * is used for P values between 0.05 and 0.01; ** for P values between $P > 0.01$ and 0.001. *** is used for P values < 0.001 . The quality of the fit was determined using the prediction error.

RESULTS

Two GABA_A Conductances in Neonatal PCs

The single-channel properties of GABA_A receptors have been extensively studied in neuronal cultures and brain slices. In cerebellar granule cells, three main conductance (28, 17, 12 pS) have been characterized and are attributed to distinct GABA_A receptor subtypes (Brickley et al., 1999). We analyzed currents activated by isoguvacine or muscimol, two GABA_A receptor agonists, recorded from 108 cell-attached patches from PCs in acute cerebellar slices from male and female mice, between P5 and P45. In 10 patches, two conductance levels were recorded simultaneously (Figure 1). Figure 1A1 illustrates current traces showing two channels subtypes with a slope conductance of 19 pS and 7.3 pS, reversing at the same potential, indicating a similar ionic selectivity (Figure 1A3). The amplitude distribution in Figure 1A2 shows that the dominant channel conductance in this patch is level 1, and that it is not the result of simultaneous openings of two level 2 channels. The mean conductance slope value is 17.7 ± 0.9 pS for level 1 and 8.1 ± 0.5 pS for

level 2 (Figure 1B, $n = 10$); these are significantly different ($P < 0.001$).

The histogram distribution of the slope conductance of level 1 (in red) and 2 (in blue) channels are illustrated in Figure 1C. For both channel types the amplitude distribution is normal and fitted with a Gaussian function but with distinct peak values, 17 pS for level 1 and 7.5 pS for level 2.

GABA Conductance Switch During PC Development

A switch in the dominant GABA_A receptor channel conductance occurs during development, from primarily level 1 in immature PCs (P5–12) to primarily level 2 in mature (P26–45) PCs in both sexes. Two recordings from PCs (female mice) illustrating this switch are shown in Figure 2A1. At P6, the slope conductance of the dominant GABA_A receptor channel is 18 pS, whereas at P24 it is 10.8 pS (Figure 2A2).

Figure 2B summarizes and compares the conductances of the dominant channels recorded in males (left panel) at P5–12 (newborn) and at P28–45 (young adult) and in females (right panel) at P6–12 and P26–36. In males the mean conductance of the dominant GABA_A channel switch from 17.3 ± 1.6 pS ($n = 14$) at P5–12 to 10.5 ± 1.7 pS ($n = 15$, $p < 0.001$) at P28–45; and in females from 18.5 ± 3.0 pS ($n = 11$) at P6–12 to 9.8 ± 8 pS ($n = 6$, $p < 0.001$) at P26–36. In newborn mice (both sexes), the mean conductance of the dominant GABA_A channel is not significantly different from the level 1 conductance illustrated in Figure 1; similarly, the mean conductance of the dominant GABA_A channel in young-adult mice (both sexes) is not significantly different from the level 2 conductance illustrated in Figure 1. Thus GABA_A channels in PCs switch from level 1 to level 2 during post-natal development.

Sexual Dimorphism of the Chloride Gradient Shift

We then determined the reversal potential of the dominant GABA_A receptor channel relative to the resting membrane potential (RP) during PC development in males and females. Figure 3 illustrates current recordings obtained in PCs from a P16 male (Figure 3A) and a P16 female (Figure 3B). The reversal potential of the GABA_A receptor channel is determined by the linear regression used to fit the current/voltage (*I/V*) relationship of a single GABA_A receptor channel. At P16, the reversal potential is negative to RP (−14 mV) in males (Figure 3A, bottom panel), but positive to RP (+4 mV) in females (Figure 3B, bottom panel).

The changes in GABA reversal potential relative to RP in cerebellar PCs from males and females is illustrated in Figure 3C. The curve in males can be fitted with a sigmoidal function (four parameters, X_0 14.4 days). Between P5–P11 the reversal potential is stable, around +10 mV relative to RP; the reversal potential then rapidly reaches a negative value around P14 and stabilizes at P26 around −10 mV relative to RP (-10.3 ± 5.0 mV, $n = 10$ at $P \geq 26$, see bottom graph in inset). Therefore, GABA exerts depolarizing effects in male PCs prior to P15 and hyperpolarizing effects thereafter.

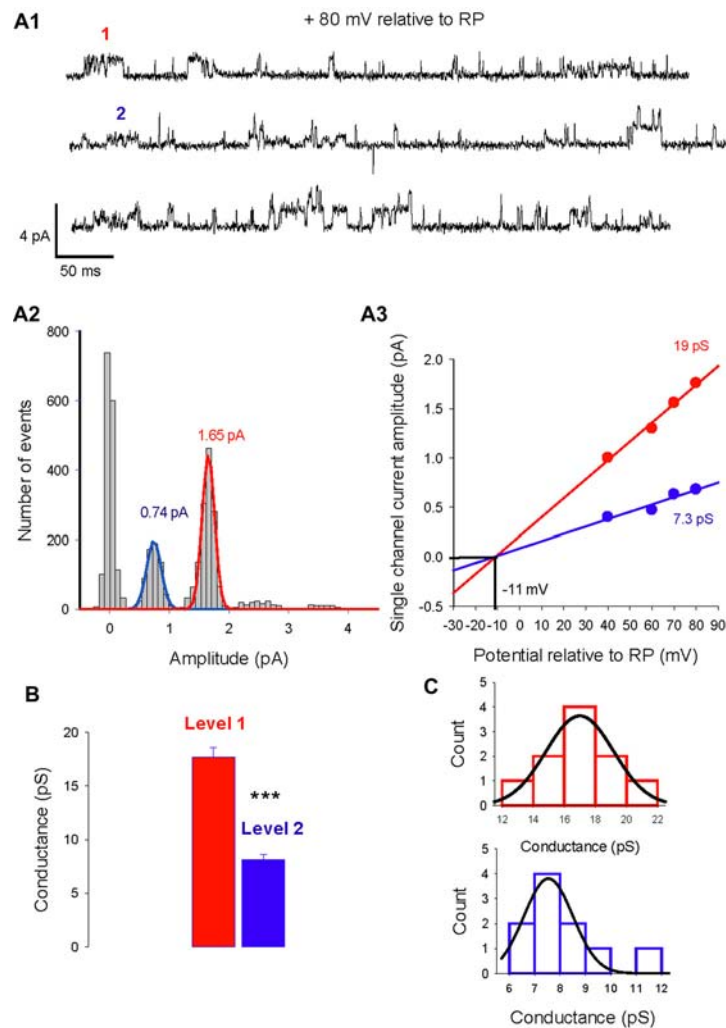


FIGURE 1 | Two levels of type A gamma-aminobutyric acid (GABA_A) receptor channel conductances can be recorded from the same Purkinje cell (PC) membrane patch. **(A1)** Current traces recorded in cell-attached conditions at a potential of 80 mV relative to resting potential (RP). Two amplitude levels of GABA_A receptor channels are seen (level 1 in red, level 2 in blue). **(A2)** Data from the same patch as in panel **(A1)** is illustrated in a current amplitude histogram. The distribution is fitted by two Gaussians, with peaks at 1.65 pA and 0.74 pA. **(A3)** The relation between single channel current amplitude and the potential relative to RP for the two conductance levels. Linear regressions give slope conductances of 19 pS (red) and 7.3 pS (blue). The reversal potential for the two conducting levels is -11 mV relative to RP. **(B)** Bar graphs of level 1 (red) and level 2 (blue) conductances recorded in 7 PC membrane patches. The mean value of level 1 is 17.7 ± 0.9 pA and differs significantly ($***p < 0.001$) from the mean value of level 2 (8.1 ± 0.5 pA). **(C)** Histogram distribution of the slope conductance of level 1 (red) and level 2 (blue). Each conductance distribution follows a normal distribution fitted by a Gaussian with a peak value of 17 pS for level 1 and 7.5 pS for level 2.

With the exception of the earliest post-natal days, the developmental curve of the reversal potential in female PCs also follows a sigmoid pattern from P8 to P21 but with a systematically more depolarized value compared to males (**Figure 3C**, red symbols). Although the reversal potential is not significantly more negative between P5 and P7 in females than in males ($+3.5$ mV vs. $+8.7$ mV), it then becomes significantly ($p < 0.001$) more positive between P8 and P12 ($+15.8 \pm 3.6$ mV, $n = 11$) than in males ($+9.1 \pm 4.1$ mV, $n = 8$, see top graph in inset). From this higher plateau value, the reversal potential change over time is best fitted by a sigmoid curve (four parameters, X_0 18.7 days) and decreases to -8.5 ± 3.5 mV ($n = 8$), at P26 and older (see bottom graph in inset). These

observations show that GABA exerts more depolarizing actions in female PCs than in male PCs during a period of nearly 2 weeks (P8 to P21). In addition, the GABA switch is delayed in females by 4 days (P18 vs. P14 in males), such that from P15–19 the reversal potential is negative relative to RP in males (-15.9 ± 7.4 mV, $n = 17$) but still positive in females ($+7.6 \pm 5$ mV, $n = 10$; see top graph in inset).

An important step in cerebellar synaptic maturation during the early postnatal period is the refinement of climbing fiber synapses on PCs, from a multiple climbing fiber innervation to mono-innervation (Hashimoto and Kano, 2003). To determine possible links between GABA signaling and circuit refinement in terms of climbing fiber synapse elimination, we measured

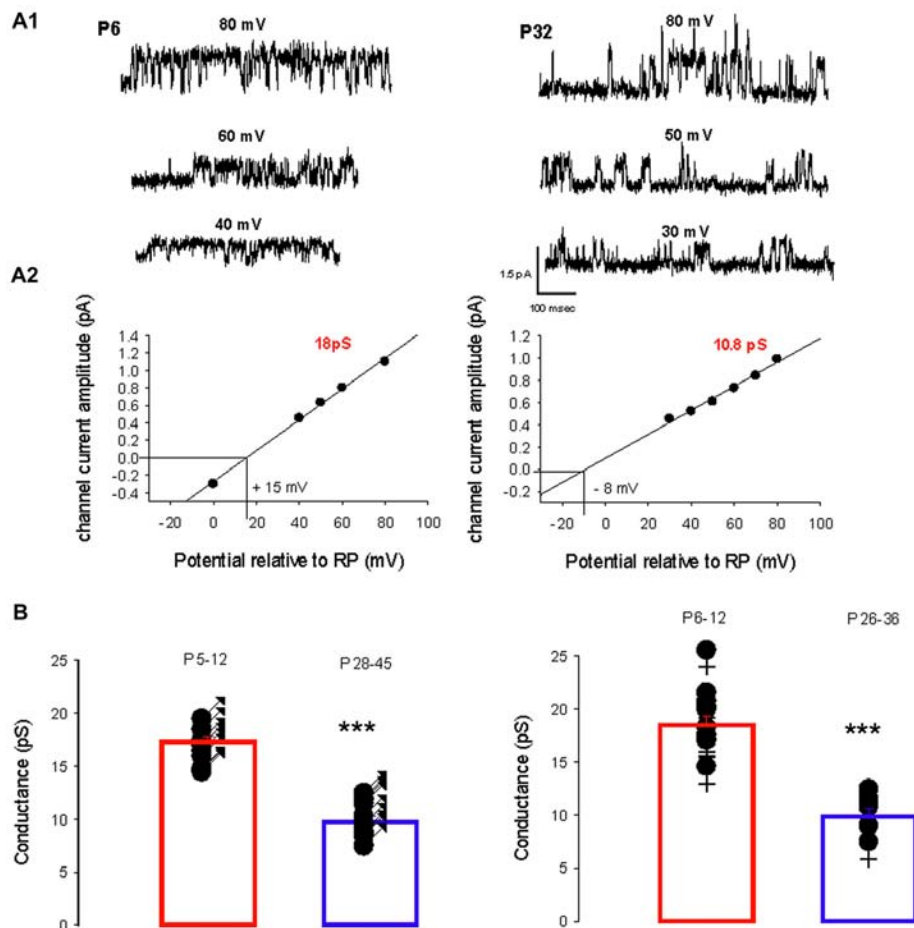


FIGURE 2 | Developmental evolution of the main GABA_A receptor channel conductance. **(A1)** Current traces recorded in cell-attached conditions at different potentials relative to RP as indicated, from a female at P6 (left) and at P32 (right). **(A2)** Current-voltage relationship for the channel recorded at P6 (left) and at P32 (right). Linear regressions yield a conductance of 18 pS (level 1) and a reversal potential at +15 mV relative to RP for the channel recorded at P6; and a conductance of 10.8 pS (level 2) and reversal potential at -8 mV relative to RP for the channel recorded at P32. **(B)** The left panel shows the conductance of the dominant GABA_A receptor channel recorded from males between P5–P12 ($n = 14$) and P28–45 ($n = 15$). Each point represents an individual cell. The bar graphs show the mean values \pm SD from P5–12 (red) and P28–45 (blue). These mean values (17.3 and 10.1 pS) are significantly different ($***p < 0.001$). The right panel illustrates the conductance of the dominant GABA_A receptor channel recorded from females between P6–P12 ($n = 11$) and P26–36 ($n = 6$). Each point represents an individual cell. The bar graphs show the mean values \pm SD at P6–12 (red) and P26–36 (blue). These mean values (18.5 and 10.5 pS) are significantly different ($***p < 0.001$). The conductances at P5–12 in males and at P6–12 in females are not significantly different and neither is significantly different from the mean level 1 conductance. The conductances at P24–45 in males and at P26–36 in females are not significantly different and neither is significantly different from the mean level 2 conductance.

the number of climbing fiber synapses on each PC from males and females at different ages (**Figure 3D**). The progress of synapse elimination in both sexes was very similar, indicating that sex-dependent differences in GABAergic signaling does not disrupt this fundamental developmental process.

The Developmental Switch of the Chloride Gradient Is Delayed in the Valproate Mouse Model of Autism

In the valproate rat model of autism, the developmental regulation of the chloride gradient, which determines the effects of GABA_A receptor activation on neuronal excitability,

is disrupted in hippocampal neurons. As a result, the developmental excitatory-inhibitory switch of GABAergic effects is abolished in hippocampal neurons from valproate rats, with depolarizing actions from birth onwards (Tyzio et al., 2014). We used this same model in mice to analyze the developmental changes in GABA_A receptor channel conductance and the chloride gradient. We recorded 57 PC-attached recordings of GABA_A receptor channels from 35 males and 22 females from valproate-treated dams, at different postnatal ages. As in control mice, recordings from valproate mice revealed two conductance levels (level 1 mean value 15.8 ± 0.4 pS and level 2 mean value 7.8 ± 0.5 pS, $p < 0.001$) that could occasionally be recorded from the same patch (five patches, **Figure 4A**). Furthermore,

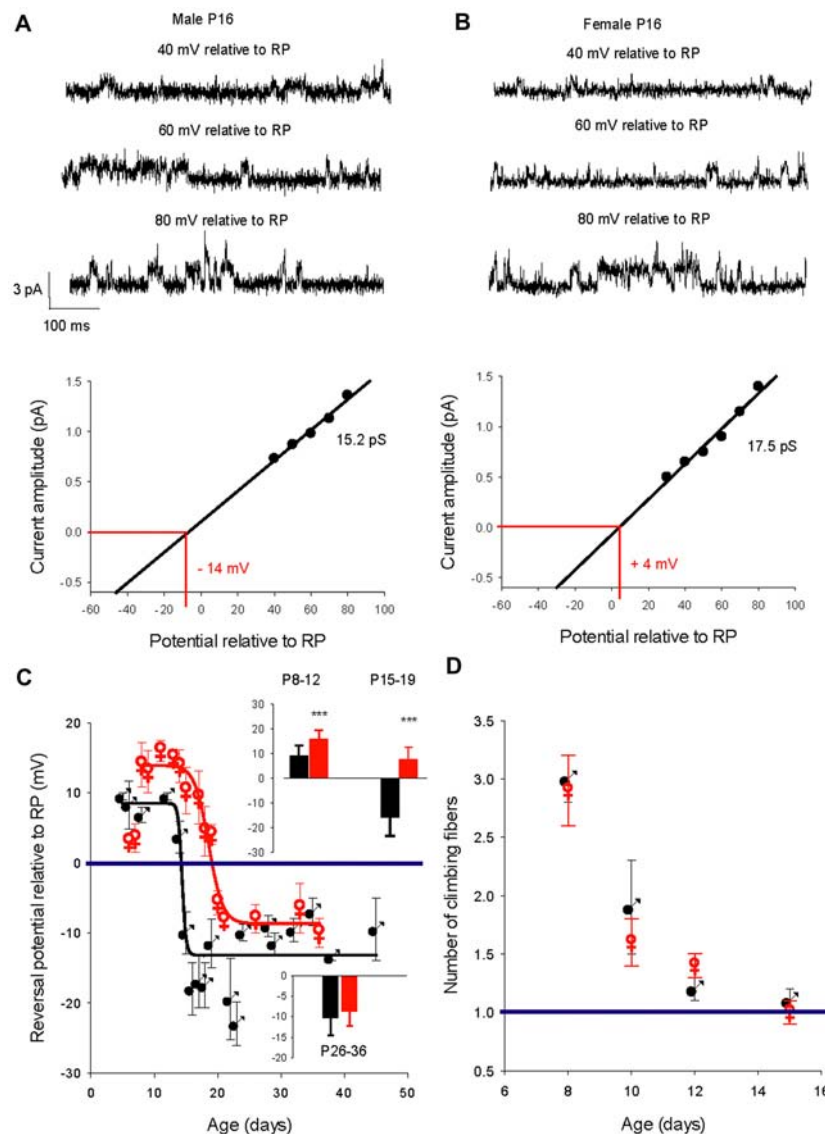


FIGURE 3 | Developmental evolution of the GABA_A receptor channel reversal potential in males and females and climbing fiber synapse elimination. **(A)** Recordings from a P16 male. Current traces show the GABA_A receptor channel recorded from a PC membrane patch at three potentials as indicated on top of each trace. The I/V curve below, a linear regression of the data from this channel, gives a conductance of 15.2 pS and a reversal potential with an extrapolated value of -14 mV relative to RP. **(B)** Recordings from a P16 female. Current traces show the GABA_A receptor channel recorded from a PC membrane patch at three potentials as indicated on top of each trace. The I/V curve below, a linear regression of the data from this channel, gives a conductance of 17.5 pS and a reversal potential with an extrapolated value of +4 mV relative to RP. Note that at the same post-natal age the GABA_A receptor channel reverses at a negative potential relative to RP in the male, but in the female reversal occurs at a positive potential relative to RP. **(C)** Left graph, evolution of the mean reversal potential of the dominant GABA_A receptor channel as a function of the age in males (black) and females (red). The data were best fit ($R = 0.98$) by a sigmoidal hill function with four parameters ($f = Y_0 + a/(1 + \exp(-(X - X_0)/b))$) between P5 and P48 in males (black line, a (max) = 22, b (slope) = -0.31, $X_0 = 14.4$ and Y_0 (min) = -13.5) and in between P8 and P36 in females (red line, $a = 24.2$, $b = -1.25$, $X_0 = 18.5$, $Y_0 = -8.3$). The horizontal line at 0 mV shows the depolarizing/hyperpolarizing switch. The bar graphs in inset compare the mean values of the reversal potential relative to RP in males (black) and in females (red) at P8-12, P15-19 and P26-36. A significant difference between males and females ($***p < 0.001$) was found at P8-12 and P15-19. **(D)** Right graph: regression of climbing fiber multi-innervation of Purkinje cells (PCs) is similar in males and females, indicating that this basic circuit maturation during this developmental period is not sex-dependent.

as in control mice, PCs from valproate-treated male or female newborn mice show a dominant level 1 conductance channel, and PCs from juvenile and young adult PCs showed a dominant level 2 conductance channel. In males, the mean conductance switches from 17.1 ± 1.6 pS ($n = 13$) at P6-10, to 13.1 pS ± 1.8 pS

($n = 5$) at P24-30 (**Figure 4B**, $p = 0.002$). In females, the mean conductance switches from 17.7 ± 3.2 pS ($n = 5$) at P7-10, to 10.9 pS ± 1.6 pS ($n = 7$) at P23-30 (**Figure 4C**, $p < 0.001$). These conductance levels are not different between the sexes nor are they different from conductance levels 1 and 2 (**Figures 1B, 4A**)

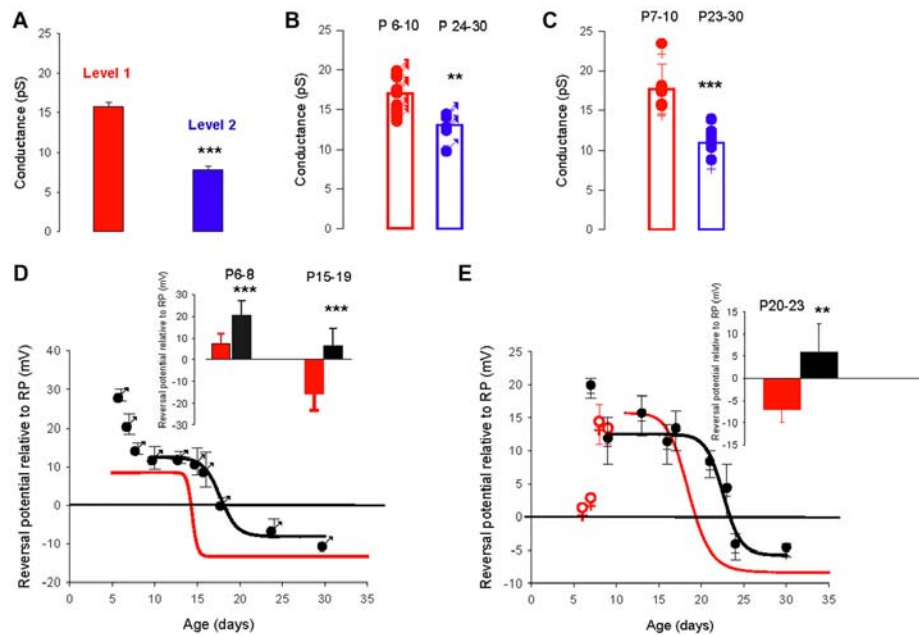


FIGURE 4 | The valproate mouse model of autism alters developmental evolution of GABA_A channel reversal potential. **(A)** Mean slope conductance of the two conductance levels found simultaneously in five cell-attached recordings from PCs of male and female mice prenatally exposed to valproate. The level 1 (red) conductance (15.8 ± 0.4 pS) is significantly different from the level 2 (blue) conductance (7.8 ± 0.5 pS; *** $p < 0.001$). **(B)** Conductance of the dominant GABA_A receptor channel recorded in PCs from male valproate mice at P6–10 ($n = 13$) and at P24–30 ($n = 5$). Each symbol represents a single cell-attached recording. The bar graphs show the mean values \pm SD between P6–10 (red) and between P24–30 (blue). These mean values (17.1 and 13.1 pS) are significantly different (** $p = 0.002$). **(C)** Conductance of the dominant GABA_A receptor channel recorded from female valproate mice at P7–10 ($n = 5$) and at P23–30 ($n = 7$). Each symbol represents a single cell-attached recording. The bar graphs show the mean values \pm SD at P7–10 (red) and at P23–30 (blue). These mean values (18.5 and 10.5 pS) are significantly different (*** $p < 0.001$). The mean conductances at P6–10 in males and at P7–10 in females are not significantly different, and neither is significantly different from the level 1 channel conductance. The mean conductances at P24–30 in males and at P23–30 in females are not significantly different and neither is significantly different from the level 2 conductance. **(D,E)** Reversal potential of GABA_A receptor channels during development, in PCs recorded from male **(D)** and female **(E)** valproate mice. **(D)** In males, the depolarizing/hyperpolarizing switch is delayed in valproate animals (black symbols). Evolution of the GABA_A reversal potential with age (P5–P30). From P10 to P30 the data are best fit using a sigmoidal hill function with four parameters (black line, $a = 21$, $b = -0.16$, $X_0 = 17.7$ and $Y_0 = -8$). The curve in red represents the same curve but for control males. The inset bar graphs compare the mean values of the reversal potential relative to RP in control males (black) and valproate males (red) at P6–8 and P15–19. A significant difference between control males and valproate males (*** $p < 0.001$) is detected. **(E)** In females, the depolarizing/hyperpolarizing switch is less altered in valproate animals (black symbols). Evolution of the GABA_A receptor channel reversal potential with age (P6–P30) in valproate females. Data are best fit by a sigmoidal function four parameters (black curve, $a = 17$, $b = -0.28$, $X_0 = 23$ and $Y_0 = -5$). The red curve is a sigmoidal fit of the evolution of the reversal potential in control females and the red open dots the mean value in control females not included in the fit by the red line. The bar graphs in inset compare the mean values of the reversal potential relative to RP in control females (black) and valproate females (red) at P20–23. A significant difference between control females and valproate females (** $p = 0.003$) is reported.

in control mice. Therefore, the conductance shift is not impacted in this ASD model.

However, the developmental change in the GABA_A receptor channel reversal potential was clearly more complicated in valproate-treated male mice (**Figure 4D**, black symbols) than in control male mice (red sigmoid, from **Figure 3C**). At P6–8 the reversal potential is significantly ($p < 0.001$, see graph in inset) more positive relative to RP ($+20.6 \pm 6.5$ mV, $n = 10$) in valproate males compared to control males ($+7.4 \pm 4.6$ mV, $n = 9$), decreases to a plateau value around $+12$ mV at P10, then reaches a negative value around P20 (sigmoid curve, $X_0 = P17.7$ days). Thus, the switch from depolarizing to hyperpolarizing effect of GABA is delayed by 3 days in valproate male mice compared to control males. Therefore during a relatively long period, GABAergic currents are more depolarizing in valproate mice than in age matched control mice. Indeed, at P15–19 the

mean reversal potential of the GABA_A channel is still positive in valproate mice ($+6.6 \pm 4.4$ mV, $n = 17$ compared to -15.9 ± 7.4 mV, $n = 11$ in control male mice, $p < 0.001$, see graph in inset). These differences are less evident in females (**Figure 4E**). Yet at P7 in valproate female mice the reversal potential of GABA_A channels is around $+20$ mV relative to RP whereas it is about $+5$ mV relative to RP in control females. Furthermore, a comparison between the sigmoidal fit of the data obtained from valproate females (black curve, $X_0 = 22.7$ days) and the sigmoidal fit of the data obtained in control females (red curve, from **Figure 3C**) reveals a delay of the GABA switch of almost 4 days. As a consequence, at P20–P23 the mean reversal potential of the GABA_A channels is positive relative to RP ($+5.8 \pm 6.5$ mV, $n = 8$) in valproate treated females but negative (-7.0 ± 3.0 mV, $n = 8$, $p = 0.003$) in control females (see inset **Figure 4D**).

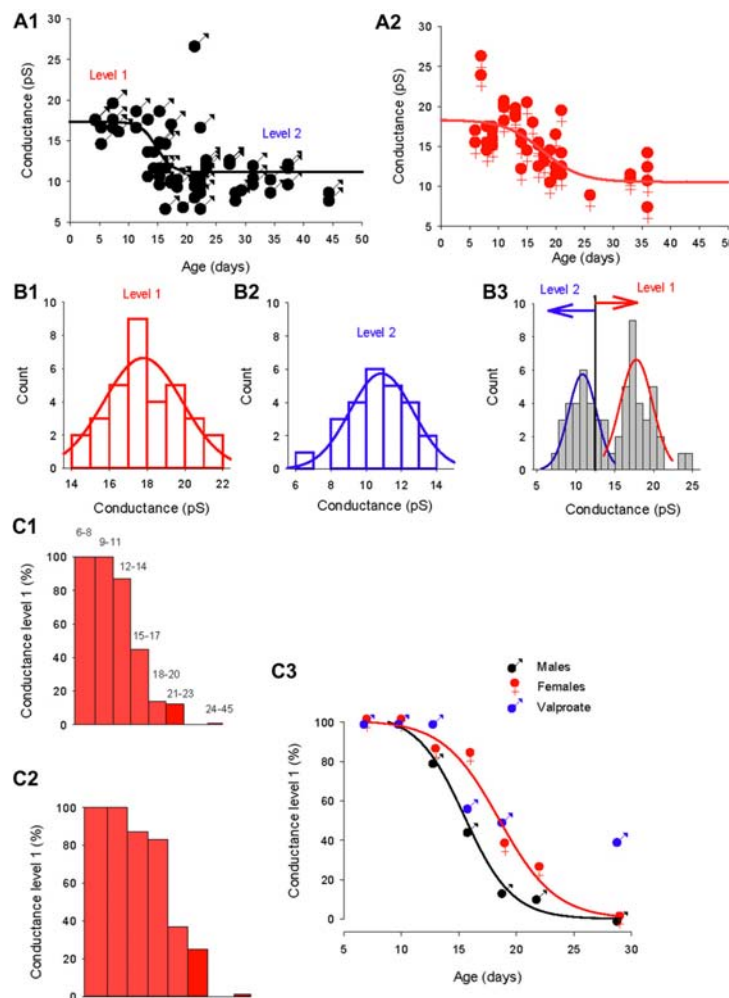
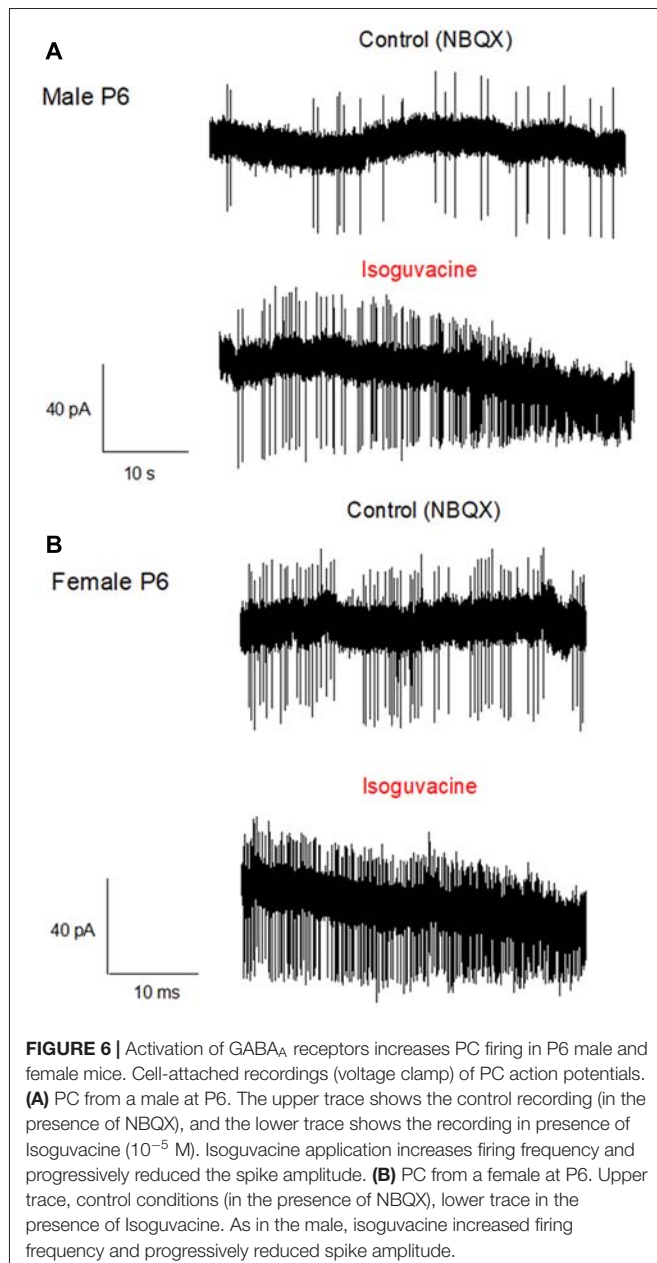


FIGURE 5 | Distinct evolution of the GABA switch between conductance levels 1 and 2 in males, females and valproate-treated males. **(A1)** Dominant GABA_A channel conductance from level 1 to level 2 as a function of the post-natal age in males (each point represents a single cell). Data are best fit with a sigmoidal hill function with four parameters (black line, $a = 6.2$, $b = -1.33$, $X_0 = 14.7$ and $Y_0 = 11.1$). **(A2)** Dominant GABA_A channel conductance from level 1 to level 2 as a function of the post-natal age in females (each point represents a single cell). Data are best fit with a sigmoidal hill function with four parameters (red line, $a = 7.8$, $b = -3.3$, $X_0 = 17.7$ and $Y_0 = 10.5$). Note the presence of three channels with a conductance around 25 pS. **(B1)** Histogram distribution of the slope conductance of level 2 channels (pooled data from **Figures 1B, 2B, 4A**). The distribution is normal and fit by a Gaussian (blue line) with a peak value at 10.9 pA. **(B2)** Histogram distribution of the slope conductance of level 1 channels (pooled data from **Figures 1B, 2B, 4A**). The distribution is normal and fit by a Gaussian function (red line) with a peak value at 17.8 pA. **(B3)** Histogram distribution of the slope conductance of level 1 and level 2 channels (pooled data from **B1** and **B2**). To determine the limit of conductance between level 2 (blue line) and level 1 (red line) the Gaussian fits obtained in **(A1, A2)** were superimposed. The limit between levels 1 and 2 is 14 pS. Channels with conductances ≥ 14 pS are classified as level 1 channels and channels with conductances < 14 pS are classified as level 2 channels. **(C1)** Data from male mice. The bar plots show the % of level 1 channels (conductance ≥ 14 pS) at increasing post-natal age ranges, as indicated on top of each bar. **(C2)** Data from female mice. The bar plots show the % of level 1 channels (conductance ≥ 14 pS) at increasing post-natal age ranges (the same range as in **C1**). **(C3)** Percentage of conductance level 1 as a function of the age in male mice (black symbols) female mice (red symbols) and valproate treated male mice (blue symbols). Data for control males (black curve) and females (red curve) are best fit using a sigmoidal function with the following parameters: $a = 99$, $b = -1.9$, $X_0 = 15.3$ and $Y_0 = 3.2$ for males; and $a = 100$, $b = -2.42$, $X_0 = 18.5$, $Y_0 = 0.43$ for females.

Sex Dependence of the GABA Conductance Shift: Parallel Development of GABA_A Channel Reversal Potential and Conductance

To determine whether the GABA_A channel conductance and the reversal potential switch occur in parallel, we compared the development of the GABA_A channels conductance in males and

females (**Figure 5**). As a first approach, the slope conductance of the dominant GABA_A channel was plotted as a function of age in males (**Figure 5A1**) and females (**Figure 5A2**). The evolution of the conductance could be fitted in both sexes by a sigmoidal function (black and red lines) but with distinct parameters (slope = -1.33 , $X_0 = 14.7$ days for males and slope = -3.3 , $X_0 = 17.7$ days for females) indicating that the shift in conductance is slower and later in females compared



to males. In both sexes, a single channel with larger slope conductance (25–27 pS, not included in the fit) was recorded in three patches and may indicate the presence of a rarely-occurring third conductance level of GABA_A receptor channel, as previously described for cerebellar granule cells (Brickley et al., 1999).

In order to quantitatively analyze the conductance switch, we determined the conductance ranges of the two levels. We first constructed separate histogram distributions of conductance levels 1 and 2 channels by pooling conductance values of GABA_A channels recorded in both sexes between P5–12 for conductance level 1 (Figure 5B1) and conductance values of GABA_A channels recorded at P28–45 in males and P26–36 in females for conductance level 2 (Figure 5B2). The distributions

are fitted with distinct Gaussian functions, giving a peak of 17.8 pS for level 1 and 10.9 pS for level 2. Next, we combined the two distributions and associated fits (Figure 5B3), to show that the two fits intercept at a value of 13.9 pS. From this observation, we classified channels with a slope conductance of 14–22 pS as level 1, and channels with a slope conductance <14 pS as level 2.

Then, we determined the developmental alterations of level 1 channel percentage at different post-natal ages (Figures 5C1–C3). In both sexes the proportion of patches displaying dominant level 1 GABA_A receptor channel decreases with age; but the histograms in Figures 5C1,C2 show that this drop in level 1 conductance (defined as presence in less than 50% of patches) occurred earlier in males (P14; Figure 5C1) than in females (P17; Figure 5C2). Therefore, during a transitional period (around P15–20), PCs in females have a higher-conductance dominant channel than male PCs.

The evolution of the proportion of level 1 GABA_A channel as a function of age (Figure 5C3) is similar in both males and females to the evolution of the chloride reversal potential. Both curves are sigmoidal (four parameters) with similar X_0 s (14.4 days for the level 1 plot and 15.3 days for the chloride reversal potential plot in males; and 18.5 days for both the level 1 plot and the chloride reversal potential in females). Interestingly the switch of GABA_A channel conductance is also altered in valproate male mice with 25% of level 1 channel dominant in young adult animals.

Sexual Dimorphism of the GABA Excitatory/Inhibitory Shift

Finally, we determined possible links between the chloride driving force and the excitatory or inhibitory actions of the GABA_A agonist isoguvacine on PC firing, with or without NBQX. Similar effects of isoguvacine were observed in the presence of NBQX suggesting that glutamatergic neurotransmission was not involved (not shown; $n = 80$). When the reversal potential of the GABA_A channel was positive to RP (at P6), isoguvacine increased the firing rate in males (Figure 6A, $n = 3$ out of 5) and in females (Figure 6B, $n = 3$ out of 6). This effect was accompanied by a progressive decrease in the size of the spikes due to the sodium channel inactivation produced by a strong depolarization. In the remaining recordings, PCs were silent and isoguvacine applications led to a depolarization. In older PCs, when the reversal potential of the GABA_A channels is negative to RP, isoguvacine decreased spontaneous activity of PCs, without altering the spike amplitude in both males (P27; Figure 7A) and females (P25; Figure 7B).

Additional experiments confirmed the sex and age difference in the actions of isoguvacine. In males at P15, after 2 min isoguvacine application, PC firing was blocked by $75 \pm 35\%$ in all cells tested ($n = 4$; example in Figure 8A), and completely blocked (100%) for PCs recorded from P16 to P29 ($n = 14$; example in Figure 7A). However in females at P17, 2 min of isoguvacine increased PC firing frequency by $220 \pm 161\%$, accompanied by a reduction in spike amplitude in 5 out of 13 PCs (example in Figure 8B), sometimes preceded by a temporary reduction in the firing frequency ($n = 2$, including the example in Figure 8B). Isoguvacine had no effect on firing frequency in two PCs from female mice, and inhibited firing frequency in seven of these

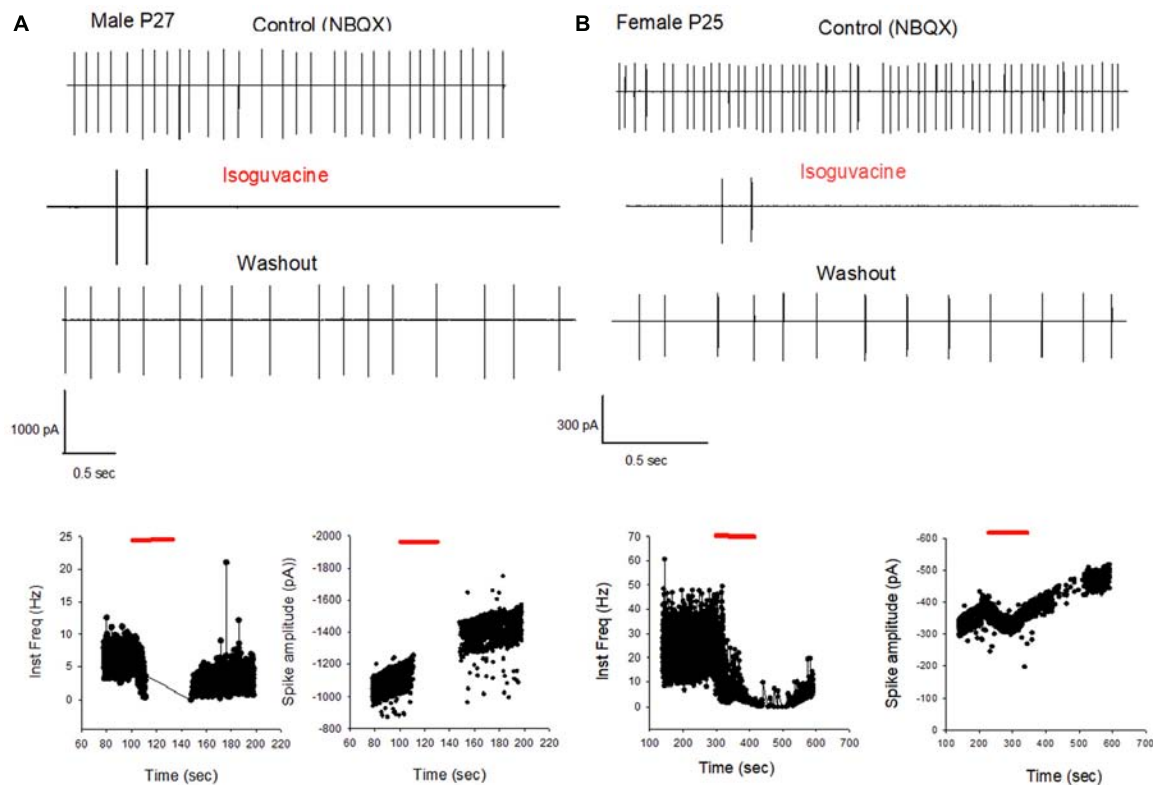


FIGURE 7 | GABA_A receptor activation inhibits PC firing in young adult male and female mice. **(A)** Cell-attached recording (voltage clamp) of the spontaneous spiking activity of a PC from a male P27 mouse. Upper panel: current traces recorded in control conditions (in the presence of NBQX), in the presence of Isoguvacine, and after washout. Isoguvacine silences the cell, and activity recovers after washout. Lower panel: data from the same cell showing instantaneous action potential frequency (left) and action potential amplitude (right) over time. Isoguvacine application is indicated by the red line. The control spike frequency is about 7 Hz; isoguvacine abolishes the spiking activity of the cell; and this effect is reversible upon washout. Note that spike amplitude is not reduced before the silencing of the cell. **(B)** As in panel **(A)**, but from a female P25 mouse. Upper panel: current traces recorded in control conditions, in the presence of Isoguvacine, and following washout. Isoguvacine silences the cell, and activity recovers after washout. Lower panel: data from the same cell, showing instantaneous action potential frequency (left) and action potential amplitude (right) over time. Isoguvacine is applied as indicated by the red line. The control spike frequency is around 30 Hz. In presence of isoguvacine the spiking activity of the cell is almost abolished, but the spike amplitude is not altered.

PCs. The excitatory effect of isoguvacine continued to be seen in female PCs ($n = 2$ out of 5) until P19; then at P20–25 isoguvacine had only inhibitory effects ($87\% \pm 8\%$ inhibition, $n = 6$).

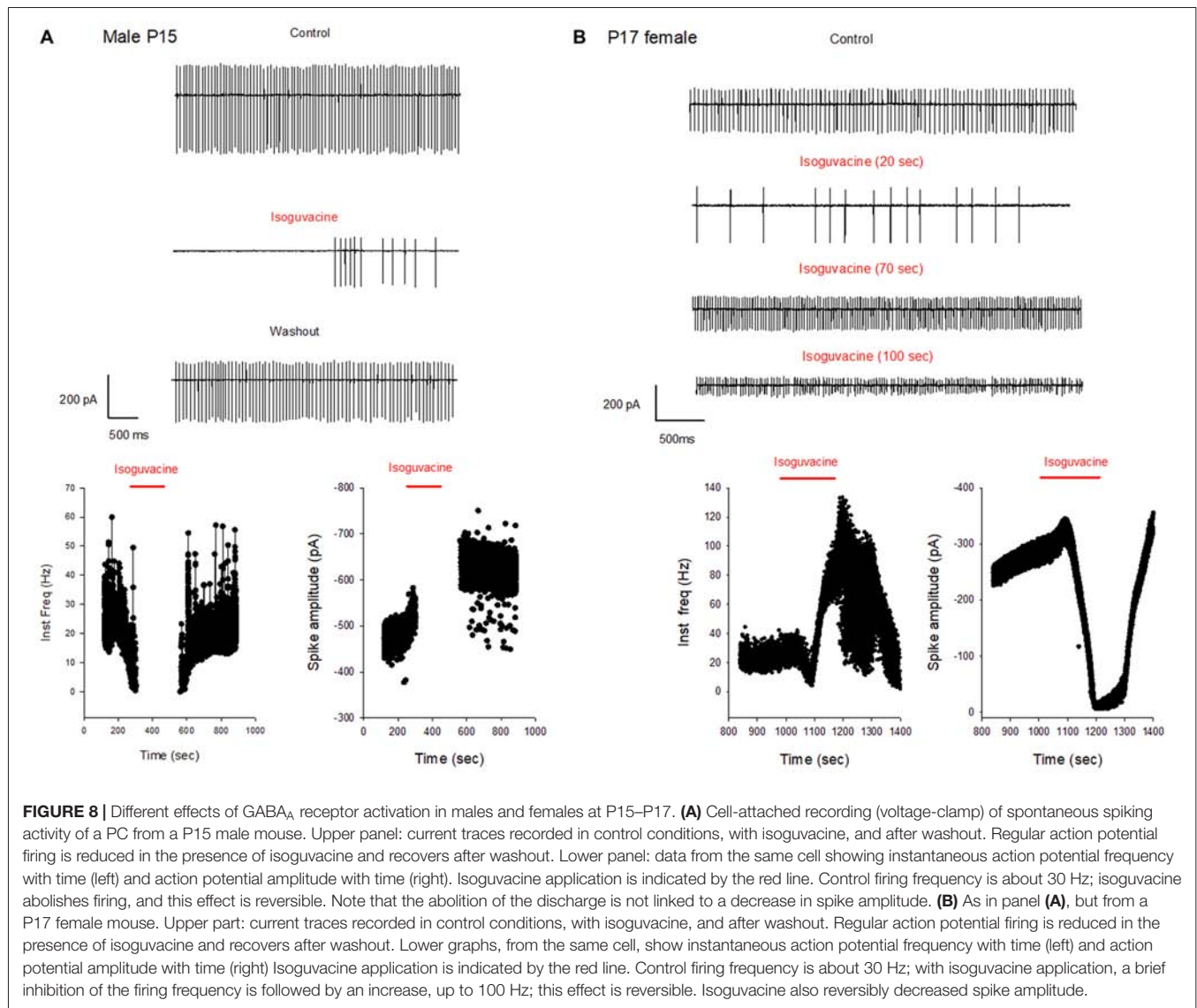
To summarize the effects of isoguvacine on spontaneous PC, firing we assigned a value of +1 when isoguvacine produced an increased firing frequency, 0 when the increase was preceded by a short inhibition of firing, 0 when isoguvacine had no effect and –1 when isoguvacine inhibited firing. **Figure 9** shows the mean valence as a function of age for PCs from male and female mice, and clearly illustrates the different time course of the shift to inhibitory isoguvacine effects between male and females.

DISCUSSION

Development of GABA_A Receptor Channel Subunit Composition in Cerebellar PCs

Somatic GABA_A receptor channels in adult vertebrate neurons have complex gating and multiple conductance states ranging from 7 to 36 pS, with a single dominant conductance state in

each cell type (Newland et al., 1991; Robello et al., 1998; Brickley et al., 1999; Mortensen and Smart, 2006). We found three main conductance levels in PC, with conductances of 7–12 pS, 15–18 pS, and occasionally 25–28 pS. Similar conductance values are observed in adult cerebellar granule cells, but with a shift of the dominant conductance from medium (15–18 pS) to small (7–12 pS) during maturation. This shift likely reflects a reorganization of GABA_A channel subunit composition (Moss et al., 1990; Verdoorn et al., 1990; Mortensen and Smart, 2006). Although it is difficult to equate GABA conductance levels with specific subunits combinations (Brickley et al., 1999), it is likely that in young-adult PCs, receptors lack the γ subunit (Verdoorn et al., 1990; Fisher and Macdonald, 1997; Amato et al., 1999; Hörtnagl et al., 2013). The dominant medium conductance level (18 pS) in newborn PCs suggests the presence of an $\alpha 1\beta 1$ GABA_A receptor at this developmental stage (Moss et al., 1990). The very rare occurrence of the 25–28 pS conducting level is may be related to a low level of expression of the $\gamma 2$ subunit (Mortensen and Smart, 2006). Our observations suggest a subunit reorganization during development (but see

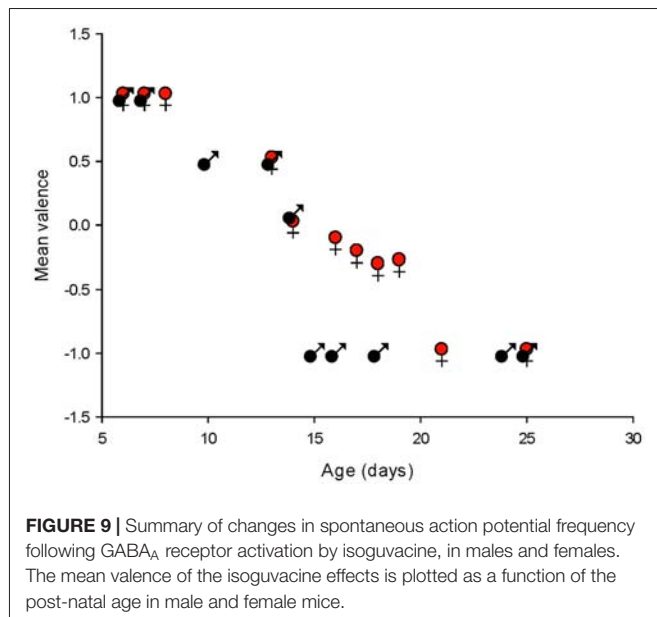


Nadler et al., 1994; Haghiri et al., 2013) but further experiments are required to determine if this is associated with changes in IPSCs kinetics.

Sexual Dimorphism of GABA Driving Force in Wild Type Mice and in the Valproate Model of Autism

In a wide range of brain structures, the polarity of GABA_A receptor effects is regulated by the expression and activity of two chloride membrane transporters: NKCC1 and KCC2. NKCC1 is expressed in immature neurons and actively transports chloride ions into the cell; KCC2 is expressed in mature neurons and actively transports chloride ions out of the cell. This changes in transporter expression leads to depolarizing effects of GABA in immature neurons and hyperpolarizing effects in mature neurons (Ben-Ari, 2014; Watanabe and Fukuda, 2015; Raimondo et al., 2017) with a developmental switch around

birth (Tyzio et al., 2014; Watanabe and Fukuda, 2015). However, PCs do not express NKCC1 (Mikawa et al., 2002), suggesting that alternative mechanisms are required to regulate chloride homeostasis, including chloride channels (Zhang et al., 2015; Rahmati et al., 2016) and KCC2. The developmental GABA switch occurs in PCs at the end of the second post-natal week (see also Eilers et al., 2001), when profound morphological and functional alterations occur in PCs (Dusart and Flamant, 2012). The timing of the switch is strongly dependent on the specific cerebral structure; it is similar in the antero-ventral cochlear nucleus (Song et al., 2012) and substantia nigra pars reticulata (SNR; Kyrozis et al., 2006), and earlier in other brain structures (Stein et al., 2004; Tyzio et al., 2007; Allain et al., 2011; Witte et al., 2014). Our results also suggest that the regulation of chloride homeostasis is sex dependent, since it is delayed in female mice. A similar sex dependence of chloride homeostasis has been observed in the substantia nigra (Galanopoulou, 2008).



The mechanisms underlying these sex differences are poorly understood. The testosterone surge in males that occurs during late gestation and shortly after birth (Dean and McCarthy, 2008) has been suggested to promote the expression and the activity of NKCC1 and to depress the synthesis and activity of KCC2 (Waddell and McCarthy, 2012), and thus make the GABA switch occurs later in males than in females. This effect has been shown in hippocampal cultures (Nuñez and McCarthy, 2007), SNR neurons in acute slices (Kyrozis et al., 2006), and embryonic hypothalamic neurons in culture (Mir et al., 2017). However, the GABA switch in PCs is delayed in females, rather than in males, despite this testosterone effect on KCC2, suggesting that alternative mechanisms must be present. PCs synthesize estradiol from cholesterol in the neonatal period and the enzymes involved in this synthesis are developmentally regulated with a different profile in males and in females (Dean and McCarthy, 2008). In PCs, estradiol promotes BDNF-mediated dendritic growth, spinogenesis and synaptogenesis during neonatal life (Tsutsui et al., 2011), and BDNF inhibits KCC2 activity (Huang et al., 2013). Furthermore, the development of the cerebellar expression of insulin receptors (IR) and insulin-like growth factor-1 receptors (IGF-1R) differs in males and females. IR and IGF-1R expression increase between P0–P7 and is down regulated at P14 in males, whereas in females IR and IGF-1R are stable between P0–P7 and up-regulated at P14 (Haghir et al., 2013). IGF-1 accelerates the developmental switch between NKCC1 and KCC2 chloride transporters in the visual cortex (Baroncelli et al., 2017). Collectively, these observations converge to suggest multiple mechanisms to explain the differences between chloride homeostasis regulation in males and females.

Using the valproate mouse model of autism, we observed that the chloride reversal potential in P5–6 valproate males is more positive than in controls (by about 10–20 mV), and that the GABA switch is delayed by 3–4 days in both males and females, extending this experimental model to the cerebellum.

Increased excitatory-inhibitory ratio is suggested to underlie the pathogenesis of autism and successful clinical trials have shown that the NKCC1 antagonist bumetanide, which restores low (Cl^-)_i and GABAergic inhibition, also attenuates the severity of autism (Rubenstein and Merzenich, 2003; Lemonnier and Ben-Ari, 2010; Tyzio et al., 2014; Lee et al., 2016; Uzunova et al., 2016; Lemonnier et al., 2017). It is now accepted that the cerebellum is involved in higher order functions (Schmahmann and Sherman, 1998) including perceptual processes (Baumann et al., 2015), in addition to its roles in balance, posture, and motor control. The cerebellum has been implicated in many psychiatric disorders (Phillips et al., 2015) and cerebellar abnormality is associated with ASD (Tsai et al., 2012). Several reports in individuals with autism or animal models of autism describe alterations in PC density and properties (Skefos et al., 2014; Tsai, 2016). Thus, chloride gradient modifications and alterations in the GABA switch in cerebellar PCs that we show here may be particularly relevant for further studies of autism and the role of the cerebellum.

Parallel Development of GABA_A Receptor Channel Subunit Composition and Chloride Gradient

Our data show that the kinetics of the shift of the dominant conductance levels during development, from medium (15–18 pS) to small conductance (7–12 pS), are similar to the kinetics of the development of the chloride gradient. Both phenomena followed a similar sigmoidal process, are delayed in females, and are altered in valproate mice, suggesting interactions between the subunit composition of GABA_A channels and intracellular chloride concentration (Succol et al., 2012).

Interestingly, in PCs, it has been suggested that an interaction between KCC2 and a specific subunit of the GABA_A receptor represents a fundamental mechanism of regulation of GABAergic synapses (Huang et al., 2013). Furthermore, membrane expression of the β 3 GABA_A receptor subunit at different postnatal developmental stages is observed in rats exposed prenatally to valproic acid (Li et al., 2017). Finally, alterations in the efficacy of neuronal inhibition mediated by GABA_A receptors containing β 3 subunits have been implicated in autism (Vien et al., 2015). Collectively, these observations raise the possibility of parallel convergent developmental alterations of GABAergic signals, linking chloride gradient and subunit composition.

CONCLUSIONS AND PERSPECTIVES

The conductance properties of GABA_A receptors as well as the chloride equilibrium potential and the polarity of GABA effects in PCs are developmentally regulated in parallel, occurring later than in other brain structures, which is coherent with the delayed development of cerebellar PCs to the postnatal period. The switch is also delayed by 4 days in females, indicating sexual dimorphism in keeping with recently reported sex differences in synaptic excitation, inhibition and intrinsic

properties (Mercer et al., 2016). Finally, we show that the valproate model of autism produced a shift in the chloride gradient in developing PCs from males and females, providing important potential implications for the cerebellum in the pathology of autism.

REFERENCES

- Allain, A. E., Le Corrion, H., Delpy, A., Cazenave, W., Meyrand, P., Legendre, P., et al. (2011). Maturation of the GABAergic transmission in normal and pathologic motoneurons. *Neural Plast.* 2011:905624. doi: 10.1155/2011/905624
- Amato, A., Connolly, C. N., Moss, S. J., and Smart, T. G. (1999). Modulation of neuronal and recombinant GABA_A receptors by redox reagents. *J. Physiol.* 517, 35–50. doi: 10.1111/j.1469-7793.1999.00352.x
- Baroncelli, L., Cenni, M. C., Melani, R., Deidda, G., Landi, S., Narducci, R., et al. (2017). Early IGF-1 primes visual cortex maturation and accelerates developmental switch between NKCC1 and KCC2 chloride transporters in enriched animals. *Neuropharmacology* 113, 167–177. doi: 10.1016/j.neuropharm.2016.02.034
- Baumann, O., Borra, R. J., Bower, J. M., Cullen, K. E., Habas, C., Ivry, R. B., et al. (2015). Consensus paper: the role of the cerebellum in perceptual processes. *Cerebellum* 14, 197–220. doi: 10.1007/s12311-014-0627-7
- Ben-Ari, Y. (2002). Excitatory actions of GABA during development: the nature of the nurture. *Nat. Rev. Neurosci.* 3, 728–739. doi: 10.1038/nrn920
- Ben-Ari, Y. (2014). The GABA excitatory/inhibitory developmental sequence: a personal journey. *Neuroscience* 279, 187–219. doi: 10.1016/j.neuroscience.2014.08.001
- Ben-Ari, Y. (2017). NKCC1 chloride importer antagonists attenuate many neurological and psychiatric disorders. *Trends Neurosci.* 40, 536–554. doi: 10.1016/j.tins.2017.07.001
- Ben-Ari, Y., Cherubini, E., Corradetti, R., and Gaiarsa, J. L. (1989). Giant synaptic potentials in immature rat CA3 hippocampal neurones. *J. Physiol.* 416, 303–325. doi: 10.1113/jphysiol.1989.sp017762
- Brickley, S. G., Cull-Candy, S. G., and Farrant, M. (1999). Single-channel properties of synaptic and extrasynaptic GABA_A receptors suggest differential targeting of receptor subtypes. *J. Neurosci.* 19, 2960–2973. doi: 10.1523/JNEUROSCI.19-08-02960.1999
- Dean, S. L., and McCarthy, M. M. (2008). Steroids, sex and the cerebellar cortex: implications for human disease. *Cerebellum* 7, 38–47. doi: 10.1007/s12311-008-0003-6
- Dusart, I., and Flamant, F. (2012). Profound morphological and functional changes of rodent Purkinje cells between the first and the second postnatal weeks: a metamorphosis? *Front. Neuroanat.* 6:11. doi: 10.3389/fnana.2012.00011
- Eilers, J., Plant, T. D., Marandi, N., and Konnerth, A. (2001). GABA-mediated Ca²⁺ signalling in developing rat cerebellar Purkinje neurones. *J. Physiol.* 536, 429–437. doi: 10.1111/j.1469-7793.2001.0429c.xd
- Fatemi, S. H., Aldinger, K. A., Ashwood, P., Bauman, M. L., Blaha, C. D., Blatt, G. J., et al. (2012). Consensus paper: pathological role of the cerebellum in autism. *Cerebellum* 11, 777–807. doi: 10.1007/s12311-012-0355-9
- Fisher, J. L., and Macdonald, R. L. (1997). Single channel properties of recombinant GABA_A receptors containing γ 2 or delta subtypes expressed with α 1 and β 3 subtypes in mouse L929 cells. *J. Physiol.* 505, 283–297. doi: 10.1111/j.1469-7793.1997.283bb.x
- Fritschy, J. M., Paysan, J., Enna, A., and Mohler, H. (1994). Switch in the expression of rat GABA_A-receptor subtypes during postnatal development: an immunohistochemical study. *J. Neurosci.* 14, 5302–5324. doi: 10.1523/JNEUROSCI.14-09-05302.1994
- Galanopoulou, A. S. (2008). Sexually dimorphic expression of KCC2 and GABA function. *Epilepsy Res.* 80, 99–113. doi: 10.1016/j.eplepsyres.2008.04.013
- Haghir, H., Rezaee, A. A., Nomani, H., Sankian, M., Kheradmand, H., and Hami, J. (2013). Sexual dimorphism in expression of insulin and insulin-like growth factor-I receptors in developing rat cerebellum. *Cell. Mol. Neurobiol.* 33, 369–377. doi: 10.1007/s10571-012-9903-6
- Hashimoto, K., and Kano, M. (2003). Functional differentiation of multiple climbing fiber inputs during synapse elimination in the developing cerebellum. *Neuron* 38, 785–796. doi: 10.1016/s0896-6273(03)00298-8
- Hörtnagl, H., Tasan, R. O., Wieselthaler, A., Kirchmair, E., Sieghart, W., and Sperk, G. (2013). Patterns of mRNA and protein expression for 12 GABA_A receptor subunits in the mouse brain. *Neuroscience* 236, 345–372. doi: 10.1016/j.neuroscience.2013.01.008
- Huang, Y., Wang, J. J., and Yung, W. H. (2013). Coupling between GABA-A receptor and chloride transporter underlies ionic plasticity in cerebellar Purkinje neurons. *Cerebellum* 12, 328–330. doi: 10.1007/s12311-013-0453-3
- Ingram, J. L., Peckham, S. M., Tisdale, B., and Rodier, P. M. (2000). Prenatal exposure of rats to valproic acid reproduces the cerebellar anomalies associated with autism. *Neurotoxicol. Teratol.* 22, 319–324. doi: 10.1016/s0892-0362(99)00083-5
- Kyrozis, A., Chudomel, O., Moshé, S. L., and Galanopoulou, A. S. (2006). Sex-dependent maturation of GABA_A receptor-mediated synaptic events in rat substantia nigra reticulata. *Neurosci. Lett.* 398, 1–5. doi: 10.1016/j.neulet.2005.12.018
- Laurie, D. J., Wisden, W., and Seeburg, P. H. (1992). The distribution of thirteen GABA_A receptor subunit mRNAs in the rat brain: III. Embryonic and postnatal development. *J. Neurosci.* 11, 4151–4172. doi: 10.1523/JNEUROSCI.12-11-04151.1992
- Lee, K., Goodman, L., Fourie, C., Schenk, S., Leitch, B., and Montgomery, J. M. (2016). AMPA receptors as therapeutic targets for neurological disorders. *Adv. Protein Chem. Struct. Biol.* 103, 203–261. doi: 10.1016/bs.apcsb.2015.10.004
- Lemonnier, E., and Ben-Ari, Y. (2010). The diuretic bumetanide decreases autistic behaviour in five infants treated during 3 months with no side effects. *Acta Paediatr.* 99, 1885–1888. doi: 10.1111/j.1651-2227.2010.01933.x
- Lemonnier, E., Villeneuve, N., Sonie, S., Serret, S., Rosier, A., Roue, M., et al. (2017). Effects of bumetanide on neurobehavioral function in children and adolescents with autism spectrum disorders. *Transl. Psychiatry* 7:e1124. doi: 10.1038/tp.2017.101
- Li, Y., Zhou, Y., Peng, L., and Zhao, Y. (2017). Reduced protein expressions of cytomembrane GABA_A β 3 at different postnatal developmental stages of rats exposed prenatally to valproic acid. *Brain Res.* 1671, 33–42. doi: 10.1016/j.brainres.2017.06.018
- Mercer, A. A., Palarz, K. J., Tabatadze, N., Woolley, C. S., and Raman, I. M. (2016). Sex differences in cerebellar synaptic transmission and sex-specific responses to autism-linked Gabrb3 mutations in mice. *Elife* 5:e07596. doi: 10.7554/eLife.07596
- Mikawa, S., Wang, C., Shu, F., Wang, T., Fukuda, A., and Sato, K. (2002). Developmental changes in KCC1, KCC2 and NKCC1 mRNAs in the rat cerebellum. *Dev. Brain Res.* 136, 93–100. doi: 10.1016/s0165-3806(02)00345-0
- Mir, F. R., Carrer, H. F., and Cambiasso, M. J. (2017). Sex differences in depolarizing actions of GABA_A receptor activation in rat embryonic hypothalamic neurons. *Eur. J. Neurosci.* 45, 521–527. doi: 10.1111/ejn.13467
- Mortensen, M., and Smart, T. G. (2006). Extrasynaptic $\alpha\beta$ subunit GABA_A receptors on rat hippocampal pyramidal neurons. *J. Physiol.* 577, 841–856. doi: 10.1113/jphysiol.2006.117952
- Moss, S. J., Smart, T. G., Porter, N. M., Nayeem, N., Devine, J., Stephenson, F. A., et al. (1990). Cloned GABA receptors are maintained in a stable cell line: allosteric and channel properties. *Eur. J. Pharmacol.* 189, 77–88. doi: 10.1016/0922-4106(90)90232-m
- Nadler, L. S., Guirguis, E. R., and Siegel, R. E. (1994). GABA_A receptor subunit polypeptides increase in parallel but exhibit distinct distributions in the developing rat cerebellum. *J. Neurobiol.* 25, 1533–1544. doi: 10.1002/neu.480251206
- Newland, C. F., Colquhoun, D., and Cull-Candy, S. G. (1991). Single channels activated by high concentrations of GABA in superior cervical ganglion

AUTHOR CONTRIBUTIONS

SR, AL, YB-A, BP and J-LB wrote the manuscript. SR, AL and J-LB designed the research, performed the experiments and analyzed the data.

- neurones of the rat. *J. Physiol.* 432, 203–233. doi: 10.1113/jphysiol.1991.sp018382
- Núñez, J. L., and McCarthy, M. M. (2007). Evidence for an extended duration of GABA-mediated excitation in the developing male versus female hippocampus. *Dev. Neurobiol.* 67, 1879–1890. doi: 10.1002/dneu.20567
- Pangratz-Fuehrer, S., Sieghart, W., Rudolph, U., Parada, I., and Huguenard, J. R. (2016). Early postnatal switch in GABA_A receptor α -subunits in the reticular thalamic nucleus. *J. Neurophysiol.* 115, 1183–1195. doi: 10.1152/jn.00905.2015
- Phillips, J. R., Hewedi, D. H., Eissa, A. M., and Moustafa, A. A. (2015). The cerebellum and psychiatric disorders. *Front. Public Health* 3:66. doi: 10.3389/fpubh.2015.00066
- Rahmati, N., Vinuela Veloz, M. F., Xu, J., Barone, S., Rodolfo Ben Hamida, N., Schonewille, M., et al. (2016). SLC26A11 (KBAT) in purkinje cells is critical for inhibitory transmission and contributes to locomotor coordination. *eNeuro* 3:ENEURO.0028–16. doi: 10.1523/ENEURO.0028-16.2016
- Raimondo, J. V., Richards, B. A., and Woodin, M. A. (2017). Neuronal chloride and excitability—the big impact of small changes. *Curr. Opin. Neurobiol.* 43, 35–42. doi: 10.1016/j.conb.2016.11.012
- Rivera, C., Voipio, J., Payne, J. A., Ruusuvuori, E., Lahtinen, H., Lamsa, K., et al. (1999). The K⁺/Cl[−] co-transporter KCC2 renders GABA hyperpolarizing during neuronal maturation. *Nature* 397, 251–255. doi: 10.1038/16697
- Robello, M., Amico, C., and Cupello, A. (1998). Cerebellar granule cell GABA_A receptors studied at the single-channel level: modulation by protein kinase G. *Biochem. Biophys. Res. Commun.* 253, 768–773. doi: 10.1006/bbrc.1998.9830
- Roulet, F. I., Lai, J. K. Y., and Foster, J. (2013). *In utero* exposure to valproic acid and autism—a current review of clinical and animal studies. *Neurotoxicol. Teratol.* 36, 47–56. doi: 10.1016/j.ntt.2013.01.004
- Rubenstein, J. L. R., and Merzenich, M. M. (2003). Model of autism: increased ratio of excitation/inhibition in key neural systems. *Genes Brain Behav.* 2, 255–267. doi: 10.1034/j.1601-183x.2003.00037.x
- Schmahmann, J. D., and Sherman, J. C. (1998). The cerebellar cognitive affective syndrome. *Brain* 121, 561–579. doi: 10.1093/brain/121.4.561
- Sigel, E., and Steinmann, M. E. (2012). Structure, function, and modulation of GABA_A receptors. *J. Biol. Chem.* 287, 40224–40231. doi: 10.1074/jbc.R112.386664
- Skefos, J., Cummings, C., Enzer, K., Holiday, J., Weed, K., Levy, E., et al. (2014). Regional alterations in purkinje cell density in patients with autism. *PLoS One* 9:e81255. doi: 10.1371/journal.pone.0081255
- Song, N. Y., Shi, H. B., Li, C. Y., and Yin, S. K. (2012). Interaction between taurine and GABA_A/glycine receptors in neurons of the rat anteroventral cochlear nucleus. *Brain Res.* 1472, 1–10. doi: 10.1016/j.brainres.2012.07.001
- Stein, V., Hermans-Borgmeyer, I., Jentsch, T. J., and Hübner, C. A. (2004). Expression of the KCl cotransporter KCC2 parallels neuronal maturation and the emergence of low intracellular chloride. *J. Comp. Neurol.* 468, 57–64. doi: 10.1002/cne.10983
- Succol, F., Fiumelli, H., Benfenati, F., Cancedda, L., and Barberis, A. (2012). Intracellular chloride concentration influences the GABA_A receptor subunit composition. *Nat. Commun.* 3:738. doi: 10.1038/ncomms1744
- Tsai, P. T. (2016). Autism and cerebellar dysfunction: evidence from animal models. *Semin. Fetal Neonatal Med.* 21, 349–355. doi: 10.1016/j.siny.2016.04.009
- Tsai, P. T., Hull, C., Chu, Y., Greene-Colozzi, E., Sadowski, A. R., Leech, J. M., et al. (2012). Autistic-like behavior and cerebellar dysfunction in Purkinje cell Tsc1 mutant mice. *Nature* 488, 647–651. doi: 10.1038/nature11310
- Tsutsui, K., Ukena, K., Sakamoto, H., Okuyama, S., and Haraguchi, S. (2011). Biosynthesis, mode of action, and functional significance of neurosteroids in the purkinje cell. *Front. Endocrinol.* 2:61. doi: 10.3389/fendo.2011.00061
- Tyzio, R., Holmes, G. L., Ben-Ari, Y., and Khazipov, R. (2007). Timing of the developmental switch in GABA_A mediated signaling from excitation to inhibition in CA3 rat hippocampus using gramicidin perforated patch and extracellular recordings. *Epilepsia* 48, 96–105. doi: 10.1111/j.1528-1167.2007.01295.x
- Tyzio, R., Nardou, R., Ferrari, D. C., Tsintsadze, T., Shahrokhi, A., Eftekhari, S., et al. (2014). Oxytocin-mediated GABA inhibition during delivery attenuates autism pathogenesis in rodent offspring. *Science* 343, 675–679. doi: 10.1126/science.1247190
- Uzunova, G., Pallanti, S., and Hollander, E. (2016). Excitatory/inhibitory imbalance in autism spectrum disorders: implications for interventions and therapeutics. *World J. Biol. Psychiatry* 17, 174–186. doi: 10.3109/15622975.2015.1085597
- Verdoorn, T. A., Draguhn, A., Ymer, S., Seeburg, P. H., and Sakmann, B. (1990). Functional properties of recombinant rat GABA_A receptors depend upon subunit composition. *Neuron* 4, 919–928. doi: 10.1016/0896-6273(90)90145-6
- Vien, T. N., Modgil, A., Abramian, A. M., Jurd, R., Walker, J., Brandon, N. J., et al. (2015). Compromising the phosphodependent regulation of the GABA_A β 3 subunit reproduces the core phenotypes of autism spectrum disorders. *Proc. Natl. Acad. Sci. U S A* 112, 14805–14810. doi: 10.1073/pnas.1514657112
- Waddell, J., and McCarthy, M. M. (2012). Sexual differentiation of the brain and ADHD: what is a sex difference in prevalence telling us? *Curr. Top. Behav. Neurosci.* 9, 341–360. doi: 10.1007/7854_2010_114
- Watanabe, M., and Fukuda, A. (2015). Development and regulation of chloride homeostasis in the central nervous system. *Front. Cell. Neurosci.* 9:371. doi: 10.3389/fncel.2015.00371
- Witte, M., Reinert, T., Dietz, B., Nerlich, J., Rübsamen, R., and Milenkovic, I. (2014). Depolarizing chloride gradient in developing cochlear nucleus neurons: underlying mechanism and implication for calcium signaling. *Neuroscience* 261, 207–222. doi: 10.1016/j.neuroscience.2013.12.050
- Zhang, L., Pathak, H. R., Coulter, D. A., Freed, M. A., and Vardi, N. (2006). Shift of intracellular chloride concentration in ganglion and amacrine cells of developing mouse retina. *J. Neurophysiol.* 95, 2404–2416. doi: 10.1152/jn.00578.2005
- Zhang, W., Schmelzeisen, S., Parthier, D., Fring, S., and Möhrle, F. (2015). Anoctamin calcium-activated chloride channels may modulate inhibitory transmission in the cerebellar cortex. *PLoS One* 10:e0142160. doi: 10.1371/journal.pone.0142160

Conflict of Interest Statement: YB-A is CEO of Neurochlore, a biotech company devoted to treat autism.

The remaining authors declare that the research was conducted in the absence of any commercial or financial relationships that could be construed as a potential conflict of interest.

Copyright © 2018 Roux, Lohof, Ben-Ari, Poulain and Bossu. This is an open-access article distributed under the terms of the Creative Commons Attribution License (CC BY). The use, distribution or reproduction in other forums is permitted, provided the original author(s) and the copyright owner(s) are credited and that the original publication in this journal is cited, in accordance with accepted academic practice. No use, distribution or reproduction is permitted which does not comply with these terms.



Intracellular Dynamics in Cuneate Nucleus Neurons Support Self-Stabilizing Learning of Generalizable Tactile Representations

Udaya B. Rongala¹, Anton Spanne², Alberto Mazzoni¹, Fredrik Bengtsson², Calogero M. Oddo¹ and Henrik Jörntell^{2*}

¹ The BioRobotics Institute, Scuola Superiore Sant'Anna, Pisa, Italy, ² Section for Neurobiology, Department of Experimental Medical Sciences, Biomedical Center, Lund University, Lund, Sweden

OPEN ACCESS

Edited by:

Philippe Isope,
Centre National de la Recherche
Scientifique (CNRS), France

Reviewed by:

Jesus Garrido,
Universidad de Granada, Spain
Natasha Alexandra Cayco Gajic,
University College London,
United Kingdom

*Correspondence:

Henrik Jörntell
henrik.jorntell@med.lu.se

Received: 26 March 2018

Accepted: 26 June 2018

Published: 31 July 2018

Citation:

Rongala UB, Spanne A, Mazzoni A, Bengtsson F, Oddo CM and Jörntell H (2018) Intracellular Dynamics in Cuneate Nucleus Neurons Support Self-Stabilizing Learning of Generalizable Tactile Representations. *Front. Cell. Neurosci.* 12:210. doi: 10.3389/fncel.2018.00210

How the brain represents the external world is an unresolved issue for neuroscience, which could provide fundamental insights into brain circuitry operation and solutions for artificial intelligence and robotics. The neurons of the cuneate nucleus form the first interface for the sense of touch in the brain. They were previously shown to have a highly skewed synaptic weight distribution for tactile primary afferent inputs, suggesting that their connectivity is strongly shaped by learning. Here we first characterized the intracellular dynamics and inhibitory synaptic inputs of cuneate neurons *in vivo* and modeled their integration of tactile sensory inputs. We then replaced the tactile inputs with input from a sensorized bionic fingertip and modeled the learning-induced representations that emerged from varied sensory experiences. The model reproduced both the intrinsic membrane dynamics and the synaptic weight distributions observed in cuneate neurons *in vivo*. In terms of higher level model properties, individual cuneate neurons learnt to identify specific sets of correlated sensors, which at the population level resulted in a decomposition of the sensor space into its recurring high-dimensional components. Such vector components could be applied to identify both past and novel sensory experiences and likely correspond to the fundamental haptic input features these neurons encode *in vivo*. In addition, we show that the cuneate learning architecture is robust to a wide range of intrinsic parameter settings due to the neuronal intrinsic dynamics. Therefore, the architecture is a potentially generic solution for forming versatile representations of the external world in different sensor systems.

Keywords: cuneate nucleus, neurophysiology, neuronal plasticity, intrinsic dynamics, tactile, touch, synaptic integration

INTRODUCTION

The problem of how to represent a complex external world to support non-trivial versatility of action has a deadening presence both in neuroscience (Loeb and Fishel, 2014; Spanne and Jörntell, 2015), robotics and artificial intelligence (AI) systems (Service, 2014). For neuroscience, the issue is closely associated with the understanding of the brain—without

knowledge of how information of the world is represented in neuronal circuitry, it is difficult to decipher its functional mechanisms. An important related issue is how biological systems can generalize previously learnt sensory experiences to apply them to the interpretation of novel contexts—lack of generalization capability is a limitation in classical pattern recognition systems (Spanne and Jorntell, 2015), to which AI and DNN systems has an ancestry, and likely an important reason why such systems can be comparatively easily fooled (Nguyen et al., 2015). As versatility of interaction with the external world is a hallmark of brain function, an important question is how that versatility can be supported.

The skin is an interface that directly interacts with the physical world, using 10,000's of tactile sensors (Johansson and Flanagan, 2009). Current models of the organization of tactile neural systems to a large extent build on assumptions that the brain needs to identify edges, shapes or other physical parameters that human external observers may deem important to represent (Pei et al., 2011; Sathian, 2016). Using sparse-coding interpretations of neural coding combined with grandmother neuron-like theory (Barlow, 1972) such a system can be expected to work in the classification of a large range of tactile experiences. However, classifying systems based on pattern recognition can suffer from problems with generalization, i.e., where learning from one situation can be scaled or adapted to apply to new ones (Spanne and Jorntell, 2015). An alternative mode of representation of tactile information would be one that automatically arises out of experienced interactions through learning. Indeed, during early development, mammals generate seemingly random movements and interactions with the environment, which would engage a wide set of sensors from large parts of the body (Shao et al., 2016) and play a crucial role for development (Forssberg et al., 1995; Petersson et al., 2003; Blumberg et al., 2013). Such interactions result in spatiotemporal patterns of skin sensor activation, that depend on, and therefore abstract, the properties of the objects we touch, the laws of physics describing the interactions that can take place (Hayward, 2011), the types of movement we make, the mechanical effects inducible in the skin and how the tactile sensors are tuned to them (Jörntell et al., 2014). The available set of sensors will respond across these conditions and their activations will have specific relationships depending on the condition. Hence, rather than viewing brain integration of tactile sensors as occurring in a pixel-by-pixel fashion, we here consider the often overlooked fact that individual neurons integrate information from several sensors. It follows that what is being learnt is likely to involve the relationships between the activations of these sensors. To learn such relationships is here hypothesized to be an important component of being able to form representations of the external world that is applicable or generalizable to novel experiences.

As tactile inputs are first processed in the cuneate nucleus, before they reach the cortex, it is likely that the basic constraints on the brain's representation of the tactile part of the physical world are formed here. *In vivo* whole cell recordings from these neurons indicate that their synaptic weights for tactile inputs are highly skewed, which indicates that they are highly learnt (Bengtsson et al., 2013). The important question why

that learning occurs recently found a possible answer, when the cuneate neurons were found to code for unique combinations of the fundamental haptic input features (Jörntell et al., 2014), which tentatively correspond to the dimensions or the vector decompositions of the contact mechanics effects arising between two objects (Hayward, 2011). Here, we emulated the learning that would arise from a set of varied sensory experiences given the biological constraints provided by the recording data we obtained on the intrinsic membrane dynamics and the synaptic inputs of the neurons of the cuneate nucleus. We find that the main effect of the cuneate learning is a utility-based decomposition of the tactile sensory space into vector components that made it possible to generalize the learning to novel tactile experiences. This is a different form of representation of sensory input data than a direct identification of sensory input patterns, which is a potential explanation for the large versatility in the identification of sensor input data in biological systems.

METHODS

All biological data was obtained under acute conditions identical to those of a previous study on the cuneate nucleus *in vivo* (Bengtsson et al., 2013). Briefly, adult cats of both sexes were initially prepared under propofol anesthesia and subsequently decerebrated to allow cuneate neuronal recordings under non-anesthetized conditions. This study was carried out in accordance with the recommendations of Malmö-Lund Animal Research Ethics Committee. All experimental procedures were approved in advance by the Malmö/Lund Animal Research Ethics Committee (permit number and approval-ID: M32-09).

This section contains four main parts. First, we describe how recordings were made from projection neurons and inhibitory interneurons of the cuneate nucleus using the *in vivo* whole cell patch clamp technique. Secondly, the recorded characteristics of the cuneate projection neurons and the inhibition from the interneurons were approximated by constructing a model of individual cuneate projection neurons (CNs) and their afferent network. Thirdly, the responses of a population of skin sensors that provided synaptic input to the CN network across a range of different real world stimuli were generated by a bionic fingertip. Fourthly, the CN synaptic learning process for skin sensor input was inferred from generic neuronal learning mechanisms *in vivo* and our estimation of intracellular calcium responses. The theoretical basis for the construction of the CN model and its learning process is also provided for each step.

Biological Data

Briefly, under initial deep propofol anesthesia, adult cats were prepared for acute *in vivo* recordings with artificial respiration, strict monitoring of blood pressure, end-expiratory carbon dioxide and temperature. Thereafter, the animals were decerebrated and the anesthesia discontinued. To monitor the level of anesthesia before decerebration, we continuously measured the blood pressure and verified the absence of withdrawal reflexes to noxious stimulation. To monitor the state of the preparation after the decerebration, we in addition made EEG recordings from intact parts of the neocortex. EEG

recordings were characterized by a 1–4 Hz oscillatory activity that was periodically interrupted by large-amplitude 7–14 Hz spindle oscillations lasting for 0.5 s or more. Such EEG patterns are associated with deep stages of sleep (Niedermeyer and Da Silva, 2005). The EEG activity and the blood pressure remained stable, also on noxious stimulation, throughout the experiments. Mounting in a stereotaxic frame, drainage of cerebrospinal fluid, pneumothorax and clamping the spinal processes of a few cervical and lumbar vertebral bodies served to increase the mechanical stability of the preparation.

In vivo whole cell patch clamp recordings were made in the exposed cuneate nucleus. The recorded neurons were identified with respect to the location of their excitatory receptive field on the skin (Bengtsson et al., 2013). Stimulation in relation to the location of this receptive field was done using force-time controlled touch as well as by local electrical activation of skin afferents. Current injections to characterize the intrinsic membrane responses were made through the recording pipette. All intracellular signals were analyzed off-line using custom-made software. Identification of unitary IPSPs was made using a tailored template matching routine with manually constructed templates. The templates consisted of a time series of voltage ranges into which the signal had to fit to be counted. The template was adjusted to allow the detection of gradually smaller events until it started to include events that on visual inspection did not resemble the event time course of IPSPs evoked by skin stimulation (Bengtsson et al., 2013). Hence, the similarity of time course between evoked and unitary IPSPs was taken as an indication that they were derived from the same type of inhibitory synapses.

A difference with our previous analysis of EPSPs (Bengtsson et al., 2013), was that the voltage deflections of the unitary IPSPs were much smaller. Thereby, the noise of the recording system prevented the detection of IPSPs of amplitudes below a certain level. Therefore, our reported values of the median peak unitary IPSP amplitudes for each neuron are most likely overestimates. For population data, we report the mean and standard deviation of the median IPSP amplitudes recorded for at least 100 spontaneous IPSPs in each of the 15 recorded cuneate projection neurons.

Modeling Design

Based on our present biological observations, as well as previously published data on cuneate neurons (Bengtsson et al., 2013) and generic neuronal physiology and plasticity, we aimed to simulate how these parameters and processes could support learning when brought together in a functional system. Our simulation consisted of two main components,

- (a) A bionic fingertip covered with silicon skin and equipped with tactile sensors that transduced local mechanical skin strain patterns into spatiotemporal patterns of sensor spike output data in response to physical interactions with external objects/surfaces. This was the counterpart of the tactile primary afferents (PAs) in biological systems. The bionic fingertip provided the important feature of a system of PA sensors where there is a consistent relationship between

the activation of the different sensors across conditions or tactile experiences. As discussed in the introduction, rather than viewing brain integration of tactile sensors as occurring in a pixel-by-pixel fashion, we here consider the often overlooked fact that each cuneate nucleus neurons integrate information from several sensors. It follows that what is being learnt is likely to involve the relationships between the activations of these sensors. To learn such relationships is here hypothesized to be an important component of being able to form representations of the external world that is applicable to novel experiences.

- (b) A simulated cuneate nucleus neuronal network containing a set of cuneate neurons receiving synaptic input from those PAs. Each model cuneate projection neuron (CN) was simulated individually, capturing the intrinsic responsiveness observed *in vivo* and the generic subcellular processes involved in synaptic plasticity. The accumulative effects of the synaptic plasticity during the learning process were evaluated by the changes in synaptic weights of the PA inputs in each CN.

In the account that follows, we present the design of the simulation starting with the low level neuronal properties, the dynamic model describing the intrinsic responsiveness of the cuneate neurons, synaptic weight initialization, the sensory input data and the bionic fingertip used to generate it, the learning process and the evaluation of the end effect of the learning process. The design and performance of the bionic fingertip has already been reported in previous papers, therefore we merely present the specific adaptations made for the present simulation. The modeling software is available on: https://figshare.com/projects/Artificial_Cuneate_Neuron_Model/34886.

Network Connectivity

Based on biological data of cuneate neurons (Bengtsson et al., 2013; **Figures 1, 2**), our network model (**Figure 3A**) was comprised of sensory afferents projecting as excitatory synapses on each individual model CN. In addition to the excitatory synapses, and based on our biological observations (**Figure 1**), the sensory afferents also drove local inhibitory interneurons that provided inhibitory synapses to the CNs (**Figure 3A**). The model CN had equal numbers of excitatory and inhibitory synapses. The synaptic weights of these synapses were given initial starting weights (or seed weights, see below) that were gradually learnt on a trial-by-trial basis.

The simulated network model had 80 sensory input channels (PAs) that innervated each individual CN. This number of afferents was less than biological estimates, which suggest in the order of 1,000's of PAs per CN (Bengtsson et al., 2013). However, the lower number of simulated afferents is still realistic because out of these 1,000 synapses, many are likely to represent anatomically present synaptic inputs from PA axons mediating input from several different fingers, which in the adult animal mostly provide “silent” synaptic inputs (Weinberg et al., 1990; Bengtsson et al., 2013). In contrast, our inputs were generated from the tip of one finger alone. Synaptic inhibition was simulated as being provided by 80 independent interneurons that

were each directly activated by one out of the 80 PA afferents available in our simulated system. Because all unitary inhibitory synaptic inputs were found to be of comparable, low weights in the biological cuneate neuron (**Figure 1**), inhibitory synapses were here simplified to one lump inhibitory synapse per CN (total inhibitory synaptic weight, **Figure 3**). Hence, interneurons were not explicitly simulated, but instead the spiking activity of each PA afferent was fed directly to an inhibitory synapse on the CN.

Neuron Model

The model cuneate projection neuron (CN) was implemented as a conductance based Exponential Integrate and Fire (EIF) model (Fourcaud-Trocmé et al., 2003), which can recreate the fast dynamics (~ 1 ms timescale) of neuronal spike generation. In addition to the basic EIF model, voltage sensitive calcium channels and calcium dependent potassium channels were also modeled in order to recreate intermediate cuneate neuron dynamics (~ 10 ms timescale) observed *in vivo* (**Figures 1E,F**). The complete dynamics of the CN membrane potential are given by:

$$C_m \frac{dV_m}{dt} = I_L + I_{spike} + I_{ion} + I_{ext} + I_{syn} \quad (1)$$

where C_m is the membrane capacitance, $I_L = -\bar{g}_L(V_m - E_L)$ is the leak current, I_{spike} is the spike currents (fast dynamics), I_{ion} is the ion channel currents (intermediate dynamics), I_{syn} is the synaptic input currents and I_{ext} denotes external injected currents that were used to evaluate the intrinsic CN neuron responsiveness to current step commands (**Figure 1F**). The model values for these and other parameters are given in **Table 2**. The membrane resistance and time constant/capacitance were within the range of values recorded *in vivo* (Bengtsson et al., 2013), whereas other intrinsic parameter values were chosen through an optimization process (see below).

Neuron Model-Fast Dynamics

The spike current (I_{spike}) is generated using a basic EIF model (Equation 2) to achieve the fast dynamics and recreate the initiation of the action potential (Ostojic and Brunel, 2011).

$$I_{spike} = \bar{g}_L \Delta_T \exp\left(\frac{V_m - V_t}{\Delta_T}\right) \quad (2)$$

As the depolarization reaches a threshold speed, an action potential is said to be generated, and the membrane potential is immediately reset by a fast afterhyperpolarization (AHP) to the membrane potential at which the spike was initiated, i.e., mimicking the fast spike AHP of the recorded cuneate projection neurons (see **Figure 2A**).

Neuron Model-Intermediate Dynamics

The intermediate dynamics include currents from additional ion channels (I_{ion} , Equation 1) that are not directly involved in forming action potentials, but have more of a modulating role in episodes leading up to the generation of action potential and the episodes between action potentials when the synaptic input activity is high. The intermediate dynamics of the

model were optimized to mimic the reactive conductances that could generate the types of responses to current injections we recorded in the cuneate neurons *in vivo* (**Figures 1E,F**). Such responses, i.e., post-inhibitory rebound responses and a tendency to generate bursts of action potential firing, have been observed in other neuron types (Llinás and Jahnsen, 1982; Huguenard, 1996; Molineux et al., 2008) and has at least partly been attributed to by *low-threshold voltage gated calcium channels* (LVA) and *calcium-activated potassium channels* (CAP). Hence, I_{ion} can be divided according to:

$$I_{ion} = I_{Ca} + I_K \quad (3)$$

where I_{Ca} is the current through LVA channels or equivalent channels and I_K the current through the CAP channels. These are modeled as two separate pools of ion channels (Saarinen et al., 2008) according to:

$$\begin{aligned} I_{Ca} &= -\bar{g}_{Ca} x_{Ca,a}^3 x_{Ca,i} (V_m - E_{Ca}) \\ I_K &= -\bar{g}_K x_{KCa}^4 x_{KVm}^4 (V_m - E_K) \end{aligned} \quad (4)$$

where \bar{g}_{Ca} and \bar{g}_K are the maximum conductances of the respective channels, E_{Ca} and E_K are the reversal potentials of the respective ions, and x_{KCa} , x_{KVm} , $x_{Ca,a}$, $x_{Ca,i}$ are the activity states of the channels (Saarinen et al., 2008).

The activation states of the LVA channels were modeled using the following differential equations:

$$\begin{aligned} \frac{d(x_{Ca,a})}{dt} &= (\bar{x}_{Ca,a}(V_m) - x_{Ca,a}) / \tau_{Ca,a} \\ \frac{d(x_{Ca,i})}{dt} &= (\bar{x}_{Ca,i}(V_m) - x_{Ca,i}) / \tau_{Ca,i} \end{aligned} \quad (5)$$

where tau is the time constant at which the states move toward the voltage dependent equilibrium described by $\bar{x}_{Ca}(V_m)$. These equilibrium functions are two parameters sigmoid of the form:

$$\begin{aligned} \bar{x}_{Ca,a}(V_m) &= \left(1 + \exp \frac{p_{Ca,a,1} - V_m}{p_{Ca,a,2}}\right)^{-1} \\ \bar{x}_{Ca,i}(V_m) &= 1 - \left(1 + \exp \frac{p_{Ca,i,1} - V_m}{p_{Ca,i,2}}\right)^{-1} \end{aligned} \quad (6)$$

Since the calcium sensitive subunits of the CAP channels are located on the inner surface of the cell membrane, the intracellular concentration of calcium ($[Ca^{2+}]$) is modeled for small volumes rather than as an overall concentration within the cell. The calcium concentration within the cell will change both due to ion channels through which calcium ions enter to the inside of the membrane, and diffusion of ions into the remaining intracellular volume. From this line of reasoning, and in accordance with Saarinen et al. (2008), Equation 7 is constructed

$$\begin{aligned} \frac{d([Ca^{2+}])}{dt} &= B_{Ca} \bar{g}_{Ca} x_{Ca,a}^3 x_{Ca,i} (V_m - E_{Ca}) \\ &\quad + ([Ca^{2+}]_{rest} - [Ca^{2+}]) / \tau_{[Ca^{2+}]} \end{aligned} \quad (7)$$

The activation states of the CAP channels were modeled using the following differential equations:

$$\begin{aligned}\frac{d(x_{K_{Ca}})}{dt} &= (\bar{x}_{K_{Ca}}([Ca^{2+}]) - x_{K_{Ca}}) / \tau_{K_{Ca}} \\ \frac{d(x_{K_{Vm}})}{dt} &= (\bar{x}_{K_{Vm}}(V_m) - x_{K_{Vm}}) / \tau_{K_{Vm}}\end{aligned}\quad (8)$$

where the two time constants ($\tau_{K_{Ca}}$ and $\tau_{K_{Vm}}$) indicate the times at which the states move toward the voltage dependent equilibrium described by $\bar{x}_{K_{Vm}}$ and the calcium dependent equilibrium described by $\bar{x}_{K_{Ca}}$. These equilibrium functions are two parameters sigmoid of the form:

$$\begin{aligned}\bar{x}_{K_{Vm}}(V_m) &= \left(1 + \exp \frac{p_{K_{Vm},1} - V_m}{p_{K_{Vm},2}}\right)^{-1} \\ \bar{x}_{K_{Ca}}([Ca^{2+}]) &= 1 - \left(1 + \exp \frac{p_{K_{Ca},1} - [Ca^{2+}]}{p_{K_{Ca},2}}\right)^{-1}\end{aligned}\quad (9)$$

The values for these parameters were chosen through an optimization procedure (see below) and are indicated in **Table 2**. Note that we observed a range of variance between cuneate neurons *in vivo* in terms of their intermediate dynamics. Our aim was to provide a simple model that at the same time could capture the main principles of the rebound and burst responses that we could demonstrate in our recorded cuneate neurons. Therefore, we do not expect that our parameter values have a direct correspondence with biophysical measures, and we do not expect to precisely capture the properties of the intermediate dynamic response of any single neuron (which likely would have required a larger set of parameters).

Neuron Model-Synaptic Inputs

The synaptic current (I_{syn}) through the cell membrane is the summated synaptic currents of the activated synapses. Each individual synapse (i) is activated by a primary afferent spike generated by a single sensor of the bionic fingertip. Once activated, this spike gives rise to a stereotyped time course of conductance injection at the synapse (I_{syn}) which is described by

$$\begin{aligned}I_{syn} &= g_{max} \sum_i w_{exc,i} \exp(-\tau(t - t^*)) (E_{rev,exc} - V_m) \\ &+ g_{max} w_{inh} \sum_i \exp(-\tau(t - t^*)) (E_{rev,inh} - V_m)\end{aligned}\quad (10)$$

where E_{rev} is the reversal potential of the type of synapse ($E_{rev,exc}$ or $E_{rev,inh}$ depending on whether the synapse is excitatory or inhibitory, see **Table 2**), V_m is the membrane potential and t^* is the time of activation of the synapse. Each spike in each sensory afferent was converted into a synaptic conductance in the simulated neuron. For each synapse, the peak amplitude of the synaptic response was determined by the product of their individual weight (w_{exc} or w_{inh}) and the overall *maximum synaptic conductance constant* (g_{max} , see **Table 1**). Through g_{max} the relative leak conductance (i.e., the ratio of the synaptic and the leak conductances) could be adjusted to simulate cuneate

TABLE 1 | Specification of the intrinsic CN parameter values used.

| Parameters | Initial value/range |
|---|--|
| Maximum synaptic conductance constant (g_{max}) | 23e-9 S, 9e-9 S, 23e-8 S , 9e-7 S, 23e-7 S |
| Calcium activity set point ($SetPoint_{Ca^{2+}}$) | 20 Hz , 40 Hz, 60 Hz, 80 Hz, 100 Hz |
| Synaptic local Ca^{2+} time constant ($\tau_{Ca^{2+}_{loc}}$) | $[\tau_d, \tau_r, \tau_m] = 50\%, \mathbf{100\%}, 150\%, 200\%, 250\%$ |
| Seed weight distribution spread (SW Spread) | 0% , -20%, -40%, -60%, -80% |

The values of the basic CN configuration, or default values, are indicated in bold.

neurons with different sizes. The time constant of the decay of the synaptic membrane potential responses, τ , was 6.4 ms for both excitatory and inhibitory synapses, in accordance with the time courses recorded in the cuneate nucleus neurons *in vivo* (Bengtsson et al., 2013; **Figure 1**). Note that as all the PA synapses of our system stayed well below 200 Hz of firing activity, we did not simulate any rate adaptation of the PA synapses as such adaptation *in vivo* primarily occurs at intervals shorter than 5 ms (Jörntell and Ekerot, 2006).

Optimization of the Neuronal Calcium Dynamic Model Against Measured Data

The complete model was optimized during three steps. During each simulation, the model was fed with six 100 ms current steps with amplitudes of 100, 200, 300, 400, 600, and 800 pA. The results from the six trials were then optimized against intracellular recordings where the cuneate neurons were fed with the same currents *in vivo* (**Figure 1F**).

The first step is to manually choose suitable initial parameters, using both previously known values to some of the parameters, and estimating others using trial and error simulations. The second step is to use the Nelder-Mead algorithm, but with an objective function where the simulated traces is compared to the measured traces. The third step also uses the Nelder-Mead algorithm, but with an objective function that measure the discrepancy between the action-potential timing in the simulated trace and the measured trace. As there is no guarantee that the simulated trace contains the same number of action potentials as the measured trace, discontinuities appear when the number of action potentials in the simulated trace change. The use of the Nelder-Mead method is motivated by that this is a commonly applied numerical method used to find the minimum or maximum of an objective function in a multidimensional space, in particular for nonlinear optimization problems. Equation 11 contains the complete objective function:

$$e = \begin{cases} e_t \omega_s \sum_{T, \hat{T} \in \mathbb{T}} (|\hat{T}| - |T|)^2 & \exists T, \hat{T} \in \mathbb{T} \quad |\hat{T}| \neq |T| \\ e_t & \forall T, \hat{T} \in \mathbb{T} \quad |\hat{T}| = |T| \end{cases}\quad (11)$$

TABLE 2 | Neuron model parameters.

| Parameter | Symbol | Value |
|---|-------------------|-----------------------------|
| Membrane capacitance | C_m | 4.270e-11 F |
| Leak conductance | g_L | 8.100e-09 S |
| Leak reverse potential | E_L | -62.309 mV |
| Width of the spike (EIF model) | Δ_t | 1.3063 |
| Spike threshold (EIF model) | V_t | -57.129 mV |
| Maximum potassium conductance | g_K | 2.022e-08 S |
| EPSP reversal potential | $E_{rev,exc}$ | 0 mV |
| IPSP reversal potential | $E_{rev,inh}$ | -80 mV |
| Potassium reversal potential | E_K | -104.514 mV |
| Maximum calcium conductance | g_{Ca} | 2.082e-08 S |
| Calcium reversal potential | E_{Ca} | 121.436 mV |
| Conversion factor between calcium current and concentration | B_{Ca} | 3.374e-15 |
| Calcium concentration at rest (equilibrium) | Ca_{rest}^{2+} | 1.010e-07 |
| Time constant of the calcium concentration leak | $\tau_{Ca^{2+}}$ | 0.0063 |
| Time constant of the calcium activation state | $\tau_{Ca,a}$ | 2.722e-04 |
| Time constant of the calcium inactivation state | $\tau_{Ca,i}$ | 0.0207 |
| Time constant of the potassium calcium dependent activation state | $\tau_{K_{Ca}}$ | 0.0013 |
| Time constant of the potassium voltage gated activation state | $\tau_{K_{Vm}}$ | 0.0011 |
| Constant for sigmoid function of intermediate dynamic model | $\rho_{Ca,a,1}$ | -60.8369 mV |
| Constant for sigmoid function of intermediate dynamic model | $\rho_{Ca,a,2}$ | 6.3419 mV ⁻¹ |
| Constant for sigmoid function of intermediate dynamic model | $\rho_{Ca,i,1}$ | -68.0100 mV |
| Constant for sigmoid function of intermediate dynamic model | $\rho_{Ca,i,2}$ | 1.3008 mV ⁻¹ |
| Constant for sigmoid function of intermediate dynamic model | $\rho_{K_{Vm},1}$ | -64.0785 mV |
| Constant for sigmoid function of intermediate dynamic model | $\rho_{K_{Vm},2}$ | 0.7833 mV ⁻¹ |
| Constant for sigmoid function of intermediate dynamic model | $\rho_{K_{Ca},1}$ | 2.2166e-07 mV |
| Constant for sigmoid function of intermediate dynamic model | $\rho_{K_{Ca},2}$ | 4.7923e-08 mV ⁻¹ |

where e is the objective function value, ω_s a weight used to punish any discrepancy in the number of action potentials, and e_t the total time error between simulated and measured action potentials:

$$e_t = \sum_{T, \hat{T} \in \mathbb{T}} \begin{cases} \sum_{t \in T} \min_{\hat{t} \in \hat{T}} |t - \hat{t}|^2 & |T| \geq |\hat{T}| \\ \sum_{\hat{t} \in \hat{T}} \min_{t \in T} |t - \hat{t}|^2 & |T| < |\hat{T}| \end{cases} \quad (12)$$

where \mathbb{T} is the set of all pairs of T, \hat{T} , where T and \hat{T} are the sets of all measured and simulated action potentials, respectively, during a single current step. The list of all optimized parameters used in the model is shown in **Table 2**.

Subsynaptic Local Calcium Activity

In the learning process, excitatory synaptic weight learning was driven by the calcium activity in the main compartment of the cuneate neuron (i.e., as calculated by the calcium dynamic model above) in combination with the calcium activity in the individual synapses. An essential component of this combination is the intensity of activation of the individual synapses. According to the learning rule that we used (see below), a synapse that fires at high frequency with a high degree of correlation with the main compartment total calcium activity ($A_{tot}^{Ca^{2+}} = k[Ca^{2+}]$, where k is an arbitrary constant that is here assumed to be 1), will be “rewarded” as due to the strong correlation with the learning signal $A_{tot}^{Ca^{2+}}$. Conversely, strong firing in a synapse in relation to low or zero $A_{tot}^{Ca^{2+}}$ will be “punished” (i.e., similar to the classical BCM rule for Hebbian plasticity) (Bienenstock et al., 1982). Therefore, the *local calcium time constants* ($\tau_{Ca_{loc}^{2+}}$,

Table 1), defining the temporal properties of the calcium signal in the local space underneath each individual synapse, play a major role in the learning process (the local postsynaptic calcium activity can be considered an analogy with the calcium activity in a local dendritic spine; Koester and Sakmann, 1998; Tigaret et al., 2016). The learning rule critically depends on this time constant. For instance, if $\tau_{Ca_{loc}^{2+}}$ time constants are too high, the rewarding effects on synapses that have a high degree of correlation with the $A_{loc}^{Ca^{2+}}$ will be lost. However, as there is no data on the relevant time constants in the cuneate neurons *in vivo*, we had to make assumptions of the values of this time constant. In order to avoid pitfalls in relation to this assumption, we studied a range of time constants for $A_{loc}^{Ca^{2+}}$ (**Table 1**) during the CN learning process.

For each synapse, each input spike at time t^* contributes to the subsynaptic spine calcium concentration, the time course of which is given by the kernel (Mazzoni et al., 2008) of Equation 13,

$$\alpha = \frac{\tau_l}{\tau_d - \tau_r}$$

$$\Delta A_{loc}^{Ca^{2+}}(t) = \alpha * \left[\exp\left(-\frac{t - \tau_l - t^*}{\tau_d}\right) - \exp\left(-\frac{t - \tau_l - t^*}{\tau_r}\right) \right] \quad (13)$$

In its basic configuration, the parameters describing the relative local calcium concentration (or activity), are the decay time $\tau_d = 12.5$ ms and the rise time $\tau_r = 4$ ms multiplied with a constant $\tau_l = 21$ ms (which is a constant to calculate the ratio) for $\tau_{Ca_{loc}^{2+}} = 100\%$ (**Table 1**). τ_l is the latency time which is zero in our case. The initial values chosen were derived from our assumption that the time course of the slow afterhyperpolarization of the cuneate neuron spike (**Figure 1B**), which is known to reflect the activation of calcium-dependent potassium channels, matched the time course of the calcium concentration induced in the synapse. This resulted in a somewhat faster but still comparable time course of spine calcium than reported for single spines *in vitro* (Tigaret et al., 2016), but the rise time of our subsynaptic calcium signal was slower than in previous simulations of the

properties of calcium-dependent learning (Graupner and Brunel, 2012). As the temporal properties of this calcium signal clearly were assumptions with large uncertainty, we tested a wide range of different values for these parameters (Table 1). In order to achieve supralinearity in the local calcium activity (Wang et al., 2000), we used an approximative approach of subtracting an offset from the local calcium signal (an offset corresponding to 75% of the peak activity of the single pulse activation was subtracted) and this was the value of the local calcium activity ($A_{loc}^{Ca^{2+}}$). With this approach, repetitive activation of the same synapse resulted in a supralinear increase in the intensity of the local calcium activity depending on the frequency of the PA afferent activity for that synapse.

Synaptic Weights

The synaptic weight in our model was a gain factor ranging between 0.001 and 1, where 1 signified the maximum weight of a synapse. As there is no information on perinatal synaptic weights for the CNs, we needed to make assumptions. The first assumption was that synapses have different initial synaptic weights, or seed weights. The second assumption was that all synapses had initial non-zero up to medium strong synaptic seed weights. In our model, the distribution of synaptic weights across the primary afferent synapses of the CN model, or the *initial excitatory synaptic weights* ($w_{init,exc}$), were normal distributions ranging between 0.001 and 0.5 across the 80 primary afferent inputs. We used 5 different pseudo-randomized initial weight distributions, referred to as “Seed weights 1–5.” Pseudo-randomization here implies that the distribution is randomized but that the same distribution is kept constant across different learning process runs. This had the advantage that the effects of specific intrinsic CN configurations (see “Variations of initial intrinsic CN parameters” below) could be tested for the same initial weight distributions (Figure 12).

Synaptic inhibition was simulated as being provided by 80 independent interneurons that were each directly activated by one out of the 80 PA afferents available in our simulated system. Each PA synapse had the same weight on its targeted inhibitory interneuron. The collective, or total, *inhibitory synaptic weight* ($w_{init,inh}$) was initially set to 0.125 evenly distributed across all the inhibitory synapses between the interneurons and the CN neuron they contacted, meaning that each PA synapse provided equally weighted inhibition to the CN neuron (as suggested by our biological data accounted for in the Results).

Sensory Inputs

Our aim was to simulate the learning process in the cuneate neurons driven by simulated sensory activation of the PAs. The main idea was to simulate a varied set of interactions between the skin and the physical world, and let the resulting spatiotemporal patterns of skin sensor activation determine the outcome of the learning process in the cuneate neurons. Rather than designing an arbitrary set of spatiotemporal patterns of skin sensor activations, we wanted to use a physical model of a fingertip to generate the spatiotemporal spike patterns of PA input that the cuneate neurons of our model (CNs) learned from. This is because across the different kinds of interactions that

the skin may experience, there may be relationships between the skin sensors that are not easily calculated across all conceivable conditions/interactions.

Bionic Fingertip

To generate the sensor patterns, we used a set of touch protocols based on different stimulus conditions (Table S1). The sensory fingertip comprises a 2×2 array of Micro Electro Mechanical System (MEMS) based bio-inspired tactile sensors (Oddo et al., 2011) to generate spatio-temporal sensory input patterns (Figure S2). Each individual sensor comprises a four transducing piezoresistors mesh (totaling 16 sensory channels for each fingertip), arranged in cross-shaped fashion able to generate precise response magnitudes for both normal and tangential forces, applied across the surface of the sensor (Beccai et al., 2005; Oddo et al., 2007). However, only four of the 16 sensor channels were sufficiently dynamically sensitive to the range of forces arising for the stimuli used to be used in the present experiment. We created 80 PA sensory input channels from these four sensors' analog data (Figure 4) by multiplexing them with multiple neuron models and signal processing as explained below. Each of these 80 PA sensor spike output patterns were considered a unique PA signal provided as synaptic input to the CNs, where sensor#1 was used to create PA input #1-20, sensor #2 to create PA input #21-40 and so on.

The normalized analog output of the tactile sensor is fed as virtual current input to a fine-tuned Izhikevich neuron models (Izhikevich, 2003) in-order to achieve the spatiotemporal spike output (Figure S2) as described previously (Oddo et al., 2016; Rongala et al., 2017). The Izhikevich model was chosen in order to reproduce the adaptation dynamics, that is a characteristic of mechanoreceptors (Johansson and Flanagan, 2009). Per the Izhikevich model, the membrane potential v and the adaptation variable u were updated via the following nonlinear differential equations discretized using Euler's method:

$$\begin{aligned}\dot{v} &= Av^2 + Bv + C - u + \frac{I_{input}}{C_m} \\ \dot{u} &= a(bv - u)\end{aligned}\quad (14)$$

When the membrane potential reached the spike depolarization threshold of 30 mV, one spike was produced followed by a reset:

$$\text{if } v \geq 30 \text{ mV, then } \begin{cases} v \leftarrow c \\ u \leftarrow u + d \end{cases} \quad (15)$$

The A , B , C and the spiking threshold are the standard ones of the Izhikevich artificial neuron model, whereas the parameters a , b , c and d were selected (Table S2) to allow a regular spiking behavior.

From the existing 16 sensory channels, we consider 4 active channels (2, 5, 12, and 15) (Figure S2). We further derivated the analog sensor data to mimic both Merkel Slowly Adapting (SA) type I mechanoreceptors, sensitive to the sustained level of mechanical interactions, and Meissner Fast Adapting (FA) type I mechanoreceptors, mostly sensitive to dynamic changes (Vallbo and Johansson, 1984; Abaira and Ginty, 2013). For each physical stimulus, the stimulation was repeated five times and the

corresponding consecutive five analog signals were considered as the response of a unique sensor. As we had four physical sensors, this procedure thus generated 20 analog unique sensory signals per physical stimulus. In addition, each analog sensor signal was derivated to obtain a total of 40 different analog sensory signals (Figure 4). Moreover, by implementing the Izhikevich neuron model (Izhikevich, 2003) with two different settings, we obtained a total of 80 different PA spike output patterns for each physical stimulus.

For the learning process, we used the sensor outputs obtained using five different physical stimuli (Figure 4), and in addition the PA spike output responses to five other physical stimuli were provided as “non-training” stimuli (see Results text).

Learning Protocol

In order to induce learning in the CNs, we used a series of 1,500 stimulus presentations. Each of the 1,500 stimuli hence corresponded to a spatiotemporal pattern of PA spike inputs (Figure 4), where all of the 80 PAs were activated during each stimulus presentation. The 1500 presentations were generated from the 5 physical stimulus presentations. Each stimulus presentation was hence repeated 300 times. Rather than feeding the system with identical spatiotemporal spike patterns for each of these 300 repetitions, we added a spike time jitter to all tactile sensor spike output responses. Gaussian noise with zero mean and standard deviation σ ($\sigma = 5$ ms) was added to the individual spike times of each PA. The motivation for this injection of noise rather than repeating identical patterns of PA spike responses was because we observed it to make the learning more robust. It also allowed an identification of the spread of learning outcome (end weight “landscapes”) for each model setting (Figures 5B,C).

Excitatory Synaptic Weight Learning

During the learning process, the individual excitatory synaptic weights were gradually learnt, i.e., there was an alteration in the weight of each synapse. All the synaptic weights were updated after each stimulus presentation. The weight change for the individual excitatory synapse (i) is given by Equation 16.

$$w_{exc,i} = \int_{t_0}^{t_{\max}} \left\{ \left(A_{tot}^{Ca^{2+}}(t) - (Avg_{A_{tot}^{Ca^{2+}}} \cdot Syn_{EQ}) \right) \cdot A_{loc}^{Ca^{2+}}(t) \right\} \cdot K \cdot dt \quad (16)$$

The driving force for the net synaptic weight change ($w_{exc,i}$) is given by the integral of the correlation between main compartment total calcium ($A_{tot}^{Ca^{2+}}$) and local calcium activity for each synapse ($A_{loc}^{Ca^{2+}}$) from t_0 to t_{\max} (corresponding to the start and end of each stimulus presentation). The $A_{tot}^{Ca^{2+}}$ is offset to zero by the *Learning threshold* (Figure 3D), where $A_{tot}^{Ca^{2+}}$ above the Learning threshold is in the positive zone (potentiation) and below is the negative zone (depression) (similar to Graupner and Brunel, 2012). In other words, the main compartment calcium activity is a gate for the plastic reaction in the local synaptic compartment, deciding whether potentiation or depression should occur. Therefore, the product of the counterbalanced

$A_{tot}^{Ca^{2+}}$ and individual synapse $A_{loc}^{Ca^{2+}}$ (Figures 3E–G) defines the net learning drive for each respective synapse as a function over time (Figures 3F–H). The value of the time integral of the net learning drive attained at t_{\max} decides to what extent each specific synapse should be potentiated (Figure 3F) or depressed (Figure 3H). The strength of the potentiation/depression for that individual synapse is further multiplied with a constant given by a sigmoid function (Figure 3I) of the current synaptic weight ($w_{exc,i}$), a constant which we called the synaptic weight compensation. This is motivated by that the insertion of a synaptic receptor ion channel in the synaptic membrane can be regarded as a chemical reaction, where the addition of a new channel will become less likely the higher the number of ion channels already inserted and vice versa. The sigmoid function is defined by $S(t) = \frac{1}{1+e^{-t}}$, with an arbitrarily chosen steepness gain of 0.005.

The *Learning threshold* is given by the product of the average total calcium ($Avg_{A_{tot}^{Ca^{2+}}}$) and synaptic equilibrium (Syn_{EQ}) where $Avg_{A_{tot}^{Ca^{2+}}}$ is the mean of $A_{tot}^{Ca^{2+}}$ across the last three consecutive stimulus presentations. The averaging was required to avoid instability in the learning and could in principle correspond to the dampening effect of the time required in biological systems for protein synthesis and/or ion channel insertion. The Syn_{EQ} is a gain factor, used to attain a homeostatic synaptic plasticity (Turrigiano and Nelson, 2004; Turrigiano, 2011) to keep the sum of the excitatory synaptic weights in control. It is defined as a linear function of the total excitatory synaptic weight ($\sum w_{exc}$), with a dual slope having zero point preset to $SetPoint_{\sum w_{exc}}$ (in our model, that point is set to 10). The slopes intercepts for this linear function are defined such that, when total excitatory synaptic weight is 10 the Syn_{EQ} is 1. When $\sum w_{exc}$ is >10 , the slope is 0.12, whereas for $\sum w_{exc} < 10$, the slope is 0.04. The differences in slopes were necessary to prevent neurons from being stuck in a depressed state, and to prevent unstable, rapid potentiation once above the set point. In principle, the slope differences can be regarded as corresponding to that the insertion and the removal of synaptic conductances in biology is handled by partly separate chemical reactions (Jörntell and Hansel, 2006).

Inhibitory Synaptic Weight Learning

In model CNs without adaptation of synaptic inhibition, we observed that synaptic weight changes in the PA synapses tended to make the CNs unstable, which degraded learning stability (Figure 10). Instability was attained gradually during the learning process and typically resulted in that either the CN had excessive calcium activity or no calcium activity at all. In such cases, the CN would often swing between these two extremities several times during the learning process. We found that it was important that the model system prevented the CNs from entering such unstable states and a main effective regulator was found to be gradual adaptation of the total inhibitory synaptic weight around a set point of the total calcium activity of the neuron.

Therefore, during the learning process, after each stimulus presentation, also the total inhibitory weight was adapted toward a set point, which was defined by the activity of the calcium

spike rate, closely related to $A_{tot}^{Ca^{2+}}$. A high calcium activity during the stimulus presentations was countered by an increase in total inhibitory synaptic weight, whereas a low calcium activity was countered by a decrease in this weight. A plastic regulation of the weight of inhibitory synapses against postsynaptic calcium activity or postsynaptic calcium-dependent bursting activity has previously been found in various neurons across the brain (Kawaguchi et al., 2011; Hulme and Connelly, 2014; Lourenço et al., 2014). In our model, we found this feature to prevent overexcitation in the simulated CNs as the learning of the synaptic weights progressed. A function with dual linear slope was used to define the rate of *inhibitory weight change* with respect to the calcium spike rate. Inhibitory weight change is summed with the existing inhibitory synaptic weights (w_{inh}). The *calcium activity set point* ($SetPoint_{Ca^{2+}}$) (Table 1) is the critical factor that defines the calcium spike rate, around which the inhibitory weight adapts to keep the system in balance. These slope functions are built zeroing from the preset point ($SetPoint_{Ca^{2+}}$), where the range of weight change is set between -0.01 and 0.01 for calcium spike rates between 0 and 200 Hz, respectively. In order to dampen the rate of adaptation, we used a moving average of the calcium spike rate across the last three stimulus presentations as the input to the adaptation.

Adaptation of the total inhibitory synaptic weights was implemented because the change in the weights of the excitatory PA synapses on the CN neuron could lead to large changes in the levels of the LVA (voltage-activated calcium channel) activity, which in turn led to unstable learning (as in Figure 10). Adaptation of the inhibitory synaptic weights balanced the LVA activity and resulted in a maintained stable learning process. All adaptation of the weight of the synaptic inhibition was evenly distributed across all the inhibitory synapses. Calcium-dependent potentiation of inhibitory synapses has previously been found to be confined to the inhibitory synapses that were active during the calcium activity (Kawaguchi et al., 2011; Hulme and Connelly, 2014; Lourenço et al., 2014)—indeed, in our simulated set of inhibitory synapses, all of them were active under all stimulus presentations as described above.

Variations of Initial Intrinsic CN Parameters

In addition to testing the effects of excitatory synaptic seed weight distributions on the outcome of the learning process (see below) we also wanted to test the effects of intrinsic CN parameters. Moreover, the values of these parameters to some extent relied on assumptions, and we wanted to know the sensitivity of the model to these assumptions. Therefore, in separate simulation runs, some of the intrinsic CN parameters were varied as described by Table 1. All of the initial parameters were kept constant during the learning process.

MODEL DATA ANALYSIS

Correlation Index

The *correlation index* measure (Figure 5D) was used to quantify the degree of correlation between the spiking activities of two or more PAs while being provided with sensory inputs. We compared PAs whose synapses after learning ended up as High

End Weight (HEW) synapses with high seed weight synapses that ended up as Low End Weight (LEW) synapses.

To compute this measure, we considered 10 HEW (green bars in Figure 5C) and 10 LEW synapses (red bars in Figure 5B). We evaluated the spike trains for these 20 PAs across all the five stimuli (Figure 4) by means of Victor-Purpura distance (VPd) (Victor and Purpura, 1996) spike train metrics. VPd gives a measure of the similarity between two spike trains by measuring the minimum cost necessary to transform one spike pattern into the other. The distance calculation is based on two rules, (i) adding/deleting a spike ($cost = 1$) and; (ii) shifting the spike by an interval of Δt ($cost = q \cdot \Delta t$, in our simulation $q = 10/s$). By making comparisons between all the primary afferent spike trains evoked by different stimuli, we obtained a matrix of comparisons between all of the stimuli used (Rongala et al., 2017). For each neuron configuration, these matrices were used to compute the correlation index value for sensors with HEW synapses (Figure 5C, green) as given by computing the average VPd across all the 10 synapses with HEW for all the 5 stimuli. The same procedure was carried out to calculate the correlation index value for sensors with LEW synapses (Figure 5C, red). The difference between correlation index values of LEW and HEW sensors was the *correlation index difference* (Figure 13).

Correlations Between Synaptic Responses

The correlation measure (Figures 7, 8) was used to compute how correlated the synaptic responses were across different learning conditions. To compute this measure, we consider all the 80 synapses. We convolute the spike trains of all 80 PAs using the same EPSP time constants as in CN *in vivo* recordings (Bengtsson et al., 2013). Further we multiply each of these convoluted signals with the respective synaptic weights of the corresponding PA. The sum of all the 80 weighted convoluted signals was the simulated intracellular signal displayed (Figures 7, 8). The correlation between two simulated intracellular signals is computed with the inbuilt MATLAB® function *xcorr* (with zero lag).

Multi-Dimensional Scaling

To further illustrate the specific distribution of synaptic weights, we used the Classical multi-dimensional scaling (MDS) method (*cmdscale*, an inbuilt MATLAB® function). The distribution of weights (w_{exc}) across the 80 PA synapses is here denoted the synaptic weight landscape. Using MDS, the differences between the synaptic landscapes of two or more CNs were visualized as distances in two-dimensional displays (Figures 9A,C,10A). The input distance vector to multi-dimensional scaling is calculated as a simple Euclidian distance between synaptic weight landscapes.

Computation of the Sparseness of the Synaptic Weight Distribution

We also measured the degree of dispersion of synaptic weights, or the sparseness of the synaptic weights, among the 80 available PA synapses (Figures 9B,D, 10B). For this purpose, we took the measured *synaptic weight sparseness* using the ratio between the l_2 and l_1 norm of the weight vector (Yin et al., 2014). This measure will report its minimal value when all synapses have

exactly the same weight and a value of one when one synapse has maximum weight and all other synapses have zero weight. It was used to track the evolution of the synaptic weight dispersion during consecutive stimulus presentations and was therefore also an indicator of the stability of the learning.

Statistical Tests

After the learning process, the correlation index of the High End Weight (HEW) PA synapses ($N = 10$) was compared to that of the Low End Weight (LEW) PA synapses ($N = 10$) for each CN configuration using paired t -test (these distributions were on visual inspection comparable to normal distributions, see **Figure 5D**). The changes in correlation between the synaptic responses, of different CNs to the same stimulus and of the same CN to different stimuli, induced by training were statistically quantified using the paired, two-sided Wilcoxon signed rank test.

RESULTS

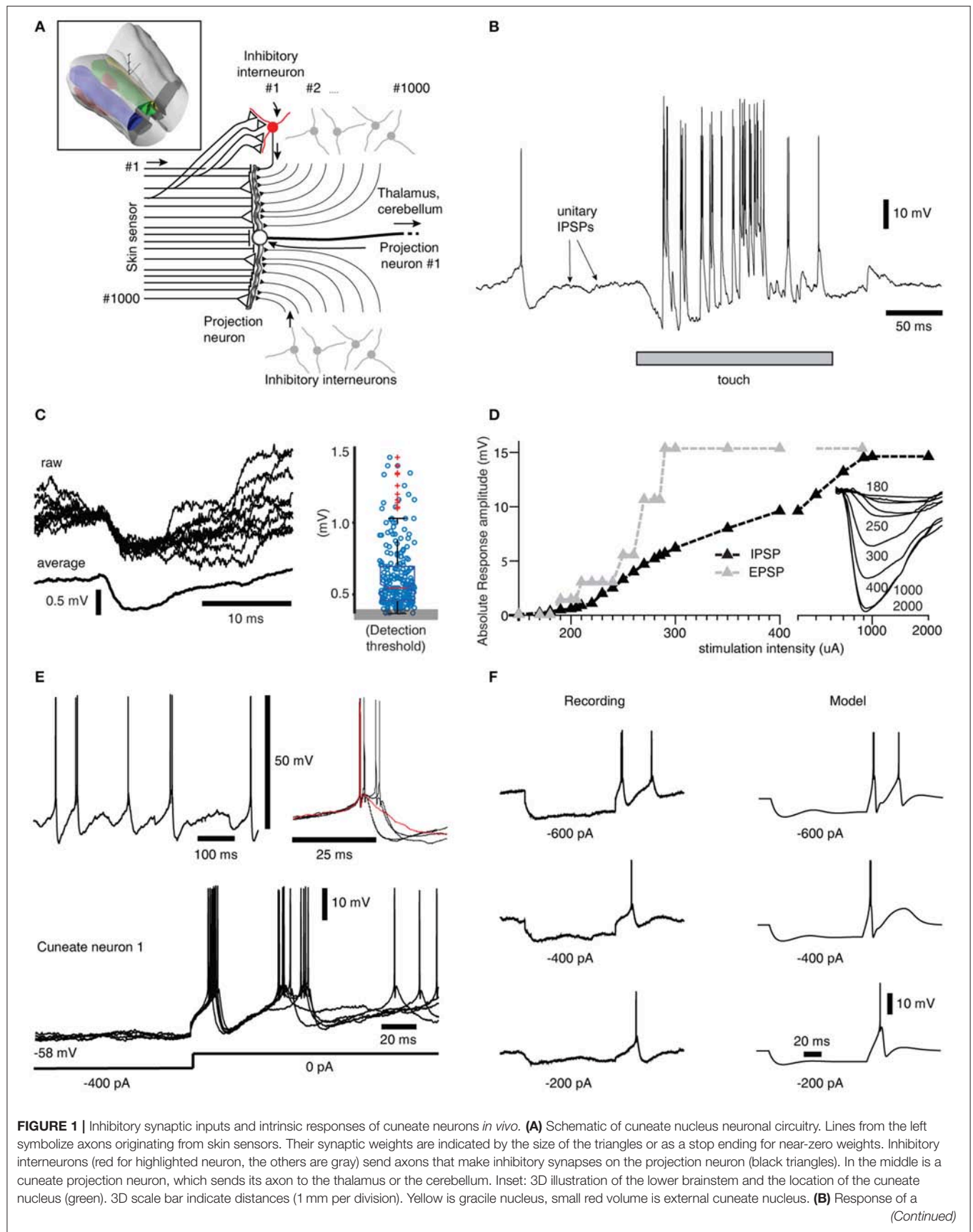
Inhibitory Synaptic Inputs and Intrinsic Responses of Cuneate Neurons *in Vivo*

To support the construction of our model, we started out by extending a previous characterization of the projection neurons of the cuneate nucleus in the decerebrate cat (Bengtsson et al., 2013) to also include their inhibitory synaptic inputs and intrinsic membrane responses, using a set of *in vivo* whole cell intracellular recordings from projection neurons ($N = 15$) and interneurons ($N = 8$) (**Figure 1A**). A touch to the receptive field of a cuneate projection neuron activated both excitatory and inhibitory synaptic inputs (**Figures 1A,B**) and the interneurons, which are responsible for synaptic inhibition evoked by skin stimulation in this preparation (Bengtsson et al., 2013). Spontaneous unitary inhibitory postsynaptic potentials (IPSPs), presumably driven by spontaneous interneuron spiking, were very small (**Figures 1B,C**) (the average median IPSP amplitude was -0.55 ± 0.08 mV, recorded from $N = 15$ cuneate projection neurons). In fact, this amplitude is an overestimate since many of the apparent IPSPs were too small to be detected from baseline noise using our template based identification method. In contrast, maximal evoked compound IPSPs (evoked from outside the receptive field of the excitatory input, see Bengtsson et al., 2013) were large (-14.3 ± 2.1 mV) and recruited in a continuous, gradable fashion (**Figure 1D**). Such maximal compound IPSPs had a response onset latency of 6.1 ± 0.7 ms, which is about 1.0 ms longer than the latency time of primary afferent EPSPs in the same type of preparation (Bengtsson et al., 2013). This observation strongly suggests that the compound IPSPs were due to primary afferent activation of the inhibitory interneurons. Together, these findings indicated that a high number of interneurons (>30 , but possibly 100's) innervated each projection neuron with relatively uniformly low weighted inhibitory synapses.

A strong involvement of intrinsic voltage-activated conductances in shaping the membrane potential trajectory over time was suggested by the subthreshold spontaneous activity of the cuneate projection neurons recorded near resting potential (**Figure 1E**). Note the doublets, triplets or quadruplets

of spike firing, which were observed in all projection neurons, but none of the interneurons. Occasional single spike firing events dramatically altered the spike afterhyperpolarization phase (red trace in **Figure 1E**), which further suggested the presence of intrinsic membrane potential dynamics. Indeed, using current clamp to generate temporary hyperpolarization of the membrane potential resulted in strong rebound excitation (**Figure 1E**), which demonstrates the contribution of such active intrinsic conductances. Similar intrinsic responses were recorded in all cuneate projection neurons when hyperpolarized by at least -200 pA for at least 200 ms ($N = 15$). Since such intrinsic responses can be expected to be an important part of defining the time course of calcium influx into the neuron, which in turn will be important for its learning process during a time-varying synaptic input, an important component of our full model below was the “intermediate dynamics” model of the of the cuneate projection neurons. We observed that there were relatively wide differences in the intensity and the speed of the intrinsic responses (**Figure 1E**) between the cuneate projection neurons. Therefore, we designed the intermediate dynamics model of these membrane potential dynamics against one of our recorded cuneate projection neurons, with the primary aim of approximating its overall dynamics across a range of conditions rather than focusing on capturing its behavior under any single condition exactly (for the full model, we later also will show model experiments in which parameters influencing the intermediate dynamics are adjusted to modify the intrinsic responses of the cuneate projection neurons, showing that model behavior was robust across a range of intermediate dynamics). Our intermediate dynamics model approximated the observed membrane potential dynamics well across a range of hyperpolarizations (**Figure 1F**). The model also resulted in a reproduction at least of the overall dynamics for responses evoked by touch (**Figure S1**).

In order to verify that the recorded IPSPs (**Figure 1**) could be generated by the local interneurons, we made intracellular recordings also from these neurons. Intracellular recordings were identified as projection neurons and interneurons based on their characteristic spike shapes (**Figure 2A**). The spontaneous spike firing frequencies were 11 ± 4.8 Hz (mean \pm sd.) vs. 8.8 ± 2.2 Hz for projection neurons ($N = 15$) and interneurons ($N = 8$), respectively. Interneurons responded well to touch to the skin (**Figure 2B**) and on electrical skin stimulation (**Figure 2C**). The EPSPs evoked by electrical skin stimulation in the interneurons were considered monosynaptic based on the response latency time and the low variability of the EPSPs (Bengtsson et al., 2013; **Figure 2C**). Based on a qualitative analysis of the extent of their receptive fields on the skin (**Figure 2B**), interneurons were found to have much wider excitatory receptive fields than the cuneate projection neurons (which were previously quantitatively defined in Bengtsson et al., 2013). Combined with the rapid responses of the interneurons to PA synaptic input (**Figure 2C**), these observations made it plausible that their activation was responsible for the compound IPSPs recorded in the cuneate projection neurons on stimulation within or in the vicinity of their receptive fields (**Figure 1D**). The apparent absence of intrinsic regenerative responses to skin stimulation



(Continued)

FIGURE 1 | projection neuron *in vivo* to a light skin touch within its receptive area. Arrows indicate putative spontaneous IPSPs, which are so small they are barely visible at this magnification of the voltage trace. **(C)** At a different magnification, examples of spontaneous IPSPs from one cuneate projection neuron are superimposed and averaged to the left. The peak amplitudes of 500 consecutive spontaneous IPSPs are shown in the box plot at right. **(D)** The gradual recruitment of summated, or compound, IPSPs with increased electrical stimulation intensity to a skin area adjacent to the excitatory receptive skin area of a sample projection neuron (black curve). Gray curve illustrates corresponding recruitment of unitary EPSPs (Bengtsson et al., 2013). Inset traces, average evoked IPSPs (averages of 20–50 repetitions) at different stimulation intensities. **(E)** Spontaneous activity of a projection neuron with zoomed-in, superimposed spikes to the right. Red trace indicates a case of a spontaneous single spike event, whereas most spontaneous firing occurred in doublets with an associated difference in voltage trajectory after the spike. Bottom, examples of rebound responses elicited by release from hyperpolarizing current injections (−400 pA for 200 ms). **(F)** Comparison between the rebound responses of a cuneate neuron *in vivo* and the CN model.

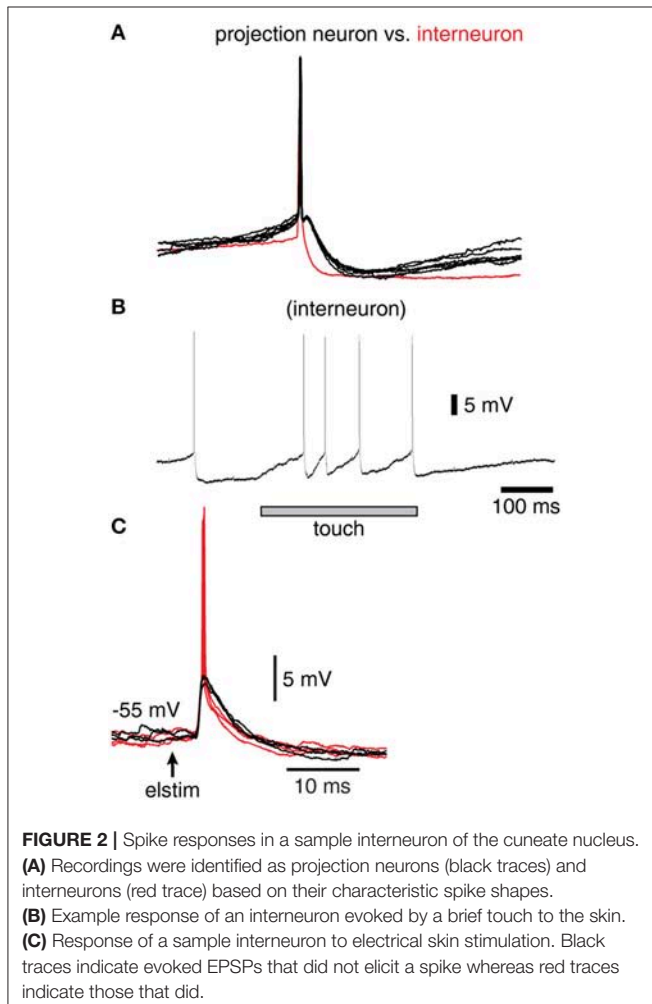


FIGURE 2 | Spike responses in a sample interneuron of the cuneate nucleus. **(A)** Recordings were identified as projection neurons (black traces) and interneurons (red trace) based on their characteristic spike shapes. **(B)** Example response of an interneuron evoked by a brief touch to the skin. **(C)** Response of a sample interneuron to electrical skin stimulation. Black traces indicate evoked EPSPs that did not elicit a spike whereas red traces indicate those that did.

in the interneurons (Figure 2B) suggested the function of the cuneate interneurons to be a linear transfer of PA input, inverted to IPSPs, to the projection neurons. These findings motivated our simplification of the inhibitory synaptic inputs to the cuneate projection neurons to be modeled as a set of unitary weight inhibitory synaptic inputs directly generated by the spikes of the individual PAs (Figures 3A,B).

Functional Structure of the CN Model

In our integrated cuneate model, the biological sensorized skin was replaced with a bionic fingertip (Oddo et al., 2016; Figure 3A

and Figure S2). The model cuneate projection neuron (CN) was composed of the intermediate dynamics model described above (Figure 1F), that implemented input- and time-varying intrinsic responsiveness, and the excitatory and inhibitory synaptic inputs from the sensors that drove the activation of the intermediate dynamics of the CN (“Total calcium activity” in Figure 3B). The factor g_{\max} allowed an adjustment of the ratio between the synaptic conductances and the background, leak, conductance, which is later in the paper used for simulating CNs with different input resistances or sizes. The rest of the diagram in Figure 3B indicates adaptation mechanisms for the excitatory and inhibitory synaptic weights, which implemented a Hebbian-type of learning combined with synaptic weight scaling as described below.

Depending on the correlation between the calcium activity in the main compartment and in the individual synaptic spaces (Figures 3C,D), the weight of each excitatory synapse was updated after each stimulus presentation (Figures 3E–H). To illustrate this process, Figure 3E shows that the local synaptic calcium activity crossed the learning threshold twice in this example. But for calculating the learning signal, also the calcium activity in the main compartment (Figure 3D) was taken into account. For the first episode of suprathreshold calcium activity in the synapse (Figure 3E), the calcium activity in the main compartment was in the “positive zone,” i.e., sufficiently high to permit potentiation of the synaptic weight. Therefore, this first episode made the net learning drive of this synapse positive (Figure 3F). The second episode of suprathreshold calcium elevation in the synapse (Figure 3E) instead coincided with calcium activity in the main compartment being partly in the “negative zone” (Figure 3D). Therefore, the net learning drive for this episode was partly negative (Figure 3F). The net learning effect of each stimulus presentation and each synapse was the integral of all of these episodes, which in this case ended up positive (Figure 3F). For another synapse, the suprathreshold calcium activity (Figure 3G) mostly coincided with main compartment calcium activity being in the negative zone (Figure 3D), which resulted in a negative integral of the net learning drive (Figure 3H).

For each update of synaptic weights, the weight of the synapse itself was an additional factor used to scale the synaptic weight change (Figure 3I; synaptic weight compensation in Figure 3B) (Bi and Poo, 1998). Altogether, this architecture resulted in a Hebbian form of plasticity (Hebb, 1949). The end result was a form of plasticity that had properties being related to spike-time dependent plasticity (STDP) (Markram

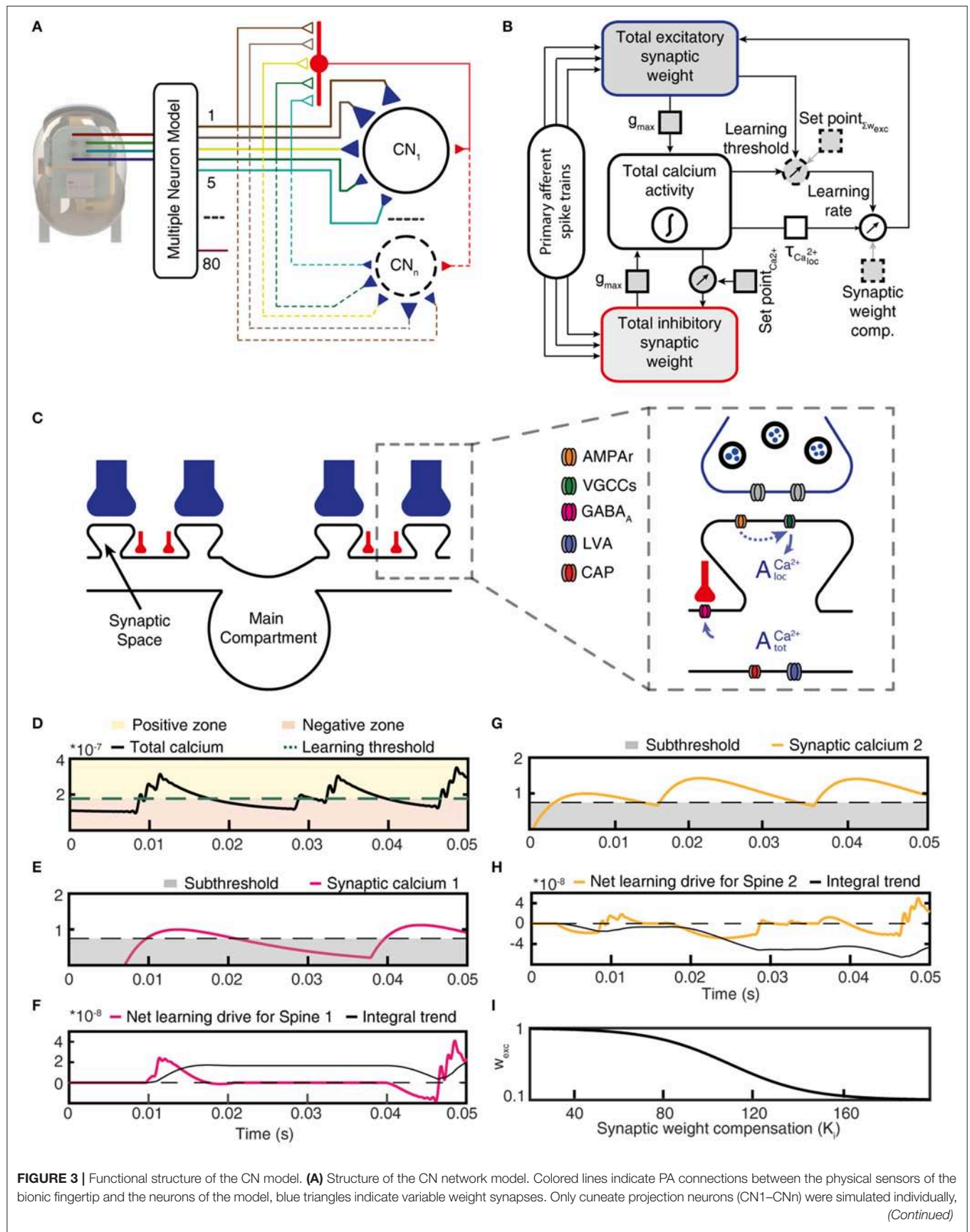


FIGURE 3 | Functional structure of the CN model. **(A)** Structure of the CN network model. Colored lines indicate PA connections between the physical sensors of the bionic fingertip and the neurons of the model, blue triangles indicate variable weight synapses. Only cuneate projection neurons (CN1–CNn) were simulated individually, (Continued)

FIGURE 3 | where the number identifies a specific initial synaptic weight configuration (see **Figure 5B**). PA inputs were also provided to the CNs as a lump inhibitory synaptic input via an interneuron (red). **(B)** Graphic representation of the functional structure of the CN model. Components indicated with a dashed outline were the only elements with fixed parameters, whereas parameters with solid outlines were adjusted in the later part of this paper to simulate CNs with different intrinsic properties. **(C)** Subcellular factors involved in the synaptic plasticity of the CN, with variable weight PA synapses (blue) and inhibitory synapses (red). The CN neuron is divided into a main compartment, with reactive LVA and CAP conductances and synaptic spaces containing VGCCs (Higley and Sabatini, 2012) and a variable number of AMPA:s. AMPA, excitatory glutamate receptors; VGCCs, voltage gated calcium channels; GABA_A, inhibitory synaptic receptors; LVA, low-threshold voltage activated calcium channels; CAP, calcium-dependent potassium channels. **(D)** The calcium activity of the main compartment varied over time due to synaptic input and the responses they elicited via the intermediate dynamics model of the CN. The level of the calcium activity, in relationship to the learning threshold, defined when the cell was in the positive zone (i.e., potentiation mode) or in the negative zone (depression mode). **(E)** The local calcium activity threshold used to define the eligibility for plasticity for each PA synapse. **(F)** The net learning drive for the PA synapse varied depending on the temporal correlation between the zero-offset main compartment calcium activity and the local, or synapse space, calcium activity. **(G)** The activity of another PA synapse under the same stimulus presentation and; **(H)** its net learning drive. **(I)** The synaptic weight compensation constant that was multiplied with the integral net learning drive to calculate the final weight change per stimulus presentation. For **(D,E,G)**, note that the y axes indicate the relative magnitude of calcium signals for each compartment and not an actual estimation of the calcium concentration.

et al., 1997; Graupner and Brunel, 2012) but being less sharply dependent on the exact spike timing (Helias et al., 2008). The motivation for taking this approach to formulate the driving forces for the learning rule was to let the dynamics of the cellular learning signal, and its shaping by the integration of peripheral synaptic input have its origin in biological data recorded from cuneate projection neurons *in vivo* (**Figures 1E,F**) rather than in assumptions made for other learning systems. We believe that overall, net learning effects are comparable to those obtained under some settings of those previous models (Graupner and Brunel, 2012) (Discussion) but more specifically constrained to the effects that might arise in the cuneate projection neurons.

The integrated model also used two separate feedback regulatory systems. First, the total inhibitory synaptic weight was updated based on the total calcium activity, according to a fixed set point (**Figure 3B**). Adaptation of the total inhibitory synaptic weights was implemented because we found that the change in the weights of the excitatory PA synapses on the CN neuron could lead to large changes in the levels of activity in the voltage-activated calcium channels, which in turn led to unstable learning. A plastic regulation of the weight of inhibitory synapses against postsynaptic calcium activity or postsynaptic calcium-dependent bursting activity has previously been found in various neurons across the brain (Kawaguchi et al., 2011; Hulme and Connelly, 2014; Lourenço et al., 2014).

Secondly, $SetPoint_{\sum w_{exc}}$ is a control signal used to implement a homeostatic synaptic plasticity mechanisms (Turrigiano and Nelson, 2004; Turrigiano, 2011) through which the sum of the excitatory synaptic weights is kept under control. The total excitatory synaptic weight was driven toward this set point by adjusting the learning threshold for synaptic potentiation vs. depression (**Figure 3B**; positive vs. negative zone in **Figure 3D**). Hence, the propensity for LTP or LTD was affected by the current total synaptic weight and the effect of the learning threshold was therefore a synaptic weight scaling. The set point of the learning threshold (**Figure 3B**) is the fixed sum of the excitatory synaptic weights toward which the adaptation of the learning threshold strives to bring the system. Further details and motivations are given in Methods.

Synaptic Weight Changes During the Learning Process

The sensorized bionic fingertip was used to provide the CN with training data. The bionic fingertip provided the important feature of a system of PA sensors where there is a consistent relationship between the activation of the different sensors across different conditions or tactile experiences. The CN learning process consisted of 1,500 presentations of five training stimuli, each activating all of the 80 PA sensory inputs but in different spatiotemporal patterns (**Figure 4**), presented in a pseudorandom order. The training stimuli consisted in three touch-an-slide conditions and in two dynamic indentation stimuli (**Figure 4**). During the learning process, the gradual transition from initial, or “seed,” synaptic weights to the final distribution of synaptic weights (“end weight”) was monitored (**Figure 5A**). Interestingly, the weight of a synapse could for example evolve from a very low seed weight to a high end weight (green thick line), or from high seed weight to near-zero end weight (red thick line) and any intermediate or mixed development. Such examples showed that the fate of an individual synaptic weight during the learning process was not depending on its starting point but suggested some underlying functional principle.

The learning process resulted in a transformation of the initial random distribution of low-moderate weight synapses (seed weight, SW) (**Figure 5B**) to a highly skewed distribution with a few high weight synapses (end weight, EW) (**Figure 5C**), similar to cuneate neurons in adult animals (Bengtsson et al., 2013). We simulated CNs with five different pseudo-randomized SWs, which below are referred to as CN1-5, based on the assumption that initial random synaptic weight distributions likely differ between biological cuneate neurons in the same animal. For each CN, there was at the end of the learning process a unique end weight distribution (EW), dominated by different specific synapses with high weights (**Figure S3**). The seed weight losers (red bars in **Figure 5B**) differed from the end weight winners (green bars in **Figure 5C** and **Figure S3**) in that they conveyed sensor spiking activity that was less correlated across the training stimuli (**Figure 5D**), as measured by the Victor-Purpura distance metric for comparisons between spike trains. During the learning process, the overall adaptive regulation of the total excitatory and inhibitory synaptic weights in the model

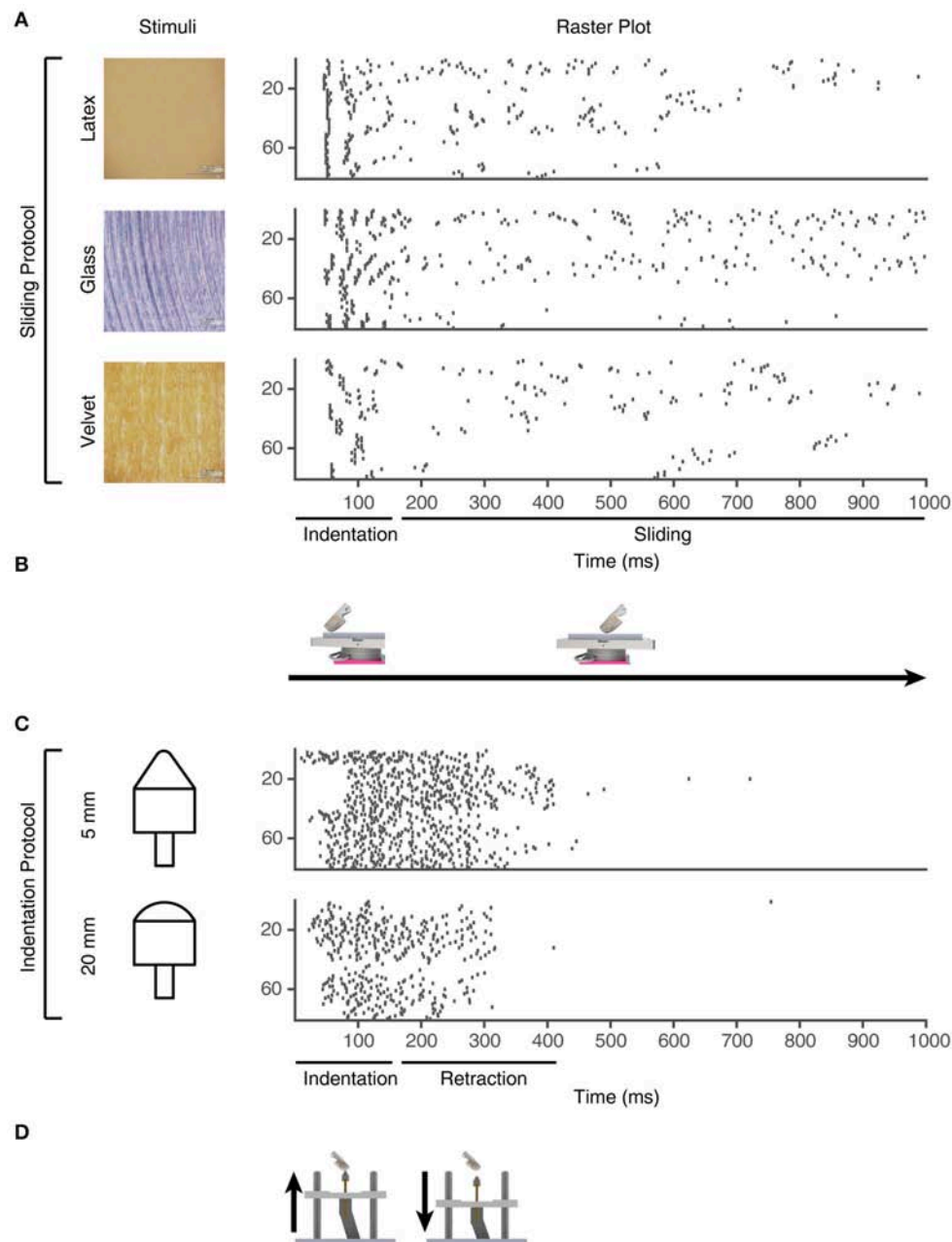


FIGURE 4 | Training stimuli. Physical stimuli and corresponding sensor spiking responses in PA sensory inputs #1-80 for the training stimuli used in the learning process. **(A)** Three of the physical stimulus conditions consisted in the artificial fingertip first indenting and subsequently sliding across surfaces with different textures, as shown in **(B)**. **(C)** The two indentation stimuli, where the artificial fingertip was dynamically indented against two different shapes, as shown in **(D)**.

(Figure 3B) helped stabilizing the activity of the CN (Figure 6), which was important for a stable learning outcome. In addition, in parallel with the acquisition of highly skewed synaptic weight distributions, the cuneate neurons also gradually acquired a firing that was dominated by brief, episodic bursts of spike output, similar to the firing mode observed for these neurons in adulthood *in vivo* (Bengtsson et al., 2013; Figures 1, 6D, Figure S1).

Learning Resulted in Decorrelations of Synaptic Inputs Between Neurons and Stimuli

The next question asked was what functional effects the learning process resulted in. We found that between the individual CNs, the learning process resulted in a decorrelation of the initially highly correlated temporal patterns of the synaptic responses to each given training stimulus (Figures 7A,B).

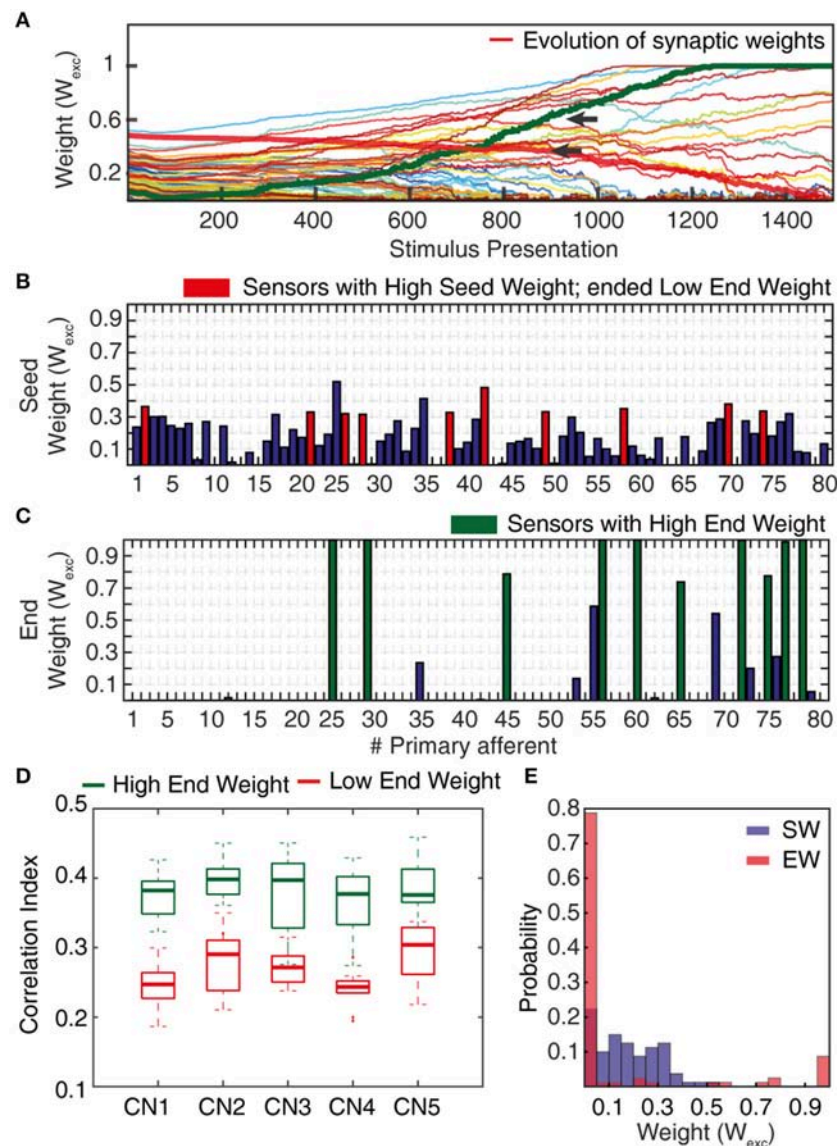


FIGURE 5 | Synaptic weight changes during the learning process. **(A)** Evolution of the synaptic weights during a learning process of 1,500 stimulus presentations, with the evolutions of two highlighted synapses indicated by red and green thick lines. **(B)** Starting weights of the PA synapses (“seed weights”) for the sample learning process. Red bars indicate a set of 10 sensors/PA synapses that started with high weight but ended up as low weight synapses (“losers”). **(C)** The end weights of the PA synapses after a completed learning process. Green bars indicate the ten synapses with the highest end weights (“winners”). **(D)** Box plots of the correlation indexes for the end weight “winners” and for the end weight “losers” for each of the five seed weight configurations tested. The differences in correlation index between the winners and losers was statistically different in each of these five cases ($p < 0.001$, paired t -test). **(E)** Histogram of the distribution of synaptic weights before and after learning in the example CN (CN1).

Hence, a consequence of the learning process was an increased differentiation of the CN responses to a given input, which was statistically significant at $p \leq 0.001$ (Wilcoxon signed rank test). In addition to testing the stimuli that the CNs were trained to, we also used a set of previously non-encountered stimuli, consisting of three types of texture sliding and two touch indentations, here referred to as non-training stimuli. Similar to the case with the training stimuli, the learning process resulted in a decorrelation of the synaptic responses of the CNs also to the non-training stimuli (Figures 7C,D; $p < 0.001$, Wilcoxon

signed rank test). Moreover, in the individual CN, whereas the differences in the spatiotemporal patterns of PA input between stimuli to some extent generated specific synaptic responses already in the “naïve” state, the responses became markedly differentiated with learning (Figures 8A,B). For each of the five CNs, CN1-5, the learning process resulted in a statistically significant decrease in the correlation between the synaptic responses to the five training stimuli ($p < 0.001$, Wilcoxon signed rank test). Such synaptic response differentiation is a basis for tactile input feature segregation (Jörntell et al., 2014)

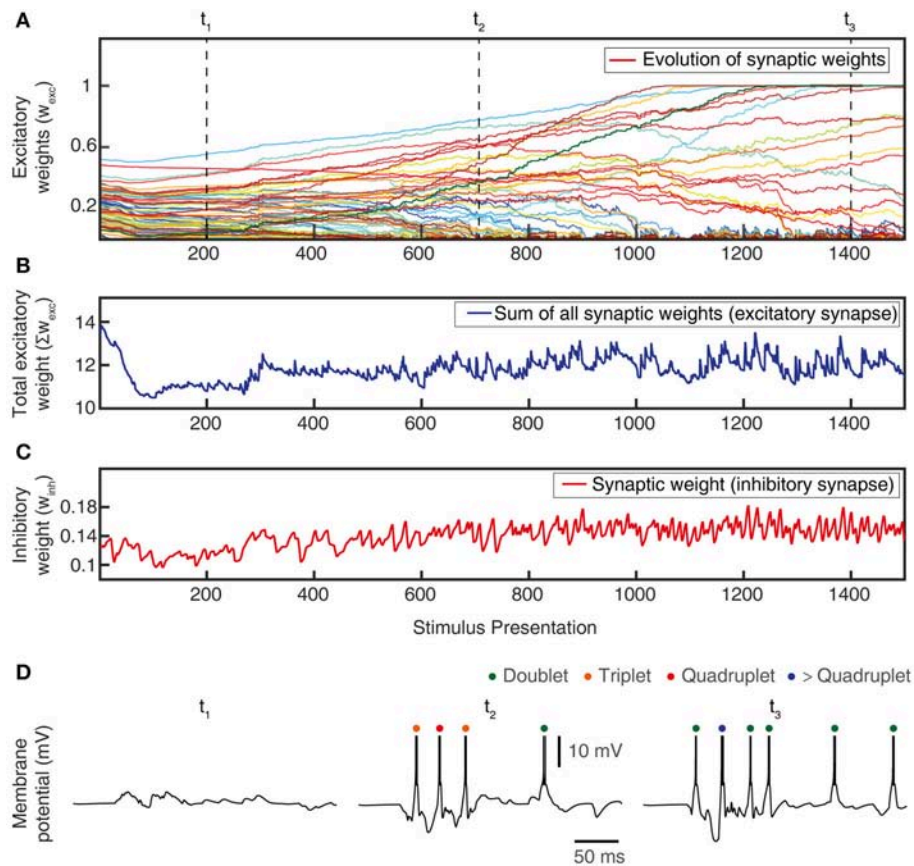


FIGURE 6 | Total synaptic weights and response evolution during learning. Relationship between synaptic weight evolution during the learning process (A) and the sum of the excitatory synaptic weights (B) and of the inhibitory synaptic weights (equal for all inhibitory synapses) (C). Note that the latter two parameters were controlled by the feedback mechanisms to ensure stability of the sum of the excitatory synaptic weights on the CN (by homeostatic plasticity) and of the total calcium activity (by the weight of the inhibitory synapses) (Figure 3B). (D) Example responses of the CN to the same stimulus condition (indentation 20 mm, see Figure 4) at three different time points during the learning process (indicated in A).

and the mechanism described here can hence be expected to improve the resolution at which the neuronal segregation of spatiotemporal PA sensory input patterns occurs. The learning process also resulted in that the individual CN increased the segregation of its responses to different non-training stimuli (Figures 8C,D). For the illustrated CN, the learning process resulted in a statistically significant decrease in the correlation between the synaptic responses to the five training stimuli at $p = 0.027$ whereas the p values for the other four CNs were below 0.001 (Wilcoxon signed rank test). The results with non-training stimuli hence indicated that the acquired learning was generalizable to previously non-encountered experiences, which is difficult to achieve in traditional pattern recognition systems (Spanne and Jorntell, 2015).

Evolution of Synaptic Weight Landscapes and Sparseness During the Learning Process

The gradual evolution of the synaptic weight distributions (or their “landscapes”) during the learning process was further

studied by plotting the weights of all the 80 PA synapses of each CN in an 80-dimensional space, embedded in 2D plots using multi-dimensional scaling (MDS). First, the analysis showed that the end weight landscape, which is the basis for the segregation of responses between neurons and inputs shown in Figures 7, 8, depended on the seed weight landscape of the CN (Figure 9A). Secondly, it showed that the evolution of the synaptic weight landscape initially accelerated but later decelerated to hover around a relatively stable end point (Figure 9A), suggesting that the learning was self-stabilizing. Self-stabilization is further quantified in Figure 9B, which shows the temporal evolution of the sparseness of the synaptic weight distribution. This self-stabilization was lost on removal of the supralinearity in the calcium dynamic responses and in the local synaptic calcium activity (Figure 10). In this case, the main compartment calcium was the sum of the local calcium activity in all the synapses, i.e., without intrinsic calcium dynamics in the main compartment and without supralinear local calcium activity subsynaptically. Under such conditions, the learning process became chaotic, without any stable end point and without any development of sparseness of the synaptic weight distribution (cf. Figure 9A).

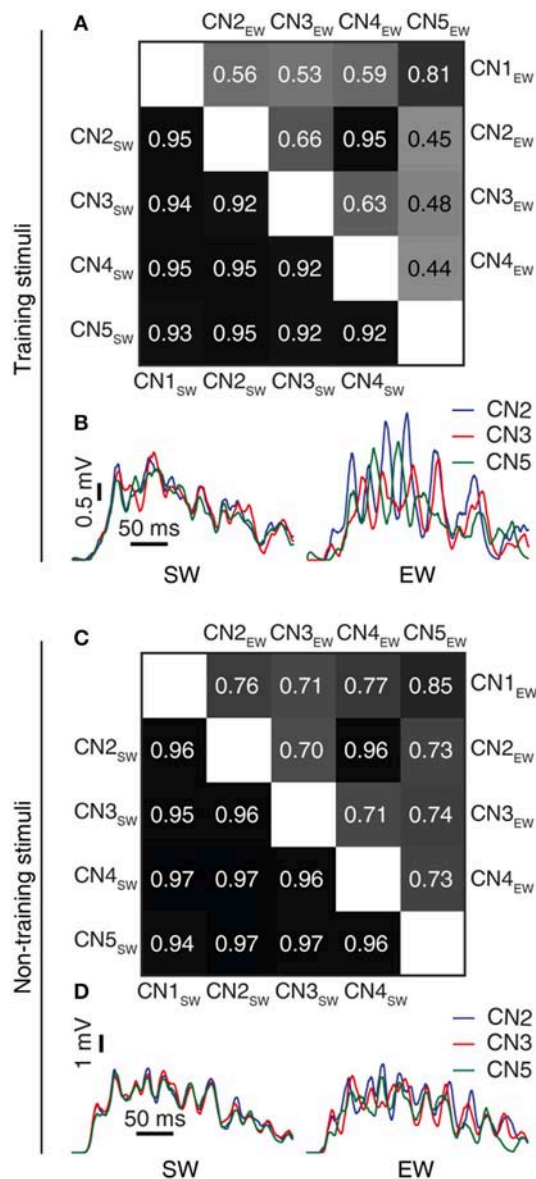


FIGURE 7 | Learning resulted in decorrelated responses between neurons to the same stimulus. **(A)** Triangle matrix for the correlations between synaptic responses evoked by the same training stimulus before (CN1_{SW}-CN5_{SW}) and after learning for all five cuneate neurons (CN1_{EW}-CN5_{EW}). The difference in correlation between the two groups was statistically significant ($p = 0.001$, Wilcoxon signed rank test) **(B)** Averaged synaptic responses to the stimulus ("indentation 20 mm") repeated 100 times for three different CNs (CN2, CN3, CN5) before and after training. **(C,D)** Similar displays as in **(A,B)** but for a novel stimulus that was not part of the training set ("indentation 10 mm;" Oddo et al., 2017). The difference in correlation before and after learning was statistically significant ($p < 0.001$, Wilcoxon signed rank test).

As we will describe in greater detail further below, we found that not only the seed weight landscape but also the intrinsic CN properties affected the outcome of the learning process. Of particular interest in relation to the effects of the calcium dynamic response (**Figure 10**) was the coupling between the synaptic

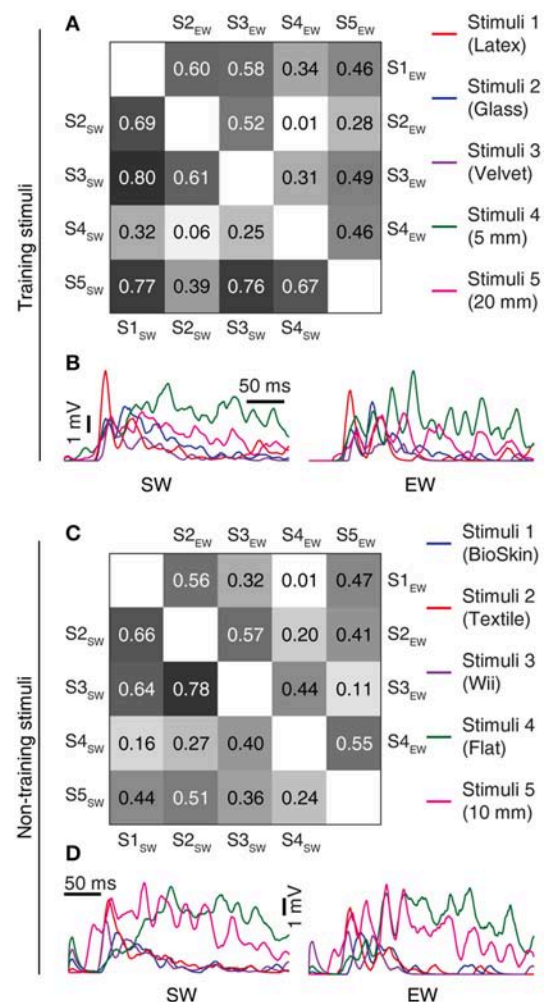
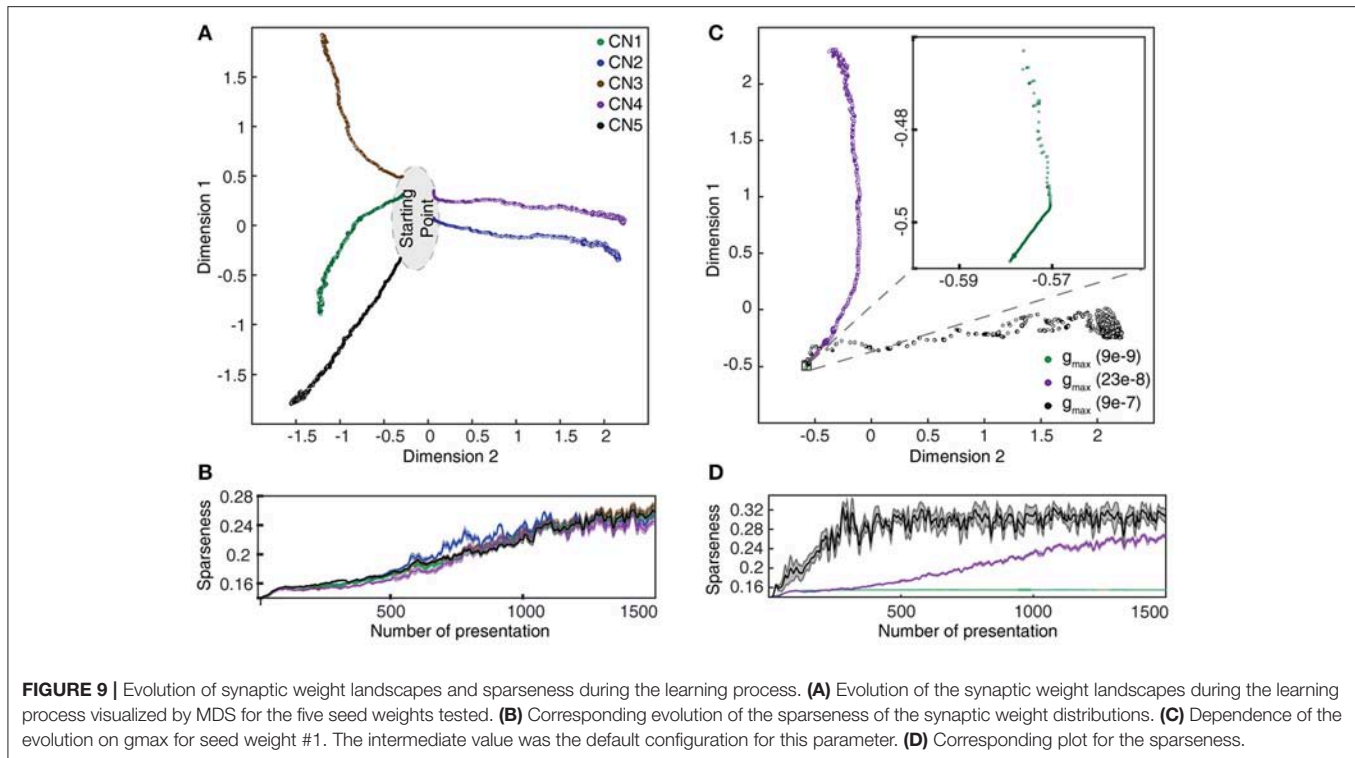


FIGURE 8 | Learning resulted in decorrelation of the responses to different stimuli in the individual CN. **(A)** Triangle matrix for the correlations between synaptic responses evoked by the training stimuli before and after learning in the same CN. Otherwise the display is similar to **Figure 7A**. The difference in correlation before and after learning was statistically significant ($p < 0.001$, Wilcoxon signed rank test) **(B)** Averaged synaptic responses of the CN (CN1) to the full set of training stimuli. **(C,D)** Similar display as in **(A,B)** but for non-training stimuli previously reported for shapes (Oddo et al., 2017) and for textures (Rongala et al., 2017). The difference in correlation between the two groups was statistically significant ($p = 0.028$, Wilcoxon signed rank test).

input and the intermediate dynamics model of the CN, since the intermediate dynamics model governed the time course of the calcium signal and thereby the learning process. This coupling was strongly affected by the Maximum synaptic conductance constant (g_{\max}), which was the ratio between the maximum synaptic conductance and the leak conductance of the neuron. A decrease in this ratio, or coupling, substantially reduced the learning rate whereas an increase instead caused the learning to become rapid, unstable and with dramatic shifts, unlike the more gradual process when the learning system was in balance (**Figure 9C**). Interestingly, even in the setting with high g_{\max} the system found a relatively stable end point in the synaptic weight



landscape but with a different location compared to the basic configuration (**Figures 9C,D**). However, a high learning speed, or learning rate, may not be beneficial if the aim is to allow the result of the learning process to take a variety of experiences into account, which in turn could limit the range of conditions and novel experiences that the learnt network structure would be applicable to. To explore this, we tested the effects of “monotypic” sensory training.

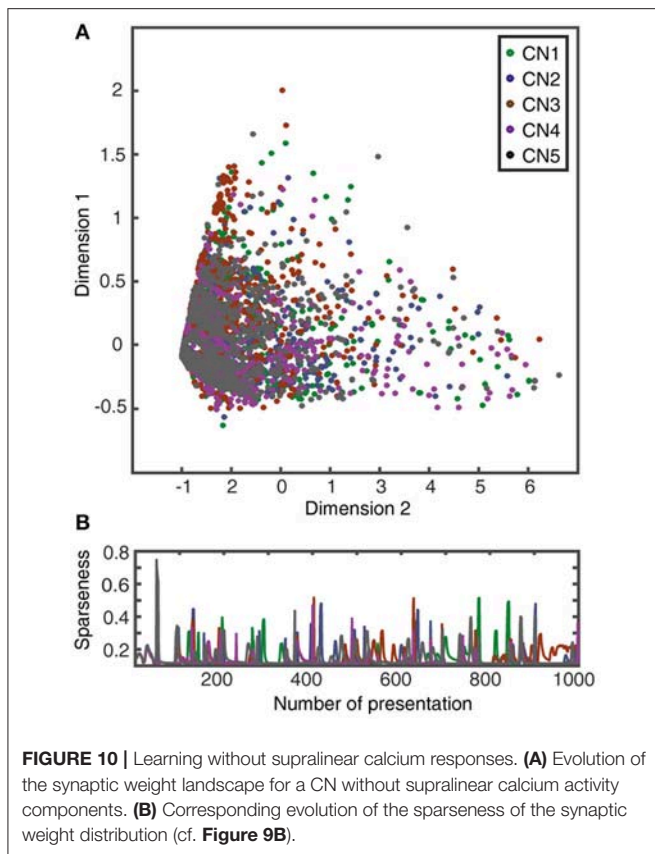
Importance of Varied Sensory Experiences

Monotypic sensory training is here referring to a situation where the same sensory experience, or stimulus, is repeated a high number of times in succession. i.e., instead of using the regular learning process protocol with 1,500 presentations of the set of five stimulus presentations mixed in a pseudo-random order, here we ran the learning process with one single type of stimulus for the whole learning process. Similar to diversified sensory training (**Figure 9A**), monotypic sensory training also resulted in gradual changes in the synaptic weight landscape (**Figure 11A**). However, the type of stimulus applied had a decisive influence on the direction of development of the synaptic weight landscape (**Figures 11A–C**), and that a switch from one monotypic stimulus to another could sharply turn the evolution of the synaptic weight landscape in a new direction (**Figures 11B–D**). Also, with monotypic stimulus presentations, stable end points of synaptic weight landscapes were not clearly identified, in contrast to the relatively stable end points obtained when a mixture of stimuli was used in the learning process (**Figure 9A**). Indeed, instead of reaching a stable end point well before 1,500 trials (as in **Figure 9A**), monotypic sensory training instead could

result in rapid changes in synaptic weight distribution at this time point (**Figure 11A**), which on inspection was found to be due to that the calcium activity of the CN could not be held within its set point and started to generate chaotic behavior (as in **Figure 10**). Hence, the order of presentation of the sensory experiences influenced the outcome of the learning process (**Figure 11D**), which indicates that the presence of a mixed, diversified set of sensory experiences over time will influence the result of the learning process. In addition, these findings also suggest that a high learning speed as in **Figures 9C,D** would make the CN more sensitive to individual sensory experiences and their order of presentation than in the basic configuration (**Figures 9A,B**).

The Intrinsic CN Properties Profoundly Influenced Learning Outcome

Whereas the above analysis (**Figures 5–8**, **Figure S3**) indicated that the seed synaptic weight distribution was an important factor influencing learning outcome, i.e., which set of correlated sensors the CNs picked to selectively strengthen, also the intrinsic CN parameters could conceivably act as a seed factor. Morphological differences between cuneate neurons (Fyffe et al., 1986) is an example of a source of variability in intrinsic neuronal behavior, the level of expression of different ionic conductances another. To explore this issue, we tested to separately vary the time constant of the calcium signal in the local synaptic space, the coupling between the synaptic input and the intrinsic dynamics (already shown in **Figures 9C,D**) and the set point of allowed calcium activity in the intermediate dynamics model (which was controlled by adapting the gain of the inhibitory synaptic



input, see **Figure 3B**). All intrinsic CN parameters, for all values tested (**Table 1**) influenced the outcome of the learning in terms of the end weight landscape (**Figure 12A**). Given that these intrinsic parameters influenced the behavior of the intermediate dynamics model and the calcium signal, either on a per stimulus presentation basis or over longer time, this was in itself perhaps not a surprising finding. However, the impact of these intrinsic parameters was profound and almost of comparative magnitude to the impact of the synaptic seed weight landscapes. The only apparent exceptions were the two lowest values of the g_{max} (inset) and the lowest τ for the calcium activity in the local synaptic space (triangle) (**Figure 12A**). However, the effect of these latter settings was that they reduced learning speed to a minimum and consequently resulted in little change from seed weight (black dot in **Figure 12A**). To estimate the relative stability of the learning, each configuration was run through the learning process five different times where each process was different as a minor noise was always injected in the sensor spike trains. The highest g_{max} value, with the fastest learning, resulted in the largest variability between learning processes (star in **Figure 12A**). All other parameter values were associated with lower variability in the learning outcome.

We tested the impact of varying the intrinsic CN parameters for all SWs by plotting them on the same MDS plot. The effect of the seed weight on the end weight landscape was larger than those of the intrinsic CN parameters (**Figure 12B**), but

it is clear that both categories of seed factors had a major impact on learning outcome. But irrespective of seed weight or intrinsic seed factors, the learning process always resulted in a selection of correlated sensors to become the end weight winner synapses (**Figure 13**). The fact that the learning worked in a similar fashion across a range of settings of intrinsic parameters for defining the intrinsic dynamics of the CN shows that the model architecture has some degree of robustness, i.e., it is independent of having precise constraints on neuron intrinsic behavior and will work similarly across a population of neurons with different intrinsic dynamics. Such differences within a CN population may be important to identify different subsets of correlated sensors in the learning process, and hence creating a diversification in the tuning of across the population of cuneate neurons, similar to the one observed *in vivo* (Jörntell et al., 2014).

DISCUSSION

Using an integrated model of cuneate nucleus neurons, based on the present *in vivo* whole cell recording data, and a bionic tactile sensor system, this study investigated what form of representations the brain could automatically learn from tactile interactions with the world. At the single neuron level, the CN learning resulted in the identification of sets of functionally correlated sensors (**Figures 5, 13**). By reducing or eliminating the synaptic weights of other sensors, this process essentially equals a dimensionality reduction of the sensory space at the single neuron level. At the population level, each CN, as defined by its unique seed factors, gradually identified different sets of functionally correlated sensors (**Figures 7–9, 13**). As a consequence, the learning process induced decorrelations in the synaptic responses of the different CNs to the same stimulus as well as for the individual CN to different stimuli (**Figures 7, 8**).

Such decorrelated synaptic responses is a key requirement for a population of cuneate neurons to be able to segregate the high-dimensional tactile sensory space, where each sensor potentially represents a unique dimension (Spanne and Jörntell, 2013), into specific projections (Jörntell et al., 2014). These projections are defined by the types of sensory experiences made (**Figure 11**) and the physical-mechanical effects involved (see Introduction). Hence, the representation of the physical world that naturally unfolded given the neurophysiological constraints of the cuneate neurons *in vivo* (**Figure 1**) was a utility-based decomposition of the sensory space. Thereby, the architecture of the cuneate nucleus network (**Figure 3**) would help the brain focusing to focus on the statistically recurring elements of experienced tactile sensory activation patterns. It follows that an early rich variation of tactile sensory experiences (Pape et al., 2012; Loeb and Fishel, 2014), such as achieved by motor babbling in the infant (Forssberg et al., 1995; Blumberg et al., 2013), is important for the brain because it would be needed to form representations with a sufficiently high dimensionality.

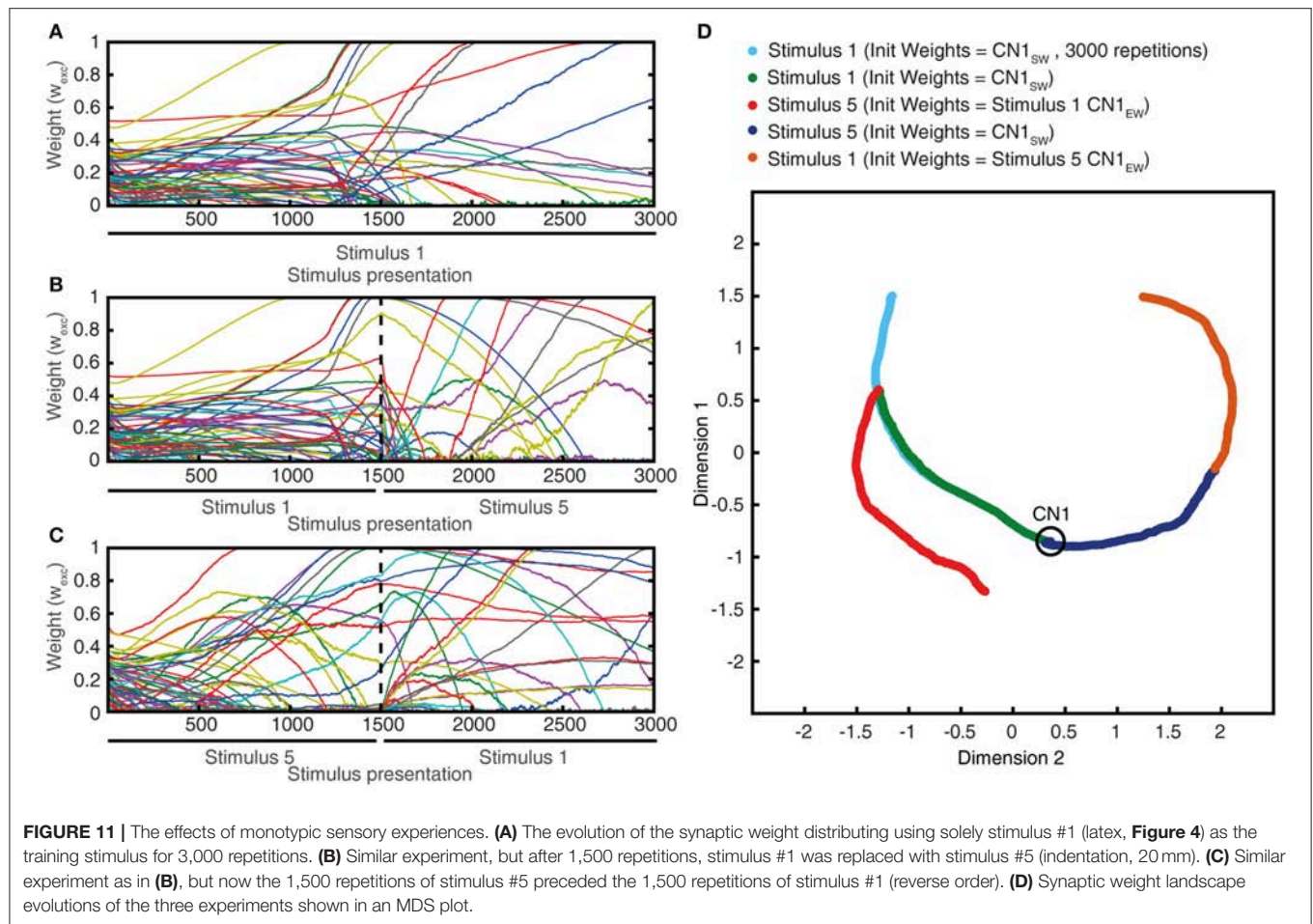


FIGURE 11 | The effects of monotypic sensory experiences. **(A)** The evolution of the synaptic weight distributing using solely stimulus #1 (latex, **Figure 4**) as the training stimulus for 3,000 repetitions. **(B)** Similar experiment, but after 1,500 repetitions, stimulus #1 was replaced with stimulus #5 (indentation, 20 mm). **(C)** Similar experiment as in **(B)**, but now the 1,500 repetitions of stimulus #5 preceded the 1,500 repetitions of stimulus #1 (reverse order). **(D)** Synaptic weight landscape evolutions of the three experiments shown in an MDS plot.

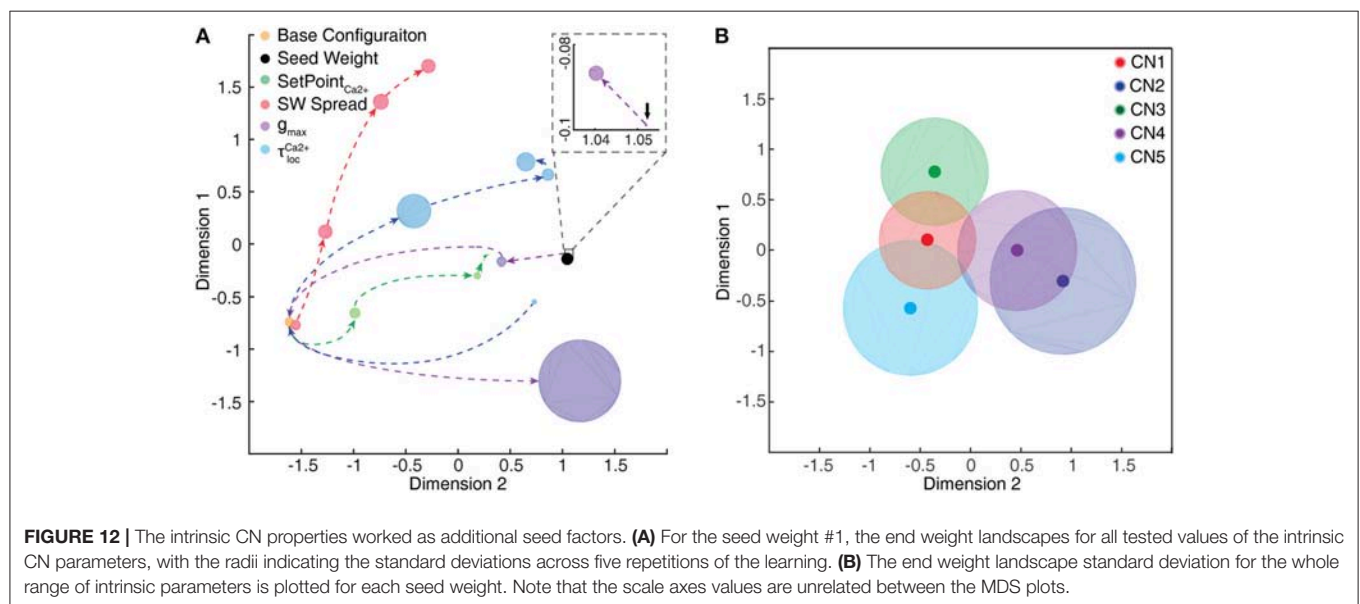


FIGURE 12 | The intrinsic CN properties worked as additional seed factors. **(A)** For the seed weight #1, the end weight landscapes for all tested values of the intrinsic CN parameters, with the radii indicating the standard deviations across five repetitions of the learning. **(B)** The end weight landscape standard deviation for the whole range of intrinsic parameters is plotted for each seed weight. Note that the scale axes values are unrelated between the MDS plots.

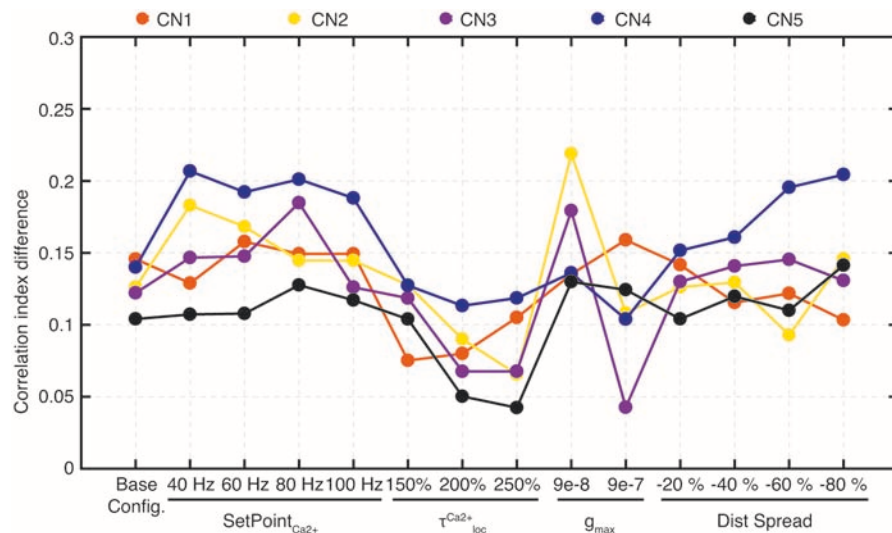


FIGURE 13 | Improvements in correlation indexes for learning with different seed factors. The differences in correlation index between end weight winners and end weight losers (see **Figure 5**) plotted for all values of intrinsic CN parameters and all synaptic seed weights. Note that for some values of intrinsic parameters (g_{\max} of $23e-9$ and g_{\max} of $9e-9$, and τ for the local calcium activity of 50%) no learning took place (**Figure 12**) and the learning effects of those intrinsic parameter settings are hence omitted from this figure. Based on five CNs and 14 conditions, statistical comparisons were made for 70 conditions. The differences in correlation index between the end weight winners and losers was statistically different in each of these 70 cases ($p < 0.05$, paired t -test), except one ($p = 0.11$ for CN3 at g_{\max} of $9e-7$).

Robustness of the Learning Process Suggests Little Dependence on Assumptions

In order to address a breadth of issues that related to the representation of haptic input features in the cuneate nucleus neurons (Jörntell et al., 2014) and their intrinsic properties, but which are too complex to be resolved by experimental recordings, we needed to model the cuneate neurons. Whereas, the model system naturally could have featured a higher number of sensors or a larger number of contexts across which the generalization capability was tested, we find no reason to believe that would have altered the principles reported here. An important component of the model was the learning process that we envisage to be one of the earliest developmental steps toward a functional tactile neural system. Although there are several indications that the PA synapses on the cuneate neurons are extensively plastic at least during some phase of development (Bengtsson et al., 2013) and following removal of PA inputs (Kambi et al., 2014; Mowery et al., 2014), the direct synaptic mechanisms underlying the plasticity have not been explored. Therefore, in order to model this learning process, we used an already validated idea of a calcium activity-dependent mechanism (Helias et al., 2008), which to some extent can be regarded a general synaptic plasticity mechanisms of neurons. It is in principle a variant of the BCM learning rule (Bienenstock et al., 1982) for which we obtained specific data from the biological cuneate projection neurons to approximate how their internal calcium signal can be expected to vary over time and with the input. In comparison with a previous study of how calcium-dependent STDP varies across a range of parameter settings (Graupner and Brunel, 2012), our

approach had a less steep rising phase in the postsynaptic calcium response, which can be expected to dampen the dependence of our model on exact spike timings and instead make it rely to a larger extent on the temporal variation in the intensity of the synaptic activation (Graupner et al., 2016) and how it correlated with the overall activity of the postsynaptic neuron. Naturally, the actual cuneate learning process is likely to differ from ours in many details but the fundamental properties of our model, i.e., an extreme dimensionality reduction in each neuron and the identification of different correlated sets of sensors by the population of CNs (**Figure 7**), were remarkably robust to manipulation of a wide variety of neuronal parameters that influenced the learning process (**Figures 12, 13**). It can also be noted that after learning, our CNs had synaptic weight distributions that were similar to adult cuneate neurons (**Figure 5C** and **Figure S3**) (Bengtsson et al., 2013) as well as response dynamics that qualitatively captured the dynamics recorded *in vivo* (**Figure 6D**, **Figure S1**).

Plasticity in inhibitory synaptic inputs could in principle help improving segregation of inputs (Garrido et al., 2016). Our analysis of the biological inhibitory synaptic inputs in the cuneate nucleus did not overtly support a specific role in such function, though. The recorded inhibitory interneurons in the cuneate nucleus were activated from wide receptive fields and in the projection neurons inhibition was found to originate from similar wide receptive fields, with relatively uniform inhibitory synaptic weights (**Figures 1C,D**). This is in contrast to the excitatory synaptic inputs from PAs, which in cuneate projection neurons have been found to have strongly differentiated weights and hence suggestive of an

extensive learning history in these synapses (Bengtsson et al., 2013). In our CN model, the plasticity in the inhibitory synapses instead assumed the role of activity balancing, i.e., ensuring that the excitable calcium responses did not go out of bounds (neither upwards, nor downwards), which was an important function to ensure stable, gradual learning (cf. Figure 10).

Advantages of the Representational Format and of the Architecture

The utility-based decomposition of the tactile sensory space learned with our CN architecture is likely to correspond to an early level acquisition of a representation of the experienced, and therefore useful, haptic input features, which were previously found to be represented in cuneate neurons *in vivo* in adult animals (Jörntell et al., 2014). Being based on physical-mechanical effects (Hayward, 2011; Hayward et al., 2014), correspondences between the haptic input features and sensory information from other modalities such as vision and hearing can be expected to be abundant. Hence, this type of tactile representation would provide a basis for rich cross-modality representations of rules of object interactions that can be learnt by the higher level centers of the brain to conceptualize the external world (O'Regan and Noe, 2001). This model does not contradict the possibility that the activity of individual cuneate neurons or neurons of the somatosensory cortex could correlate with physical parameters such as edge orientation or texture or even adaptation rate, but indicates that the underlying organizational and coding principle is likely to be more intricate than that.

These principles are potentially portable to AI and robotic systems, which faces challenges of how to design sensor systems to support more general functionality in the interactions with the external world (Brooks, 1991; Davis et al., 1993; Service, 2014). AI systems are generally designed to deliver performance on specific tasks, such as the game of Go (Gibney, 2016), where they deliver impressive performance if given very large amounts of training data (Lecun et al., 2015). However, they seem to be lacking the wide versatility or generalization capability of biological systems (Nguyen et al., 2015; Athalye and Sutskever, 2017), which could be related to the known problems of classical pattern recognition systems (Spanne and Jörntell, 2015) and which the current alternative mode of representation of sensory input data may help resolving. These technical systems also in general suffer from a strong dependence on the initial weight configuration (Glorot and Bengio, 2010; He et al., 2015). This dependence can be eliminated by specifically dedicated computational mechanisms calculating appropriate initial weights or by other computationally intensive methods (Williams and Hinton, 1986; Földiák, 1990; Glorot and Bengio, 2010), which, however, may not be available to the brain. Our architecture, featuring a set of neuronal auto-regulatory mechanisms and self-stabilizing learning, provide

potential solutions also for these challenges within DNN and AI systems.

CONCLUDING REMARKS

A main advantage of representing tactile experiences by decomposing them into vector components of their constituent physical effects, rather than by pattern recognition applied to pixelated sensory data directly, is the powerful generalization possibilities (Spanne and Jörntell, 2015). With this mode of representation, the brain could in principle learn to identify the extent of the space of the theoretically possible physical effects within a short time using just a few types of disparate skin-object interactions and later subsequently learn to interpolate new points within this space at a gradually higher resolution. A major issue for future studies is to explore if brain processing operates in terms of such vector components also globally in the neocortex.

AUTHOR CONTRIBUTIONS

UR, AS, and HJ designed the model. FB and HJ performed the patch clamp recording experiments and analyzed the biological data. UR, AM, and CO developed and experimented the bionic finger for electrophysiological and translational bioengineering studies. UR, AS, AM, CO, and HJ designed the analysis of the model data. UR, CO, AM, and HJ wrote the paper.

ACKNOWLEDGMENTS

This work was supported by the Ministry of Education, Universities and Research of the Italian Republic and the Swedish Research Council, via the Italy-Sweden bilateral research project J52I15000030005 SensBrain (Brain network mechanisms for integration of natural tactile input patterns), by the EU Grant FET 611687 NEBIAS Project (NEurocontrolled BiDirectional Artificial upper limb and hand prosthesis), by the EU Grant FP7-NMP 228844 NANOBIOTOUCH project (Nanoresolved multi-scan investigations of human tactile sensations and tissue engineered nanobiosensors), and by the national project B81J12002680008 PRIN/HandBot (Biomechatronic hand prostheses endowed with bio-inspired tactile perception, bi-directional neural interfaces and distributed sensori-motor control), SENSOPAC (EU FP6, IST-028056-SENSOPAC), The Hand Embodied (EU FP7 IST-248587-THE) and the Swedish Research Council (project grant no. K2014-63X-147 80-12-3).

SUPPLEMENTARY MATERIAL

The Supplementary Material for this article can be found online at: <https://www.frontiersin.org/articles/10.3389/fncel.2018.00210/full#supplementary-material>

REFERENCES

- Abraira, V. E., and Ginty, D. D. (2013). The sensory neurons of touch. *Neuron* 79, 618–639. doi: 10.1016/j.neuron.2013.07.051
- Athalye, A., and Sutskever, I. (2017). Synthesizing robust adversarial examples. *arXiv [preprint] arXiv:1707.07397*.
- Barlow, H. B. (1972). Single units and sensation: a neuron doctrine for perceptual psychology? *Perception* 1, 371–394. doi: 10.1068/p010371
- Beccai, L., Roccella, S., Arena, A., Valvo, F., Valdastri, P., Menciassi, A., et al. (2005). Design and fabrication of a hybrid silicon three-axial force sensor for biomechanical applications. *Sens. Actuators. A Phys.* 120, 370–382. doi: 10.1016/j.sna.2005.01.007
- Bengtsson, F., Brasselet, R., Johansson, R. S., Arleo, A., and Jorntell, H. (2013). Integration of sensory quanta in cuneate nucleus neurons *in vivo*. *PLoS ONE* 8:e56630. doi: 10.1371/journal.pone.0056630
- Bi, G. Q., and Poo, M. M. (1998). Synaptic modifications in cultured hippocampal neurons: dependence on spike timing, synaptic strength, and postsynaptic cell type. *J. Neurosci.* 18, 10464–10472. doi: 10.1523/JNEUROSCI.18-24-10464.1998
- Bienenstock, E. L., Cooper, L. N., and Munro, P. W. (1982). Theory for the development of neuron selectivity: orientation specificity and binocular interaction in visual cortex. *J. Neurosci.* 2, 32–48. doi: 10.1523/JNEUROSCI.02-01-00032.1982
- Blumberg, M. S., Marques, H. G., and Iida, F. (2013). Twitching in sensorimotor development from sleeping rats to robots. *Curr. Biol.* 23, R532–537. doi: 10.1016/j.cub.2013.04.075
- Brooks, R. A. (1991). “Intelligence without reason,” in *Proceedings of International Joint Conference on Artificial Intelligence* (Sydney, NSW), 569–595.
- Davis, R., Shrobe, H., and Szolovits, P. (1993). What is a knowledge representation? *AI magazine* 14, 17
- Földiák, P. (1990). Forming sparse representations by local anti-Hebbian learning. *Biol. Cybern.* 64, 165–170. doi: 10.1007/BF02331346
- Forssberg, H., Eliasson, A., Kinoshita, H., Westling, G., and Johansson, R. (1995). Development of human precision grip. *Exp. Brain Res.* 104, 323–330. doi: 10.1007/BF00242017
- Fourcaud-Trocmé, N., Hansel, D., Van Vreeswijk, C., and Brunel, N. (2003). How spike generation mechanisms determine the neuronal response to fluctuating inputs. *J. Neurosci.* 23, 11628–11640. doi: 10.1523/JNEUROSCI.23-37-11628.2003
- Fyffe, R. E., Cheema, S. S., Light, A. R., and Rustioni, A. (1986). Intracellular staining study of the feline cuneate nucleus. II. Thalamic projecting neurons. *J. Neurophysiol.* 56, 1284–1296. doi: 10.1152/jn.1986.56.5.1284
- Garrido, J. A., Luque, N. R., Tolu, S., and D’angelo, E. (2016). Oscillation-driven spike-timing dependent plasticity allows multiple overlapping pattern recognition in inhibitory interneuron networks. *Int J Neural Syst.* 26, 1650020. doi: 10.1142/S0129065716500209
- Gibney, E. (2016). Google AI algorithm masters ancient game of Go. *Nature* 529, 445–446. doi: 10.1038/529445a
- Glorot, X., and Bengio, Y. (2010). “Understanding the difficulty of training deep feedforward neural networks,” in *Proceedings of Artificial Intelligence and Statistics* (Sardinia), 249–256.
- Graupner, M., and Brunel, N. (2012). Calcium-based plasticity model explains sensitivity of synaptic changes to spike timing, rate, and dendritic location. *Proc. Natl. Acad. Sci. U.S.A.* 109, 3991–3996. doi: 10.1073/pnas.1109359109
- Graupner, M., Wallisch, P., and Ostojic, S. (2016). Natural firing patterns imply low sensitivity of synaptic plasticity to spike timing compared with firing rate. *J. Neurosci.* 36, 11238–11258. doi: 10.1523/JNEUROSCI.0104-16.2016
- Hayward, V. (2011). Is there a ‘plenaptic’ function? *Phil. Trans. R. Soc. B.* 366, 3115–3122. doi: 10.1098/rstb.2011.0150
- Hayward, V., Terekhov, A. V., Wong, S. C., Geborek, P., Bengtsson, F., and Jorntell, H. (2014). Spatio-temporal skin strain distributions evoke low variability spike responses in cuneate neurons. *J. R. Soc. Inter.* 11, 20131015. doi: 10.1098/rsif.2013.1015
- He, K., Zhang, X., Ren, S., and Sun, J. (2015). “Delving deep into rectifiers: Surpassing human-level performance on imagenet classification,” in *Proceedings of the IEEE International Conference on Computer Vision* (Santiago), 1026–1034.
- Hebb, D. O. (1949). *The Organization of Behavior: A Neuropsychological Approach*. Oxford: John Wiley & Sons.
- Helias, M., Rotter, S., Gewaltig, M. O., and Diesmann, M. (2008). Structural plasticity controlled by calcium based correlation detection. *Front. Comput. Neurosci.* 2, 7. doi: 10.3389/neuro.10.007.2008
- Higley, M. J., and Sabatini, B. L. (2012). Calcium signaling in dendritic spines. *Cold Spring Harb. Perspec. Biol.* 4:a005686. doi: 10.1101/cshperspect.a005686
- Huguenard, J. R. (1996). Low-threshold calcium currents in central nervous system neurons. *Annu. Rev. Physiol.* 58, 329–348. doi: 10.1146/annurev.ph.58.030196.001553
- Hulme, S. R., and Connelly, W. M. (2014). L-type calcium channel-dependent inhibitory plasticity in the thalamus. *J. Neurophysiol.* 112, 2037–2039. doi: 10.1152/jn.00918.2013
- Izhikevich, E. M. (2003). Simple model of spiking neurons. *IEEE Trans. Neural Netw.* 14, 1569–1572. doi: 10.1109/TNN.2003.820440
- Johansson, R. S., and Flanagan, J. R. (2009). Coding and use of tactile signals from the fingertips in object manipulation tasks. *Nat. Rev. Neurosci.* 10, 345–359. doi: 10.1038/nrn2621
- Jorntell, H., Bengtsson, F., Geborek, P., Spanne, A., Terekhov, A. V., and Hayward, V. (2014). Segregation of tactile input features in neurons of the cuneate nucleus. *Neuron* 83, 1444–1452. doi: 10.1016/j.neuron.2014.07.038
- Jorntell, H., and Ekerot, C. F. (2006). Properties of somatosensory synaptic integration in cerebellar granule cells *in vivo*. *J. Neurosci.* 26, 11786–11797. doi: 10.1523/JNEUROSCI.2939-06.2006
- Jorntell, H., and Hansel, C. (2006). Synaptic memories upside down: bidirectional plasticity at cerebellar parallel fiber-Purkinje cell synapses. *Neuron* 52, 227–238. doi: 10.1016/j.neuron.2006.09.032
- Kambi, N., Halder, P., Rajan, R., Arora, V., Chand, P., Arora, M., et al. (2014). Large-scale reorganization of the somatosensory cortex following spinal cord injuries is due to brainstem plasticity. *Nat. Commun.* 5, 3602. doi: 10.1038/ncomms4602
- Kawaguchi, S., Nagasaki, N., and Hirano, T. (2011). Dynamic impact of temporal context of Ca^{2+} signals on inhibitory synaptic plasticity. *Sci. Rep.* 1:143. doi: 10.1038/srep00143
- Koester, H. J., and Sakmann, B. (1998). Calcium dynamics in single spines during coincident pre- and postsynaptic activity depend on relative timing of back-propagating action potentials and subthreshold excitatory postsynaptic potentials. *Proc. Natl. Acad. Sci. U.S.A.* 95, 9596–9601. doi: 10.1073/pnas.95.16.9596
- Lecun, Y., Bengio, Y., and Hinton, G. (2015). Deep learning. *Nature* 521, 436–444. doi: 10.1038/nature14539
- Linás, R., and Jahnsen, H. (1982). Electrophysiology of mammalian thalamic neurones *in vitro*. *Nature* 297, 406–408. doi: 10.1038/297406a0
- Loeb, G. E., and Fishel, J. A. (2014). Bayesian action&perception: representing the world in the brain. *Front. Neurosci.* 8:341. doi: 10.3389/fnins.2014.00341
- Lourenço, J., Pacioni, S., Rebola, N., Van Woerden, G. M., Marinelli, S., Digregorio, D., et al. (2014). Non-associative potentiation of perisomatic inhibition alters the temporal coding of neocortical layer 5 pyramidal neurons. *PLoS Biol.* 12:e1001903. doi: 10.1371/journal.pbio.1001903
- Markram, H., Lubke, J., Frotscher, M., and Sakmann, B. (1997). Regulation of synaptic efficacy by coincidence of postsynaptic APs and EPSPs. *Science* 275, 213–215. doi: 10.1126/science.275.5297.213
- Mazzoni, A., Panzeri, S., Logothetis, N. K., and Brunel, N. (2008). Encoding of naturalistic stimuli by local field potential spectra in networks of excitatory and inhibitory neurons. *PLoS Comput. Biol.* 4:e1000239. doi: 10.1371/journal.pcbi.1000239
- Molineux, M. L., Mehaffey, W. H., Tadayonnejad, R., Anderson, D., Tennent, A. F., and Turner, R. W. (2008). Ionic factors governing rebound burst phenotype in rat deep cerebellar neurons. *J. Neurophysiol.* 100, 2684–2701. doi: 10.1152/jn.90427.2008
- Mowery, T. M., Kostylev, P. V., and Garraghty, P. E. (2014). AMPA and GABA(A/B) receptor subunit expression in the cuneate nucleus of adult squirrel monkeys during peripheral nerve regeneration. *Neurosci. Lett.* 559, 141–146. doi: 10.1016/j.neulet.2013.11.054
- Nguyen, A., Yosinski, J., and Clune, J. (2015). “Deep neural networks are easily fooled: High confidence predictions for unrecognizable images,” in *Proceedings of the IEEE Conference on Computer Vision and Pattern Recognition* (Boston, MA), 427–436.

- Niedermeyer, E., and Da Silva, F. L. (2005). *Electroencephalography: Basic Principles, Clinical Applications, and Related Fields*. London: Lippincott Williams & Wilkins.
- Oddo, C. M., Controzzi, M., Beccai, L., Cipriani, C., and Carrozza, M. C. (2011). Roughness encoding for discrimination of surfaces in artificial active-touch. *IEEE. Trans. Robot.* 27, 522–533. doi: 10.1109/TRO.2011.2116930
- Oddo, C. M., Mazzoni, A., Spanne, A., Enander, J. M., Mogensen, H., Bengtsson, F., et al. (2017). Artificial spatiotemporal touch inputs reveal complementary decoding in neocortical neurons. *Sci. Rep.* 8:45898. doi: 10.1038/srep45898
- Oddo, C. M., Raspopovic, S., Artoni, F., Mazzoni, A., Spigler, G., Petrini, F., et al. (2016). Intraneural stimulation elicits discrimination of textural features by artificial fingertip in intact and amputee humans. *Elife* 5:e09148. doi: 10.7554/eLife.09148
- Oddo, C. M., Valdastrì, P., Beccai, L., Roccella, S., Carrozza, M. C., and Dario, P. (2007). Investigation on calibration methods for multi-axis, linear and redundant force sensors. *Meas. Sci. Tech.* 18, 623–631. doi: 10.1088/0957-0233/18/3/011
- O'Regan, J. K., and Noe, A. (2001). A sensorimotor account of vision and visual consciousness. *Behav. Brain Sci.* 24, 939–973. discussion: 973–1031. doi: 10.1017/S0140525X01000115
- Ostojic, S., and Brunel, N. (2011). From spiking neuron models to linear-nonlinear models. *PLoS Comput. Biol.* 7:e1001056. doi: 10.1371/journal.pcbi.1001056
- Pape, L., Oddo, C. M., Controzzi, M., Cipriani, C., Förster, A., Carrozza, M. C., et al. (2012). Learning tactile skills through curious exploration. *Front. Neur.* 6:6. doi: 10.3389/fnbot.2012.00006
- Pei, Y. C., Hsiao, S. S., Craig, J. C., and Bensmaia, S. J. (2011). Neural mechanisms of tactile motion integration in somatosensory cortex. *Neuron* 69, 536–547. doi: 10.1016/j.neuron.2010.12.033
- Petersson, P., Waldenström, A., Fähræus, C., and Schouenborg, J. (2003). Spontaneous muscle twitches during sleep guide spinal self-organization. *Nature* 424, 72–75. doi: 10.1038/nature01719
- Rongala, U. B., Mazzoni, A., and Oddo, C. M. (2017). Neuromorphic artificial touch for categorization of naturalistic textures. *IEEE. Trans. Neur. Net. Learn. Syst.* 28, 819–829. doi: 10.1109/TNNLS.2015.2472477
- Saarienen, A., Linne, M. L., and Yli-Harja, O. (2008). Stochastic differential equation model for cerebellar granule cell excitability. *PLoS Comput. Biol.* 4:e1000004. doi: 10.1371/journal.pcbi.1000004
- Sathian, K. (2016). Analysis of haptic information in the cerebral cortex. *J. Neurophysiol.* 116, 1795–1806. doi: 10.1152/jn.00546.2015
- Service, R. F. (2014). Minds of their own. *Science* 346, 182–183. doi: 10.1126/science.346.6206.182
- Shao, Y., Hayward, V., and Visell, Y. (2016). Spatial patterns of cutaneous vibration during whole-hand haptic interactions. *Proc. Natl. Acad. Sci. U.S.A.* 113, 4188–4193. doi: 10.1073/pnas.1520866113
- Spanne, A., and Jörntell, H. (2015). Questioning the role of sparse coding in the brain. *Trends Neurosci.* 38, 417–427. doi: 10.1016/j.tins.2015.05.005
- Spanne, A., and Jörntell, H. (2013). Processing of multi-dimensional sensorimotor information in the spinal and cerebellar neuronal circuitry: a new hypothesis. *PLoS Comput. Biol.* 9:e1002979. doi: 10.1371/journal.pcbi.1002979
- Tigaret, C. M., Olivo, V., Sadowski, J. H. L. P., Ashby, M. C., and Mellor, J. R. (2016). Coordinated activation of distinct Ca^{2+} sources and metabotropic glutamate receptors encodes Hebbian synaptic plasticity. *Nat. Comm.* 7:10289. doi: 10.1038/ncomms10289
- Turrigiano, G. (2011). Too Many Cooks? Intrinsic and Synaptic Homeostatic Mechanisms in Cortical Circuit Refinement. *Ann. Rev. Neurosci.* 34, 89–103. doi: 10.1146/annurev-neuro-060909-153238
- Turrigiano, G. G., and Nelson, S. B. (2004). Homeostatic plasticity in the developing nervous system. *Nat. Rev. Neurosci.* 5, 97–107. doi: 10.1038/nrn1327
- Vallbo, A. B., and Johansson, R. S. (1984). Properties of Cutaneous Mechanoreceptors in the Human Hand Related to Touch Sensation. *Human Neurobiol.* 3, 3–14.
- Victor, J. D., and Purpura, K. P. (1996). Nature and precision of temporal coding in visual cortex: A metric-space analysis. *J. Neurophysiol.* 76, 1310–1326. doi: 10.1152/jn.1996.76.2.1310
- Wang, S. S. H., Denk, W., and Häusser, M. (2000). Coincidence detection in single dendritic spines mediated by calcium release. *Nat. Neurosci.* 3, 1266–1273. doi: 10.1038/81792
- Weinberg, R. J., Pierce, J. P., and Rustioni, A. (1990). Single fiber studies of ascending input to the cuneate nucleus of cats: I. Morphometry of primary afferent fibers. *J. Comp. Neurol.* 300, 113–133. doi: 10.1002/cne.903000108
- Williams, D., and Hinton, G. (1986). Learning representations by back-propagating errors. *Nature* 323, 533–538. doi: 10.1038/323533a0
- Yin, P., Esser, E., and Xin, J. (2014). Ratio and difference of l1 and l2 norms and sparse representation with coherent dictionaries. *Commun. Inform. Syst.* 14, 87–109. doi: 10.4310/CIS.2014.v14.n2.a2

Conflict of Interest Statement: The authors declare that the research was conducted in the absence of any commercial or financial relationships that could be construed as a potential conflict of interest.

Copyright © 2018 Rongala, Spanne, Mazzoni, Bengtsson, Oddo and Jörntell. This is an open-access article distributed under the terms of the Creative Commons Attribution License (CC BY). The use, distribution or reproduction in other forums is permitted, provided the original author(s) and the copyright owner(s) are credited and that the original publication in this journal is cited, in accordance with accepted academic practice. No use, distribution or reproduction is permitted which does not comply with these terms.



Decreased Number and Expression of nNOS-Positive Interneurons in Basolateral Amygdala in Two Mouse Models of Autism

Xiaona Wang¹, Jisheng Guo², Yinsen Song¹, Qi Wang³, Shunan Hu¹, Lingshan Gou⁴ and Yinbo Gao^{1*}

¹Henan Provincial Key Laboratory of Children's Genetics and Metabolic Diseases, Children's Hospital Affiliated of Zhengzhou University, Zhengzhou, China, ²Center for Translational Medicine, The Sixth People's Hospital of Zhengzhou, Zhengzhou, China, ³Department of Histology and Embryology, Guizhou Medical University, Guiyang, China, ⁴Center for Genetic Medicine, Xuzhou Maternity and Child Health Care Hospital, Xuzhou, China

The basolateral amygdala (BLA) controls socio-emotional behaviors and is involved in the etiology of autism. We have recently shown that virtually every neuronal nitric oxide synthase (nNOS) positive cell is a GABAergic inhibitory interneuron in the mouse BLA. Here, stereology was used to quantify the number of nNOS-expressing interneurons in valproic acid (VPA)-exposed C57BL/6J (B6) and BTBR T⁺Itpr3^{tf}/J (BTBR) mice models of autism. Additionally, the protein and mRNA levels of nNOS in the BLA were quantitatively assessed by western blot and qRT-PCR analysis, respectively. Our results showed the decreased number of nNOS interneurons in the BLA of animal models relative to autism. Consistently, nNOS was significantly reduced in the VPA-exposed and BTBR mice at both protein and mRNA levels. Together, these preliminary findings suggest that down-regulation of nNOS may be an attractive target for the pharmacological intervention in autism.

Keywords: autism spectrum disorders, interneuron, nNOS, basolateral amygdala, mouse models

INTRODUCTION

Autism spectrum disorders are a group of common neurodevelopmental disorders, characterized by repetitive behaviors, restricted interests, social deficits and communication difficulties (Lin et al., 2013). Altered function of several brain areas is thought to underlie the social and cognitive phenotype in autism. Identified brain regions include the amygdala, prefrontal and temporal cerebral cortex and hippocampus, striatum, among others (Sosa-Díaz et al., 2014; Hashemi et al., 2017). Accumulating evidence suggests loss of GABAergic cells in the hippocampus and cerebral cortex of autism (Sgadò et al., 2013; Sabanov et al., 2017; Ariza et al., 2018). Noteworthy, it is reported that morphology and neurophysiology change in the amygdala of autism (Markram et al., 2007; Bringas et al., 2013). Recent efforts have shown the remarkable decrease in neuronal numbers in the lateral nucleus amygdala of autistic subjects (Varghese et al., 2017). Studying in animals has confirmed that GABAergic interneurons within the basolateral amygdala (BLA) are strongly implicated in autistic-relevant behaviors (Prager et al., 2016). Collectively, these results demonstrate that BLA dysfunction may contribute to social and emotional disturbance in autism (Todd and Anderson, 2009; Lin et al., 2013).

OPEN ACCESS

Edited by:

Marylka Yoe Uusisaari,
Okinawa Institute of Science and
Technology, Japan

Reviewed by:

Valerie J. Bolivar,
Wadsworth Center, United States
Crystal C. Watkins,
School of Medicine, Johns Hopkins
University, United States

*Correspondence:

Yinbo Gao
xiaonawang2015@163.com

Received: 29 March 2018

Accepted: 23 July 2018

Published: 13 August 2018

Citation:

Wang X, Guo J, Song Y, Wang Q,
Hu S, Gou L and Gao Y
(2018) Decreased Number and
Expression of nNOS-Positive
Interneurons in Basolateral Amygdala
in Two Mouse Models of Autism.
Front. Cell. Neurosci. 12:251.
doi: 10.3389/fncel.2018.00251

Emerging evidence suggests that deficits in GABAergic inhibitory interneurons are the pathophysiological mechanism of autism (Dong et al., 2016; Lee and Kim, 2017). In particular, glutamic acid decarboxylase 65 and 67 (GAD₆₅, GAD₆₇) are reduced in the cortex of valproic acid (VPA)-treated animals (Oblak et al., 2011a). Studies have also shown decreased GAD₆₅ and GAD₆₇ mRNA levels of the cerebellum in autistic patients (Yip et al., 2007, 2009). Remarkably, it has been established that the subpopulations of GABAergic interneurons in the mouse BLA consist of calcium-binding proteins (parvalbumin (PV), calbindin and calretinin, neuropeptide Y and neuronal nitric oxide synthase (nNOS); Wang et al., 2017). At the behavioral level, mice with reduced PV interneurons expression display the robust autism-relevant behaviors (Filice et al., 2016). The reduced number of PV-containing cells could disrupt the balance of excitation/inhibition and alter gamma wave oscillations in the cerebral cortex of autistic subjects (Hashemi et al., 2017). Likewise, evidence has accumulated the lower density and number of calretinin, calbindin and neuropeptide Y interneurons in autism (Oblak et al., 2011b; Peñagarikano et al., 2011; Adorjan et al., 2017). Notably, we recently found that virtually every nNOS-positive cell is GABAergic interneuron in the BLA (Wang et al., 2017). Despite these observations, it remains presently unknown whether nNOS-expressing interneurons are affected in the BLA of autism.

Environmental exposure and genetic susceptibility are increasingly being recognized as potential risk factors for autism. More specifically, VPA as antiepileptic medication during pregnancy, exhibits similar to the core symptoms of autism, including impaired social interaction, stereotypic/repetitive behaviors and sensory/communication deficits (Roulet et al., 2013; Nicolini and Fahnestock, 2018). Meanwhile, BTBR T⁺Itpr3^{tf}/J (BTBR), a well-studied mouse model of idiopathic autism, displays repetitive self-grooming, deficiencies in social interactions, as well as minimal vocalization in social settings (McFarlane et al., 2008; Provenzano et al., 2016).

Therefore, in the present study, we were prompted to investigate nNOS-expressing interneurons counts in the BLA with stereological techniques in VPA-exposed and BTBR mice. Additionally, nNOS protein and mRNA levels were quantitatively determined by western blot and qRT-PCR, respectively.

MATERIALS AND METHODS

Animals

All procedures were approved by the Shandong University Animal Care and Use Committee and were carried out in compliance with the National Institutes of Health guide for the care and use of Laboratory animals (Publication No. 85-23, revised 1985). BTBR mice were obtained from Model Animal Research Center of Nanjing University. C57BL/6J (B6) mice were provided by Shandong University. Mice, 8 weeks old, were housed in plastic cages (30 cm wide × 18 cm long × 14 cm high) in humidity (30%) and temperature (23°C) maintained under a 12:12 h light/dark cycle (lights on at 07:00).

Food and water were available *ad libitum*. All efforts were made to minimize the animal suffering and the number of animals used.

Drug Administration and Experimental Groups

According to the studies of Wu et al. (2017), single female and male B6 mice were randomly allocated to mate overnight. Pregnancy was determined by the presence of a vaginal plug on embryonic day 1 (E1). We removed male mice from cages in the same day. Pregnant mice received an intraperitoneal injection of 600 mg/kg VPA sodium salt (Sigma Aldrich, St. Louis, MO, USA) on E13 (Al-Askar et al., 2017). Control mice received injection of equal volumes of saline. Pup mice were weaned on postnatal day 21 (P21) and housed in groups of four per cage. Besides, B6 animals have been routinely used as the control for the BTBR mice in autism-related studies (Cheng et al., 2017; Meyza and Blanchard, 2017). Only male offspring were used in this study.

On postnatal 35 days, four offspring groups were deeply anesthetized with pentobarbital sodium, decapitated and processed for stereology, western blot and real time-PCR analysis.

Immunohistochemistry Staining

Immunohistochemistry was conducted as we have previously described (Wang et al., 2017). Adult mice were intracardially perfused with 4% paraformaldehyde and the brain was removed immediately. The BLA was postfixed for overnight, successively placed in 30% sucrose in 0.1 M phosphate-buffered saline (PBS) overnight and cut on a sliding microtome (40 μm). Free floating sections were quenched for 30 min in 3% H₂O₂/30% methanol in PBS and incubated in a blocking solution (5% normal goat serum and 2.5% bovine serum albumin in PBST (0.25% Triton X-100)) for 30 min at room temperature. Sections were then incubated with the goat anti-rabbit nNOS (1:5000; Sigma) in the blocking serum at 4°C overnight. After rinsing in PBST (three times for 10 min), sections were reacted for 2 h at room temperature with biotinylated secondary antibody goat anti-rabbit IgG (1:500, Vector Laboratories; Burlingame, CA, USA) and incubated with avidin biotin peroxidase complex (Vector ABC Kit, Vector Laboratories). The reaction was visualized by detection solution (0.25 mg/ml 3,3'-diaminobenzidine in combination with 0.03% H₂O₂ in PBS). Sections were then transferred onto mounted on glass slides, dehydrated with ascending alcohols, rinsed in xylene and cover slipped.

Stereological Quantification

To determine the total number of nNOS-positive interneurons in the BLA in two mouse models of autism, we used the optical disector principle as previously described (Wang et al., 2017). Briefly, sections were outlined with Stereo Investigator software (MBF Biosciences, Williston, VT, USA). Brain regions of interest (ROIs) were determined based upon stereotactic coordinates provided by the Franklin and Paxinos atlas (Franklin and Paxinos, 2007) at 0.94–2.18 from bregma for the BLA. A 1-in-6 series of sections was analyzed and the counting

frame was $40 \times 40 \mu\text{m}$. The disector height was $13 \mu\text{m}$. Section thickness was measured for every section counted per mouse ($17 \mu\text{m}$). A nNOS-containing cell body was counted as it came into focus within the disector box and above the bottom exclusionary plane. Criteria for counting cells required that interneurons displayed nNOS-expressing immunoreactivity and morphological features in line with each cell type. The total number N of nNOS-expressing cells in the ROIs was calculated using the formula:

$$N = \Sigma Q * t/h * 1/asf * 1/ssf$$

where ΣQ is the total number in the BLA acquired with the optical dissect, t is the mean thickness of section, h is the optical disector height, as f represents the area sampling fraction, and ssf is the fraction of section sampling. Images of sections were captured with a Nikon TE2000U microscope.

Western Blot Analysis

Western blot analysis was carried out as we previously described (Wang et al., 2014). In brief, BLA of homogenates were centrifuged for 15 min at $10,000 g$ at 4°C to remove any cell debris. Proteins ($30 \mu\text{g}$ per well) were separated by sodium dodecyl sulfate-polyacrylamide gel electrophoresis ($100\text{--}120 \text{ V}$) and transferred to polyvinylidene difluoride membranes (Millipore, Milford, MA, USA). The membranes were blocked with 5% non-fat milk powder in Tris buffered saline containing 0.1% Tween 20 (TBST) for 60 min at room temperature. Subsequently, the membranes were probed with the primary antibodies overnight at 4°C : nNOS (1:5000; Sigma) and GAPDH (1:1000; CST, Beijing, China). The membranes were incubated with the secondary antibody horseradish peroxidase conjugated to IgG (1:1000; ZSGB-Bio, Beijing, China) and washed three times with TBST for 10 min each. Protein bands were visualized using the super enhanced chemiluminescence reagent (Pierce, Rockford, IL, USA) and images were captured by luminescent image analysis system (Fujifilm, LAS-4000 mini, Japan). Bands intensities were determined by Image J software program.

Quantitative Real-Time PCR

Total RNA (500 ng) extracted from BLA was isolated using TRIzol reagent (Invitrogen, Carlsbad, CA, USA). RNA concentrations were determined by a NanoDrop spectrophotometer (Thermo Scientific, Wilmington, MA, USA). First-strand cDNA synthesis was performed using Promega's reverse transcriptase kit (Promega, Southampton, UK) following manufacturer's instructions. qRT-PCR was performed to examine the expression of mRNA of the nNOS and GAPDH genes using the universal KAPA SYBR FAST qPCR Universal Master Mix (Kapa Biosystems, Woburn, MA, USA). The sequences of the primers used were as follows: nNOS forward $5'\text{-ACC CAA CGT CAT TTC TGT CC-3'}$ and reverse $5'\text{-AAG GTG GTC TCC AGG TGT GT-3'}$; GAPDH forward $5'\text{-CGGAGTCAACGGATTTGGTCGTAT-3'}$ and reverse $5'\text{-AGCCTTCTCCATGGTGGTGAAGAC-3'}$. Gene expression quantitation was carried out in a DNA thermal cycler (Bio-Rad, San Diego, CA, USA) as follows: a denaturation step of 95°C

for 15 min, 50 cycles of denaturation at 94°C for 15 s and annealing/extension/data acquisition ranging from 60°C to 72°C for 20 s. The housekeeping gene GAPDH mRNA was used as an internal reference to normalize the mRNA content for each sample. Gene expression data were expressed as a proportion of GAPDH gene, as a reference, using a $1/\Delta\text{Ct}$ calculation.

Statistical Analysis

Statistical analysis was performed with GraphPad Prism 5.01 (GraphPad Software, San Diego, CA, USA), using the Student's t test. The level of statistical significance was set at $p < 0.05$.

RESULTS

Stereological Quantification

To determine the extent of nNOS-expressing cell loss in the current study, we first counted the total number of nNOS-containing interneurons in the VPA and BTBR mice models of autism. As illustrated in **Figure 1**, the total number of nNOS interneurons in the BLA of saline-treated offspring, estimated by stereologically counting nNOS-positive interneurons, was $(5.63 \pm 0.92) \times 10^3/\text{mm}^3$ ($N = 8$). However, in the VPA-induced autism model, the total number of nNOS-containing cells was $(4.23 \pm 0.75) \times 10^3/\text{mm}^3$, a 15% reduction compared to B6 controls ($N = 8$, $p < 0.01$, **Figures 1A,C**).

Similarly, the total number of nNOS-immunoreactive interneurons in the BLA of B6 group was $(5.63 \pm 1.30) \times 10^3/\text{mm}^3$ ($N = 8$). In the BTBR mice, the total number of nNOS-expressing cells was $(4.23 \pm 0.92) \times 10^3/\text{mm}^3$, a 43% reduction as compared to B6 strains ($N = 8$, $p < 0.05$, **Figures 1B,D**), indicating that nNOS-containing interneurons in the BLA are vulnerable to VPA-exposed and BTBR mice.

Alterations in Protein and Gene Levels of nNOS

These nNOS-positive interneurons are suggested to play a crucial role in the regulation of neuronal excitability in the BLA (Mańko et al., 2012). Next, we compared the nNOS protein levels in the VPA mouse model of autism with those in saline-exposed offspring. As shown in **Figure 2**, the results showed that exposure of mice to VPA significantly decreased nNOS protein expression in the BLA compared with the corresponding controls ($N = 6$, $p < 0.01$, **Figure 2A**). Likewise, nNOS expression of VPA-treated mice was remarkably decreased as compared to B6 mice ($N = 6$, $p < 0.05$, **Figure 2B**). Thus, nNOS protein expression was down-regulated in nNOS-positive GABAergic cells in the BLA of VPA-exposed and BTBR mice.

Furthermore, our results demonstrated that mice treated with VPA markedly exhibited lower nNOS mRNA levels when compared to saline group ($N = 6$, $p < 0.01$, **Figure 3A**). As expected, nNOS mRNA expression in the BLA of VPA-treated offspring was dramatically decreased compared with B6 mice ($N = 6$, $p < 0.001$, **Figure 3B**). Thus, the nNOS mRNA was dramatically reduced in the nNOS-expressing interneurons in the BLA of VPA-treated and BTBR mice.

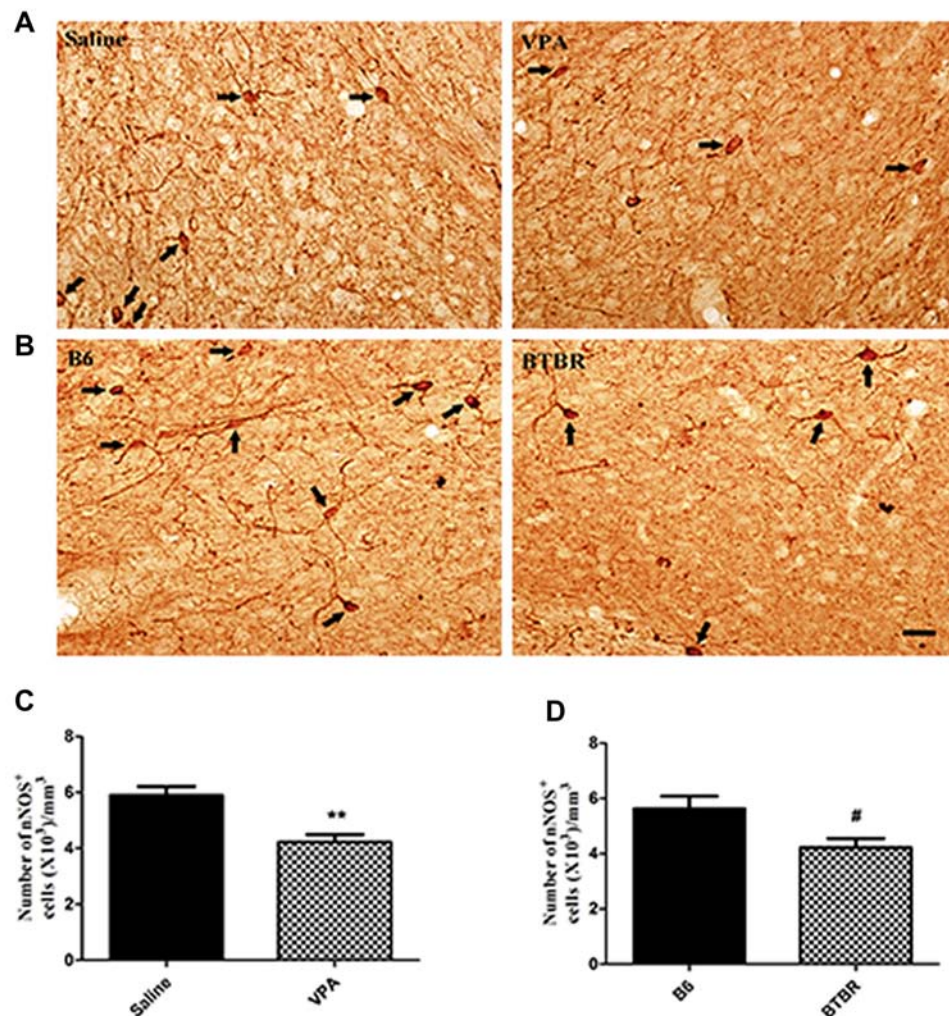


FIGURE 1 | Stereological estimations of neuronal nitric oxide synthase (nNOS)-expressing interneurons in valproic acid (VPA)-exposed (**A**) and BTBR $T^{+}Itpr3^{fl/J}$ (BTBR; **B**) mice in comparison to those in saline-treated and C57BL/6J (B6) mice, respectively. Some nNOS immunoreactive interneurons have been pointed with arrow. Significant differences are observed in nNOS-containing cells in two animal models of autism (**C,D**). ** $p < 0.01$ vs. saline-treated mice. # $p < 0.05$ vs. B6 mice. Scale bars: 25 μ m.

DISCUSSION

Our study demonstrated that number of nNOS interneurons in BLA was reduced in two well-established mouse models of autism. Furthermore, nNOS expression was remarkably decreased in VPA-exposed and BTBR mice at both protein and mRNA levels.

Converging evidence indicates altered GABAergic signaling is related to autism, culminating in the proposal that increase in excitation/inhibition ratio is critical cause of autism (Han et al., 2012, 2014; Lee and Kim, 2017). Specifically, postmortem neuropathological studies of individuals with autism have shown decreased GABA precursors in certain neuron populations and reduced number, density and expression of GABA receptors in the cortex (Blatt and Fatemi, 2011). Moreover, structural amygdala abnormalities such as reduced neuron number and

changes in volume have been observed in individuals with autism (Schumann et al., 2004; Schumann and Amaral, 2006). It has been widely reported that decreasing GABA function decreases sociability in the BLA (Paine et al., 2017). Numerous studies have demonstrated that prenatal exposure to VPA and BTBR mice lead to autism phenotype, which can be used to model the complexity of autism symptoms (Han et al., 2014; Barrett et al., 2017). Accordingly, we first ascertained by stereology that the number of nNOS-expressing cells was altered in the BLA of VPA-exposed and BTBR mice. Of particular noteworthy, our data showed that there was indication of the decrease of nNOS-expressing cells in the BLA of autism, consistent with previous results obtained in the decreased number and density of PV interneurons in the prefrontal cortex in autism (Filice et al., 2016; Ariza et al., 2018). The reduced number of PV-immunoreactive cells could

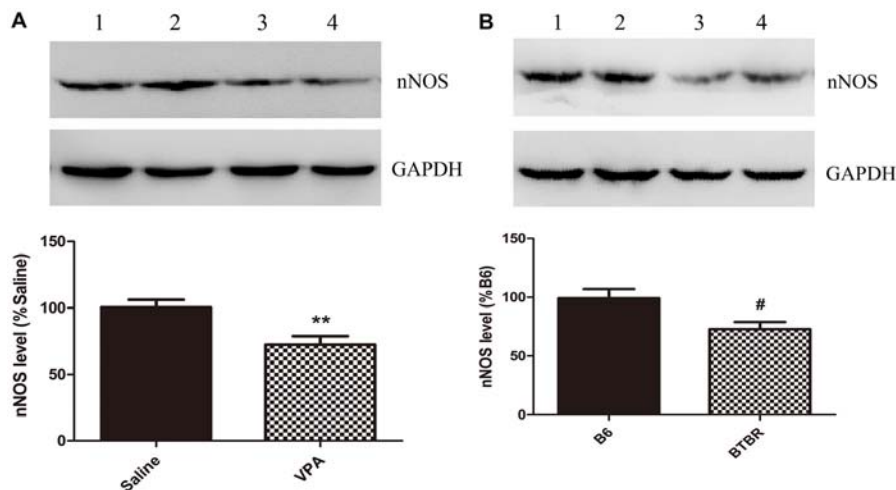


FIGURE 2 | Quantitative western blot analysis of nNOS expression in basolateral amygdala (BLA) samples of VPA-treated and BTBR mice. A representative western blot and the quantification of nNOS protein levels in VPA-exposed (**A**) and BTBR (**B**) mice are shown. (**A**) Band 1, 2 saline-treated group; Band 3, 4 VPA-exposed group. (**B**) Band 1, 2 B6 group; Band 3, 4 BTBR group. Data are from six independent experiments and are shown as mean \pm SEM. Results are expressed as a percentage of normalized nNOS levels measured in controls, defined as 100%. GAPDH signals served as loading controls and were used for the normalization of the nNOS signals. ** $p < 0.01$ vs. saline-treated group. # $p < 0.05$ vs. B6 group.

disrupt the balance of excitation/inhibition and elicit core deficits of autism (Wohr et al., 2015; Hashemi et al., 2017). Of relevance, animal models that exhibit an imbalance in the ratio of pyramidal cells to interneurons in the cortex show core autism-related deficits, including abnormalities in reciprocal social interactions and stereotyped behaviors (Helmeke et al., 2008). It is therefore possible that disruptions in the BLA region through synaptic connectivity formed by reduction of nNOS interneurons may result in disrupted socio-emotional behaviors of autism. Additional researches including direct recordings from nNOS interneurons during the behavioral experiment in autism and observing autism-related phenotypes after modulating the excitation/inhibition balance due to decreased nNOS levels could give us the opportunity to prove the relationship between the two.

While an involvement of nNOS interneurons in autism is rather undoubted, it remains unclear whether the observed reduced nNOS-expressing cells in the BLA of autism are the result of: (I) a truly decreased number of nNOS-positive interneurons due to developmentally immature or perturbed state (e.g., region-improper localization of nNOS-containing cells, enhanced susceptibility, precursor and premature neuronal death) or (II) alternatively from the reduction of nNOS protein (or mRNA) levels or the inability to express sufficient levels of the protein (or mRNA). To resolve this question, one needs to clarify whether the decrease in nNOS-expressing cells in two canonical autism mouse models might in part the result of nNOS down-regulation. Noticeably, the present data showed the decrease in nNOS protein expression for nNOS-positive

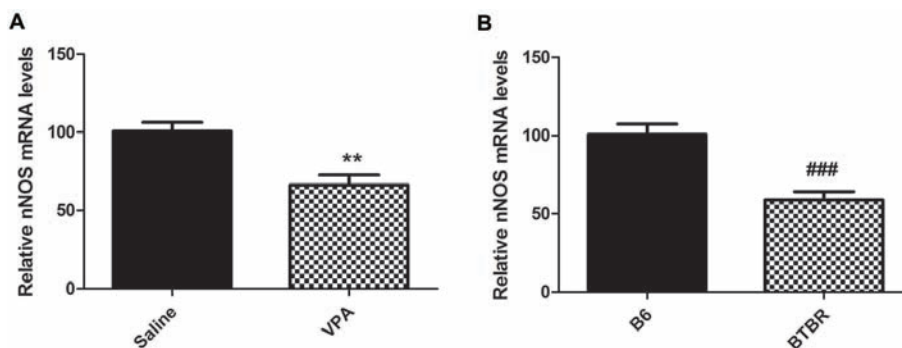


FIGURE 3 | qRT-PCR values from VPA-treated (**A**) and BTBR (**B**) mice representing nNOS mRNA levels were normalized to GAPDH mRNA levels and expressed as fold change compared to controls. Data from six independent experiments were pooled together and are shown as mean \pm SEM. ** $p < 0.01$ vs. saline-treated controls. ### $p < 0.001$ vs. B6 mice.

cells in the VPA-exposed and BTBR mouse models. The similar magnitude in down-regulation of nNOS mRNA manifests the regulation at the level of transcription, in agreement with the reduced GABA content, GAD₆₅ and GAD₆₇ mRNA levels in autism (Chao et al., 2010). Future investigation is necessary to identify possible mechanisms for nNOS interneurons vulnerability and to illustrate the functional consequences for potentially developing autism-like features.

Accumulating evidence indicates that nNOS-containing cells are implicated in inhibitory synaptic transmission (Armstrong et al., 2012; Lange et al., 2012). Particularly, Li et al. (2014) reported that firing of hippocampal nNOS interneurons creates suppression of synaptic inhibition. Previous work has revealed that nNOS-expressing cells evoke a slow inhibitory postsynaptic current (IPSC) caused by volume transmission of GABA and modulate neurons slow inhibition in the BLA (Capogna and Pearce, 2011; Mańko et al., 2012). It should be noted that nNOS-mediated long-term regulation of inhibitory transmission might contribute to fear learning in amygdala (Lange et al., 2012). Following this line of reasoning, thus, identification the slow inhibition properties of nNOS-containing cells within the BLA is crucial for understanding how emotional and cognitive impairments in addition to autistic symptoms are processed. Consequently, the demonstration that nNOS levels are reduced may suggest a shift in the excitation/inhibition balance to a reduced inhibition, considering the proven function of nNOS in synaptic transmission on autism-related defects.

In a complementary fashion, one limitation is that molecular alterations in the VPA model are similar but not identical to those demonstrated in individuals with idiopathic autism (Nicolini and Fahnstock, 2018). On the other hand, the striking feature of BTBR mice is lack of corpus callosum, which is rare among autistic individuals (Meyza et al., 2013). Disc1 mutation, carried by BTBR mice, has been related with autism in some cases. Indeed, a substantial body of evidence indicates that a child is predisposed to autism due to dynamic interplay between environment and genetics (Olexová et al., 2012). Therefore, to further explore the function of nNOS-expressing interneurons in autism, more attention is needed for the development of a combined-model approach, in which the core symptoms and etiological character of autism are represented.

To conclude, the present study has indicated the decrease in the number and expression of nNOS-positive interneurons in autism, which is a fundamental step that will shed light on the origins of altered excitation/inhibition balance in autistic amygdala. As well, testing whether approaches aimed at restoring normal nNOS expression levels and/or nNOS interneuron function might ameliorate autism relevant behavioral phenotypes appears therefore warranted and may represent potential promise for novel therapeutic strategies.

AUTHOR CONTRIBUTIONS

XW and YG designed the research and wrote the manuscript. JG, YS, QW, SH and LG conducted experiments and analyzed the data.

REFERENCES

- Adorjan, I., Ahmed, B., Feher, V., Torso, M., Krug, K., Esiri, M., et al. (2017). Calretinin interneuron density in the caudate nucleus is lower in autism spectrum disorder. *Brain* 140, 2028–2040. doi: 10.1093/brain/awx131
- Al-Askar, M., Bhat, R. S., Selim, M., Al-Ayadhi, L., and El-Ansary, A. (2017). Postnatal treatment using curcumin supplements to amend the damage in VPA-induced rodent models of autism. *BMC Complement. Altern. Med.* 17:259. doi: 10.1186/s12906-017-1763-7
- Ariza, J., Rogers, H., Hashemi, E., Noctor, S. C., and Martínez-Cerdeño, V. (2018). The number of Chandelier and Basket cells are differentially decreased in prefrontal cortex in autism. *Cereb. Cortex* 28, 411–420. doi: 10.1093/cercor/bhw349
- Armstrong, C., Krook-Magnuson, E., and Soltesz, I. (2012). Neurogliaform and Ivy cells: a major family of nNOS expressing GABAergic neurons. *Front. Neural Circuits* 6:23. doi: 10.3389/fncir.2012.00023
- Barrett, C. E., Hennessey, T. M., Gordon, K. M., Ryan, S. J., McNair, M. L., Ressler, K. J., et al. (2017). Developmental disruption of amygdala transcriptome and socioemotional behavior in rats exposed to valproic acid prenatally. *Mol. Autism* 8:42. doi: 10.1186/s13229-017-0160-x
- Blatt, G. J., and Fatemi, S. H. (2011). Alterations in GABAergic biomarkers in the autism brain: research findings and clinical implications. *Anat. Rec.* 294, 1646–1652. doi: 10.1002/ar.21252
- Bringas, M. E., Carvajal-Flores, F. N., López-Ramírez, T. A., Atzori, M., and Flores, G. (2013). Rearrangement of the dendritic morphology in limbic regions and altered exploratory behavior in a rat model of autism spectrum disorder. *Neuroscience* 241, 170–187. doi: 10.1016/j.neuroscience.2013.03.030
- Capogna, M., and Pearce, R. A. (2011). GABA_{A,slow}: causes and consequences. *Trends Neurosci.* 34, 101–112. doi: 10.1016/j.tins.2010.10.005
- Chao, H. T., Chen, H., Samaco, R. C., Xue, M., Chahrouh, M., Yoo, J., et al. (2010). Dysfunction in GABA signalling mediates autism-like stereotypies and Rett syndrome phenotypes. *Nature* 468, 263–269. doi: 10.1038/nature09582
- Cheng, N., Alshammari, F., Hughes, E., Khanabaei, M., and Rho, J. M. (2017). Dendritic overgrowth and elevated ERK signaling during neonatal development in a mouse model of autism. *PLoS One* 12:e0179409. doi: 10.1371/journal.pone.0179409
- Dong, F., Jiang, J., McSweeney, C., Zou, D., Liu, L., and Mao, Y. (2016). Deletion of CTNBN1 in inhibitory circuitry contributes to autism-associated behavioral defects. *Hum. Mol. Genet.* 25, 2738–2751. doi: 10.1093/hmg/ddw131
- Filice, F., Vörckel, K. J., Sungur, A. Ö., Wöhr, M., and Schwaller, B. (2016). Reduction in parvalbumin expression not loss of the parvalbumin-expressing GABA interneuron subpopulation in genetic parvalbumin and shank mouse models of autism. *Front. Mol. Neurosci.* 9:10. doi: 10.1186/s13041-016-0192-8
- Franklin, K. B. J., and Paxinos, G. (2007). *The Mouse Brain in Stereotaxic Coordinates*. San Diego, CA: Elsevier.
- Han, S., Tai, C., Jones, C. J., Scheuer, T., and Catterall, W. A. (2014). Enhancement of inhibitory neurotransmission by GABA_A receptors having $\alpha_{2,3}$ -Subunits ameliorates behavioral deficits in a mouse model of autism. *Neuron* 81, 1282–1289. doi: 10.1016/j.neuron.2014.01.016
- Han, S., Tai, C., Westenbroek, R. E., Yu, F. H., Cheah, C. S., Potter, G. B., et al. (2012). Autistic-like behaviour in Scn1a^{+/-} mice and rescue by enhanced GABA-mediated neurotransmission. *Nature* 489, 385–390. doi: 10.1038/nature11356
- Hashemi, E., Ariza, J., Rogers, H., Noctor, S. C., and Martínez-Cerdeño, V. (2017). The number of Parvalbumin-expressing interneurons is decreased in the prefrontal cortex in autism. *Cereb. Cortex* 27, 1931–1943. doi: 10.1093/cercor/bhw021
- Helmeke, C., Ovtcharoff, W. Jr., Poeggel, G., and Braun, K. (2008). Imbalance of immunohistochemically characterized interneuron populations in the adolescent and adult rodent medial prefrontal cortex after repeated exposure

- to neonatal separation stress. *Neuroscience* 152, 18–28. doi: 10.1016/j.neuroscience.2007.12.023
- Lange, M. D., Doengi, M., Lesting, J., Pape, H. C., and Jüngling, K. (2012). Heterosynaptic long-term potentiation at interneuron-principal neuron synapses in the amygdala requires nitric oxide signalling. *J. Physiol.* 590, 131–143. doi: 10.1113/jphysiol.2011.221317
- Lee, J., and Kim, E. (2017). Excitation/inhibition imbalance in animal models of autism spectrum disorders. *Biol. Psychiatry* 81, 838–847. doi: 10.1016/j.biopsych.2016.05.011
- Li, G., Stewart, R., Canepari, M., and Capogna, M. (2014). Firing of hippocampal neurogliaform cells induces suppression of synaptic inhibition. *J. Neurosci.* 34, 1280–1292. doi: 10.1523/JNEUROSCI.3046-13.2014
- Lin, H. C., Gean, P. W., Wang, C. C., Chan, Y. H., and Chen, P. S. (2013). The amygdala excitatory/inhibitory balance in a valproate-induced rat autism model. *PLoS One* 8:e55248. doi: 10.1371/journal.pone.0055248
- Maňko, M., Bienvenu, T. C. M., Dalezio, Y., and Capogna, M. (2012). Neurogliaform cells of amygdala: a source of slow phasic inhibition in the basolateral complex. *J. Physiol.* 590, 5611–5627. doi: 10.1113/jphysiol.2012.236745
- Markram, K., Rinaldi, T., Mendola, D. L., Sandi, C., and Markram, H. (2007). Abnormal fear conditioning and amygdala processing in an animal model of autism. *Neuropsychopharmacology* 33, 901–912. doi: 10.1038/sj.npp.1301453
- McFarlane, H. G., Kusek, G. K., Yang, M., Phoenix, J. L., Bolivar, V. J., and Crawley, J. N. (2008). Autism-like behavioral phenotypes in BTBR T+tf/J mice. *Genes Brain Behav.* 7, 152–163. doi: 10.1111/j.1601-183x.2007.00330.x
- Meyza, K. Z., and Blanchard, D. C. (2017). The BTBR mouse model of idiopathic autism-current view on mechanisms. *Neurosci. Biobehav. Rev.* 76, 99–110. doi: 10.1016/j.neubiorev.2016.12.037
- Meyza, K. Z., Defensor, E. B., Jensen, A. L., Corley, M. J., Pearson, B. L., Pobbe, R. L. H., et al. (2013). The BTBR T+tf/J mouse model for autism spectrum disorders-in search of biomarkers. *Behav. Brain Res.* 251, 25–34. doi: 10.1016/j.bbr.2012.07.021
- Nicolini, C., and Fahnestock, M. (2018). The valproic acid-induced rodent model of autism. *Exp. Neurol.* 299, 217–227. doi: 10.1016/j.expneurol.2017.04.017
- Oblak, A. L., Gibbs, T. T., and Blatt, G. J. (2011a). Reduced GABA_A receptors and benzodiazepine binding sites in the posterior cingulate cortex and fusiform gyrus in autism. *Brain Res.* 1380, 218–228. doi: 10.1016/j.brainres.2010.09.021
- Oblak, A. L., Rosene, D. L., Kemper, T. L., Bauman, M. L., and Blatt, G. J. (2011b). Altered posterior cingulate cortical cytoarchitecture, but normal density of neurons and interneurons in the posterior cingulate cortex and fusiform gyrus in autism. *Autism Res.* 4, 200–211. doi: 10.1002/aur.188
- Olexová, L., Talarovičová, A., Lewis-Evans, B., Borbélyová, V., and Kršková, L. (2012). Animal models of autism with a particular focus on the neural basis of changes in social behaviour: an update article. *Neurosci. Res.* 74, 184–194. doi: 10.1016/j.neures.2012.10.004
- Paine, T. A., Swedlow, N., and Swetschinski, L. (2017). Decreasing GABA function within the medial prefrontal cortex or basolateral amygdala decreases sociability. *Behav. Brain Res.* 317, 542–552. doi: 10.1016/j.bbr.2016.10.012
- Peñarikano, O., Abrahams, B. S., Herman, E. I., Winden, K. C., Gdalyahu, A., Dong, H., et al. (2011). Absence of CNTNAP2 leads to epilepsy, neuronal migration abnormalities, and core autism-related deficits. *Cell* 147, 235–246. doi: 10.1016/j.cell.2011.08.040
- Prager, E. M., Bergstrom, H. C., Wynn, G. H., and Braga, M. F. (2016). The basolateral amygdala γ -aminobutyric acidergic system in health and disease. *J. Neurosci. Res.* 94, 548–567. doi: 10.1002/jnr.23690
- Provenzano, G., Corradi, Z., Monsorno, K., Fedrizzi, T., Ricceri, L., Scattoni, M. L., et al. (2016). Comparative gene expression analysis of two mouse models of autism: transcriptome profiling of the BTBR and *En2*^{-/-} hippocampus. *Front. Neurosci.* 10:396. doi: 10.3389/fnins.2016.00396
- Roullet, F. I., Lai, J. K., and Foster, J. A. (2013). *in utero* exposure to valproic acid and autism-a current review of clinical and animal studies. *Neurotoxicol. Teratol.* 36, 47–56. doi: 10.1016/j.ntt.2013.01.004
- Sabanov, V., Braat, S., D'Andrea, L., Willemsen, R., Zeidler, S., Rooms, L., et al. (2017). Impaired GABAergic inhibition in the hippocampus of *Fmr1* knockout mice. *Neuropharmacology* 116, 71–81. doi: 10.1016/j.neuropharm.2016.12.010
- Schumann, C. M., and Amaral, D. G. (2006). Stereological analysis of amygdala neuron number in autism. *J. Neurosci.* 26, 7674–7679. doi: 10.1523/JNEUROSCI.1285-06.2006
- Schumann, C. M., Hamstra, J., Goodlin-Jones, B. L., Lotspeich, L. J., Kwon, H., Buonocore, M. H., et al. (2004). The amygdala is enlarged in children but not adolescents with autism; the hippocampus is enlarged at all ages. *J. Neurosci.* 24, 6392–6401. doi: 10.1523/JNEUROSCI.1297-04.2004
- Sgadò, P., Genovesi, S., Kalinsky, A., Zunino, G., Macchi, F., Allegra, M., et al. (2013). Loss of GABAergic neurons in the hippocampus and cerebral cortex of Engrailed-2 null mutant mice: implications for autism spectrum disorders. *Exp. Neurol.* 247, 496–505. doi: 10.1016/j.expneurol.2013.01.021
- Sosa-Díaz, N., Bringas, M. E., Atzori, M., and Flores, G. (2014). Prefrontal cortex, hippocampus, and basolateral amygdala plasticity in a rat model of autism spectrum. *Synapse* 68, 468–473. doi: 10.1002/syn.21759
- Todd, R. M., and Anderson, A. K. (2009). Six degrees of separation: the amygdala regulates social behavior and perception. *Nat. Neurosci.* 12, 1217–1218. doi: 10.1038/nn1009-1217
- Varghese, M., Keshav, N., Jacot-Descombes, S., Warda, T., Wicinski, B., Dickstein, D. L., et al. (2017). Autism spectrum disorder: neuropathology and animal models. *Acta Neuropathol.* 134, 537–566. doi: 10.1007/s00401-017-1736-4
- Wang, X., Liu, C., Wang, X., Gao, F., and Zhan, R. Z. (2017). Density and neurochemical profiles of neuronal nitric oxide synthase-expressing interneuron in the mouse basolateral amygdala. *Brain Res.* 1663, 106–113. doi: 10.1016/j.brainres.2017.02.009
- Wang, X., Yan, S., Wang, A., Li, Y., and Zhang, F. (2014). Gastrodin ameliorates memory deficits in 3,3'-iminodipropionitrile-induced rats: possible involvement of dopaminergic system. *Neurochem. Res.* 39, 1458–1466. doi: 10.1007/s11064-014-1335-x
- Wohr, M., Orduz, D., Gregory, P., Moreno, H., Khan, U., and Vorckel, K. J. (2015). Lack of parvalbumin in mice leads to behavioral deficits relevant to all human autism core symptoms and related neural morphofunctional abnormalities. *Transl. Psychiatry* 5:e525. doi: 10.1038/tp.2015.19
- Wu, H., Wang, X., Gao, J., Liang, S., Hao, Y., Sun, C., et al. (2017). Fingolimod (FTY720) attenuates social deficits, learning and memory impairments, neuronal loss and neuroinflammation in the rat model of autism. *Life Sci.* 173, 43–54. doi: 10.1016/j.lfs.2017.01.012
- Yip, J., Soghomonian, J. J., and Blatt, G. J. (2007). Decreased GAD67 mRNA levels in cerebellar Purkinje cells in autism: pathophysiological implications. *Acta Neuropathol.* 113, 559–568. doi: 10.1007/s00401-006-0176-3
- Yip, J., Soghomonian, J. J., and Blatt, G. J. (2009). Decreased GAD65 mRNA levels in select subpopulations of neurons in the cerebellar dentate nuclei in autism: an *in situ* hybridization study. *Autism Res.* 2, 50–59. doi: 10.1002/aur.62

Conflict of Interest Statement: The authors declare that the research was conducted in the absence of any commercial or financial relationships that could be construed as a potential conflict of interest.

Copyright © 2018 Wang, Guo, Song, Wang, Hu, Gou and Gao. This is an open-access article distributed under the terms of the Creative Commons Attribution License (CC BY). The use, distribution or reproduction in other forums is permitted, provided the original author(s) and the copyright owner(s) are credited and that the original publication in this journal is cited, in accordance with accepted academic practice. No use, distribution or reproduction is permitted which does not comply with these terms.



Color Processing in Zebrafish Retina

April Meier¹, Ralph Nelson² and Victoria P. Connaughton^{1*}

¹Zebrafish Ecotoxicology, Neuropharmacology, and Vision Lab, Department of Biology, and Center for Behavioral Neuroscience, American University, Washington, DC, United States, ²Neural Circuits Unit, National Institute of Neurological Disorders and Stroke (NINDS), NIH, Bethesda, MD, United States

Zebrafish (*Danio rerio*) is a model organism for vertebrate developmental processes and, through a variety of mutant and transgenic lines, various diseases and their complications. Some of these diseases relate to proper function of the visual system. In the US, the National Eye Institute indicates >140 million people over the age of 40 have some form of visual impairment. The causes of the impairments range from refractive error to cataract, diabetic retinopathy and glaucoma, plus heritable diseases such as retinitis pigmentosa and color vision deficits. Most impairments directly affect the retina, the nervous tissue at the back of the eye. Zebrafish with long or short-wavelength color blindness, altered retinal anatomy due to hyperglycemia, high intraocular pressure, and reduced pigment epithelium are all used, and directly applicable, to study how these symptoms affect visual function. However, many published reports describe only molecular/anatomical/structural changes or behavioral deficits. Recent work in zebrafish has documented physiological responses of the different cell types to colored (spectral) light stimuli, indicating a complex level of information processing and color vision in this species. The purpose of this review article is to consolidate published morphological and physiological data from different cells to describe how zebrafish retina is capable of complex visual processing. This information is compared to findings in other vertebrates and relevance to disorders affecting color processing is discussed.

OPEN ACCESS

Edited by:

Philippe Isope,
Centre National de la Recherche
Scientifique (CNRS), France

Reviewed by:

Susan E. Brockerhoff,
University of Washington,
United States
Elvir Becirovic,
Ludwig-Maximilians-Universität
München, Germany

*Correspondence:

Victoria P. Connaughton
vconn@american.edu

Received: 18 July 2018

Accepted: 10 September 2018

Published: 03 October 2018

Keywords: *Danio rerio*, color vision, red, green, blue, ultraviolet

ZEBRAFISH RETINAL STRUCTURE AND DEVELOPMENT

Zebrafish retina, like those of other vertebrates, contains five neural types organized into layers. Distal-most are photoreceptors (PRs) with cell bodies in the outer nuclear layer (ONL) and terminals forming synaptic contacts with the dendritic processes of bipolar (BCs) and horizontal (HCs) cells in the outer plexiform layer (OPL). The cell bodies of these second order neurons, as well as those of third order amacrine cells (ACs), reside in the inner nuclear layer (INL). BCs are presynaptic to AC and ganglion cell (GC) dendrites in the inner plexiform layer (IPL), where processes in the distal IPL, or sublamina *a*, mediate OFF-type responses and processes in sublamina *b* mediate ON-type responses. GC bodies are in the most proximal layer, the GC layer (GCL).

Development of Neurons and Circuits

Eye morphogenesis in zebrafish begins at 12 h postfertilization (hpf; Schmitt and Dowling, 1994). Subsequent structural changes to eye primordia result in well-formed optic cups at 24 hpf (Schmitt and Dowling, 1994), and development of the neural retina progresses in direction from the inner (vitreal) to the outer (scleral) retina. GC and AC form first (~32 hpf), with a small number of GC axons leaving the eye to form the optic nerve at

Citation:
Meier A, Nelson R and
Connaughton VP (2018) Color
Processing in Zebrafish Retina.
Front. Cell. Neurosci. 12:327.
doi: 10.3389/fncel.2018.00327

~34–36 hpf (Stuermer, 1988; Schmitt and Dowling, 1994, 1999; Burrill and Easter, 1995). Initial differentiation of PRs occurs in a patch ventral to the optic nerve head at ~50 hpf (Kljavin, 1987; Raymond et al., 1995; Hu and Easter, 1999; Schmitt and Dowling, 1999; Raymond and Barthel, 2004). Development in the patch continues in advance of other retinal regions until ~70 hpf, when the entire retina appears homogeneous. BC are the last cell type to form at ~60 hpf (Schmitt and Dowling, 1999) and between 60–70 hpf all neuronal cell types can be identified and synapses are apparent (Schmitt and Dowling, 1999). The vertical pathway (i.e., PR-to-BC-to-GC) appears functional at 70–74 hpf (Schmitt and Dowling, 1999), corresponding to innervation of the optic tectum (Stuermer, 1988), hatching, and the onset of visually guided behaviors (Easter and Nicola, 1996, 1997). Many of the developmental transcription factors such as cone rod homeobox gene (*crx*), atonal (*ath5*) and thyroxine $\beta 2$ nuclear receptor (*tr β 2*), which are key to retinal development in mammals, also operate in zebrafish retina (Kay et al., 2001; Shen and Raymond, 2004; Jusuf et al., 2011; Suzuki et al., 2013).

Development of Electrical Signals

Physiological studies show cone inputs dominate electroretinogram (ERG) responses in zebrafish larvae younger than days postfertilization (15 dpf; Bilotta et al., 2001) and recordings from larval GC already reveal complex cone-opponent spectral responses (Connaughton and Nelson, 2015). Rod PR density is low in larvae younger than 10 dpf (Fadool, 2003), explaining the cone-dominated electrical activity of the larval eye. Increased rod outer segment length and synaptic connections occur between 12 dpf and 15 dpf (Branchek and Bremiller, 1984) resulting in an increase in sensitivity (Branchek, 1984). However, the retina does not appear adult-like until after 20 dpf (Branchek and Bremiller, 1984) at which time both rod and cone responses can be detected in the zebrafish ERG (Bilotta et al., 2001). The early development of cones, and later development of rods, is also characteristic of mammalian retinas (Carter-Dawson and Lavail, 1979).

CONE PHOTORECEPTORS ALLOW DETECTION OF LIGHT RANGING FROM LONG (RED) TO ULTRAVIOLET (UV) WAVELENGTHS

Opsins and Cone Morphology

Zebrafish possess four morphological cone types as well as rods. The cones cover an even broader range of the optical spectrum than do human cones. In adults, the cones are classified as short single cones, long single cones, and a double cone pair based on morphology (Engström, 1960), opsin expression, and relative peak absorption wavelengths (λ_{\max}). Short single cones have a λ_{\max} ~360 nm; these are the ultraviolet (UV)-sensitive cones (SWS1 opsin). Long single cones are short wavelength sensitive (SWS2 or blue opsin) cones with a λ_{\max} ~415 nm. Double cones include an accessory member, the middle wavelength sensitive (MWS or green) cone, with a λ_{\max} ~480 nm (probably green opsin RH2-2), and a principal member, the long wavelength

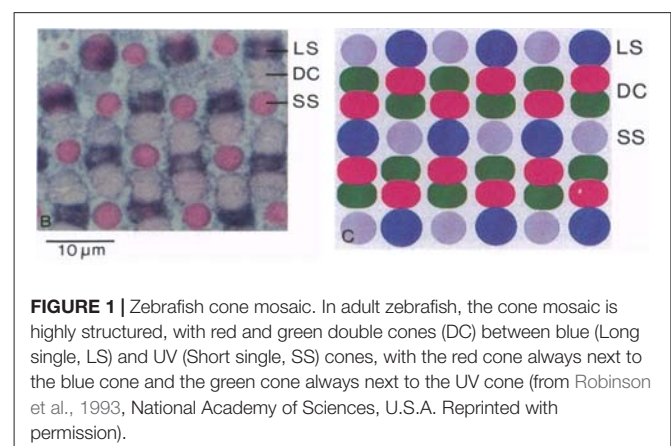
sensitive (LWS1 or adult red opsin) cone, with a λ_{\max} ~570 nm (Nawrocki, 1985; Robinson et al., 1993; Cameron, 2002; Chinen et al., 2003; Allison et al., 2004; Endeman et al., 2013). Molecular analysis of opsin expression in these different cone types has identified two genes encoding the opsins in red cones, four genes for green opsins, and a single gene each for the blue and UV opsins (Chinen et al., 2003).

Within each PR outer segment, a chromophore (11-*cis*-retinal) binds to an opsin molecule forming the visual pigment complex that absorbs light photons (Hubbard and Kropf, 1958). There are two forms of retinal, derived from either vitamin A1 or A2 (Saari, 2012). Zebrafish use only vitamin A1 based pigments, unless they are experimentally treated with thyroxine, which induces the synthesis of vitamin A2 (Allison et al., 2004; Enright et al., 2015).

Cone Mosaics in Larvae and Adults

The four cone types allow zebrafish to respond to wavelengths of light ranging from UV to red. In adults (**Figure 1**), the cones are organized into a row mosaic (Allison et al., 2010) in which double cones alternate with single cones such that the red cone is always adjacent to a blue cone and the green cone is always adjacent to a UV cone (Engström, 1960; Larison and Bremiller, 1990; Raymond et al., 1993; Allison et al., 2010). This row mosaic, first described by Engström (1960), supports a two Red: two Green: one Blue: one UV cone ratio that is constant over the entire retina, except for a small primordial region (Allison et al., 2010). Rod PRs insert into this cone mosaic, with four rods forming a square around each UV cone (Fadool, 2003; Morris and Fadool, 2005). When the retina is viewed in cross-section, it is evident that rods and cones do not form a single row but organize into tiers within the PR layer. The nuclei of short single UV cones are located most proximally. Moving distally one next identifies nuclei of long single blue cones, and then the double cones. Rod nuclei are located proximal to short single cones, while their outer segments are distal to double cones (Branchek and Bremiller, 1984; Robinson et al., 1993).

In contrast to adults, the cone mosaic in larval zebrafish (Larison and Bremiller, 1990) is less well organized and heterotypic, with regularly spaced PRs, but no row pattern (Allison et al., 2010). UV cones form first (Raymond et al., 1995;



Robinson et al., 1995; Schmitt and Dowling, 1999) and are most abundant in larval retina, followed by blue cones. Red/green double cones form last (Robinson et al., 1995; Schmitt and Dowling, 1999) and are least abundant (Allison et al., 2010). Interestingly, opsin expression displays the opposite pattern with expression of red and blue opsins occurring several hours before expression of UV opsin (Schmitt and Dowling, 1999). Red and blue opsins occur in a tandem genetic pattern under a single promoter (Chinen et al., 2003), as do the four variants of green opsins. In cone types with multiple opsin genes (i.e., red and green cones), *in situ* hybridization identified sequential expression of these opsin genes during development (Takechi and Kawamura, 2005). It is the shorter-wavelength-peaking LWS2 that is mainly expressed in larvae, while adults express a mixture of LWS1 and LWS2. For green opsins, the shorter-wavelength-peaking RH2-1 is earliest expressed, followed by the longer-wavelength-peaking RH2-2, RH2-3 and RH2-4. After the cone mosaic is present, the rod mosaic forms (Fadool, 2003; Morris and Fadool, 2005). Transition from larval to the adult mosaic occurs during the postlarval/juvenile period when the fish are >3 weeks of age (Allison et al., 2010).

OUTER RETINA—PROCESSING OF COLOR SIGNALS AT THE FIRST RETINAL SYNAPSE

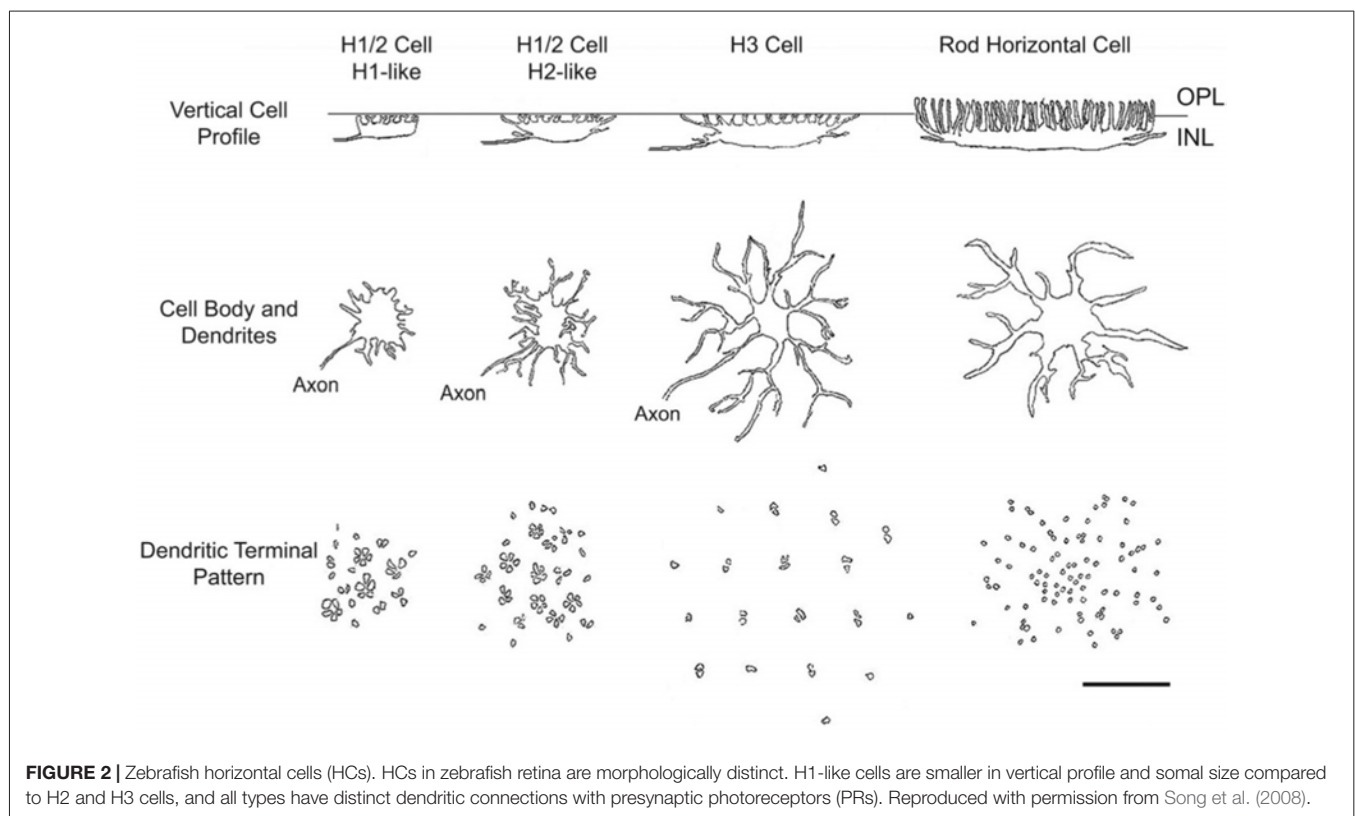
Processing of color signals from different PRs occurs in outer retina. BCs are morphologically diverse retinal interneurons that

receive combinations of inputs from rods and different cone types. Zebrafish HCs similarly contact specific combinations of PR types resulting in mono- and multiphasic spectral response properties that in total reflect inputs from all four cone types. PR inputs to BCs are modified by feedforward and feedback synapses from these spectrally-coded HCs, resulting in significant color processing at this first retinal synapse.

Vertebrate HCs

Mammalian retinas have, in general, two morphological HC types. A-cells are axonless, and large in dendritic extent; whereas the dendritic fields of B-cells are smaller and an axon ending in a terminal arbor projects from the cell body (Fisher and Boycott, 1974). Primate and rodent retinas are exceptions to the mammalian pattern. In primates, HI HCs are similar to B-cells, HII HCs are similar to A-cells, but HIII HCs more resemble teleost HCs, with a long “axon” without terminal arborization projecting from the cell body (Ahnelt and Kolb, 1994; Dacey et al., 1996, 2000). In rodents, there is only a single, B-type HC morphology (Peichl and González-Soreiano, 1994). In teleosts, all HC types bear an axon lacking terminal arborization. There are four HC morphologies in teleosts: H1–H4. Types H1–H3 are postsynaptic to cone PRs, while H4, the rod horizontal cell (HC), is postsynaptic only to rods (Stell and Lightfoot, 1975; Stell, 1975; Weiler, 1978).

In vertebrates, each HC type receives input from specific numbers and types of PRs resulting in either spectrally monophasic (L-type) or multiphasic (C-type responses; Nelson, 1977; Yang et al., 1983; Siminoff, 1986; Djamgoz et al., 1988;



Negishi et al., 1988; Dacey et al., 1996, 2000; Asi and Perlman, 1998; Twig and Perlman, 2004; Yin et al., 2006). One conspicuous difference in the physiology of mammalian HCs as compared to other vertebrates is the complete lack of C-type responses.

Cone Contacts of Horizontal Cell Types

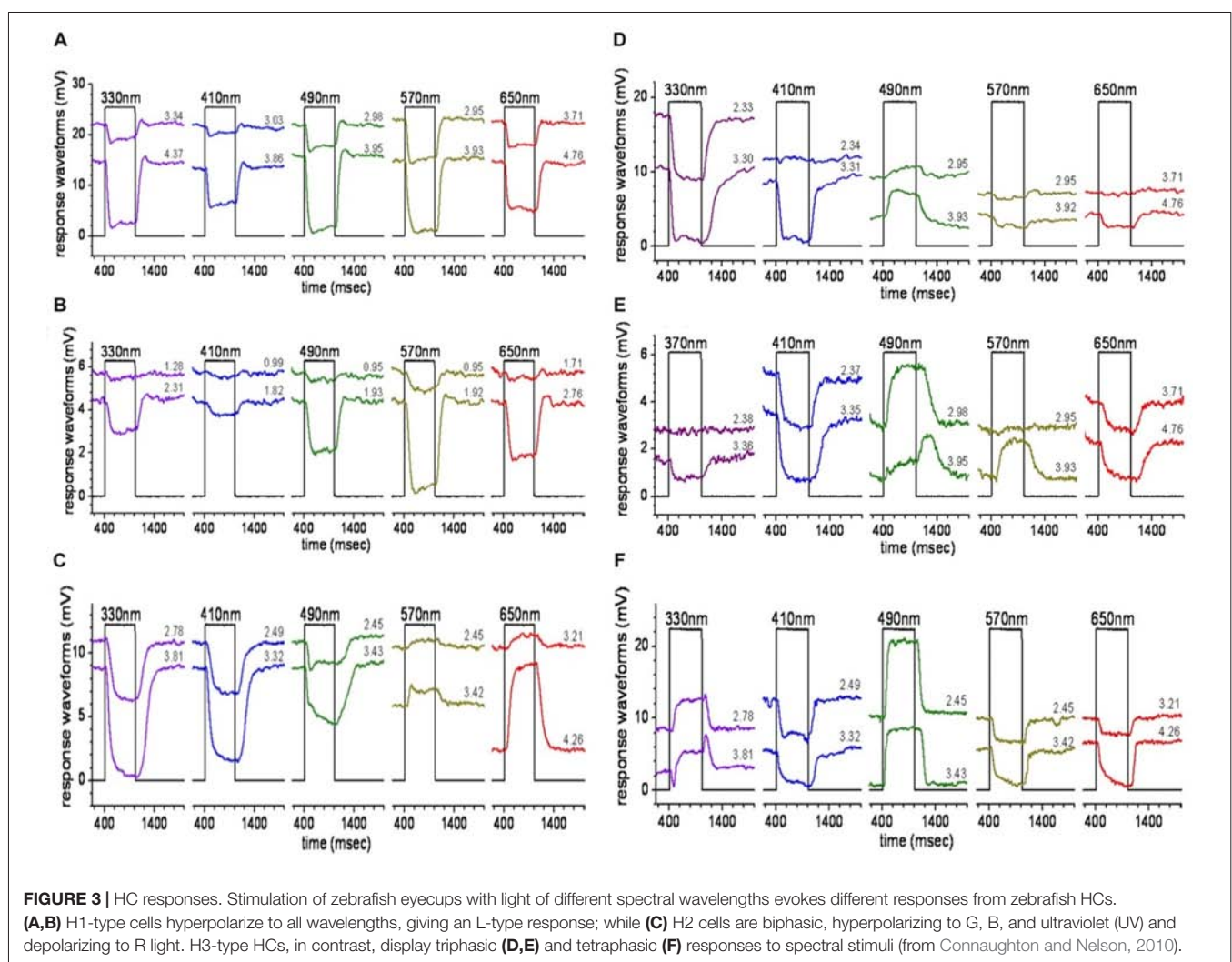
Zebrafish HC contribute to color vision by facilitating color-opponent mechanisms through feedback and feedforward connections to PR and/or BC (Song et al., 2008). As in goldfish (Stell, 1967; Stell and Lightfoot, 1975), zebrafish cone-contacting HCs are morphologically characterized as H1, H2, or H3 types, and rod horizontal cells (RHCs or H4 type) which contact rods (Song et al., 2008; Li et al., 2009). All zebrafish HC are axon-bearing, with a snake-like terminal that does not contact PRs running within the OPL (Song et al., 2008).

Zebrafish H1 HC (**Figure 2**) have a plate-shaped soma from which short dendritic processes protrude. H2 HC exhibit a wider profile than H1 HC and have an ellipsoid soma that extends tendrill-like dendritic processes. The dendritic terminals of H1 and H2 occur in clusters of 5–6 boutons arranged in a rosette. The rosettes contact both double and single cone rows.

When overlapped onto this cone mosaic, patterns consistent with contacts between HCs and either red, green and blue cones (H1 cells) or green, blue and UV cones (H2 cells) appear (Li et al., 2009). Due to H1/2 cell partial clusters and in some cases single boutons, it is probable certain individual cones may make connections with more than one HC. The remaining elements of the cluster would be contacted by another HC. H3 HC have an elongated cell body, with 3–4 long dendritic processes terminating in a rhomboid pattern with boutons arranged in doublets (Connaughton et al., 2004; Song et al., 2008). The dendritic extent of H3 is distinctly wider than either H1 or H2, making it easily recognizable. Examination of the H3 dendritic pattern on a transgenic cone mosaic where UV cone terminals are labeled suggests H3 cells selectively contact long single blue and/or short single UV cones, a pattern appearing to serve short wavelengths (Song et al., 2008; Li et al., 2009).

Development of H3 Types

The development of H3 cells was followed in larval zebrafish where the ratio of UV to blue cone synapses increased from about 2:1 at 3 dpf to 5:1 at 10 dpf. This ratio is greater than



the ratio of UV to blue cones, suggesting H3 cells actively seek out contacts with UV cones during development. The *trβ2* nuclear receptor is required for red cone development (Ng et al., 2001; Suzuki et al., 2013). When the density of UV cones was increased (and red cones decreased) by suppression of *trβ2* nuclear receptor, H3 dendrites grew and accommodated the extra UV cells with synapses. Genetic suppression of blue or UV synaptic transmission suggested that, at least for the UV to H3 synapse, activity is critical for synapse formation (Yoshimatsu et al., 2014).

Horizontal Cell Spectral Processing

Intracellular recordings of HC spectral responses identified luminosity (L-type) and chromaticity (C-type) HCs (Connaughton and Nelson, 2010), as in other teleosts (Svaetichin and Macnichol, 1958), including other cyprinidae (Naka and Rushton, 1966a,b; Kaneko, 1970). L-type, or spectrally monophasic responses hyperpolarize to light at all stimulus wavelengths and irradiances (Figures 3A,B). Most zebrafish HCs encountered (~66%) were L-type. Of these L-type responses, the majority were red-preferring L2 cells, with peak sensitivity to wavelengths ~560 nm; the rest are red/green L1 cells with a mean peak sensitivity ~490 nm (Connaughton and Nelson, 2010). C-type responses included spectrally biphasic, triphasic, and tetraphasic varieties. Biphasic cells depolarized to long wavelength stimulation (>570 nm) but hyperpolarized to wavelengths ≤530 nm (Figure 3C). Spectral responses of triphasic cells, in general, hyperpolarized to long wavelength stimuli (650, 610, and 570 nm), and depolarized to middle and short wavelengths (530, 490, and 450 nm). UV triphasic cells hyperpolarized strongly to 370 and 330 nm stimuli, while blue

triphasic cells hyperpolarized weakly to these UV stimuli, but more strongly to a 410 nm stimulus (Figures 3D,E). The final HC spectral response identified was a unique tetraphasic response (Figure 3F) characterized by hyperpolarization to red-yellow (650–570 nm), depolarization to green and green-blue (530, 490 nm), hyperpolarization to 450, 410 and/or 370 nm, and depolarization to UV (330 nm; Connaughton and Nelson, 2010). Dye fills of recorded cells indicate HCs with L-type and biphasic spectral responses were similar in morphology (Connaughton and Nelson, 2010) and distinct from cells with triphasic and tetraphasic responses. Combining images of microelectrode stains and response properties with the anatomical studies of HC morphologies and PR terminals (Li et al., 2009), suggests: (a) L-type responses occur in H1 HCs; (b) biphasic cells are H2 cells; and (c) triphasic and tetraphasic responses occur in H3-type HC (Li et al., 2009; Connaughton and Nelson, 2010).

CONE SYNAPSES WITH BIPOLAR CELLS

Vertebrate BCs Are Similar in Glutamatergic Mechanisms and Axonal Stratification Patterns

Zebrafish BCs were initially classified by their glutamate-gated currents, which identified both ON- and OFF-type cells. ON-cells express metabotropic glutamate receptors and a chloride channel forming glutamate transporter on their dendritic arbor (Grant and Dowling, 1995); whereas, OFF-type cells express AMPA/kainate receptors (Connaughton and Nelson, 2000). The ON-BC dendritic “glutamate transporter channel” is not seen in mammals as it provides presynaptic inhibition on axon

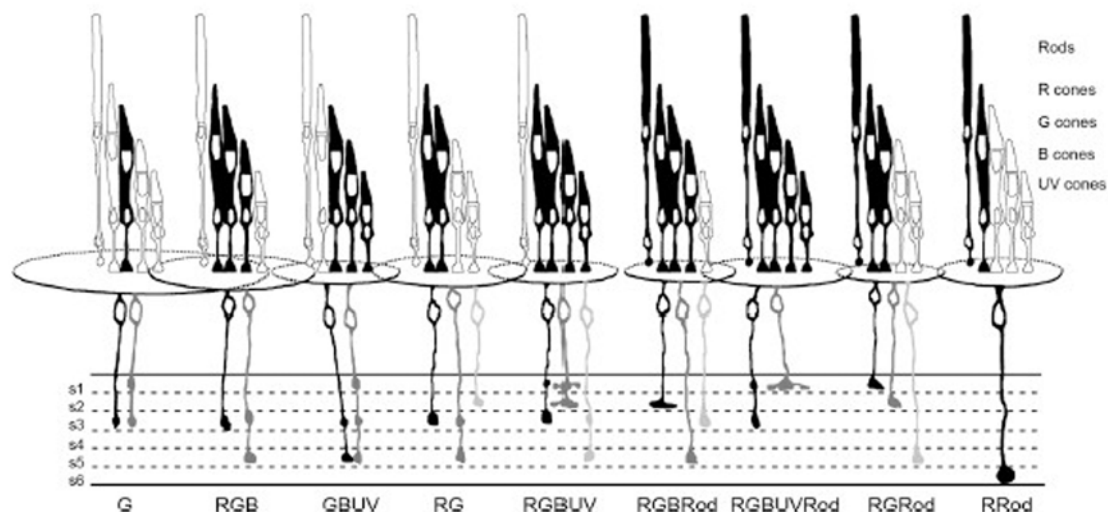


FIGURE 4 | Bipolar cells make diverse connections with PRs. Summary figure (reproduced with permission from Li et al., 2012) showing the different PR connections associated with morphologically-distinct types of BCs. Each BC was identified by axon terminal ramification within the six sublaminae (s1–s6) of the inner plexiform layer (IPL) and by dendritic connections with specific cone types. Most BC types make connections with multiple (>2) PR types, except for two types that exclusively contact green cones (at left of figure) Rod, contacts rods; R, red cones; G, green cones; B, blue cones; UV, UV cones. Shading reflects frequency of identification of a given type, with the darker (black) color indicating the most commonly observed type.

terminals of mammalian ON-type BCs (Wersinger et al., 2006). Morphologically, the axon terminals of physiologically ON-BCs were found within IPL sublamina *b* while OFF-BC terminals were in sublamina *a* (Connaughton and Nelson, 2000). These sublamina divide the IPL roughly in half, with sublamina *a* represented by the outer half, near ACs, and sublamina *b* by the inner half, near GCs, consistent with IPL structure and BC morphology in other vertebrates. Subsequent studies using dye-labeling methods (DiI) introduced a 6-stratum scheme for classifying bipolar axon terminal depth within the zebrafish IPL and identified ~17 morphological types of BCs based on axonal stratification patterns (Connaughton et al., 2004; Li et al., 2012). This number of types was large as compared to mammals (Kolb et al., 1981; Haverkamp et al., 2005; Masland, 2012) and amphibians (Wu et al., 2000), but similar to the 15 types identified in goldfish with Golgi staining (Sherry and Yazulla, 1993). Of the 17 types in zebrafish, ~7 were OFF-cells, ~6 were ON-cells, and ~4 were presumed ON-OFF cells with axon terminals in both sublamina *a* and *b* (Connaughton et al., 2004). This latter type, with bistratified axon terminals, physiologically expressed either OFF-type or ON-type glutamate receptors (Connaughton and Nelson, 2000).

Bipolar Cells Differentially Contact Multiple Cone Types

Superposition of DiI-stained BC dendrites onto the zebrafish cone mosaic revealed BC type-specific synaptic connection patterns with PRs, and further expanded the number of BC

types to ~33 (Li et al., 2012). Nine dominant patterns of PR connections accounted for 96% of a total of 18 patterns found (Figure 4). These dominant patterns included both cone-only BCs, exclusively postsynaptic to cone PRs, and mixed-rod-cone input BCs (Li et al., 2012). Only one of the cone-selective patterns was restricted to a single cone type (green cones), and one of the mixed rod-cone patterns received input from all PR types. Examining the axon-terminal stratification types among these PR connectivity patterns, six of the nine patterns included monostratified ON types, with terminals in s4–s6 and either monostratified or bistratified OFF types, with all terminals in s1–s3. Four of the patterns included ON-OFF axon terminal stratification types. The variety in presynaptic connections, the dendritic field size of each BC, and the terminal ramification patterns in the IPL (Li et al., 2012) suggest selective and elaborate color circuits involving BCs across the entire retina.

Bipolar Cell Spectral Properties

Recent calcium-imaging 2-photon microscopy of BC axon terminals in live zebrafish larvae found BCs that were chromatic (wavelength selective), achromatic (responding to all wavelengths), or opponent (opposite responses at two wavelengths; Figure 5). To image light-driven calcium activity, a transgene, consisting of the *ribeyeA/ctbp2* promoter, which is selectively expressed by retinal BCs, and the synaptophysin-GCaMP6f fusion protein, a synaptically localized calcium sensor (Dreosti et al., 2009; Zimmermann et al., 2018), was inserted into the zebrafish genome.

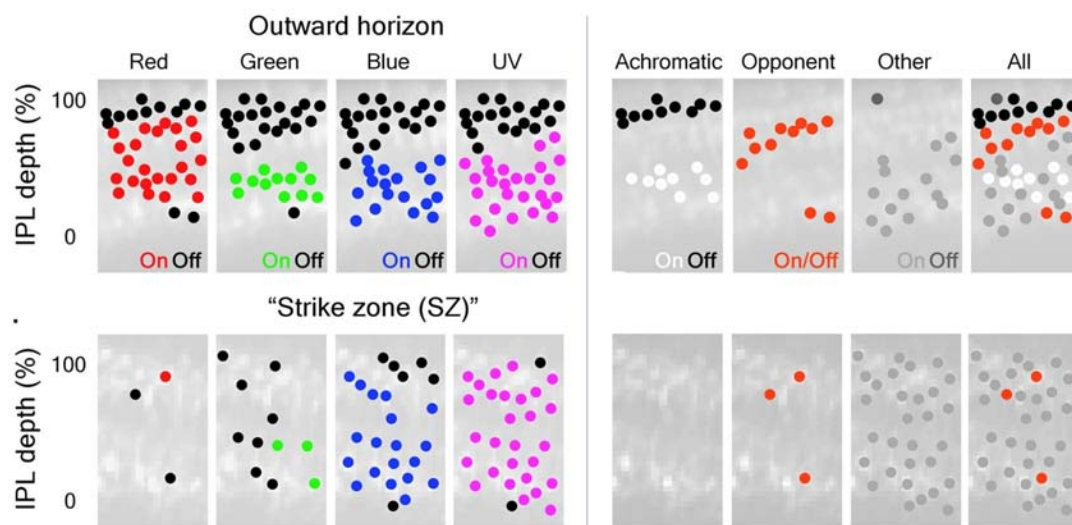


FIGURE 5 | Color inputs to inner retina are segregated in the IPL. BC terminals in the larval zebrafish IPL can be segregated based on the spectral inputs they respond to across the visual scene. (Left) BC-terminal excitation by R, G, B, and UV stimuli are represented as red, green, blue and magenta dots located throughout the IPL; inhibitory responses are represented as black dots. The distribution of ON-responses varies based on the spectral stimulus and which part of the visual scene (outer horizon vs. “strike zone (SZ)”) is being viewed. The “SZ” represents looking forward and upward at prey items. (Right) Subsequent classification of the different spectral inputs from BCs into the IPL identified achromatic and color-opponent regions in this synaptic layer that were most evident outside the “SZ”. For the right panels: black dots = achromatic OFF-responses, white dots = achromatic ON-responses, red dots = color-opponent responses, gray dots = “other” (taken from Figure 3, Zimmermann et al., 2018).

A blue-UV chromatic response was found to be regionally selective, with a preponderance of ON-type UV-excited BC terminals throughout the IPL. In retinal topology, these cells densely occupy a temporal-ventral “strike zone (SZ),” the region looking forward and upward at prey (Zimmermann et al., 2018). Both ON and OFF achromatic types responded with excitation or inhibition to all wavelengths tested. Opponent responses included red excited, green, blue and UV inhibited, as well as blue and UV excited, but red, green inhibited. These results are broadly consistent with neuroanatomical connectivity of BCs, particularly in respect to the many cone signals represented in BC terminals throughout the depth of the IPL, which attests to the idea that multi-cone contacting BCs may connect to cones in a color-opponent manner.

To date, there have been no studies reporting the spectral responses of zebrafish BCs using either whole-cell patch or sharp electrode techniques. In the closely related Giant Danio retina (*Danio aequipinnatus*), however, patch recordings of bistratified cone BCs with axonal boutons in both sublamina *a* and sublamina *b* (Cab BCs) revealed color-opponent responses, excited by one wavelength, but inhibited by another. The Cab cells subtract signals from cones with different opsin expression, and multiple spectral patterns were observed. There was evidence that different types of BC dendritic glutamate receptors were stimulated by different spectral types of cone (Wong and Dowling, 2005). Further, spectral light stimulation (red, green, or blue), evoked double color-opponent responses. Selectively blocking AMPA/kainate receptors or glutamate transporter associated chloride channels on these cells revealed that the responses to stimulation with short and long wavelengths are mediated by these two-different glutamate-gated mechanisms (Wong and Dowling, 2005).

ERG b-Waves Suggest Bipolar-Cell Spectral Properties

The ERG is a light-evoked retinal field potential that sums activities of retinal neurons. ERG b- and d-waves represent, and are dominated by, the massed activity of ON- and OFF-BC types in zebrafish, respectively. The b-wave in adult zebrafish receives contributions from all four cone types and exhibits evidence of red-green color-opponent mechanisms (Hughes et al., 1998). Modeling these inputs, (Cameron, 2002) separated b-wave signals into four different processing channels, one for each cone type. Two color channels (long and middle wavelengths) were involved in color-opponent processing, while the short and UV wavelength channels were not (Cameron, 2002). This suggests BCs detect wavelength-dependent differences in both chromatic and luminance contrast (Cameron, 2002).

ERG b-wave responses in larval zebrafish are different from those in adults. Adult ERG responses include a-wave, b-wave, and d-wave components at all stimulus wavelengths and irradiance levels (Bilotta et al., 2005). The components present in a larval ERG, however, are wavelength dependent. For example, in response to UV light stimulation, the larval ERG includes a large a-wave, delayed b-wave, and small/no

d-wave. However, if middle/long wavelength stimuli are used, the ERG has a small/no a-wave followed by large amplitude b- and d-waves (Bilotta et al., 2005). The ERG of larval zebrafish retina is dominated by UV cones, and the physiological differences in a-wave amplitude evoked using UV vs. longer wavelength stimuli can be attributed to differences in cone representation in larval responses (Bilotta et al., 2005). However, differences in larval b-wave (ON-BC) responses may also be due to differences in glutamate receptor expression on these cells. For example, UV and short wavelength stimuli seemed to be mediated by APB-sensitive metabotropic glutamate receptors on ON-BC dendrites, while longer wavelength stimuli were not (Bilotta et al., 2005). Multiple glutamate-gated mechanisms are present on adult zebrafish ON-BCs (Connaughton and Nelson, 2000; Nelson and Singla, 2009) and it appears that the mechanisms may be somewhat selective for cone type.

SPECTRAL PROCESSING IN AMACRINE CELLS

AC Characteristics

As a group, and across all vertebrates, ACs are the most diverse class of retinal neuron. ACs are categorized by their physiological response to light, their great variety of neurotransmitter expression as determined using immunolabeling, their dendritic morphology, and dendritic lamination patterns in the IPL. The different types of ACs range from 43 in roach (Wagner and Wagner, 1988) to 22 in cat (Kolb et al., 1981) to ~30 in rabbit (MacNeil et al., 1999; Masland, 2012). Physiological responses of ACs are similarly diverse. Light stimulation evokes sustained or transient, ON, OFF, or ON-OFF responses in both mammalian (Nelson, 1982; Nelson and Kolb, 1985; Stafford and Dacey, 1997; Menger and Wässle, 2000) and non-mammalian (Kaneko, 1970, 1973; Pang et al., 2002; Miller et al., 2006; Zhang and Wu, 2010) retinas.

Structural and functional diversity is also present in zebrafish ACs where ~28 morphological types have been identified in 5 dpf larval retina (Jusuf and Harris, 2009). Many larval AC types are also present in adults, as determined by dye (Connaughton et al., 2004) and/or immunolabeling (Marc and Cameron, 2001; Yazulla and Studholme, 2001; Arenzana et al., 2006; Yeo et al., 2009; Jang et al., 2011). These cells exhibit narrow, medium, or wide field dendritic arbors (Jusuf and Harris, 2009; Lewis et al., 2015) and are widely distributed over the entire retina (Yeo et al., 2009; Torvund et al., 2017); although it appears the density of parvalbumin s4, and tyrosine hydroxylase (dopaminergic) types is greater in temporal-ventral, or ventral retina than nasal retina (Yeo et al., 2009; Jang et al., 2011). In adult zebrafish, AC light responses are either transient or sustained, with excitation observed at light ON, light OFF, or both light ON and light OFF (Torvund et al., 2017). Most dendritic branching patterns are highly planar and narrowly restricted to single strata within the IPL. Both monostратified

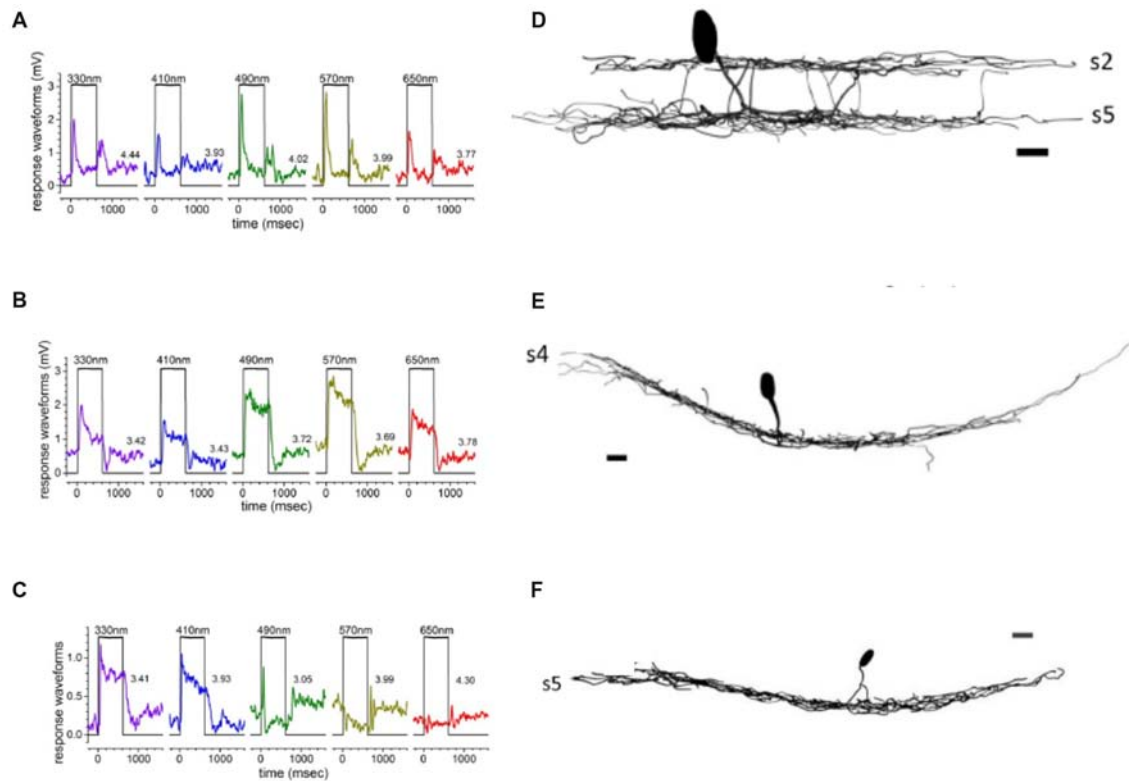


FIGURE 6 | Spectral responses of ACs are associated with specific cell types. Transient ON-OFF amacrine cells (AC) responses (**A**) were characteristic of bi-stratified ACs with dendrites in both the OFF- and ON-sublaminae (**B**). In contrast, sustained ON responses (**C**) were observed in ACs with a dendritic arbor monostratified in sublamina *b* (**D**). Spectrally multiphasic C-type responses were primarily observed in ON-cells, as shown in the biphasic response (**E**) from a monostratified AC with dendrites in s5 of sublamina *b* (**F**) (Torvund et al., 2017).

types (one branching plane) and bistratified types (two branching planes) are observed (Connaughton et al., 2004). Diffuse dendritic branching through multiple IPL strata was uncommon.

ON-OFF Amacrine Cells Select Red Cone Signals

ON-OFF responses in zebrafish are characteristic of all bistratified ACs (**Figures 6A,B**). Most of these have processes in both IPL sublamina *a* and *b*, though some ON-OFF cells have processes bistratified only within sublamina *a* (Torvund et al., 2017). These cells respond to spectral stimuli ranging from 330 nm to 650 nm; however, modeling of their responses indicates virtually exclusive input from red cones (Torvund et al., 2017), both at light ON and light OFF. For calcium imaging, ACs can be marked by the inhibitory-interneuron selective transgene *ptf1a:gal4* (Jusuf and Harris, 2009). Marked cells express the synaptic calcium reporter transgene *UAS:SyGCaMP3* (Rosa et al., 2016). In the IPL, bands of ON-OFF responding processes and synapses can be found in both sublamina *a* and sublamina *b*, a result consistent with the existence of ON-OFF bistratified AC types. This method, however, is not able to directly link both bands to actions from single

bistratified ACs. The frequency responses of these ON-OFF signals included different populations peaking at either ~5 Hz or ~10 Hz.

ON-Sustained and OFF Amacrine Sum Red and Green Cone Signals

Zebrafish OFF-type ACs, like ON-OFF types, receive dominant input from red cones, with lesser input from green or blue cones (Torvund et al., 2017). These cells are monostratified in either s1 or s2 of sublamina *a*. ON-type AC, with monostratified dendrites in s4, or rarely s3, receive mixed luminosity signals from red and green cones, leading to mid-spectral sensitivity peaks (**Figures 6C,D**). The ON ACs were sustained types, not excited at light OFF, and contributions from blue and UV cones are noticeably lacking in these non-opponent responses (Torvund et al., 2017). The dendrites of both ON and OFF *ptf1a* ACs, marked for synaptic calcium responses, labeled distinct IPL strata, with a major ON band in sublamina *b*, and a major OFF band in sublamina *a*. In addition, calcium imaging suggests a lower intensity representation of both these response types throughout retinal depth (Rosa et al., 2016). Crossover GABAergic inhibition from ON-ACs appears to shape the frequency response characteristics of OFF-BC terminals (Rosa

et al., 2016), leading to the speculation that sustained ON-ACs contribute “low pass” characteristics to OFF-BC boutons.

C-Type Amacrine Cells Subtract Cone Signals

Unique as compared to mammals, some zebrafish ACs are color-opponent. UV cone inputs contribute significantly to color-opponent (C-type) responses in zebrafish AC. The dendrites of all these C-type ACs ramify deep in sublamina *b*, indicating they are ON-type cells morphologically, though physiologically the response sign depends on wavelength (Figures 6E,F). In adult retina, both spectrally biphasic and triphasic AC responses are present, as also observed in HC spectral responses (Connaughton and Nelson, 2010). Biphasic AC responses include blue-yellow and red-green units. Red-green opponent cells depolarized to red, but hyperpolarized to green, blue and UV stimulation; while blue-yellow opponent cells responded with a sustained depolarization to short wavelength stimulation, but hyperpolarized to long wavelengths (Torvund et al., 2017). Some triphasic ACs depolarized to UV, hyperpolarized to blue, and depolarized to green. Interestingly, inclusion of (marginally significant) red cone inputs to the triphasic response would cause it to be reclassified as a tetrachromatic AC response (Torvund et al., 2017). Calcium imaging studies have found color-opponent BC terminals within the layer of dendritic branching of color-opponent ACs (Zimmermann et al., 2018). The bistratified, color-opponent Cab bipolar of Giant Danio also sends a terminal bouton to this same layer (Wong et al., 2005). Taken together these studies identify a potential synaptic input for C-type ACs. Wide dendritic fields, sometimes seen with dye coupling, suggest a wavelength-dependent modulatory role.

MORPHOLOGY AND PHYSIOLOGY OF RETINAL GANGLION CELLS

GC Physiology in Vertebrates

As the output neuron of the retina, there have been many studies documenting light responses of retinal GCs. In fact, color-opponent GCs have been documented in a variety of species, including, but not limited to, monkey (De Monasterio and Gouras, 1975; Zrenner et al., 1983; Dacey and Lee, 1994; Calkins et al., 1998; Sun et al., 2006; Crook et al., 2009; Lee and Sun, 2009; Dacey et al., 2014; Silveira et al., 2014), cat (Daw and Pearlman, 1970; Crocker et al., 1980; Guenther and Zrenner, 1993), wallaby (Hemmi et al., 2002), rabbit (Caldwell and Daw, 1978; De Monasterio, 1978; Mills et al., 2014), guinea pig (Yin et al., 2009), mouse (Chang et al., 2013), turtle (Bowling, 1980; Rocha et al., 2008), chick (Zhou et al., 2005), and fish (Wagner et al., 1960; Witkovsky, 1965; Daw, 1968; Raynauld, 1972; Spekrijse et al., 1972; Van Dijk and Spekrijse, 1984; Mackintosh et al., 1987; Bilotta and Abramov, 1989; Sakai et al., 1997). Therefore, the presence of spectrally selective GC responses in zebrafish would not be surprising. A wide range of GC characteristics/response types makes sense as these cells receive, integrate and process information from BC and AC about various parameters of the visual scene.

Zebrafish GC Morphology, Development and Tectal Projection

Mammals, in general, have a greater number of morphological types of GCs (Kolb et al., 1981; Sanes and Masland, 2015) than zebrafish (Mangrum et al., 2002). The 11 types identified in adult zebrafish (Figure 7) are grouped as either wide-field (2), narrow-field (4), multistratified (3), or diffuse (2) based on dendritic extent and patterns of stratification (Mangrum et al., 2002). A main reason for less types in zebrafish is a closer grouping of cell body diameters (5–8 μm) and dendritic field diameters (80–200 μm) as compared to mammals (cat: 10–40 μm cell bodies; 20–900 μm dendritic fields; Kolb et al., 1981). A wide spread of metrics allows for more type-features to be distinguished. In mouse retina, similar to zebrafish, GC dendritic fields are restricted in range (150–450 μm ; Sun et al., 2002). The greatest density of zebrafish GCs occurs in a temporal-ventral patch similar to the “SZ”, a visual space used for feeding (Mangrum et al., 2002; Zimmermann et al., 2018).

Time-lapse imaging experiments in larval zebrafish (Mumm et al., 2006) discovered diverse dendritic growth patterns and laminar targeting mechanisms used by GCs in the IPL, resulting in 15 stratification patterns. GC input to the tectum is somewhat segregated, with inputs relaying similar information (such as stimulus direction) going to similar tectal areas (Johnston and Lagnado, 2012). Though these inputs to the tectum are functional by 66 hpf, it is not until 78 hpf that tectal neurons begin to display mature responses. This suggests that GCs are capable of information processing before structural development in the retina is complete (Niell and Smith, 2005).

Ganglion Cell Light Responses

Light responses of larval zebrafish GCs are either transient or sustained, with ON-, OFF- and ON-OFF subtypes (Emran et al., 2007). Most ON-OFF cells are bistratified in sublaminae *a* and *b*, while ON- and OFF-cells are monostatified (Zhang et al., 2010). Between 2 dpf and 4 dpf zebrafish GCs undergo depolarizing to hyperpolarizing shift in GABAergic inhibitory E_{Cl} (Zhang et al., 2010), a process common to vertebrate early neuronal development (Li et al., 1998). Stable light responses are recorded as early as 4 dpf (Zhang et al., 2010) and color-opponent and non-opponent responses are evident at 5 dpf and 6 dpf, when responses are dominated by spectrally multiphasic types (Connaughton and Nelson, 2015). The most common spectral type is the triphasic GC response with bursts of spikes to both long and short wavelength stimuli, but inhibited firing at middle wavelengths. Other multiphasic responses include biphasic, tetraphasic and pentaphasic units (Connaughton and Nelson, 2015). Like adult ACs, red cone inputs are prominent in larval GC spectral responses. However, most GC responses include significant and commonly dominant, UV excitation, resulting in multiphasic spectral properties. Very few larval zebrafish GCs are spectrally monophasic (Figure 8). In adult zebrafish, light-evoked spike discharges are seen in the optic nerve, particularly ON-OFF types (Li and Dowling, 2000; Huang et al., 2005), but the spectral properties are not known.

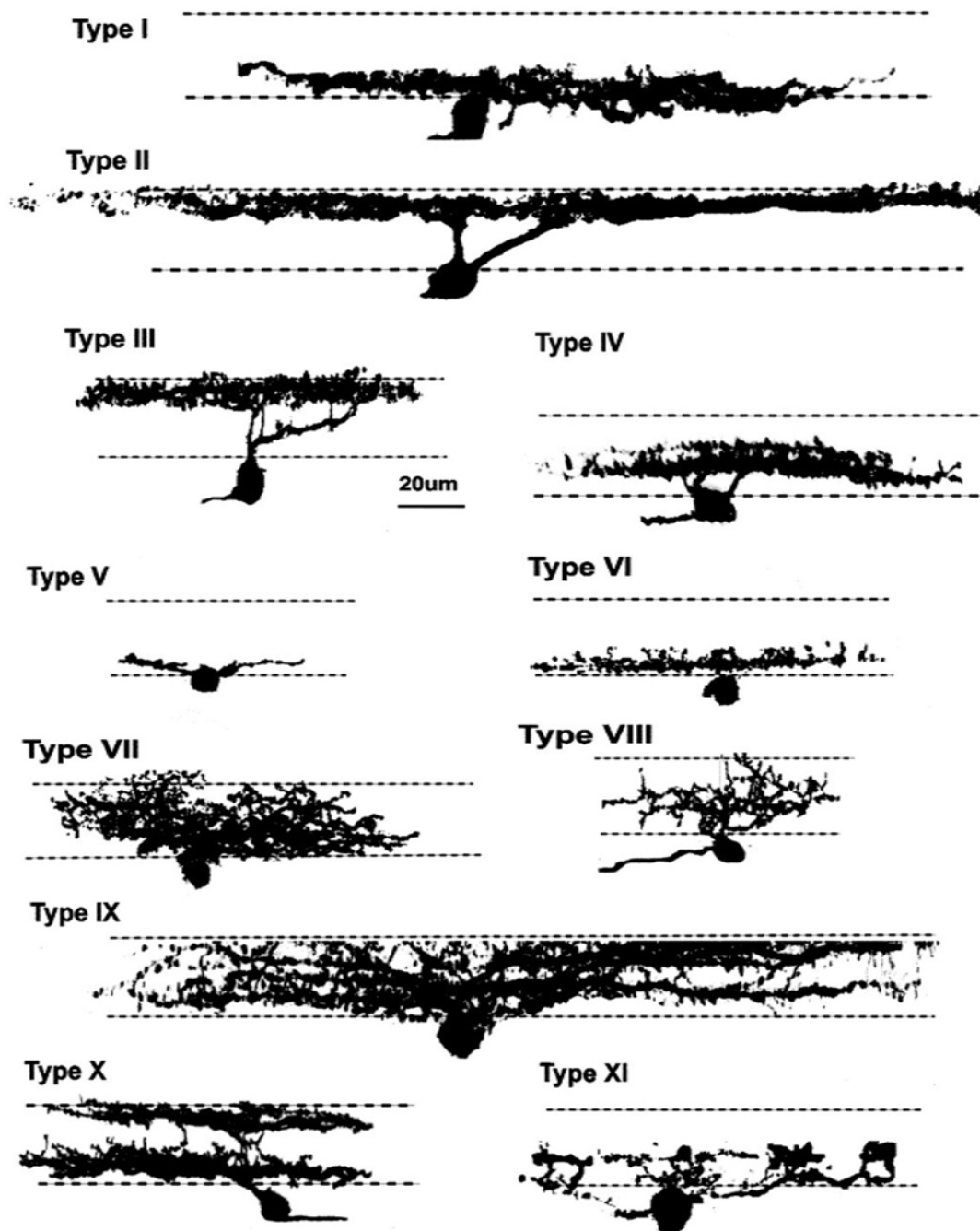
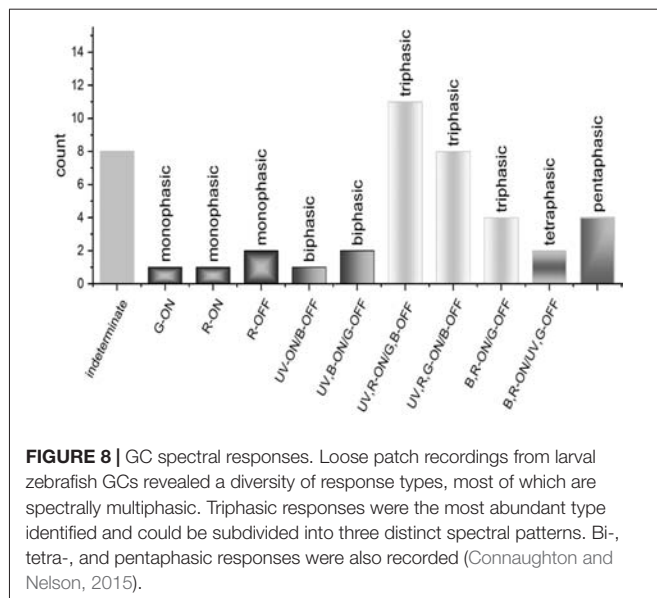


FIGURE 7 | Zebrafish ganglion cells (GCs). Di-I labeling of GCs in whole mount tissue identified 11 morphological types, based on dendritic arborization patterns in the IPL. These patterns included processes restricted to 1–2 sublaminae, as well as more diffuse arborization patterns. Reproduced with permission from Mangrum et al. (2002).

WAVELENGTH PROCESSING CIRCUITRY IN ZEBRAFISH

The different subtypes of second- and third-order neurons in zebrafish receive inputs from single or, more often, multiple cone PRs, resulting in spectrally monophasic and multiphasic responses. As a result, the signals from each cone type are relayed,

through both feedforward and feedback circuitry, throughout the entire retina. One feature of this intermixing of cone signals is both synergistic and antagonistic interactions between different cone signals in distal neurons, such as HC and BC, a feature also noted in AC and GC of the inner retina. The spectral properties of GCs, retinal output neurons, are similar to the color-opponent spectral responses of HCs, suggesting one of the



origins of GC spectral processing lies in distal retina, with the cone connectivity patterns of HC and BC. One expects there is further selective integration of BC and AC physiological types onto the dendrites of GC receptive fields in the IPL, resulting in even greater diversification and refinement of spectral properties. The dominance of red cone signals in spectrally monophasic AC types is reminiscent of the L-type signals from H1 HCs, suggesting the existence of an L-type BC pathway. Despite the evidence for a mixing of cone signals in the image-processing circuits of the inner retina, existing evidence suggests that signals from the 4 retinal cone types in zebrafish are not treated equally.

Red Cone Signals

Red cones are only 1/3 of adult cone types. Nonetheless, red cone signals dominate spectral responses in HC and AC. These red (LWS) signals are relayed directly from the principal member of the double cone to H1 HCs (Li et al., 2009) resulting in red-dominated monophasic (L1- or L2-type) physiologies in 2/3 of HCs studied (Connaughton and Nelson, 2010). Even though contacting them, H1 HCs do not receive physiological signals from blue (SWS2) cones, and do not contact UV (SWS1) cones at all. LWS cones are included in seven of nine of BC connectivity patterns or 87% of 321 BCs studied (Li et al., 2012), potentially accounting for the prevalence of red cone signals seen in ACs (Torvund et al., 2017). However, these BC pathways, while contacting red cones, are not red cone selective, as green (MWS) cones overlap, comingling in all but one of these same BC connectivity patterns and 93% of BCs studied (Li et al., 2012).

Non-color-opponent AC responses are either selective for or dominated by red cone signals; these cells are OFF-stratified, ON-stratified, and ON-OFF bistratified cells, altogether accounting for 89% of recorded cells (Torvund et al., 2017). The variety of AC stratification patterns in this group suggest that AC processes receiving LWS-selective cone inputs are present throughout the depth of the IPL

(Torvund et al., 2017), consistent with direct input from red cone contacting, and physiologically red cone dominated BCs, also presumably of multiple stratification types. In contrast to adult ACs, LWS inputs to GCs in larval zebrafish retinas contribute mainly to spectrally multiphasic responses. For the latter, red cone inputs are always excitatory (Connaughton and Nelson, 2015), but the responses are dominated by excitation from UV cones. The contrast between dominant AC and GC red cone spectral patterns presents a dilemma, and it is unclear at present how large a role larval development plays, as b-wave spectral sensitivity progresses from UV-dominated in larvae to a more broadly sensitive pattern in juveniles and adults (Saszik et al., 1999). A reasonable conjecture is that both non-opponent and opponent BC pathways exist for red cone signals. This idea is consistent with the finding of a population of red cone opponent ACs in adults with a unique stratification pattern (Torvund et al., 2017).

Green Cone Signals

Despite a numerical representation in adults identical to red cones, green cone signals are not dominant in zebrafish physiology. In the outer retina, while red cones dominate H1 HC responses, UV cones dominate one physiological subtype of H3, and blue cones dominate the other, there is no HC strictly devoted to excitation from green cones. These signals appear as complementary components in H1 HC, particularly the L2-type response and H2 HC biphasic signals, where they combine with blue cone signals. The most selective and prominent role of green cone signals in the outer retina are as the inhibitory (depolarizing) elements in triphasic and tetraphasic HC responses (Connaughton and Nelson, 2010).

In ACs, green cone inputs to non-color-opponent cells were small and found mainly in sustained-ON AC, with processes monostratified either in the OFF sublamina or in the distal-most layer of the ON sublamina (Torvund et al., 2017). Green cone signals were seldom identified in the numerically dominant ON-OFF types. No ACs that selectively represent green cone signals have been encountered (Torvund et al., 2017). The relative absence of MWS signals in ACs is mysterious, unless green cone-to-BC synapses are commonly either inactive, inhibitory, or opponent. In calcium imaging physiology of BC boutons (Zimmermann et al., 2018) it does appear that the most common form of BC color opponency is red excitatory, green inhibitory (Figure 5). These red-ON, green-OFF boutons localize mainly in s2, s3 of IPL sublamina *a*. Green cones are the only type that selectively innervate BCs, in fact there are three varieties of OFF stratifying BCs that only contact green cones (Li et al., 2012). The green cone signals appear to be largely inhibitory (Connaughton and Nelson, 2015), and speculatively, the inhibition might involve OFF-type, or color-opponent OFF-type, green cone BCs. However, in adults, the spectrally triphasic, green cone inhibited, color-opponent AC did not co-stratify with green cone BC terminals in sublamina *a*.

Blue and UV Cone Signals

In outer retina, blue and UV cone signals are represented in about 1/3 of recorded HC. Blue (SWS2) cones contact H1,

H2 and H3 HC (Li et al., 2009), but only contribute signals to biphasic (H2) and blue-preferring triphasic (H3) responses (Connaughton and Nelson, 2010). UV cones directly connect only to H3 cells (Li et al., 2009). However, UV inputs to H3 cells appear variable, as this morphological type can generate three different spectral responses (Connaughton and Nelson, 2010): (1) UV-excited spectrally triphasic responses dominated by UV cone excitation; (2) tetraphasic (UV-inhibitory); and (3) blue-preferring triphasic responses excited by both UV and blue cones. Spectrally multiphasic patterns are presumed evidence of feedback to blue and UV cones from HC types receiving stimulation from LWS cones (Li et al., 2009; Connaughton and Nelson, 2010) to generate HC multiphasic responses.

In adult inner retina, stimulation of blue and UV cones contributes to biphasic and triphasic responses in zebrafish ACs, a pattern similar to outer retina. These include a UV-depolarizing blue-yellow opponent biphasic unit and UV-depolarizing triphasic responses (Torvund et al., 2017). Short wavelength inputs to larval GCs elicit spectrally triphasic responses, similar to triphasic HC responses (Connaughton and Nelson, 2015). Interestingly, adult ACs with C-type responses have processes exclusively in sublamina *b*, suggesting a functional segregation of short wavelength BC-to-AC synapses in the IPL. Adult connectomic analysis identified 3 BC types directly postsynaptic to UV cones with axon terminals in sublamina *b*, and 5 BC types postsynaptic to blue cones (Li et al., 2012), suggesting there are a relatively few, possibly selective, circuits that relay short wavelength signals to inner retina, and that short wavelength cone signals are commonly conveyed in a color-opponent pathway.

Stratification of IPL Cone Signals

There may be some segregation of cone signals in the zebrafish IPL. BC connectomics provides pathways for red, green, blue and UV cone signals into all IPL strata. This homogeneity is partly enforced by BCs with multistratified axon terminals, as well as the prevalence of BCs contacting multiple cone types (Li et al., 2012). The finding of dominant red cone signals in all non-opponent ACs, regardless of stratification pattern, is in accord with a distribution of L-type, or achromatic, red cone signals throughout the IPL (Torvund et al., 2017). Nonetheless, there are some imbalances. The RRod type BC conducts red cone (and rod) signals only, and projects to IPL sublamina *b*. The solely green cone contacting BCs project only to s1 and s3 of sublamina *a*, with most boutons in s3 (Li et al., 2012). Depolarizing sustained ACs stratify in s3-s4. In addition to red cone signals, these cells are strongly excited by green cone stimulation (Torvund et al., 2017). Over 60% of BC types project to sublamina *a* (Li et al., 2012), a curious imbalance. In calcium imaging studies of BC boutons, Zimmermann et al. (2018) found that the IPL strata containing achromatic OFF-BC boutons may be much narrower than previously supposed, localized to s1 and not all strata of sublamina *a*. The remaining s2-s3 band contains color-opponent BC boutons of various types. There is also an s5 color-opponent band, perhaps innervating the color-opponent ACs that branch in s5 (Torvund et al., 2017). Torvund et al. (2017)

proposed that the multistratified GBUV BC types (Li et al., 2012) might be the color-opponent pathway innervating color-opponent ACs, a theory yet to be tested but consistent with the color-opponent BC axon terminal distribution (Wong and Dowling, 2005; Zimmermann et al., 2018). Stratum s4 and thereabouts is the true achromatic ON-type band. Zimmermann et al. (2018) find that IPL banding varies with retinal region as well, with UV excited boutons being broadly prevalent in the "SZ". The indications are that there are multiple functional layers in zebrafish IPL, both for chromatic and achromatic processing.

COMPARISON WITH MAMMALIAN COLOR CIRCUITRY

In mammals, there are well-defined, specific inner and outer retinal circuits for rod and cone signals. Rod signals are relayed through rod BCs (RBCs) to AII ACs and then to ON-GCs through gap junctions with ON-BC terminals (Kolb and Famiglietti, 1974). Cone signals are relayed through cone BCs to GCs (Kolb, 1970). As true for most fish, zebrafish have mixed input (mb) BCs, a close analog of mammalian RBCs, but receiving inputs from both rods and cones. In mammals, cones synapse on HC dendrites, and rods synapse on HC axon terminals (Nelson et al., 1975; Kolb, 1977; Dacheux and Raviola, 1982). In zebrafish, rods synapse on a separate HC type, while cones selectively innervate 3 distinct HC types and 4 different BC types (Li et al., 2012). Overall, it appears that rod and cone signals in zebrafish, like mammals, are selectively sampled by retinal interneurons. Zebrafish HCs are either spectrally monophasic (red cone signals) or multiphasic (color opponency among cone signals, (Connaughton and Nelson, 2010); while only spectrally monophasic patterns appear in mammalian HCs. Mammalian HC axon terminals are physiologically rod selective, while the mammalian HC cell bodies mix red cone, rod and UV/blue cone signals (Steinberg, 1969; Dacheux and Raviola, 1982; Nelson, 1985; Dacey et al., 1996).

There are BCs selective for UV cones in mammals (Mariani, 1984; Haverkamp et al., 2005). In contrast, there is no anatomically UV cone selective BC in zebrafish (Li et al., 2012). Nonetheless, UV-selective BC physiology is likely present (Saszik et al., 2002; Zimmermann et al., 2018). Zebrafish GC responses include short-wavelength color-opponent responses, as reported in other species. In primate retina, for example, the blue-ON/yellow-OFF response of small bistratified GCs has been particularly well described (Dacey, 1999; Marshak and Mills, 2014). This spectrally multiphasic response is due to feedback circuitry involving HCs in outer retina. In inner retina, it is attributed to separate inputs from ON- and OFF-BCs, which themselves are postsynaptic to different cone types, as well as chromatic AC inputs (Marshak and Mills, 2014). It is likely that the multiphasic responses dominated by UV signals observed in larval zebrafish GCs similarly integrate and reflect inputs from UV-selective outer retinal circuitry involving HCs and direct inputs from spectrally selective presynaptic BCs and/or ACs.

COLOR PREFERENCE, PERCEPTION AND BEHAVIOR

Zebrafish display color discrimination or preference when given a choice between different sections of a tank that have different background colors (Colwill et al., 2005; Risner et al., 2006; Avdesh et al., 2012; Ahmad and Richardson, 2013; Oliveira et al., 2015; Park et al., 2016). Most studies report a natural preference for blue/short wavelength light in both adult (Colwill et al., 2005; Risner et al., 2006; Bault et al., 2015; Oliveira et al., 2015; Peeters et al., 2016) and larval (Park et al., 2016; Peeters et al., 2016) fish. A few studies, in contrast, report a natural preference for red/long wavelength light (Avdesh et al., 2012; Ahmad and Richardson, 2013), which may be associated with food/foraging and be related to color of prey items (Spence and Smith, 2008).

In behavioral testing, color preference is best explained by a multiple-mechanisms model that includes both non-opponent (UV, B) and opponent (G-B and G-R) systems (Risner et al., 2006). This model is also most accurate in describing spectral sensitivities of ERG b-wave and ON-tectal responses in zebrafish (McDowell et al., 2004), suggesting behavioral responses reflect physiological processing of the visual scene. Interestingly, though color choice experiments indicate zebrafish can behaviorally distinguish color stimuli, the optomotor response (OMR), a standard vision-based behavior used to identify mutant strains, is “color blind” (Krauss and Neumeyer, 2003; Orger and Baier, 2005) as it is dominated by LWS (red) cones in adults (Krauss and Neumeyer, 2003) and pooled inputs from red and green cones in larvae (Orger and Baier, 2005). OMRs can be reduced, though, when UV or B cones are selectively ablated (Hagerman et al., 2016), suggesting short wavelength cones do contribute to the OMR, possibly in an inhibitory manner (Krauss and Neumeyer, 2003; Hagerman et al., 2016).

ZEBRAFISH AS MODELS OF RETINAL DISEASE

There have been several recent reviews detailing the applicability of zebrafish to the study of ocular/retinal diseases (Gross and Perkins, 2008; Bibliowicz et al., 2011; Link and Collery, 2015). These reviews highlight the experimental strengths of zebrafish: similar retinal/eye anatomy with humans, rapid development and large clutch size, easy manipulation and phenotype observation, and amenability of genome editing techniques to generate mutant and transgenic lines (Bibliowicz et al., 2011; Link and Collery, 2015). Of the >20 diseases for which zebrafish are used, ~50% target PRs/PR layer (Link and Collery, 2015), and 13 specific genes associated with PR degeneration have been identified (Brockerhoff and Fadool, 2011). Behavioral studies using the optokinetic response (OKR; Brockerhoff et al., 1995), the escape response (Li and Dowling, 1997), or the visual motor response (Emran et al., 2008), coupled to ERG recordings allowed functional assessment of mutant phenotypes. Interestingly, many of the mutations leading to PR degeneration are not associated with transduction, but with protein trafficking (Brockerhoff and Fadool, 2011), consistent with the high metabolic demand and

almost-constant functioning of retinal PRs. Here, we focus on those zebrafish lines with mutations in cone PRs. These studies have largely been performed with larval (5–7 dpf) zebrafish because, at this age, the cone-rich retina contains few/no rods (Holzhausen et al., 2009).

Mutations Affecting All Cone Types

The OKR is a visually-guided behavior based on saccadic eye movements as a stationary animal tracks a moving grating. This is a reliable test that can be elicited as early as ~4 dpf in zebrafish (Brockerhoff et al., 1995; Neuhauss, 2003). Brockerhoff et al. (1995, 1997, 1998) were the first to apply this technique to the identification of mutant phenotypes. Most of these behaviorally-identified zebrafish were later found to have mutations in cone-specific genes.

One of the first mutants identified was *no optokinetic response a* (*noa*). As the name suggests, *noa* larvae do not display an OKR. These mutants have ERG recordings with normal a-waves, but abnormal b-waves (Brockerhoff et al., 1995), consistent with altered glutamate responses in postsynaptic BCs (Connaughton, 2001). Subsequent, molecular analysis identified two alleles of *noa*: *m631* and *a13* (Taylor et al., 2004). *noa*^{a13} mutants (originally *no optokinetic response b*, (Taylor et al., 2004) have a deficient *dihydrolipoamide-S-acetyltransferase* (*dlat*) gene, resulting in the absence of the E2 subunit of the enzyme pyruvate dehydrogenase (PDH; Taylor et al., 2004). PDH is a critical enzyme involved in ATP production in mitochondria because it catalyzes the reaction that converts pyruvate to Acetyl Co A (Karp, 1999). Absence of this enzyme results in PDH deficiency, an inherited metabolic disorder (Barnerias et al., 2010; Patel et al., 2012). The *dlat* (*noa*^{a13}) mutant is, therefore, a model for human PDH deficiency.

no optokinetic response c (*nrc*) mutants, in addition to an absent OKR, have a diverse phenotype that includes floating ribbons in cone pedicles (Allwardt et al., 2001) and reduced numbers of unevenly distributed synaptic vesicles (Van Epps et al., 2004). Abnormal ERG recordings (Allwardt et al., 2001) revealed a light adaptation defect in distal retina (Van Epps et al., 2001). ON-GC responses in inner retina are also reduced/absent (Emran et al., 2007). Molecular analysis identified the *nrc* mutation as a premature stop codon in the *synaptojanin 1* (*SynJ1*) gene (Van Epps et al., 2004) in cone PRs (Holzhausen et al., 2009). *Synaptojanin-1* is strongly expressed in brain¹ and the synaptojanin-1 protein is involved in endocytosis of clathrin-coated vesicles (Perera et al., 2006) in nerve terminals.

A cone-specific mutation is also observed in zebrafish *no optokinetic response f* (*nof*) mutants. *nof* fish have a nonsense mutation in the gene coding for the α -subunit of cone transducin (T α C; Brockerhoff et al., 2003). Development of the transgenic line *TG(3.2T α CP-EGFP)* allowed visualization of T α C in all zebrafish cone types, making *nof* mutants a model for achromatopsia (Kennedy et al., 2007). Interestingly, though *nof* cones lack transducin, they do respond to bright light stimuli, albeit at a much-reduced level (Brockerhoff et al., 2003).

¹<https://www.ncbi.nlm.nih.gov/gene/8867>

A mutation in the cone cGMP-phosphodiesterase α subunit (*pde6a*¹ or *pde6c*), also causes cone degeneration (Stearns et al., 2007; Nishiwaki et al., 2008) in zebrafish. cGMP-PDE is an enzyme complex located in PR outer segments that is part of the phototransduction cascade (Rodieck, 1998). In mouse rods, absence/mutations in either the α (Huang et al., 1995), β (Pittler and Baehr, 1991), or γ (Tsang et al., 1996) subunits of cGMP-PDE result in rod degeneration. cGMP-PDE in zebrafish cones is similarly required as mutations lead to cone-specific degeneration.

Mutations/Treatments Affecting Specific Cone Types

The generation of knockout (KO) and mutant lines has also identified genes specific to a given cone type. The transcription factor *Tbx2b*, for example, is necessary for UV cone formation (Alvarez-Delfin et al., 2009) as a mutation in *tbx2b* results in the conversion of UV cones to rods, resulting in the *lots-of-rods* (*lor*) phenotype (Alvarez-Delfin et al., 2009). Though *lor* zebrafish have a strong OKR, UV opsin expression in larval retinas is deficient. All other cone types are present and *tbx2b* mutants have an even and abundant distribution of rods over the entire retina. Similarly, the transcription factor *sine oculis homeobox homolog 7* (*six7*) is required for green cone development (Ogawa et al., 2015). PRs in *six7* KO larvae don't express any of the four, green opsin (RH2-1 to RH2-4) genes, resulting in a loss of green cones that persists to adulthood. Interestingly, the *six7* KO phenotype also includes reduced blue opsin expression (larval stage), increased number of rods (larvae), and a switch in red opsin expression (adults; Ogawa et al., 2015). Finally, red cone fate is determined by thyroid hormone receptor $\beta 2$ (*trb2*) expression (Suzuki et al., 2013) as knockdown of *trb2* results in a loss of red cones, but an increase in UV cones (Suzuki et al., 2013). Red cone loss is also selective in *partial optokinetic response b* (*pob*) mutants (Brockerhoff et al., 1997). *pob* zebrafish are red color blind due to rapid degeneration of red cones. PR loss in *pob* is due to a mutation in the *pob* gene, which codes for a protein required for red cone survival (Taylor et al., 2005).

Allison and colleagues have developed transgenic zebrafish lines in which a single class of PR can be chemically ablated (Fraser et al., 2013; Hagerman et al., 2016). These lines are key in determining how removal of one cone type may alter the existing PR mosaic as well as how the retina will respond. The zebrafish retina continues to grow throughout the life of the fish and is able to regenerate cells in response to damage (reviewed in Brockerhoff and Fadool, 2011). Chemical ablation of a single cone type in adult retina can trigger retinal regeneration (Fraser et al., 2013; Hagerman et al., 2016). For example, selective ablation of UV cones stimulates the formation of new UV cones, at a higher density than predicted (Fraser et al., 2013). This recovery and regeneration is rapid: behavioral responses (OMR) are restored in 72 h

(Hagerman et al., 2016). Selective loss of blue cones, however, results in an even faster regenerative response, with behavioral responses restored in 24 h (Hagerman et al., 2016). The rapid regeneration capabilities of zebrafish retinal tissue, and the ability of this tissue to respond to the selective loss of a given cone type, is an important step in determining mechanisms that could be used to restore cell loss after retinal degeneration.

Finally, other studies have induced diseases with retinal complications using non-molecular mechanisms. For example, prolonged hyperglycemia, characteristic of diabetes, can be induced by either immersing zebrafish in a glucose solution (Gleeson et al., 2007; Alvarez et al., 2010) or through streptozotocin injection (Olsen et al., 2010; Intine et al., 2013), both of which result in changes to the retina, making zebrafish a model for diabetic retinopathy. In addition to retinal thinning (Gleeson et al., 2007; Olsen et al., 2010) and changes to retinal vasculature (Alvarez et al., 2010), there are also marked changes to cone PRs in hyperglycemic zebrafish retinas with double cones displaying the most severe alterations (Alvarez et al., 2010).

CONCLUSION

Zebrafish are capable of rich color processing due to the presence of four cone types that allow detection of light ranging from UV to red. After stimulation of the phototransduction cascade in cones, spectral signals are immediately processed and modified in outer retina through synapses with HC. BC signaling relays spectral information to inner retina, where multiple feedforward inputs converge on AC and GC and feedback inputs from AC further modify spectral signals. These ON-signals are faithfully relayed to the tectum. As a result, zebrafish are able to behaviorally discriminate color and display innate color preferences. This elaborate signaling, coupled to well-known retinal anatomy and targeted genetic manipulation, has resulted in zebrafish that exhibit mutation-induced red blindness (Brockerhoff et al., 1997), UV blindness (Alvarez-Delfin et al., 2009), and green blindness (Ogawa et al., 2015). Zebrafish also serve as models for vision disorders, such as diabetic retinopathy (Gleeson et al., 2007; Alvarez et al., 2010), retinitis pigmentosa (Baye et al., 2011), achromatopsia (Kennedy et al., 2007) and Leber's congenital amaurosis (Baye et al., 2011), making zebrafish a model of choice for study of human retinal disorders.

AUTHOR CONTRIBUTIONS

AM, RN and VC all contributed to writing the article and selection of figures. Supported by funds from the College of Arts and Science and the American University Library (to VPC).

REFERENCES

- Ahmad, F., and Richardson, M. K. (2013). Exploratory behavior in the open field test adapted for larval zebrafish: impact of environmental complexity. *Behav. Processes* 92, 88–98. doi: 10.1016/j.beproc.2012.10.014
- Ahnelt, P., and Kolb, H. (1994). Horizontal cells and cone photoreceptors in primate retina: a Golgi-light microscopic study of spectral connectivity. *J. Comp. Neurol.* 343, 387–405. doi: 10.1002/cne.903430305
- Allison, W. T., Barthel, L. K., Skebo, K. M., Takechi, M., Kawamura, S., and Raymond, P. A. (2010). Ontogeny of cone photoreceptor mosaics

- in zebrafish. *J. Comp. Neurol.* 518, 4182–4195. doi: 10.1002/cne.22447
- Allison, W. T., Haimberger, T. J., Hawryshyn, C. W., and Temple, S. E. (2004). Visual pigment composition in zebrafish: evidence for a rhodopsin-porphyrin interchange system. *Vis. Neurosci.* 21, 945–952. doi: 10.1017/S0952523804216145
- Allwardt, B. A., Lall, A. B., Brockerhoff, S. E., and Dowling, J. E. (2001). Synapse formation is arrested in retinal photoreceptors of the zebrafish *nrc* mutant. *J. Neurosci.* 21, 2330–2342. doi: 10.1523/jneurosci.21-07-02330.2001
- Alvarez, Y., Chen, K., Reynolds, A. L., Waghorne, N., O'Connor, J. J., and Kennedy, B. N. (2010). Predominant cone photoreceptor dysfunction in a hyperglycaemic model of non-proliferative diabetic retinopathy. *Dis. Model. Mech.* 3, 236–245. doi: 10.1242/dmm.003772
- Alvarez-Delfin, K., Morris, A. C., Snelson, C. D., Gamse, J. T., Gupta, T., Marlow, F. L., et al. (2009). Tbx2b is required for ultraviolet photoreceptor cell specification during zebrafish retinal development. *Proc. Natl. Acad. Sci. U S A* 106, 2023–2038. doi: 10.1073/pnas.0809439106
- Arenzana, F. J., Arévalo, R., Sánchez-González, R., Clemente, D., Aijón, J., and Porteros, A. (2006). Tyrosine hydroxylase immunoreactivity in the developing visual pathway of the zebrafish. *Anat. Embryol.* 211, 323–334. doi: 10.1007/s00429-006-0084-2
- Asi, H., and Perlman, I. (1998). Neural interactions between cone photoreceptors and horizontal cells in the turtle (*Mauremys caspica*) retina. *Vis. Neurosci.* 15, 1–13. doi: 10.1017/s0952523898146047
- Avdesh, A., Martin-Iverson, M. T., Mondal, A., Chen, M., Askra, S., Morgan, N., et al. (2012). Evaluation of color preference in zebrafish for learning and memory. *J. Alzheimers Dis.* 28, 459–469. doi: 10.3233/JAD-2011-110704
- Barnerias, C., Saudubray, J.-M., Touati, G., De Lonlay, P., Dulac, O., Ponsot, G., et al. (2010). Pyruvate dehydrogenase complex deficiency: four neurological phenotypes with differing pathogenesis. *Dev. Med. Child Neurol.* 52, e1–e9. doi: 10.1111/j.1469-8749.2009.03541.x
- Bault, Z. A., Peterson, S. M., and Freeman, J. L. (2015). Directional and color preference in adult zebrafish: implications in behavioral and learning assays in neurotoxicology studies. *J. Appl. Toxicol.* 35, 1502–1510. doi: 10.1002/jat.3169
- Baye, L. M., Patrino, X., Swaminathan, S., Beck, J. S., Zhang, Y., Stone, E. M., et al. (2011). The N-terminal region of centrosomal protein 290 (CEP290) restores vision in a zebrafish model of human blindness. *Human Mol. Gen.* 20, 1467–1477. doi: 10.1093/hmg/ddr025
- Bibliowicz, J., Tittle, R. K., and Gross, J. M. (2011). Towards a better understanding of human eye disease: insights from the zebrafish, *Danio rerio*. *Prog. Mol. Biol. Transl. Sci.* 100, 287–330. doi: 10.1016/B978-0-12-384878-9.00007-8
- Bilotta, J., and Abramov, I. (1989). Spatiotemporal properties of goldfish retinal ganglion cells. *J. Neurophysiol.* 62, 1140–1148. doi: 10.1152/jn.1989.62.5.1140
- Bilotta, J., Saszik, S., and Sutherland, S. (2001). Rod contributions to the electroretinogram of the dark-adapted developing zebrafish. *Dev. Dyn.* 222, 564–570. doi: 10.1002/dvdy.1188
- Bilotta, J., Trace, S. E., Vukmanic, E. V., and Risner, M. L. (2005). Ultraviolet- and short-wavelength cone contributions alter the early components of the ERG of young zebrafish. *Int. J. Dev. Neurosci.* 23, 15–25. doi: 10.1016/j.ijdevneu.2004.09.004
- Bowling, D. B. (1980). Light responses of ganglion cells in the retina of the turtle. *J. Physiol.* 299, 173–196. doi: 10.1113/jphysiol.1980.sp013118
- Branchek, T. (1984). The development of photoreceptors in the zebrafish, *Brachydanio rerio*: II. Function. *J. Comp. Neurol.* 224, 116–122. doi: 10.1002/cne.902240110
- Branchek, T., and Bremiller, R. (1984). The development of photoreceptors in the zebrafish, *Brachydanio rerio*. I. Structure. *J. Comp. Neurol.* 224, 107–115. doi: 10.1002/cne.902240109
- Brockerhoff, S. E., Dowling, J. E., and Hurley, J. B. (1998). Zebrafish retinal mutants. *Vision Res.* 38, 1335–1339. doi: 10.1016/s0042-6989(97)00227-7
- Brockerhoff, S. E., and Fadool, J. M. (2011). Genetics of photoreceptor degeneration and regeneration in zebrafish. *Cell. Moll. Life Sci.* 68, 651–659. doi: 10.1007/s00018-010-0563-8
- Brockerhoff, S. E., Hurley, J. B., Janssen-Bienhold, U., Neuhauss, S. C., Driever, W., and Dowling, J. E. (1995). A behavioral screen for isolating zebrafish mutants with visual system defects. *Proc. Natl. Acad. Sci. U S A* 92, 10545–10549. doi: 10.1073/pnas.92.23.10545
- Brockerhoff, S. E., Hurley, J. B., Niemi, G. A., and Dowling, J. E. (1997). A new form of inherited red-blindness identified in zebrafish. *J. Neurosci.* 17, 4236–4242. doi: 10.1523/jneurosci.17-11-04236.1997
- Brockerhoff, S. E., Rieke, F., Matthews, H. R., Taylor, M. R., Kennedy, B., Ankoudinova, I., et al. (2003). Light stimulates a transducin-independent increase of cytoplasmic Ca^{2+} and suppression of current in cones from the zebrafish mutant *nof*. *J. Neurosci.* 23, 470–480. doi: 10.1523/jneurosci.23-02-00470.2003
- Burrill, J. D., and Easter, S. S. Jr. (1995). The first retinal axons and their microenvironment in zebrafish cryptic pioneers and the pretract. *J. Neurosci.* 15, 2935–2947. doi: 10.1523/jneurosci.15-04-02935.1995
- Caldwell, J. H., and Daw, N. W. (1978). New properties of rabbit retinal ganglion cells. *J. Physiol.* 276, 257–276. doi: 10.1113/jphysiol.1978.sp012232
- Calkins, D. J., Tsukamoto, Y., and Sterling, P. (1998). Microcircuitry and mosaic of a blue-yellow ganglion cell in the primate retina. *J. Neurosci.* 18, 3373–3385. doi: 10.1523/jneurosci.18-09-03373.1998
- Cameron, D. A. (2002). Mapping absorbance spectra, cone fractions and neuronal mechanism to photopic spectral sensitivity in the zebrafish. *Vis. Neurosci.* 19, 365–372. doi: 10.1017/s0952523802192121
- Carter-Dawson, L. D., and Lavail, M. M. (1979). Rods and cones in the mouse retina: II. Autoradiographic analysis of cell generation using tritiated thymidine. *J. Comp. Neurol.* 188, 263–272. doi: 10.1002/cne.901880205
- Chang, L., Breuninger, T., and Euler, T. (2013). Chromatic coding from cone-type unselective circuits in the mouse retina. *Neuron* 77, 559–571. doi: 10.1016/j.neuron.2012.12.012
- Chinen, A., Hamaoka, T., Yamada, Y., and Kawamura, S. (2003). Gene duplication and spectral diversification of cone visual pigments of zebrafish. *Genetics* 163, 663–675.
- Colwill, R. M., Raymond, M. P., Ferreira, L., and Escudero, H. (2005). Visual discrimination learning in zebrafish (*Danio rerio*). *Behav. Processes* 70, 19–31. doi: 10.1016/j.beproc.2005.03.001
- Connaughton, V. P. (2001). Organization of ON- and OFF-pathways in the zebrafish retina: neurotransmitter localization, electrophysiological responses of bipolar cells and patterns of axon terminal stratification. *Prog. Brain Res.* 131, 161–176. doi: 10.1016/s0079-6123(01)31014-2
- Connaughton, V. P., Graham, D., and Nelson, R. (2004). Identification and morphological classification of horizontal, bipolar, and amacrine cells within the zebrafish retina. *J. Comp. Neurol.* 477, 371–385. doi: 10.1002/cne.20261
- Connaughton, V. P., and Nelson, R. (2000). Axonal stratification patterns and glutamate-gated conductance mechanisms in zebrafish retinal bipolar cells. *J. Physiol.* 524, 135–146. doi: 10.1111/j.1469-7793.2000.t01-1-00135.x
- Connaughton, V. P., and Nelson, R. (2010). Spectral responses in zebrafish horizontal cells include a tetraphasic response and a novel UV-dominated triphasic response. *J. Neurophysiol.* 104, 2407–2422. doi: 10.1152/jn.00644.2009
- Connaughton, V. P., and Nelson, R. (2015). Ultraviolet dominates ganglion cell responses in larval zebrafish retinas. *Invest. Ophthalmol. Vis. Sci.* 56, 3251.
- Crocker, R. A., Ringo, J., Wolbarsht, M. L., and Wagner, H. G. (1980). Cone contributions to cat retinal ganglion cell receptive fields. *J. Gen. Physiol.* 76, 763–785. doi: 10.1085/jgp.76.6.763
- Crook, J. D., Davenport, C. M., Peterson, B. B., Packer, O. S., Detwiler, P. B., and Dacey, D. M. (2009). Parallel ON and OFF cone bipolar inputs establish spatially coextensive receptive field structure of blue-yellow ganglion cells in primate retina. *J. Neurosci.* 29, 8372–8387. doi: 10.1523/jneurosci.1218-09.2009
- Dacey, D. M. (1999). Primate retina: cell types, circuits and color opponency. *Prog. Retin Eye Res.* 18, 737–763. doi: 10.1016/s1350-9462(98)00013-5
- Dacey, D. M., Crook, J. D., and Packer, O. S. (2014). Distinct synaptic mechanisms create parallel S-ON and S-OFF color opponent pathways in the primate retina. *Vis. Neurosci.* 31, 139–151. doi: 10.1017/s0952523813000230
- Dacey, D. M., Diller, L. C., Verweij, J., and Williams, D. R. (2000). Physiology of L- and M-cone inputs to H1 horizontal cells in the primate retina. *J. Opt. Soc. Am. A Opt. Image Sci. Vis.* 17, 589–596. doi: 10.1364/josaa.17.000589
- Dacey, D. M., and Lee, B. B. (1994). The 'blue-on' opponent pathway in primate retina originates from a distinct bistratified ganglion cell type. *Nature* 367, 731–735. doi: 10.1038/367731a0

- Dacey, D. M., Lee, B. B., Stafford, D. K., Pokorny, J., and Smith, V. C. (1996). Horizontal cells of the primate retina: cone specificity without spectral opponency. *Science* 271, 656–659. doi: 10.1126/science.271.5249.656
- Dacheux, R. F., and Raviola, E. (1982). Horizontal cells in the retina of the rabbit. *J. Neurosci.* 2, 1486–1493. doi: 10.1523/jneurosci.02-10-01486.1982
- Daw, N. W. (1968). Colour-coded ganglion cells in the goldfish retina: extension of their receptive fields by means of new stimuli. *J. Physiol.* 197, 567–592. doi: 10.1113/jphysiol.1968.sp008575
- Daw, N. W., and Pearlman, A. L. (1970). Cat colour vision: evidence for more than one process. *J. Physiol.* 211, 125–137. doi: 10.1113/jphysiol.1970.sp009270
- De Monasterio, F. M. (1978). Spectral interactions in horizontal and ganglion cells of the isolated and arterially-perfused rabbit retina. *Brain Res.* 150, 239–258. doi: 10.1016/0006-8993(78)90278-0
- De Monasterio, F. M., and Gouras, P. (1975). Functional properties of ganglion cells of the rhesus monkey retina. *J. Physiol.* 251, 167–195. doi: 10.1113/jphysiol.1975.sp011086
- Djamgoz, M. B., Downing, J. E., Kirsch, M., Prince, D. J., and Wagner, H.-J. (1988). Plasticity of cone horizontal cell functioning in cyprinid fish retina: effects of background illumination of moderate intensity. *J. Neurocytol.* 17, 701–710. doi: 10.1007/bf01260997
- Dreosti, E., Odermatt, B., Dorostkar, M. M., and Lagnado, L. (2009). A genetically encoded reporter of synaptic activity *in vivo*. *Nat. Methods* 6, 883–889. doi: 10.1038/nmeth.1399
- Easter, S. S. Jr., and Nicola, G. N. (1996). The development of vision in the zebrafish (*Danio rerio*). *Dev. Biol.* 180, 646–663. doi: 10.1006/dbio.1996.0335
- Easter, S. S. Jr., and Nicola, G. N. (1997). The development of eye movements in the zebrafish (*Danio rerio*). *Dev. Psychobiol.* 31, 267–276. doi: 10.1002/(sici)1098-2302(199712)31:4<267::aid-dev4>3.0.co;2-p
- Emran, F., Rihel, J., Adolph, A., Wong, K., Kraves, S., and Dowling, J. (2007). OFF ganglion cells cannot drive the optokinetic reflex in zebrafish. *Proc. Natl. Acad. Sci. U S A* 104, 19126–19131. doi: 10.1073/pnas.0709337104
- Emran, F., Rihel, J., and Dowling, J. E. (2008). A behavioral assay to measure responsiveness of zebrafish to changes in light intensities. *J. Vis. Exp.* 20:e923. doi: 10.3791/923
- Endeman, D., Klaassen, L. J., and Kamermans, M. (2013). Action spectra of zebrafish cone photoreceptors. *PLoS One* 8:e68540. doi: 10.1371/journal.pone.0068540
- Engström, K. (1960). Cone types and cone arrangement in the retina of some cyprinids. *Acta Zoologica* 41, 277–295. doi: 10.1111/j.1463-6395.1960.tb00481.x
- Enright, J. M., Toomey, M. B., Sato, S.-Y., Temple, S. E., Allen, J. R., Fujiwara, R., et al. (2015). Cyp27c1 red-shifts the spectral sensitivity of photoreceptors by converting vitamin A1 into A2. *Curr. Biol.* 25, 3048–3057. doi: 10.1016/j.cub.2015.10.018
- Fadool, J. M. (2003). Development of a rod photoreceptor mosaic revealed in transgenic zebrafish. *Dev. Biol.* 258, 277–290. doi: 10.1016/s0012-1606(03)00125-8
- Fisher, S. K., and Boycott, B. B. (1974). Synaptic connections made by horizontal cells within the outer plexiform layer of the retina of the cat and the rabbit. *Proc. R. Soc. Lond. B Biol. Sci.* 186, 317–331. doi: 10.1098/rspb.1974.0052
- Fraser, B., Duval, M. G., Wang, H., and Allison, W. T. (2013). Regeneration of cone photoreceptors when cell ablation is primarily restricted to a particular cone subtype. *PLoS One* 8:e55410. doi: 10.1371/journal.pone.0055410
- Gleeson, M., Connaughton, V., and Arneson, L. S. (2007). Induction of hyperglycemia in zebrafish, *Danio rerio*, leads to morphological changes in the retina. *Acta Diabetol.* 44, 157–163. doi: 10.1007/s00592-007-0257-3
- Grant, G. B., and Dowling, J. E. (1995). A glutamate-activated chloride current in cone-driven ON-bipolar cells of the white perch retina. *J. Neurosci.* 15, 3852–3862. doi: 10.1523/jneurosci.15-05-03852.1995
- Gross, J. M., and Perkins, B. D. (2008). Zebrafish mutants as models for congenital ocular disorders in humans. *Mol. Reprod. Dev.* 75, 547–555. doi: 10.1002/mrd.20831
- Guenther, E., and Zrenner, E. (1993). The spectral sensitivity of dark- and light-adapted cat retinal ganglion cells. *J. Neurosci.* 13, 1543–1550. doi: 10.1523/jneurosci.13-04-01543.1993
- Hagerman, G. F., Noell, N. C., Cao, S. Y., Duval, M. G., Oel, A. P., and Allison, W. T. (2016). Rapid recovery of visual function associated with blue cone ablation in zebrafish. *PLoS One* 11:e0166932. doi: 10.1371/journal.pone.0166932
- Haverkamp, S., Wässle, H., Dübels, J., Künér, T., Augustine, G., Feng, G., et al. (2005). The primordial, blue-cone color system of the mouse retina. *J. Neurosci.* 25, 5438–5445. doi: 10.1523/jneurosci.1117-05.2005
- Hemmi, J. M., James, A., and Taylor, W. R. (2002). Color opponent retinal ganglion cells in the tammar wallaby retina. *J. Vis.* 2, 608–617. doi: 10.1167/2.9.3
- Holzhausen, L. C., Lewis, A. A., Cheong, K. K., and Brockerhoff, S. E. (2009). Differential role of synaptotagmin 1 in rod and cone photoreceptors. *J. Comp. Neurol.* 517, 633–644. doi: 10.1002/cne.22176
- Hu, M., and Easter, S. S. (1999). Retinal neurogenesis: the formation of the initial central patch of postmitotic cells. *Dev. Biol.* 207, 309–321. doi: 10.1006/dbio.1998.9031
- Huang, L., Maaswinkel, H., and Li, L. (2005). Olfactorectal centrifugal input modulates zebrafish retinal ganglion cell activity: a possible role for dopamine-mediated Ca^{2+} signaling pathways. *J. Physiol.* 569, 939–948. doi: 10.1113/jphysiol.2005.099531
- Huang, S. H., Pittler, S. J., Huang, X., Oliveira, L., Berson, E., and Dryja, T. P. (1995). Autosomal recessive retinitis pigmentosa caused by mutations in the α -subunit of rod cGMP phosphodiesterase. *Nat. Genet.* 11, 468–471. doi: 10.1038/ng1295-468
- Hubbard, R., and Kropf, A. (1958). The action of light on rhodopsin. *Proc. Natl. Acad. Sci. U S A* 44, 130–139. doi: 10.1073/pnas.44.2.130
- Hughes, H., Saszik, S., Bilotta, J., Demarco, P., and Patterson, W. (1998). Cone contributions to the photopic spectral sensitivity of the zebrafish ERG. *Vis. Neurosci.* 15, 1029–1037. doi: 10.1017/s095252389815602x
- Intine, R. V., Olsen, A. S., and Sarra, M. P. (2013). A zebrafish model of diabetes mellitus and metabolic memory. *J. Vis. Exp.* 72:e50232. doi: 10.3791/50232
- Jang, Y.-J., Yu, S.-H., Lee, E.-S., and Jeon, C.-J. (2011). Two types of tyrosine hydroxylase-immunoreactive neurons in the zebrafish retina. *Neurosci. Res.* 71, 124–133. doi: 10.1016/j.neures.2011.07.002
- Johnston, J., and Lagnado, L. (2012). What the fish's eye tells the fish's brain. *Neuron* 76, 257–259. doi: 10.1016/j.neuron.2012.10.006
- Jusuf, P. R., Almeida, A. D., Randlett, O., Joubin, K., Poggi, L., and Harris, W. (2011). Origin and determination of inhibitory cell lineages in the vertebrate retina. *J. Neurosci.* 31, 2549–2562. doi: 10.1523/jneurosci.4713-10.2011
- Jusuf, P. R., and Harris, W. A. (2009). Ptf1a is expressed transiently in all types of amacrine cells in the embryonic zebrafish retina. *Neural Dev.* 4:34. doi: 10.1186/1749-8104-4-34
- Kaneko, A. (1970). Physiological and morphological identification of horizontal, bipolar and amacrine cells in goldfish retina. *J. Physiol.* 207, 623–633. doi: 10.1113/jphysiol.1970.sp009084
- Kaneko, A. (1973). Receptive field organization of bipolar and amacrine cells in the goldfish retina. *J. Physiol.* 235, 133–153. doi: 10.1113/jphysiol.1973.sp010381
- Karp, G. (1999). *Cell and Molecular Biology*. New York, NY: John Wiley & Sons, Inc.
- Kay, J. N., Finger-Baier, K. C., Roeser, T., Staub, W., and Baier, H. (2001). Retinal ganglion cell genesis required lakritz, a zebrafish atonal homolog. *Neuron* 30, 725–736. doi: 10.1016/s0896-6273(01)00312-9
- Kennedy, B. N., Alvarez, Y., Brockerhoff, S. E., Stearns, G. W., Sapetto-Rebow, B., Taylor, M. R., et al. (2007). Identification of a zebrafish cone photoreceptor-specific promoter and genetic rescue of achromatopsia in the nof mutant. *Invest. Ophthalmol. Vis. Sci.* 48, 522–529. doi: 10.1167/iovs.06-0975
- Klavin, I. (1987). Early development of photoreceptors in the ventral retina of the zebrafish embryo. *J. Comp. Neurol.* 260, 461–471. doi: 10.1002/cne.902600311
- Kolb, H. (1970). Organization of the outer plexiform layer of the primate retina: electron microscopy of Golgi-impregnated cells. *Philos. Trans. R. Soc. Lond. B Biol. Sci.* 258, 261–283. doi: 10.1098/rstb.1970.0036
- Kolb, H. (1977). The organization of the outer plexiform layer in the retina of the cat: electron microscopic observations. *J. Neurocytol.* 6, 131–153. doi: 10.1007/bf01261502
- Kolb, H., and Famiglietti, E. V. (1974). Rod and cone pathways in the inner plexiform layer of cat retina. *Science* 186, 47–49. doi: 10.1126/science.186.4158.47

- Kolb, H., Nelson, R., and Mariani, A. (1981). Amacrine cells, bipolar cells and ganglion cells of the cat retina: a Golgi study. *Vision Res.* 21, 1081–1114. doi: 10.1016/0042-6989(81)90013-4
- Krauss, A., and Neumeyer, C. (2003). Wavelength dependence of the optomotor response in zebrafish (*Danio rerio*). *Vision Res.* 43, 1275–1282. doi: 10.1016/s0042-6989(03)00090-7
- Larison, K. D., and Bremiller, R. (1990). Early onset of phenotype and cell patterning in the embryonic zebrafish retina. *Development* 109, 567–576.
- Lee, B. B., and Sun, H. (2009). The chromatic input to cells of the magnocellular pathway of primates. *J. Vis.* 9, 1–18. doi: 10.1167/9.2.15
- Lewis, A. A., Mahoney, J. T., Wilson, N., and Brockerhoff, S. E. (2015). Identification of amacrine subtypes that express the atypical cadherin celsr3. *Exp. Eye Res.* 130, 51–57. doi: 10.1016/j.exer.2014.12.003
- Li, L., and Dowling, J. E. (1997). A dominant form of inherited retinal degeneration caused by a non-photoreceptor cell-specific mutation. *Proc. Natl. Acad. Sci. U S A* 94, 11645–11650. doi: 10.1073/pnas.94.21.11645
- Li, L., and Dowling, J. E. (2000). Effects of dopamine depletion on visual sensitivity of zebrafish. *J. Neurosci.* 20, 1893–1903. doi: 10.1523/jneurosci.20-05-0189.3.2000
- Li, Y. N., Matsui, J. I., and Dowling, J. E. (2009). Specificity of the horizontal cell-photoreceptor connections in the zebrafish (*Danio rerio*) retina. *J. Comp. Neurol.* 516, 442–453. doi: 10.1002/cne.22135
- Li, Y. X., Schaffner, A. E., Walton, M. K., and Barker, J. L. (1998). Astrocytes regulate developmental changes in the chloride ion gradient of embryonic rat ventral spinal cord neurons in culture. *J. Physiol.* 509, 847–858. doi: 10.1111/j.1469-7793.1998.847bm.x
- Li, Y. X., Tsujimura, T., Kawamura, S., and Dowling, J. E. (2012). Bipolar cell-photoreceptor connectivity in the zebrafish (*Danio rerio*) retina. *J. Comp. Neurol.* 520, 3786–3802. doi: 10.1002/cne.23168
- Link, B. A., and Coltery, R. F. (2015). Zebrafish models of retinal disease. *Annu. Rev. Vis. Sci.* 1, 125–153. doi: 10.1146/annurev-vision-082114-035717
- Mackintosh, R. M., Bilotta, J., and Abramov, I. (1987). Contributions of short-wavelength cones to goldfish ganglion cells. *J. Comp. Physiol. A* 161, 85–94. doi: 10.1007/bf00609457
- MacNeil, M. A., Heussy, J. K., Dacheux, R. F., Raviola, E., and Masland, R. H. (1999). The shapes and numbers of amacrine cells: matching of photofilled with Golgi-stained cells in the rabbit retina and comparison with other mammalian species. *J. Comp. Neurol.* 413, 305–326. doi: 10.1002/(sici)1096-9861(19991018)413:2<305::aid-cne10>3.0.co;2-e
- Mangrum, W. I., Dowling, J. E., and Cohen, E. D. (2002). A morphological classification of ganglion cells in the zebrafish retina. *Vis. Neurosci.* 19, 767–779. doi: 10.1017/s0952523802196076
- Marc, R., and Cameron, D. (2001). A molecular phenotype atlas of the zebrafish retina. *J. Neurocytol.* 30, 593–654. doi: 10.1023/A:1016516818393
- Mariani, A. P. (1984). Bipolar cells in monkey retina selective for the cones likely to be blue-sensitive. *Nature* 308, 184–186. doi: 10.1038/308184a0
- Marshak, D. W., and Mills, S. L. (2014). Short-wavelength cone-opponent retinal ganglion cells in mammals. *Vis. Neurosci.* 31, 165–175. doi: 10.1017/s095252381300031x
- Masland, R. H. (2012). The neuronal organization of the retina. *Neuron* 76, 266–280. doi: 10.1016/j.neuron.2012.10.002
- McDowell, A. L., Dixon, L. J., Houchens, J. D., and Bilotta, J. (2004). Visual processing of the zebrafish optic tectum before and after optic nerve damage. *Vis. Neurosci.* 21, 97–106. doi: 10.1017/s0952523804043019
- Menger, N., and Wässle, H. (2000). Morphological and physiological properties of the A17 amacrine cell of the rat retina. *Vis. Neurosci.* 17, 769–780. doi: 10.1017/s0952523800175108
- Miller, R. F., Staff, N. P., and Velte, T. J. (2006). Form and function of ON-OFF amacrine cells in the amphibian retina. *J. Neurophysiol.* 95, 3171–3190. doi: 10.1152/jn.00090.2005
- Mills, S. L., Tian, L.-M., Hoshi, H., Whitaker, C. M., and Massey, S. C. (2014). Three distinct blue-green color pathways in a mammalian retina. *J. Neurosci.* 34, 1760–1768. doi: 10.1523/JNEUROSCI.3901-13.2014
- Morris, A. C., and Fadool, J. M. (2005). Studying rod photoreceptor development in zebrafish. *Physiol. Behav.* 86, 306–313. doi: 10.1016/j.physbeh.2005.08.020
- Mumm, J. S., Williams, P. R., Godinho, L., Koerber, A., Pittman, A. J., Roeser, T., et al. (2006). *In vivo* imaging reveals dendritic targeting of laminated afferents by zebrafish retinal ganglion cells. *Neuron* 52, 609–621. doi: 10.1016/j.neuron.2006.10.004
- Naka, K. I., and Rushton, W. A. (1966a). S-potentials from colour units in the retina of fish (Cyprinidae). *J. Physiol.* 185, 536–555. doi: 10.1113/jphysiol.1966.sp008001
- Naka, K. I., and Rushton, W. A. (1966b). S-potentials from luminosity units in the retina of fish (Cyprinidae). *J. Physiol.* 185, 587–599. doi: 10.1113/jphysiol.1966.sp008003
- Nawrocki, L. W. (1985). *Development of the Neural Retina in the Zebrafish, Brachydanio rerio*. PhD. Thesis. Eugene, OR: University of Oregon.
- Negishi, K., Salas, R., Parthe, V., and Drujan, B. D. (1988). Identification of horizontal cells generating different spectral responses in the retina of a teleost fish (*Eugerres plumieri*). *J. Neurosci. Res.* 20, 246–256. doi: 10.1002/jnr.490200214
- Nelson, R. (1977). Cat cones have rod input: a comparison of the response properties of cones and horizontal cell bodies in the retina of the cat. *J. Comp. Neurol.* 172, 109–136. doi: 10.1002/cne.901720106
- Nelson, R. (1982). AII amacrine cells quicken time course of rod signals in the cat retina. *J. Neurophysiol.* 47, 928–947. doi: 10.1152/jn.1982.47.5.928
- Nelson, R. (1985). Spectral properties of cat horizontal cells. *Neurosci. Res. Suppl.* 2, S167–S183. doi: 10.1016/0921-8696(85)90015-5
- Nelson, R., and Kolb, H. (1985). A17: a broad-field amacrine cell in the rod system of the cat retina. *J. Neurophysiol.* 54, 592–614. doi: 10.1152/jn.1985.54.3.592
- Nelson, R. F., and Singla, N. (2009). A spectral model for signal elements isolated from zebrafish photopic electroretinogram. *Vis. Neurosci.* 26, 349–363. doi: 10.1017/s0952523809990113
- Nelson, R., von Lutzow, A., Kolb, H., and Gouras, P. (1975). Horizontal cells in cat retina with independent dendritic systems. *Science* 189, 137–139. doi: 10.1126/science.1138370
- Neuhauß, S. C. (2003). Behavioral genetic approaches to visual system development and function in zebrafish. *J. Neurobiol.* 54, 146–160. doi: 10.1002/neu.10165
- Ng, L., Hurley, J. B., Dierks, B., Srinivas, M., Saltó, C., Vennström, B., et al. (2001). A thyroid hormone receptor that is required for the development of green cone photoreceptors. *Nat. Genet.* 27, 94–98. doi: 10.1038/83829
- Niell, C. M., and Smith, S. J. (2005). Functional imaging reveals rapid development of visual response properties in the zebrafish tectum. *Neuron* 45, 941–951. doi: 10.1016/j.neuron.2005.01.047
- Nishiwaki, Y., Komori, A., Sagara, H., Suzuki, E., Manabe, T., Hosoya, T., et al. (2008). Mutation of cGMP phosphodiesterase-6 α -subunit gene causes progressive degeneration of cone photoreceptors in zebrafish. *Mech. Dev.* 125, 932–946. doi: 10.1016/j.mod.2008.09.001
- Ogawa, Y., Shiraki, T., Kojima, D., and Fukada, Y. (2015). Homeobox transcription factor Six7 governs expression of green opsin genes in zebrafish. *Proc. R. Soc. B Biol. Sci.* 282:20150659. doi: 10.1098/rspb.2015.0659
- Oliveira, J., Silveira, M., Chacon, D., and Luchiar, A. (2015). The zebrafish world of colors and shapes: preference and discrimination. *Zebrafish* 12, 166–173. doi: 10.1089/zeb.2014.1019
- Olsen, A. S., Sarras, M. P. Jr., and Intine, R. V. (2010). Limb regeneration is impaired in an adult zebrafish model of diabetes mellitus. *Wound Repair. Regen.* 18, 532–542. doi: 10.1111/j.1524-475x.2010.00613.x
- Orger, M. B., and Baier, H. (2005). Channeling of red and green cone inputs to the zebrafish optomotor response. *Vis. Neurosci.* 22, 275–281. doi: 10.1017/s0952523805223039
- Pang, J.-J., Gao, F., and Wu, S. M. (2002). Segregation and integration of visual channels: layer-by-layer computation of ON-OFF signals by amacrine cell dendrites. *J. Neurosci.* 22, 4693–4701. doi: 10.1523/JNEUROSCI.22-11-0469.3.2002
- Park, J.-S., Tyu, J.-H., Choi, T.-I., Bae, Y.-K., Lee, S., Kang, H., et al. (2016). Innate color preference of zebrafish and its use in behavioral analysis. *Mol. Cells* 39, 750–755. doi: 10.14348/molcells.2016.0173
- Patel, K. P., O'Brien, T. W., Subramony, S. H., Shuster, J., and Stacpoole, P. W. (2012). The spectrum of pyruvate dehydrogenase complex deficiency: clinical, biochemical and genetic features in 371 patients. *Mol. Genet. Metab.* 106, 385–394. doi: 10.1016/j.ymgme.2011.09.032
- Peeters, B. W., Mesokops, M., and Veenliet, A. R. (2016). Color preference in *Danio rerio*: effects of age and anxiolytic treatments. *Zebrafish* 13, 330–334. doi: 10.1089/zeb.2015.1150

- Peichl, L., and González-Soreiano, J. (1994). Morphological types of horizontal cell in rodent retinae: a comparison of rat, mouse, gerbil, and guinea pig. *Vis. Neurosci.* 11, 501–517. doi: 10.1017/s095252380000242x
- Perera, R. M., Zoncu, R., Lucast, L., De Camilli, P., and Toomre, D. (2006). Two synaptotagmin 1 isoforms are recruited to clathrin-coated pits at different stages. *Proc. Natl. Acad. Sci. U S A* 103, 19332–19337. doi: 10.1073/pnas.0609795104
- Pittler, S. J., and Baehr, W. (1991). Identification of a nonsense mutation in the rod photoreceptor cGMP phosphodiesterase B-subunit of the rd mouse. *Proc. Natl. Acad. Sci. U S A* 88, 8322–8326. doi: 10.1073/pnas.88.19.8322
- Raymond, P. A., and Barthel, L. K. (2004). A moving wave patterns the cone photoreceptor mosaic array in the zebrafish retina. *Int. J. Dev. Biol.* 48, 935–945. doi: 10.1387/ijdb.041873pr
- Raymond, P. A., Barthel, L. K., and Curran, G. A. (1995). Developmental patterning of rod and cone photoreceptors in embryonic zebrafish. *J. Comp. Neurol.* 359, 537–550. doi: 10.1002/cne.903590403
- Raymond, P. A., Barthel, L. K., Rounsifer, M. E., Sullivan, S. A., and Knight, J. K. (1993). Expression of rod and cone visual pigments in goldfish and zebrafish: a rhodopsin-like gene is expressed in cones. *Neuron* 10, 1161–1174. doi: 10.1016/0896-6273(93)90064-x
- Raynauld, J.-P. (1972). Goldfish retina: sign of the rod input in opponent color ganglion cells. *Science* 177, 84–85. doi: 10.1126/science.177.4043.84
- Risner, M. L., Lemerise, E., Vukmanic, E. V., and Moore, A. (2006). Behavioral spectral sensitivity of the zebrafish (*Danio rerio*). *Vision Res.* 46, 2625–2635. doi: 10.1016/j.visres.2005.12.014
- Robinson, J., Schmitt, E. A., and Dowling, J. E. (1995). Temporal and spatial patterns of opsin gene expression in zebrafish (*Danio rerio*). *Vis. Neurosci.* 12, 895–906. doi: 10.1017/s0952523800009457
- Robinson, J., Schmitt, E. A., Hárosi, F. I., Reece, R. J., and Dowling, J. E. (1993). Zebrafish ultraviolet visual pigment: absorption spectrum, sequence, and localization. *Proc. Natl. Acad. Sci. U S A* 90, 6009–6012. doi: 10.1073/pnas.90.13.6009
- Rocha, F. A., Saito, C. A., Silveira, L. C., de Souza, J. M., and Ventura, D. F. (2008). Twelve chromatically opponent ganglion cell types in turtle retina. *Vis. Neurosci.* 25, 307–315. doi: 10.1017/s0952523808080516
- Rodiek, R. (1998). *The First Steps in Seeing*. Sunderland, MA: Sinauer Associates, Inc.
- Rosa, J. M., Ruehle, S., Ding, H., and Lagnado, L. (2016). Crossover inhibition generates sustained visual responses in the inner retina. *Neuron* 90, 308–319. doi: 10.1016/j.neuron.2016.03.015
- Saari, J. C. (2012). Vitamin A metabolism in rod and cone visual cycles. *Annu. Rev. Nutr.* 32, 125–145. doi: 10.1146/annurev-nutr-071811-150748
- Sakai, H. M., Machuca, H., Korenberg, M. J., and Naka, K.-I. (1997). Processing of color- and noncolor-coded signals in the gourami retina: III. ganglion cells. *J. Neurophysiol.* 78, 2034–2047. doi: 10.1152/jn.1997.78.4.2034
- Sanes, J. R., and Masland, R. H. (2015). The types of retinal ganglion cells: current status and implications for neuronal classification. *Annu. Rev. Neurosci.* 38, 221–246. doi: 10.1146/annurev-neuro-071714-034120
- Saszik, S., Alexander, A., Lawrence, T., and Bilotta, J. (2002). APB differentially affects the cone contributions to the zebrafish ERG. *Vis. Neurosci.* 19, 521–529. doi: 10.1017/s0952523802194144
- Saszik, S., Bilotta, J., and Givin, C. M. (1999). ERG assessment of zebrafish retinal development. *Vis. Neurosci.* 16, 881–888. doi: 10.1017/s0952523899165076
- Schmitt, E. A., and Dowling, J. E. (1994). Early-eye morphogenesis in the zebrafish, *Brachydanio rerio*. *J. Comp. Neurol.* 344, 532–542. doi: 10.1002/cne.903440404
- Schmitt, E. A., and Dowling, J. E. (1999). Early retinal development in the zebrafish, *Danio rerio*: light and electron microscopic analysis. *J. Comp. Neurol.* 404, 515–536. doi: 10.1002/(sici)1096-9861(19990222)404:4<515::aid-cne8>3.0.co;2-a
- Shen, Y. C., and Raymond, P. A. (2004). Zebrafish cone-rod (crx) homeobox gene promotes retinogenesis. *Dev. Biol.* 269, 237–251. doi: 10.1016/j.ydbio.2004.01.037
- Sherry, D. M., and Yazulla, S. (1993). Goldfish bipolar cells and axon terminal patterns: a Golgi study. *J. Comp. Neurol.* 329, 188–200. doi: 10.1002/cne.903290204
- Silveira, L. C., Saito, C. A., Da Dilva Filho, M., Kremers, J., Bowmaker, J. K., and Lee, B. B. (2014). Alouatta trichromatic color vision: cone spectra and physiological responses studied with microspectrophotometry and single unit retinal electrophysiology. *PLoS One* 9:e113321. doi: 10.1371/journal.pone.0113321
- Siminoff, R. (1986). Dynamics of chromaticity horizontal cells in the freshwater turtle retina. *Biol. Cybern.* 54, 269–279. doi: 10.1007/bf00318423
- Song, P. I., Matsui, J. I., and Dowling, J. E. (2008). Morphological types and connectivity of horizontal cells found in the adult zebrafish (*Danio rerio*) retina. *J. Comp. Neurol.* 506, 328–338. doi: 10.1002/cne.21549
- Spekreijse, H., Wagner, H. G., and Wolbarsht, M. L. (1972). Spectral and spatial coding of ganglion cell responses in goldfish retina. *J. Neurophysiol.* 35, 73–86. doi: 10.1152/jn.1972.35.1.73
- Spence, R., and Smith, C. (2008). Innate and learned colour preference in the zebrafish, *Danio rerio*. *Ethology* 114, 582–588. doi: 10.1111/j.1439-0310.2008.01515.x
- Stafford, D. K., and Dacey, D. M. (1997). Physiology of the A1 amacrine: a spiking, axon-bearing interneuron of the macaque monkey retina. *Visual Neurosci.* 14, 507–522. doi: 10.1017/s0952523800012165
- Stearns, G., Evangelista, M., Fadool, J. M., and Brockerhoff, S. E. (2007). A mutation in cone-specific pde6 gene causes rapid cone photoreceptor degeneration in zebrafish. *J. Neurosci.* 27, 13866–13874. doi: 10.1523/JNEUROSCI.3136-07.2007
- Steinberg, R. H. (1969). Rod and cone contributions to S-potentials from the cat retina. *Vision Res.* 9, 1319–1329. doi: 10.1016/0042-6989(69)90069-8
- Stell, W. K. (1967). The structure and relationships of horizontal cells and photoreceptor-bipolar synaptic complexes in goldfish retina. *Am. J. Anat.* 121, 401–423. doi: 10.1002/aja.1001210213
- Stell, W. K. (1975). Horizontal cell axons and axon terminals in goldfish retina. *J. Comp. Neurol.* 159, 503–519. doi: 10.1002/cne.901590405
- Stell, W. K., and Lightfoot, D. O. (1975). Color-specific interconnections of cones and horizontal cells in the retina of the goldfish. *J. Comp. Neurol.* 159, 473–501. doi: 10.1002/cne.901590404
- Stuermer, C. A. (1988). Retinotopic organization of the developing retinotectal projection in the zebrafish embryo. *J. Neurosci.* 8, 4513–4530. doi: 10.1523/JNEUROSCI.08-12-04513.1988
- Sun, W., Li, N., and He, S. (2002). Large-scale morphological survey of mouse retinal ganglion cells. *J. Comp. Neurol.* 451, 115–126. doi: 10.1002/cne.10323
- Sun, H., Smithson, H. Z., Zaidi, Q., and Lee, B. B. (2006). Specificity of cone inputs to macaque retinal ganglion cells. *J. Neurophysiol.* 95, 837–849. doi: 10.1152/jn.00714.2005
- Suzuki, S. C., Bleckert, A., Williams, P. R., Takechi, M., Kawamura, S., and Wong, R. O. (2013). Cone photoreceptor types in zebrafish are generated by symmetric terminal divisions of dedicated precursors. *Proc. Natl. Acad. Sci. U S A* 110, 15109–15114. doi: 10.1073/pnas.1303551110
- Svaetichin, G., and Macnichel, E. F. Jr. (1958). Retinal mechanisms for chromatic and achromatic vision. *Ann. N Y Acad. Sci.* 74, 385–404. doi: 10.1111/j.1749-6632.1958.tb39560.x
- Takechi, M., and Kawamura, S. (2005). Temporal and spatial changes in the expression pattern of multiple red and green subtype opsin genes during zebrafish development. *J. Exp. Biol.* 208, 1337–1345. doi: 10.1242/jeb.01532
- Taylor, M. R., Hurley, J. B., Van Epps, H. A., and Brockerhoff, S. E. (2004). A zebrafish model for pyruvate dehydrogenase deficiency: rescue of neurological dysfunction and embryonic lethality using a ketogenic diet. *Proc. Natl. Acad. Sci. U S A* 101, 4584–4589. doi: 10.1073/pnas.0307074101
- Taylor, M. R., Kikkawa, S., Diez-Juan, A., Ramamurthy, V., Kawakami, K., Carmeliet, P., et al. (2005). The zebrafish pob gene encodes a novel proetin required for survival of red cone photoreceptor cells. *Genetics* 170, 263–273. doi: 10.1534/genetics.104.036434
- Torvund, M. M., Ma, T. S., Connaughton, V. P., Ono, F., and Nelson, R. F. (2017). Cone signals in the monostriated and bistratified amacrine cells of adult zebrafish retina. *J. Comp. Neurol.* 525, 1532–1557. doi: 10.1002/cne.24107
- Tsang, S. H., Gouras, P., Yamashita, C. K., Kjeldbye, H., Fisher, J., Barber, D. B., et al. (1996). Retinal degeneration in mice lacking the γ -subunit of the rod cGMP phosphodiesterase. *Science* 272, 1026–1029. doi: 10.1126/science.272.5264.1026
- Twig, G., and Perlman, I. (2004). Homogeneity and diversity of color-opponent horizontal cells in the turtle retina: consequences for potential wavelength discrimination. *J. Vis.* 4, 403–414. doi: 10.1167/4.5.5
- Van Dijk, B. W., and Spekreijse, H. (1984). Linear color opponency in carp retinal ganglion cells. *Vision Res.* 24, 1865–1872. doi: 10.1016/0042-6989(84)90019-1

- Van Epps, H. A., Hayashi, M., Lucast, L., Stearns, G. W., Hurley, J. B., De Camilli, P., et al. (2004). The zebrafish nrc mutant reveals a role for the polyphosphoinositide phosphatase synaptojanin 1 in cone photoreceptor ribbon anchoring. *J. Neurosci.* 24, 8641–8650. doi: 10.1523/JNEUROSCI.2892-04.2004
- Van Epps, H. A., Yim, C. M., Hurley, J. B., and Brockerhoff, S. E. (2001). Investigations of photoreceptor synaptic transmission and light adaptation in the zebrafish visual mutant nrc. *Invest. Ophthalmol. Vis. Sci.* 42, 868–874.
- Wagner, H. G., Macnichol, E. F., and Wolbarsht, M. L. (1960). The response properties of single ganglion cells in the goldfish retina. *J. Gen. Physiol.* 43, 45–62. doi: 10.1085/jgp.43.6.45
- Wagner, H. G., and Wagner, E. (1988). Amacrine cells in the retina of a teleost fish, the roach (*Rutilus rutilus*): a Golgi study on differentiation and layering. *Philos. Trans. R. Soc. Lond. B Biol. Sci.* 321, 263–324. doi: 10.1098/rstb.1988.0094
- Weiler, R. (1978). Horizontal cells of the carp retina: Golgi impregnation and Procion-Yellow injection. *Cell Tissue Res.* 195, 515–526. doi: 10.1007/bf00233893
- Wersinger, E., Schwab, Y., Sahel, J., Rendon, A., Pow, D., Picaud, S., et al. (2006). The glutamate transporter EAAT5 works as a presynaptic receptor in mouse rod bipolar cells. *J. Physiol.* 557, 221–234. doi: 10.1113/jphysiol.2006.118281
- Witkovsky, P. (1965). The spectral sensitivity of retinal ganglion cells in the carp. *Vision Res.* 5, 603–614. doi: 10.1016/0042-6989(65)90034-9
- Wong, K. Y., Cohen, E. D., and Dowling, J. E. (2005). Retinal bipolar cell input mechanisms in giant danio: II. Patch-clamp analysis of on bipolar cells. *J. Neurophysiol.* 93, 94–107. doi: 10.1152/jn.00270.2004
- Wong, K. Y., and Dowling, J. E. (2005). Retinal bipolar cell input mechanisms in giant danio. III. ON-OFF bipolar cells and their color-opponent mechanisms. *J. Neurophysiol.* 94, 265–272. doi: 10.1152/jn.00271.2004
- Wu, S. M., Gao, F., and Maple, B. R. (2000). Functional architecture of synapses in the inner retina: segregation of visual signals by stratification of bipolar cell axon terminals. *J. Neurosci.* 20, 4462–4470. doi: 10.1523/JNEUROSCI.20-12-04462.2000
- Yang, X.-L., Tauchi, M., and Kaneko, A. (1983). Convergence of signals from red-sensitive and green-sensitive cones onto L-type external horizontal cells of the goldfish retina. *Vision Res.* 23, 371–380. doi: 10.1016/0042-6989(83)90084-6
- Yazulla, S., and Studholme, K. M. (2001). Neurochemical anatomy of the zebrafish retina as determined by immunocytochemistry. *J. Neurocytol.* 30, 551–592. doi: 10.1023/A:1016512617484
- Yeo, J.-Y., Lee, E.-S., and Jeon, C.-J. (2009). Parvalbumin-immunoreactive neurons in the inner nuclear layer of zebrafish retina. *Exp. Eye Res.* 88, 553–560. doi: 10.1016/j.exer.2008.11.014
- Yin, L., Smith, R. G., Sterling, P., and Brainard, D. H. (2006). Chromatic properties of horizontal and ganglion cell responses follow a dual gradient in cone opsin expression. *J. Neurosci.* 26, 12351–12361. doi: 10.1523/JNEUROSCI.1071-06.2006
- Yin, L., Smith, R. G., Sterling, P., and Brainard, D. H. (2009). Physiology and morphology of color-opponent ganglion cells in a retina expressing a dual gradient of S and M opsins. *J. Neurosci.* 29, 2706–2724. doi: 10.1523/JNEUROSCI.5471-08.2009
- Yoshimatsu, T., Williams, P. R., D'Orazi, F. D., Suzuki, S. C., Fadool, J. M., Allison, W., et al. (2014). Transmission from the dominant input shapes the stereotypic ratio of photoreceptor inputs onto horizontal cells. *Nat. Commun.* 5:3699. doi: 10.1038/ncomms4699
- Zhang, R.-W., Wei, H.-P., Xia, Y.-M., and Du, J.-L. (2010). Development of light response and GABAergic excitation-to-inhibition switch in zebrafish retinal ganglion cells. *J. Physiol.* 588, 2557–2569. doi: 10.1113/jphysiol.2010.187088
- Zhang, A.-J., and Wu, S. M. (2010). Responses and receptive fields of amacrine cells and ganglion cells in the salamander retina. *Vision Res.* 50, 614–622. doi: 10.1016/j.visres.2010.01.009
- Zhou, Y., Chen, A.-H., Gong, H.-Q., and Liang, P.-J. (2005). Color information encoded by the spatiotemporal patterns of light response in ganglion cells of chick retina. *Brain Res.* 1059, 1–6. doi: 10.1016/j.brainres.2005.07.077
- Zimmermann, M. J. Y., Nevala, N. E., Yoshimatsu, T., Osorio, D., Nilsson, D.-E., Berns, P., et al. (2018). Zebrafish differentially process colour across visual space to match natural scenes. *Curr. Biol.* 28, 2018.e5–2032.e5. doi: 10.1016/j.cub.2018.04.075
- Zrenner, E., Nelson, R., and Mariani, A. (1983). Intracellular recordings from a biplexiform ganglion cell in macaque retina, stained with horseradish peroxidase. *Brain Res.* 262, 181–185. doi: 10.1016/0006-8993(83)91007-7

Conflict of Interest Statement: The authors declare that the research was conducted in the absence of any commercial or financial relationships that could be construed as a potential conflict of interest.

Copyright © 2018 Meier, Nelson and Connaughton. This is an open-access article distributed under the terms of the Creative Commons Attribution License (CC BY). The use, distribution or reproduction in other forums is permitted, provided the original author(s) and the copyright owner(s) are credited and that the original publication in this journal is cited, in accordance with accepted academic practice. No use, distribution or reproduction is permitted which does not comply with these terms.



Modulation of Hyperpolarization-Activated Inward Current and Thalamic Activity Modes by Different Cyclic Nucleotides

Maia Datunashvili^{1*}, Rahul Chaudhary¹, Mehrnoush Zobeiri¹, Annika Lüttjohann¹, Evanthia Mergia², Arnd Baumann³, Sabine Balfanz³, Björn Budde¹, Gilles van Luijtelea⁴, Hans-Christian Pape¹, Doris Koesling² and Thomas Budde^{1*}

¹Institut für Physiologie I, Westfälische Wilhelms-Universität, Münster, Germany, ²Institut für Pharmakologie und Toxikologie, Ruhr-Universität Bochum, Bochum, Germany, ³Institute of Complex Systems, Forschungszentrum Jülich, Jülich, Germany, ⁴Donders Centre for Cognition, Radboud University, Nijmegen, Netherlands

OPEN ACCESS

Edited by:

Lisa Mapelli,
University of Pavia, Italy

Reviewed by:

Christian Wahl-Schott,
Ludwig-Maximilians-Universität
München, Germany
Andrea Nistri,
Scuola Internazionale Superiore di
Studi Avanzati (SISSA), Italy

*Correspondence:

Maia Datunashvili
datunasm@ukmuenster.de
Thomas Budde
tbudde@uni-muenster.de

Received: 03 August 2018

Accepted: 28 September 2018

Published: 24 October 2018

Citation:

Datunashvili M, Chaudhary R, Zobeiri M, Lüttjohann A, Mergia E, Baumann A, Balfanz S, Budde B, van Luijtelea G, Pape H-C, Koesling D and Budde T (2018) Modulation of Hyperpolarization-Activated Inward Current and Thalamic Activity Modes by Different Cyclic Nucleotides. *Front. Cell. Neurosci.* 12:369. doi: 10.3389/fncel.2018.00369

The hyperpolarization-activated inward current, I_h , plays a key role in the generation of rhythmic activities in thalamocortical (TC) relay neurons. Cyclic nucleotides, like 3',5'-cyclic adenosine monophosphate (cAMP), facilitate voltage-dependent activation of hyperpolarization-activated cyclic nucleotide-gated (HCN) channels by shifting the activation curve of I_h to more positive values and thereby terminating the rhythmic burst activity. The role of 3',5'-cyclic guanosine monophosphate (cGMP) in modulation of I_h is not well understood. To determine the possible role of the nitric oxide (NO)-sensitive cGMP-forming guanylyl cyclase 2 (NO-GC2) in controlling the thalamic I_h , the voltage-dependency and cGMP/cAMP-sensitivity of I_h was analyzed in TC neurons of the dorsal part of the lateral geniculate nucleus (dLGN) in wild type (WT) and NO-GC2-deficit (NO-GC2^{-/-}) mice. Whole cell voltage clamp recordings in brain slices revealed a more hyperpolarized half maximal activation ($V_{1/2}$) of I_h in NO-GC2^{-/-} TC neurons compared to WT. Different concentrations of 8-Br-cAMP/8-Br-cGMP induced dose-dependent positive shifts of $V_{1/2}$ in both strains. Treatment of WT slices with lyase enzyme (adenylyl and guanylyl cyclases) inhibitors (SQ22536 and ODQ) resulted in further hyperpolarized $V_{1/2}$. Under current clamp conditions NO-GC2^{-/-} neurons exhibited a reduction in the I_h -dependent voltage sag and reduced action potential firing with hyperpolarizing and depolarizing current steps, respectively. Intrathalamic rhythmic bursting activity in brain slices and in a simplified mathematical model of the thalamic network was reduced in the absence of NO-GC2. In freely behaving NO-GC2^{-/-} mice, delta and theta band activity was enhanced during active wakefulness (AW) as well as rapid eye movement (REM) sleep in cortical local field potential (LFP) in comparison to WT. These findings indicate

Abbreviations: AW, active wakefulness; DSWS, deep slow wave sleep; EEG, electroencephalogram; HCN, hyperpolarization-activated cyclic nucleotide-gated channels; IC, internal capsule; I_h , hyperpolarization activated current; LFP, local field potential; LSWS, light slow wave sleep; LTS, low-threshold Ca^{2+} spike; NO, nitric oxide; nonREM, non-rapid eye movement sleep; nRT, reticular thalamus; PIR, passive infrared recording system; REM, rapid eye movement sleep; Rin, input resistance; RMP, resting membrane potential; SSC, somatosensory cortex; SWS, slow wave sleep; TC, thalamocortical; $V_{1/2}$, half maximal activation; VB, ventrobasal thalamus.

that cGMP facilitates I_h activation and contributes to a tonic activity in TC neurons. On the network level basal cGMP production supports fast rhythmic activity in the cortex.

Keywords: thalamus, dLGN, cyclic nucleotides, NO-GC2, HCN channels, I_h current, I_{KIR} current, slow oscillations

INTRODUCTION

Cyclic nucleotides, like cyclic adenosine monophosphate (cAMP) and cyclic guanosine monophosphate (cGMP) bind to the hyperpolarization-activated cyclic nucleotide-gated (HCN) channels and stabilize their open state (Zagotta et al., 2003). HCN channels represent the molecular basis of the hyperpolarization-activated current, termed I_h (Pape, 1996). HCN isoforms (HCN1-4) reveal different characteristics with respect to voltage dependency, activation kinetics and cyclic nucleotide sensitivity (He et al., 2014). HCN2 and the HCN4 isoforms (Ludwig et al., 2003; Notomi and Shigemoto, 2004) are strongly modulated by cAMP in thalamocortical (TC) relay neurons (Kanyshkova et al., 2009, 2012). A number of brain rhythms are controlled by HCN channels, and epileptogenesis in the TC system is accompanied by changes in HCN expression levels and altered properties of I_h , including cAMP—sensitivity (Budde et al., 2005; Kanyshkova et al., 2012). In thalamic neurons of the rodent brain, I_h contributes to the resting membrane potential (RMP) and determines cell type-specific firing patterns and postnatal changes in HCN isoform expression profiles are accompanied by the maturation of sleep-related slow oscillations (Meuth et al., 2006; Kanyshkova et al., 2009).

In the dorsal lateral geniculate nucleus (dLGN), neuronal nitric oxide synthase (nNOS) was found in interneurons and cholinergic afferents arising from the ascending brainstem system (Gabbott and Bacon, 1994). NO exerts an important role in behavioral state-dependent gating of visual information and regulating TC oscillations (Pape and Mager, 1992; Yang and Cox, 2008). Thalamic NO concentrations increase during wakefulness and rapid eye movement (REM) sleep and decrease during slow wave sleep (SWS; Burlet and Cespuglio, 1997), pointing to a possible role of NO in regulation of arousal and REM sleep.

NO has been identified as an important modulator of HCN channel activity mediated by the NO-sensitive soluble NO-GC1 and NO-GC2 (Russwurm et al., 2013). Although cyclic nucleotide-dependent modulation of I_h in the thalamus under physiological and pathophysiological conditions has been assessed before (Pape, 1996; He et al., 2014), it is not known whether I_h in TC neurons is under the simultaneous control of both cAMP and cGMP. To address this issue, we studied I_h properties in wild type (WT) and NO-GC2-deficient mice, in the presence of adenylyl and guanylyl cyclase inhibitors as well as by intracellular application of cyclic nucleotides. By combining *in vitro* voltage and current clamp methods, we examined the characteristics of I_h current as well as the passive and active properties of NO-GC2^{-/-} TC cells. By means of *in vitro* and *in vivo* field potential recordings we studied intrathalamic and cortical activities. Based on these results the present study provides a detailed description of the role of cGMP in the regulation of intrathalamic and cortical activities.

MATERIALS AND METHODS

Preparation of Coronal dLGN Slices

All animal work has been approved by local authorities (review board institution: Landesamt für Natur, Umwelt und Verbraucherschutz Nordrhein-Westfalen; approval ID: 84-02.04.2015.A574, 84-02.05.50.15.026). Experiments were performed on NO-GC2-deficient mice (Mergia et al., 2006) ranging in age from postnatal day P16 to P35. These mice lack the $\alpha 2$ subunit of NO-dependent soluble guanylyl cyclase while the $\alpha 1$ and $\beta 1$ subunits can assemble to enzymatically active NO-GC1. NO-GC2^{-/-} mice were produced by breeding heterozygous mice or homozygous mice of the F1 generation. Genotyping of the mice was performed by PCR analysis of DNA extracted from ear biopsies. As the knockout strain was backcrossed over 10 generations onto C57BL/6J background, C57BL/6J mice (postnatal day P16 to P35) were used as WT controls (WT). Mice were anesthetized with isoflurane (3.5 vol%) and sacrificed. After surgically removing their skull cap caudal to bregma, a block of brain tissue containing the thalamus was removed from the cranial vault and submerged in ice-cold aerated (O₂) saline containing (in mM): sucrose, 200; PIPES, 20; KCl, 2.5; NaH₂PO₄, 1.25; MgSO₄, 10; CaCl₂, 0.5; dextrose, 10; pH 7.35, with NaOH. Thalamic slices (250–300 μ m thick) were prepared as coronal sections on a vibratome. Slices were transferred to a holding chamber and kept submerged (at 30°C for 30 min, thereafter at room temperature) in artificial cerebrospinal fluid (ACSF) containing (in mM): NaCl, 125; KCl, 2.5; NaH₂PO₄, 1.25; NaHCO₃, 24; MgSO₄, 2; CaCl₂, 2; dextrose, 10; pH adjusted to 7.35 by bubbling with carbogen (95% O₂ and 5% CO₂ gas mixture).

Voltage Clamp Recordings

Recordings were done on visually identified TC neurons of the dLGN in a solution containing (in mM): NaCl, 120; KCl, 2.5; NaH₂PO₄, 1.25; HEPES, 30; MgSO₄, 2; CaCl₂, 2; dextrose, 10; pH 7.35 adjusted with HCl. For some recordings, bicarbonate (NaHCO₃) buffered ACSF was used (in mM): NaCl, 125; KCl, 2.5; NaH₂PO₄, 1.25; NaHCO₃, 24; MgSO₄, 2; CaCl₂, 2; dextrose, 10; pH adjusted to 7.35 by bubbling with carbogen. In order to block inward rectifying K⁺ and K_{2P} channels, 0.5 mM BaCl₂ was added to the solution. Whole-cell recordings were made from the soma of TC neurons at 30–32°C. Membrane currents were measured with glass microelectrodes pulled from borosilicate glass capillaries (GC150T-10; Clark Electromedical Instruments, Pangbourne, UK) filled with (in mM): K-gluconate, 95; K₃-citrate, 20; NaCl, 10; HEPES, 10; MgCl₂, 1; CaCl₂, 0.5; BAPTA, 3; Mg-ATP, 3; Na₂-GTP, 0.5. The internal solution was set to a pH of 7.25 with KOH and an osmolality of 295 mOsm/kg. A 0.2 μ m pore size sterile filter (MP, Hennigsdorf, Germany) was placed between the needle and the syringe to fill the electrodes.

Patch electrodes were connected to an EPC-10 amplifier (HEKA Elektronik, Lamprecht, Germany) via a chlorinated silver wire. The resistances of electrodes were in the range of 2.5–3.5 MΩ. Access resistances were between 8 MΩ and 20 MΩ. Series resistance compensation of >50% was routinely applied. Recordings started 2–3 min after obtaining the whole-cell configuration. Voltage clamp experiments were controlled by the software Pulse or PatchMaster (HEKA Elektronik) operating on an IBM-compatible personal computer. All recordings were corrected offline for a liquid junction potential of 10 mV ($V_M = V_P - 10$ mV; with V_M = membrane potential and V_P = pipette voltage). Care was exercised to monitor series resistance and recordings were terminated whenever a significant increase (>20%) occurred.

The voltage protocol used to examine I_h (Kanyshkova et al., 2012) was designed in order to increase the stability of whole cell recordings and account for increasingly fast activation kinetics of the current. Therefore the pulse length was shortened by 500 ms with increasing hyperpolarization (3.5 s pulse length at −130 mV). Steady-state activation of I_h , $p(V)$, was estimated by normalizing the mean tail current amplitudes (I) 50–100 ms after stepping to a constant potential from a variable amplitude step using the following function (equation 1):

$$P(V) = (I - I_{\min}) / (I_{\max} - I_{\min}) \quad (1)$$

with I_{\max} being the tail current amplitude for the voltage step from −130 mV to −100 mV and I_{\min} for the voltage step from −40 mV to −100 mV, respectively. I_h activation was well accounted for by a Boltzmann function of the following form (equation 2):

$$p(V) = 1 / (1 + \exp((V - V_{1/2})/k)) \quad (2)$$

where $V_{1/2}$ is the voltage of half-maximal activation and k the slope factor.

The current density was calculated by dividing the I_h amplitude at −130 mV (i.e., subtracting the instantaneous current amplitude from the steady-state current) by the membrane capacitance obtained during whole cell recordings.

The time course of I_h activation in TC neurons at a temperature of 30–32°C was best approximated by the following double-exponential equation:

$$I_h(t) = A_1(1 - \exp^{-t/\tau_{\text{fast}}}) + A_2(1 - \exp^{-t/\tau_{\text{slow}}}), \quad (3)$$

Where $I_h(t)$ is the time (ms), A_1 and A_2 are current amplitudes (pA), and τ_{fast} and τ_{slow} are time constants (ms), respectively. Currents evoked by voltage steps to −130 mV were analyzed.

A series of hyperpolarizing (500 ms) voltage steps in −10 mV increments were injected from the holding potential of −60 to −130 mV in order to evoke inwardly rectifying potassium (I_{KIR}) current. I_{KIR} currents were isolated from I_h by applying 20 μM ZD7288. I_{KIR} amplitudes were measured manually as the difference of the peak and the steady state current at the beginning and at the end of voltage pulses, respectively.

Current Clamp Recordings and Determination of the Intrinsic Electrophysiological Properties

The active and passive membrane properties of TC neurons were determined in current clamp mode. Recordings were performed at RMP in Ba^{2+} -free extracellular solution containing (in mM): NaCl, 125; KCl, 2.5; NaH_2PO_4 , 1.25; NaHCO_3 , 24; MgSO_4 , 2; CaCl_2 , 2; dextrose, 10; pH adjusted to 7.35 by bubbling with carbogen. In order to compare the effects of different buffers and Ba^{2+} ions on intrinsic membrane properties of TC neurons, 0.5 mM BaCl_2 was added in HEPES and NaHCO_3 buffered extracellular solutions. Analysis was performed according to established procedures (Leist et al., 2016). Only cells with overshooting APs were included for analysis. The stimulation protocol contained hyperpolarizing and depolarizing current steps (1 s duration, from −230 pA to +370 pA with 40 pA increments; for 8-Br-cGMP experiments, a protocol with steps of 1 s duration, from −120 pA to +260 pA with 20 pA increments, was used). Membrane input resistance (R_{in}) was deduced from the slope of the current-voltage (I - V) relationship obtained from current injections of −30 and 50 pA. Membrane time constants (τ_m) were obtained by fitting single or double exponentials (FitMaster, HEKA Elektronik) to negative voltage deflections induced by hyperpolarizing current injections of −30 pA. The I_h -dependent anomalous rectification (or voltage sag) of current injection of −230 pA was calculated as the change between the maximal and steady state voltage deflection (at the end of hyperpolarizing current injection). APs were detected manually by setting an amplitude threshold (V_{thresh}). FitMaster (HEKA Elektronik) and Clampfit 10.7 (Axon Molecular Devices, Sunnyvale, CA, USA) software was used for the analyses.

Immunofluorescence

WT mice were transcardially perfused with 4% (w/v) phosphate-buffered paraformaldehyde (PFA). Brains were removed and post fixed overnight in 4% PFA and later in 30% (w/v) sucrose for 48–72 h. Free-floating coronal sections (40 μm) were cut and slices were collected in phosphate-buffered saline (PBS). Sections were rinsed three times for 10 min in PBS. Slices were then incubated for 2 h in PBS supplemented with 10% (v/v) normal goat serum, Triton-X100 (0.3% (w/v)), and 3% (w/v) bovine serum albumin (BSA). Finally sections were incubated with primary antibodies overnight at 4°C. Polyclonal rabbit (rb) anti-NO-GCα₂ (1:1,000; ab42108, Abcam, USA) antibody was utilized to detect a localization of dLGN. Several studies using this antibody revealed detecting of a single protein band of the correct size in quantitative Western blot experiments, thereby pointing to specificity of the reaction (Backer et al., 2008; Thoonen et al., 2015; product data sheet Abcam). In a similar way the monoclonal mouse anti-postsynaptic density protein 95 (PSD95; 1:1,000; 10011435, Cayman, USA) antibody which marks the postsynaptic membrane revealed a single protein band in Western blots (Yao et al., 2004). After incubation with primary antibodies, sections were washed three times for 10 min in PBS and then transferred to the secondary antibody solution

(Alexa Fluor 488 goat anti-rabbit-IgG, 1:1,000 and Alexa Fluor 568 goat anti-mouse-IgG, 1:1,000) for 2 h. Finally, sections were washed three times for 10 min in PBS and mounted with a mounting medium (VECTASHIELD, Vector Laboratories Inc., Burlingame, CA, USA) for confocal microscopy (Nikon eC1plus) equipped with a CFI75 LWD \times 16/0.8 NA objective (Nikon). Omission of primary or secondary antibodies from the staining procedure resulted in a lack of fluorescent signals.

Quantification of cGMP in Tissue Samples

WT mice of different postnatal development age (P7, P21 and P105) were sacrificed and coronal slices were prepared on a vibratome. Separate tissues containing dLGN, ventrobasal thalamic complex (VB) and somatosensory cortex (SSC) were placed in ice-cold buffer containing (in mM): sucrose, 200; PIPES, 20; KCl, 2.5; NaH_2PO_4 , 1.25; MgSO_4 , 10; CaCl_2 , 0.5; dextrose, 10; pH 7.35 with NaOH and further incubated in an oxygenated salt solution (in mM: NaCl, 125; KCl, 2.5; NaH_2PO_4 , 1.25; HEPES, 30; glucose, 10; CaCl_2 , 2; MgCl_2 , 1; IBMX, 0.05; pH 7.3) for 2 h. Samples were mechanically homogenized at room temperature. To eliminate any non-solubilized material, samples were centrifuged at $1,000\times g$ for 10 min at 4°C . The supernatant was transferred to a new Eppendorf cup and kept on ice, snap frozen in liquid nitrogen and stored at -80°C before further use.

Prior to cGMP quantification, samples were thawed on ice and 50 μl was used for Bradford protein assay. A cyclic GMP ELISA Kit (Prod. No. 581021, Cayman Chemicals, Ann Arbor, MI, USA) was used to quantify cGMP. Briefly, all samples were treated with trichloroacetic acid (TCA, final concentration 5% (w/v)) to precipitate proteins. After centrifugation, the supernatant was extracted with ether to remove any TCA residuals. An acetylation step for tissue samples was performed according to the manufacturer's protocol. The final assay set up, luminescent measurement and analysis was performed as suggested by the manufacturer. We used a Fluostar Omega fluorescence reader (BMG Labtech, Ortenberg, Germany) for data acquisition and Microsoft Excel 2011 version 14.0 to analyze the data.

Rhythmic Burst Activity Recordings in Thalamic Slices

Horizontal brain slices were transferred to an interface chamber and recordings were performed at $32 \pm 1^\circ\text{C}$. The superfusion solution consisted of (in mM): NaCl, 125; KCl, 2.5; NaHCO_3 , 26; NaH_2PO_4 , 1.25; MgCl_2 , 1; CaCl_2 , 2; glucose, 10; pH 7.35 adjusted with carbogen. Rhythmic burst activity was induced through stimulation (1 ms, 1.45 mA) of the internal capsule (IC) using a pair of tungsten electrodes (with 50–100 $\text{M}\Omega$ resistance). Stimulation electrodes were connected to custom-made amplifier and stimulus isolator, and duration of stimulus was controlled by WinLTPd101 software (WinLTP Ltd, University of Bristol, UK). Network activity was measured in VB using a glass electrode (GC150T-10; Clark Electromedical Instruments, Harvard, UK) with a resistance of 0.5–2 $\text{M}\Omega$. Burst firing was characterized by at least three high-frequency spikes with an intra-burst frequency

interval of >100 Hz and inter-burst interval not more than 500 ms. Activity was analyzed in a time interval ranging from 50 ms to 100 ms up to 2–3 s after stimulation of the IC. Analysis was performed offline using Clampfit 10.7 and Peak v1.0 software.

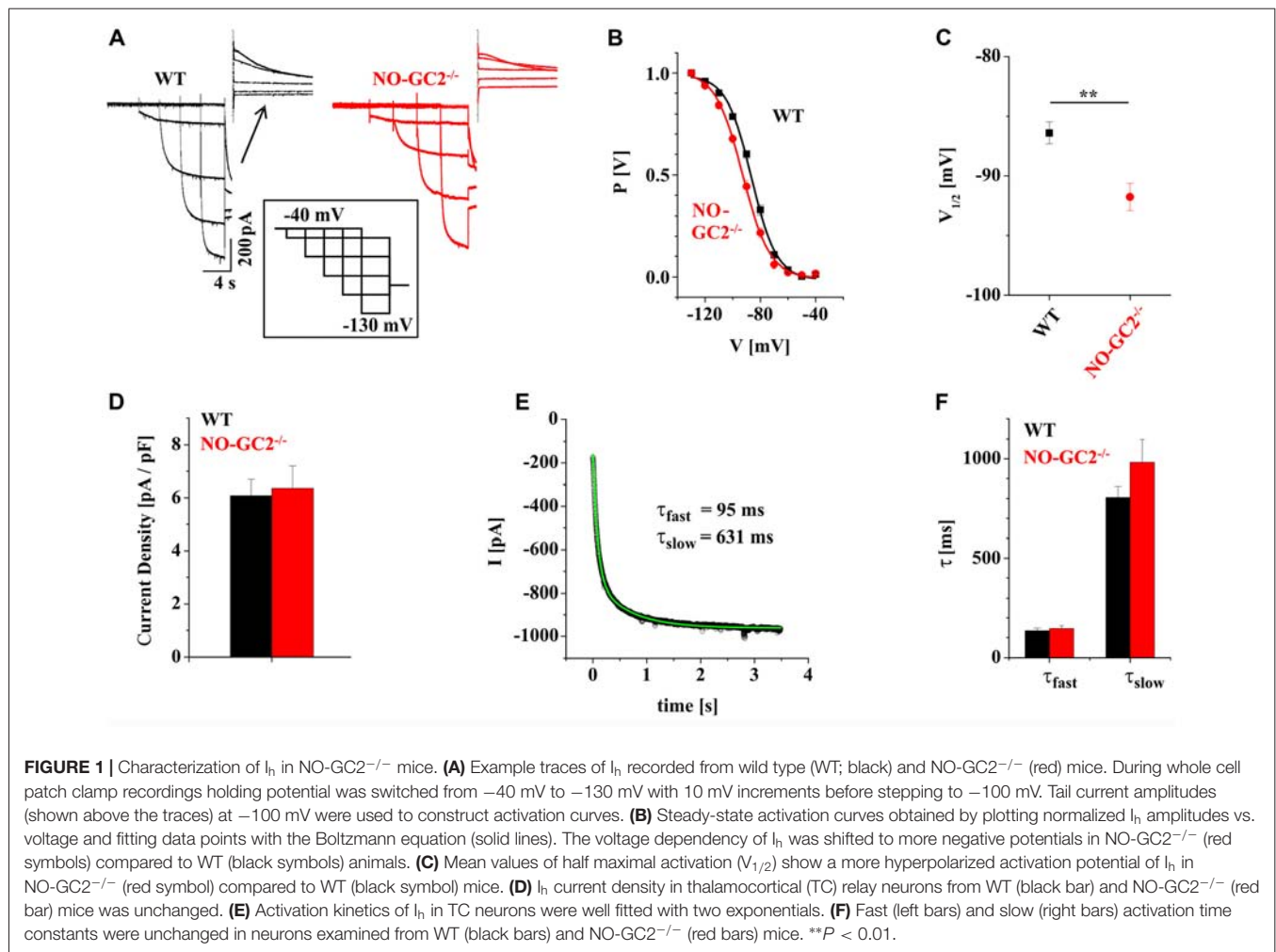
Electrode Implantation and LFP Recordings for *in vivo* Electrophysiology

Mature properties of I_h were reached in young mice postnatal between P20 and P30. Similar mature sleep pattern were found in young (P18) and adult (P90) rodents based on the analyses of cortical electroencephalogram (EEG) recordings, in which well-developed high amplitude delta waves distinguished NREM sleep from wakefulness. 3 to 5 months old adult male $\text{NO-GC2}^{-/-}$ and WT mice were used for the *in vivo* experiments. Before surgery each animal was kept individually for 1 week in 12 h light/dark conditions (6 a.m.–6 p.m. light on period) and had unrestricted access to water and food. Implantation of the local field potential (LFP) recording electrodes was performed in a stereotactic frame (David Kopf Instruments, Tujunga, CA, USA) in animals under pentobarbital anesthesia (50 mg kg^{-1} i.p.) supplemented by a subcutaneous injection of carprofen (rimadyl; 5 mg/kg^{-1}). Holes were drilled into the skull of the right hemisphere for inserting the silver recording electrode within the somatosensory cortex (SSC) (A/P = 0, M/L = 3, depth = -1.2 ; referenced to Bregma according to the mouse brain atlas), as well as for the reference and ground electrodes, which were placed over the cerebellum. The electrode assembly was fixed to the skull using dental acrylic cement (Pulpdent Glasslute, Watertown, MA, USA). After 1 week of recovery period the mice were habituated to the recording chamber. The LFP signal of each mouse was recorded for 2 h between 6 and 8 a.m. corresponding to the first 2 h of the light period. The LFP signal was amplified with a physiological amplifier (DPA-2F, Science Products, Hofheim, Germany), filtered by a band pass filter with cut-off points at 1 (HP) and 30 (LP) Hz and digitalized with a constant sampling rate of 2 kHz by multichannel continuous recording system (CED1401, Cambridge Electronic Design, Cambridge, England). In parallel, behavioral activity of mice was registered using a Passive Infrared Recording System (PIR, RK2000DPC LuNAR PR Ceiling Mount, Rokonet RISCO Group S.A., Drogenbos, Belgium). Following LFP recordings, animals were deeply anesthetized with an overdose of pentobarbital (i.p. injection) and the brains were removed for histological verification of the correct electrode positions.

Analysis of LFP Activity

LFPs were inspected offline by trained electrophysiologist (blinded for genotype) using Spike2 analysis software (Version 7.08, Cambridge Electronic Design, Germany). Recordings were subjected to Fast Fourier Transformation (FFT) in the 1–30 Hz range. Twenty epochs of 10 s duration were chosen from four behavioral states for power spectral density (PSD) analyses: active wakefulness (AW), REM sleep, light SWS (LSWS) and deep SWS (DSWS). For all epochs the EEG power in the delta (δ = 1–4 Hz), theta (θ = 5–8 Hz), alpha (α = 9–12 Hz)

October 2018 | Volume 12 | Article 369



NO-GC2^{-/-} revealed increased sensitivity to all applied concentrations of 8-Br-cGMP ($\Delta V_{1/2}$: $1 \mu\text{M} = 14.2 \pm 1.7$ mV, $n = 7$; $10 \mu\text{M} = 16.5 \pm 1.2$ mV, $n = 8$; $100 \mu\text{M} = 20.7 \pm 1.5$ mV, $n = 9$), compared to WT ($\Delta V_{1/2}$: $1 \mu\text{M} = 3.4$ mV, $n = 8$; $10 \mu\text{M} = 9.6 \pm 1.3$ mV, $n = 11$; $100 \mu\text{M} = 10.3 \pm 1.1$ mV, $n = 9$; P 's < 0.05 ; **Figure 2D**). Preincubation of slices in $10 \mu\text{M}$ ODQ induced a negative shift of $V_{1/2}$ in WT ($V_{1/2} = -93.6 \pm 1.3$ mV; $\Delta V_{1/2} = -7.2 \pm 1.1$ mV, $n = 8$), while it did not cause significant changes in GC2 knockout mice ($V_{1/2} = -94.1 \pm 0.9$ mV; $\Delta V_{1/2} = -2.2 \pm 0.5$ mV, $n = 5$; **Figures 2B,D**). No effects of 8-Br-cGMP and ODQ were found on I_h current density in both strains (data not shown).

Next, we manipulated intracellular cAMP levels by applying different concentrations of 8-Br-cAMP via the patch pipette. This resulted in a dose-dependent depolarizing shift in voltage-dependent activation (**Figure 2E**) accompanied by reduced activation time constants (**Figure 2F**) of I_h in both strains. $\Delta V_{1/2}$ revealed significant changes during application of $1 \mu\text{M}$ ($\Delta V_{1/2}$: WT = 8.5 ± 0.9 mV, $n = 10$; NO-GC2^{-/-} = 17.1 ± 1.6 mV, $n = 8$; $P < 0.05$) and $10 \mu\text{M}$ 8-Br-cAMP ($\Delta V_{1/2}$: WT = 17.4 ± 1.6 mV, $n = 11$; NO-GC2^{-/-} = 21.9 ± 1.7 mV, $n = 8$; $P < 0.05$; **Figure 2D**).

Preincubation of slices with $200 \mu\text{M}$ SQ 22536 shifted activation potentials of I_h to more negative values in both strains. The effect was stronger in WT ($V_{1/2} = -95.5 \pm 0.6$ mV, $n = 11$), compared to NO-GC2^{-/-} mice ($V_{1/2} = -95.2 \pm 0.8$ mV, $n = 10$; $\Delta V_{1/2} = -3.5 \pm 0.7$ mV, $n = 10$; P 's < 0.05 ; **Figures 2D,E**). 8-Br-cAMP and SQ 22536 did not change I_h current density in TC neurons (data is not shown).

More recently, the modulation of HCN2 and HCN4 channels by cCMP and cUMP has been reported (Zong et al., 2012). Both channel isoforms are major constituents of I_h in murine TC neurons (Ludwig et al., 2003; Leist et al., 2016). Thus, we examined the effect of cCMP and cUMP on I_h currents in WT neurons. cCMP is a partial agonist of HCN channels with an EC_{50} value of $\sim 30 \mu\text{M}$ compared to $1 \mu\text{M}$ for cAMP (Zong et al., 2012). Therefore, we applied $30 \mu\text{M}$ cCMP and cUMP. Both compounds induced depolarizing shifts of $V_{1/2}$ in TC compared to control cells (cCMP: $V_{1/2} = -77.44 \pm 2.3$ mV; $\Delta V_{1/2} = 8.9 \pm 2.3$ mV; $n = 6$; P 's < 0.05); cUMP: $V_{1/2} = -78.9 \pm 3.6$ mV, $\Delta V_{1/2} = 7.6 \pm 3.5$ mV; $n = 6$; P 's < 0.05 ; **Figures 2D,G**).

In order to allow better comparison between voltage and current clamp recordings and to assess potential effects of pH

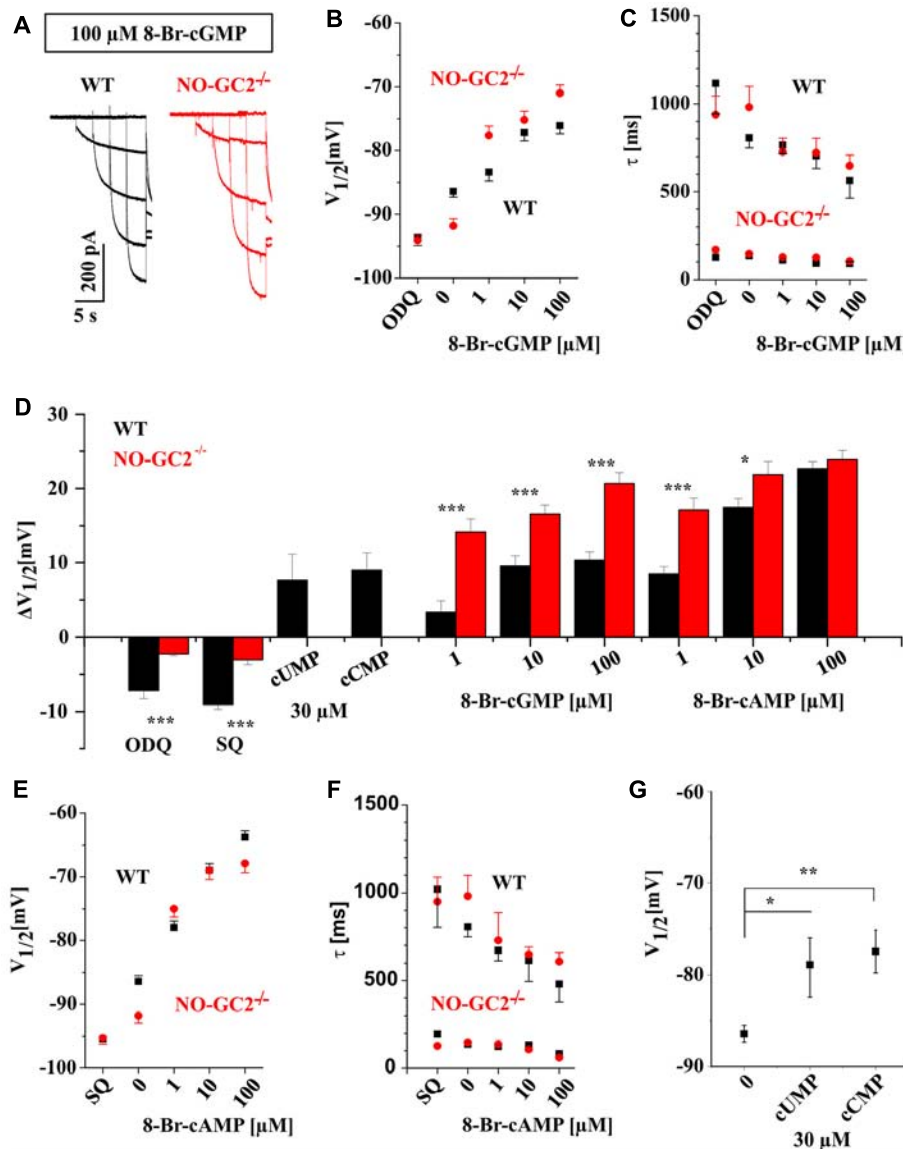


FIGURE 2 | Thalamic I_h is modulated by different cyclic nucleotides. **(A)** Example traces of I_h recorded from WT (black) and NO-GC2^{-/-} (red) mice in the presence of 100 μM 8-Br-cyclic guanosine monophosphate (cGMP) in the intracellular solution. **(B)** Different concentrations of 8-Br-cGMP induced a dose-dependent depolarizing shift of $V_{1/2}$ in both mouse strains. Stronger effects were found in NO-GC2^{-/-} (red symbols) for some concentrations compared to WT (black symbols). The selective sGC inhibitor ODQ significantly shifted $V_{1/2}$ to more negative potentials in WT but not in NO-GC2^{-/-} mice. **(C)** Activation kinetics of hyperpolarization-activated cyclic nucleotide-gated (HCN) channels were enhanced by different concentrations of 8-Br-cGMP in both strains (WT—black symbols; NO-GC2^{-/-}—red symbols). The upper and lower panels show the slow and fast time constants of activation. ODQ slowed the slow component of HCN channel kinetics in WT but not in NO-GC2^{-/-} mice. **(D)** Calculation of $\Delta V_{1/2}$ revealed different sensitivity of thalamic I_h current to cyclic nucleotides and adenylyl- and guanylyl-cyclase inhibitors between WT and NO-GC2^{-/-} mice. **(E)** Effects of various concentrations of 8-Br-cyclic adenosine monophosphate (cAMP) and the adenylyl cyclase inhibitor SQ22536 on $V_{1/2}$ (WT—black symbols; NO-GC2^{-/-}—red symbols). **(F)** Effects of various concentrations of 8-Br-cAMP and the adenylyl cyclase inhibitor SQ22536 on activation time constants of HCN channels (WT—black symbols; NO-GC2^{-/-}—red symbols). **(G)** Modulation of $V_{1/2}$ of I_h by cUMP and cCMP as indicated. ***,*** indicate $P < 0.05$, $P < 0.01$, $P < 0.001$, respectively.

buffering conditions, we compared I_h current from WT TC neurons in NaHCO_3 and HEPES buffered extracellular solutions in the presence of 0.5 mM BaCl_2 . Half maximal activation potential of I_h (NaHCO_3 : $V_{1/2} = -89.7 \pm 0.8$ mV, $n = 6$; HEPES: $V_{1/2} = -88.2 \pm 1.2$ mV, $n = 5$; $P > 0.05$) and current density (NaHCO_3 : $I_h = 5.2 \pm 0.6$ pA/pF; HEPES: $I_h = 6.9 \pm 1.2$ pA/pF,

$n = 5$; $P > 0.05$) did not differ between the two recording conditions (data not shown).

Since Kir channels have been found to be modulated by cyclic nucleotides and are important in setting the RMP and determining the firing pattern of neurons, the effect of 8-Br-cGMP was studied on WT inwardly rectifying potassium

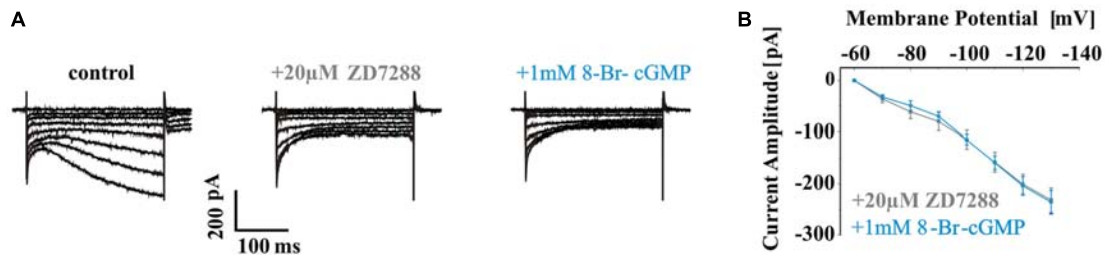


FIGURE 3 | Effects of 8-Br-cGMP on WT inwardly rectifying potassium (I_{KIR}) current. **(A)** Representative current traces evoked by increasing hyperpolarizing voltage steps (from -60 mV to -130 mV with 10 mV increments) of WT TC neurons under control condition (left panel; no blocker present) and in the presence of $20 \mu\text{M}$ ZD7288 (middle panel) and additional application of 1 mM 8-Br-cGMP (right panel). Typical I_{KIR} was seen in $20 \mu\text{M}$ ZD7288. **(B)** I_{KIR} amplitudes elicited by each voltage steps were plotted as I-V curves for different recording conditions as indicated. Please note that 8-Br-cGMP did not change the amplitude of I_{KIR} in dorsal lateral geniculate nucleus (dLGN) TC neurons.

(I_{KIR}) current. I_{KIR} was evoked by hyperpolarizing voltage steps and was isolated from I_h by applying $20 \mu\text{M}$ ZD7288. Extracellular application of 1 mM 8-Br-cGMP did not change the amplitude of I_{KIR} (ZD7288: 231.9 ± 23.9 pA at -130 mV, $n = 6$; 8-Br-cGMP: 235.8 ± 22.8 pA, $n = 6$; $P > 0.05$; **Figures 3A,B**) in dLGN TC neurons.

Influence of cGMP on TC Neurons Firing Patterns

To determine the functional impact of NO-GC2 activity on passive membrane properties and neuronal firing, TC neurons were recorded under current clamp conditions from the RMP (**Figure 4A**). While the RMP (WT: -67.1 ± 0.9 mV, $n = 16$; NO-GC2 $^{-/-}$: -69.3 ± 0.9 mV, $n = 14$; $P > 0.05$) did not differ between the strains, R_{in} was significantly reduced in NO-GC2 $^{-/-}$ (WT: $224.9 \pm 13.1 \text{ M}\Omega$, $n = 16$; NO-GC2 $^{-/-}$: $175.9 \pm 8.7 \text{ M}\Omega$, $n = 14$; $P < 0.05$; **Figure 4B**). Negative current injections (-230 to -30 pA, 1 s duration) induced significantly smaller voltage sags in the absence of NO-GC2 (WT: 13.5 ± 1.6 mV at -230 pA, $n = 16$; NO-GC2 $^{-/-}$: 6.2 ± 0.9 mV at -230 pA, $n = 14$; $P < 0.05$; **Figures 4A,B**). Upon release from the hyperpolarizing pulse NO-GC2 $^{-/-}$ mice generated less rebound low-threshold Ca^{2+} spikes (LTS) with action potentials riding on top of it. Out of 16 WT cells 12 cells showed an LTS which triggered action potentials (number of action potentials per LTS: 1.25 ± 0.3 , $n = 16$), whereas only 4 out of 14 NO-GC2-deficient cells displayed an LTS triggering action potentials (number of action potentials per LTS: 0.38 ± 0.2 , $n = 14$; $P < 0.05$; **Figure 4B**). When TC neurons from NO-GC2 $^{-/-}$ mice were challenged with depolarizing currents (10 – 370 pA, 1 s duration), tonic activity was characterized by less APs compared to WT mice (WT: 65.1 ± 3.6 at 370 pA, $n = 16$; NO-GC2 $^{-/-}$: 40.9 ± 4.3 at 370 pA, $n = 14$; $P < 0.05$; **Figures 4A,B**). Preincubation of slices from WT in $10 \mu\text{M}$ ODQ was performed to mimic the effects of NO-GC2 deficiency under current clamp conditions. No changes in the RMP (control: -67.1 ± 0.9 mV, $n = 16$; $10 \mu\text{M}$ ODQ: -69.1 ± 0.9 mV, $n = 7$; $P > 0.05$) and R_{in} (control: $224.9 \pm 13.1 \text{ M}\Omega$, $n = 16$; $10 \mu\text{M}$ ODQ: $193.6 \pm 19.6 \text{ M}\Omega$, $n = 7$; $P > 0.05$) were found (**Figure 4C**). Voltage sag amplitudes were marginally decreased (control: 13.5 ± 1.6 mV at -230 pA, $n = 16$; $10 \mu\text{M}$ ODQ: 7.7 ± 2.8 mV, $n = 7$; $P > 0.05$), generation

of LTS was less pronounced (number of action potentials per LTS: control: 1.25 ± 0.3 , $n = 16$; $10 \mu\text{M}$ ODQ: 0.29 ± 0.2 , $n = 7$; $P < 0.05$; **Figure 4C**) and number of APs was reduced in TC cells treated with ODQ (control: 65.1 ± 3.6 at 370 pA, $n = 16$; ODQ: 48.5 ± 6.4 at 370 pA, $n = 7$; $P < 0.05$; **Figure 4C**).

Next, effects of exogenously increased cGMP concentrations were assessed. Application of $10 \mu\text{M}$ 8-Br-cGMP via the patch pipette in WT TC neurons resulted in a more positive RMP (control: -70.43 ± 0.69 mV, $n = 7$; cGMP: -65.57 ± 1.7 mV, $n = 7$; $P < 0.05$; **Figure 5A**) and increased occurrence of LTS. All cGMP treated cells showed LTS (number of action potentials per LTS: control: 0.7 ± 0.3 , $n = 7$; $10 \mu\text{M}$ 8-Br-cGMP: 1.7 ± 1.8 , $n = 7$; $P < 0.05$; **Figure 5A**). Under these conditions, TC neurons fired significantly more tonic APs (**Figure 5A**). To assess to what extent these changes may be related to modulation of I_h , neurons from WT and NO-GC2 $^{-/-}$ mice were washed with the HCN channel blocker ZD7288 ($20 \mu\text{M}$) and then subjected to an extracellular application of 8-Br-cGMP (1 mM ; **Figure 5B**). In all cells tested, ZD7288 completely abolished the voltage sag. In WT, ZD7288 strongly hyperpolarized the RMP (control: -64 ± 1.3 mV, $n = 7$; ZD7288: -70.3 ± 1.5 mV, $n = 7$; $P < 0.05$), while 8-Br-cGMP caused depolarization of the RMP (8-Br-cGMP: -60.7 ± 2.8 mV, $n = 7$; $P < 0.05$, **Figure 5C**). Although ZD7288 did not change the R_{in} of WT cells (control: $191.9 \pm 25.4 \text{ M}\Omega$, $n = 7$; ZD7288: $182.2 \pm 16.9 \text{ M}\Omega$, $n = 7$; $P > 0.05$), administration of 8-Br-cGMP strongly increased R_{in} to $272.3 \pm 33.4 \text{ M}\Omega$ ($n = 7$; $P < 0.05$; **Figure 5C**). Tonic firing was only nominally increased after the application of ZD7288 (**Figure 5C**). With injected currents up to 90 pA, WT TC neurons fired slightly more APs after additional application of 8-Br-cGMP. Stronger current injections however were associated with partial depolarization block (**Figure 5B**; inset), thereby pointing to the loss of hyperpolarizing influences (**Figures 5B,C**). When hyperpolarizing K^+ currents are reduced, neurons may enter the state of depolarization block where under sustained input current of increasing strength neurons eventually reduce or stop firing, while membrane potential fluctuations above threshold are present (Bianchi et al., 2012). In NO-GC2 $^{-/-}$ the direction of changes in RMP induced by ZD7288 and 8-Br-cGMP was similar to WT (control: -67.2 ± 1.1 mV, $n = 6$; ZD7288:

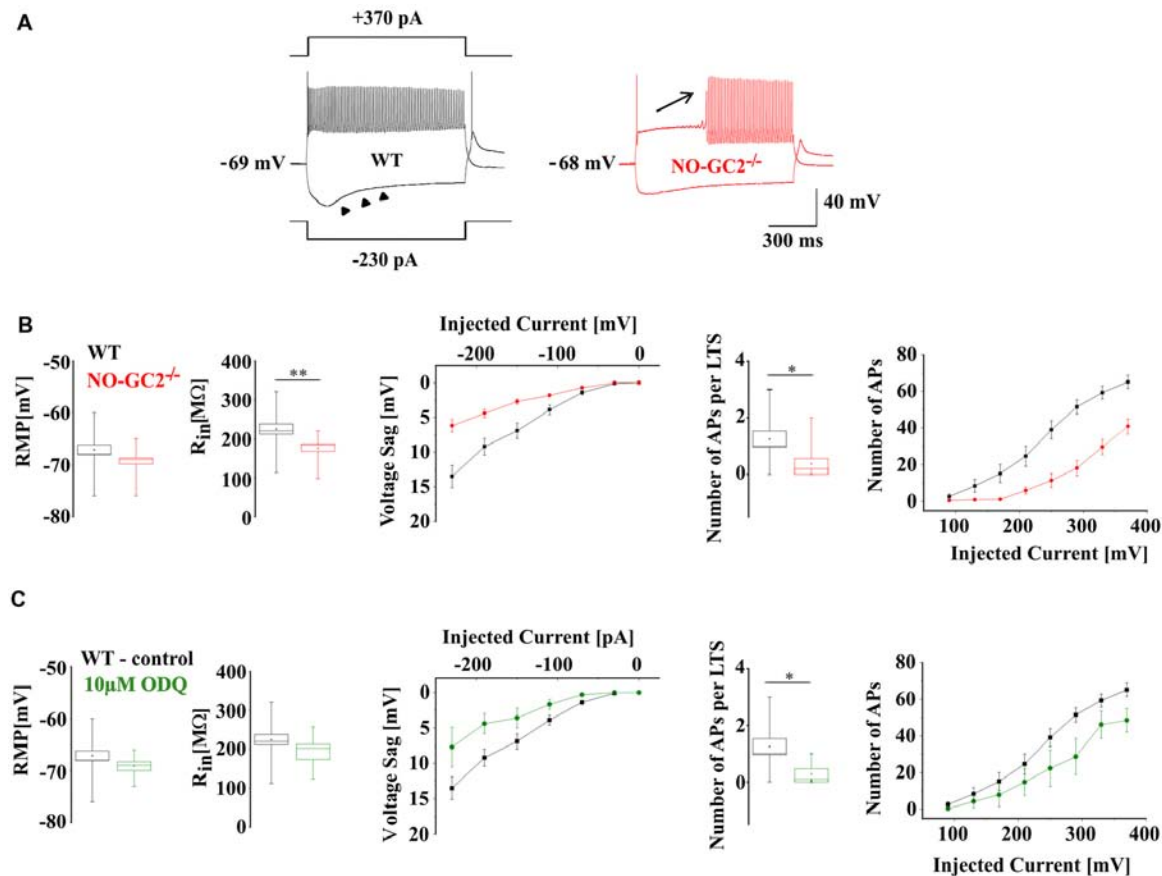


FIGURE 4 | Passive and active membrane properties of TC neurons in WT and NO-GC2^{-/-}. **(A)** Voltage responses of TC neurons recorded under current clamp conditions at rest. Both WT (black) and NO-GC2^{-/-} (red) neurons were injected with a series of hyperpolarizing and depolarizing currents. **(B)** Box and whisker plot showing the resting membrane potential (RMP) and R_{in} of NO-GC2^{-/-} (red box) and WT (black box) TC neurons. The amplitude of anomalous rectification induced by hyperpolarizing current injection was less pronounced in NO-GC2^{-/-} (red symbols) compared to WT (black symbols) mice. Upon release from membrane hyperpolarization the occurrence of low-threshold Ca²⁺ spikes (LTS) and the number of action potentials per LTS was higher in WT neurons (black box) in comparison to NO-GC2^{-/-} (red box). Depolarizing currents evoked less number of action potentials in NO-GC2^{-/-} (red symbols) compared to WT (black symbols) neurons. **(C)** Preincubation of WT slices in 10 μ M ODQ (green box) did not change either RMP nor R_{in} , compared to control conditions (black box). Voltage sag amplitudes were nominally reduced, occurrence of LTS and the number of action potentials per LTS was less pronounced and the number of APs in response to depolarizing current injections was nominally decreased after the blockage of GC (green symbols) in comparison to control (black symbols). *** indicate $P < 0.05$, $P < 0.01$, respectively.

-71.7 ± 2.7 mV, $n = 6$; 8-Br-cGMP: -63.6 ± 3.7 mV, $n = 6$; P 's > 0.05 ; **Figure 5D**). Both compounds increased the R_{in} of NO-GC2-deficient cells (control: 165.9 ± 17.7 MΩ, $n = 6$; ZD7288: 227.7 ± 28.4 MΩ, $n = 6$, $P > 0.05$; 8-Br-cGMP: 278 ± 16.9 MΩ, $n = 6$; $P < 0.05$; **Figure 5D**). Both ZD7288 and 8-Br-cGMP increased the excitability of NO-GC2^{-/-} TC neurons, compared to control recordings. Again, AP firing in the presence of both compounds was characterized by a partial depolarization block (**Figure 5D**). RMP, R_{in} and firing did not differ between the strains after ZD7288 and cGMP application (**Figures 5C,D**). When WT slices were preincubated with 10 μ M ODQ, application of ZD7288 (20 μ M) marginally hyperpolarized the RMP (ODQ: -65.5 ± 1.6 mV, $n = 6$; ZD7288: -70.5 ± 2.4 mV, $n = 6$; $P > 0.05$) and increased the R_{in} (ODQ: 192.1 ± 23.2 MΩ, $n = 6$; ZD7288: 221.9 ± 27.3 MΩ, $n = 6$; $P > 0.05$) of TC. The number of spikes with depolarizing current

injections was slightly increased after the application of ZD7288 (**Figure 5E**).

Effect of Ba²⁺ on Membrane Properties of TC Neurons

In order to allow better comparison between current and voltage clamp recordings and to assess the contribution of Ba²⁺-sensitive inward rectifier and K_{2P} channels, like TASK and TREK channels, BaCl₂ (0.5 mM) was added to NaHCO₃- and HEPES-buffered extracellular solutions. Results were compared to the data described above (i.e., Ba²⁺ free NaHCO₃-buffered solution; **Figure 6**). In both genotypes Ba²⁺ significantly changed passive and active membrane properties of TC neurons. In the presence of Ba²⁺, the RMP was strongly depolarized, R_{in} was increased, voltage sags were unmasked, and the number of APs was significantly increased (**Figures 6A–C**). In the presence of Ba²⁺

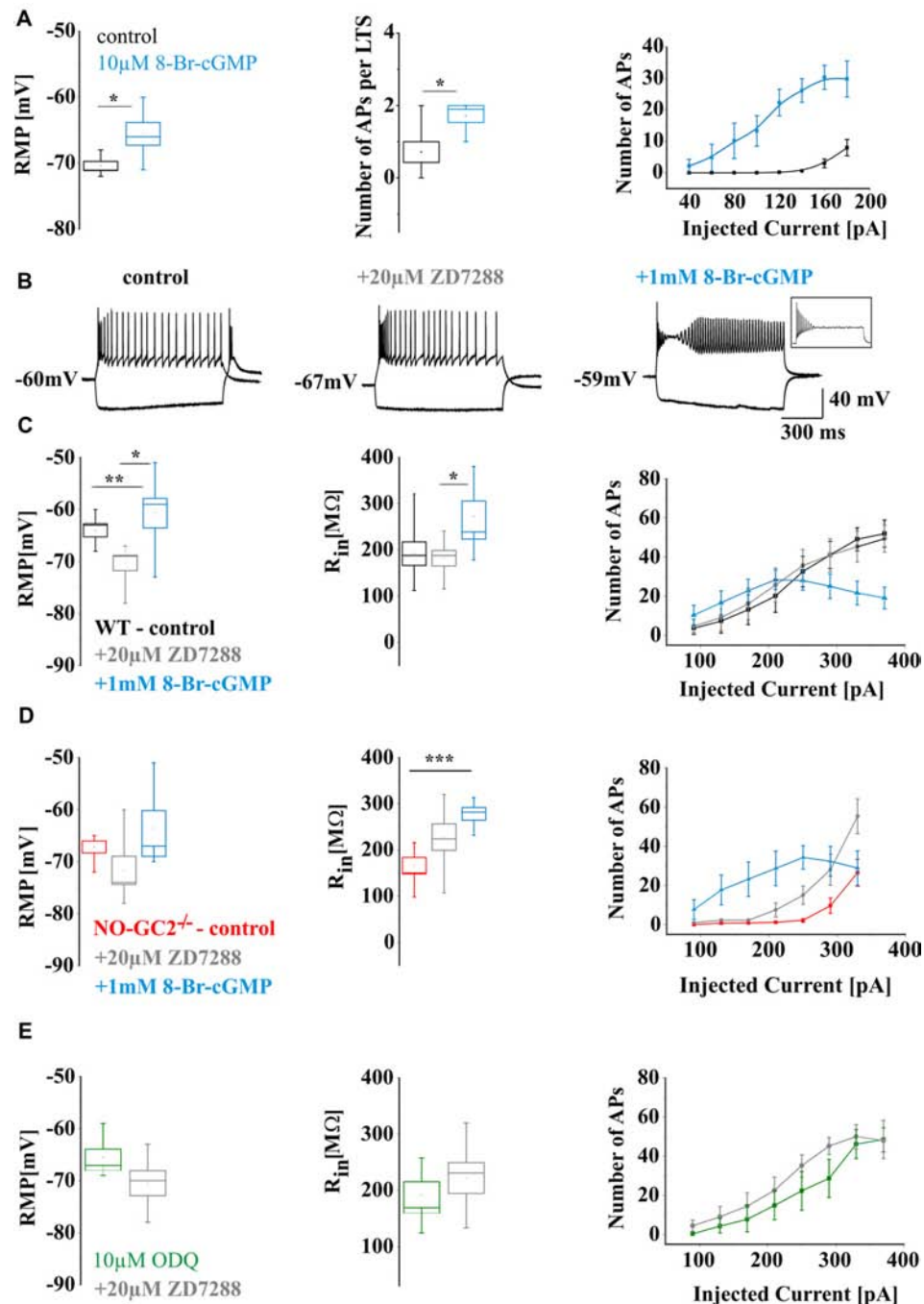


FIGURE 5 | Effects of increased intracellular levels of cGMP on the electrical properties of WT and NO-GC2^{-/-} mice TC neurons. **(A)** Perfusion of WT TC neurons with an intracellular solution containing 10 μ M 8-Br-cGMP. Left panel: the RMP of control TC cells (black box) and the cells treated by 10 μ M 8-Br-cGMP (blue box). Middle panel: the number of APs per LTS induced upon release from the hyperpolarizing pulse in control (black box) and 10 μ M 8-Br-cGMP (blue box) infused cells. Right panel: the number of APs induced by positive current injection in control (black symbols) and 10 μ M 8-Br-cGMP (blue symbols) treated cells. **(B)** Example traces of WT neurons at -230 pA and 210 pA current injection recorded under control (black heading) condition and in the presence of 20 μ M ZD-7288 (gray heading) and 1 mM 8-Br-cGMP (blue heading). Inset: please notice an example of depolarization block with 250 pA depolarizing current injection. **(C)** The passive and active membrane properties of WT neurons: the RMP (left panel), R_{in} (middle panel) and the number of APs (right panel) under control conditions (black box, symbols) and in the presence of 20 μ M ZD-7288 (gray box, symbols) and 1 mM 8-Br-cGMP (blue box, symbols). **(D)** The passive and active membrane properties of NO-GC2 deficient neurons: the RMP (left panel), R_{in} (middle panel) and the number of APs (right panel) under control conditions (red box, symbols) and in the presence of 20 μ M ZD-7288 (gray box, symbols) and 1 mM 8-Br-cGMP (blue box, symbols). **(E)** The RMP (left panel), R_{in} (middle panel) and the number of APs (right panel) of WT neurons incubated in 10 μ M ODQ (green box, symbols) and in the presence of 20 μ M ZD7288 (gray box, symbols). ***,*** indicate $P < 0.05$, $P < 0.01$, $P < 0.001$, respectively.

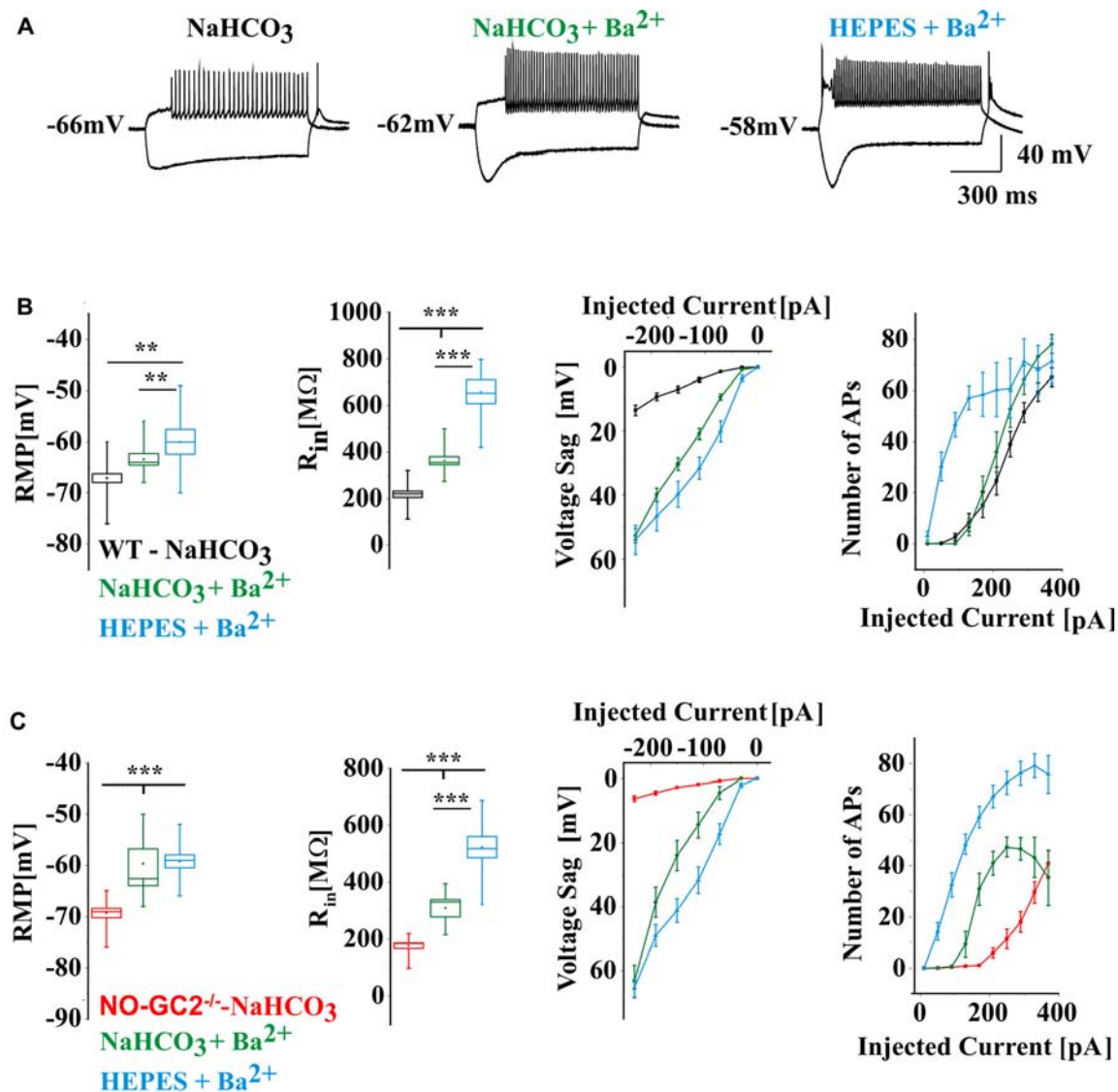


FIGURE 6 | (A) Example traces of WT current clamp recordings at -230 pA and 210 pA current injections. The recordings were done in bicarbonate (NaHCO_3) buffered, Ba^{2+} free extracellular solution (black heading), in bicarbonate buffered solution contained 0.5 mM BaCl_2 (green heading) and in HEPES buffered solution contained 0.5 mM BaCl_2 (blue heading). **(B)** Active and passive membrane properties of WT cells recorded in different extracellular solutions. **(C)** Active and passive membrane properties of $\text{NO-GC2}^{-/-}$ cells recorded in different extracellular solutions. ***,*** indicate $P < 0.01$, $P < 0.001$, respectively.

voltage sag amplitudes were significantly larger in $\text{NO-GC2}^{-/-}$ in comparison to WT ($\text{NaHCO}_3 + \text{Ba}^{2+}$: WT: 52.74 ± 2.25 mV at -230 pA, $n = 12$; $\text{NO-GC2}^{-/-}$: 63.38 ± 5 mV at -230 pA, $n = 6$; HEPES: WT: 53.95 ± 4.48 mV at -230 pA, $n = 7$; $\text{NO-GC2}^{-/-}$: 65.45 ± 2.8 mV at -230 pA, $n = 10$, P 's < 0.05 ; **Figures 6B,C**).

To assess the possible contribution of I_{KIR} to hyperpolarization-induced voltage deflections and firing pattern of TC neurons, WT slices were washed for 15 min with the Kir channel inhibitor Tertiapin-Q, thereafter effects of extracellular application of 8-Br-cGMP on membrane properties were studied. Tertiapin-Q (200 nM) did not change either the RMP (control: -69 ± 0.7 mV, $n = 6$;

Tertiapin-Q: -68.8 ± 1.4 mV, $n = 6$; $P > 0.05$), nor R_{in} (control: 215.5 ± 7.3 MΩ, $n = 6$; Tertiapin-Q: 239.4 ± 9.9 MΩ; $P > 0.05$) and voltage sag amplitudes (control: 21.3 ± 2.9 mV at -230 pA, $n = 6$; Tertiapin-Q: 21.8 ± 3.6 mV at -230 pA, $n = 6$; $P > 0.05$; **Figure 7A**) of TC neurons. Application of 8-Br-cGMP significantly depolarized the RMP (8-Br-cGMP: -62.8 ± 1.4 mV; $P < 0.05$), increased R_{in} (8-Br-cGMP: 297.4 ± 19.4 MΩ, $n = 6$; $P < 0.05$) and voltage sag amplitudes (8-Br-cGMP: 31.9 ± 4.7 mV, $n = 6$; $P < 0.05$; **Figure 7A**). Firing was slightly increased by Tertiapin-Q and 8-Br-cGMP caused further excitation of TC neurons, eventually resulting in a depolarization block with higher depolarizing current injections (**Figure 7A**).

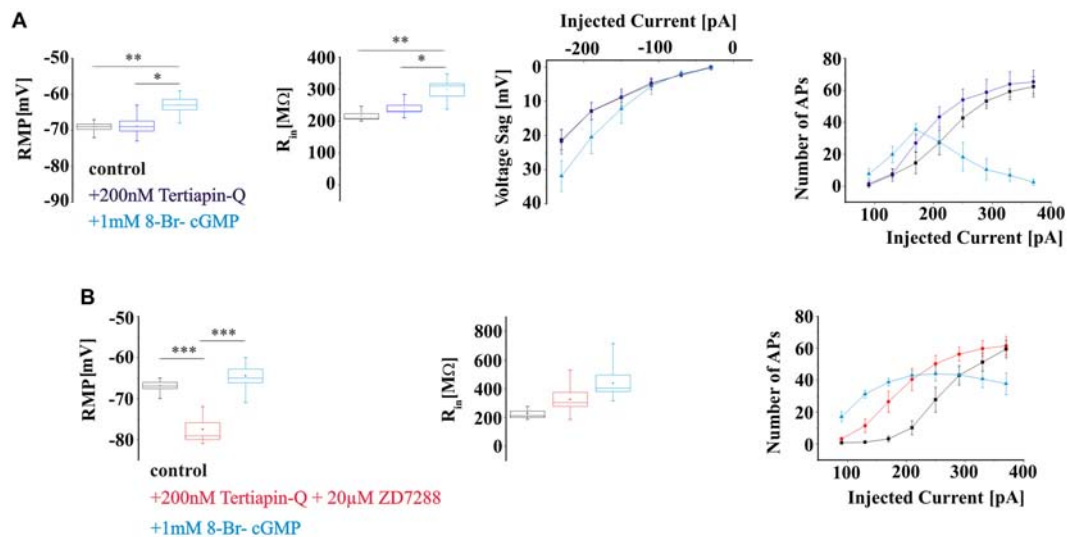


FIGURE 7 | Effects of elevated 8-Br-cGMP levels on electrical properties of WT TC neurons in the presence of Kir and HCN channels blockers. **(A)** Passive and active properties of TC in control (black) and after the application of Kir channels blocker Tertiapin-Q (ilac) and 8-Br-cGMP (blue). **(B)** Effects of 8-Br-cGMP on electrical properties of TC in the presence of Kir and HCN channels blockers (red). ***,*** indicate $P < 0.05$, $P < 0.01$, $P < 0.001$, respectively.

Next, the effects of elevated levels of 8-Br-cGMP on TC neurons membrane properties were studied in the presence of Kir and HCN channels inhibitors Tertiapin-Q and ZD7288, respectively (**Figure 7B**). Co-administration of the two inhibitors significantly hyperpolarized the RMP (control: -66.8 ± 0.7 mV, $n = 6$; Tertiapin-Q + ZD7288: -77.5 ± 1.6 mV, $n = 6$; $P < 0.05$) and nominally increased R_{in} (control: 228.3 ± 0.7 MΩ; Tertiapin-Q + ZD7288: 325.6 ± 48.8 MΩ, $n = 6$; $P > 0.05$; **Figure 7B**) of TC neurons. The RMP was significantly depolarized (8-Br-cGMP: -64.5 ± 1.7 mV, $n = 6$; $P < 0.05$) and R_{in} was increased (8-Br-cGMP: 438.4 ± 57.7 MΩ, $n = 6$; $P > 0.05$) following extracellular application of 1 mM 8-Br-cGMP. Inhibition of Kir and HCN channels resulted in an increased number of APs with small depolarizing current injections and the occurrence of a depolarization block was noticed in the presence of 8-Br-cGMP in TC neurons (**Figure 7B**).

GC Activity in dLGN

The presence and localization of NO-GC2 in the thalamus was analyzed immunohistochemically. A strong fluorescent signal was detected in dLGN (**Figure 8A**). Higher magnification images revealed expression in the cellular boundaries. Co-staining for NO-GCα2 and the PSD95 revealed a strong overlap of the fluorescent signals, pointing to a postsynaptic localization.

In order to address a potential contribution of cGMP in TC neurons signaling, we quantified the amount of cGMP in tissue from different brain areas at different developmental stages. In all samples (dLGN, VB, SSC) the highest cGMP levels were consistently detected in young animals (postnatal day 7, P7) with the SSC containing the largest amount of cGMP. During postnatal development (P21 and P107) the tissue contained lower cGMP levels (**Figure 8B**).

Reduction of Burst Activity in the Thalamic Network in the Absence of NO-GC2

The intrathalamic network activity is involved in the generation of different thalamic oscillations such as sleep spindle and delta oscillations which critically depend on activation of I_h (Kanyshkova et al., 2009, 2012). Rhythmic bursting is a property of thalamic cells and has frequently been used as a measure of intrathalamic rhythmicity in horizontal thalamic slices conserving axonal connections between nRT and VB TC neurons (Huguenard and Prince, 1994; Yue and Huguenard, 2001). In this model system intrathalamic oscillations are generated by reciprocal interactions between inhibitory nRT neurons and excitatory TC neurons. Stimulation of nRT neurons evokes IPSPs in VB neurons and triggers rebound burst activity in TC. Rebound bursts of TC neurons re-excite the nRT and the cycle starts again. Here dampened oscillatory activity (i.e., up to 6–8 cycles) was induced by stimulation of the IC (containing TC and corticothalamic fibers) and recorded in VB (**Figure 9A**). Compared to control animals, NO-GC2^{-/-} mice revealed a significantly lower number of bursts in response to a single stimulus (NO-GC2^{-/-}: 5.8 ± 0.3 bursts, $n = 12$; WT: 7.1 ± 0.5 bursts, $n = 8$; $P < 0.05$; **Figures 9B,C**).

To further assess the influence of NO-GC2 activity on rhythmic activity in the thalamic network, a mathematical modeling approach was used (Kanyshkova et al., 2009, 2012; **Figure 9D**). Spontaneous rhythmic bursting was analyzed in an interconnected four-cell model of two TC and two nRT neurons which was used for simulation of the intrathalamic network activity (Kanyshkova et al., 2009, 2012). Compared to WT, the number of bursts generated within the stimulation period of 2 s based on NO-GC2^{-/-}-derived parameters was significantly lower (NO-GC2^{-/-}: 4.7 ± 0.5 bursts,

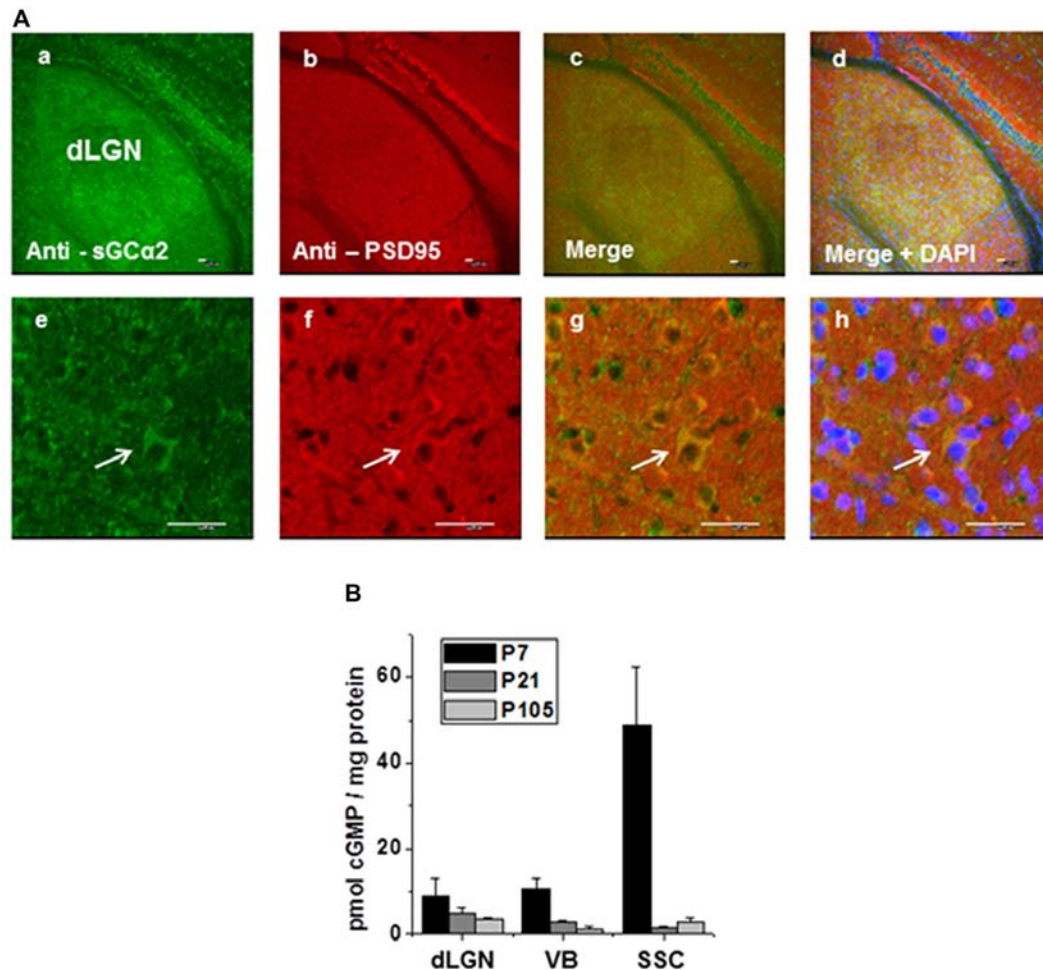


FIGURE 8 | Immunohistochemical staining of NO-GC α 2, postsynaptic density protein 95 (PSD95) in dLGN of WT mice. **(A)** Immunoreactivity of triple-stained thalamic tissue with antibodies against the α 2 subunit of NO-GC2 (green), postsynaptic density protein, PSD 95 (red) and nuclear marker, DAPI (blue) is shown in lower **(a,b,c,d)** and higher **(e,f,g,h)** magnification. Scale bars = 25 μ m. **(B)** Quantification of basal cGMP levels (pmol cGMP/mg protein) at different postnatal ages in the dLGN, ventrobasal thalamus (VB) and somatosensory cortex (SSC).

$n = 11$; WT: 8.0 ± 0.8 bursts, $n = 11$; $P < 0.05$; **Figure 9E**).

Spectral Power Characteristics of NO-GC2 $^{-/-}$ Mice During Different Behavioral States

Thalamic bursting is involved in the generation of TC rhythms such as delta oscillations which are found on the LFP and EEG recordings during SWS sleep and anesthesia (Steriade et al., 1993; Timofeev, 2011). Therefore, we assessed the effects of NO-GC2 deficiency on cortical oscillations by performing LFP recordings from the SSC of freely moving mice (**Figures 10, 11**). Recordings made during the first 2 h of the light period were taken for analysis. Absolute spectral power of LFP signals recorded from NO-GC2 $^{-/-}$ ($n = 4$) and WT ($n = 5$) mice was assessed for the delta, theta, alpha and beta bands and compared between strains during

the four different behavioral states (AW, REM, LSWS and DSWS).

During AW both strains show predominant theta activity in the LFP, characteristic for a moving rodent (**Figure 10A**). NO-GC2 $^{-/-}$ mice displayed more power than WT mice within the δ (WT: $51 \pm 9.5 \mu\text{V}^2/\text{Hz}$; NO-GC2 $^{-/-}$: $267 \pm 41 \mu\text{V}^2/\text{Hz}$; $P < 0.05$), θ (WT: $132 \pm 80 \mu\text{V}^2/\text{Hz}$; NO-GC2 $^{-/-}$: $450 \pm 89 \mu\text{V}^2/\text{Hz}$; $P < 0.05$) as well as within the α frequency band (WT: $119 \pm 64 \mu\text{V}^2/\text{Hz}$; NO-GC2 $^{-/-}$: $354 \pm 72 \mu\text{V}^2/\text{Hz}$; $P < 0.05$), whereas the β power did not significantly differ between the strains (WT: $19 \pm 4 \mu\text{V}^2/\text{Hz}$; NO-GC2 $^{-/-}$: $32 \pm 4 \mu\text{V}^2/\text{Hz}$; $P > 0.05$; **Figures 10B,C**). The percentage of EEG frequencies (%) were nominally enhanced in δ (WT: $16.6 \pm 2.2\%$; NO-GC2 $^{-/-}$: $28.6 \pm 8.2\%$; $P > 0.05$) and significantly decreased in β frequency range in NO-GC2 $^{-/-}$ ($3.3 \pm 0.69\%$), compared to WT ($5.9 \pm 0.44\%$; $P < 0.05$, **Figure 10D**) mice.

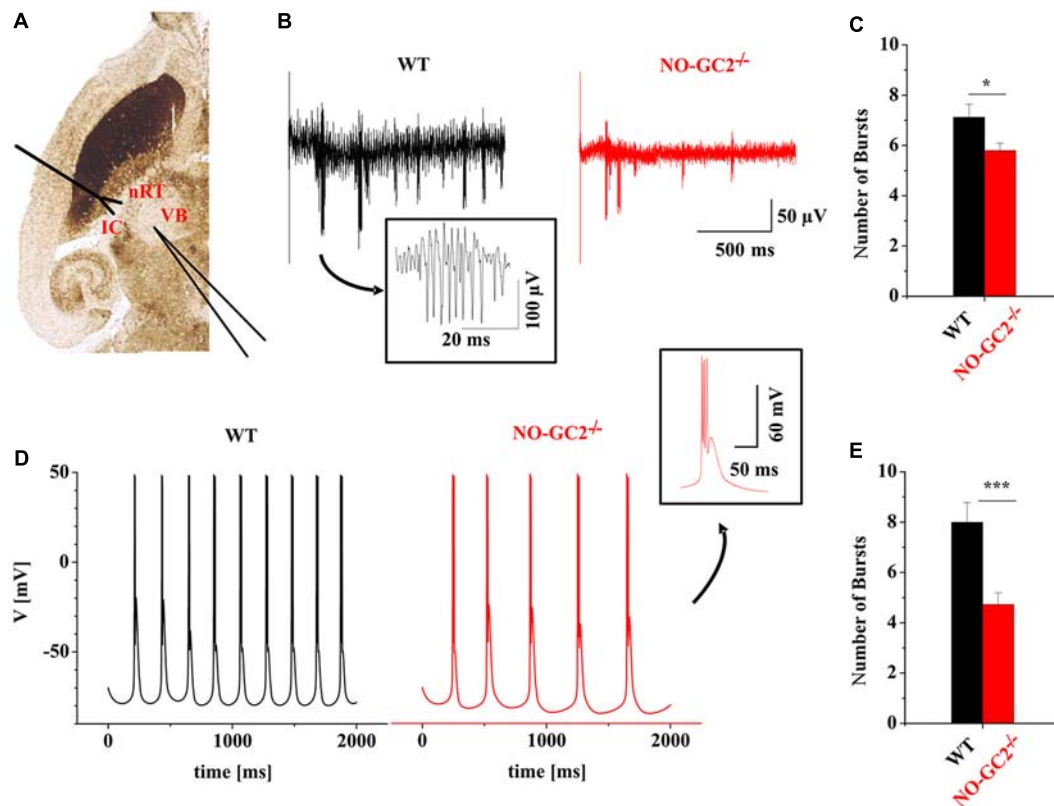


FIGURE 9 | Dysfunction of the NO-GC2 signaling pathway changes thalamic oscillations. **(A)** Dampened rhythmic activity was induced by exciting neurons in the reticular thalamus (nRT) via stimulation of the internal capsule (IC) in horizontal thalamic slices. Neuronal responses were measured in the ventrobasal thalamus (VB). **(B)** Example traces of rhythmic burst activities from WT (black) and NO-GC2^{-/-} (red) mice. **(C)** The number of bursts (red bar) was significantly decreased in NO-GC2^{-/-} compared to WT (black bar) mice. **(D)** Computer simulation of rhythmic activity in a mathematical model. In this simulation two nRT neurons reciprocally communicate via GABA_A-mediated connections and project to two TC neurons via GABA_A and GABA_B signaling. The feedback from TC neurons is carried by AMPA receptors to both nRT neurons. Rhythmic bursting profiles with I_h properties taken from TC neurons of WT (black) and NO-GC2^{-/-} (red) mice are shown. **(E)** With I_h parameters set to the values obtained from TC cells of WT (black bar) and NO-GC2^{-/-} (red bar) mice, the number of bursts was significantly lower in NO-GC2^{-/-} mice. *,*** indicate $P < 0.05$, $P < 0.001$, respectively.

Both strains show a typical REM sleep spectrum, characterized by the presence of theta activity in the LFP (**Figure 11A**). NO-GC2^{-/-} mice had a significantly higher spectral power than WT mice in the δ band during REM sleep (WT: $76 \pm 28 \mu\text{V}^2/\text{Hz}$; NO-GC2^{-/-}: $199 \pm 31 \mu\text{V}^2/\text{Hz}$; $P < 0.05$). However, strains did not differ in power of θ , α and β frequency bands (**Figures 11B,C**). The normalized values of different frequencies showed increased δ (WT: $14.3 \pm 1.58\%$; NO-GC2^{-/-}: $24.7 \pm 3.62\%$; $P < 0.05$) and decreased α (WT: $38.92 \pm 1.2\%$; NO-GC2^{-/-}: $28.64 \pm 2.4\%$; $P < 0.05$) and β (WT: $5 \pm 0.42\%$; $P < 0.05$; NO-GC2^{-/-}: $3.58 \pm 0.33\%$; **Figure 11D**) activities in NO-GC2^{-/-} mice.

During LSWS and DSWS there were no strain differences in any of the bands of the raw LFPs, as well as in the normalized data (data not shown).

DISCUSSION

The modulation of I_h in TC neurons of different mammalian species by cAMP is well established (McCormick and Pape,

1990; Budde et al., 2005; Leist et al., 2016). Fewer studies have addressed effects mediated by cGMP. While the increase in current and the shift to depolarized potentials in the activation curve by NO donors and cGMP as well as the involvement of GC activity in I_h modulation have been described before (Pape and Mager, 1992; Yang and Cox, 2008), the GC subtype involved in these phenomena has not been yet identified. Experimental data suggested low to moderate mRNA expression of GC α_1 , α_2 and β_1 subunits which form the heterodimeric NO-GC1 ($\alpha_1\beta_1$) and NO-GC2 ($\alpha_2\beta_1$) isoforms in different thalamic nuclei (Giuili et al., 1994; Gibb and Garthwaite, 2001). Notably, V_{1/2} of I_h in TC neurons of NO-GC2^{-/-} mice was found to be more hyperpolarized compared to WT, indicating that the current is controlled by the basal activity of postsynaptic NO-GC2. The control of I_h by basal cGMP production is in good agreement with electrophysiological analyses of CA1 pyramidal neurons (Neitz et al., 2014).

It has recently been suggested that cCMP and cUMP should also be considered in HCN channel-regulated processes (Zong

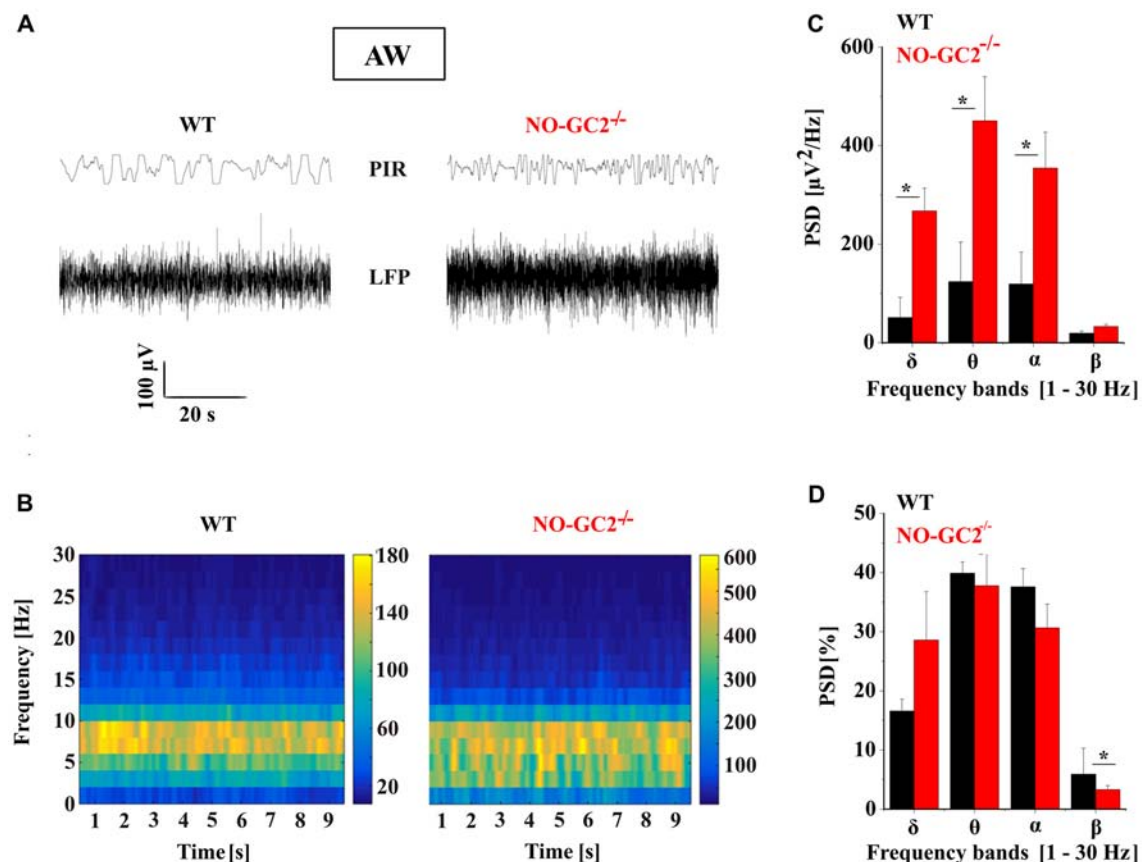


FIGURE 10 | Effect of NO-GC2-deficiency on active waking (AW) state. **(A)** Raw local field potential (LFP) example traces during AW from SSC and movement detector (Passive Infrared Recording System, PIR) in WT (left) and NO-GC2^{-/-} (right) mice. **(B)** The mean power spectrum of the LFPs between 1 Hz and 30 Hz obtained from 20 epochs of 10 s duration analyzed during the first 2 h of the light on period. **(C)** The mean values of raw PSD during AW showed enhanced δ (1–4 Hz), θ (5–8 Hz) and α (9–12 Hz) activity in NO-GC2^{-/-} (red bar) compared to WT (black bar) mice. **(D)** The normalized PSD values are presented as percentage for WT (black bar) and NO-GC2^{-/-} (red bar) mice. * $P < 0.05$.

et al., 2012) and soluble GC might also synthesize cCMP and cUMP in the presence of NO and Mn^{2+} (Beste et al., 2012). In agreement with this previous notion, we found that I_h in native neurons is moderately modulated by cCMP and cUMP.

In other neuronal cell types an increase in AP firing induced by NO donors which was sensitive to ODQ has been previously observed, suggesting participation of cGMP-dependent mechanisms (Kim et al., 2004). Intracellular application of 8-Br-cGMP strongly increased tonic firing in WT TC neurons and a number of distinct changes in electrophysiological properties were found in TC neurons following knock out or inhibition of NO-GC2. While NO-GC2^{-/-} mice revealed reduced voltage sag amplitudes and tonic firing, RMP was unchanged. With respect to the number of triggered action potentials, LTS firing was less pronounced in NO-GC2-deficient mice. It has been shown before that the voltage-dependent properties of I_h crucially influence LTS generation and burst firing in TC neurons (Hughes et al., 1998). Positive shifts in the voltage-dependency of I_h increase the amplitude and duration of the LTS while negative shifts have opposite effects. Thus in line with our findings the reduced availability of I_h

is associated with a decreased number of action potentials in the LTS.

Although we registered a decreased availability of I_h in TC neurons of NO-GC2^{-/-} mice which is generally in line with some of our functional findings, the intrinsic membrane properties of TC neurons are expected to depend on several membrane currents. Setting of the RMP (Meuth et al., 2006), rhythmic bursting (Amarillo et al., 2014) and tonic firing (Kasten et al., 2007) of rodent TC neurons is based on the dynamic interaction of multiple membrane currents, with some of them being modulated by cGMP in a differential manner. While HCN channels are activated by direct binding of cGMP to the cyclic nucleotide binding domain (CNBD), the situation is more complex when it comes to K_2P channels. PKG-dependent activation of TASK-1 and TREK-1 (Toyoda et al., 2010) as well as inhibition of heteromeric TASK-1/TASK-3 (Gonzalez-Forero et al., 2007) channels have been described. In addition, inward rectifier K^+ currents have been shown to be inhibited in a cGMP-dependent manner (Dixon and Copenhagen, 1997) and a number of Kir channel subtypes (including members of the Kir2, Kir3 and Kir6 families) are expressed in thalamic cells

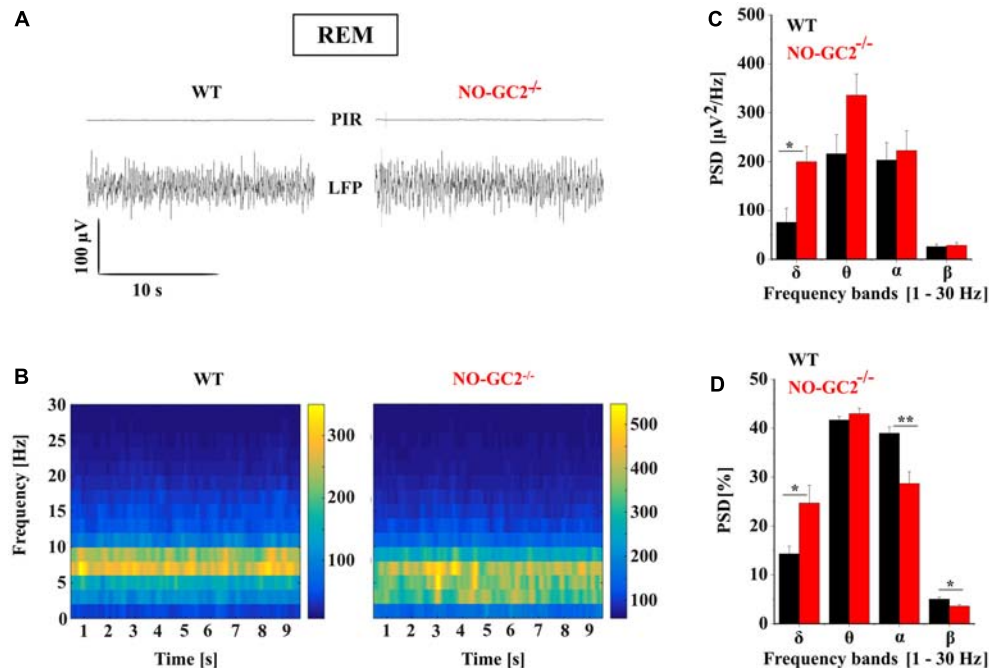


FIGURE 11 | Effect of NO-GC2-deficiency on rapid eye movement (REM) sleep. **(A)** Raw LFP example traces during REM sleep in WT (left) and NO-GC2^{-/-} (right) mice. Note, during REM sleep no movements are detected on PIR, indicating the immobility of the animal. **(B)** LFP power spectrum of different frequencies (1–30 Hz) over time. **(C)** During REM sleep, electroencephalogram (EEG) spectral power density is increased in the δ (1–4 Hz) and θ (5–8 Hz) band in NO-GC2^{-/-} (red bar) compared to WT (black bar) mice. **(D)** The normalized PSD values are presented as percentage in WT (black bar) and NO-GC2^{-/-} (red bar) mice. *,** indicate $P < 0.05$, $P < 0.01$, respectively.

(Thomzig et al., 2005). In TC neurons of different species several K_{2P} (TASK-1, TASK-3, TREK-1, TREK-2) and Kir channels (Kir2, Kir3) are expressed and have important contributions to the RMP, anomalous rectification and firing pattern (Meuth et al., 2003, 2006; Bista et al., 2015), thereby pointing to a complex scenario when cGMP-dependent effector functions are considered. The knockout of NO-GC2 and application of ODQ which both decrease the basal cGMP levels may have inhibited depolarizing HCN channels and (positively and negatively) modulated diverse hyperpolarizing K^+ channels in a way that the net effects on RMP and R_{in} in the present study were inconspicuous. When taking the effects of exogenous cGMP application also into account, the strong effect of 8-Br-cGMP on RMP, R_{in} and tonic firing in the presence of ZD7288 (i.e., with HCN channels blocked) clearly points to the involvement of further ion channels. Here the combination of membrane depolarization and increased R_{in} is in line with the inhibition of TASK1/TASK3 heteromers which are present in TC neurons (Meuth et al., 2006). Indeed, application of Ba^{2+} which blocks TASK, TREK and Kir channels was associated with strong membrane depolarization, increased R_{in} and strongly enhanced tonic firing. Specific inhibition of some Kir channel types by Tertiapin-Q however, did not change the RMP and R_{in} in WT TC neurons. Moreover, extracellular application of 8-Br-cGMP had no influence on I_{KIR} amplitudes in Voltage clamp recordings. Taken together, the pharmacological manipulations indicate that altered modulation of cGMP-sensitive K_{2P} channels (Ma et al.,

2011) may contribute to the phenotype of NO-GC2-deficient mice. But it does not exclude other ion channels as well.

Sleep is a complex process and controlled by several mechanisms (Borbély and Tobler, 2011) such as homeostatic, allostatic and circadian components. All regulators must ultimately target the thalamus to affect the cellular mechanisms that induce stable and global sleep-related oscillatory activity and allow the state-dependent gating of sensory information (Coulon et al., 2012). NO-dependent signaling is critically involved in the regulation of sleep homeostasis (Kalinchuk et al., 2006) and variations of NO and cGMP levels in the brain have been observed during the sleep-wake cycle (Kostin et al., 2013). We observed a strong increase in delta activity of the EEG as a consequence of NO-GC2 deficiency during AW and REM sleep. The nerve terminals of the mesopontine tegmentum cholinergic neurons which are part of the ascending reticular activating system have the ability to synthesis NO (Vincent, 2000). The release of NO from these thalamic afferents during arousal or REM sleep is followed by depolarization of TC neurons. It is possible that lack of postsynaptically located NO-GC2 receptors and decreased excitability of TC neurons in NO-GC2 mice disrupt the transition to AW and REM sleep and increases periods of slow oscillations in the EEG. The decreased availability to HCN channels may additionally hamper their pacemaker function and slow down oscillatory activity. We suggest that in the thalamus the cellular mechanisms of cGMP action may involve activation of HCN channels in addition to

cGMP-dependent protein kinases. In addition, complete loss of the HCN2 channel gene and decreased responsiveness of I_h were associated with the appearance of pathological slow high amplitude oscillations (5–7 Hz) in the EEG in form of spike-and-wave discharges (Ludwig et al., 2003; Kuisle et al., 2006). These pathological activities were not found in NO-GC2^{-/-}. Furthermore loss of HCN1 expression in the forebrain is associated with increased theta oscillations during AW and REM sleep (Nolan et al., 2004), and deletion of HCN channels auxiliary subunit TRIP8b increases delta oscillations during AW (Zobeiri et al., 2018). Therefore the effects of the NO-GC2 gene knockout are in agreement with reduced activation of I_h in forebrain neurons which result in increased slow frequency bands in EEG recordings.

The involvement of the NO/GC/cGMP pathway in the regulation of sleep and wakefulness are not fully conclusive and in part even contradictory (Cavas and Navarro, 2006). While some studies indicate that NOS inhibition increases SWS and NO is required for arousal (Burlet and Cespuglio, 1997), opposite responses and differential effects on REM and non-REM sleep have been described (Hars, 1999). Nevertheless, the use of NOS inhibitors, NO donors and 8-Br-cGMP in cats *in vivo* supported the role of cGMP in controlling rhythmic neuronal activity in thalamic and cortical neurons, which may play a role in sleep/wake transition (Cudeiro et al., 2000). Divergent findings might be due to variances in timing and dosage of drug administration, acute pharmacological treatment vs. genetic background (transgenic animals), and NO-independent cGMP signaling (Hess et al., 2005). The fact that cGMP-dependent signaling has multiple effectors throughout the brain which are difficult to control experimentally may have additionally contributed to the ongoing discussion (Russwurm et al., 2013).

Neurons of the nRT reveal intrinsic pacemaking properties and participate in intrathalamic network operations which allow them to generate and synchronize spindle waves (7–15 Hz), a hallmark of early sleep stages (Fuentealba and Steriade, 2005). Since nRT and TC neurons are interconnected in a loop, and we reported decreased LTS characteristics and damped burst activities *in vitro* from NO-GC2^{-/-} slice preparation, changed intrinsic properties of TC neurons may affect spindle oscillations. In addition, it was suggested that deactivation of I_h is important to terminate spindle activity (Bal and McCormick, 1996). It

is therefore expected that the number or the shape of spindle waves is changed in NO-GC2^{-/-} animals. Analysis of the cellular effects of NO-GC2-deficiency in nRT neurons and combined electrophysiological recordings in nRT and VB *in vivo* may be well suited to investigate this aspect in future studies.

Based on our results, we conclude that thalamic HCN channels are modulated by different cyclic nucleotides and that cGMP is a good candidate to regulate intrathalamic and cortical activities. However, the action of cGMP is broad, involving complex signaling pathways and is thus not limited to the modulation of HCN channels. Since reduced basal levels of cGMP decrease the excitability of TC cells, our data are in agreement with previous studies and supports the idea that the role of cGMP in thalamus is excitatory. The increased occurrence of delta and theta band activity during AW characterizes the loss of NO-GC2 as a TC dysrhythmia syndrome (Llinás et al., 1999) and supports the view that slow oscillations are an intrinsic property of the TC system (Timofeev, 2011).

AUTHOR CONTRIBUTIONS

MD, RC, EM, AL, MZ, BB, SB and AB performed experiments and analyzed/interpreted data. TB designed and supervised the project and reviewed all experiments. H-CP, DK and GvL provided important scientific input. MD and TB wrote the manuscript. All authors edited and agreed on the final version of the manuscript.

FUNDING

This work has been supported by DFG (BU1019/15-1, BU1019/16-1; Cells-in-Motion Cluster of Excellence), IZKF Münster (Bud3/001/16) and DAAD (fellowships to MD and RC).

ACKNOWLEDGMENTS

We would like to thank Manuela Cerina for her scientific contribution. The authors thank Elke Naß, Svetlana Kiesling and Julia Schröer for excellent technical assistance. This work was done in partial fulfillment of the Ph.D. theses of MD and RC.

REFERENCES

- Amarillo, Y., Zagha, E., Mato, G., Rudy, B., and Nadal, M. S. (2014). The interplay of seven subthreshold conductances controls the resting membrane potential and the oscillatory behavior of thalamocortical neurons. *J. Neurophysiol.* 112, 393–410. doi: 10.1152/jn.00647.2013
- Backer, O. D., Elinck, E., Sips, P., Buys, E., Brouckaert, P., and Lefebvre, R. A. (2008). Role of the soluble guanylyl cyclase α_1/α_2 subunits in the relaxant effect of CO and CORM-2 in murine gastric fundus. *Neuyn Schmiedeberts Arch. Pharmacol.* 378, 493–502. doi: 10.1007/s00210-008-0315-6
- Bal, T., and McCormick, D. A. (1996). What stops synchronized thalamocortical oscillations? *Neuron* 17, 297–308. doi: 10.1016/s0896-6273(00)80161-0
- Beste, K. Y., Burhenne, H., Kaefer, V., Stasch, J.-P., and Seifert, R. (2012). Nucleotidyl cyclase activity of soluble guanylyl cyclase $\alpha_1\beta_1$. *Biochemistry* 51, 194–204. doi: 10.1021/bi201259y
- Bianchi, D., Marasco, A., Limongiello, A., Marchetti, C., Marie, H., Tirozzi, B., et al. (2012). On the mechanisms underlying the depolarization block in the spiking dynamics of CA1 pyramidal neurons. *J. Comput. Neurosci.* 33, 207–225. doi: 10.1007/s10827-012-0383-y
- Bista, P., Cerina, M., Ehling, P., Leist, M., Pape, H.-C., Meuth, S. G., et al. (2015). The role of two-pore-domain background K^+ (K_2p) channels in the thalamus. *Pflugers Arch.* 467, 895–905. doi: 10.1007/s00424-014-1632-x
- Borbély, A. A., and Tobler, I. (2011). Manifestations and functional implications of sleep homeostasis. *Handb. Clin. Neurol.* 98, 205–213. doi: 10.1016/b978-0-444-52006-7.00013-7
- Budde, T., Caputi, L., Kanyshkova, T., Staak, R., Abrahamczik, C., Munsch, T., et al. (2005). Impaired regulation of thalamic pacemaker channels through an imbalance of subunit expression in absence epilepsy. *J. Neurosci.* 25, 9871–9882. doi: 10.1523/jneurosci.2590-05.2005
- Burlet, S., and Cespuglio, R. (1997). Voltammetric detection of nitric oxide (NO) in the rat brain: its variations throughout the sleep-wake

- cycle. *Neurosci. Lett.* 226, 131–135. doi: 10.1016/s0304-3940(97)00247-4
- Cavas, M., and Navarro, J. F. (2006). Effects of selective neuronal nitric oxide synthase inhibition on sleep and wakefulness in the rat. *Prog. Neuro-Psychopharmacology Biol. Psychiatry* 30, 56–67. doi: 10.1016/j.pnpbp.2005.06.013
- Coulon, P., Budde, T., and Pape, H.-C. (2012). The sleep relay—the role of the thalamus in central and decentral sleep regulation. *Pflügers Arch.* 463, 53–71. doi: 10.1007/s00424-011-1014-6
- Cudeiro, J., Rivadulla, C., and Grieve, K. L. (2000). A possible role for nitric oxide at the sleep/wake interface. *Sleep* 23, 829–835. doi: 10.1093/sleep/23.6.1j
- Destexhe, A., Neubig, M., Ulrich, D., and Huguenard, J. (1998). Dendritic low-threshold calcium currents in thalamic relay cells. *J. Neurosci.* 18, 3574–3588. doi: 10.1523/jneurosci.18-10-03574.1998
- Dixon, D. B., and Copenhagen, D. R. (1997). Metabotropic glutamate receptor-mediated suppression of an inward rectifier current is linked via a cGMP cascade. *J. Neurosci.* 17, 8945–8954. doi: 10.1523/jneurosci.17-23-08945.1997
- Fuentealba, P., and Steriade, M. (2005). The reticular nucleus revisited: intrinsic and network properties of a thalamic pacemaker. *Prog. Neurobiol.* 75, 125–141. doi: 10.1016/j.pneurobio.2005.01.002
- Gabbott, P. L. A., and Bacon, S. J. (1994). Two types of interneuron in the dorsal lateral geniculate nucleus of the rat: a combined NADPH diaphorase histochemical and GABA immunocytochemical study. *J. Comp. Neurol.* 350, 281–301. doi: 10.1002/cne.903500211
- Gibb, B. J., and Garthwaite, J. (2001). Subunits of the nitric oxide receptor, soluble guanylyl cyclase, expressed in rat brain. *Eur. J. Neurosci.* 13, 539–544. doi: 10.1046/j.1460-9568.2001.01421.x
- Giulii, G., Luzzi, A., Poyard, M., and Guellaën, G. (1994). Expression of mouse brain soluble guanylyl cyclase and NO synthase during ontogeny. *Brain Res. Dev. Brain Res.* 81, 269–283. doi: 10.1016/0165-3806(94)90313-1
- Gonzalez-Forero, D., Portillo, F., Gomez, L., Montero, F., Kasparov, S., and Moreno-Lopez, B. (2007). Inhibition of resting potassium conductances by long-term activation of the NO/cGMP/protein kinase G pathway: a new mechanism regulating neuronal excitability. *J. Neurosci.* 27, 6302–6312. doi: 10.1523/jneurosci.1019-07.2007
- Hars, B. (1999). Endogenous nitric oxide in the rat pons promotes sleep. *Brain Res.* 816, 209–219. doi: 10.1016/s0006-8993(98)01183-4
- He, C., Chen, F., Li, B., and Hu, Z. (2014). Neurophysiology of HCN channels: from cellular functions to multiple regulations. *Prog. Neurobiol.* 112, 1–23. doi: 10.1016/j.pneurobio.2013.10.001
- Hess, D. T., Matsumoto, A., Kim, S.-O., Marshall, H. E., and Stamler, J. S. (2005). Protein S-nitrosylation: purview and parameters. *Nat. Rev. Mol. Cell Biol.* 6, 150–166. doi: 10.1038/nrm1569
- Hines, M. L., and Carnevale, N. T. (2001). NEURON: a tool for neuroscientist. *Neuroscientist* 7, 123–135. doi: 10.1177/107385840100700207
- Hughes, S. W., Cope, D. W., and Crunelli, V. (1998). Dynamic clamp study of I_h modulation of burst firing and δ oscillations in thalamocortical neurons *in vitro*. *Neuroscience* 87, 541–550. doi: 10.1016/s0306-4522(98)00170-5
- Huguenard, J. R., and Prince, D. A. (1994). Intrathalamic rhythmicity studied *in vitro*: nominal T-current modulation causes robust antioscillatory effects. *J. Neurosci.* 14, 5485–5502. doi: 10.1523/jneurosci.14-09-05485.1994
- Kalinchuk, A. V., Lu, Y., Stenberg, D., Rosenberg, P. A., and Porkka-Heiskanen, T. (2006). Nitric oxide production in the basal forebrain is required for recovery sleep. *J. Neurochem.* 99, 483–498. doi: 10.1111/j.1471-4159.2006.04077.x
- Kanyshkova, T., Meuth, P., Bista, P., Liu, Z., Ehling, P., Caputi, L., et al. (2012). Differential regulation of HCN channel isoform expression in thalamic neurons of epileptic and non-epileptic rat strains. *Neurobiol. Dis.* 45, 450–461. doi: 10.1016/j.nbd.2011.08.032
- Kanyshkova, T., Pawlowski, M., Meuth, P., Dube, C., Bender, R. A., Brewster, A. L., et al. (2009). Postnatal expression pattern of HCN channel isoforms in thalamic neurons: relationship to maturation of thalamocortical oscillations. *J. Neurosci.* 29, 8847–8857. doi: 10.1523/jneurosci.0689-09.2009
- Kasten, M. R., Rudy, B., and Anderson, M. P. (2007). Differential regulation of action potential firing in adult murine thalamocortical neurons by Kv3.2, Kv1, and SK potassium and N-type calcium channels. *J. Physiol.* 584, 565–582. doi: 10.1113/jphysiol.2007.141135
- Kim, H. W., Park, J.-S., Jeong, H.-S., Jang, M. J., Kim, B.-C., Kim, M.-K., et al. (2004). Nitric oxide modulation of the spontaneous firing of rat medial vestibular nuclear neurons. *J. Pharmacol. Sci.* 96, 224–228. doi: 10.1024/jphs.scj04006x
- Kostin, A., McGinty, D., Szymusiak, R., and Alam, M. N. (2013). Sleep-wake and diurnal modulation of nitric oxide in the perifornical-lateral hypothalamic area: real-time detection in freely behaving rats. *Neuroscience* 254, 275–284. doi: 10.1016/j.neuroscience.2013.09.022
- Kuisle, M., Wanaverbecq, N., Brewster, A. L., Frère, S. G. A., Pinault, D., Baram, T. Z., et al. (2006). Functional stabilization of weakened thalamic pacemaker channel regulation in rat absence epilepsy. *J. Physiol.* 575, 83–100. doi: 10.1113/jphysiol.2006.110486
- Leist, M., Datanashvili, M., Kanyshkova, T., Zobeiri, M., Aissaoui, A., Cerina, M., et al. (2016). Two types of interneurons in the mouse lateral geniculate nucleus are characterized by different h-current density. *Sci. Rep.* 6:24904. doi: 10.1038/srep24904
- Llinás, R. R., Ribary, U., Jeanmonod, D., Kronberg, E., and Mitra, P. P. (1999). Thalamocortical dysrhythmia: a neurological and neuropsychiatric syndrome characterized by magnetoencephalography. *Proc. Natl. Acad. Sci. U S A* 96, 15222–15227. doi: 10.1073/pnas.96.26.15222
- Ludwig, A., Budde, T., Stieber, J., Moosmang, S., Wahl, C., Holthoff, K., et al. (2003). Absence epilepsy and sinus dysrhythmia in mice lacking the pacemaker channel HCN2. *EMBO J.* 22, 216–224. doi: 10.1093/emboj/cdg032
- Ma, X.-Y., Yu, J.-M., Zhang, S.-Z., Liu, X.-Y., Wu, B.-H., Wei, X.-L., et al. (2011). External Ba^{2+} block of the two-pore domain potassium channel TREK-1 defines conformational transition in its selectivity filter. *J. Biol. Chem.* 286, 39813–39822. doi: 10.1074/jbc.M111.264788
- McCormick, D. A., and Pape, H. C. (1990). Noradrenergic and serotonergic modulation of a hyperpolarization-activated cation current in thalamic relay neurones. *J. Physiol.* 431, 319–342. doi: 10.1113/jphysiol.1990.sp018332
- Mergia, E., Friebe, A., Dangel, O., Russwurm, M., and Koesling, D. (2006). Spare guanylyl cyclase NO receptors ensure high NO sensitivity in the vascular system. *J. Clin. Invest.* 116, 1731–1737. doi: 10.1172/jci27657
- Meuth, P., Meuth, S. G., Jacobi, D., Broicher, T., Pape, H.-C., and Budde, T. (2005). Get the rhythm: modeling neuronal activity. *J. Undergrad. Neurosci. Educ.* 4, A1–A11.
- Meuth, S. G., Budde, T., Kanyshkova, T., Broicher, T., Munsch, T., and Pape, H.-C. (2003). Contribution of TWIK-related acid-sensitive K^+ channel 1 (TASK1) and TASK3 channels to the control of activity modes in thalamocortical neurons. *J. Neurosci.* 23, 6460–6469. doi: 10.1523/jneurosci.23-16-06460.2003
- Meuth, S. G., Kanyshkova, T., Meuth, P., Landgraf, P., Munsch, T., Ludwig, A., et al. (2006). Membrane resting potential of thalamocortical relay neurons is shaped by the interaction among TASK3 and HCN2 channels. *J. Neurophysiol.* 96, 1517–1529. doi: 10.1152/jn.01212.2005
- Neitz, A., Mergia, E., Imbrosci, B., Petrasch-Parwez, E., Eysel, U. T., Koesling, D., et al. (2014). Postsynaptic NO/cGMP increases NMDA receptor currents via hyperpolarization-activated cyclic nucleotide-gated channels in the hippocampus. *Cereb. Cortex* 24, 1923–1936. doi: 10.1093/cercor/bht048
- Nolan, M. F., Malleret, G., Dudman, J. T., Buhl, D. L., Santoro, B., Gibbs, E., et al. (2004). A behavioral role for dendritic integration: HCN1 channels constrain spatial memory and plasticity at inputs to distal dendrites of CA1 pyramidal neurons. *Cell* 119, 719–732. doi: 10.1016/j.cell.2004.11.020
- Notomi, T., and Shigemoto, R. (2004). Immunohistochemical localization of Ih channel subunits, HCN1–4, in the rat brain. *J. Comp. Neurol.* 471, 241–276. doi: 10.1002/cne.11039
- Oostenveld, R., Fries, P., Maris, E., and Schoffelen, J.-M. (2011). FieldTrip: open source software for advanced analysis of MEG, EEG, and invasive electrophysiological data. *Comput. Intell. Neurosci.* 2011, 1–9. doi: 10.1155/2011/156869
- Pape, H. C. (1996). Queer current and pacemaker: the hyperpolarization-activated cation current in neurons. *Annu. Rev. Physiol.* 58, 299–327. doi: 10.1146/annurev.ph.58.030196.001503
- Pape, H. C., and Mager, R. (1992). Nitric oxide controls oscillatory activity in thalamocortical neurons. *Neuron* 9, 441–448. doi: 10.1016/0896-6273(92)90182-d
- Russwurm, M., Russwurm, C., Koesling, D., and Mergia, E. (2013). NO/cGMP: the past, the present and the future. *Methods Mol. Biol.* 1020, 1–16. doi: 10.1007/978-1-62703-459-3_1

- Steriade, M., McCormick, D. A., and Sejnowski, T. J. (1993). Thalamocortical oscillations in the sleeping and aroused brain. *Science* 262, 679–685. doi: 10.1126/science.8235588
- Thomzig, A., Laube, G., Prüss, H., and Veh, R. W. (2005). Pore-forming subunits of K-ATP channels, Kir6.1 and Kir6.2, display prominent differences in regional and cellular distribution in the rat brain. *J. Comp. Neurol.* 484, 313–330. doi: 10.1002/cne.20469
- Thoonen, R., Cauwels, A., Decaluwe, K., Geschka, S., Tainsh, R. E., Delanghe, J., et al. (2015). Cardiovascular and pharmacological implications of haem-deficient NO-unresponsive soluble guanylate cyclase knock-in mice. *Nat. Commun.* 6:8482. doi: 10.1038/ncomms9482
- Timofeev, I. (2011). Neuronal plasticity and thalamocortical sleep and waking oscillations. *Prog. Brain Res.* 193, 121–144. doi: 10.1016/B978-0-444-53839-0.00009-0
- Toyoda, H., Saito, M., Okazawa, M., Hirao, K., Sato, H., Abe, H., et al. (2010). Protein kinase G dynamically modulates TASK1-mediated leak K⁺ currents in cholinergic neurons of the basal forebrain. *J. Neurosci.* 30, 5677–5689. doi: 10.1523/jneurosci.5407-09.2010
- Vincent, S. R. (2000). The ascending reticular activating system - from aminergic neurons to nitric oxide. *J. Chem. Neuroanat.* 18, 23–30. doi: 10.1016/s0891-0618(99)00048-4
- Yang, S., and Cox, C. L. (2008). Excitatory and anti-oscillatory actions of nitric oxide in thalamus. *J. Physiol.* 586, 3617–3628. doi: 10.1113/jphysiol.2008.153312
- Yao, W. D., Gainetdinov, R. R., Arbuckle, M. I., Sotnikova, T. D., Cyr, M., Beaulieu, J. M., et al. (2004). Identification of PSD-95 as a regulator of dopamine-mediated synaptic and behavioral plasticity. *Neuron* 41, 625–638. doi: 10.1016/s0896-6273(04)00048-0
- Yue, B. W., and Huguenard, J. R. (2001). The role of H-current in regulating strength and frequency of thalamic network oscillations. *Thalamus Relat. Syst.* 1, 95–103. doi: 10.1016/S1472-9288(01)00009-7
- Zagotta, W. N., Olivier, N. B., Black, K. D., Young, E. C., Olson, R., and Gouaux, E. (2003). Structural basis for modulation and agonist specificity of HCN pacemaker channels. *Nature* 425, 200–205. doi: 10.3410/f.1006733.197501
- Zobeiri, M., Chaudhary, R., Datunashvili, M., Heuermann, R. J., Lüttjohann, A., Narayanan, V., et al. (2018). Modulation of thalamocortical oscillations by TRIP8b, an auxiliary subunit for HCN channels. *Brain Struct. Funct.* 223, 1537–1564. doi: 10.1007/s00429-017-1559-z
- Zong, X., Krause, S., Chen, C.-C., Krüger, J., Gruner, C., Cao-Ehlker, X., et al. (2012). Regulation of hyperpolarization-activated cyclic nucleotide-gated (HCN) channel activity by cCMP. *J. Biol. Chem.* 287, 26506–26512. doi: 10.1074/jbc.M112.357129

Conflict of Interest Statement: The authors declare that the research was conducted in the absence of any commercial or financial relationships that could be construed as a potential conflict of interest.

Copyright © 2018 Datunashvili, Chaudhary, Zobeiri, Lüttjohann, Mergia, Baumann, Balfanz, Budde, van Luijtelea, Pape, Koesling and Budde. This is an open-access article distributed under the terms of the Creative Commons Attribution License (CC BY). The use, distribution or reproduction in other forums is permitted, provided the original author(s) and the copyright owner(s) are credited and that the original publication in this journal is cited, in accordance with accepted academic practice. No use, distribution or reproduction is permitted which does not comply with these terms.



Oscillatory Cortical Activity in an Animal Model of Dystonia Caused by Cerebellar Dysfunction

Elena Laura Georgescu^{1,2†}, Ioana Antoaneta Georgescu^{1†}, Carmen Denise Mihaela Zahiu¹, Alexandru Răzvan Șteopoaie¹, Vlad Petru Morozan¹, Adrian Ștefan Pană¹, Ana-Maria Zăgrean^{1*‡} and Daniela Popa^{1,2*‡}

¹Division of Physiology and Neuroscience, Carol Davila University of Medicine and Pharmacy, Bucharest, Romania, ²Institut de Biologie de l'Ecole Normale Supérieure (IBENS), Ecole Normale Supérieure, CNRS, INSERM, PSL Research University, Paris, France

OPEN ACCESS

Edited by:

Marylka Yoe Uusisaari,
Okinawa Institute of Science and
Technology Graduate University,
Japan

Reviewed by:

Laurens Bosman,
Erasmus Medical Center, Erasmus
University Rotterdam, Netherlands
Wolf-Julian Neumann,
Charité Universitätsmedizin Berlin,
Germany

*Correspondence:

Ana-Maria Zăgrean
ana-maria.zagrean@umfcd.ro
Daniela Popa
daniela.popa@ens.fr

[†]These authors have contributed
equally to this work

[‡]These authors have jointly directed
this work

Received: 20 July 2018

Accepted: 10 October 2018

Published: 06 November 2018

Citation:

Georgescu EL, Georgescu IA, Zahiu CDM, Șteopoaie AR, Morozan VP, Pană AȘ, Zăgrean A-M and Popa D (2018) Oscillatory Cortical Activity in an Animal Model of Dystonia Caused by Cerebellar Dysfunction. *Front. Cell. Neurosci.* 12:390. doi: 10.3389/fncel.2018.00390

The synchronization of neuronal activity in the sensorimotor cortices is crucial for motor control and learning. This synchrony can be modulated by upstream activity in the cerebello-cortical network. However, many questions remain over the details of how the cerebral cortex and the cerebellum communicate. Therefore, our aim is to study the contribution of the cerebellum to oscillatory brain activity, in particular in the case of dystonia, a severely disabling motor disease associated with altered sensorimotor coupling. We used a kainic-induced dystonia model to evaluate cerebral cortical oscillatory activity and connectivity during dystonic episodes. We performed microinjections of low doses of kainic acid into the cerebellar vermis in mice and examined activities in somatosensory, motor and parietal cortices. We showed that repeated applications of kainic acid into the cerebellar vermis, for five consecutive days, generate reproducible dystonic motor behavior. No epileptiform activity was recorded on electrocorticogram (ECoG) during the dystonic postures or movements. We investigated the ECoG power spectral density and coherence between motor cortex, somatosensory and parietal cortices before and during dystonic attacks. During the baseline condition, we found a phenomenon of permanent adaptation with a change of baseline locomotor activity coupled to an ECoG gamma band increase in all cortices. In addition, after kainate administration, we observed an increase in muscular activity, but less signs of dystonia together with modulations of the ECoG power spectra with an increase in gamma band in motor, parietal and somatosensory cortices. Moreover, we found reduced coherence in all measured frequency bands between the motor cortex and somatosensory or parietal cortices compared to baseline. In conclusion, examination of cortical oscillatory activities in this animal model of chronic dystonia caused by cerebellar dysfunction reveals a disruption in the coordination of neuronal activity across the cortical sensorimotor/parietal network, which may underlie motor skill deficits.

Keywords: cerebellum, intra-cortical oscillations, dystonia, kainate, mice

INTRODUCTION

There is increasing evidence that oscillations in the sensorimotor cortices can be modulated by the cerebellum via cerebello-thalamo-cortical pathways. The cerebellum provides a putative synchronization mechanism across multiple regions of the brain in both rodents and humans (O'Connor et al., 2002; Kujala et al., 2007; Courtemanche et al., 2013; Popa et al., 2013). Yet, the role of the cerebellum in modulating cerebral oscillations and associated coherence between brain regions involved in motor execution remains poorly understood.

Dystonia is a motor disorder in which a cerebellar dysfunction has been recently recognized, despite the absence of cardinal cerebellar signs (ataxia, dysmetria). Abnormal oscillatory activities in the motor cortex and abnormal learning are recognized as dystonic typical traits. This has led to propose that a distorted cerebellar output in the cerebello-thalamo-cortical pathway may pathologically influence the motor cortex (Prudente et al., 2014). Results of recent animal studies corroborate such a view (Caligiore et al., 2017). Indeed, abnormalities restricted to cerebellum were sufficient to cause dystonia and the cerebellar dysfunction was coupled to dystonic movements (LeDoux, 2011; Raïke et al., 2013; Fremont et al., 2014; White and Sillitoe, 2017).

So far, studies in dystonia have focused on cortical oscillations during simple movements and did not provide information on cerebellar contribution to these oscillations. Dystonic patients have impaired movement-related beta band coherence during simple movements in primary sensorimotor cortices (Jin et al., 2011). In focal hand dystonia patients, a significant decrease in high gamma power in the sensorimotor cortex was identified during the preparation of simple movements of the affected hand, when compared to healthy subjects (Hinkley et al., 2012). Furthermore, recent studies provide evidence of reduced functional connectivity in theta, alpha and beta bands in the somatosensory network in patients with Writer's Cramp dystonia (Cheng et al., 2016).

Dystonia can be pharmacologically modeled in mice by direct application of a glutamate receptor agonist (kainic acid) on the cerebellar cortex. In this case, abnormal cerebellar output is the source of dystonia (Pizoli et al., 2002). When dystonic movements were triggered by pharmacological stimulation of the cerebellum, microdialysis revealed significant reductions in striatal dopamine release. These results suggest that dystonia may originate from the alteration of a motor network involving both the basal ganglia and the cerebellum (Chen et al., 2014; Neumann et al., 2015, 2017), rather than an isolated dysfunction of only these motor areas.

Structural changes of white matter connectivity between the red nucleus and internal pallidum in the basal ganglia have been described in dystonic patients (Blood et al., 2012; Blood, 2013). The neurons from magnocellular red nucleus receive excitatory input from the contralateral cerebellar nuclei (dentate and interposed) and release output through the descending rubrospinal tract that sends the information to the interneurons of the ventral gray column that synapse with the contralateral

motoneurons (Fedina et al., 1975). Because the motoneurons also receive input directly from the rubrospinal axons, they will be activated both through the rubrospinal tract (directly) and also through the propriospinal neurons (indirectly). Thus, an abnormal cerebellar output may cause a deficient agonist and antagonist muscle coordination which occurs in dystonia (Pizoli et al., 2002). Abnormal cerebellar output coupled with dystonia-like behavior was also induced in mice by blocking the glutamatergic olivocerebellar signaling and eliminating the Purkinje cell complex spikes activity. In addition, *in vivo* lidocaine infusions in the cerebellar nuclei of these mice reduced dystonic tremor. Also, deep brain stimulation of the interposed cerebellar nuclei improved movement in severely dystonic mice (White and Sillitoe, 2017).

Abnormal activities in another cortical area, the parietal cortex, were also described in dystonic patients (Gallea et al., 2016). Intricate sensory maps for the planning of eye or hand reaching movements represent the form in which the parietal cortex is involved in creating cognitive plans. Each movement is individually represented on the parietal intentional map that serves as an integrator of various sensory inputs and as a coordination area. Also, the parietal cortex undergoes rapid plastic and interpersonal variations (Andersen and Buneo, 2002).

The present study examined the contribution of the cerebellum to motor, somatosensory and parietal oscillatory activities by using a mouse model of dystonia (chronic kainic acid administration to the cerebellar vermis). Kainic acid is an excitatory glutamate agonist proven to induce generalized dystonia when injected into the cerebellar vermis (Pizoli et al., 2002). We combined *in vivo* recordings of motor behavior, electrocorticogram (ECoG) and electromyogram (EMG) in order to characterize oscillatory activity in somatosensory, motor and parietal cortices during five consecutive days of sustained dystonic motor behavior. Moreover, our multi-site recording technique allowed us to calculate the coherence between motor cortex and somatosensory cortex, or between motor and parietal cortices, before and during dystonic attacks. Coherence describes the spectral distribution of oscillatory synchronization between simultaneously recorded signals and may reflect interactions or communication between brain areas or as areas sharing a common drive (Bowyer, 2016).

MATERIALS AND METHODS

The study was carried out with the approval of the local committee (Comisia de Etică a Cercetării Științifice; number PO-35-F-01) for animal research of "Carol Davila" University of Medicine and Pharmacy (Bucharest, Romania). The European Communities Council Directive 86/609/EEC and national policies for the good practice on animals used for scientific purposes were respected.

Animals

Experiments were performed on 3-month-old Swiss albino mice ($n = 20$), divided into two groups, motor-somatosensory group ($n = 10$) and motor-parietal group ($n = 10$), weighing between

45 g and 52 g. Mice were provided access to water and food *ad libitum* and housed on a 12 h light/dark cycle.

Chronic Electrode Implantation Surgery

Inhalatory isoflurane anesthesia (3%–4% concentration) was used for induction and 1.5%–2% for maintenance together with buprenorphine (50 $\mu\text{g/kg}$) applied subcutaneously for pain management. During surgical preparation, anesthetic efficiency was assessed by checking the withdrawal reflex to a noxious stimulus; if necessary, isoflurane dose was increased. Mice were maintained at 37°C through the entire procedure. After a local subcutaneous anesthetic injection (lidocaine, 1 ml, 2%), the scalp was incised medially, and skin and subcutaneous tissue were removed from the skull. Four small (1 mm diameter) craniotomies were drilled with stereotaxic guidance for the insertion of in-house made insulated nichrome (Kanthal, Palm Coast, FL, USA), flexible wire (0.15 mm) ECoG electrodes, on the dura mater surface. All the electrodes were manually de-insulated at both ends, 2 mm each, by mechanical abrasion. The two groups of implanted mice differed only by the position of the somatosensory or the parietal electrode. The placement of the electrodes was above both the left and the right motor cortices (2.2 mm anterior and 2.2 mm lateral relative to Bregma) and the ground electrode at 2 mm posterior and 2 mm lateral to the right

relative to lambda. An EMG electrode, made from the same wire, was placed in the neck muscles. For the somatosensory cortex group another electrode was placed above the left somatosensory cortex (1.3 mm anterior and 3.2 mm lateral relative to the Bregma) and, for the parietal cortex group, the electrode was fixed at 2.06 mm posterior and 2.3 mm lateral relative to the Bregma (**Figure 1A**). The skull was then coated with Super Bond (Dental Adhesive Resin Cement, Sun Medical CO, Japan). The electrodes were then fixed with dental cement (Pi-Ku-Plast HP 36, Bredent GmbH, Germany) and connected to the pins through which the headstage would be attached. At 7 mm posterior to Bregma, on the cerebellar vermal lobule VI, we inserted on the surface of the dura mater a guide cannula vertically with a 0.6 mm internal diameter. After the surgery, another dose of buprenorphine (50 $\mu\text{g/kg}$) was applied. The mice were individually housed and were allowed a minimum of 4 days of recovery after implantation.

Data Acquisition

Recordings (ECoG along with EMG activity) were performed in awake, freely moving animals for 150 min for six consecutive days using a Multi Channel Systems W2100 wireless interface board with an acquisition frequency of 1 KHz and a 4-channel W2100-HS4-opto Headstage (weight of 1.9 g + 3.8 g for

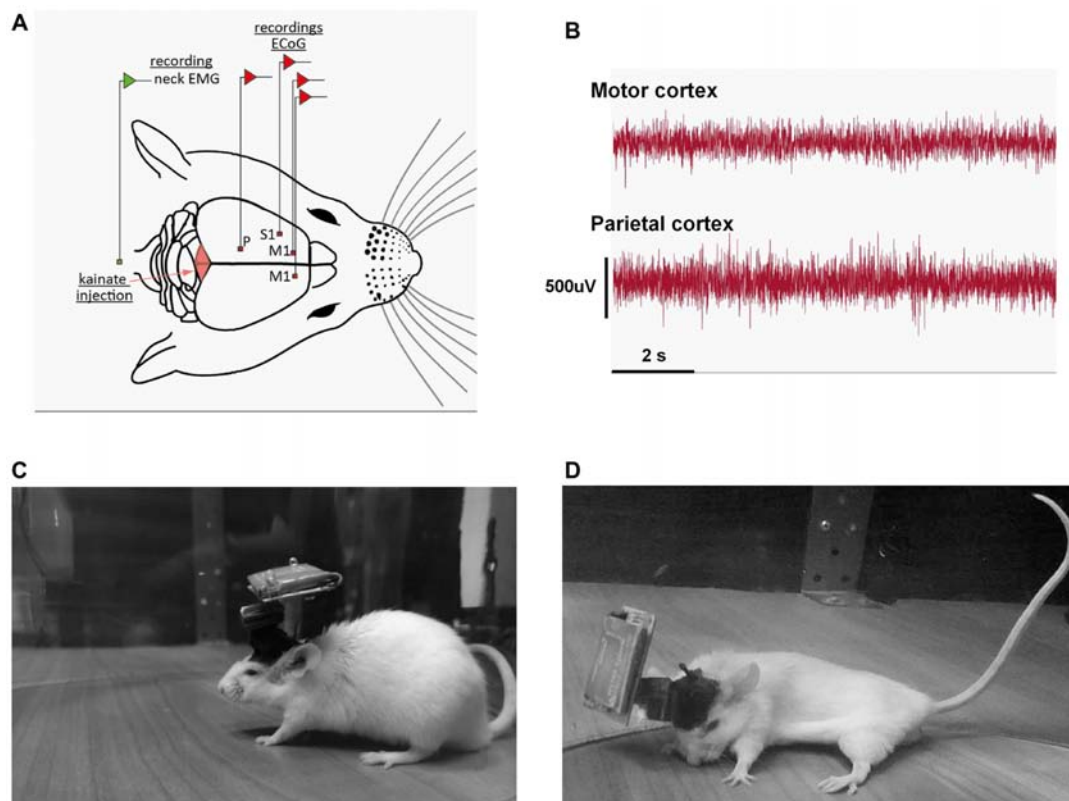


FIGURE 1 | (A) Schematic representation of the recording conditions; example of the position of the electrodes for the motor (M1), somatosensory (S1) and parietal (P) group. **(B)** Example of a motor, parietal electrocorticograms (ECoGs) during a dystonic attack. **(C)** Example of recording of a mouse in the pre-kainate state. **(D)** Example of dystonic attack during a post-kainate recording session.

the battery). In addition, video tracking of the mice was carried out for all experiments. After surgery, all mice were kept in the same room where the recordings followed. We also habituated the animals to the recording arena 2 days before the recordings. In the first day of experiment (baseline day), no injection was performed. On the next five consecutive days, recordings were performed before (10 min) and after 150 (min) kainic acid (Sigma) injections. Mice were briefly anesthetized with isoflurane (SC. Rompharm Company S.R.L., Romania) for the kainate injection and, after 1 min from waking up, the recording started. The ECoG demonstrated the absence of epileptic seizures after the injection.

Data Analysis

We only included data acquired from confirmed recording sites. All data were visually inspected, and intervals contaminated by artifacts were excluded from further analysis. Consequently, an average of 80% of recordings was retained. Power spectral density estimates were obtained with the Welch method with 2 s windows overlapping 1 s from the 1 KHz signal (MATLAB function *pwelch*). Changes in the ECoG power spectral density bands (Delta: 0.5–3.5 Hz, Theta: 4–12 Hz; Beta: 13–30 Hz; Low-Gamma: 30.5–48 Hz; High-Gamma: 52–100 Hz) were analyzed before and during all days of kainic acid administration for all the areas examined: motor, somatosensory and parietal cortices. Moreover, the real and imaginary coherence variations per band were investigated, as well as the evolution in time throughout the 5 days of chronic application of kainic acid for all the investigated brain regions. Coherence estimates were obtained using the MATLAB function *mscohere*, from power spectral density estimates of pairs of ECoG recordings, using the same parameters investigating the coherence between motor and sensorimotor and between motor and parietal cortices. The imaginary part of the coherence was also computed to estimate the coherence avoiding contamination by volume conduction (Nolte et al., 2004). Data were normalized by expressing the results as percentages of the baseline values (the values from the first day of recording).

The data obtained were processed in the Excel 2016 software, and then in GraphPrism 6.0 using repeated measures ANOVA, Dunnett's multiple comparisons test, Friedman test, Dunn's multiple comparisons test, Multiple *t*-test, Mann Whitney test and Kruskal-Wallis test after testing the normality distribution of the data, as appropriate. Results were presented as mean \pm the standard error of the mean (SEM). A *p*-value < 0.05 was considered statistically significant.

Electromyography analysis consisted of first calculating the power spectral density for each EMG recording for the whole 1–100-Hz frequency range. To quantitatively compare the EMG spectra for the two functional states, pre-kainate and post-kainate, mean power frequency was calculated. In addition, the median frequency was calculated as the frequency at which the EMG power spectrum is divided into two regions with equal amplitude. We also analyzed the EMG amplitude estimators: root mean square (RMS) and average rectified value (ARV; μ V).

To investigate the effects on the EMG spectral power and amplitude, the analysis consisted of ANOVA with repeated measures.

Video Recordings Monitored Behavior and Focused on the Animals' Motor Behavior in an Open Field

We induced dystonia using administration of $0.75 \pm 0.1 \mu$ l (100 μ g/ml) of kainate directly on the vermis surface of the cerebellum (Pizoli et al., 2002). The first day of recordings (without injection) was considered the baseline for each mouse. Periods of paroxysmal dystonic attacks were identified offline based upon the neck EMG recordings and video recordings. The presence and severity of dystonia in mice was quantified using a previously published scale (Pizoli et al., 2002; Calderon et al., 2011) in which 0 = normal motor behavior; 1 = abnormal motor behavior, no dystonic postures; 2 = mild motor impairment, dystonic-like postures when disturbed; 3 = moderate impairment, frequent spontaneous dystonic postures; and 4 = severe impairment, sustained dystonic postures. The percentage rate of active wake behavior from the total time of a recording (active wake percentages, AW%) was also calculated for both states, pre and post-kainate. In order to assess the general locomotor activity, we considered active wake behavior as the exploring activity during which the mice were walking inside the open field. Dystonia severity was evaluated for each 10-min epoch and several reviewers performed the assessment of the behavior independently (DZ, AŞ, VM and AP). The reviewers were blind to the procedures that were done, and their scores were averaged and decoded.

Correlations Between Behavior and Neuronal Activity

We assessed the link between behavior, dystonia and neuronal activity by computing the correlations between dystonic behavior (dystonia score or active wake) and the ECoG coherence for both motor cortex-somatosensory cortex and motor cortex-parietal cortex. Linear regressions were analyzed and Pearson correlation coefficients (*r*) and significance (*P*) values were added to **Supplementary Tables**.

RESULTS

Mice Displayed Dystonic Motor Behavior After Cerebellar Kainic Acid Application on the Cerebellar Vermis

Wild-type mice displayed a reproducible dystonic behavior after kainate injection on the lobule VI of the cerebellar vermis (Figures 1A–D). The produced phenotype was similar to that previously described (Pizoli et al., 2002).

ECoG (motor, somatosensory, parietal) recordings during dystonic attacks indicated no epileptiform activity (Figure 1B). The first signs of dystonia appeared after ~2–3 min following the injection with a general slowing down of movements or the hind limb being held near the trunk while the mouse

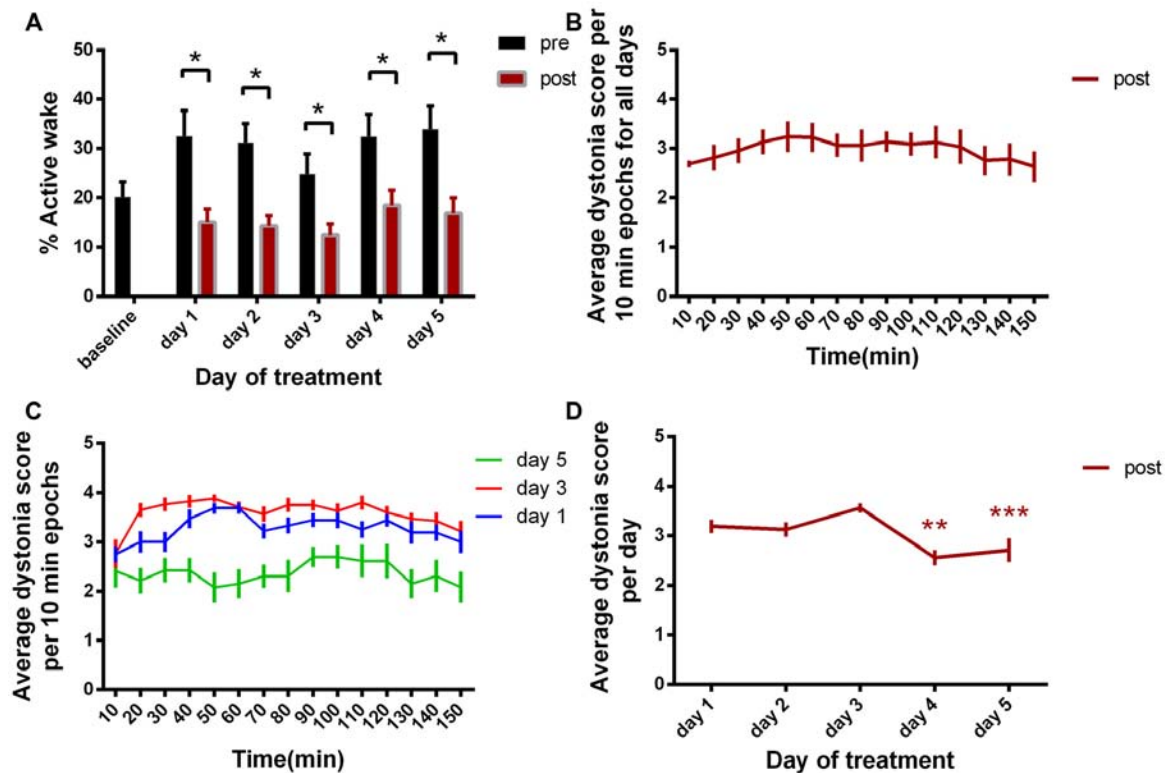


FIGURE 2 | (A) Active wake percentage averages \pm standard error of the mean (SEM) from baseline day to day 5 evolution. **(B)** Average score of dystonia during the recording sessions \pm SEM. **(C)** Average dystonia score during day 1, day 3, day 5. **(D)** Average total dystonia score per day \pm SEM evolution from day 1 to day 5. Results are expressed as average \pm the SEM (* $p < 0.05$, ** $p < 0.01$, *** $p < 0.001$, Table 1).

was exploring. After a few minutes, the mice began to show attacks of generalized dystonia with the muscles of the trunk, neck, tail and limbs being contracted (arched back, flexed neck, tail held in an upright position; Figure 1D). Mice usually remained in an immobilized severe dystonic position for a few minutes, followed by periods of lessening of the symptoms.

When comparing baseline day with all pre-kainate and post-kainate behavior of the same mice, we found that the mice were less active in post-kainate states (Figure 2A, Table 1). We also observed differences between the AW% during the pre-administration periods across all 5 days of dystonia. These results showed a sustained decrease in the time spent in exploratory activity after kainic injections. Interestingly, we also found an increase of the AW% before the injection across days (Figure 2A, Table 1), suggesting the possible presence of long-lasting plastic changes in the motor system following recurring kainate injections.

Evaluation of Dystonia Score

We then examined the average dystonia score for every 10 min recording periods (Figure 2B, Table 1). The results showed a high score over the complete duration of the recording, with a peak at approximately 50 min from the

recording start. This progress was followed by descending scores, constantly until the end of the recording (150 min). Figure 2C represents the evolution of the average dystonia score from the beginning to the end of the recording during day 1, 3 and 5 of kainic acid administration that shows a maximum of scores during day 3 and a minimum during day 5. Moreover, we analyzed the variation over time of the average score of these changes for the five consecutive days. When comparing each day to day 1, we found statistically significant decreased total average scores on day 4 and day 5 of kainic acid administration (Figure 2D, Table 1). The findings also implied that the severity of dystonia increased until day 3 and afterwards it started to decrease significantly to a minimum on the last day of the experiment, day 5, demonstrating that the susceptibility to kainate was possibly reduced at the end, suggesting a compensation mechanism or receptor desensitization.

Electromyography Demonstrates Higher Muscular Activity After Cerebellar Kainate Injections

During the dystonic attacks, mice had a predominantly tonic pattern of muscle activity (Figure 3A). We examined the electromyographic recordings and we found that the median

TABLE 1 | Behavior (active wake percentages, AW%).

| Behavior (Figure 2A) | Test | P value |
|---|-------------------------------------|-----------------------------|
| AW% baseline vs. AW% post day1 | Multiple <i>t</i> -test | $P = 0.0044$ |
| AW% baseline vs. AW% post day2 | Multiple <i>t</i> -test | $P = 0.0004$ |
| AW% baseline vs. AW% post day3 | Multiple <i>t</i> -test | $P = 0.0123$ |
| AW% baseline vs. AW% post day4 | Multiple <i>t</i> -test | $P = 0.0140$ |
| AW% baseline vs. AW% post day5 | Multiple <i>t</i> -test | $P = 0.0080$ |
| Dystonia score (Figure 2D) | Friedman test | $P < 0.0001$ |
| day1 vs. day2 | +Dunn's multiple comparisons test | ns |
| day1 vs. day3 | +Dunn's multiple comparisons test | ns |
| day1 vs. day4 | +Dunn's multiple comparisons test | ** |
| day1 vs. day5 | +Dunn's multiple comparisons test | *** |
| EMG median/mean frequency (Figures 3B,C) | 1-way ANOVA | $F_{(1,134,226.7)} = 9.025$ |
| day0 vs. day1 | Dunnett's multiple comparisons test | *** |
| day0 vs. day2 | Dunnett's multiple comparisons test | ns |
| day0 vs. day3 | Dunnett's multiple comparisons test | ** |
| day0 vs. day4 | Dunnett's multiple comparisons test | ** |
| day0 vs. day5 | Dunnett's multiple comparisons test | * |
| RMS EMG (Figure 3E) | Kruskal-Wallis test | $P = 0.6832$ |
| day0 vs. day1 | Dunn's multiple comparisons test | ns |
| day0 vs. day2 | Dunn's multiple comparisons test | ns |
| day0 vs. day3 | Dunn's multiple comparisons test | ns |
| day0 vs. day4 | Dunn's multiple comparisons test | ns |
| day0 vs. day5 | Dunn's multiple comparisons test | ns |
| ARV EMG (Figure 3F) | Kruskal-Wallis test | $P = 0.9260$ |
| day0 vs. day1 | Dunn's multiple comparisons test | ns |
| day0 vs. day2 | Dunn's multiple comparisons test | ns |
| day0 vs. day3 | Dunn's multiple comparisons test | ns |
| day0 vs. day4 | Dunn's multiple comparisons test | ns |
| day0 vs. day5 | Dunn's multiple comparisons test | ns |

Electromyogram (EMG) median and mean frequency. Statistical data. * $p < 0.05$, ** $p < 0.01$, *** $p < 0.001$, ns, not significant.

frequency of the muscular power spectral density was increased in day 1, day 4 and day 5 of experiment and decreased in day 3 (Figure 3B). The values recorded a maximum on day 4 and, in day 5, they fell again below the previous day ones. The mean frequency had a continuous increase since day 1 until day 4 of recordings and started to decrease in day 5 (Figure 3C, Table 1). Still, the values were higher than in the baseline condition. After the kainic acid injection, the power spectral density peak amplitude (Figure 3D) increased gradually from the baseline day until day 5.

We further analyzed the EMG amplitude estimators (Figures 3E,F). RMS revealed high amplitudes in the first and last days of kainate administration and minimum ones in day 3. The ARV estimator showed minimum changes in the first 3 days, recorded a maximum in day 4 and dropped immediately in the 5th day of experiment. The values recorded in day 5 were still higher than those recorded in the first 3 days. However, these changes were not statistically significant. This data suggests that kainic acid still has a muscular effect (increased mean frequency) during the last days of recording, even though dystonic score decreases.

Motor Cortex ECoG Power Spectral Density Evolution

For the motor cortex, we found significant power spectral density increases in the high frequency bands, especially in low and high gamma bands, for both pre and post-kainate recordings. Here, changes were visible since the first day of kainic acid

administration; significant changes were also found in low frequency bands (Figures 4A–E, Table 2).

Overall, except for delta band, all motor cortex ECoG power spectral densities bands showed a gradual increase that reached its maximum in the 5th day of examination for both conditions. Moreover, the pre-kainate data demonstrated a significant increase in high frequency bands in day 5 of examination, when compared with day 4. For high frequency bands post-kainate recordings, a significant increase was also shown between day 3 and day 4 of kainic acid administration (Figure 4, Table 2). This might suggest a plastic redistribution of the motor cortex activity as a reaction to the repeated kainic acid cerebellar administration a reaction to the injections across days. The increase in gamma band in the pre-kainate state concomitant with the increase in the active wake behavior and decrease in the average dystonia score in day 4 and 5, despite the enhanced EMG activation, suggests a possible adaptive process to correct the dystonic behavior.

Somatosensory Cortex ECoG Power Spectral Density

We next investigated the ECoG power spectral density for the somatosensory cortex and we found important progressive increases in high frequency bands, reaching the maximum in the last day of experiment. These results have been observed since the first day of recordings for both pre and post-administration periods (Figures 5A–F, Table 3). In addition, few significant changes were also found in the low-frequency bands (Figures 5A,B).

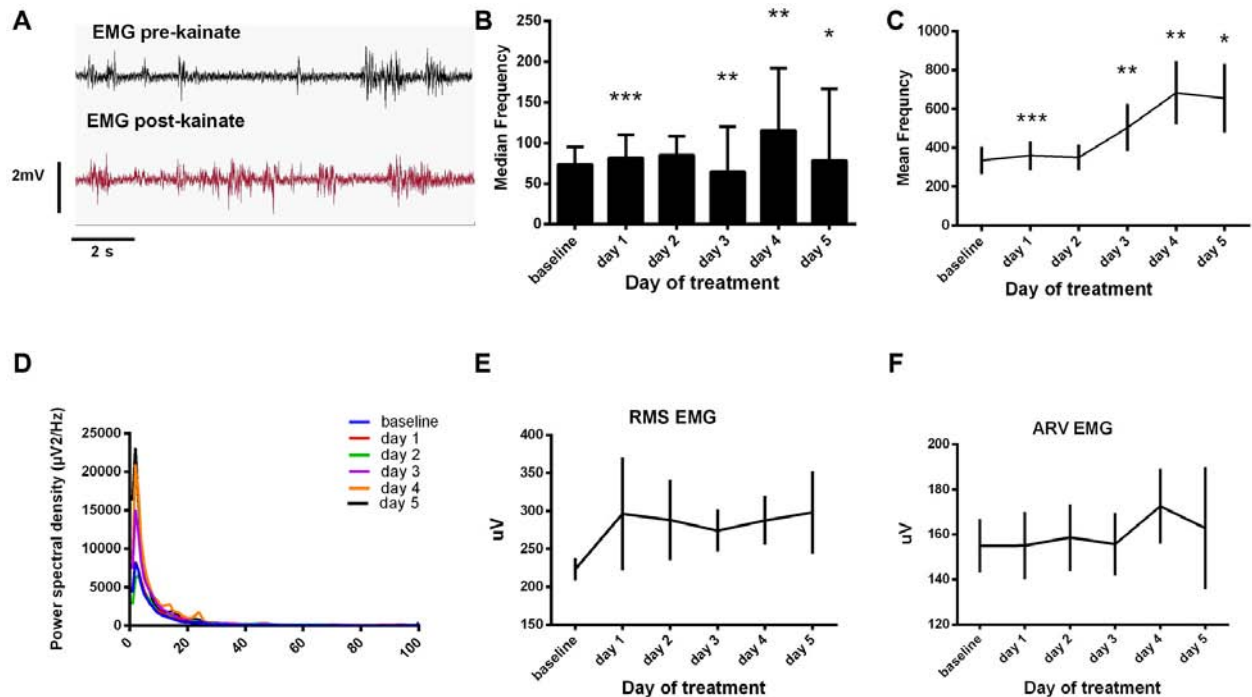


FIGURE 3 | (A) Raw electromyogram (EMG) recordings. Examples of raw EMG recordings during the dystonic attack. **(B)** Median frequency of the EMG power spectra \pm SEM. **(C)** Mean frequency of the EMG power spectra \pm SEM. **(D)** Average EMG power spectral density evolution from baseline day to day 5. **(E)** Average root mean square (RMS) during each day of experiment (μ V). **(F)** Average rectified value (ARV) during all days of experiment (μ V). **(B,C)** Repeated measures ANOVA, Dunnett's multiple comparisons test, each day vs. baseline day, **Table 1**. * $p < 0.05$, ** $p < 0.01$, *** $p < 0.001$.

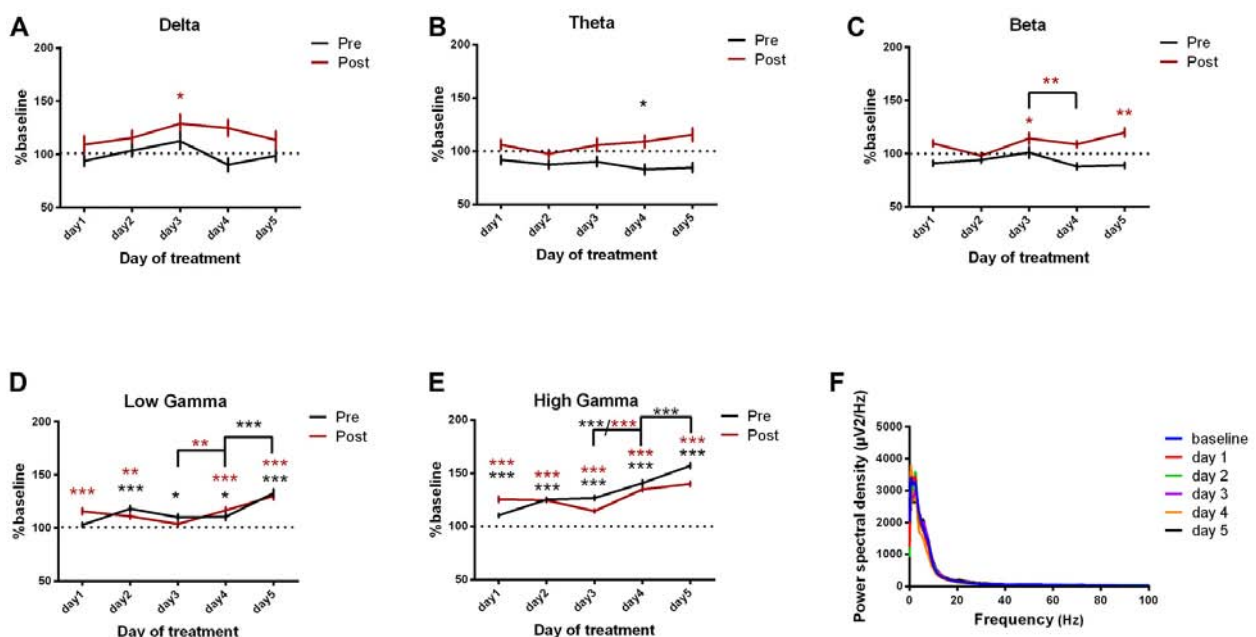


FIGURE 4 | Power spectral density of motor cortex ECoGs represented as percentage from baseline day across different bands. (A) Delta (0.5–3.5 Hz). **(B)** Theta (4–12 Hz). **(C)** Beta (13–30 Hz). **(D)** Low Gamma (30.5–48 Hz). **(E)** High Gamma (52–100 Hz) oscillations from baseline day to day 1, day 2, day 3, day 4, day 5 of intracerebellar kainic acid administration. **(F)** Average ECoG power spectral density evolution from baseline day to the 5th day. For each frequency band, the spectra are expressed as average \pm the SEM (* $p < 0.05$, ** $p < 0.01$, *** $p < 0.001$, repeated measures ANOVA, Dunnett's multiple comparisons test, each day vs. baseline day with the values of baseline group being normalized as 100%, **Table 2**).

Furthermore, for post-kainate recordings, we noticed a significant increase in the somatosensory ECoG power spectral density for all high-frequency bands in day 4 of dystonia, when compared to day 3. Also, the pre-kainate data revealed an important increase in gamma band in the 4th and 5th day, when compared to the previous one (Figures 5C–E). Our results show that increases occur especially in the last 2 days of examination for both pre-kainate and post-kainate recordings.

Parietal Cortex ECoG Power Spectral Density

In addition, we investigated the changes in the parietal cortex ECoGs (Figures 6A–F, Table 4) and we found an important increase in power spectral density before and after the kainic acid administration in the high frequency bands (Figures 6C–E). In gamma band, this increase was observed across all days of experiment. The parietal cortex revealed higher power spectral densities for pre-kainate recordings in high-gamma band than for post-kainate ones. For the low-frequency bands, only theta showed a significant decrease in day 5 of post-kainate recordings (Figures 6A,B).

Interestingly, when compared to the previous day, the parietal cortex power spectral density also increased significantly in the last 2 days of examination in the high-frequency bands, for both pre and post-kainate recordings (Figures 6C–E).

Motor-Ipsilateral Somatosensory Cortices Coherence

We then assessed the coherence between motor and ipsilateral somatosensory cortices (Figures 7A–F, Table 5). Notably, when comparing it to the baseline day, the cortical coherence of motor-somatosensory post-kainate recordings was significantly reduced in theta and beta bands (Figures 7B,C). Conversely, high gamma band showed increased coherence since the 1st day of kainate administration, with a recorded maximum in day 5 (Figure 7E). Pre-kainate administration periods revealed significantly lower motor-somatosensory coherence in low-frequency bands (Figures 7A,B). In the high frequency bands, except for day 5 in high gamma band, the pre-kainate coherence was also decreased (Figures 7C–E).

We further investigated the changes that occurred in the last 2 days of experiment. For pre-kainate recordings, the coherence decreased in day 4 (when comparing it to day 3) in all frequency bands, except high gamma (Figures 7A–E). Starting with day 4, an increasing trend has been observed for all frequency bands. Day 5 revealed significantly higher coherences in theta and high frequency bands (Figures 7B–E). In conclusion, motor-somatosensory coherence decreased in all frequency bands for both pre and post-kainate periods, but, since day 4, it started to increase.

Motor-Ipsilateral Parietal Cortices Coherence

Motor-parietal cortex coherence was significantly reduced from the baseline day to all dystonia days across all the tested frequency bands (Figures 8A–F, Table 6). For the post-kainate recordings, we found an increased coherence in high gamma band in day 5 of dystonia.

Over the last 2 days of recordings we found that, between day 4 and day 5, the motor-parietal cortex coherence was significantly increased in high-frequency bands for the pre and

post-administration periods. However, between day 3 and day 4, a significant decrease was observed for all pre-kainate data and also for post-kainate recordings in the high frequency bands (Figures 8A–E).

The analysis of motor-somatosensory and motor-parietal coherences coupled with dystonia scores suggest a negative correlation between the average dystonia score and high gamma frequency band.

We also calculated the imaginary part of coherence (Nolte et al., 2004; Stam et al., 2007) to estimate the coherence avoiding contamination by volume conduction. We found a very clear imaginary coherence coupling in low frequencies and in gamma band (Supplementary Figures S1C,D) that exclude volume conduction. We also yielded consistent results of the quantification of coherences in pre and post kainate injections in the cerebellum compared with the real part of the coherence, with an increased coherence post kainate injection (Supplementary Figures S1A,B).

Changes in Neural Activity Predict Changes in Motor Behavior

We assessed the link between behavior, dystonia and neuronal activity by computing the correlations between dystonic behavior (dystonia score or active wake) and the ECoG power spectral densities for motor, somatosensory and parietal cortices and also for motor-somatosensory and motor-parietal coherences (Supplementary Tables S1–S10). We found correlations notably in the first day of dystonia (Supplementary Figures S2–S6). The following days there was little or no relationship between dystonia scores and motor, sensory or parietal cortices activity because of the lack of variability for dystonia scores (Supplementary Tables S1–S10). Indeed, we found a very severe phenotype of dystonia after kainate injections in all our mice (Figure 2), while we found a reorganization of cortical neuronal activity across motor, somatosensory and parietal network (Figures 4–8). Specifically, for the motor cortex, we found a negative linear regression between dystonia score and motor cortex power spectral density in high gamma band in day 1 and day 4 (Supplementary Figure S2A, Supplementary Table S2). Also, a positive correlation was found for delta band and AW% (post-administration) in day 4 (Supplementary Figure S2C, Supplementary Table S1). Somatosensory cortex power spectral density revealed negative linear regressions with dystonia score in beta (day 3), low gamma (day 3, day 4) and high gamma bands (day 4; Supplementary Figure S3A, Supplementary Table S4). Also, positive correlations were found with AW% in delta (pre-administration, in day 3 and day 5 and post-administration in day 4; Supplementary Figures S3B,C, Supplementary Table S3). In the parietal cortex, positive correlations were found between delta power spectral density and AW% (post-administration, day 1; Supplementary Figure S4C, Supplementary Table S5), as well as between delta and dystonia score in day 3 (Supplementary Figure S4A, Supplementary Table S6). We further examined the motor-somatosensory and motor-parietal cortices coherence in relationship with behavior. For the motor-somatosensory cortex we found a negative correlation with AW% (post-

TABLE 2 | Motor cortex power spectral density bands.

| Motor cortex spectral density (Figure 4) | Test | $F_{(DFn,DFd)}$ | P value |
|--|--------------------------------------|------------------------|--------------|
| Delta pre | 1-way ANOVA | $F_{(5,701)} = 1.558$ | $P = 0.1698$ |
| day0 vs. day1 | +Dunnett's multiple comparisons test | | ns |
| day0 vs. day2 | +Dunnett's multiple comparisons test | | ns |
| day0 vs. day3 | +Dunnett's multiple comparisons test | | ns |
| day0 vs. day4 | +Dunnett's multiple comparisons test | | ns |
| day0 vs. day5 | +Dunnett's multiple comparisons test | | ns |
| Delta post | 1-way ANOVA | $F_{(5,694)} = 1.982$ | $P = 0.0792$ |
| day0 vs. day1 | +Dunnett's multiple comparisons test | | ns |
| day0 vs. day2 | +Dunnett's multiple comparisons test | | ns |
| day0 vs. day3 | +Dunnett's multiple comparisons test | | * |
| day0 vs. day4 | +Dunnett's multiple comparisons test | | ns |
| day0 vs. day5 | +Dunnett's multiple comparisons test | | ns |
| Theta pre | 1-way ANOVA | $F_{(5,1711)} = 1.947$ | $P = 0.0838$ |
| day0 vs. day1 | +Dunnett's multiple comparisons test | | ns |
| day0 vs. day2 | +Dunnett's multiple comparisons test | | ns |
| day0 vs. day3 | +Dunnett's multiple comparisons test | | ns |
| day0 vs. day4 | +Dunnett's multiple comparisons test | | * |
| day0 vs. day5 | +Dunnett's multiple comparisons test | | ns |
| Theta post | 1-way ANOVA | $F_{(5,1694)} = 1.481$ | $P = 0.1930$ |
| day0 vs. day1 | +Dunnett's multiple comparisons test | | ns |
| day0 vs. day2 | +Dunnett's multiple comparisons test | | ns |
| day0 vs. day3 | +Dunnett's multiple comparisons test | | ns |
| day0 vs. day4 | +Dunnett's multiple comparisons test | | ns |
| day0 vs. day5 | +Dunnett's multiple comparisons test | | ns |
| Beta pre | 1-way ANOVA | $F_{(5,3529)} = 2.536$ | $P = 0.0267$ |
| day0 vs. day1 | +Dunnett's multiple comparisons test | | ns |
| day0 vs. day2 | +Dunnett's multiple comparisons test | | ns |
| day0 vs. day3 | +Dunnett's multiple comparisons test | | ns |
| day0 vs. day4 | +Dunnett's multiple comparisons test | | ns |
| day0 vs. day5 | +Dunnett's multiple comparisons test | | ns |
| Beta post | 1-way ANOVA | $F_{(5,3494)} = 5.058$ | $P = 0.0001$ |
| day0 vs. day1 | +Dunnett's multiple comparisons test | | ns |
| day0 vs. day2 | +Dunnett's multiple comparisons test | | ns |
| day0 vs. day3 | +Dunnett's multiple comparisons test | | * |
| day0 vs. day4 | +Dunnett's multiple comparisons test | | ns |
| day0 vs. day5 | +Dunnett's multiple comparisons test | | ** |
| Low gamma pre | 1-way ANOVA | $F_{(5,3630)} = 17.78$ | $P < 0.0001$ |
| day0 vs. day1 | +Dunnett's multiple comparisons test | | ns |
| day0 vs. day2 | +Dunnett's multiple comparisons test | | *** |
| day0 vs. day3 | +Dunnett's multiple comparisons test | | * |
| day0 vs. day4 | +Dunnett's multiple comparisons test | | * |
| day0 vs. day5 | +Dunnett's multiple comparisons test | | *** |
| Low gamma post | 1-way ANOVA | $F_{(5,3594)} = 13.56$ | $P < 0.0001$ |
| day0 vs. day1 | +Dunnett's multiple comparisons test | | *** |
| day0 vs. day2 | +Dunnett's multiple comparisons test | | ** |
| day0 vs. day3 | +Dunnett's multiple comparisons test | | ns |
| day0 vs. day4 | +Dunnett's multiple comparisons test | | *** |
| day0 vs. day5 | +Dunnett's multiple comparisons test | | *** |
| High gamma pre | 1-way ANOVA | $F_{(5,9791)} = 100.7$ | $P < 0.0001$ |
| day0 vs. day1 | +Dunnett's multiple comparisons test | | *** |
| day0 vs. day2 | +Dunnett's multiple comparisons test | | *** |
| day0 vs. day3 | +Dunnett's multiple comparisons test | | *** |
| day0 vs. day4 | +Dunnett's multiple comparisons test | | *** |
| day0 vs. day5 | +Dunnett's multiple comparisons test | | *** |
| High gamma post | 1-way ANOVA | $F_{(5,9694)} = 45.23$ | $P < 0.0001$ |
| day0 vs. day1 | +Dunnett's multiple comparisons test | | *** |
| day0 vs. day2 | +Dunnett's multiple comparisons test | | *** |
| day0 vs. day3 | +Dunnett's multiple comparisons test | | *** |
| day0 vs. day4 | +Dunnett's multiple comparisons test | | *** |
| day0 vs. day5 | +Dunnett's multiple comparisons test | | *** |

(Continued)

TABLE 2 | (Continued)

| Motor cortex spectral density (Figure 4) | Test | $F_{(DFn,DFd)}$ | P value |
|--|-------------------|-----------------|--------------|
| Delta pre | | | |
| day3 vs. day4 | Mann Whitney test | | $P = 0.1239$ |
| day4 vs. day5 | Mann Whitney test | | $P = 0.1975$ |
| Delta post | | | |
| day3 vs. day4 | Mann Whitney test | | $P = 0.8639$ |
| day4 vs. day5 | Mann Whitney test | | $P = 0.2458$ |
| Theta pre | | | |
| day3 vs. day4 | Mann Whitney test | | $P = 0.4611$ |
| day4 vs. day5 | Mann Whitney test | | $P = 0.8121$ |
| Theta post | | | |
| day3 vs. day4 | Mann Whitney test | | $P = 0.1490$ |
| day4 vs. day5 | Mann Whitney test | | $P = 0.4406$ |
| Beta pre | | | |
| day3 vs. day4 | Mann Whitney test | | $P = 0.5772$ |
| day4 vs. day5 | Mann Whitney test | | $P = 0.1614$ |
| Beta post | | | |
| day3 vs. day4 | Mann Whitney test | | $P = 0.0023$ |
| day4 vs. day5 | Mann Whitney test | | $P = 0.1052$ |
| Low gamma pre | | | |
| day3 vs. day4 | Mann Whitney test | | $P = 0.6894$ |
| day4 vs. day5 | Mann Whitney test | | $P < 0.0001$ |
| Low gamma post | | | |
| day3 vs. day4 | Mann Whitney test | | $P = 0.0037$ |
| day4 vs. day5 | Mann Whitney test | | $P = 0.1339$ |
| High gamma pre | | | |
| day3 vs. day4 | Mann Whitney test | | $P < 0.0001$ |
| day4 vs. day5 | Mann Whitney test | | $P < 0.0001$ |
| High gamma post | | | |
| day3 vs. day4 | Mann Whitney test | | $P < 0.0001$ |
| day4 vs. day5 | Mann Whitney test | | $P = 0.4010$ |

Statistical data. * $p < 0.05$, ** $p < 0.01$, *** $p < 0.001$, ns, not significant.

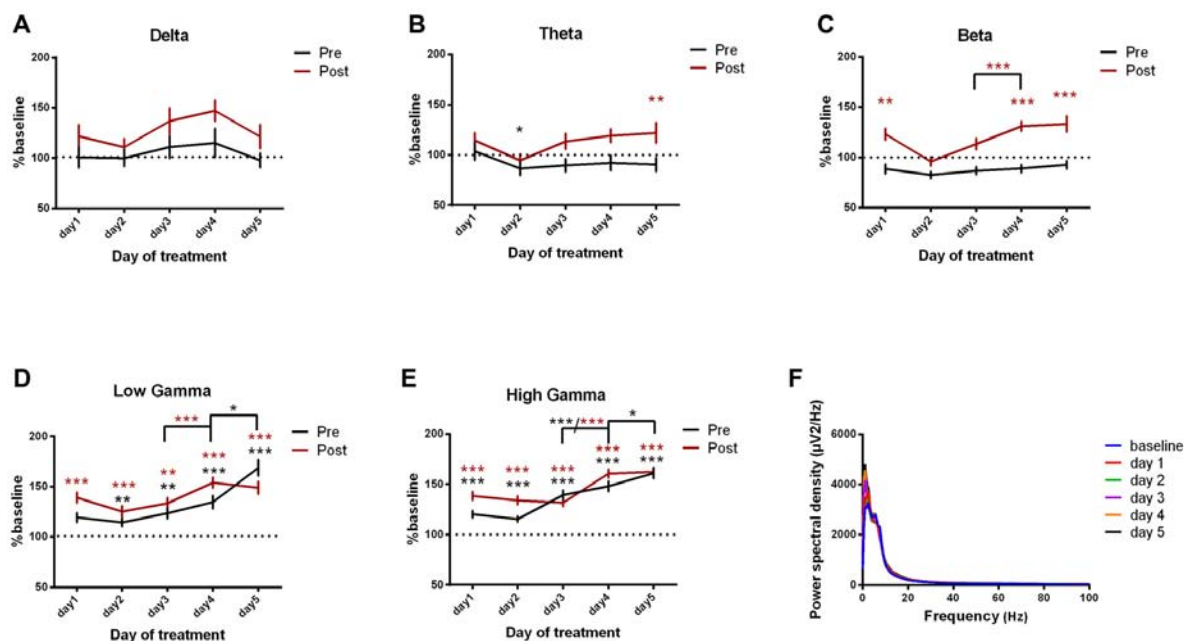


FIGURE 5 | Power spectral density of somatosensory cortex ECoGs represented as percentage from baseline day across different bands. **(A)** Delta (0.5–3.5 Hz). **(B)** Theta (4–12 Hz). **(C)** Beta (13–30 Hz). **(D)** Low-gamma (30.5–48 Hz). **(E)** High-gamma (52–100 Hz) oscillations from Baseline day to day 1, day 2, day 3, day 4, day 5 of intracerebellar kainic acid administration. **(F)** Average ECoG power spectral density evolution from baseline day to the 5th day. For each frequency band, the spectra are expressed as average \pm SEM (* $p < 0.05$, ** $p < 0.01$, *** $p < 0.001$, repeated measures ANOVA, Dunnett's multiple comparisons test, each day vs. baseline day with the values of baseline group being normalized as 100%, Table 3).

TABLE 3 | Somatosensory cortex power spectral density bands.

| Somatosensory cortex spectral density bands (Figure 5) | Test | $F_{(DFn,DFd)}$ | P value |
|--|--------------------------------------|------------------------|--------------|
| Delta pre | 1-way ANOVA | $F_{(5,610)} = 0.7700$ | $P = 0.5716$ |
| day0 vs. day1 | +Dunnett's multiple comparisons test | | ns |
| day0 vs. day2 | +Dunnett's multiple comparisons test | | ns |
| day0 vs. day3 | +Dunnett's multiple comparisons test | | ns |
| day0 vs. day4 | +Dunnett's multiple comparisons test | | ns |
| day0 vs. day5 | +Dunnett's multiple comparisons test | | ns |
| Delta post | 1-way ANOVA | $F_{(5,603)} = 1.380$ | $P = 0.2301$ |
| day0 vs. day1 | +Dunnett's multiple comparisons test | | ns |
| day0 vs. day2 | +Dunnett's multiple comparisons test | | ns |
| day0 vs. day3 | +Dunnett's multiple comparisons test | | ns |
| day0 vs. day4 | +Dunnett's multiple comparisons test | | ns |
| day0 vs. day5 | +Dunnett's multiple comparisons test | | ns |
| Theta pre | 1-way ANOVA | $F_{(5,1507)} = 1.827$ | $P = 0.1045$ |
| day0 vs. day1 | +Dunnett's multiple comparisons test | | ns |
| day0 vs. day2 | +Dunnett's multiple comparisons test | | * |
| day0 vs. day3 | +Dunnett's multiple comparisons test | | ns |
| day0 vs. day4 | +Dunnett's multiple comparisons test | | ns |
| day0 vs. day5 | +Dunnett's multiple comparisons test | | ns |
| Theta post | 1-way ANOVA | $F_{(5,1473)} = 3.733$ | $P = 0.0023$ |
| day0 vs. day1 | +Dunnett's multiple comparisons test | | ns |
| day0 vs. day2 | +Dunnett's multiple comparisons test | | ns |
| day0 vs. day3 | +Dunnett's multiple comparisons test | | ns |
| day0 vs. day4 | +Dunnett's multiple comparisons test | | ns |
| day0 vs. day5 | +Dunnett's multiple comparisons test | | ** |
| Beta pre | 1-way ANOVA | $F_{(5,3146)} = 1.715$ | $P = 0.1277$ |
| day0 vs. day1 | +Dunnett's multiple comparisons test | | ns |
| day0 vs. day2 | +Dunnett's multiple comparisons test | | ns |
| day0 vs. day3 | +Dunnett's multiple comparisons test | | ns |
| day0 vs. day4 | +Dunnett's multiple comparisons test | | ns |
| day0 vs. day5 | +Dunnett's multiple comparisons test | | ns |
| Beta post | 1-way ANOVA | $F_{(5,3039)} = 14.59$ | $P < 0.0001$ |
| day0 vs. day1 | +Dunnett's multiple comparisons test | | ** |
| day0 vs. day2 | +Dunnett's multiple comparisons test | | ns |
| day0 vs. day3 | +Dunnett's multiple comparisons test | | ns |
| day0 vs. day4 | +Dunnett's multiple comparisons test | | *** |
| day0 vs. day5 | +Dunnett's multiple comparisons test | | *** |
| Low gamma pre | 1-way ANOVA | $F_{(5,3162)} = 23.94$ | $P < 0.0001$ |
| day0 vs. day1 | +Dunnett's multiple comparisons test | | ns |
| day0 vs. day2 | +Dunnett's multiple comparisons test | | ** |
| day0 vs. day3 | +Dunnett's multiple comparisons test | | ** |
| day0 vs. day4 | +Dunnett's multiple comparisons test | | *** |
| day0 vs. day5 | +Dunnett's multiple comparisons test | | *** |
| Low gamma post | 1-way ANOVA | $F_{(5,3126)} = 17.70$ | $P < 0.0001$ |
| day0 vs. day1 | +Dunnett's multiple comparisons test | | *** |
| day0 vs. day2 | +Dunnett's multiple comparisons test | | *** |
| day0 vs. day3 | +Dunnett's multiple comparisons test | | ** |
| day0 vs. day4 | +Dunnett's multiple comparisons test | | *** |
| day0 vs. day5 | +Dunnett's multiple comparisons test | | *** |
| High gamma pre | 1-way ANOVA | $F_{(5,8530)} = 85.14$ | $P < 0.0001$ |
| day0 vs. day1 | +Dunnett's multiple comparisons test | | *** |
| day0 vs. day2 | +Dunnett's multiple comparisons test | | *** |
| day0 vs. day3 | +Dunnett's multiple comparisons test | | *** |
| day0 vs. day4 | +Dunnett's multiple comparisons test | | *** |
| day0 vs. day5 | +Dunnett's multiple comparisons test | | *** |
| High gamma post | 1-way ANOVA | $F_{(5,8439)} = 64.12$ | $P < 0.0001$ |
| day0 vs. day1 | +Dunnett's multiple comparisons test | | *** |
| day0 vs. day2 | +Dunnett's multiple comparisons test | | *** |
| day0 vs. day3 | +Dunnett's multiple comparisons test | | *** |
| day0 vs. day4 | +Dunnett's multiple comparisons test | | *** |
| day0 vs. day5 | +Dunnett's multiple comparisons test | | *** |

(Continued)

TABLE 3 | (Continued)

| Somatosensory cortex spectral density bands (Figure 5) | Test | $F_{(DFn,DFd)}$ | P value |
|--|-------------------|-----------------|--------------|
| Delta pre | | | |
| day3 vs. day4 | Mann Whitney test | | $P = 0.6585$ |
| day4 vs. day5 | Mann Whitney test | | $P = 0.9723$ |
| Delta post | | | |
| day3 vs. day4 | Mann Whitney test | | $P = 0.5757$ |
| day4 vs. day5 | Mann Whitney test | | $P = 0.1021$ |
| Theta pre | | | |
| day3 vs. day4 | Mann Whitney test | | $P = 0.5030$ |
| day4 vs. day5 | Mann Whitney test | | $P = 0.6922$ |
| Theta post | | | |
| day3 vs. day4 | Mann Whitney test | | $P = 0.0551$ |
| day4 vs. day5 | Mann Whitney test | | $P = 0.8825$ |
| Beta pre | | | |
| day3 vs. day4 | Mann Whitney test | | $P = 0.3119$ |
| day4 vs. day5 | Mann Whitney test | | $P = 0.6042$ |
| Beta post | | | |
| day3 vs. day4 | Mann Whitney test | | $P < 0.0001$ |
| day4 vs. day5 | Mann Whitney test | | $P = 0.6332$ |
| Low gamma pre | | | |
| day3 vs. day4 | Mann Whitney test | | $P = 0.1936$ |
| day4 vs. day5 | Mann Whitney test | | $P = 0.0122$ |
| Low gamma post | | | |
| day3 vs. day4 | Mann Whitney test | | $P < 0.0001$ |
| day4 vs. day5 | Mann Whitney test | | $P = 0.5692$ |
| High gamma pre | | | |
| day3 vs. day4 | Mann Whitney test | | $P < 0.0001$ |
| day4 vs. day5 | Mann Whitney test | | $P = 0.0125$ |
| High gamma post | | | |
| day3 vs. day4 | Mann Whitney test | | $P < 0.0001$ |
| day4 vs. day5 | Mann Whitney test | | $P = 0.0806$ |

Statistical data. * $p < 0.05$, ** $p < 0.01$, *** $p < 0.001$, ns, not significant.

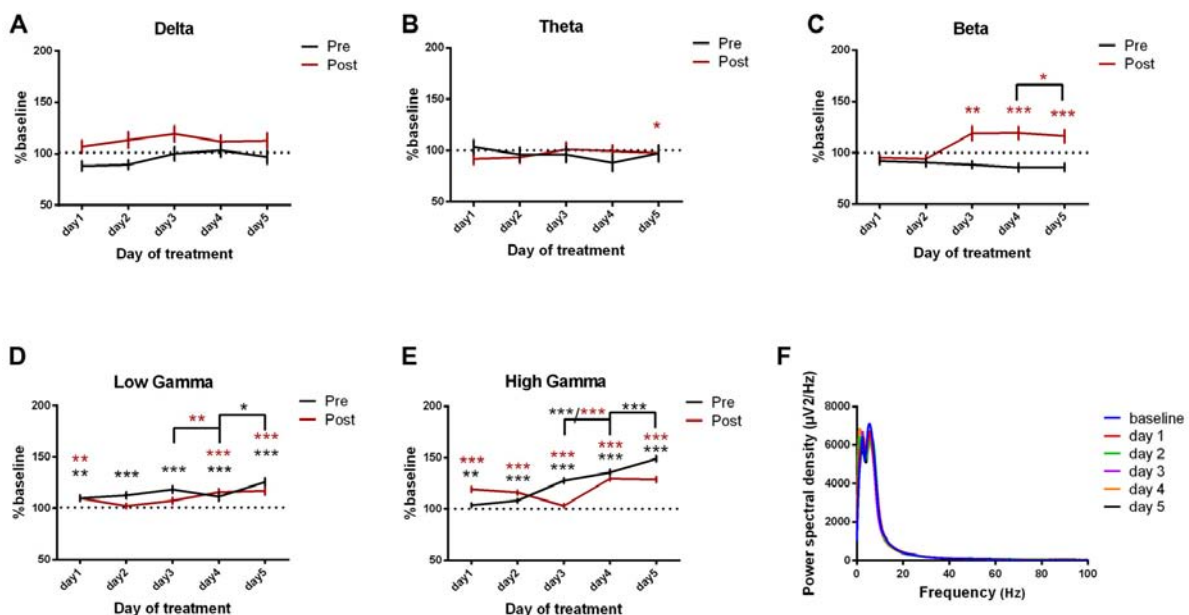


FIGURE 6 | Power spectral density of parietal cortex ECoGs represented as percentage from baseline day across different bands. **(A)** Delta (0.5–3.5 Hz). **(B)** Theta (4–12 Hz). **(C)** Beta (13–30 Hz). **(D)** Low-gamma (30.5–48 Hz). **(E)** High-gamma (52–100 Hz) oscillations from baseline day to day 1, day 2, day 3, day 4, day 5 of intracerebellar kainic acid administration. **(F)** Average ECoG power spectral density evolution from baseline day to the 5th day. For each frequency band, the spectra are expressed as average \pm SEM (* $p < 0.05$, ** $p < 0.01$, *** $p < 0.001$, repeated measures ANOVA, Dunnett's multiple comparisons test, each day vs. baseline day with the values of baseline group being normalized as 100%, Table 4).

TABLE 4 | Parietal cortex power spectral density bands.

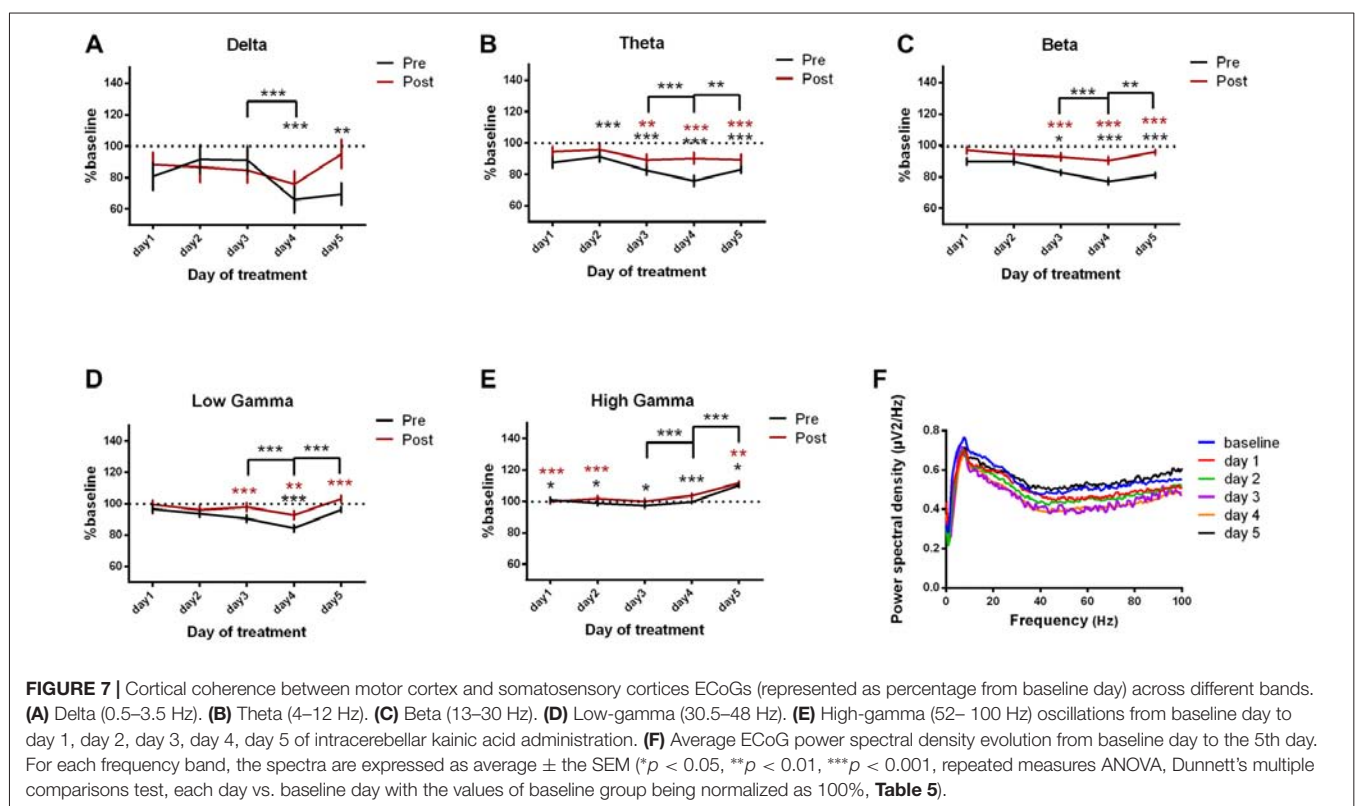
| Parietal cortex spectral density bands (Figure 6) | Test | $F_{(DFn,DFd)}$ | P value |
|---|--------------------------------------|-------------------------|--------------|
| Delta pre | 1-way ANOVA | $F_{(5,624)} = 1.561$ | $P = 0.1692$ |
| day0 vs. day1 | +Dunnett's multiple comparisons test | | ns |
| day0 vs. day2 | +Dunnett's multiple comparisons test | | ns |
| day0 vs. day3 | +Dunnett's multiple comparisons test | | ns |
| day0 vs. day4 | +Dunnett's multiple comparisons test | | ns |
| day0 vs. day5 | +Dunnett's multiple comparisons test | | ns |
| Delta post | 1-way ANOVA | $F_{(5,624)} = 1.457$ | $P = 0.2021$ |
| day0 vs. day1 | +Dunnett's multiple comparisons test | | ns |
| day0 vs. day2 | +Dunnett's multiple comparisons test | | ns |
| day0 vs. day3 | +Dunnett's multiple comparisons test | | ns |
| day0 vs. day4 | +Dunnett's multiple comparisons test | | ns |
| day0 vs. day5 | +Dunnett's multiple comparisons test | | ns |
| Theta pre | 1-way ANOVA | $F_{(5,1524)} = 0.4282$ | $P = 0.8292$ |
| day0 vs. day1 | +Dunnett's multiple comparisons test | | ns |
| day0 vs. day2 | +Dunnett's multiple comparisons test | | ns |
| day0 vs. day3 | +Dunnett's multiple comparisons test | | ns |
| day0 vs. day4 | +Dunnett's multiple comparisons test | | ns |
| day0 vs. day5 | +Dunnett's multiple comparisons test | | ns |
| Theta post | 1-way ANOVA | $F_{(5,1524)} = 2.904$ | $P = 0.0129$ |
| day0 vs. day1 | +Dunnett's multiple comparisons test | | ns |
| day0 vs. day2 | +Dunnett's multiple comparisons test | | ns |
| day0 vs. day3 | +Dunnett's multiple comparisons test | | ns |
| day0 vs. day4 | +Dunnett's multiple comparisons test | | ns |
| day0 vs. day5 | +Dunnett's multiple comparisons test | | * |
| Beta pre | 1-way ANOVA | $F_{(5,3216)} = 0.6552$ | $P = 0.6575$ |
| day0 vs. day1 | +Dunnett's multiple comparisons test | | ns |
| day0 vs. day2 | +Dunnett's multiple comparisons test | | ns |
| day0 vs. day3 | +Dunnett's multiple comparisons test | | ns |
| day0 vs. day4 | +Dunnett's multiple comparisons test | | ns |
| day0 vs. day5 | +Dunnett's multiple comparisons test | | ns |
| Beta post | 1-way ANOVA | $F_{(5,3144)} = 14.86$ | $P < 0.0001$ |
| day0 vs. day1 | +Dunnett's multiple comparisons test | | ns |
| day0 vs. day2 | +Dunnett's multiple comparisons test | | ns |
| day0 vs. day3 | +Dunnett's multiple comparisons test | | ** |
| day0 vs. day4 | +Dunnett's multiple comparisons test | | *** |
| day0 vs. day5 | +Dunnett's multiple comparisons test | | *** |
| Low gamma pre | 1-way ANOVA | $F_{(5,3234)} = 15.84$ | $P < 0.0001$ |
| day0 vs. day1 | +Dunnett's multiple comparisons test | | ns |
| day0 vs. day2 | +Dunnett's multiple comparisons test | | ** |
| day0 vs. day3 | +Dunnett's multiple comparisons test | | *** |
| day0 vs. day4 | +Dunnett's multiple comparisons test | | *** |
| day0 vs. day5 | +Dunnett's multiple comparisons test | | *** |
| Low gamma post | 1-way ANOVA | $F_{(5,3234)} = 14.39$ | $P < 0.0001$ |
| day0 vs. day1 | +Dunnett's multiple comparisons test | | ** |
| day0 vs. day2 | +Dunnett's multiple comparisons test | | ns |
| day0 vs. day3 | +Dunnett's multiple comparisons test | | ns |
| day0 vs. day4 | +Dunnett's multiple comparisons test | | *** |
| day0 vs. day5 | +Dunnett's multiple comparisons test | | *** |
| High gamma pre | 1-way ANOVA | $F_{(5,8724)} = 137.3$ | $P < 0.0001$ |
| day0 vs. day1 | +Dunn multiple comparisons test | | ** |
| day0 vs. day2 | +Dunn multiple comparisons test | | *** |
| day0 vs. day3 | +Dunn multiple comparisons test | | *** |
| day0 vs. day4 | +Dunn multiple comparisons test | | *** |
| day0 vs. day5 | +Dunn multiple comparisons test | | *** |
| High gamma post | 1-way ANOVA | $F_{(5,8730)} = 53.57$ | $P < 0.0001$ |
| day0 vs. day1 | +Dunn multiple comparisons test | | *** |
| day0 vs. day2 | +Dunn multiple comparisons test | | *** |
| day0 vs. day3 | +Dunn multiple comparisons test | | *** |
| day0 vs. day4 | +Dunn multiple comparisons test | | *** |
| day0 vs. day5 | +Dunn multiple comparisons test | | *** |

(Continued)

TABLE 4 | (Continued)

| Parietal cortex spectral density bands (Figure 6) | Test | $F_{(DFn,DFd)}$ | P value |
|---|-------------------|-----------------|--------------|
| Delta pre | | | |
| day3 vs. day4 | Mann Whitney test | | $P = 0.5624$ |
| day4 vs. day5 | Mann Whitney test | | $P = 0.3381$ |
| Delta post | | | |
| day3 vs. day4 | Mann Whitney test | | $P = 0.6417$ |
| day4 vs. day5 | Mann Whitney test | | $P = 0.7438$ |
| Theta pre | | | |
| day3 vs. day4 | Mann Whitney test | | $P = 0.9601$ |
| day4 vs. day5 | Mann Whitney test | | $P = 0.7127$ |
| Theta post | | | |
| day3 vs. day4 | Mann Whitney test | | $P = 0.1778$ |
| day4 vs. day5 | Mann Whitney test | | $P = 0.1067$ |
| Beta pre | | | |
| day3 vs. day4 | Mann Whitney test | | $P = 0.5185$ |
| day4 vs. day5 | Mann Whitney test | | $P = 0.8966$ |
| Beta post | | | |
| day3 vs. day4 | Mann Whitney test | | $P = 0.1108$ |
| day4 vs. day5 | Mann Whitney test | | $P = 0.0165$ |
| Low gamma pre | | | |
| day3 vs. day4 | Mann Whitney test | | $P = 0.9334$ |
| day4 vs. day5 | Mann Whitney test | | $P = 0.0106$ |
| Low gamma post | | | |
| day3 vs. day4 | Mann Whitney test | | $P = 0.0049$ |
| day4 vs. day5 | Mann Whitney test | | $P = 0.0821$ |
| High gamma pre | | | |
| day3 vs. day4 | Mann Whitney test | | $P < 0.0001$ |
| day4 vs. day5 | Mann Whitney test | | $P < 0.0001$ |
| High gamma post | | | |
| day3 vs. day4 | Mann Whitney test | | $P < 0.0001$ |
| day4 vs. day5 | Mann Whitney test | | $P = 0.7735$ |

Statistical data. * $p < 0.05$, ** $p < 0.01$, *** $p < 0.001$, ns, not significant.



administration) in delta (day 1, day 2), theta (day 1, day 2), beta (day 2) and low gamma (day 2; **Supplementary Figure S5C, Supplementary Table S7**). The motor-parietal cortex coherence was positively correlated with dystonia score in delta (day 1; **Supplementary Figure S6A, Supplementary Table S10**).

DISCUSSION

Our study examined the relationship between the activation of the cerebellar cortex with kainate and the intra-cortical oscillatory activities in normal and dystonic conditions. We found functional reorganization of multiple cerebral cortical areas and new coordination of their activity. In this model (Pizoli et al., 2002), the dystonia occurred only after the kainic acid administration and it lasted for 3 h, without visible signs of dystonia in the next day. The injection was performed for five consecutive days. We obtained a phenomenon of permanent adaptation with a change of baseline locomotor activity together with an ECoG high gamma band increase in the motor and parietal cortices. In addition, in the post-kainate state we noticed an adaptation in the motor circuit across days with an increase in muscular activity in day 4 and day 5, but with less signs of dystonia and with changes in power spectral of ECoG of all frequency bands in the motor circuit. Our results revealed less signs of dystonia in the last 2 days, coupled with a reduced motor-somatosensory coherence in all bands, except for day 5 in gamma band. The increase in the locomotor activity suggests improved control of muscular contraction across days of dystonia.

Furthermore, we found a reduction of the motor-somatosensory and motor-parietal cortex oscillations coherences in low and high frequency ranges, after cerebellar kainate injections. This data is consistent with other lines of recent evidence (Mantel et al., 2018) that writer's cramp patients have reduced functional connectivity for the right motor and S1, supramarginal gyrus and also posterior parietal cortex. Interestingly, beginning day 4 of cerebellar kainate administration, intra-cortical coherence started to return to normal values. This phenomenon might be explained by a compensatory mechanism or a reduction of the sensibility of the kainate receptors after multiple administrations, even though the kainate might still have a muscular effect as indicated by the increase in mean frequency of EMG and median frequency of EMG consistent with a prolongation of muscle activation. This reflects the EMG pattern of movement in dystonia, characterized by excessive motor activation that can be due to excessive activation of antagonist muscles, redundant activation of muscles and maintenance of muscle activation producing abnormal muscle contraction and lack of coordination (Mima et al., 2000).

Cerebellum and Dystonia

We found that mice developed sustained and reproducible dystonic motor behavior after daily kainate application on the cerebellar vermis in agreement with previous studies.

Multiple applications of kainic acid into the cerebellar vermis resulted in increased neuronal activation (indicated by c-fos expression) in the cerebellum in all three layers of the cerebellar cortex and in the ventro-anterior thalamus. Also, Hsp70 expression was increased in the Purkinje cell layer and in the magnocellular part of the red nucleus, which is the first output of the cerebellar nuclei, suggesting that an altered neuronal network may be part of the pathogenesis of the disorder (Alvarez-Fischer et al., 2012). Moreover, kainic acid cerebellar application induced a significantly lower degree of dystonia in mice lacking Purkinje cells, this underlying the critical role of these cells in the pathogenesis of the disorder (Pizoli et al., 2002). Glutamate receptor activation, specifically AMPA receptor activation by kainic acid was necessary to produce dystonia, whereas a nonspecific increase in cerebellar excitability was not enough to induce dystonic behavior (Fan et al., 2012).

The cerebellum and the cerebello-forebrain pathways have been implicated in several animal models of dystonia (Chen et al., 2014; Shakkottai et al., 2017). Indeed, the cerebellar vermis was proven to be involved in controlling anticipatory postural motor behavior and to be connected to the motor cortex (Diedrichsen et al., 2005). It was previously believed that postural dystonia might be related to its impaired function (Coffman et al., 2011). Also, in human studies, cerebellar structural neuroimaging abnormalities such as atrophy (Delmaire et al., 2007), anatomical disturbance of cerebellar output (Niethammer et al., 2011) or lesions (Batla et al., 2015) have been reported. Additionally, PET imaging studies have revealed that many different forms of dystonia are characterized by abnormal increases in cerebellar metabolic activity (Hutchinson et al., 2000; Carbon et al., 2013). In mutant tottering mice, which exhibit paroxysmal dystonia due to an inherited defect affecting calcium channels, prior studies have shown that abnormal cerebellar output is essential for the generation of dystonic movements with slow oscillations occurring in the cerebellar cortex in relation with dystonic movements (Chen et al., 2009). In another genetic model of dystonia in the mice, a recent study showed that dystonia is eliminated following surgical removal of the cerebellum (Devanagondi et al., 2007). Cerebellectomy also relieved the motor symptoms in a genetic model of dystonia in the rat (LeDoux, 2011). In other genetic models of dystonia—*dt* rat, tottering mouse and mouse with invalidation of type 1 inositol triphosphate receptor in the cerebellum/brainstem—removal of the cerebellum, or only cerebellar Purkinje neurons or deep cerebellar nuclei, eliminates dystonic movements, showing that abnormalities in the cerebellum are the source of the movement disorders (LeDoux et al., 1993, 1995; Campbell et al., 1999; Neychev et al., 2008; Hisatsune et al., 2013). In addition, the block of the olivocerebellar excitatory neurotransmission has been shown to eliminate Purkinje cell complex spikes and to produce aberrant cerebellar nuclear activity while inducing dystonic behavior (White and Sillitoe, 2017). These findings lead to the proposal that dystonia in these models is linked to an increase in neuronal activity in the cerebellum. This hypothesis is confirmed by studies showing that excitation of the cerebellum by local application of the glutamate agonist kainic acid evokes

TABLE 5 | Motor-ipsilateral somatosensory coherence.

| Motor-somatosensory coherence (Figure 7) | Test | $F_{(DFn,DFd)}$ | P value |
|--|--------------------------------------|------------------------|--------------|
| Delta pre | 1-way ANOVA | $F_{(5,666)} = 4.469$ | $P = 0.0005$ |
| day0 vs. day1 | +Dunnett's multiple comparisons test | | ns |
| day0 vs. day2 | +Dunnett's multiple comparisons test | | ns |
| day0 vs. day3 | +Dunnett's multiple comparisons test | | ns |
| day0 vs. day4 | +Dunnett's multiple comparisons test | | *** |
| day0 vs. day5 | +Dunnett's multiple comparisons test | | ** |
| Delta post | 1-way ANOVA | $F_{(5,631)} = 2.443$ | $P = 0.0331$ |
| day0 vs. day1 | +Dunnett's multiple comparisons test | | ns |
| day0 vs. day2 | +Dunnett's multiple comparisons test | | ns |
| day0 vs. day3 | +Dunnett's multiple comparisons test | | ns |
| day0 vs. day4 | +Dunnett's multiple comparisons test | | ns |
| day0 vs. day5 | +Dunnett's multiple comparisons test | | ns |
| Theta pre | 1-way ANOVA | $F_{(5,1626)} = 14.69$ | $P < 0.0001$ |
| day0 vs. day1 | +Dunnett's multiple comparisons test | | ns |
| day0 vs. day2 | +Dunnett's multiple comparisons test | | *** |
| day0 vs. day3 | +Dunnett's multiple comparisons test | | *** |
| day0 vs. day4 | +Dunnett's multiple comparisons test | | *** |
| day0 vs. day5 | +Dunnett's multiple comparisons test | | *** |
| Theta post | 1-way ANOVA | $F_{(5,1541)} = 11.81$ | $P < 0.0001$ |
| day0 vs. day1 | +Dunnett's multiple comparisons test | | ns |
| day0 vs. day2 | +Dunnett's multiple comparisons test | | ns |
| day0 vs. day3 | +Dunnett's multiple comparisons test | | ** |
| day0 vs. day4 | +Dunnett's multiple comparisons test | | *** |
| day0 vs. day5 | +Dunnett's multiple comparisons test | | *** |
| Beta pre | 1-way ANOVA | $F_{(5,3426)} = 14.07$ | $P < 0.0001$ |
| day0 vs. day1 | +Dunnett's multiple comparisons test | | ns |
| day0 vs. day2 | +Dunnett's multiple comparisons test | | ns |
| day0 vs. day3 | +Dunnett's multiple comparisons test | | * |
| day0 vs. day4 | +Dunnett's multiple comparisons test | | *** |
| day0 vs. day5 | +Dunnett's multiple comparisons test | | *** |
| Beta post | 1-way ANOVA | $F_{(5,3179)} = 16.68$ | $P < 0.0001$ |
| day0 vs. day1 | +Dunnett's multiple comparisons test | | ns |
| day0 vs. day2 | +Dunnett's multiple comparisons test | | ns |
| day0 vs. day3 | +Dunnett's multiple comparisons test | | *** |
| day0 vs. day4 | +Dunnett's multiple comparisons test | | *** |
| day0 vs. day5 | +Dunnett's multiple comparisons test | | *** |
| Low gamma pre | 1-way ANOVA | $F_{(5,3450)} = 9.262$ | $P < 0.0001$ |
| day0 vs. day1 | +Dunnett's multiple comparisons test | | ns |
| day0 vs. day2 | +Dunnett's multiple comparisons test | | ns |
| day0 vs. day3 | +Dunnett's multiple comparisons test | | ns |
| day0 vs. day4 | +Dunnett's multiple comparisons test | | *** |
| day0 vs. day5 | +Dunnett's multiple comparisons test | | ns |
| Low gamma post | 1-way ANOVA | $F_{(5,3270)} = 15.02$ | $P < 0.0001$ |
| day0 vs. day1 | +Dunnett's multiple comparisons test | | ns |
| day0 vs. day2 | +Dunnett's multiple comparisons test | | ns |
| day0 vs. day3 | +Dunnett's multiple comparisons test | | *** |
| day0 vs. day4 | +Dunnett's multiple comparisons test | | ** |
| day0 vs. day5 | +Dunnett's multiple comparisons test | | *** |
| High gamma pre | 1-way ANOVA | $F_{(5,9306)} = 12.67$ | $P < 0.0001$ |
| day0 vs. day1 | +Dunnett's multiple comparisons test | | * |
| day0 vs. day2 | +Dunnett's multiple comparisons test | | * |
| day0 vs. day3 | +Dunnett's multiple comparisons test | | * |
| day0 vs. day4 | +Dunnett's multiple comparisons test | | *** |
| day0 vs. day5 | +Dunnett's multiple comparisons test | | * |
| High gamma post | 1-way ANOVA | $F_{(5,8827)} = 32.84$ | $P < 0.0001$ |
| day0 vs. day1 | +Dunnett's multiple comparisons test | | *** |
| day0 vs. day2 | +Dunnett's multiple comparisons test | | *** |
| day0 vs. day3 | +Dunnett's multiple comparisons test | | ns |
| day0 vs. day4 | +Dunnett's multiple comparisons test | | ns |
| day0 vs. day5 | +Dunnett's multiple comparisons test | | ** |

(Continued)

TABLE 5 | (Continued)

| Motor-somatosensory coherence (Figure 7) | Test | $F_{(DFn,DFd)}$ | <i>P</i> value |
|--|-------------------|-----------------|----------------|
| Delta pre | | | |
| day3 vs. day4 | Mann Whitney test | | $P = 0.0005$ |
| day4 vs. day5 | Mann Whitney test | | $P = 0.0790$ |
| Delta post | | | |
| day3 vs. day4 | Mann Whitney test | | $P = 0.4940$ |
| day4 vs. day5 | Mann Whitney test | | $P = 0.8762$ |
| Theta pre | | | |
| day3 vs. day4 | Mann Whitney test | | $P < 0.0001$ |
| day4 vs. day5 | Mann Whitney test | | $P = 0.0077$ |
| Theta post | | | |
| day3 vs. day4 | Mann Whitney test | | $P = 0.9324$ |
| day4 vs. day5 | Mann Whitney test | | $P = 0.1112$ |
| Beta pre | | | |
| day3 vs. day4 | Mann Whitney test | | $P < 0.0001$ |
| day4 vs. day5 | Mann Whitney test | | $P = 0.0063$ |
| Beta post | | | |
| day3 vs. day4 | Mann Whitney test | | $P = 0.3153$ |
| day4 vs. day5 | Mann Whitney test | | $P = 0.5027$ |
| Low gamma pre | | | |
| day3 vs. day4 | Mann Whitney test | | $P < 0.0001$ |
| day4 vs. day5 | Mann Whitney test | | $P < 0.0001$ |
| Low gamma post | | | |
| day3 vs. day4 | Mann Whitney test | | $P = 0.1747$ |
| day4 vs. day5 | Mann Whitney test | | $P = 0.5429$ |
| High gamma pre | | | |
| day3 vs. day4 | Mann Whitney test | | $P < 0.0001$ |
| day4 vs. day5 | Mann Whitney test | | $P < 0.0001$ |
| High gamma post | | | |
| day3 vs. day4 | Mann Whitney test | | $P = 0.8062$ |
| day4 vs. day5 | Mann Whitney test | | $P = 0.2107$ |

Statistical data. * $p < 0.05$, ** $p < 0.01$, *** $p < 0.001$, ns, not significant.

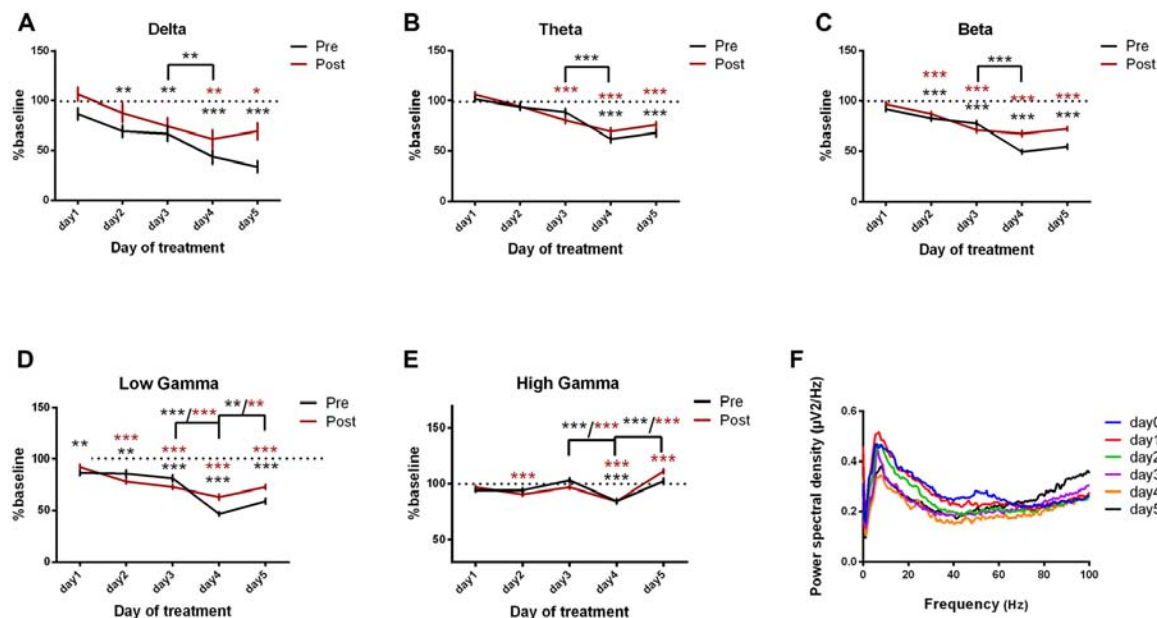


FIGURE 8 | Cortical coherence between motor cortex and parietal cortices ECoGs (represented as percentage from baseline day) across different bands. **(A)** Delta (0.5–3.5 Hz). **(B)** Theta (4–12 Hz). **(C)** Beta (13–30 Hz). **(D)** Low-gamma (30.5–48 Hz). **(E)** High-gamma (52–100 Hz) oscillations from baseline day to day 1, day 2, day 3, day 4, day 5 of intracerebellar kainic acid administration. **(F)** Average ECoG power spectral density evolution from baseline day to the 5th day in post-kainate state. For each frequency band, the spectra are expressed as average \pm the SEM (* $p < 0.05$, ** $p < 0.01$, *** $p < 0.001$, repeated measures ANOVA, Dunnett's multiple comparisons test, each day vs. baseline day with the values of baseline group being normalized as 100%, Table 6).

TABLE 6 | Motor-ipsilateral parietal coherence.

| Motor-parietal coherence (Figure 8) | Test | $F_{(DFn,DFd)}$ | P value |
|-------------------------------------|--------------------------------------|------------------------|--------------|
| Delta pre | 1-way ANOVA | $F_{(5,351)} = 14.51$ | $P < 0.0001$ |
| day0 vs. day1 | +Dunnett's multiple comparisons test | | ns |
| day0 vs. day2 | +Dunnett's multiple comparisons test | | ** |
| day0 vs. day3 | +Dunnett's multiple comparisons test | | ** |
| day0 vs. day4 | +Dunnett's multiple comparisons test | | *** |
| day0 vs. day5 | +Dunnett's multiple comparisons test | | *** |
| Delta post | 1-way ANOVA | $F_{(5,365)} = 4.809$ | $P = 0.0003$ |
| day0 vs. day1 | +Dunnett's multiple comparisons test | | ns |
| day0 vs. day2 | +Dunnett's multiple comparisons test | | ns |
| day0 vs. day3 | +Dunnett's multiple comparisons test | | ns |
| day0 vs. day4 | +Dunnett's multiple comparisons test | | ** |
| day0 vs. day5 | +Dunnett's multiple comparisons test | | * |
| Theta pre | 1-way ANOVA | $F_{(5,861)} = 26.64$ | $P < 0.0001$ |
| day0 vs. day1 | +Dunnett's multiple comparisons test | | ns |
| day0 vs. day2 | +Dunnett's multiple comparisons test | | ns |
| day0 vs. day3 | +Dunnett's multiple comparisons test | | ns |
| day0 vs. day4 | +Dunnett's multiple comparisons test | | *** |
| day0 vs. day5 | +Dunnett's multiple comparisons test | | *** |
| Theta post | 1-way ANOVA | $F_{(5,895)} = 22.43$ | $P < 0.0001$ |
| day0 vs. day1 | +Dunnett's multiple comparisons test | | ns |
| day0 vs. day2 | +Dunnett's multiple comparisons test | | ns |
| day0 vs. day3 | +Dunnett's multiple comparisons test | | *** |
| day0 vs. day4 | +Dunnett's multiple comparisons test | | *** |
| day0 vs. day5 | +Dunnett's multiple comparisons test | | *** |
| Beta pre | 1-way ANOVA | $F_{(5,1779)} = 64.37$ | $P < 0.0001$ |
| day0 vs. day1 | +Dunnett's multiple comparisons test | | ns |
| day0 vs. day2 | +Dunnett's multiple comparisons test | | *** |
| day0 vs. day3 | +Dunnett's multiple comparisons test | | *** |
| day0 vs. day4 | +Dunnett's multiple comparisons test | | *** |
| day0 vs. day5 | +Dunnett's multiple comparisons test | | *** |
| Beta post | 1-way ANOVA | $F_{(5,1849)} = 33.06$ | $P < 0.0001$ |
| day0 vs. day1 | +Dunnett's multiple comparisons test | | ns |
| day0 vs. day2 | +Dunnett's multiple comparisons test | | *** |
| day0 vs. day3 | +Dunnett's multiple comparisons test | | *** |
| day0 vs. day4 | +Dunnett's multiple comparisons test | | *** |
| day0 vs. day5 | +Dunnett's multiple comparisons test | | *** |
| Low gamma pre | 1-way ANOVA | $F_{(5,1830)} = 46.99$ | $P < 0.0001$ |
| day0 vs. day1 | +Dunnett's multiple comparisons test | | ** |
| day0 vs. day2 | +Dunnett's multiple comparisons test | | ** |
| day0 vs. day3 | +Dunnett's multiple comparisons test | | *** |
| day0 vs. day4 | +Dunnett's multiple comparisons test | | *** |
| day0 vs. day5 | +Dunnett's multiple comparisons test | | *** |
| Low gamma post | 1-way ANOVA | $F_{(5,1902)} = 29.69$ | $P < 0.0001$ |
| day0 vs. day1 | +Dunnett's multiple comparisons test | | ns |
| day0 vs. day2 | +Dunnett's multiple comparisons test | | *** |
| day0 vs. day3 | +Dunnett's multiple comparisons test | | *** |
| day0 vs. day4 | +Dunnett's multiple comparisons test | | *** |
| day0 vs. day5 | +Dunnett's multiple comparisons test | | *** |
| High gamma pre | 1-way ANOVA | $F_{(5,4941)} = 11.30$ | $P < 0.0001$ |
| day0 vs. day1 | +Dunnett's multiple comparisons test | | ns |
| day0 vs. day2 | +Dunnett's multiple comparisons test | | ns |
| day0 vs. day3 | +Dunnett's multiple comparisons test | | ns |
| day0 vs. day4 | +Dunnett's multiple comparisons test | | *** |
| day0 vs. day5 | +Dunnett's multiple comparisons test | | ns |
| High gamma post | 1-way ANOVA | $F_{(5,5135)} = 26.34$ | $P < 0.0001$ |
| day0 vs. day1 | +Dunnett's multiple comparisons test | | ns |
| day0 vs. day2 | +Dunnett's multiple comparisons test | | *** |
| day0 vs. day3 | +Dunnett's multiple comparisons test | | ns |
| day0 vs. day4 | +Dunnett's multiple comparisons test | | *** |
| day0 vs. day5 | +Dunnett's multiple comparisons test | | *** |

(Continued)

TABLE 6 | (Continued)

| Motor-Parietal coherence (Figure 8) | Test | $F_{(DFn,DFd)}$ | P value |
|-------------------------------------|-------------------|-----------------|--------------|
| Delta pre | | | |
| day3 vs. day4 | Mann Whitney test | | $P = 0.0078$ |
| day4 vs. day5 | Mann Whitney test | | $P = 0.2144$ |
| Delta post | | | |
| day3 vs. day4 | Mann Whitney test | | $P = 0.1434$ |
| day4 vs. day5 | Mann Whitney test | | $P = 0.4075$ |
| Theta pre | | | |
| day3 vs. day4 | Mann Whitney test | | $P < 0.0001$ |
| day4 vs. day5 | Mann Whitney test | | $P = 0.2441$ |
| Theta post | | | |
| day3 vs. day4 | Mann Whitney test | | $P = 0.0502$ |
| day4 vs. day5 | Mann Whitney test | | $P = 0.1605$ |
| Beta pre | | | |
| day3 vs. day4 | Mann Whitney test | | $P < 0.0001$ |
| day4 vs. day5 | Mann Whitney test | | $P = 0.2699$ |
| Beta post | | | |
| day3 vs. day4 | Mann Whitney test | | $P = 0.7344$ |
| day4 vs. day5 | Mann Whitney test | | $P = 0.3052$ |
| Low gamma pre | | | |
| day3 vs. day4 | Mann Whitney test | | $P < 0.0001$ |
| day4 vs. day5 | Mann Whitney test | | $P = 0.0017$ |
| Low gamma post | | | |
| day3 vs. day4 | Mann Whitney test | | $P = 0.0003$ |
| day4 vs. day5 | Mann Whitney test | | $P = 0.0015$ |
| High gamma pre | | | |
| day3 vs. day4 | Mann Whitney test | | $P = 0.0001$ |
| day4 vs. day5 | Mann Whitney test | | $P < 0.0001$ |
| High gamma post | | | |
| day3 vs. day4 | Mann Whitney test | | $P < 0.0001$ |
| day4 vs. day5 | Mann Whitney test | | $P < 0.0001$ |

Statistical data. * $p < 0.05$, ** $p < 0.01$, *** $p < 0.001$, ns, not significant.

in normal mice movements that have similarities with human dystonia (Pizoli et al., 2002). When dystonic movements were triggered by pharmacological stimulation of the cerebellum, microdialysis revealed significant reductions in striatal dopamine release (Pizoli et al., 2002). These results suggest that dystonia may occur from disruption of a motor network involving both the basal ganglia and the cerebellum (Chen et al., 2014; Bostan and Strick, 2018), rather than isolated dysfunction of only one motor system. By using conditional genetics to regionally limit cerebellar dysfunction, Raïke et al. (2013) demonstrated that abnormalities restricted to cerebellar Purkinje cells are sufficient to cause dystonia and that the extent of cerebellar dysfunction determines the extent of dystonic movements. Recently it was shown that conditional knockout mice lacking type 1 inositol 1,4,5-trisphosphate receptor (IP3R1) specifically in the cerebellum and brainstem, experienced dystonia the symptoms of which were independent of the basal ganglia, and could be rescued by inactivation of the cerebellum, inferior olive or in the absence of Purkinje cells (Hisatsune et al., 2013). Heterozygous animals carrying the DYT1 dystonia mutation in the TOR1a gene exhibit no behavioral defect, but defects in the cerebello-cortical pathway are similar to those found in human non-manifesting gene carriers, confirming the role of this pathway in the penetrance of the disease (Uluğ et al., 2011). Therefore, the changes that we found in intra-cerebral oscillatory activity could be in part results from depressed cerebello-cortical coupling.

Cerebellum, Oscillations and Dystonia

We found changes in the coordination of cortical networks following cerebellar kainate injections. Previous studies on dystonia examined cortical oscillations during simple movements without providing cerebellar activity. Dystonic patients have impaired movement-related beta decrease during simple movements in primary somatosensory cortices (Jin et al., 2011). Recently in focal hand dystonia patients, a significant decrease in high gamma power in the somatosensory cortex was identified during the preparation of simple movements of the affected hand compared to healthy subjects (Hinkley et al., 2012). Oscillation studies in deep structures were limited to the internal globus pallidus (Neumann et al., 2017), where a high gamma synchrony was observed when patients performed a reaction-time task with their unaffected hand. It was related to the scaling of ongoing movements (Brücke et al., 2012). Moreover, when performing voluntary movements, patients with primary dystonia showed an increase in synchronization in the high frequency range (Liu et al., 2008). It has also been suggested that, due to their neuronal activity synchronization in high frequency bands, the basal ganglia may contribute to hyperkinesias (Chen et al., 2006). These results suggest complex changes in oscillatory dynamics of high rhythms in dystonia.

We found changes in intra-cortical oscillations particularly in gamma band in motor, somatosensory and parietal cortices. Among the oscillations generated during intense neuronal communication, gamma rhythms appear to function

as a temporal code, facilitating the dynamic formation of neuronal assemblies by permitting synchronous firing among multiple, spatially separate subpopulations of neurons (Schoffelen et al., 2005). The networks supporting gamma oscillations critically depend on the inhibitory neurotransmitter γ -aminobutyric acid (GABA; Cardin et al., 2009; Gallea et al., 2018). Gamma oscillations represent reference signals for polysensory integration (Mishra et al., 2007), sensory-motor coordination (Schoffelen et al., 2005) and formation of long-term memories through spike timing-dependent plasticity (STDP; Wespata et al., 2004). The ability of the cerebellar cortex to generate rhythms within the gamma bands (30–80 and 80–160 Hz), as does the motor cortex, suggests that these rhythms may represent a common spatiotemporal code for the cortico-cerebellar dialog (Middleton et al., 2008). In humans, high gamma synchronization was observed in the cerebellum and the inferior parietal cortex during internal generation of decision and actions (Guggisberg et al., 2008) and in bilateral cerebellum after learning a bimanual complex motor tasks (Houweling et al., 2008). High gamma activity in the cerebellum and somatosensory cortex was observed during paced finger movement (Dalal et al., 2008). Our results of changes in coordination of neuronal activity across the cortical somatosensory/parietal network may underlie deficits in motor skills in dystonia.

Compensatory Activity and Motor Circuit Plasticity

We found that the severity of dystonia was sustained during the first 3 days of cerebellar kainate administrations and it decreased for the last 2 days. This was coupled with increased activity particularly in gamma bands in motor cortex. This change might induce frequency modulations in cortical networks and basal ganglia and compensatory activities that can rescue the behavior. In our model, dystonia resulted from abnormalities in cerebellar cortical activity due to kainate administration and this induced subsequent compensatory activities in motor systems (Shakkottai et al., 2017). However, the role of the motor cortex in cerebellar-induced dystonia is limited. Indeed, cortical activity contributes to the severity of cerebellar-induced dystonic postured, but dystonia can manifest in the absence of overt cortical activity (Calderon et al., 2011). We also found a correlation between the behavior, dystonia and motor cortex activity notably during the first day of induction of dystonia suggesting that changes in motor cortex activity induced by changes in cerebellum could predict changes in motor behavior. However, in the following days there was little or no relationship between dystonia scores and motor cortex activity and compensatory or adaptive cortical activities were observed after multiple injections of kainate in cerebellum.

Gallea et al. (2018) suggested that there is a loss of cerebellar modulation of M1 in dystonia and that this originated from GABAergic changes in cerebellar structures that could be compensatory or adaptive.

We also observed changes in parietal cortex activities during dystonia. This result is in line with the abnormal activation of the parietal cortex that was found in dystonic patients without

task-specific symptoms (Delnooz et al., 2013), as well as in task specific dystonia during non-symptomatic tasks or at rest (Gallea et al., 2016). An abnormal processing of multisensory input is a key pathophysiologic concept in dystonia because sensory activation can improve dystonic symptoms (Stamelou et al., 2012), and amelioration of reduced parietal activity has been shown during sensory activation in cervical dystonia (Mantel et al., 2018).

While human studies have established a cerebellar contribution to cortical plasticity (Popa et al., 2013, 2018), the counterpart phenomenon has not yet been studied in animal models. Indirect electron-microscopy evidence the presence of plastic changes in the cerebello-thalamic pathway (Aumann and Horne, 1999). The cerebello-thalamo-cortical pathway contacts the pyramidal neurons via a di- or trisynaptic pathway, and notably excites the pyramidal tract neurons (Futami et al., 1986) and the cortico-thalamic neurons (Na et al., 1997). The cerebellum indeed regulates motor cortex excitability (Oulad Ben Taib et al., 2005). Moreover, we recently demonstrated an important role of the cerebellum in the somatosensory coupling of the cortex where it was found that the cerebellum baselines the gamma-band synchronization of the sensori-motor cortex during active tactile exploration in the rodent (Popa et al., 2013). The cerebellum thus controls the gamma-band synchronization of the sensori-motor cortex during active tactile exploration in the rodent. Therefore, this decrease in the intra-cortical activity in gamma band could directly result from the contribution of the cerebellum to the sensorimotor coordination after cerebellar kainate administration during dystonia (Popa et al., 2013).

Functional Implications

Motor disorders that are consecutive to brain dysfunction (e.g., Parkinson's disease, dystonia, ataxia, tremors, etc.) are associated with a wide variety of symptoms, but typically involve a set of several brain structures: somatosensory and premotor cortices, basal ganglia and cerebellum. Of these structures, the cerebellum is probably the least studied, despite the strong evidence for its involvement in a large spectrum of movement disorders: dystonia (Hubsch et al., 2013), essential tremor (Louis, 2014), Parkinson's tremor (Helmich et al., 2011) and ataxia (Bastian, 2006). The cerebellum exhibits reciprocal connections with the motor cortex (Kelly and Strick, 2003; Proville et al., 2014) and the basal ganglia (Bostan and Strick, 2010). While the coarse anatomy and connectivity of the cerebello-thalamo-cortical pathway have been documented (Steriade, 1995), the cerebellar contribution to motor function and dysfunction remains unclear (Shakkottai et al., 2017). Still, this pathway is notably the site of functional reorganizations in the course of motor diseases (Brighina et al., 2009; Ni et al., 2010) anomalies in the cerebello-cortical pathway co-vary with the severity of the symptoms, but the nature of their contribution to the pathology remains unclear. We showed in our study that local anomalies in the cerebellum could induce sustained dystonia coupled with intra-cortical changes in oscillatory activities suggesting that the cerebellum is a gateway for changing motor circuits.

In conclusion, examination of cortical oscillatory activities in this animal model of dystonia caused by cerebellar dysfunction

reveals a disruption of the coordination of neuronal activity across the cortical somatosensory/parietal network, which may underlie deficits in motor skills.

AUTHOR CONTRIBUTIONS

EG, IG, A-MZ and DP designed the experiments and wrote the manuscript. EG, IG, CZ, AŞ, VM and AP performed the experiments and analyzed the data.

FUNDING

This work was supported by TE European Young Team: “CEROSCO”, PN-II-RU-TE-2014-4 project/UEFISCDI (Executive Unit for Higher Education, Research, Development

and Innovation), public institution with legal personality subordinated to the Ministry of Education, Romania and by Agence Nationale de Recherche to DP (ANR-16-CE37-0003-02 Amedyst).

ACKNOWLEDGMENTS

We are grateful to Clément Léna and Thomas C. Watson for the careful reading of the manuscript.

SUPPLEMENTARY MATERIAL

The Supplementary Material for this article can be found online at: <https://www.frontiersin.org/articles/10.3389/fncel.2018.00390/full#supplementary-material>

REFERENCES

- Alvarez-Fischer, D., Grundmann, M., Lu, L., Samans, B., Fritsch, B., Möller, J. C., et al. (2012). Prolonged generalized dystonia after chronic cerebellar application of kainic acid. *Brain Res.* 1464, 82–88. doi: 10.1016/j.brainres.2012.05.007
- Andersen, R. A., and Buneo, C. A. (2002). Intentional maps in posterior parietal cortex. *Annu. Rev. Neurosci.* 25, 189–220. doi: 10.1146/annurev.neuro.25.112701.142922
- Aumann, T. D., and Horne, M. K. (1999). Ultrastructural change at rat cerebellothalamic synapses associated with volitional motor adaptation. *J. Comp. Neurol.* 409, 71–84. doi: 10.1002/(sici)1096-9861(19990621)409:1<71::aid-cne6>3.0.co;2-c
- Bastian, A. J. (2006). Learning to predict the future: the cerebellum adapts feedforward movement control. *Curr. Opin. Neurobiol.* 16, 645–649. doi: 10.1016/j.conb.2006.08.016
- Batla, A., Sánchez, M. C., Erro, R., Ganos, C., Stamelou, M., Balint, B., et al. (2015). The role of cerebellum in patients with late onset cervical/segmental dystonia?—evidence from the clinic. *Parkinsonism Relat. Disord.* 21, 1317–1322. doi: 10.1016/j.parkreldis.2015.09.013
- Blood, A. J. (2013). Imaging studies in focal dystonias: a systems level approach to studying a systems level disorder. *Curr. Neuropharmacol.* 11, 3–15. doi: 10.2174/157015913804999513
- Blood, A. J., Kuster, J. K., Woodman, S. C., Kirlic, N., Makhlof, M. L., Multhaupt-Buell, T. J., et al. (2012). Evidence for altered basal ganglia-brainstem connections in cervical dystonia. *PLoS One* 7:e31654. doi: 10.1371/journal.pone.0031654
- Bostan, A. C., and Strick, P. L. (2010). The cerebellum and basal ganglia are interconnected. *Neuropsychol. Rev.* 20, 261–270. doi: 10.1007/s11065-010-9143-9
- Bostan, A. C., and Strick, P. L. (2018). The basal ganglia and the cerebellum: nodes in an integrated network. *Nat. Rev. Neurosci.* 19, 338–350. doi: 10.1038/s41583-018-0002-7
- Bowyer, S. M. (2016). Coherence a measure of the brain networks: past and present. *Neuropsychiatr. Electrophysiol.* 2:1. doi: 10.1186/s40810-015-0015-7
- Brighina, F., Romano, M., Giglia, G., Saia, V., Puma, A., Giglia, F., et al. (2009). Effects of cerebellar TMS on motor cortex of patients with focal dystonia: a preliminary report. *Exp. Brain Res.* 192, 651–656. doi: 10.1007/s00221-008-1572-9
- Brücke, C., Huebel, J., Schonecker, T., Neumann, W.-J., Yarrow, K., Kupsch, A., et al. (2012). Scaling of movement is related to pallidal γ oscillations in patients with dystonia. *J. Neurosci.* 32, 1008–1019. doi: 10.1523/jneurosci.3860-11.2012
- Calderon, D. P., Fremont, R., Kraenzlin, F., and Khodakhah, K. (2011). The neural substrates of rapid-onset Dystonia-Parkinsonism. *Nat. Neurosci.* 14, 357–365. doi: 10.1038/nn.2753
- Caligiore, D., Pezzulo, G., Baldassarre, G., Bostan, A. C., Strick, P. L., Doya, K., et al. (2017). Consensus paper: towards a systems-level view of cerebellar function: the interplay between cerebellum, basal ganglia and cortex. *Cerebellum* 16, 203–229. doi: 10.1007/s12311-016-0763-3
- Campbell, D. B., North, J. B., and Hess, E. J. (1999). Tottering mouse motor dysfunction is abolished on the Purkinje cell degeneration (*pcd*) mutant background. *Exp. Neurol.* 160, 268–278. doi: 10.1006/exnr.1999.7171
- Carbon, M., Raymond, D., Ozelius, L., Saunders-Pullman, R., Frucht, S., Dhawan, M. V., et al. (2013). Metabolic changes in DYT11. *Neurology* 80, 385–391. doi: 10.1212/wnl.0b013e31827f0798
- Cardin, J. A., Carlén, M., Meletis, K., Knoblich, U., Zhang, F., Deisseroth, K., et al. (2009). Driving fast-spiking cells induces gamma rhythm and controls sensory responses. *Nature* 459, 663–667. doi: 10.1038/nature08002
- Chen, C. H., Fremont, R., Arteaga-Bracho, E. E., and Khodakhah, K. (2014). Short latency cerebellar modulation of the basal ganglia. *Nat. Neurosci.* 17, 1767–1775. doi: 10.1038/nn.3868
- Chen, C. C., Kühn, A. A., Hoffmann, K.-T., Kupsch, A., Schneider, G. H., Trottenberg, T., et al. (2006). Oscillatory pallidal local field potential activity correlates with involuntary EMG in dystonia. *Neurology* 66, 418–420. doi: 10.1212/01.wnl.0000196470.00165.7d
- Chen, G., Popa, L. S., Wang, X., Gao, W., Barnes, J., Hendrix, C. M., et al. (2009). Low-frequency oscillations in the cerebellar cortex of the tottering mouse. *J. Neurophysiol.* 101, 234–245. doi: 10.1152/jn.90829.2008
- Cheng, C.-H., Tseng, Y.-J., Chen, R.-S., and Lin, Y.-Y. (2016). Reduced functional connectivity of somatosensory network in writer's cramp patients. *Brain Behav.* 6:e00433. doi: 10.1002/brb3.433
- Coffman, K. A., Dum, R. P., and Strick, P. L. (2011). Cerebellar vermis is a target of projections from the motor areas in the cerebral cortex. *Proc. Natl. Acad. Sci. U S A* 108, 16068–16073. doi: 10.1073/pnas.1107904108
- Courtetmanche, R., Robinson, J. C., and Aponte, D. I. (2013). Linking oscillations in cerebellar circuits. *Front. Neural Circuits* 7:125. doi: 10.3389/fncir.2013.00125
- Dalal, S. S., Guggisberg, A. G., Edwards, E., Sekihara, K., Findlay, A. M., Canolty, R. T., et al. (2008). Five-dimensional neuroimaging: localization of the time-frequency dynamics of cortical activity. *Neuroimage* 40, 1686–1700. doi: 10.1016/j.neuroimage.2008.01.023
- Delmaire, C., Vidailhet, M., Elbaz, A., Bourdain, F., Bleton, J. P., Sangla, S., et al. (2007). Structural abnormalities in the cerebellum and sensorimotor circuit in writer's cramp. *Neurology* 69, 376–380. doi: 10.1212/01.wnl.0000266591.49624.1a
- Delnoot, C. C. S., Pasman, J. W., Beckmann, C. F., and van de Warrenburg, B. P. C. (2013). Task-free functional mri in cervical dystonia reveals multi-network changes that partially normalize with botulinum toxin. *PLoS One* 8:e62877. doi: 10.1371/journal.pone.0062877
- Devanagondi, R., Egami, K., LeDoux, M. S., Hess, E. J., and Jinnah, H. A. (2007). Neuroanatomical substrates for paroxysmal dyskinesia in lethargic mice. *Neurobiol. Dis.* 27, 249–257. doi: 10.1016/j.nbd.2007.05.001
- Diedrichsen, J., Hashambhoy, Y., Rane, T., and Shadmehr, R. (2005). Neural correlates of reach errors. *J. Neurosci.* 25, 9919–9931. doi: 10.1523/jneurosci.1874-05.2005

- Fan, X., Hughes, K. E., Jinnah, H. A., and Hess, E. J. (2012). Selective and sustained α -amino-3-hydroxy-5-methyl-4-isoxazolepropionic acid receptor activation in cerebellum induces dystonia in mice. *J. Pharmacol. Exp. Ther.* 340, 733–741. doi: 10.1124/jpet.111.190082
- Fedina, L., Hultborn, H., and Illert, M. (1975). Facilitation from contralateral primary afferents of interneuronal transmission in the Ia inhibitory pathway to motoneurons. *Acta Physiol. Scand.* 94, 198–221. doi: 10.1111/j.1748-1716.1975.tb05880.x
- Fremont, R., Calderon, D. P., Maleki, S., and Khodakhah, K. (2014). Abnormal high-frequency burst firing of cerebellar neurons in rapid-onset dystonia-parkinsonism. *J. Neurosci.* 34, 11723–11732. doi: 10.1523/JNEUROSCI.1409-14.2014
- Futami, T., Kano, M., Sento, S., and Shinoda, Y. (1986). Synaptic organization of the cerebello-thalamo-cerebral pathway in the cat. III. Cerebellar input to corticofugal neurons destined for different subcortical nuclei in areas 4 and 6. *Neurosci. Res.* 3, 321–344. doi: 10.1016/0168-0102(86)90024-6
- Gallea, C., Herath, P., Voon, V., Lerner, A., Ostuni, J., Saad, Z., et al. (2018). Loss of inhibition in sensorimotor networks in focal hand dystonia. *Neuroimage Clin.* 17, 90–97. doi: 10.1016/j.nicl.2017.10.011
- Gallea, C., Horowitz, S. G., 'Ali Najee-Ullah, M., and Hallett, M. (2016). Impairment of a parieto-premotor network specialized for handwriting in writer's cramp. *Hum. Brain Mapp.* 37, 4363–4375. doi: 10.1002/hbm.23315
- Guggisberg, A. G., Dalal, S. S., Findlay, A. M., and Nagarajan, S. S. (2008). High-frequency oscillations in distributed neural networks reveal the dynamics of human decision making. *Front. Hum. Neurosci.* 1:14. doi: 10.3389/fneuro.09.014.2007
- Helmich, R. C., Janssen, M. J. R., Oyen, W. J. G., Bloem, B. R., and Toni, I. (2011). Pallidal dysfunction drives a cerebellothalamic circuit into Parkinson tremor. *Ann. Neurol.* 69, 269–281. doi: 10.1002/ana.22361
- Hinkley, L. B. N., Dolberg, R., Honma, S., Findlay, A., Byl, N. N., and Nagarajan, S. S. (2012). Aberrant oscillatory activity during simple movement in task-specific focal hand dystonia. *Front. Neurol.* 3:165. doi: 10.3389/fneuro.2012.00165
- Hisatsune, C., Miyamoto, H., Hirono, M., Yamaguchi, N., Sugawara, T., Ogawa, N., et al. (2013). IP3R1 deficiency in the cerebellum/brainstem causes basal ganglia-independent dystonia by triggering tonic Purkinje cell firings in mice. *Front. Neural Circuits* 7:156. doi: 10.3389/fncir.2013.00156
- Houweling, S., Daffertshofer, A., van Dijk, B. W., and Beek, P. J. (2008). Neural changes induced by learning a challenging perceptual-motor task. *Neuroimage* 41, 1395–1407. doi: 10.1016/j.neuroimage.2008.03.023
- Hubsch, C., Roze, E., Popa, T., Russo, M., Balachandran, A., Pradeep, S., et al. (2013). Defective cerebellar control of cortical plasticity in writer's cramp. *Brain* 136, 2050–2062. doi: 10.1093/brain/awt147
- Hutchinson, M., Nakamura, T., Moeller, J. R., Antonini, A., Belakhlef, A., Dhawan, V., et al. (2000). The metabolic topography of essential blepharospasm: a focal dystonia with general implications. *Neurology* 55, 673–677. doi: 10.1212/wnl.55.5.673
- Jin, S.-H., Lin, P., Auh, S., and Hallett, M. (2011). Abnormal functional connectivity in focal hand dystonia: mutual information analysis in EEG. *Mov. Disord.* 26, 1274–1281. doi: 10.1002/mds.23675
- Kelly, R. M., and Strick, P. L. (2003). Cerebellar loops with motor cortex and prefrontal cortex of a nonhuman primate. *J. Neurosci.* 23, 8432–8444. doi: 10.1523/jneurosci.23-23-08432.2003
- Kujala, J., Pammer, K., Cornelissen, P., Roebroek, A., Formisano, E., and Salmelin, R. (2007). Phase coupling in a cerebro-cerebellar network at 8–13 Hz during reading. *Cereb. Cortex* 17, 1476–1485. doi: 10.1093/cercor/bhl059
- LeDoux, M. S. (2011). Animal models of dystonia: Lessons from a mutant rat. *Neurobiol. Dis.* 42, 152–161. doi: 10.1016/j.nbd.2010.11.006
- LeDoux, M. S., Lorden, J. F., and Ervin, J. M. (1993). Cerebellectomy eliminates the motor syndrome of the genetically dystonic rat. *Exp. Neurol.* 120, 302–310. doi: 10.1006/exnr.1993.1064
- LeDoux, M. S., Lorden, J. F., and Meinzen-Derr, J. (1995). Selective elimination of cerebellar output in the genetically dystonic rat. *Brain Res.* 697, 91–103. doi: 10.1016/0006-8993(95)00792-0
- Liu, X., Wang, S., Yianni, J., Nandi, D., Bain, P. G., Gregory, R., et al. (2008). The sensory and motor representation of synchronized oscillations in the globus pallidus in patients with primary dystonia. *Brain* 131, 1562–1573. doi: 10.1093/brain/awn083
- Louis, E. D. (2014). From neurons to neuron neighborhoods: the rewiring of the cerebellar cortex in essential tremor. *Cerebellum* 13, 501–512. doi: 10.1007/s12311-013-0545-0
- Mantel, T., Meindl, T., Li, Y., Jochim, A., Gora-Stahlberg, G., Kräenbring, J., et al. (2018). Network-specific resting-state connectivity changes in the premotor-parietal axis in writer's cramp. *Neuroimage Clin.* 17, 137–144. doi: 10.1016/j.nicl.2017.10.001
- Middleton, S. J., Racca, C., Cunningham, M. O., Traub, R. D., Monyer, H., Knöpfel, T., et al. (2008). High-frequency network oscillations in cerebellar cortex. *Neuron* 58, 763–774. doi: 10.1016/j.neuron.2008.03.030
- Mima, T., Steger, J., Schulman, A. E., Gerloff, C., and Hallett, M. (2000). Electroencephalographic measurement of motor cortex control of muscle activity in humans. *Clin. Neurophysiol.* 111, 326–337. doi: 10.1016/s1388-2457(99)00229-1
- Mishra, J., Martinez, A., Sejnowski, T. J., and Hillyard, S. A. (2007). Early cross-modal interactions in auditory and visual cortex underlie a sound-induced visual illusion. *J. Neurosci.* 27, 4120–4131. doi: 10.1523/JNEUROSCI.4912-06.2007
- Na, J., Kakei, S., and Shinoda, Y. (1997). Cerebellar input to corticothalamic neurons in layers V and VI in the motor cortex. *Neurosci. Res.* 28, 77–91. doi: 10.1016/s0168-0102(97)00031-x
- Neumann, W.-J., Horn, A., Ewert, S., Huebl, J., Brücke, C., Slentz, C., et al. (2017). A localized pallidal physiologic marker in cervical dystonia. *Ann. Neurol.* 82, 912–924. doi: 10.1002/ana.25095
- Neumann, W.-J., Jha, A., Bock, A., Huebl, J., Horn, A., Schneider, G.-H., et al. (2015). Cortico-pallidal oscillatory connectivity in patients with dystonia. *Brain* 138, 1894–1906. doi: 10.1093/brain/awv109
- Neychev, V. K., Fan, X., Mitev, V. I., Hess, E. J., and Jinnah, H. A. (2008). The basal ganglia and cerebellum interact in the expression of dystonic movement. *Brain* 131, 2499–2509. doi: 10.1093/brain/awn168
- Ni, Z., Pinto, A. D., Lang, A. E., and Chen, R. (2010). Involvement of the cerebellothalamocortical pathway in Parkinson disease. *Ann. Neurol.* 68, 816–824. doi: 10.1002/ana.22221
- Niethammer, M., Carbon, M., Argyelan, M., and Eidelberg, D. (2011). Hereditary dystonia as a neurodevelopmental circuit disorder: evidence from neuroimaging. *Neurobiol. Dis.* 42, 202–209. doi: 10.1016/j.nbd.2010.10.010
- Nolte, G., Bai, O., Wheaton, L., Mari, Z., Vorbach, S., and Hallett, M. (2004). Identifying true brain interaction from EEG data using the imaginary part of coherency. *Clin. Neurophysiol.* 115, 2292–2307. doi: 10.1016/j.clinph.2004.04.029
- O'Connor, S. M., Berg, R. W., and Kleinfeld, D. (2002). Coherent electrical activity between vibrissa sensory areas of cerebellum and neocortex is enhanced during free whisking. *J. Neurophysiol.* 87, 2137–2148. doi: 10.1152/jn.00229.2001
- Oulad Ben Taib, N., Manto, M., Laute, M.-A., and Brotschi, J. (2005). The cerebellum modulates rodent cortical motor output after repetitive somatosensory stimulation. *Neurosurgery* 56, 811–820. doi: 10.1227/01.neu.0000156616.94446.00
- Pizoli, C. E., Jinnah, H. A., Billingsley, M. L., and Hess, E. J. (2002). Abnormal cerebellar signaling induces dystonia in mice. *J. Neurosci.* 22, 7825–7833. doi: 10.1523/jneurosci.22-17-07825.2002
- Popa, T., Hubsch, C., James, P., Richard, A., Russo, M., Pradeep, S., et al. (2018). Abnormal cerebellar processing of the neck proprioceptive information drives dysfunctions in cervical dystonia. *Sci. Rep.* 8:2263. doi: 10.1038/s41598-018-20510-1
- Popa, T., Russo, M., Vidailhet, M., Roze, E., Lehericy, S., Bonnet, C., et al. (2013). Cerebellar rTMS stimulation may induce prolonged clinical benefits in essential tremor and subjunct changes in functional connectivity: an open label trial. *Brain Stimul.* 6, 175–179. doi: 10.1016/j.brs.2012.04.009
- Proville, R. D., Spolidoro, M., Guyon, N., Dugué, G. P., Selimi, F., Isopé, P., et al. (2014). Cerebellum involvement in cortical sensorimotor circuits for the control of voluntary movements. *Nat. Neurosci.* 17, 1233–1239. doi: 10.1038/nn.3773
- Prudente, C. N., Hess, E. J., and Jinnah, H. A. (2014). Dystonia as a network disorder: what is the role of the cerebellum? *Neuroscience* 260, 23–35. doi: 10.1016/j.neuroscience.2013.11.062
- Raika, R. S., Pizoli, C. E., Weisz, C., van den Maagdenberg, A. M. J. M., Jinnah, H. A., and Hess, E. J. (2013). Limited regional cerebellar dysfunction

- induces focal dystonia in mice. *Neurobiol. Dis.* 49, 200–210. doi: 10.1016/j.nbd.2012.07.019
- Schoffelen, J.-M., Oostenveld, R., and Fries, P. (2005). Neuronal coherence as a mechanism of effective corticospinal interaction. *Science* 308, 111–113. doi: 10.1126/science.1107027
- Shakkottai, V. G., Batla, A., Bhatia, K., Dauer, W. T., Dresel, C., Niethammer, M., et al. (2017). Current opinions and areas of consensus on the role of the cerebellum in dystonia. *Cerebellum* 16, 577–594. doi: 10.1007/s12311-016-0825-6
- Stam, C. J., Nolte, G., and Daffertshofer, A. (2007). Phase lag index: assessment of functional connectivity from multi channel EEG and MEG with diminished bias from common sources. *Hum. Brain Mapp.* 28, 1178–1193. doi: 10.1002/hbm.20346
- Stamelou, M., Edwards, M. J., Hallett, M., and Bhatia, K. P. (2012). The non-motor syndrome of primary dystonia: clinical and pathophysiological implications. *Brain* 135, 1668–1681. doi: 10.1093/brain/awr224
- Steriade, M. (1995). Two channels in the cerebellothalamocortical system. *J. Comp. Neurol.* 354, 57–70. doi: 10.1002/cne.903540106
- Uluğ, A. M., Vo, A., Argyelan, M., Tanabe, L., Schiffer, W. K., Dewey, S., et al. (2011). Cerebellothalamocortical pathway abnormalities in torsinA DYT1 knock-in mice. *Proc. Natl. Acad. Sci. U S A* 108, 6638–6643. doi: 10.1073/pnas.1016445108
- Wespatat, V., Tennigkeit, F., and Singer, W. (2004). Phase sensitivity of synaptic modifications in oscillating cells of rat visual cortex. *J. Neurosci.* 24, 9067–9075. doi: 10.1523/jneurosci.2221-04.2004
- White, J. J., and Sillitoe, R. V. (2017). Genetic silencing of olivocerebellar synapses causes dystonia-like behaviour in mice. *Nat. Commun.* 8:14912. doi: 10.1038/ncomms14912
- Conflict of Interest Statement:** The authors declare that the research was conducted in the absence of any commercial or financial relationships that could be construed as a potential conflict of interest.

Copyright © 2018 Georgescu, Georgescu, Zahiu, Șteopoaie, Morozan, Pană, Zăgrean and Popa. This is an open-access article distributed under the terms of the Creative Commons Attribution License (CC BY). The use, distribution or reproduction in other forums is permitted, provided the original author(s) and the copyright owner(s) are credited and that the original publication in this journal is cited, in accordance with accepted academic practice. No use, distribution or reproduction is permitted which does not comply with these terms.



How Do Cells of the Oligodendrocyte Lineage Affect Neuronal Circuits to Influence Motor Function, Memory and Mood?

Renee E. Pepper[†], Kimberley A. Pitman[†], Carlie L. Cullen and Kaylene M. Young^{*}

Menzies Institute for Medical Research, University of Tasmania, Hobart, TAS, Australia

Oligodendrocyte progenitor cells (OPCs) are immature cells in the central nervous system (CNS) that can rapidly respond to changes within their environment by modulating their proliferation, motility and differentiation. OPCs differentiate into myelinating oligodendrocytes throughout life, and both cell types have been implicated in maintaining and modulating neuronal function to affect motor performance, cognition and emotional state. However, questions remain about the mechanisms employed by OPCs and oligodendrocytes to regulate circuit function, including whether OPCs can only influence circuits through their generation of new oligodendrocytes, or can play other regulatory roles within the CNS. In this review, we detail the molecular and cellular mechanisms that allow OPCs, newborn oligodendrocytes and pre-existing oligodendrocytes to regulate circuit function and ultimately influence behavioral outcomes.

Keywords: NG2 glia, myelin, oligodendrocyte, anxiety, motor function, depression, learning, neuronal activity

OPEN ACCESS

Edited by:

Philippe Isopé,
Centre National de la Recherche
Scientifique (CNRS), France

Reviewed by:

Fernando de Castro,
Instituto Cajal (IC), Spain
Herbert Hildebrandt,
Hannover Medical School, Germany

*Correspondence:

Kaylene M. Young
kaylene.young@utas.edu.au

[†]These authors have contributed
equally to this work

Received: 30 July 2018

Accepted: 17 October 2018

Published: 16 November 2018

Citation:

Pepper RE, Pitman KA, Cullen CL
and Young KM (2018) How Do Cells
of the Oligodendrocyte Lineage
Affect Neuronal Circuits to Influence
Motor Function, Memory and Mood?
Front. Cell. Neurosci. 12:399.
doi: 10.3389/fncel.2018.00399

INTRODUCTION

Within the central nervous system (CNS), cells of the oligodendrocyte lineage are critical regulators of circuit function. Oligodendrocyte progenitor cells (OPCs) generate oligodendrocytes that elaborate myelin membrane to ensheath discrete axon segments, effectively reducing axonal capacitance and enabling the saltatory conduction of action potentials. However, their role in circuit regulation does not stop there. Herein, we detail the maturation of OPCs into pre-myelinating and myelinating oligodendrocytes and outline how each cell type can influence neural network construction, operation and plasticity to ensure healthy CNS function.

OLIGODENDROCYTE PROGENITOR CELLS

Origin and Other Sources of Heterogeneity

OPCs, also known as oligodendrocyte precursors or NG2-glia, can be identified by their expression of platelet-derived growth factor receptor α (PDGFR α ; Stallcup and Beasley, 1987; Hart et al., 1989; Pringle et al., 1992; Rivers et al., 2008) or the NG2 proteoglycan (Zhu et al., 2008) and the transcription factors SOX10 (Kuhlbrodt et al., 1998) and OLIG2 (Lu et al., 2000; Zhou et al., 2000; Dimou et al., 2008; **Figure 1**). In human brain development, PDGFR α ⁺ OPCs are detected in the forebrain at ~10 weeks of gestation and increase in number until ~15 weeks (Jakovcevski et al., 2009). A high density of OPCs in the ventricular and subventricular zones of the ganglionic eminence and cortex suggests that OPCs are

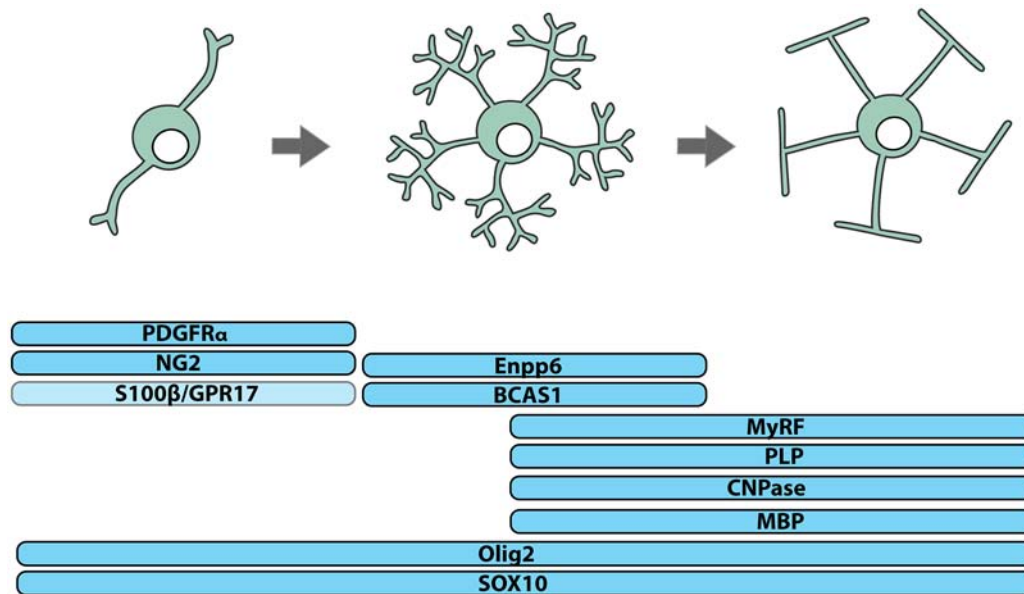


FIGURE 1 | Identifying cells of the oligodendrocyte lineage. Cells of the oligodendrocyte lineage can be subdivided into three stages of differentiation based on protein expression: oligodendrocyte progenitor cells (OPCs), premyelinating oligodendrocytes and myelinating oligodendrocytes. Essentially all OPCs co-express the NG2 proteoglycan and PDGFR α , while only a subset express S100 β and/or the G-protein coupled receptor, GPR17. Premyelinating oligodendrocytes express Breast Carcinoma Amplified Sequence-1 (BCAS1) and Ectonucleotide Pyrophosphatase Phosphodiesterase 6 (Enpp6), and upregulate Myelin Regulatory Factor (MyRF). Myelinating oligodendrocytes express myelin-related proteins including Myelin Basic Protein (MBP), Proteolipid Protein (PLP) and 2',3'-Cyclic-nucleotide 3'-phosphodiesterase (CNPase). All cells of the oligodendrocyte lineage express the transcription factors OLIG2 and SOX10.

generated by ventral and dorsal neural stem cell populations (Jakovcevski et al., 2009) and a stream of PDGFR α ⁺ OPCs bridging the ganglionic eminence and cortex, suggests that OPCs of ventral origin migrate to populate the cortex (Rakic and Zecevic, 2003).

The mixed dorsal and ventral origin of cortical OPCs has been verified by histological (Ivanova et al., 2003) and cre-lox lineage tracing (Kessaris et al., 2006) studies of the developing mouse forebrain, which revealed that OPCs are first generated in the ventricular zone of the medial ganglionic eminence (MGE) at embryonic day (E)12 and migrate in a number of directions, including into the developing cortex, arriving by ~E16. OPCs are subsequently generated from the ventricular zones of the lateral ganglionic eminence (LGE) and cortex (Kessaris et al., 2006), and while MGE-derived OPCs do not persist postnatally, those derived from the LGE and cortex remain throughout adulthood (Kessaris et al., 2006).

OPCs in the spinal cord have a similarly mixed origin. In the human (Hajihosseini et al., 1996) and mouse (Fu et al., 2002; Masahira et al., 2006) spinal cord, the ventrally-located premotor neuron (pMN) domain is the first and major source of OPCs. However, studies of mouse development indicate that ~3 days after these OPCs are produced, others are generated from more dorsal domains (Cai et al., 2005; Fogarty et al., 2005; Vallstedt et al., 2005; Tripathi et al., 2011).

OPCs of different embryonic origin can have similar electrophysiological properties (Tripathi et al., 2011) and following the conditional ablation of OPCs from one site of origin, OPCs from another expand to occupy the unpopulated

territory (Kessaris et al., 2006), indicating that a level of phenotypic and functional redundancy exists between different OPC populations. However, the long-term consequence of ablating OPCs from a given origin has not been explored, and it is unclear how origin contributes to reports of postnatal OPC phenotypic and functional heterogeneity. In the postnatal CNS, only some OPCs express S100 β (Vives et al., 2003; Hachem et al., 2005) or the G protein-coupled receptor 17 (GPR17), and GPR17⁺ OPCs are less likely to differentiate to produce oligodendrocytes than GPR17-negative OPCs (Viganò et al., 2016; **Figure 1**). It is important to consider that such differences in gene expression and function could result from divergent signaling within the postnatal CNS, as adult human OPCs have been shown to locally upregulate the fibroblast growth factor receptor (FGFR)1 when they are associated with active demyelinating lesions (Clemente et al., 2011).

OPCs Interact With the CNS Vasculature

Once generated, human and mouse OPCs associate with the vascular endothelium and migrate along and between blood vessels, extending a leading process prior to translocation of the cell body (Tsai et al., 2016). As OPCs migrate, they also divide, so that they expand in number to occupy the CNS (van Heyningen et al., 2001; Kelenis et al., 2018). Postnatally, OPCs continue to proliferate (Rivers et al., 2008; Psachoulia et al., 2009; Zhu et al., 2011; Clarke et al., 2012; Hughes et al., 2013). In acute brain slices generated from early postnatal mice, OPCs divide asymmetrically to produce an OPC and a new oligodendrocyte or symmetrically to produce two OPCs

or two oligodendrocytes (Zhu et al., 2011). Symmetric and asymmetric OPC divisions also occur in the adult mouse brain, however, *in vivo* imaging has revealed that OPCs occupy and maintain spatially discrete domains through a process of self-repulsion and that proliferation rarely immediately precedes differentiation—rather OPC differentiation appears to trigger the proliferation of adjacent OPCs, ensuring homeostatic progenitor cell replacement (Hughes et al., 2013).

In development, while using the vasculature as a scaffold for migration, OPCs exert a strong regulatory influence over angiogenesis and vascular cell function (Figure 2). OPCs secrete transforming growth factor (TGF) β 1 to promote tight junction protein expression by endothelial cells, which enhances the integrity of the blood brain barrier (BBB; Seo et al., 2014). They also secrete unidentified factors that enhance the proliferation of endothelial cells (Yuen et al., 2014) and pericytes (Maki et al., 2015). Furthermore, as OPCs expand to occupy the brain, they enter regions that have insufficient vasculature to meet oxygen demands. Hypoxia activates the oxygen-sensing subunits of the hypoxia-inducible factor (HIF) complex within OPCs and drives their secretion of Wnt7a/7b, to promote angiogenesis and increase oxygen supply to that region of the developing brain (Yuen et al., 2014; Figure 2).

OPCs Modulate Neuroinflammation

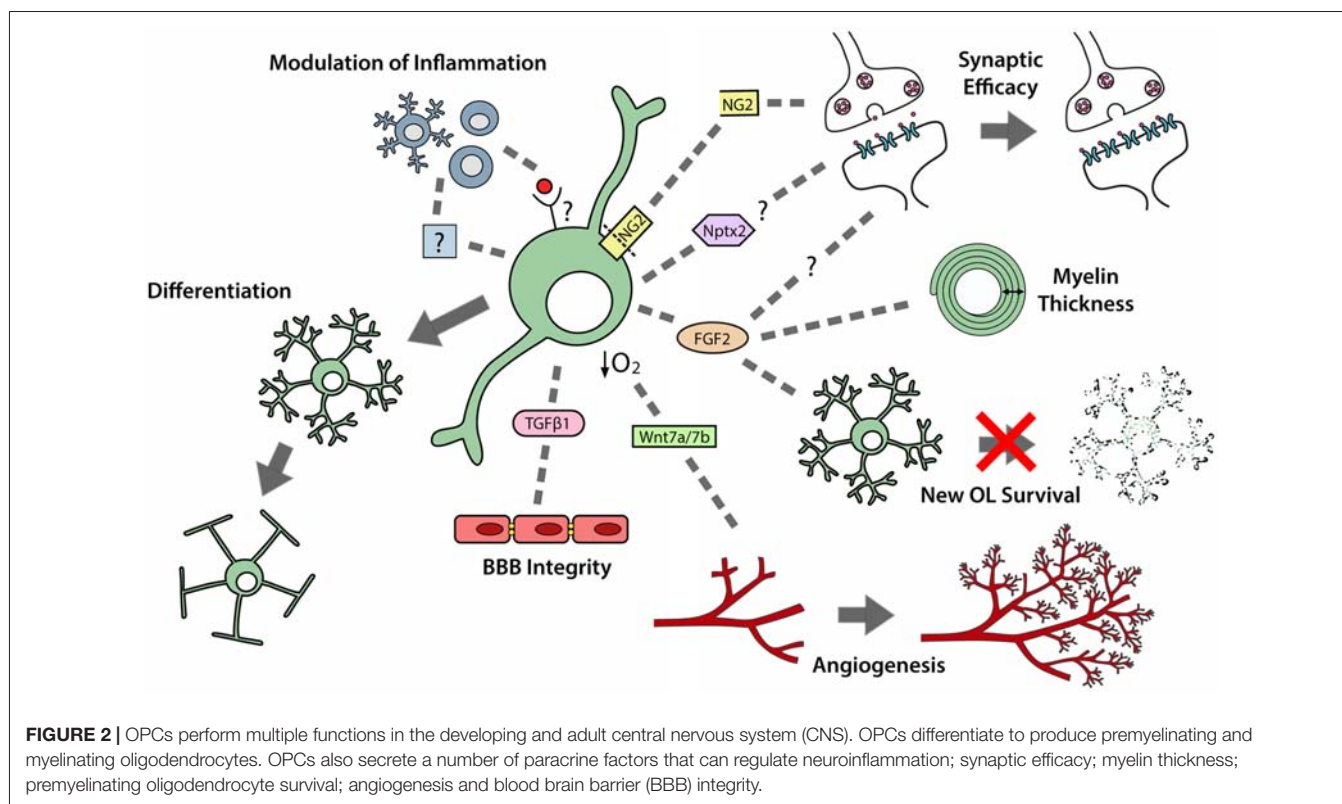
In postnatal development, microglia are important regulators of OPC maintenance and oligodendrogenesis, as their pharmacological depletion results in fewer OPCs populating the corpus callosum and impaired oligodendrogenesis in the

corpus callosum, cerebellum and cortex (Hagemeyer et al., 2017). This effect may, in part, result from a loss of microglial-derived transglutaminase-2 (Tgm2), as *Tgm2* knockout mice also have reduced OPC proliferation in the corpus callosum and the conditional deletion of *Tgm2* from microglia produces a small but significant decrease in the number of callosal oligodendrocytes produced by P28 (Giera et al., 2018). OPCs can reciprocally regulate microglial function, as the transgenic ablation of NG2⁺ cells from the adult rat brain activates microglia (Figure 2), leading to hippocampal neuronal cell death (Nakano et al., 2017).

The extent to which OPCs interact with peripheral immune cells in the healthy CNS is unclear, however their expression of genes associated with antigen presentation and inflammation (Zhang et al., 2014) suggests that they can modulate or even exacerbate neuroinflammation (Figure 2). Data obtained using an adoptive transfer model of experimental autoimmune encephalomyelitis (EAE) support this idea, as they show that OPCs can respond to activated Th17 cells (Wang et al., 2017). Th17 cells are known to secrete the cytokine interleukin-17 (IL-17), which can bind to IL-17 receptors expressed by OPCs to activate notch1 signaling and a pro-inflammatory cascade that leads to immune-mediated demyelination of the CNS (Wang et al., 2017).

OPCs Modulate Synaptic Efficacy

Postnatally, cortical OPCs play an important role in memory formation, as the activity-dependent cleavage of NG2 can modulate α -amino-3-hydroxy-5-methyl-4-isoxazolepropionic



acid (AMPA) and *N*-methyl-D-aspartate (NMDA) receptor mediated currents, and enhance NMDA receptor-dependent long-term potentiation in pyramidal neurons (Sakry et al., 2014; **Figure 2**). As OPCs are found throughout the CNS, it is possible that they influence synaptic strength in other regions via cleaved NG2 or the secretion of other factors able to modulate neuronal communication and synaptic plasticity (reviewed by Parolisi and Boda, 2018). For example, Nptx2 (neuronal pentraxin 2), also known as neuronal activity regulated pentraxin (Narp), is a secreted immediate-early gene product that can modulate the clustering of AMPA receptors (O'Brien et al., 1999), regulate excitatory synapse function (Gu et al., 2013; Pelkey et al., 2015), and influence the functional integration of interneurons into neural circuits (Pelkey et al., 2015). As developmental OPCs express Nptx2 (Sakry et al., 2015), Nptx2 secretion may be another mechanism by which OPCs influence synaptic efficacy (**Figure 2**).

PRE-MYELINATING OLIGODENDROCYTES

While OPCs perform a number of functions in the CNS, their best-known function is the life-long generation of oligodendrocytes (**Figures 1, 2**). OPCs differentiate to produce oligodendrocytes during postnatal development (Zhu et al., 2008, 2011) and throughout adulthood (Dimou et al., 2008; Rivers et al., 2008; Kang et al., 2010; Zhu et al., 2011; Young et al., 2013). They initially differentiate into pre-myelinating oligodendrocytes, retaining their expression of SOX10 and OLIG2, losing PDGFR α and NG2, and gaining expression of Breast Carcinoma Amplified Sequence 1 (BCAS1; Zhang et al., 2014; Fard et al., 2017), Ectonucleotide Pyrophosphatase Phosphodiesterase 6 (ENPP6; Zhang et al., 2014; Xiao et al., 2016) and Myelin Regulator Factor (MyRF; Cahoy et al., 2008; Emery et al., 2009; **Figure 1**). This early differentiation step also involves significant morphological change, most obviously the symmetric elaboration of a dense network of fine processes (Trapp et al., 1997).

In the P7–P21 rat cortex ~20% of pre-myelinating oligodendrocytes are degenerating at any one time (Trapp et al., 1997) and ~78% die within 2 days of differentiation in the adult mouse cortex (Hughes et al., 2018). The survival of pre-myelinating oligodendrocytes is enhanced by FGFR signaling *in vitro* (Palser et al., 2009) and β 1-integrin (Benninger et al., 2006) or glutamatergic (Kougioumtzidou et al., 2017) signaling *in vivo*. While it is possible that this largely transient cell population performs currently unknown regulatory functions in the CNS, its only known function is to act as a reservoir of cells available for further differentiation into mature, myelinating oligodendrocytes.

MYELINATING OLIGODENDROCYTES

Myelination

The major function of oligodendrocytes is to add myelin internodes to both excitatory (Young et al., 2013; Tomassy et al., 2014) and inhibitory (Micheva et al., 2016; Stedehouder and Kushner, 2017; Stedehouder et al., 2017, 2018) neurons

in the CNS (**Figure 3**). Oligodendrocyte maturation requires the transcription factor MyRF (Emery et al., 2009), but is influenced by extrinsic signals, including neuronal activity (Barres and Raff, 1999; Lundgaard et al., 2013; Gibson et al., 2014). At the onset of myelination, oligodendrocytes extend motile processes to contact axons (Kirby et al., 2006; Hughes et al., 2013). Following contact, the oligodendrocyte process flattens to form a sheet that is tightly attached at the cytoplasmic surfaces. The leading edge of this growing myelin sheath spirals around the axon, extending the new wrap underneath the preceding one, while simultaneously extending laterally along the axon (Snaidero et al., 2014). Myelin initiation requires Arp2/3 complex-dependent actin assembly (Zuchero et al., 2015) and ADF/cofilin-1-dependent actin depolymerization drives myelin wrapping (Nawaz et al., 2015). The major myelin protein, myelin basic protein (MBP), is also necessary for actin disassembly and myelin compaction, while 2', 3'-Cyclic-nucleotide 3'-phosphodiesterase (CNPase) counteracts myelin compaction allowing myelin formation, as well as the formation of uncompacted myelinic channels within the sheath (Snaidero et al., 2017).

A single oligodendrocyte elaborates and supports myelin sheaths on numerous axons. Time-lapse imaging of the developing zebrafish spinal cord has revealed that oligodendrocytes initially over-produce short myelin sheaths (Czopka et al., 2013; Hines et al., 2015; Mensch et al., 2015) and that sheath retraction and extension is regulated by local calcium signaling induced by neuronal activity (Baraban et al., 2018; Krasnow et al., 2018). Long-duration, high-amplitude calcium bursts facilitate calpain-mediated sheath retraction, while lower-amplitude, short-duration calcium bursts correlate with the rate of sheath extension (Baraban et al., 2018; Krasnow et al., 2018). Sheath retraction, stabilization and extension occurs within a 5-h window (Czopka et al., 2013) and while final internode length is influenced by intrinsic properties of the maturing oligodendrocyte, it can also be influenced by extrinsic factors such as axon diameter (Bechler et al., 2015). Extrinsic factors also regulate myelin thickness, for example, activation of FGFR2 in the paranodal loops of the adult mouse spinal cord, enhances MyRF expression and increases Extracellular Signal-Related Kinase (ERK)1/2 and, in turn, mammalian Target of Rapamycin (mTOR)C1 activity to increase myelin thickness (Furusato et al., 2017).

Myelinating Oligodendrocyte Survival

Once formed, oligodendrocytes are long-lived cells (Yeung et al., 2014; Tripathi et al., 2017; Hill et al., 2018; Hughes et al., 2018). In mice, the overall density of CC1⁺ oligodendrocytes was found to increase in the corpus callosum, motor cortex and spinal cord throughout adulthood, but the density of GFP⁺ oligodendrocytes born prior to P60 (*Opalin-CreER^{T2} :: Tau-mGFP* mice) remained unchanged until old age (\geq P240; (Tripathi et al., 2017). Consistent with these data, the *in vivo* imaging of oligodendrocytes in the somatosensory cortex of adult mice, revealed that mature oligodendrocytes are remarkably stable (Hill et al., 2018; Hughes et al., 2018). However, these

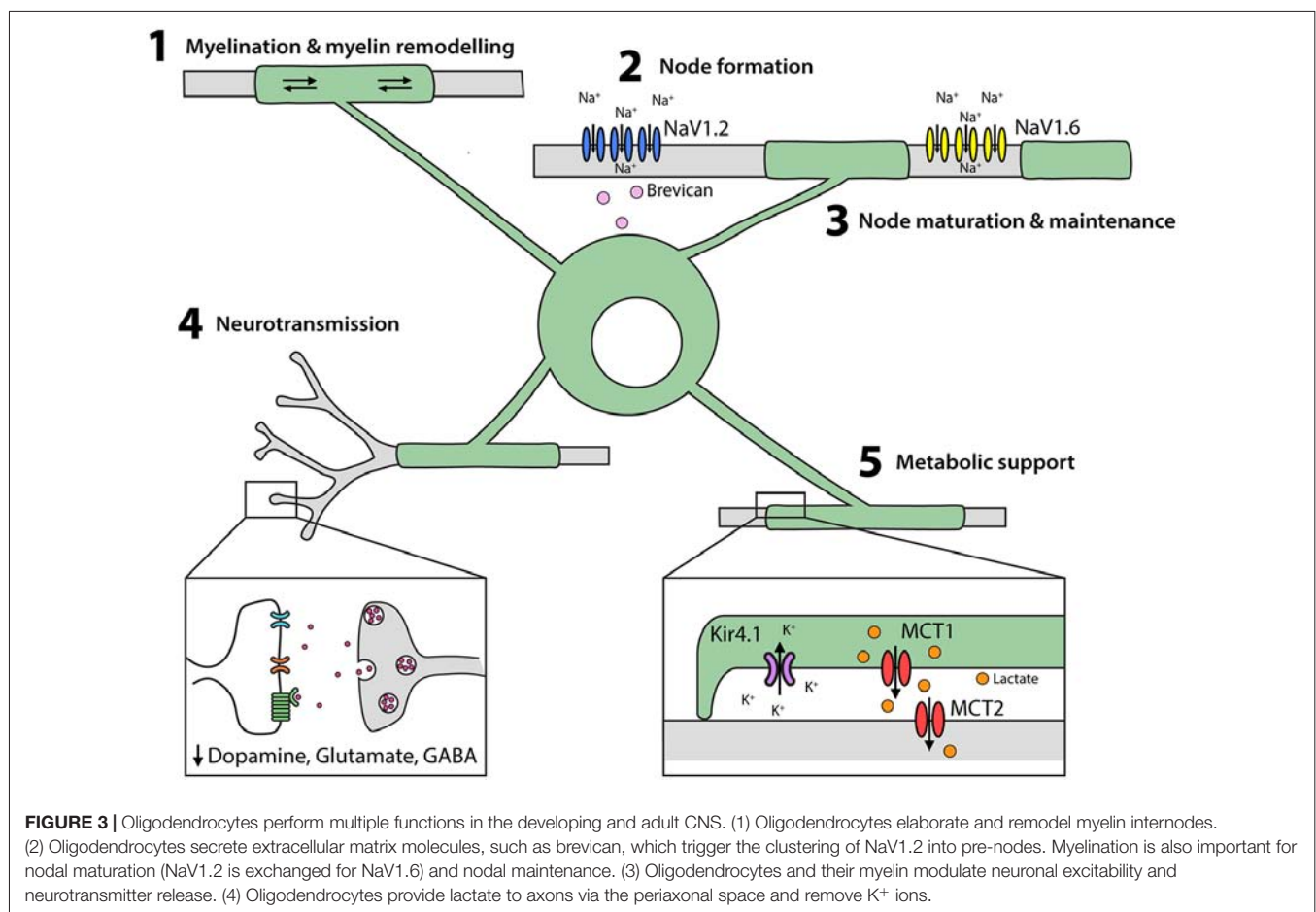
experiments also revealed that adult-born oligodendrocytes add new myelin internodes to partially myelinated axons throughout life, and that this addition is not accompanied by the loss of pre-existing internodes (Hill et al., 2018), suggesting that adult oligodendrogenesis is not simply required for cell replacement or myelin turnover, but instead represents a novel form of neural plasticity, that modifies the myelination of existing circuits.

Myelin Remodeling

Axons are not uniformly myelinated along their length in the adult mouse brain—some are unmyelinated, at least for long stretches, and others are partially myelinated (Tomassy et al., 2014). The myelin profile of individual axons can be modified by the addition of new internodes or by modifying existing internodes in a process termed myelin remodeling. When new oligodendrocytes are added to the adult mouse somatosensory cortex, they elaborate an equivalent number of internodes, that are similar in length to those produced by developmentally-born oligodendrocytes in the same region (Hughes et al., 2018). However, the myelin internodes retain a certain level of plasticity after elaboration (Hill et al., 2018). For a single oligodendrocyte, some sheaths remain stable over time while others change in length (Figure 3), suggesting that internode plasticity is modulated at the level

of the internode, rather than the level of the oligodendrocyte. Overall, ~81% of sheaths are stable, ~15% extend and ~4% retract between P60 and P90 (Hill et al., 2018) and this drops to ~1% of sheaths extending or retracting between P300 and P420 (Hughes et al., 2018), suggesting that myelin remodeling decreases with ageing. As internode extension would require uncoupling of the paranodal junction and either stretching of the existing myelin sheath or the addition of new myelin membrane, it is difficult to imagine how this might occur. It is also unclear what regulates this subtle form of myelin remodeling, or the purpose of this plasticity for axon function. However, it conceivably provides a mechanism for the fine-tuning of myelination after internode elaboration is complete.

The process of myelin remodeling differs between the mouse optic nerve and cortex, perhaps because optic nerve axons are essentially fully myelinated during development. In the optic nerve, adult-born oligodendrocytes morphologically differ from those generated in the same region during postnatal development (Young et al., 2013). Oligodendrocytes born between 4 and 6 months of age elaborate more internodes that are significantly shorter than those elaborated in development (Butt et al., 1994; Young et al., 2013). Additionally, the number of new oligodendrocytes added over this period exceeds the number that would be required to myelinate



the small number of unmyelinated or partially myelinated optic nerve axons remaining (Young et al., 2013). These data may suggest that oligodendrocytes are less stable in the optic nerve compared to the cortex, as oligodendrocyte and myelin turnover could explain the need for so many additional oligodendrocytes. Alternatively, developmentally-born oligodendrocytes may significantly remodel their sheaths, to provide space for adult-born oligodendrocytes to elaborate short myelin sheaths. The addition of numerous short myelin sheaths by adult-born oligodendrocytes is predicted to modify axonal conduction velocity (Young et al., 2013), but may also ensure that a larger number of oligodendrocytes are available to meet the metabolic needs of axons (see below).

The Generation and Maintenance of Nodes of Ranvier

While the dendrites and soma of neurons receive input, the axon supports output i.e., action potential initiation and propagation. The myelination of axons reduces their effective membrane capacitance and speeds up action potential conduction (Rasminsky and Sears, 1972), with action potentials being regenerated at the small ($\sim 1 \mu\text{m}$) excitable axon domains called nodes of Ranvier. Nodes of Ranvier are characterized by a high density of voltage-gated sodium channels (NaV) and are immediately flanked by the paranodal and juxtaparanodal domains of myelin internodes. In the CNS, clustering of NaV at the nodes of Ranvier is coordinated by oligodendrocytes (reviewed by Freeman et al., 2016; Zhang and Rasband, 2016).

In the early stages of node formation, the NaV subunits NaV1.1 and NaV1.2 cluster to form pre-nodes, and this process can be triggered in cultured retinal ganglion and hippocampal neurons by exposure to oligodendrocyte-conditioned medium (Kaplan et al., 2001; Freeman et al., 2015). *In vivo*, it has been shown that glial-derived extracellular matrix molecules, such as brevican, regulate NaV clustering in an ankyrin G-dependent manner (Feinberg et al., 2010; Freeman et al., 2016; **Figure 3**), with ankyrin-G bridging Neurofascin 186 in the axonal cytoskeleton and NaV in the axonal membrane (Wang et al., 2014; Xu and Cooper, 2015). Node formation along cortical projection neurons is concomitant with myelination, however pre-nodes containing NaV1.2 form along excitatory axons in the developing rat optic nerve (Kaplan et al., 2001) and on GABAergic axons in the rat and mouse cortex before the onset of myelination (Freeman et al., 2015). Cell-attached patch clamp recordings from cultured hippocampal interneurons support the ability of these pre-nodes to increase conduction velocity (Freeman et al., 2015), however, myelination is required for nodal maturation and the maintenance of saltatory conduction.

During nodal maturation NaV1.2 is replaced with NaV1.6 (**Figure 3**). While oligodendrocyte-conditioned medium is insufficient to induce the clustering of NaV1.6, this process does occur in neurons that are co-cultured with astrocytes and oligodendrocytes (Freeman et al., 2015). During myelination, the axonal proteins contactin and contactin-associated protein

(caspr) interact with neurofascin 155 in the oligodendrocyte myelin loops (Peles et al., 1997; Bhat et al., 2001; Charles et al., 2002; Sherman et al., 2005) to form the paranodal junctions that stabilize the nodes. Disruption of the paranodal junctions by gene deletion (Suzuki et al., 2004) or demyelination (Hamada and Kole, 2015) has significant effects on sodium channel (particularly NaV1.6) expression and clustering, and NaV and voltage-gated potassium channels (KV) diffuse between the node and the paranode, short-circuiting the node (Rosenbluth, 2009). These data indicate that oligodendrocytes play a role in node of Ranvier formation, maturation and maintenance (**Figure 3**).

Myelinating Oligodendrocytes Regulate Neuronal Excitability

It has been suggested that myelination can affect the intrinsic excitability of axons, as spontaneous supra-threshold depolarizations and antidromic action potentials are ectopically generated in the distal regions of demyelinated axons (Hamada and Kole, 2015). This may relate to the ability of oligodendrocytes to regulate potassium homeostasis in highly myelinated white matter regions (Larson et al., 2018). In mice, the conditional deletion of the inwardly rectifying potassium channel, Kir4.1, from mature oligodendrocytes, does not alter myelination but slows potassium clearance in the corpus callosum and optic nerve, causing pathological neuronal hyperexcitability (Larson et al., 2018).

Oligodendrocytes and their associated myelin may also influence neurotransmitter release and efficacy in the CNS (**Figure 3**), as mice with reduced oligodendrocyte number and/or impaired myelination have enhanced evoked dopamine release in the striatum (Roy et al., 2007) and elevated dopamine expression in the prefrontal cortex (Xu et al., 2010). Furthermore, in mice with altered myelin ultrastructure, glutamate and glycine expression is increased in the superior olivary complex and GABA expression increased in the amygdala and ventral hippocampus (Maheras et al., 2018). These findings may reflect the ability of myelination to reduce neuronal excitability, but may alternatively be a secondary effect of myelin loss, whereby neurons undergo pre- or post-synaptic modifications in an attempt to compensate for impaired regulation of the circuit.

Myelination Regulates Conduction Velocity and Synchronicity

Myelination not only allows the rapid arrival of action potentials, but coordinates action potential synchrony (Freeman et al., 2016). It has been suggested that for large-diameter myelinated axons, such as motor-neurons, in which action potentials can travel at 80 ms^{-1} , myelination may principally enable speed, however, in cortical neurons where conduction is much slower ($\sim 0.5\text{--}4.5 \text{ ms}^{-1}$), myelination may principally promote synchrony (Freeman et al., 2016). Cortical neurons generate action potentials in an oscillatory rhythm, which synchronizes their discharge with high precision (Gray et al., 1989) and the maturation of neural synchrony across adolescence is associated with the development of cognitive functions,

including working memory and executive processes (James et al., 2008). GABAergic interneurons, particularly parvalbumin (PV)⁺ basket cells, are critical for establishing neural synchrony, and while a single interneuron may be sufficient to synchronize the firing of multiple pyramidal neurons, when coupled to other interneurons, via gap junctions, they can precisely synchronize the oscillations of many pyramidal neurons within the network (reviewed Uhlhaas et al., 2009). Oligodendrocytes and their associated myelin may facilitate the long-range synchronization of different cortical regions by ensuring the precision and frequency of the neural oscillations (Uhlhaas et al., 2009).

Oligodendrocytes are known to coordinate action potential arrival times and allow neurons to fire at high frequencies. Following the demyelination of layer V cortical pyramidal neurons, action potential conduction is no longer saltatory, but instead propagates as a slow, broad, continuous wave, and fails at high firing frequencies (Hamada et al., 2017). In systems such as the auditory system, the fidelity of timing of action potential arrival is critical, and in mice lacking CNS expression of *claudin11*, in which the passive properties of compact CNS myelin are altered, the myelinated, small diameter axons of the auditory pathway have slowed conduction and the resulting temporal dispersion (loss of synchronicity) is predicted to distort auditory perception (Maheras et al., 2018). Furthermore, dysmyelination of auditory system neurons is associated with spike failure and action potential “jitters” (Kim et al., 2013).

For myelination to precisely regulate action potential arrival time across multiple axons in any circuit, internodes must either: (i) be laid down with incredible precision during ensheathment; (ii) retain some level of plasticity, to allow adjustments to be made in internode length after ensheathment, or (iii) possess the ability to modify their ultrastructure in order to regulate conduction. While there is evidence that internode length can be adjusted (Hill et al., 2018; Hughes et al., 2018), the level of remodeling reported in the cortex appears insufficient to achieve synchronicity. However, node of Ranvier length may also be modulated, and on a larger scale, to fine-tune conduction velocity (Ford et al., 2015; Arancibia-Cárcamo et al., 2017). This has been difficult to reconcile experimentally as both the conditional deletion of a cohesion regulatory protein, *Esco2*, from all cells of the oligodendrocyte lineage (Schneider et al., 2016), and the overexpression of Anosmin-1 in mouse development (Murcia-Belmonte et al., 2016), lengthen nodes of Ranvier, but have opposing effects on action potential conduction velocity in the corpus callosum. Such differences may be explained by associated changes in internode length, axon diameter, myelin thickness, NaV1.6 density or axonal metabolic support, but highlight the need for carefully designed experiments that can selectively examine the contribution of nodal plasticity to conduction velocity regulation. While the mechanisms that underpin conduction velocity tuning are not fully elucidated, oligodendrocyte depolarization has been shown to directly increase conduction velocity (Yamazaki et al., 2007, 2014).

Oligodendrocytes Provide Metabolic Support to Axons

Oligodendrocytes provide metabolic support to axons, allowing them to influence neuronal homeostasis independently of conduction velocity modulation (Figure 3). It is for this reason, that mice lacking proteolipid protein (PLP), that have compact, though unstable myelin, are initially able to sustain conduction, but ultimately experience axon degeneration (Klugmann et al., 1997; Griffiths et al., 1998). Similarly, mice lacking CNPase have normal appearing myelin, but elaborate internodes that have abnormal inner tongue processes and paranodal loops (Lappe-Siefke et al., 2003; Rasband et al., 2005; Edgar et al., 2009), and, in the case of large caliber axons, have disrupted myelinic channels—a phenotype sufficient to cause progressive axonal degeneration (Zuchero et al., 2015). By contrast, oligodendrocytes in mice lacking MBP produce thin, uncompacted myelin sheaths that are insufficient to support saltatory conduction, but largely prevent axon degeneration (Loers et al., 2004). By comparing the phenotypes of these mice, it is clear that oligodendrocytes play an important role in supporting neuron survival, and that the elements of the myelin sheath that are critical for supporting action potential conduction, differ from those required for neuronal survival.

Oligodendrocytes require cytoplasmic myelinic channels to transfer short carbon-chain energy metabolites, such as pyruvate and lactate, to axons (reviewed Philips and Rothstein, 2017; Figure 3). Neuronal activity is associated with glutamate release, which binds NMDA receptors on oligodendrocytes and increases their glucose uptake and lactate production (Saab et al., 2016). Oligodendrocytes express the monocarboxylate transporter (MCT)1 which transports monocarboxylate metabolites and has a high affinity for lactate transport (Lee et al., 2012). As oligodendrocytes accumulate intracellular lactate it is transported via MCT1 into the periaxonal space and taken into neurons by MCT2 (Fünfschilling et al., 2012; Lee et al., 2012). Consistent with this mechanism, the conditional deletion of *Mct1* from oligodendrocytes results in severe axonal injury and motor neuron death in mice (Lee et al., 2012). Furthermore, in brain slices, MCT1- and MCT2-deficiency result in axonal degeneration, but only MCT1-deficiency can be rescued by the exogenous application of L-Lactate (Suzuki et al., 2011; Lee et al., 2012), as MCT2 can transport lactate directly into the axon.

Within the axon, lactate is converted to pyruvate that enters the mitochondrial citric acid cycle to drive oxidative phosphorylation and the generation of ATP, which is necessary to maintain the activity of NaV and KV to sustain the continuous, repetitive firing of action potentials (Almeida et al., 2001; Saez et al., 2014). Indeed, the failure of de/dys-myelinated axons to fire at high firing frequencies (Kim et al., 2013; Hamada et al., 2017), may be explained by the loss of oligodendrocyte-derived metabolic support. In this way, the lactate-shuttle overcomes the limited ability of axons to meet their own energy demands and is a critical role fulfilled by oligodendrocytes and myelin across a number of circuits (Figure 3).

OLIGODENDROCYTE LINEAGE CELLS AFFECT MOTOR CIRCUIT FUNCTION

Multiple sclerosis (MS) is an autoimmune and neurodegenerative disease in which central demyelination and axonal loss are associated with significant motor impairment (reviewed by Trapp and Nave, 2008) and changes in motor function and coordination are frequently used as behavioral indicators of the onset of demyelination in preclinical models of MS, particularly in the EAE model (Tripathi et al., 2010; Moore et al., 2013; Grace et al., 2017). The requirement of myelination for normal motor circuit function is also highlighted by the motor phenotype that develops in *Plp1*-null mice, in which subtle changes in myelin structure slow action potential conduction in the brain (Gould et al., 2018) and spinal cord (Klugmann et al., 1997; Petit et al., 2014). A detailed behavioral analysis of these mice revealed that gross motor coordination on the rotorod test was unaffected, but that fine motor coordination was disrupted, as evidenced by gait abnormalities, uncoordinated and slower swimming, extended time to complete a puzzle box and reduced marble burying by 3 months of age, as well as reduced swimming distance and less digging time by 9 months of age (Gould et al., 2018). Furthermore, ablation of the oligodendrocyte-specific transcription factor *Myrf* from all cells of the oligodendrocyte lineage or from oligodendrocytes disrupts central myelination and severely impairs motor performance in the rotorod test (Koenning et al., 2012; McKenzie et al., 2014). While these phenotypes may directly result from myelin dysfunction in the CNS, they could alternatively be a secondary consequence of altered microglial or astrocytic function, as the pharmacological depletion of microglia from *Cnp1* knockout mice relieves their catatonia, suggesting that, at least in this instance, motor dysfunction was not the direct result of myelin abnormalities (Janova et al., 2018).

While developmental myelination is required for normal motor function, it is not yet clear whether motor function is influenced by ongoing adult myelination. Preventing the formation of new myelinating oligodendrocytes in adulthood, by conditionally deleting *Myrf* from adult OPCs, does not disrupt existing myelination or elicit detectable dysfunction in rotorod performance, but does impair coordinated motor performance, as evidenced by a reduced running speed on the complex running wheel (McKenzie et al., 2014). By contrast, the conditional deletion of *Esco2*, from all Sox10⁺ cells, to induce apoptosis of the proliferating OPCs, produces a severe deficit in motor coordination, that can be detected in the beam crossing and grid walk tests after 6 weeks (Schneider et al., 2016). In this model, the ablated OPCs were primarily GPR17-negative OPCs, and a compensatory increase in the proliferation of un-recombined GPR17⁺ OPCs meant that OPC number was equivalent between control and gene-deleted mice. However, the number of newborn (BrdU-labeled) oligodendrocytes added to the white matter was effectively halved, the nodes of Ranvier and paranodes lengthened and the conduction velocity of callosal axons slowed (Schneider et al., 2016). While this phenotype may be the result of reduced oligodendrogenesis,

it may also partially reflect a change in OPC composition, which is not a feature of the *Myrf*-deletion model. Further research is needed to fully understand the role that adult OPCs and ongoing myelination play in the regulation of motor function.

OLIGODENDROCYTE LINEAGE CELLS AFFECT LEARNING AND COGNITION

As more than half of all people with MS experience cognitive decline (reviewed; Rocca et al., 2015), it is likely that myelination also exerts a significant influence on cognitive circuits. Cognitive impairment can be an early feature of this disease, as ~20% of people with early MS or clinically isolated syndrome fail four or more neuropsychological assessment tasks, indicating significant impairment in attention, executive function and learning and memory (Baysal Kiraç et al., 2014). The development of cognitive impairment temporally correlates with demyelination of gray matter regions, including the neocortex, particularly the cingulate cortex, thalamus, hippocampus, cerebellum and spinal cord (Geurts and Barkhof, 2008) and cortical lesion load and cortical volume independently correlate with the level of cognitive impairment (Calabrese et al., 2009).

The idea that myelination is critical for normal cognitive function is also supported by rodent preclinical models that preferentially induce oligodendrocyte loss and demyelination of the corpus callosum (Xu et al., 2010), hippocampus (Xu et al., 2017) or medial prefrontal cortex (Yang et al., 2017) and impair working memory. Social isolation during development, which has no effect on oligodendrocyte number, but results in thinner myelin in the prefrontal cortex and hippocampus, also impairs working memory (Makinodan et al., 2012; Cao et al., 2017). As increasing the thickness of already elaborated myelin sheaths conversely facilitates contextual fear memory acquisition (Jeffries et al., 2016), myelin sheath thickness appears to be an important regulator of circuits relevant to cognition.

It is possible that learning not only requires developmental but adult myelination, as a strong association exists between learning and oligodendrogenesis. Indeed, training mice on a complex running wheel is associated with a rapid increase in the number of pre-myelinating oligodendrocytes present in the motor cortex and subcortical white matter (Xiao et al., 2016), and environmental enrichment, somatosensory enrichment or skilled reaching training increase the number of newly differentiated oligodendrocytes in brain regions relevant to each activity (Keiner et al., 2017; Hughes et al., 2018). In rodents, learning the skilled reaching task is also associated with an increase in fractional anisotropy of the white matter region underlying the somatosensory cortex contralateral to the trained forepaw (Sampaio-Baptista et al., 2013), and in humans, learning to juggle is similarly associated with an increase in fractional anisotropy of the white matter underlying the right posterior intraparietal sulcus (Scholz et al., 2009). In both cases, magnetic resonance imaging detected changes in fractional anisotropy in brain regions activated by the task, and in rodents, the increased fractional anisotropy correlated with an increase in MBP expression in the same brain

region (Sampaio-Baptista et al., 2013). These data suggest that the learning-induced changes detected by magnetic resonance imaging reflect myelin addition or changes in existing myelin, rather than altered axon caliber or branching.

Despite oligodendrocyte generation occurring alongside learning, few studies have examined the requirement of oligodendrogenesis and/or myelination for learning and memory functions. To address this question, McKenzie et al. (2014) used a cre-lox transgenic approach to conditionally delete *Myrf* from OPCs in the adult mouse brain. When *Myrf*-deleted mice were placed on the complex running wheel and running speed used as a surrogate for motor learning, *Myrf*-deleted mice performed worse than control mice at all time-points examined (McKenzie et al., 2014; Xiao et al., 2016). As this effect is seen within the first few hours of carrying out the learning task (Xiao et al., 2016), efficient motor learning may require the rapid production of new oligodendrocytes, but it is unclear whether pre-myelinating and/or myelinating oligodendrocytes are required. If premyelinating cells alone are required, they may be providing paracrine support to the network, however if myelinating cells are required, the new myelin may modify conduction velocity or support the increased metabolic load placed on the circuit.

OLIGODENDROCYTE LINEAGE CELLS INFLUENCE EMOTIONAL STATE

Perturbations that result in reduced central myelination can result in the development of mood disorders such as anxiety and depression. In humans this is largely correlative, with white matter abnormalities being well documented in psychiatric disorders associated with social withdrawal and anxiety (reviewed by Parnanzone et al., 2017), and demyelinating disorders often being accompanied by co-morbid depression (reviewed by Arnett et al., 2008). Similarly, in rodents, focal demyelination of the medial prefrontal cortex (Yang et al., 2017), diffuse white matter injury (van Tilborg et al., 2018) and EAE are all associated with increased anxiety- and depressive-like behaviors. Changes in myelin may contribute to this phenotype, however it is also possible that altered OPC function is a consequence of demyelination and contributes to the development of an anxiety-like phenotype. OPCs and astrocytes are known to produce interleukin 33 in the brain (Zhang et al., 2014), and the performance of *interleukin 33* knockout mice in the elevated plus maze and open field test is indicative of reduced anxiety (Dohi et al., 2017), suggesting that increased interleukin 33 release could conversely increase anxiety. The medial prefrontal cortex, amygdala and ventral hippocampus of *interleukin-33* knockout mice also contain more *cfos*⁺ neurons (Dohi et al., 2017), which may reflect increased neuronal activity, however as this is a constitutive knockout, it is unclear whether interleukin-33 affects the development or function of the circuit.

Supporting the idea that OPCs can influence anxiety, the focal genetic ablation of OPCs from the prefrontal cortex of young, adult *NG2-Cre :: iDTR* transgenic mice was sufficient to produce anxiety-like behaviors within

7 days (Birey et al., 2015). While this phenotype may result from impaired local oligodendrogenesis, knocking down FGF2 expression in prefrontal cortical OPCs recapitulates the anxiety-like phenotype (Birey et al., 2015), suggesting that FGF2 release from OPCs is a critical regulator of circuit function in this region. Glutamate uptake by astrocytes is also reduced following focal OPC ablation and the response of pyramidal neurons to glutamatergic input is impaired, as fewer GluR1-containing AMPA receptors are expressed in the membrane (Birey et al., 2015). Curiously, mice lacking OPCs only in the prefrontal cortex did not exhibit any signs of anhedonia, but ablating OPCs from the entire CNS was associated with reduced pleasure seeking in the sucrose preference test (Birey et al., 2015), suggesting that OPC function in other brain regions has a greater impact on depressive-like phenotypes.

Neonatal maternal separation, early weaning and chronic variable stress-paradigms also impair oligodendrogenesis and myelination of the medial prefrontal cortex, and produce anxiety- and depressive-like symptoms (Kodama et al., 2008; Ono et al., 2008; Yang et al., 2017; Liu et al., 2018). It has been shown that neonatal maternal separation stress reduces HDAC1/2 expression which impairs oligodendrogenesis, and that blocking HDAC1/2 recapitulates the phenotype (Yang et al., 2017). However, the mechanism by which stress induces anxiety- and depressive-like behaviors is likely to be complex, as stressed mice have narrower nodes of Ranvier and paranodes in the corpus callosum (Miyata et al., 2016), an increased number of PV⁺ interneurons in the prefrontal cortex, fewer *cfos*⁺ neurons in the prefrontal cortex (Shepard et al., 2016), and the stress hormone corticosterone can change the function of hippocampal neural stem/progenitor cells, by directing their generation of oligodendrocytes (Chetty et al., 2014). However, a role for impaired oligodendrogenesis in mediating this phenotype is further supported by genetic approaches that impair oligodendrogenesis and myelination and similarly produce an anxiety-like phenotype.

Oligodendrocyte number and myelination is impaired following the oligodendrocyte-specific knockdown of *ErbB* (Roy et al., 2007) and the oligodendrocyte-specific deletion of *Olig2* (Chen et al., 2015). In each case, mice showed impaired movement and increased anxiety-like behavior in the open field and elevated plus maze (Roy et al., 2007; Chen et al., 2015). This behavioral change was also associated with altered neurotransmitter release. *ErbB* knockdown increased evoked dopamine release in the striatum (Roy et al., 2007), while *Olig2* knockout increased glutamate expression in the cortical gray matter and increased the density of glutamatergic vesicles at synaptic terminals (Chen et al., 2015), suggesting that oligodendrocyte loss may precipitate an anxiety-like phenotype by dysregulating neurotransmitter signaling in the CNS. By contrast, mice that lack *claudin11* in the CNS have perturbed myelination that is accompanied by an increase in glutamate and glutamine expression in the superior olivary complex and an increase in GABA expression in the amygdala and ventral hippocampus, and show reduced anxiety-like behavior

(Maheras et al., 2018), suggesting that impaired myelination can have opposing effects depending on the brain regions affected.

CLOSING REMARKS

We have sufficient evidence to conclude that cells of the oligodendrocyte lineage influence motor coordination, cognition and emotional state. While the behavioral outcomes are very different in each case, it is likely that common mechanisms of circuit modification are responsible. Key mechanisms include paracrine signaling by cells of the oligodendrocyte lineage as well as conduction velocity modulation and the provision of metabolic support by myelinating oligodendrocytes. However, more research is required to fully understand how OPCs, premyelinating and myelinating oligodendrocytes contribute to brain plasticity and enable neuronal circuits to be regulated and remain adaptable to experience throughout life.

REFERENCES

- Almeida, A., Almeida, J., Bolaños, J. P., and Moncada, S. (2001). Different responses of astrocytes and neurons to nitric oxide: the role of glycolytically generated ATP in astrocyte protection. *Proc. Natl. Acad. Sci. U S A* 98, 15294–15299. doi: 10.1073/pnas.261560998
- Arancibia-Carcamo, I. L., Ford, M. C., Cossell, L., Ishida, K., Tohyama, K., and Attwell, D. (2017). Node of Ranvier length as a potential regulator of myelinated axon conduction speed. *Elife* 6:e23329. doi: 10.7554/eLife.23329
- Arnett, P. A., Barwick, F. H., and Beene, J. E. (2008). Depression in multiple sclerosis: review and theoretical proposal. *J. Int. Neuropsychol. Soc.* 14, 691–724. doi: 10.1017/s1355617708081174
- Baraban, M., Koudelka, S., and Lyons, D. A. (2018). Ca^{2+} activity signatures of myelin sheath formation and growth *in vivo*. *Nat. Neurosci.* 21, 19–23. doi: 10.1038/s41593-017-0040-x
- Barres, B. A., and Raff, M. C. (1999). Axonal control of oligodendrocyte development. *J. Cell Biol.* 147, 1123–1128. doi: 10.1083/jcb.147.6.1123
- Baysal Kırac, L., Ekmekçi, Ö., Yüceyar, N., and Sağduyu Kocaman, A. (2014). Assessment of early cognitive impairment in patients with clinically isolated syndromes and multiple sclerosis. *Behav. Neurol.* 2014:637694. doi: 10.1155/2014/637694
- Bechler, M. E., Byrne, L., and Ffrench-Constant, C. (2015). CNS myelin sheath lengths are an intrinsic property of oligodendrocytes. *Curr. Biol.* 25, 2411–2416. doi: 10.1016/j.cub.2015.07.056
- Benninger, Y., Colognato, H., Thurnherr, T., Franklin, R. J., Leone, D. P., Atanasoski, S., et al. (2006). β 1-integrin signaling mediates premyelinating oligodendrocyte survival but is not required for CNS myelination and remyelination. *J. Neurosci.* 26, 7665–7673. doi: 10.1523/JNEUROSCI.0444-06.2006
- Bhat, M. A., Rios, J. C., Lu, Y., Garcia-Fresco, G. P., Ching, W., St Martin, M., et al. (2001). Axon-glia interactions and the domain organization of myelinated axons requires neurexin IV/Caspr/Paranodin. *Neuron* 30, 369–383. doi: 10.1016/s0896-6273(01)00294-x
- Birey, F., Kloc, M., Chavali, M., Hussein, I., Wilson, M., Christoffel, D. J., et al. (2015). Genetic and stress-induced loss of NG2 glia triggers emergence of depressive-like behaviors through reduced secretion of FGF2. *Neuron* 88, 941–956. doi: 10.1016/j.neuron.2015.10.046
- Butt, A. M., Colquhoun, K., Tutton, M., and Berry, M. (1994). Three-dimensional morphology of astrocytes and oligodendrocytes in the intact mouse optic nerve. *J. Neurocytol.* 23, 469–485. doi: 10.1007/bf01184071
- Cahoy, J. D., Emery, B., Kaushal, A., Foo, L. C., Zamanian, J. L., Christopherson, K. S., et al. (2008). A transcriptome database for astrocytes, neurons, and oligodendrocytes: a new resource for understanding brain development and function. *J. Neurosci.* 28, 264–278. doi: 10.1523/JNEUROSCI.4178-07.2008
- Cai, J., Qi, Y., Hu, X., Tan, M., Liu, Z., Zhang, J., et al. (2005). Generation of oligodendrocyte precursor cells from mouse dorsal spinal cord independent of Nkx6 regulation and Shh signaling. *Neuron* 45, 41–53. doi: 10.1016/j.neuron.2004.12.028
- Calabrese, M., Agosta, F., Rinaldi, F., Mattisi, I., Grossi, P., Favaretto, A., et al. (2009). Cortical lesions and atrophy associated with cognitive impairment in relapsing-remitting multiple sclerosis. *Arch. Neurol.* 66, 1144–1150. doi: 10.1001/archneurol.2009.174
- Cao, M., Pu, T., Wang, L., Marshall, C., He, H., Hu, G., et al. (2017). Early enriched physical environment reverses impairments of the hippocampus, but not medial prefrontal cortex, of socially-isolated mice. *Brain Behav. Immun.* 64, 232–243. doi: 10.1016/j.bbi.2017.04.009
- Charles, P., Tait, S., Faivre-Sarrailh, C., Barbin, G., Gunn-Moore, F., Denisenko-Nehrbass, N., et al. (2002). Neurofascin is a glial receptor for the paranodin/Caspr-contactin axonal complex at the axoglial junction. *Curr. Biol.* 12, 217–220. doi: 10.1016/s0960-9822(01)00680-7
- Chen, X., Zhang, W., Li, T., Guo, Y., Tian, Y., Wang, F., et al. (2015). Impairment of oligodendroglia maturation leads to aberrantly increased cortical glutamate and anxiety-like behaviors in juvenile mice. *Front. Cell. Neurosci.* 9:467. doi: 10.3389/fncel.2015.00467
- Chetty, S., Friedman, A. R., Taravosh-Lahn, K., Kirby, E. D., Mirescu, C., Guo, F., et al. (2014). Stress and glucocorticoids promote oligodendrogenesis in the adult hippocampus. *Mol. Psychiatry* 19, 1275–1283. doi: 10.1038/mp.2013.190
- Clarke, L. E., Young, K. M., Hamilton, N. B., Li, H., Richardson, W. D., and Attwell, D. (2012). Properties and fate of oligodendrocyte progenitor cells in the corpus callosum, motor cortex, and piriform cortex of the mouse. *J. Neurosci.* 32, 8173–8185. doi: 10.1523/JNEUROSCI.0928-12.2012
- Clemente, D., Ortega, M. C., Arenzana, F. J., and de Castro, F. (2011). FGF-2 and anosmin-1 are selectively expressed in different types of multiple sclerosis lesions. *J. Neurosci.* 31, 14899–14909. doi: 10.1523/JNEUROSCI.1158-11.2011
- Czopka, T., Ffrench-Constant, C., and Lyons, D. A. (2013). Individual oligodendrocytes have only a few hours in which to generate new myelin sheaths *in vivo*. *Dev. Cell* 25, 599–609. doi: 10.1016/j.devcel.2013.05.013
- Dimou, L., Simon, C., Kirchhoff, F., Takebayashi, H., and Götz, M. (2008). Progeny of Olig2-expressing progenitors in the gray and white matter of the adult mouse cerebral cortex. *J. Neurosci.* 28, 10434–10442. doi: 10.1523/JNEUROSCI.2831-08.2008
- Dohi, E., Choi, E. Y., Rose, I. V. L., Murata, A. S., Chow, S., Niwa, M., et al. (2017). Behavioral changes in mice lacking interleukin-33. *eNeuro* 4:ENEURO.0147-17.2017. doi: 10.1523/eneuro.0147-17.2017
- Edgar, J. M., McLaughlin, M., Werner, H. B., McCulloch, M. C., Barrie, J. A., Brown, A., et al. (2009). Early ultrastructural defects of axons and axon-glia junctions in mice lacking expression of *Cnp1*. *Glia* 57, 1815–1824. doi: 10.1002/glia.20893

AUTHOR CONTRIBUTIONS

KY, RP, CC and KP wrote the article.

FUNDING

KY is an MS Research Australia and Macquarie Group Foundation Fellow (17-0223). CC is an MS Research Australia Fellow (15-054). KP is a National Health and Medical Research Council of Australia Fellow (1139180). RP is supported by a scholarship from the Menzies Institute for Medical Research, University of Tasmania.

ACKNOWLEDGMENTS

We would like to thank our colleagues at the University of Tasmania for their helpful feedback and comments on this manuscript.

- Emery, B., Agalliu, D., Cahoy, J. D., Watkins, T. A., Dugas, J. C., Mulinyawe, S. B., et al. (2009). Myelin gene regulatory factor is a critical transcriptional regulator required for CNS myelination. *Cell* 138, 172–185. doi: 10.1016/j.cell.2009.04.031
- Fard, M. K., van der Meer, F., Sánchez, P., Cantuti-Castelvetri, L., Mandad, S., Jäkel, S., et al. (2017). BCAS1 expression defines a population of early myelinating oligodendrocytes in multiple sclerosis lesions. *Sci. Transl. Med.* 9:eam7816. doi: 10.1126/scitranslmed.2017016
- Feinberg, K., Eshed-Eisenbach, Y., Frechter, S., Amor, V., Salomon, D., Sabanay, H., et al. (2010). A glial signal consisting of gliomedin and NrCAM clusters axonal Na⁺ channels during the formation of nodes of Ranvier. *Neuron* 65, 490–502. doi: 10.1016/j.neuron.2010.02.004
- Fogarty, M., Richardson, W. D., and Kessaris, N. (2005). A subset of oligodendrocytes generated from radial glia in the dorsal spinal cord. *Development* 132, 1951–1959. doi: 10.1242/dev.01777
- Ford, M. C., Alexandrova, O., Cossell, L., Stange-Marten, A., Sinclair, J., Kopp-Scheinflug, C., et al. (2015). Tuning of Ranvier node and internode properties in myelinated axons to adjust action potential timing. *Nat. Commun.* 6:8073. doi: 10.1038/ncomms9073
- Freeman, S. A., Desmazières, A., Fricker, D., Lubetzki, C., and Sol-Foulon, N. (2016). Mechanisms of sodium channel clustering and its influence on axonal impulse conduction. *Cell. Mol. Life Sci.* 73, 723–735. doi: 10.1007/s00018-015-2081-1
- Freeman, S. A., Desmazières, A., Simonnet, J., Gatta, M., Pfeiffer, F., Aigrot, M. S., et al. (2015). Acceleration of conduction velocity linked to clustering of nodal components precedes myelination. *Proc. Natl. Acad. Sci. USA* 112, E321–E328. doi: 10.1073/pnas.1419099112
- Fu, H., Qi, Y., Tan, M., Cai, J., Takebayashi, H., Nakafuku, M., et al. (2002). Dual origin of spinal oligodendrocyte progenitors and evidence for the cooperative role of *Olig2* and *Nkx2.2* in the control of oligodendrocyte differentiation. *Development* 129, 681–693.
- Fünfschilling, U., Supplie, L. M., Mahad, D., Boretius, S., Saab, A. S., Edgar, J., et al. (2012). Glycolytic oligodendrocytes maintain myelin and long-term axonal integrity. *Nature* 485, 517–521. doi: 10.1038/nature11007
- Furusho, M., Ishii, A., and Bansal, R. (2017). Signaling by FGF receptor 2, not FGF receptor 1, regulates myelin thickness through activation of ERK1/2-MAPK, which promotes mTORC1 activity in an Akt-independent manner. *J. Neurosci.* 37, 2931–2946. doi: 10.1523/JNEUROSCI.3316-16.2017
- Geurts, J. J., and Barkhof, F. (2008). Grey matter pathology in multiple sclerosis. *Lancet Neurol.* 7, 841–851. doi: 10.1016/S1474-4422(08)70191-1
- Gibson, E. M., Purger, D., Mount, C. W., Goldstein, A. K., Lin, G. L., Wood, L. S., et al. (2014). Neuronal activity promotes oligodendrogenesis and adaptive myelination in the mammalian brain. *Science* 344, 1252304. doi: 10.1126/science.1252304
- Giera, S., Luo, R., Ying, Y., Ackerman, S. D., Jeong, S.-J., Stoveken, H. M., et al. (2018). Microglial transglutaminase-2 drives myelination and myelin repair via GPR56/ADGRG1 in oligodendrocyte precursor cells. *Elife* 7:e33385. doi: 10.7554/elifesciences.33385
- Gould, E. A., Busquet, N., Shepherd, D., Dietz, R. M., Herson, P. S., Simoes de Souza, F. M., et al. (2018). Mild myelin disruption elicits early alteration in behavior and proliferation in the subventricular zone. *Elife* 7:e34783. doi: 10.7554/elifesciences.34783
- Grace, P. M., Loram, L. C., Christianson, J. P., Strand, K. A., Flyer-Adams, J. G., Penzkofer, K. R., et al. (2017). Behavioral assessment of neuropathic pain, fatigue, and anxiety in experimental autoimmune encephalomyelitis (EAE) and attenuation by interleukin-10 gene therapy. *Brain Behav. Immun.* 59, 49–54. doi: 10.1016/j.bbi.2016.05.012
- Gray, C. M., König, P., Engel, A. K., and Singer, W. (1989). Oscillatory responses in cat visual cortex exhibit inter-columnar synchronization which reflects global stimulus properties. *Nature* 338, 334–337. doi: 10.1038/338334a0
- Griffiths, I., Klugmann, M., Anderson, T., Yool, D., Thomson, C., Schwab, M. H., et al. (1998). Axonal swellings and degeneration in mice lacking the major proteolipid of myelin. *Science* 280, 1610–1613. doi: 10.1126/science.280.5369.1610
- Gu, Y., Huang, S., Chang, M. C., Worley, P., Kirkwood, A., and Quinlan, E. M. (2013). Obligatory role for the immediate early gene NARP in critical period plasticity. *Neuron* 79, 335–346. doi: 10.1016/j.neuron.2013.05.016
- Hachem, S., Aguirre, A., Vives, V., Marks, A., Gallo, V., and Legraverend, C. (2005). Spatial and temporal expression of S100B in cells of oligodendrocyte lineage. *Glia* 51, 81–97. doi: 10.1002/glia.20184
- Hagemeyer, N., Hanft, K.-M., Akriditou, M.-A., Unger, N., Park, E. S., Stanley, E. R., et al. (2017). Microglia contribute to normal myelinogenesis and to oligodendrocyte progenitor maintenance during adulthood. *Acta Neuropathol.* 134, 441–458. doi: 10.1007/s00401-017-1747-1
- Hajihosseini, M., Tham, T. N., and Dubois-Dalcq, M. (1996). Origin of oligodendrocytes within the human spinal cord. *J. Neurosci.* 16, 7981–7994. doi: 10.1523/JNEUROSCI.16-24-07981.1996
- Hamada, M. S., and Kole, M. H. (2015). Myelin loss and axonal ion channel adaptations associated with gray matter neuronal hyperexcitability. *J. Neurosci.* 35, 7272–7286. doi: 10.1523/JNEUROSCI.4747-14.2015
- Hamada, M. S., Popovic, M. A., and Kole, M. H. (2017). Loss of saltation and presynaptic action potential failure in demyelinated axons. *Front. Cell. Neurosci.* 11:45. doi: 10.3389/fncel.2017.00045
- Hart, I. K., Richardson, W. D., Heldin, C. H., Westermarck, B., and Raff, M. C. (1989). PDGF receptors on cells of the oligodendrocyte-type-2 astrocyte (O-2A) cell lineage. *Development* 105, 595–603.
- Hill, R. A., Li, A. M., and Grutzendler, J. (2018). Lifelong cortical myelin plasticity and age-related degeneration in the live mammalian brain. *Nat. Neurosci.* 21, 683–695. doi: 10.1038/s41593-018-0120-6
- Hines, J. H., Ravanelli, A. M., Schwindt, R., Scott, E. K., and Appel, B. (2015). Neuronal activity biases axon selection for myelination *in vivo*. *Nat. Neurosci.* 18, 683–689. doi: 10.1038/nn.3992
- Hughes, E. G., Kang, S. H., Fukaya, M., and Bergles, D. E. (2013). Oligodendrocyte progenitors balance growth with self-repulsion to achieve homeostasis in the adult brain. *Nat. Neurosci.* 16, 668–676. doi: 10.1038/nn.3390
- Hughes, E. G., Orthmann-Murphy, J. L., Langseth, A. J., and Bergles, D. E. (2018). Myelin remodeling through experience-dependent oligodendrogenesis in the adult somatosensory cortex. *Nat. Neurosci.* 21, 696–706. doi: 10.1038/s41593-018-0121-5
- Ivanova, A., Nakahira, E., Kagawa, T., Oba, A., Wada, T., Takebayashi, H., et al. (2003). Evidence for a second wave of oligodendrogenesis in the postnatal cerebral cortex of the mouse. *J. Neurosci. Res.* 73, 581–592. doi: 10.1002/jnr.10717
- Jakovcevski, I., Filipovic, R., Mo, Z., Rakic, S., and Zecevic, N. (2009). Oligodendrocyte development and the onset of myelination in the human fetal brain. *Front. Neuroanat.* 3:5. doi: 10.3389/neuro.05.005.2009
- James, L. M., Halliday, D. M., Stephens, J. A., and Farmer, S. F. (2008). On the development of human corticospinal oscillations: age-related changes in EEG-EMG coherence and cumulant. *Eur. J. Neurosci.* 27, 3369–3379. doi: 10.1111/j.1460-9568.2008.06277.x
- Janova, H., Arinrad, S., Balmuth, E., Mitjans, M., Hertel, J., Habes, M., et al. (2018). Microglia ablation alleviates myelin-associated catatonic signs in mice. *J. Clin. Invest.* 128, 734–745. doi: 10.1172/jci97032
- Jeffries, M. A., Urbanek, K., Torres, L., Wendell, S. G., Rubio, M. E., and Fyffe-Maricich, S. L. (2016). ERK1/2 activation in preexisting oligodendrocytes of adult mice drives new myelin synthesis and enhanced CNS function. *J. Neurosci.* 36, 9186–9200. doi: 10.1523/JNEUROSCI.1444-16.2016
- Kang, S. H., Fukaya, M., Yang, J. K., Rothstein, J. D., and Bergles, D. E. (2010). NG2⁺ CNS glial progenitors remain committed to the oligodendrocyte lineage in postnatal life and following neurodegeneration. *Neuron* 68, 668–681. doi: 10.1016/j.neuron.2010.09.009
- Kaplan, M. R., Cho, M. H., Ullian, E. M., Isom, L. L., Levinson, S. R., and Barres, B. A. (2001). Differential control of clustering of the sodium channels Na_v1.2 and Na_v1.6 at developing CNS nodes of Ranvier. *Neuron* 30, 105–119. doi: 10.1016/s0896-6273(01)00266-5
- Keiner, S., Niv, F., Neumann, S., Steinbach, T., Schmeer, C., Hornung, K., et al. (2017). Effect of skilled reaching training and enriched environment on generation of oligodendrocytes in the adult sensorimotor cortex and corpus callosum. *BMC Neurosci.* 18:31. doi: 10.1186/s12868-017-0347-2
- Kelenis, D. P., Hart, E., Edwards-Fligner, M., Johnson, J. E., and Yue, T. Y. (2018). ASCL1 regulates proliferation of NG2-glia in the embryonic and adult spinal cord. *Glia* 66, 1862–1880. doi: 10.1002/glia.23344
- Kessaris, N., Fogarty, M., Iannarelli, P., Grist, M., Wegner, M., and Richardson, W. D. (2006). Competing waves of oligodendrocytes in the

- forebrain and postnatal elimination of an embryonic lineage. *Nat. Neurosci.* 9, 173–179. doi: 10.1038/nn1620
- Kim, J. H., Renden, R., and von Gersdorff, H. (2013). Dysmyelination of auditory afferent axons increases the jitter of action potential timing during high-frequency firing. *J. Neurosci.* 33, 9402–9407. doi: 10.1523/JNEUROSCI.3389-12.2013
- Kirby, B. B., Takada, N., Latimer, A. J., Shin, J., Carney, T. J., Kelsh, R. N., et al. (2006). *In vivo* time-lapse imaging shows dynamic oligodendrocyte progenitor behavior during zebrafish development. *Nat. Neurosci.* 9, 1506–1511. doi: 10.1038/nn1803
- Klugmann, M., Schwab, M. H., Pühlhofer, A., Schneider, A., Zimmermann, F., Griffiths, I. R., et al. (1997). Assembly of CNS myelin in the absence of proteolipid protein. *Neuron* 18, 59–70. doi: 10.1016/s0896-6273(01)80046-5
- Kodama, Y., Kikusui, T., Takeuchi, Y., and Mori, Y. (2008). Effects of early weaning on anxiety and prefrontal cortical and hippocampal myelination in male and female Wistar rats. *Dev. Psychobiol.* 50, 332–342. doi: 10.1002/dev.20289
- Koenning, M., Jackson, S., Hay, C. M., Faux, C., Kilpatrick, T. J., Willingham, M., et al. (2012). Myelin gene regulatory factor is required for maintenance of myelin and mature oligodendrocyte identity in the adult CNS. *J. Neurosci.* 32, 12528–12542. doi: 10.1523/JNEUROSCI.1069-12.2012
- Kougoumtzidou, E., Shimizu, T., Hamilton, N. B., Tohyama, K., Sprengel, R., Monyer, H., et al. (2017). Signalling through AMPA receptors on oligodendrocyte precursors promotes myelination by enhancing oligodendrocyte survival. *Elife* 6:e28080. doi: 10.7554/elifelife.28080
- Krasnow, A. M., Ford, M. C., Valdivia, L. E., Wilson, S. W., and Attwell, D. (2018). Regulation of developing myelin sheath elongation by oligodendrocyte calcium transients *in vivo*. *Nat. Neurosci.* 21, 24–28. doi: 10.1038/s41593-017-0031-y
- Kuhlbrodt, K., Herbarth, B., Sock, E., Hermans-Borgmeyer, I., and Wegner, M. (1998). Sox10, a novel transcriptional modulator in glial cells. *J. Neurosci.* 18, 237–250. doi: 10.1523/JNEUROSCI.18-01-00237.1998
- Lappe-Siefke, C., Goebbels, C., Gravel, M., Nicksch, E., Lee, J., Braun, P. E., et al. (2003). Disruption of Cnp1 uncouples oligodendroglial functions in axonal support and myelination. *Nat. Genet.* 33, 366–374. doi: 10.1038/ng1095
- Larson, V. A., Mironova, Y., Vanderpool, K. G., Waisman, A., Rash, J. E., Agarwal, A., et al. (2018). Oligodendrocytes control potassium accumulation in white matter and seizure susceptibility. *Elife* 7:e34829. doi: 10.7554/elifelife.34829
- Lee, Y., Morrison, B. M., Li, Y., Lengacher, S., Farah, M. H., Hoffman, P. N., et al. (2012). Oligodendroglia metabolically support axons and contribute to neurodegeneration. *Nature* 487, 443–448. doi: 10.1038/nature11314
- Liu, J., Dietz, K., Hodes, G. E., Russo, S. J., and Casaccia, P. (2018). Widespread transcriptional alternations in oligodendrocytes in the adult mouse brain following chronic stress. *Dev. Neurobiol.* 78, 152–162. doi: 10.1002/dneu.22533
- Loers, G., Aboul-Enein, F., Bartsch, U., Lassmann, H., and Schachner, M. (2004). Comparison of myelin, axon, lipid, and immunopathology in the central nervous system of differentially myelin-compromised mutant mice: a morphological and biochemical study. *Mol. Cell. Neurosci.* 27, 175–189. doi: 10.1016/j.mcn.2004.06.006
- Lu, Q. R., Yuk, D., Alberta, J. A., Zhu, Z., Pawlitzky, I., Chan, J., et al. (2000). Sonic hedgehog—regulated oligodendrocyte lineage genes encoding bHLH proteins in the mammalian central nervous system. *Neuron* 25, 317–329. doi: 10.1016/s0896-6273(00)80897-1
- Lundgaard, I., Luzhynskaya, A., Stockley, J. H., Wang, Z., Evans, K. A., Swire, M., et al. (2013). Neuregulin and BDNF induce a switch to NMDA receptor-dependent myelination by oligodendrocytes. *PLoS Biol.* 11:e1001743. doi: 10.1371/journal.pbio.1001743
- Maheras, K. J., Peppi, M., Ghoddoussi, F., Galloway, M. P., Perrine, S. A., and Gow, A. (2018). Absence of claudin 11 in CNS myelin perturbs behavior and neurotransmitter levels in mice. *Sci. Rep.* 8:3798. doi: 10.1038/s41598-018-22047-9
- Maki, T., Maeda, M., Uemura, M., Lo, E. K., Terasaki, Y., Liang, A. C., et al. (2015). Potential interactions between pericytes and oligodendrocyte precursor cells in perivascular regions of cerebral white matter. *Neurosci. Lett.* 597, 164–169. doi: 10.1016/j.neulet.2015.04.047
- Makinodan, M., Rosen, K. M., Ito, S., and Corfas, G. (2012). A critical period for social experience-dependent oligodendrocyte maturation and myelination. *Science* 337, 1357–1360. doi: 10.1126/science.1220845
- Masahira, N., Takebayashi, H., Ono, K., Watanabe, K., Ding, L., Furusho, M., et al. (2006). Olig2-positive progenitors in the embryonic spinal cord give rise not only to motoneurons and oligodendrocytes, but also to a subset of astrocytes and ependymal cells. *Dev. Biol.* 293, 358–369. doi: 10.1016/j.ydbio.2006.02.029
- McKenzie, I. A., Ohayon, D., Li, H., de Faria, J. P., Emery, B., Tohyama, K., et al. (2014). Motor skill learning requires active central myelination. *Science* 346, 318–322. doi: 10.1126/science.1254960
- Mensch, S., Baraban, M., Almeida, R., Czopka, T., Ausborn, J., El Manira, A., et al. (2015). Synaptic vesicle release regulates myelin sheath number of individual oligodendrocytes *in vivo*. *Nat. Neurosci.* 18, 628–630. doi: 10.1038/nn.3991
- Micheva, K. D., Wolman, D., Mensch, B. D., Pax, E., Buchanan, J., Smith, S. J., et al. (2016). A large fraction of neocortical myelin ensheathes axons of local inhibitory neurons. *Elife* 5:e15784. doi: 10.7554/eLife.15784
- Miyata, S., Taniguchi, M., Koyama, Y., Shimizu, S., Tanaka, T., Yasuno, F., et al. (2016). Association between chronic stress-induced structural abnormalities in Ranvier nodes and reduced oligodendrocyte activity in major depression. *Sci. Rep.* 6:23084. doi: 10.1038/srep23084
- Moore, S., Khalaj, A. J., Yoon, J., Patel, R., Hannsun, G., Yoo, T., et al. (2013). Therapeutic laquinimod treatment decreases inflammation, initiates axon remyelination, and improves motor deficit in a mouse model of multiple sclerosis. *Brain Behav.* 3, 664–682. doi: 10.1002/brb3.174
- Murcia-Belmonte, V., Esteban, P. F., Martínez-Hernández, J., Gruart, A., Luján, R., Delgado-García, J. M., et al. (2016). Anosmin-1 over-expression regulates oligodendrocyte precursor cell proliferation, migration and myelin sheath thickness. *Brain Struct. Funct.* 221, 1365–1385. doi: 10.1007/s00429-014-0977-4
- Nakano, M., Tamura, Y., Yamato, M., Kume, S., Eguchi, A., Takata, K., et al. (2017). NG2 glial cells regulate neuroimmunological responses to maintain neuronal function and survival. *Sci. Rep.* 7:42041. doi: 10.1038/srep42041
- Nawaz, S., Sánchez, P., Schmitt, S., Snaidero, N., Mitkovski, M., Velte, C., et al. (2015). Actin filament turnover drives leading edge growth during myelin sheath formation in the central nervous system. *Dev. Cell* 34, 139–151. doi: 10.1016/j.devcel.2015.05.013
- O'Brien, R. J., Xu, D., Petralia, R. S., Steward, O., Haganir, R. L., and Worley, P. (1999). Synaptic clustering of AMPA receptors by the extracellular immediate-early gene product Narp. *Neuron* 23, 309–323. doi: 10.1016/s0896-6273(00)80782-5
- Ono, M., Kikusui, T., Sasaki, N., Ichikawa, M., Mori, Y., and Murakami-Murofushi, K. (2008). Early weaning induces anxiety and precocious myelination in the anterior part of the basolateral amygdala of male Balb/c mice. *Neuroscience* 156, 1103–1110. doi: 10.1016/j.neuroscience.2008.07.078
- Palser, A. L., Norman, A. L., Saffell, J. L., and Reynolds, R. (2009). Neural cell adhesion molecule stimulates survival of premyelinating oligodendrocytes via the fibroblast growth factor receptor. *J. Neurosci. Res.* 87, 3356–3368. doi: 10.1002/jnr.22248
- Parnanzone, S., Serrone, D., Rossetti, M. C., D'Onofrio, S., Splendiani, A., Micelli, V., et al. (2017). Alterations of cerebral white matter structure in psychosis and their clinical correlations: a systematic review of diffusion tensor imaging studies. *Riv. Psichiatr.* 52, 49–66. doi: 10.1708/2679.27441
- Parolisi, R., and Boda, E. (2018). NG2 glia: novel roles beyond Re-/Myelination. *Neuroglia* 1, 151–175. doi: 10.3390/neuroglia1010011
- Peles, E., Nativ, M., Lustig, M., Grumet, M., Schilling, J., Martinez, R., et al. (1997). Identification of a novel contactin-associated transmembrane receptor with multiple domains implicated in protein-protein interactions. *EMBO J.* 16, 978–988. doi: 10.1093/emboj/16.5.978
- Pelkey, K. A., Barksdale, E., Craig, M. T., Yuan, X., Sukumaran, M., Vargish, G. A., et al. (2015). Pentraxins coordinate excitatory synapse maturation and circuit integration of parvalbumin interneurons. *Neuron* 85, 1257–1272. doi: 10.1016/j.neuron.2015.02.020
- Petit, B., Giraudet, F., Bechon, C., Bardin, L., Avan, P., Boespflug-Tanguy, O., et al. (2014). Mice with a deletion of the major central myelin protein exhibit hypersensitivity to noxious thermal stimuli: involvement of central sensitization. *Neurobiol. Dis.* 65, 55–68. doi: 10.1016/j.nbd.2014.01.005
- Philips, T., and Rothstein, J. D. (2017). Oligodendroglia: metabolic supporters of neurons. *J. Clin. Invest.* 127, 3271–3280. doi: 10.1172/JCI90610
- Pringle, N. P., Mudhar, H. S., Collarini, E. J., and Richardson, W. D. (1992). PDGF receptors in the rat CNS: during late neurogenesis, PDGF α -receptor expression appears to be restricted to glial cells of the oligodendrocyte lineage. *Development* 115, 535–551.

- Psachoulia, K., Jamen, F., Young, K. M., and Richardson, W. D. (2009). Cell cycle dynamics of NG2 cells in the postnatal and ageing brain. *Neuron Glia Biol.* 5, 57–67. doi: 10.1017/S1740925X09990354
- Rakic, S., and Zecevic, N. (2003). Early oligodendrocyte progenitor cells in the human fetal telencephalon. *Glia* 41, 117–127. doi: 10.1002/glia.10140
- Rasband, M. N., Tayler, J., Kaga, Y., Yang, Y., Lappe-Siefke, C., Nave, K. A., et al. (2005). CNP is required for maintenance of axon-glia interactions at nodes of Ranvier in the CNS. *Glia* 50, 86–90. doi: 10.1002/glia.20165
- Rasminsky, M., and Sears, T. A. (1972). Internodal conduction in undissected demyelinated nerve fibres. *J. Physiol.* 227, 323–350. doi: 10.1113/jphysiol.1972.sp010035
- Rivers, L. E., Young, K. M., Rizzi, M., Jamen, F., Psachoulia, K., Wade, A., et al. (2008). PDGFRA/NG2 glia generate myelinating oligodendrocytes and piriform projection neurons in adult mice. *Nat. Neurosci.* 11, 1392–1401. doi: 10.1038/nn.2220
- Rocca, M. A., Amato, M. P., De Stefano, N., Enzinger, C., Geurts, J. J., Penner, I. K., et al. (2015). Clinical and imaging assessment of cognitive dysfunction in multiple sclerosis. *Lancet Neurol.* 14, 302–317. doi: 10.1016/S1474-4422(14)70250-9
- Rosenbluth, J. (2009). Multiple functions of the paranodal junction of myelinated nerve fibers. *J. Neurosci. Res.* 87, 3250–3258. doi: 10.1002/jnr.22013
- Roy, K., Murtie, J. C., El-Khodori, B. F., Edgar, N., Sardi, S. P., Hooks, B. M., et al. (2007). Loss of erbB signaling in oligodendrocytes alters myelin and dopaminergic function, a potential mechanism for neuropsychiatric disorders. *Proc. Natl. Acad. Sci. U S A* 104, 8131–8136. doi: 10.1073/pnas.0702157104
- Saab, A. S., Tzvetavona, I. D., Trevisiol, A., Baltan, S., Dibaj, P., Kusch, K., et al. (2016). Oligodendroglial NMDA receptors regulate glucose import and axonal energy metabolism. *Neuron* 91, 119–132. doi: 10.1016/j.neuron.2016.05.016
- Saez, I., Duran, J., Sinadinos, C., Beltran, A., Yanes, O., Tevy, M. F., et al. (2014). Neurons have an active glycogen metabolism that contributes to tolerance to hypoxia. *J. Cereb. Blood Flow Metab.* 34, 945–955. doi: 10.1038/jcbfm.2014.33
- Sakry, D., Neitz, A., Singh, J., Frischknecht, R., Marongiu, D., Binamé, F., et al. (2014). Oligodendrocyte precursor cells modulate the neuronal network by activity-dependent ectodomain cleavage of glial NG2. *PLoS Biol.* 12:e1001993. doi: 10.1371/journal.pbio.1001993
- Sakry, D., Yigit, H., Dimou, L., and Trotter, J. (2015). Oligodendrocyte precursor cells synthesize neuromodulatory factors. *PLoS One* 10:e0127222. doi: 10.1371/journal.pone.0127222
- Sampaio-Baptista, C., Khrapitchev, A. A., Foxley, S., Schlagheck, T., Scholz, J., Jbabdi, S., et al. (2013). Motor skill learning induces changes in white matter microstructure and myelination. *J. Neurosci.* 33, 19499–19503. doi: 10.1523/JNEUROSCI.3048-13.2013
- Schneider, S., Gruart, A., Grade, S., Zhang, Y., Kröger, S., Kirchhoff, F., et al. (2016). Decrease in newly generated oligodendrocytes leads to motor dysfunctions and changed myelin structures that can be rescued by transplanted cells. *Glia* 64, 2201–2218. doi: 10.1002/glia.23055
- Scholz, J., Klein, M. C., Behrens, T. E., and Johansen-Berg, H. (2009). Training induces changes in white-matter architecture. *Nat. Neurosci.* 12, 1370–1371. doi: 10.1038/nn.2412
- Seo, J. H., Maki, T., Maeda, M., Miyamoto, N., Liang, A. C., Hayakawa, K., et al. (2014). Oligodendrocyte precursor cells support blood-brain barrier integrity via TGF- β signaling. *PLoS One* 9:e103174. doi: 10.1371/journal.pone.0103174
- Shepard, R., Page, C. E., and Coutellier, L. (2016). Sensitivity of the prefrontal GABAergic system to chronic stress in male and female mice: relevance for sex differences in stress-related disorders. *Neuroscience* 332, 1–12. doi: 10.1016/j.neuroscience.2016.06.038
- Sherman, D. L., Tait, S., Melrose, S., Johnson, R., Zonta, B., Court, F. A., et al. (2005). Neurofascins are required to establish axonal domains for saltatory conduction. *Neuron* 48, 737–742. doi: 10.1016/j.neuron.2005.10.019
- Snaidero, N., Möbius, W., Czopka, T., Hekking, L. H., Mathisen, C., Verkleij, D., et al. (2014). Myelin membrane wrapping of CNS axons by PI(3,4,5)P3-dependent polarized growth at the inner tongue. *Cell* 156, 277–290. doi: 10.1016/j.cell.2013.11.044
- Snaidero, N., Velte, C., Myllykoski, M., Raasakka, A., Ignatov, A., Werner, H. B., et al. (2017). Antagonistic functions of MBP and CNP establish cytosolic channels in CNS myelin. *Cell Rep.* 18, 314–323. doi: 10.1016/j.celrep.2016.12.053
- Stallcup, W. B., and Beasley, L. (1987). Bipotential glial precursor cells of the optic nerve express the NG2 proteoglycan. *J. Neurosci.* 7, 2737–2744. doi: 10.1523/jneurosci.07-09-02737.1987
- Stedehouder, J., Brizee, D., Shpak, G., and Kushner, S. A. (2018). Activity-dependent myelination of parvalbumin interneurons mediated by axonal morphological plasticity. *J. Neurosci.* 38, 3631–3642. doi: 10.1523/JNEUROSCI.0074-18.2018
- Stedehouder, J., Couey, J. J., Brizee, D., Hosseini, B., Slotman, J. A., Dirven, C. M. F., et al. (2017). Fast-spiking parvalbumin interneurons are frequently myelinated in the cerebral cortex of mice and humans. *Cereb. Cortex* 27, 5001–5013. doi: 10.1093/cercor/bhx203
- Stedehouder, J., and Kushner, S. A. (2017). Myelination of parvalbumin interneurons: a parsimonious locus of pathophysiological convergence in schizophrenia. *Mol. Psychiatry* 22, 4–12. doi: 10.1038/mp.2016.147
- Suzuki, A., Hoshi, T., Ishibashi, T., Hayashi, A., Yamaguchi, Y., and Baba, H. (2004). Paranodal axoglial junction is required for the maintenance of the Nav1.6-type sodium channel in the node of Ranvier in the optic nerves but not in peripheral nerve fibers in the sulfatide-deficient mice. *Glia* 46, 274–283. doi: 10.1002/glia.20008
- Suzuki, A., Stern, S. A., Bozdagi, O., Huntley, G. W., Walker, R. H., Magistretti, P. J., et al. (2011). Astrocyte-neuron lactate transport is required for long-term memory formation. *Cell* 144, 810–823. doi: 10.1016/j.cell.2011.02.018
- Tomassy, G. S., Berger, D. R., Chen, H. H., Kasthuri, N., Hayworth, K. J., Vercelli, A., et al. (2014). Distinct profiles of myelin distribution along single axons of pyramidal neurons in the neocortex. *Science* 344, 319–324. doi: 10.1126/science.1249766
- Trapp, B. D., and Nave, K. A. (2008). Multiple sclerosis: an immune or neurodegenerative disorder? *J. Mol. Neurosci.* 31, 247–269. doi: 10.1146/annurev.neuro.30.051606.094313
- Trapp, B. D., Nishiyama, A., Cheng, D., and Macklin, W. (1997). Differentiation and death of premyelinating oligodendrocytes in developing rodent brain. *J. Cell Biol.* 137, 459–468. doi: 10.1083/jcb.137.2.459
- Tripathi, R. B., Clarke, L. E., Burzomato, V., Kessar, N., Anderson, P. N., Attwell, D., et al. (2011). Dorsally and ventrally derived oligodendrocytes have similar electrical properties but myelinate preferred tracts. *J. Neurosci.* 31, 6809–6819. doi: 10.1523/JNEUROSCI.6474-10.2011
- Tripathi, R. B., Jackiewicz, M., McKenzie, I. A., Kougiumtzidou, E., Grist, M., and Richardson, W. D. (2017). Remarkable stability of myelinating oligodendrocytes in mice. *Cell Rep.* 21, 316–323. doi: 10.1016/j.celrep.2017.09.050
- Tripathi, R. B., Rivers, L. E., Young, K. M., Jamen, F., and Richardson, W. D. (2010). NG2 glia generate new oligodendrocytes but few astrocytes in a murine experimental autoimmune encephalomyelitis model of demyelinating disease. *J. Neurosci.* 30, 16383–16390. doi: 10.1523/JNEUROSCI.3411-10.2010
- Tsai, H. H., Niu, J., Munji, R., Davalos, D., Chang, J., Zhang, H., et al. (2016). Oligodendrocyte precursors migrate along vasculature in the developing nervous system. *Science* 351, 379–384. doi: 10.1126/science.aad3839
- Uhlhaas, P. J., Pipa, G., Lima, B., Melloni, L., Neuenschwander, S., Nikolić, D., et al. (2009). Neural synchrony in cortical networks: history, concept and current status. *Front. Integr. Neurosci.* 3:17. doi: 10.3389/neuro.07.017.2009
- Vallstedt, A., Klos, J. M., and Ericson, J. (2005). Multiple dorsoventral origins of oligodendrocyte generation in the spinal cord and hindbrain. *Neuron* 45, 55–67. doi: 10.1016/j.neuron.2004.12.026
- van Heyningen, P., Calver, A. R., and Richardson, W. D. (2001). Control of progenitor cell number by mitogen supply and demand. *Curr. Biol.* 11, 232–241. doi: 10.1016/s0960-9822(01)00075-6
- van Tilborg, E., Achterberg, E. J. M., van Kammen, C. M., van der Toorn, A., Groenendaal, F., Dijkhuizen, R. M., et al. (2018). Combined fetal inflammation and postnatal hypoxia causes myelin deficits and autism-like behavior in a rat model of diffuse white matter injury. *Glia* 66, 78–93. doi: 10.1002/glia.23216
- Viganò, F., Schneider, S., Cimino, M., Bonfanti, E., Gelosa, P., Sironi, L., et al. (2016). GPR17 expressing NG2-Glia: oligodendrocyte progenitors serving as a reserve pool after injury. *Glia* 64, 287–299. doi: 10.1002/glia.22929
- Vives, V., Alonso, G., Solal, A. C., Joubert, D., and Legraverend, C. (2003). Visualization of S100B-positive neurons and glia in the central nervous system

- of EGFP transgenic mice. *J. Comp. Neurol.* 457, 404–419. doi: 10.1002/cne.10552
- Wang, C., Wei, Z., Chen, K., Ye, F., Yu, C., Bennett, V., et al. (2014). Structural basis of diverse membrane target recognitions by ankyrins. *Elife* 3:04353. doi: 10.7554/eLife.04353
- Wang, C., Zhang, C.-J., Martin, B. N., Bulek, K., Kang, Z., Zhao, J., et al. (2017). IL-17 induced NOTCH1 activation in oligodendrocyte progenitor cells enhances proliferation and inflammatory gene expression. *Nat. Commun.* 8:15508. doi: 10.1038/ncomms15508
- Xiao, L., Ohayon, D., McKenzie, I. A., Sinclair-Wilson, A., Wright, J. L., Fudge, A. D., et al. (2016). Rapid production of new oligodendrocytes is required in the earliest stages of motor-skill learning. *Nat. Neurosci.* 19, 1210–1217. doi: 10.1038/nn.4351
- Xu, M., and Cooper, E. C. (2015). An ankyrin-G N-terminal gate and protein kinase CK2 dually regulate binding of voltage-gated sodium and KCNQ2/3 potassium channels. *J. Biol. Chem.* 290, 16619–16632. doi: 10.1074/jbc.M115.638932
- Xu, X.-B., Fan, S.-J., He, Y., Ke, X., Song, C., Xiao, Y., et al. (2017). Loss of hippocampal oligodendrocytes contributes to the deficit of contextual fear learning in adult rats experiencing early bisphenol A exposure. *Mol. Neurobiol.* 54, 4524–4536. doi: 10.1007/s12035-016-0003-3
- Xu, H., Yang, H.-J., McConomy, B., Browning, R., and Li, X.-M. (2010). Behavioral and neurobiological changes in C57BL/6 mouse exposed to cuprizone: effects of antipsychotics. *Front. Behav. Neurosci.* 4:8. doi: 10.3389/fnbeh.2010.00008
- Yamazaki, Y., Fujiwara, H., Kaneko, K., Hozumi, Y., Xu, M., Ikenaka, K., et al. (2014). Short- and long-term functional plasticity of white matter induced by oligodendrocyte depolarization in the hippocampus. *Glia* 62, 1299–1312. doi: 10.1002/glia.22681
- Yamazaki, Y., Hozumi, Y., Kaneko, K., Sugihara, T., Fujii, S., Goto, K., et al. (2007). Modulatory effects of oligodendrocytes on the conduction velocity of action potentials along axons in the alveus of the rat hippocampal CA1 region. *Neuron Glia Biol.* 3, 325–334. doi: 10.1017/S1740925X08000070
- Yang, Y., Cheng, Z., Tang, H., Jiao, H., Sun, X., Cui, Q., et al. (2017). Neonatal maternal separation impairs prefrontal cortical myelination and cognitive functions in rats through activation of Wnt signaling. *Cereb. Cortex* 27, 2871–2884. doi: 10.1093/cercor/bhw121
- Yeung, M. S., Zdunek, S., Bergmann, O., Bernard, S., Salehpour, M., Alkass, K., et al. (2014). Dynamics of oligodendrocyte generation and myelination in the human brain. *Cell* 159, 766–774. doi: 10.1016/j.cell.2014.10.011
- Young, K. M., Psachoulia, K., Tripathi, R. B., Dunn, S. J., Cossell, L., Attwell, D., et al. (2013). Oligodendrocyte dynamics in the healthy adult CNS: evidence for myelin remodeling. *Neuron* 77, 873–885. doi: 10.1016/j.neuron.2013.01.006
- Yuen, T. J., Silbereis, J. C., Griveau, A., Chang, S. M., Daneman, R., Fancy, S. P. J., et al. (2014). Oligodendrocyte-encoded *HIF* function couples postnatal myelination and white matter angiogenesis. *Cell* 158, 383–396. doi: 10.1016/j.cell.2014.04.052
- Zhang, Y., Chen, K., Sloan, S. A., Bennett, M. L., Scholze, A. R., O'Keeffe, S., et al. (2014). An RNA-sequencing transcriptome and splicing database of glia, neurons and vascular cells of the cerebral cortex. *J. Neurosci.* 34, 11929–11947. doi: 10.1523/JNEUROSCI.1860-14.2014
- Zhang, C., and Rasband, M. N. (2016). Cytoskeletal control of axon domain assembly and function. *Curr. Opin. Neurobiol.* 39, 116–121. doi: 10.1016/j.conb.2016.05.001
- Zhou, Q., Wang, S., and Anderson, D. J. (2000). Identification of a novel family of oligodendrocyte lineage-specific basic helix-loop-helix transcription factors. *Neuron* 25, 331–343. doi: 10.1016/S0896-6273(00)80898-3
- Zhu, X., Bergles, D. E., and Nishiyama, A. (2008). NG2 cells generate both oligodendrocytes and gray matter astrocytes. *Development* 135, 145–157. doi: 10.1242/dev.004895
- Zhu, X., Hill, R. A., Dietrich, D., Komitova, M., Suzuki, R., and Nishiyama, A. (2011). Age-dependent fate and lineage restriction of single NG2 cells. *Development* 138, 745–753. doi: 10.1242/dev.047951
- Zuchero, J. B., Fu, M.-M., Sloan, S. A., Ibrahim, A., Olson, A., Zaremba, A., et al. (2015). CNS myelin wrapping is driven by actin disassembly. *Dev. Cell* 34, 152–167. doi: 10.1016/j.devcel.2015.06.011

Conflict of Interest Statement: The authors declare that the research was conducted in the absence of any commercial or financial relationships that could be construed as a potential conflict of interest.

Copyright © 2018 Pepper, Pitman, Cullen and Young. This is an open-access article distributed under the terms of the Creative Commons Attribution License (CC BY). The use, distribution or reproduction in other forums is permitted, provided the original author(s) and the copyright owner(s) are credited and that the original publication in this journal is cited, in accordance with accepted academic practice. No use, distribution or reproduction is permitted which does not comply with these terms.



PDI Knockdown Inhibits Seizure Activity in Acute Seizure and Chronic Epilepsy Rat Models via S-Nitrosylation-Independent Thiolation on NMDA Receptor

A. Ran Jeon and Ji-Eun Kim*

Department of Anatomy and Neurobiology, Institute of Epilepsy Research, College of Medicine, Hallym University, Chuncheon, South Korea

OPEN ACCESS

Edited by:

Marylka Yoe Uusisaari,
Okinawa Institute of Science
and Technology Graduate University,
Japan

Reviewed by:

Joern R. Steinert,
University of Leicester,
United Kingdom
Hee Jung Chung,
University of Illinois
at Urbana-Champaign, United States

*Correspondence:

Ji-Eun Kim
jieunkim@hallym.ac.kr

Received: 18 May 2018

Accepted: 05 November 2018

Published: 22 November 2018

Citation:

Jeon AR and Kim J-E (2018) PDI Knockdown Inhibits Seizure Activity in Acute Seizure and Chronic Epilepsy Rat Models via S-Nitrosylation-Independent Thiolation on NMDA Receptor. *Front. Cell. Neurosci.* 12:438. doi: 10.3389/fncel.2018.00438

Redox modulation and S-nitrosylation of cysteine residues are the post-translational modifications of *N*-methyl-D-aspartate receptor (NMDAR) to regulate its functionality. Recently, we have reported that protein disulfide isomerase (PDI) reduces disulfide bond (S-S) to free thiol (-SH) on NMDAR. Since PDI is a modulator of S-nitrosylation on various proteins, it is noteworthy whether PDI affects S-nitrosylation of NMDAR in acute seizure and chronic epilepsy models. In the present study, we found that acute seizures in response to pilocarpine and spontaneous seizures in chronic epilepsy rats led to the reduction in S-nitrosylated thiol (SNO-thiol)-to-total thiol ratio on NMDAR, while they elevated nitric oxide (NO) level and S-nitrosylation on NMDAR. *N*-nitro-L-arginine methyl ester (L-NAME, a non-selective NOS inhibitor) did not affect seizure activities in both models, although it decreased SNO-thiol levels on NMDAR. However, PDI knockdown effectively inhibited pilocarpine-induced acute seizures and spontaneous seizures in chronic epilepsy rats, accompanied by increasing the SNO-thiol-to-total thiol ratio on NMDAR due to diminishing the amounts of total thiols on GluN1 and GluN2A. Therefore, these findings indicate that PDI may not be a NO donor or a denitrosylase for NMDAR, and that PDI knockdown may inhibit seizure activity by the S-nitrosylation-independent thiolation on NMDAR.

Keywords: epilepsy, nitric oxide, protein disulfide isomerase, redox, siRNA, thiol

INTRODUCTION

Epilepsy is one of the common neurological disorders showing periodic spontaneous seizure activity with a prevalence of 4 – 10 per 1000 of the population (Sander, 2003). The *N*-methyl-D-aspartate receptor (NMDAR) is one of the major excitatory receptors contributing to seizures generation and epileptogenesis (Lipton and Rosenberg, 1994; Kim et al., 2016, 2017c). Since the presence of cysteine residues on the GluN1 and GluN2A subunits of NMDAR (Aizenman et al., 1989; Sullivan et al., 1994; Choi et al., 2000, 2001), redox modulation of

disulfide bond (S-S) and S-nitrosylation (-SNO) of free thiols (-SH) by nitric oxide (NO) on these residues regulate NMDAR activity (Lei et al., 1992; Choi et al., 2000; Lipton et al., 2002). Therefore, the modulation of NMDAR redox or its S-nitrosylation is one of the potential therapeutic targets for epilepsy.

Recently, we have reported that protein disulfide isomerase (PDI) knockdown and its neutralization decrease seizure susceptibility in response to pilocarpine and spontaneous seizure activity in chronic epileptic rats via inhibiting sulfhydrylation (reduction) of disulfide bonds on NMDAR (Kim et al., 2017c). PDI is a member of the thioredoxin superfamily of redox proteins, which plays a role in catalyzing disulfide bond formation, reduction, and isomerization (Rigobello et al., 2001; Turano et al., 2002; Popescu et al., 2010; Bi et al., 2011). PDI is originally a chaperone in the endoplasmic reticulum (ER), but it is also present in the nucleus, cytosol and cell surface (Edman et al., 1985; Koch, 1987; Yoshimori et al., 1990). Furthermore, it is likely that PDI would be involved in S-nitrosylation on NMDAR, since SNO-PDI acts as a transporter for NO (Uehara et al., 2006; Kallakunta et al., 2013). However, it has not been explored whether PDI reductase activity or its capacity as a NO donor affects the reduction and S-nitrosylation of cysteine residues on NMDAR, which influence seizure activity.

Here, we demonstrate that acute- and spontaneous seizures elevated NO concentration and the amounts of SNO- and total thiols on GluN1 and GluN2A subunits of NMDAR in acute seizure- and epilepsy models, accompanied by the increased PDI-NMDAR bindings. However, the SNO-thiol-to-total thiol ratios on NMDAR subunits in both models were lower those in control animals. PDI knockdown effectively inhibited seizure activities in both animal models with increasing the fraction of the amount of SNO-thiols in total thiols on NMDAR due to diminishing the total thiols levels on GluN1 and GluN2A. However, *N*-nitro-L-arginine methyl ester (L-NAME, a non-selective NOS inhibitor) did not affect seizure activities in both animal models, although it effectively inhibited NO synthesis. Furthermore, SNO-PDI was not relevant to SNO-thiol levels on NMDAR. Therefore, our findings suggest that PDI may not be a NO carrier for NMDAR, and that PDI knockdown may attenuate seizure activity, independent of S-nitrosylation on NMDAR.

MATERIALS AND METHODS

Experimental Animals and Chemicals

Male Sprague-Dawley (SD) rats (7 weeks old) were used in the present study. The colony room was maintained at $22 \pm 2^\circ\text{C}$, $55 \pm 5\%$ and a 12:12 light/dark cycle with lights, and food and water *ad libitum* throughout the experiments. All experimental protocols described below were approved by the Institutional Animal Care and Use Committee of Hallym University (Chuncheon, Republic of Korea) and all efforts were made to minimize animal suffering. All reagents were obtained from Sigma-Aldrich (St. Louis, MO, United States), except as noted.

Surgery, Chemical Infusion and PDI Knockdown

Surgery for a brain infusion kit and an electrode implantation was performed according to our previous study (Kim et al., 2017c). Briefly, animals were anesthetized with isoflurane (3% induction, 1.5–2% for surgery and 1.5% maintenance in a 65:35 mixture of $\text{N}_2\text{O}:\text{O}_2$). A brain infusion kit 1 (Alzet, United States) was implanted into the right lateral ventricle (1 mm posterior; 1.5 mm lateral; 3.5 mm depth from bregma) and connected to an osmotic pump (1007D, Alzet, United States; Reservoir volume, 100 μl) containing (1) control siRNA (20 μM), (2) PDI siRNA (20 μM), (3) vehicle (saline), (4) L-NAME (15 $\mu\text{g}/\mu\text{l}$) or (5) PACMA31 (a selective PDI inhibitor, 15 $\mu\text{g}/\mu\text{l}$), respectively. An osmotic pump supplied each animal 0.5 $\mu\text{l}/\text{h}$ of vehicle, compound or siRNA over 1 week. A 21-nt siRNA sequence targeting PDI corresponding to coding region (5' \rightarrow 3') is sense: CUGCAAAACUGAAGGCAGAUU, and antisense: UCUGCCUUCAGUUUUGCAGUU. A non-silencing RNA (5'-UAAGGCUAUGAAGAGAUAC-3') was used as the control siRNA. The pump was subcutaneously placed subcutaneously in the interscapular region. Some animals were also implanted by a monopolar stainless steel electrode (Plastics One Inc, United States) or a guide-electrode-combo (C313G-MS303/2/SPC, Plastics One, United States) into the left dorsal hippocampus (3.8 mm posterior; 2.0 mm lateral; 2.6 mm depth from bregma). One week after infusion, animals were used for EEG recording, western blot, co-immunoprecipitation or measurements of thiols and S-nitrosylation (see below).

Acute Seizure Model

Acute seizure model was generated by intraperitoneal injection of pilocarpine as described previously (Kim and Kang, 2011). One week after vehicle or siRNA infusion, rats were anesthetized (urethane, 1.5 g/kg i.p.) and placed in a stereotaxic frame. After the removal of an infusion kit, holes were drilled, and the recording electrode (Plastics One Inc.) and the NO sensor (ISO-NOPF200-L10, World Precision Instruments) were implanted into the left and right dorsal hippocampus (3.8 mm posterior; 2.0 mm lateral; 2.6 mm depth from bregma), respectively. The reference electrode was placed in the posterior cranium over the cerebellum. After establishing a stable baseline for at least 30 min, animals were treated with pilocarpine (380 mg/kg i.p.) 20 min after atropine methylbromide (5 mg/kg i.p.). Some animals were given L-NAME (30 mg/kg, i.p.) 30 min prior to PILO injection. EEG signals and NO concentration were recorded with a DAM 80 differential amplifier (0.1–3000 Hz bandpass; World Precision Instruments, United States) and Free radical analyzer (TBR4100, World Precision Instruments, United States). The data were digitized and analyzed using LabChart Pro v7 software (AD Instruments, NSW, Australia). Two hour after seizure on-set, diazepam (Valium; Hoffman la Roche, Neuilly sur-Seine, France; 10 mg/kg, i.p.) was administered and repeated, as needed. Total power and NO concentration were measured during the 270-min recording session from each animal by LabChart Pro v7 (AD Instruments, Australia). Spectrograms were automatically calculated using a Hanning sliding window with 50% overlap.

After recording, animals were immediately decapitated, and used for western blot, co-immunoprecipitation or measurements of thiols and S-nitrosylation (see below).

Generation of Chronic Epilepsy Model

Rats were treated with pilocarpine (380 mg/kg i.p.) 20 min after atropine methylbromide (5 mg/kg i.p.). Control animals received an equal volume of normal saline instead of PILO after the pretreatment with atropine methylbromide. Diazepam (Valium; Hoffman la Roche, France; 10 mg/kg, i.p.) was administered 2 h after on-set of status epilepticus (a prolonged seizure activity, SE) and repeated, as needed. Animals were video-monitored 8 h a day for general behavior and occurrence of spontaneous seizures by 6 weeks after SE. Rats showing spontaneous recurrent seizures were used as chronic epilepsy animals (Ko and Kang, 2015; Kim et al., 2017c).

Analysis of Chronic Seizure Activity

We applied a modified protocol for the effect of PDI knockdown on spontaneous seizure activity in chronic epileptic rats based on Ko and Kang (2015) and Kim et al. (2017c). After baseline seizure activity (control siRNA treatment) was determined over 2 days, PDI siRNA was administered over a 7-day period using an osmotic pump (1007D, Alzet, United States). Between trials, the minipump was changed out under isoflurane anesthesia. Every day, each animal was applied by video-EEG monitoring (2 h/day) at the same time. EEG analysis was performed by LabChart Pro v7 (AD Instruments, Australia). Behavioral seizure severity was evaluated according to Racine's scale: 1, immobility, eye closure, twitching of vibrissae, sniffing, facial clonus; 2, head nodding associated with more severe facial clonus; 3, clonus of one forelimb; 4, rearing, often accompanied by bilateral forelimb clonus; and 5, rearing with loss of balance and falling accompanied by generalized clonic seizures. After a 9-day recording, rats were used for western blot, co-immunoprecipitation or measurements of thiols and S-nitrosylation (see below). For the measurement of EEG and NO level, 1 week after vehicle or siRNA infusion, some chronic epilepsy animals were applied with the same method to the acute seizure model without atropine methylbromide, pilocarpine, and diazepam treatments. Spectrograms were automatically calculated using a Hanning sliding window with 50% overlap. After recording, rats were used for western blot, co-immunoprecipitation or measurements of thiols and S-nitrosylation (see below).

Analysis of Neuronal Activity in Responses to NMDA and AMPA

In control animals, guide-cannula (3260PGA, Plastics One Inc., United States) and monopolar stainless steel electrode (Plastics One Inc., United States) were implanted into the right lateral ventricle and the left dorsal hippocampus, respectively, and connected to an osmotic pump (1003D, Alzet, United States; Reservoir volume, 100 μ l) containing control siRNA or PDI siRNA by the same methods aforementioned. An osmotic pump supplied each animal 1 μ l/h of siRNA over 3 days. Three days

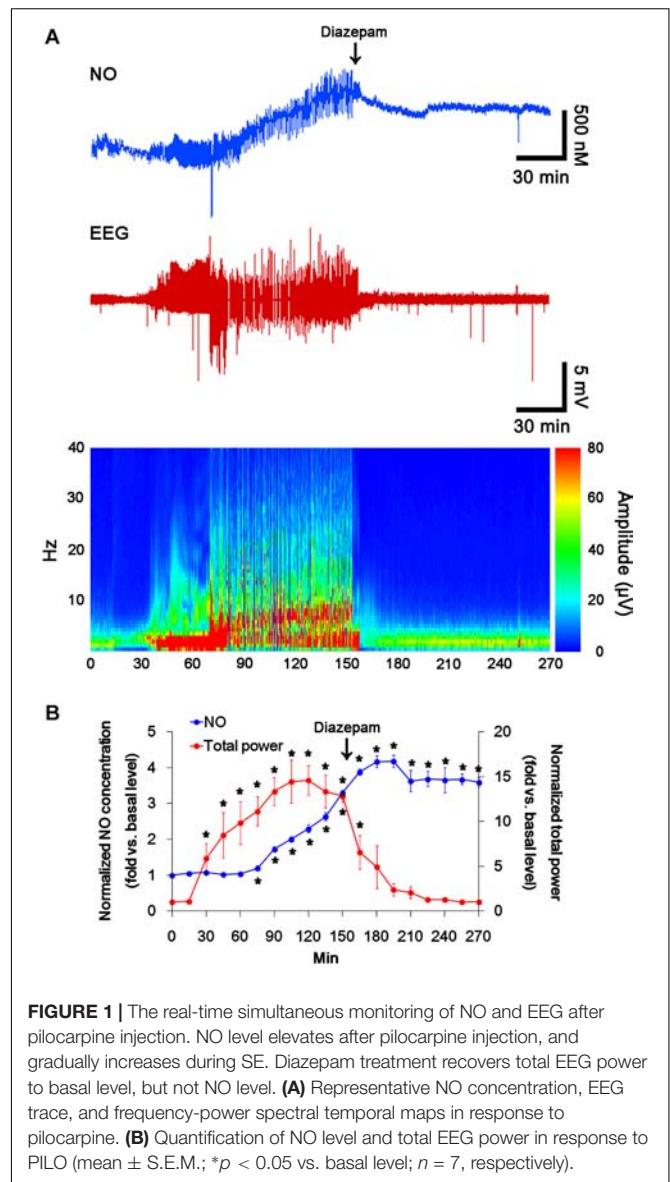
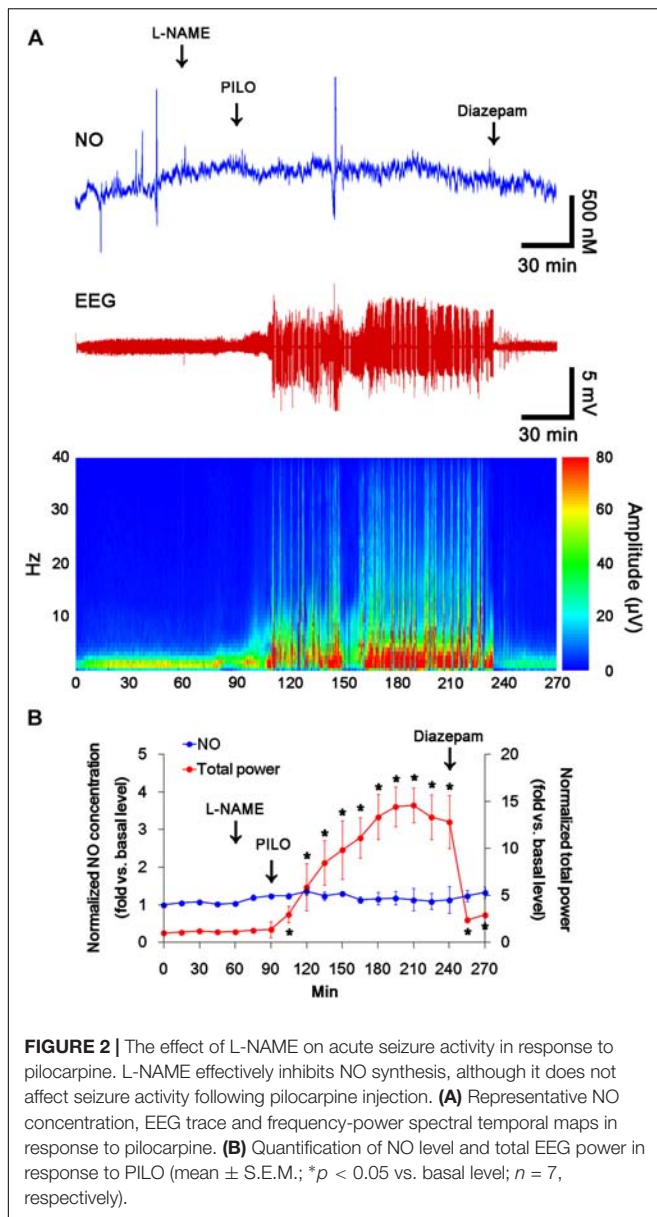


FIGURE 1 | The real-time simultaneous monitoring of NO and EEG after pilocarpine injection. NO level elevates after pilocarpine injection, and gradually increases during SE. Diazepam treatment recovers total EEG power to basal level, but not NO level. **(A)** Representative NO concentration, EEG trace, and frequency-power spectral temporal maps in response to pilocarpine. **(B)** Quantification of NO level and total EEG power in response to PILO (mean \pm S.E.M.; * p < 0.05 vs. basal level; n = 7, respectively).

after siRNA infusion, rats were anesthetized (urethane, 1.5 g/kg i.p.) and placed in a stereotaxic frame. After baseline recording for at least 30 min, an internal infusion cannula (C315IA, Plastics One, United States) was inserted into the lumen of the guide cannula to inject NMDA (20 μ M) into the ventricle over a 1-min period using a microinjection pump (1 μ l/min, KD Scientific, United States). Animals implanted with a guide-electrode-combo (C313G-MS303/2/SPC, Plastics One, United States) aforementioned were directly infused NMDA or α -amino-3-hydroxy-5-methyl-4-isoxazolepropionic acid (AMPA; 20 μ M, respectively) into the hippocampus (3.8 mm posterior; 2.0 mm lateral; 2.6 mm depth from bregma) with the same method. EEG signals were digitized and analyzed using LabChart Pro v7 (AD Instruments, Australia). Spectrograms were automatically calculated using a Hanning sliding window with 50% overlap (Kim et al., 2016, 2017b).



Western Blot

Under urethane anesthesia (1.5 g/kg, i.p.), the hippocampus was dissected out and homogenized in lysis buffer (50 mM Tris containing 50 mM 4-(2-hydroxyethyl)-1-piperazineethanesulfonic acid (pH 7.4), ethylene glycol tetraacetic acid (pH 8.0), 0.2% Tergitol type NP-40, 10 mM ethylenediaminetetraacetic acid (pH 8.0), 15 mM sodium pyrophosphate, 100 mM β -glycerophosphate, 50 mM NaF, 150 mM NaCl, 2 mM sodium orthovanadate, 1 mM phenylmethylsulfonyl fluoride, and 1 mM dithiothreitol). Total protein content was measured by BCA protein assay kit. Western blotting was performed according to standard procedures. The primary antibodies were mouse anti-PDI (1:1,000, Abcam, United Kingdom), rabbit anti-GluN1 (1:1,000, Millipore, United States) and rabbit anti-GluN2A (1:1,000,

Thermo Fisher Scientific, United States). Mouse TrueBlot (Rockland, United States) was used as a secondary antibody for PDI in co-immunoprecipitation. The rabbit anti- β -actin primary antibody (1:6000) was used as internal reference. The signals were scanned and quantified on ImageQuant LAS4000 system (GE health, United States). The values of each sample were normalized with the corresponding amount of β -actin.

Co-immunoprecipitation

The hippocampal tissues were lysed in radioimmune precipitation buffer (RIPA) with protease and phosphatase inhibitor cocktails (Roche Applied Sciences, United States) and 1 mM sodium orthovanadate. After calibration of total protein concentrations, and equal amounts of proteins were precipitated with the primary antibody and subsequent protein G sepharose at 4°C overnight (Kim et al., 2017b). Beads were collected, eluted in sample buffer and boiled at 95°C for 5 min. Next, Western blotting was performed according to standard procedures.

Measurement of Free- and Nitrosothiols

Modified biotin switch assay was performed with the S-nitrosylation Western Blot Kit (Thermo Fisher Scientific, United States) according to the manufacturer's protocol. Briefly, lysates were reacted with ascorbate in HENS buffer for specific labeling with iodoTMTzero reagents with MMT pretreatment (SNO-thiol) or not (total thiol). Protein labeling can be confirmed by Western blot using TMT antibody. Thereafter, TMT-labeled proteins were purified by Anti-TMT Resin, eluted by TMT elution buffer, and identified by Western blot according to standard procedures. For technical controls, we omitted ascorbate for each sample. The ratio of TMT-protein to total protein was described as SNO- and total thiol level. In addition, SNO-thiol over each NMDAR subunit ratio to total-thiol over each NMDAR subunit ratio was described as SNO-thiol-to-total thiol ratios.

Measurement of PDI Activity

The hippocampal tissues were lysed in RIPA buffer, and protein concentrations were determined by BCA protein assay (Pierce, Rockford, IL, United States). Equal amounts of total proteins (1 mg) were used to measure PDI activity with PROTEOSTAT® PDI assay kit (Enzo life sciences, Farmingdale, NY, United States) according to the manufacturer's protocol.

Immunohistochemistry

Rats were anesthetized with urethane anesthesia (1.5 g/kg, i.p.) and perfused transcardially with 4% paraformaldehyde in 0.1 M phosphate buffer (PB, pH 7.4). Brains were post-fixed in the same fixative overnight and then cryoprotected and sectioned at 30 μ m with a cryostat. Free-floating coronal sections were incubated in PDI antibody in PBS containing 0.3% Triton X-100 overnight at room temperature. Tissue sections were developed in 3,3'-diaminobenzidine in 0.1 M Tris buffer and mounted on gelatin-coated slides. Some sections were incubated with PDI antibody in PBS containing 0.3%

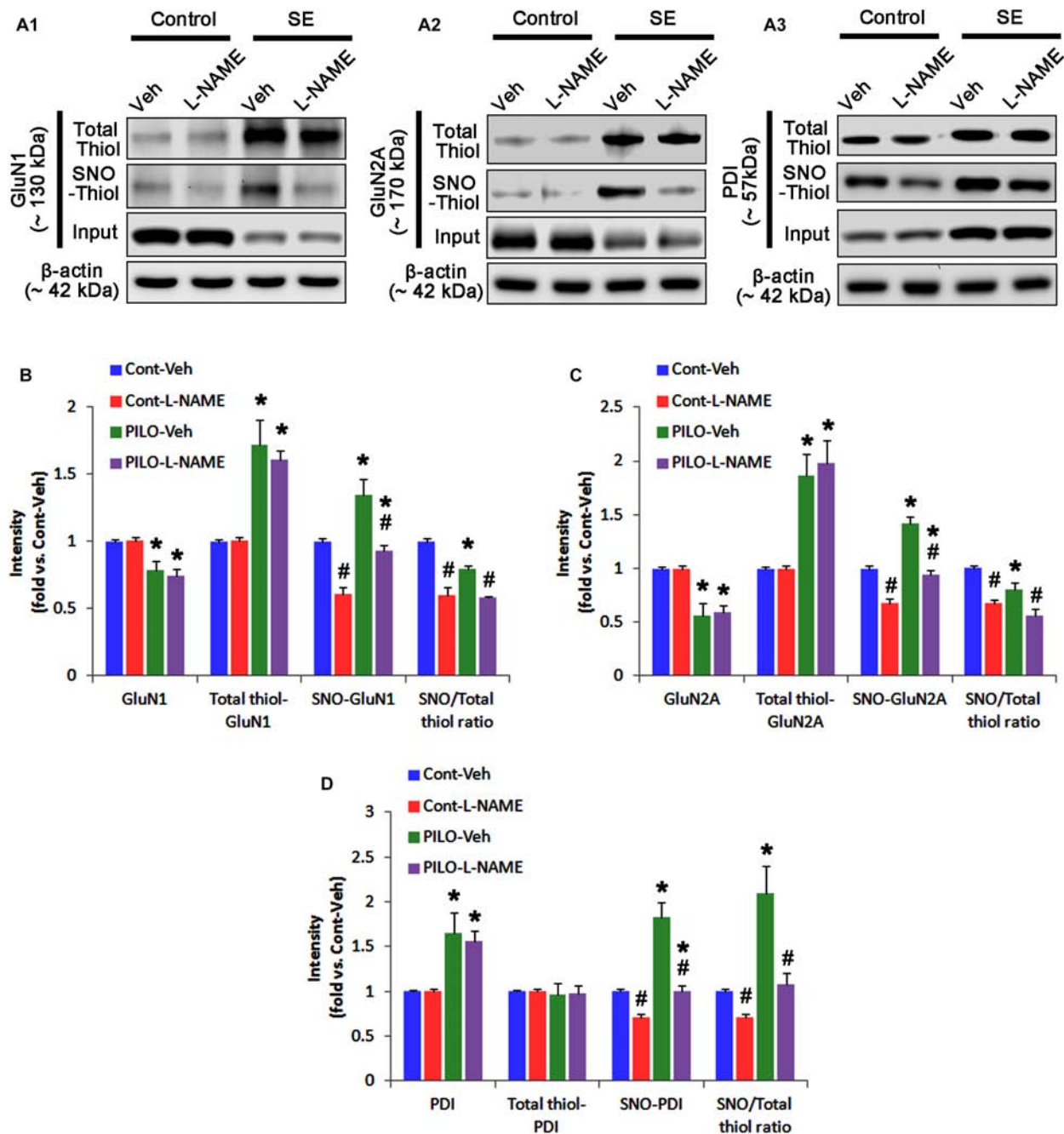


FIGURE 3 | The effect of L-NAME on SNO- and total thiol levels on NMDAR subunits and PDI in the acute seizure model. **(A)** Representative western blot for expressions, and the amounts of total- and SNO-thiol on GluN1 **(A1)**, GluN2A **(A2)**, and PDI **(A3)**. Acute seizure activity increases total- and SNO-thiol levels, but reduce the SNO-thiol-to-total thiol ratio on NMDAR. L-NAME reduces SNO-thiol level and the SNO-thiol-to-total thiol ratios on both NMDAR subunits and PDI without changing their total thiol levels. **(B–D)** Quantification of expressions (panel 1), and the amounts of total thiols (panel 2), SNO-thiol (panel 3) and the SNO-thiol-to-total thiol ratio (SNO ratio; panel 4) on GluN1 **(B)**, GluN2A **(C)**, and PDI **(D)**. Error bars indicate SEM (*, # $p < 0.05$ vs. control and vehicle, respectively; $n = 7$, respectively).

Triton X-100 overnight at room temperature. Thereafter, sections were visualized with Cy2-conjugated secondary antibody. Immunoreaction was observed using an Axio Scope microscope (Carl Zeiss Inc., Oberkochen, Germany). To establish the specificity of the immunostaining, a negative control test was

carried out with preimmune serum instead of the primary antibody. No immunoreactivity was observed for the negative control in any structures. All experimental procedures in this study were performed under the same conditions and in parallel.

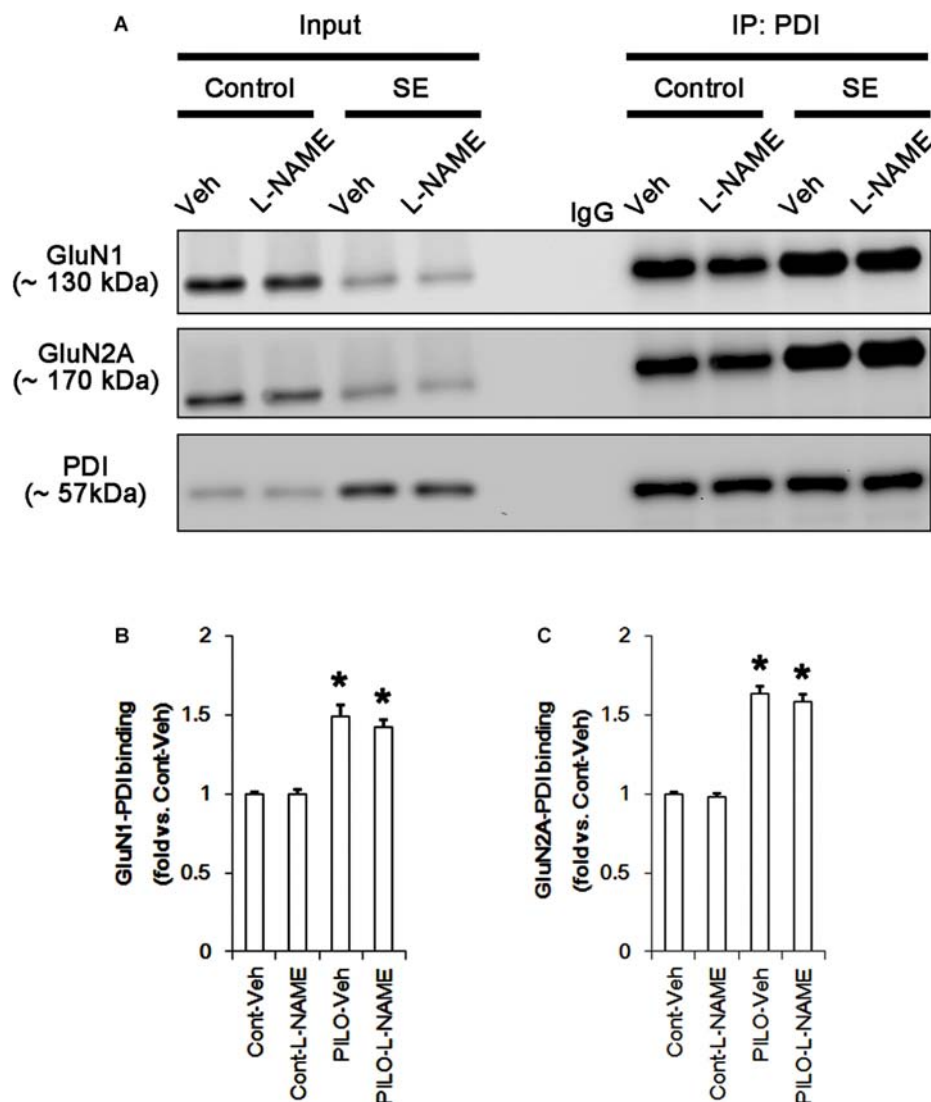


FIGURE 4 | The effect of L-NAME on the binding of PDI to NMDAR subunits in the acute seizure model. **(A)** Co-immunoprecipitation of PDI and NMDAR. Seizure activity increases PDI-NMDAR bindings that are unaffected by L-NAME. **(B,C)** Quantitative analyses of co-immunoprecipitation of PDI with GluN1 and GluN2A. Error bars indicate SEM (* $p < 0.05$ vs. control; $n = 7$, respectively).

Statistical Analysis

Quantitative data are expressed as mean \pm standard error of the mean. Data are analyzed by Student *t*-test or ANOVA followed by Newman-Keuls *post hoc* test. A $p < 0.05$ is considered to be statistically different.

RESULTS

Acute Seizures Induce the Sustained NO Synthesis Independent of Seizure Activity

In previous studies, we have reported that pilocarpine-induced SE triggers signaling cascades for the NO synthesis, and

subsequently increases NO metabolites (Kim et al., 2013; Ko et al., 2015a). Due to the microdialysis method for nitrate/nitrite products in these previous studies, the precise changes in NO synthesis during seizure activity have been limited. In the present study, thus, we applied the real-time simultaneous monitoring of NO and EEG after pilocarpine injection to directly elucidate the relationship between seizure activity and NO generation. EEG revealed seizure on-set and increase in total EEG power ~ 30 min after pilocarpine injection ($p < 0.05$ vs. basal level, **Figures 1A,B**). In addition, NO monitoring showed that NO level increased ~ 75 min after pilocarpine injection, and gradually elevated during SE ($p < 0.05$ vs. basal level, **Figures 1A,B**). After diazepam treatment, total EEG power was recovered to basal level, while increased NO level was sustained ($p < 0.05$ vs. basal level). These findings indicate that seizure on-set

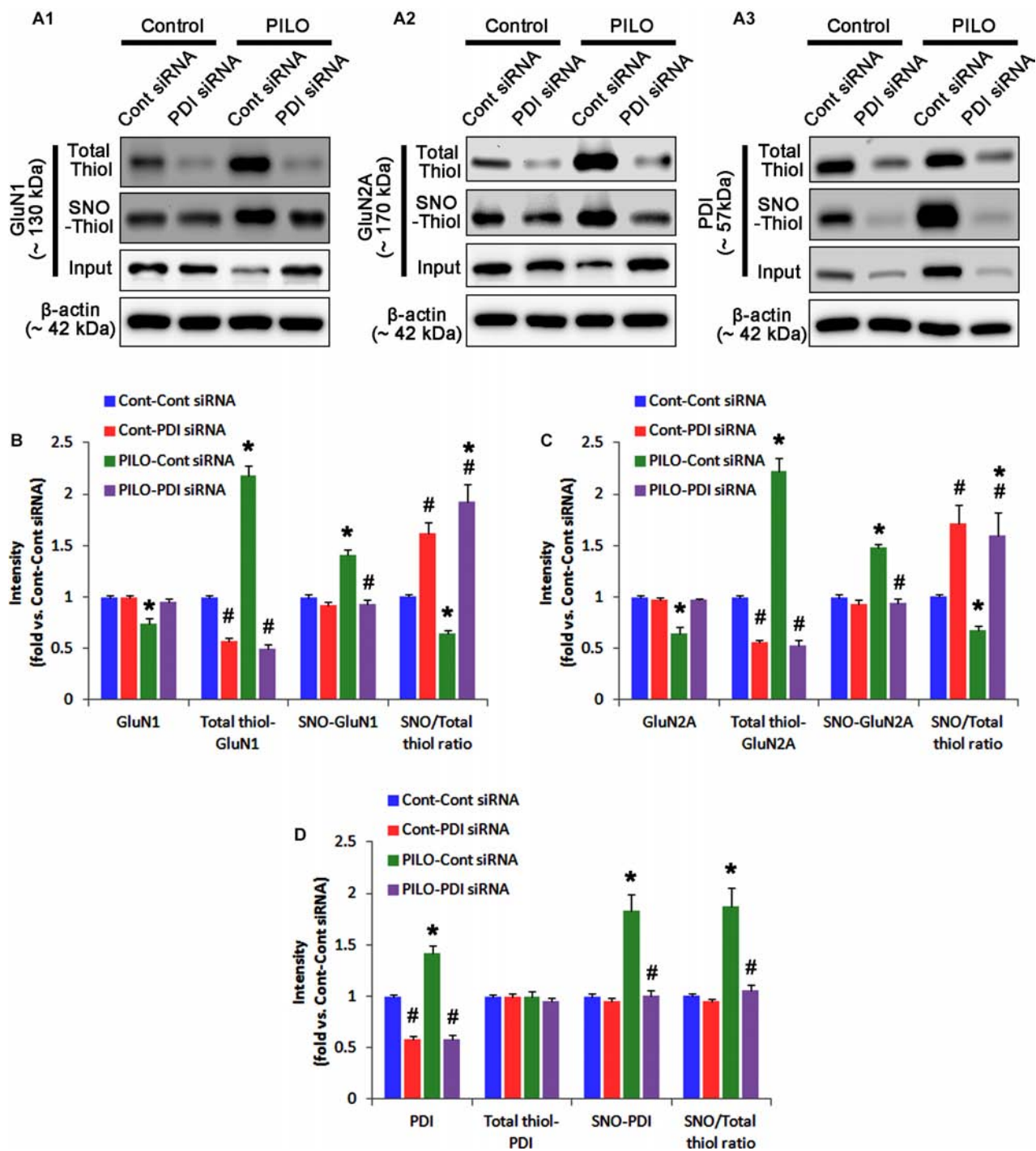


FIGURE 5 | The effect of PDI knockdown on SNO- and total thiol levels on NMDAR subunits and PDI in the acute seizure model. **(A)** Representative western blot for expressions, and the amounts of total- and SNO-thiol on GluN1 **(A1)**, GluN2A **(A2)**, and PDI **(A3)**. PDI siRNA reduces SNO- and total thiol levels on both NMDAR subunits, but increases the SNO-thiol-to-total thiol ratios on both NMDAR subunits under control and post-seizure conditions. **(B–D)** Quantification of expressions (panel 1), and the amounts of total thiols (panel 2), SNO-thiol (panel 3), and the SNO-thiol-to-total thiol ratio (SNO ratio; panel 4) on GluN1 **(B)**, GluN2A **(C)**, and PDI **(D)**. Error bars indicate SEM (*, # $p < 0.05$ vs. control and vehicle, respectively; $n = 7$, respectively).

may turn on NO generation, but seizure termination may not turn it off. For direct investigating the role of NO in seizure activity, we applied L-NAME (a non-selective NOS inhibitor) to

animals 30 min prior to SE induction. L-NAME prevented the prolonged NO generation without affecting seizure activity in response to pilocarpine (**Figures 2A,B**). Vehicle did not influence

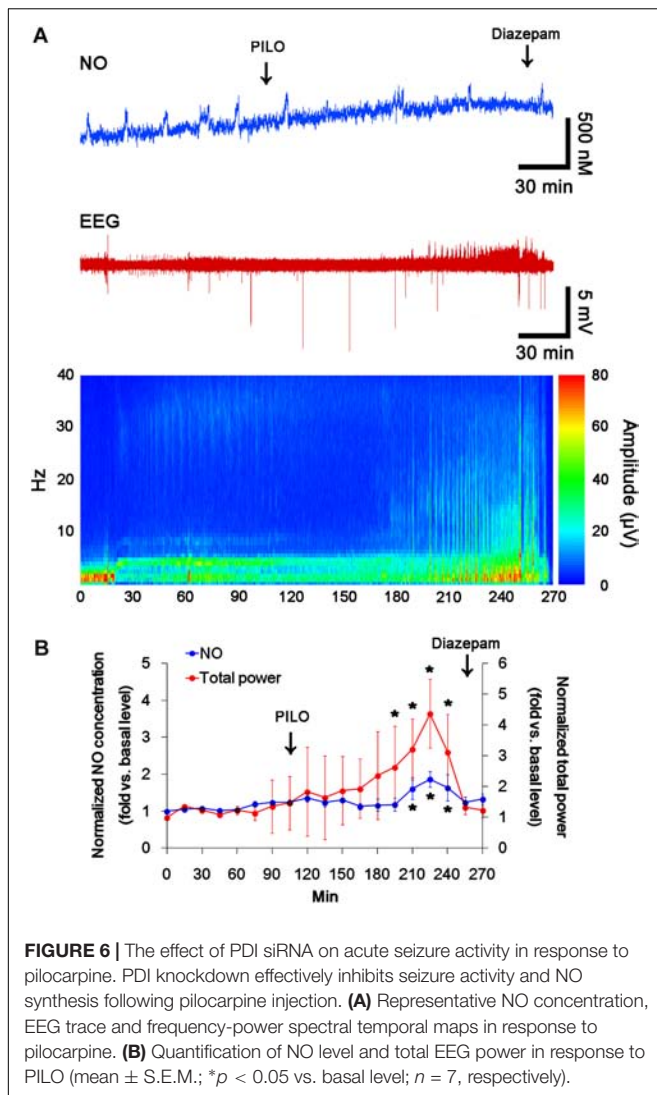


FIGURE 6 | The effect of PDI siRNA on acute seizure activity in response to pilocarpine. PDI knockdown effectively inhibits seizure activity and NO synthesis following pilocarpine injection. **(A)** Representative NO concentration, EEG trace and frequency-power spectral temporal maps in response to pilocarpine. **(B)** Quantification of NO level and total EEG power in response to PILO (mean \pm S.E.M.; * $p < 0.05$ vs. basal level; $n = 7$, respectively).

seizure susceptibility and its severity (data not shown). These findings indicate that NO may not have pro-convulsive or anti-convulsive effect. Therefore, our findings suggest that prolonged NO generation may be involved in the diverse post-SE events independent of seizure activity.

Acute Seizure Activity Increases the Amount of Total Thiol and S-Nitrosylation on NMDAR

Free thiols on GluN1 and GluN2A subunits undergo S-nitrosylation and further oxidation to disulfide bonds, which decreases NMDAR functionality (Jaffrey et al., 2001; Lipton et al., 2002). Therefore, it is likely that NO generation would be one of adaptive responses to SE for reducing seizure activity by nitrosylating free thiols on NMDAR subunits and PDI. To confirm this hypothesis, we measured the amounts of total (SH- + SNO-) thiols and SNO-thiols on NMDAR and PDI.

In control animals, L-NAME did not affect the expression levels of GluN1 and GluN2A (Figures 3A–C and Supplementary

Figure 4), while it reduced the amounts of SNO-thiols, but not total thiols, on both NMDAR subunits ($p < 0.05$ vs. vehicle; Figures 3A–C). The SNO-thiol-to-total thiol ratios on GluN1 and GluN2A were decreased to 0.6- and 0.68-fold of vehicle level, respectively ($p < 0.05$; Figures 3B,C). L-NAME did not influence PDI expression level and the amount of total thiols on PDI. Since S-nitrosylation level of PDI was decreased by L-NAME (Figures 3A3,D), the SNO-thiol-to-total thiol ratio on PDI was diminished to 0.71-fold of vehicle level ($p < 0.05$; Figure 3D).

Following acute seizures, the expression levels of GluN1 and GluN2A were reduced to 0.78- and 0.56-fold of control level, respectively ($p < 0.05$; Figures 3A–C). However, the amounts of total- and SNO-thiols on GluN1 were increased to 1.72- and 1.35-fold of control level, respectively ($p < 0.05$; Figures 3A1,B). Thus, the SNO-thiol-to-total thiol ratio on GluN1 was decreased to 0.79-fold of control level ($p < 0.05$; Figure 3B). Similarly, acute seizures increased the amount of total thiols and S-nitrosylation on GluN2A ($p < 0.05$; Figures 3A2,C), while the SNO-thiol-to-total thiol ratio on GluN2A was abolished to 0.8-fold of control level ($p < 0.05$; Figure 3C). Consistent with our previous studies (Ko et al., 2015b; Kim et al., 2017c), acute seizures elevated PDI expression and its S-nitrosylation level without altering the amount of total thiols ($p < 0.05$; Figures 3A3,D). Unlike NMDAR subunits, the SNO-thiol-to-total thiol ratio on PDI was 2.1-fold of control level ($p < 0.05$; Figure 3D). In addition, the bindings of PDI to GluN1 and GluN2A were significantly increased to 1.48- and 1.63-fold of control level, respectively ($p < 0.05$; Figures 4A–C and Supplementary Figure 5). L-NAME abolished S-nitrosylation levels of GluN1, GluN2A, and PDI without changing their expression levels following acute seizures ($p < 0.05$ vs. vehicle; Figures 3A–D). L-NAME could not affect the amount of total thiols on NMDAR subunits and PDI (Figures 3A–D). The SNO-thiol-to-total thiol ratios on GluN1, GluN2A and PDI were 0.58-, 0.56-, and 1.08-fold of vehicle level in control animals, respectively ($p < 0.05$; Figures 3B–D). As compared to vehicle, L-NAME did not influence the bindings of PDI to GluN1 and GluN2A under control and post-seizure conditions ($p < 0.05$; Figures 4A–C). Taken together, our findings indicate that seizure-induced NO generation may increase S-nitrosylation levels of NMDAR subunits and PDI without affecting their disulfide bond formations. Furthermore, the binding of PDI to NMDAR subunits may be unaffected by S-nitrosylation of PDI.

PDI siRNA Inhibits Acute Seizures in Response to Pilocarpine With Reducing the Amount of Total Thiol on NMDAR

In the present study, acute seizure activity increased PDI expression and the amounts of SNO-thiol and total thiol residues on NMDAR subunits, which regulate NMDAR functionality (Aizenman et al., 1989; Tang and Aizenman, 1993; Sanchez et al., 2000; Kim et al., 2017c). Since PDI is a redox enzyme and acts as a NO donor and a denitrosylase (Ramachandran et al., 2001; Rigobello et al., 2001; Turano et al., 2002; Root et al., 2004; Sliskovic et al., 2005; Popescu et al., 2010; Bi

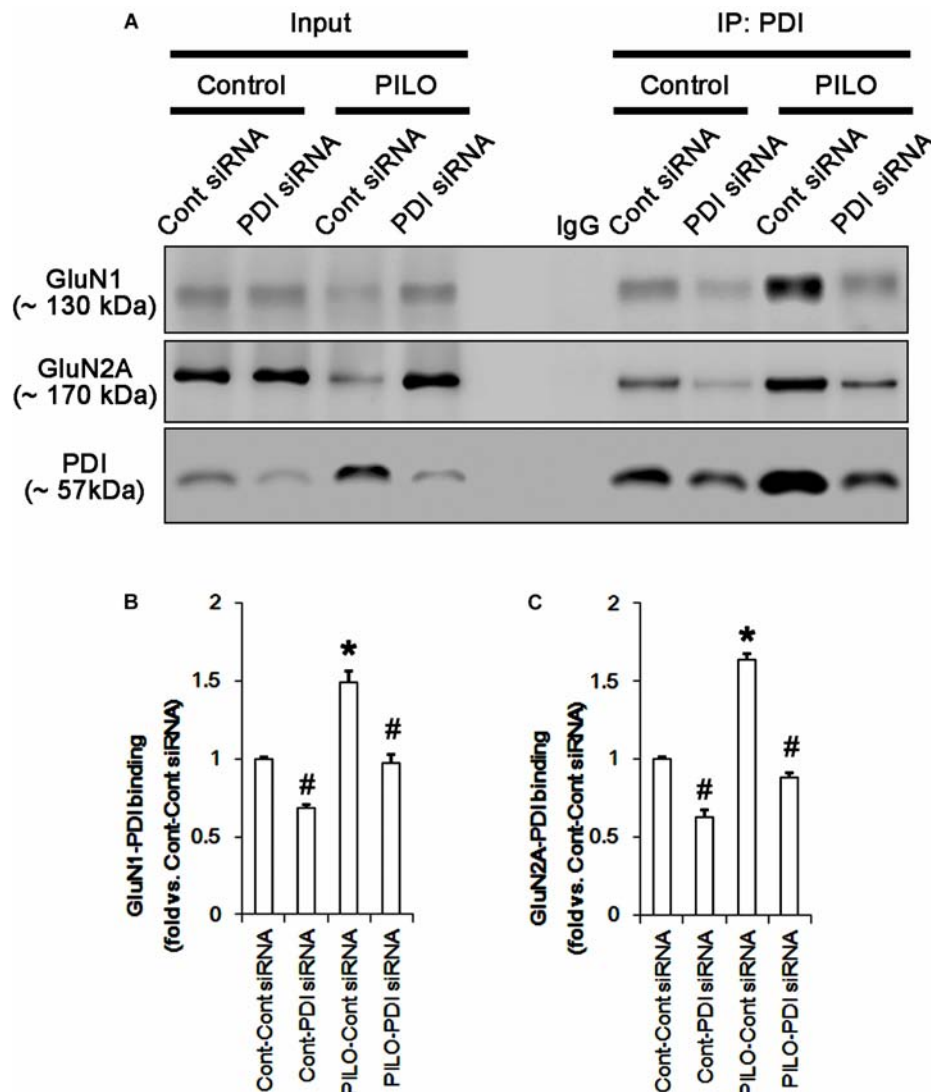


FIGURE 7 | The effect of PDI knockdown on the binding of PDI to NMDAR subunits in the acute seizure model. **(A)** Co-immunoprecipitation of PDI and NMDAR. PDI knockdown reduces PDI-NMDAR bindings under control and post-seizure conditions. **(B,C)** Quantitative analyses of co-immunoprecipitation of PDI with GluN1 and GluN2A. Error bars indicate SEM (*, # $p < 0.05$ vs. control; $n = 7$, respectively).

et al., 2011; Kallakunta et al., 2013; Kim et al., 2017c), we investigated whether the increased PDI expression affects the redox and S-nitrosylation levels on NMDAR following acute seizure activity.

Consistent with our previous studies (Kim et al., 2017c; Lee and Kim, 2018), PDI siRNA effectively reduced PDI expression, its activity and S-nitrosylation of dynamin-related protein 1 (DRP1, $p < 0.05$ vs. control siRNA; **Supplementary Figures 1, 12**). These findings confirm the efficacy of PDI siRNA in the present study. As compared to control siRNA, PDI siRNA did not influence the phosphorylation or expression levels of protein kinase RNA (PKR)-like ER kinase (PERK), inositol-requiring protein 1- α (IRE1 α), activating transcription factor 6 (ATF6) and glucose-regulated protein 78 (GRP78), which are involved in the regulation of ER stress (Ko et al., 2015b; Kim et al., 2017a;

Supplementary Figures 2, 13). These findings indicate that PDI knockdown may not provoke ER stress under physiological condition.

In control animals, PDI knockdown decreased the amount of total thiols on NMDAR subunits ($p < 0.05$ vs. control siRNA; **Figures 5A–C** and **Supplementary Figure 6**), while NMDAR subunit expressions and their S-nitrosylation were unaffected by PDI siRNA (**Figures 5A–C**). Thus, the SNO-thiol-to-total thiol ratios on GluN1 and GluN2A were increased to 1.62- and 1.49-fold of control siRNA level, respectively ($p < 0.05$; **Figures 5B,C**). PDI knockdown delayed seizure on-set and NO generation in response to pilocarpine ($p < 0.05$ vs. control siRNA; **Figures 6A,B**). However, control siRNA did not affect the seizure susceptibility and its severity in response to pilocarpine (data not shown). PDI knockdown prevented the decreased

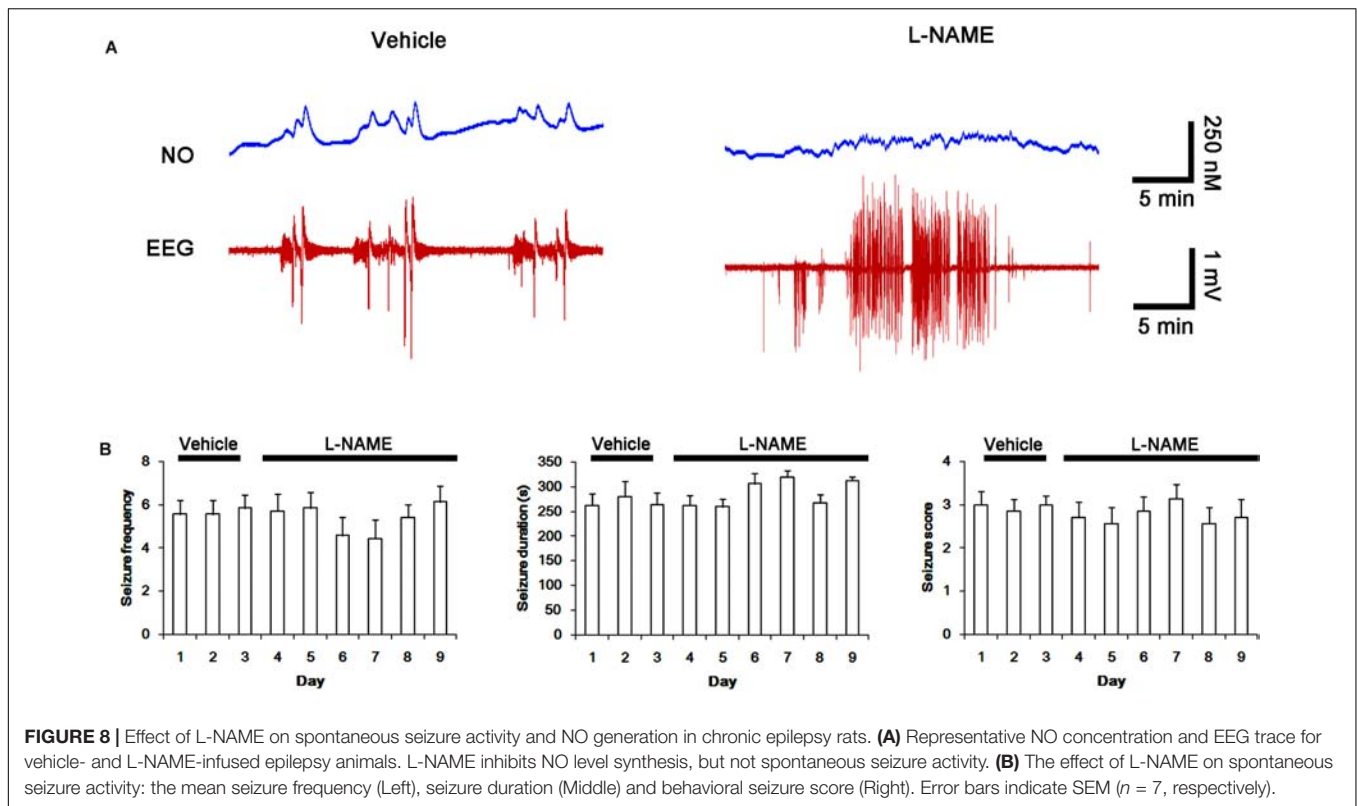


FIGURE 8 | Effect of L-NAME on spontaneous seizure activity and NO generation in chronic epilepsy rats. **(A)** Representative NO concentration and EEG trace for vehicle- and L-NAME-infused epilepsy animals. L-NAME inhibits NO level synthesis, but not spontaneous seizure activity. **(B)** The effect of L-NAME on spontaneous seizure activity: the mean seizure frequency (Left), seizure duration (Middle) and behavioral seizure score (Right). Error bars indicate SEM ($n = 7$, respectively).

NMDAR expressions induced by acute seizures ($p < 0.05$ vs. control siRNA; **Figures 5A–C**). It also abrogated the increases in the amount of total thiols and S-nitrosylation on NMDAR following acute seizure activity ($p < 0.05$ vs. control siRNA; **Figures 5A–C**). Furthermore, PDI knockdown increased the SNO-thiol-to-total thiol ratio on GluN1 and GluN2A to 1.93- and 1.85-fold of vehicle levels in control animals, respectively ($p < 0.05$ vs. control siRNA; **Figures 5B,C**). Similar to PDI siRNA, PACMA31 (a selective PDI inhibitor) also inhibited seizure activity in response to pilocarpine and diminished the amount of total thiols, but not SNO-thiols, on NMDAR subunits ($p < 0.05$ vs. vehicle; **Supplementary Figures 3, 14**). Furthermore, PACMA31 increased the SNO-thiol-to-total thiol ratios on GluN1 and GluN2A ($p < 0.05$ vs. vehicle; **Supplementary Figures 3, 14**). These data suggest that PDI may reduce the disulfide bonds on NMDAR without affecting its S-nitrosylation.

Protein disulfide isomerase siRNA abolished PDI expression ($p < 0.05$ vs. control siRNA; **Figures 5A3,D**), but not the amounts of total thiols and SNO-thiols of PDI (**Figure 5D**). The SNO-thiol-to-total thiol ratio on PDI was unaffected by PDI knockdown (**Figure 5D**). PDI siRNA inhibited the up-regulation of PDI expression, its S-nitrosylation and the SNO-thiol-to-total thiol ratio on PDI induced by acute seizures ($p < 0.05$ vs. control siRNA; **Figures 5A3,D**). PDI knockdown significantly diminished the bindings of PDI to GluN1 and GluN2A under control and post-seizure conditions ($p < 0.05$ vs. control siRNA; **Figures 7A–C** and **Supplementary Figure 7**). Therefore, our findings indicate that PDI knockdown may inhibit seizure activity

by increasing the SNO-thiol-to-total thiol ratio on NMDAR due to reducing total thiol level.

The Amounts of Total Thiol and S-Nitrosylation on NMDAR Increase in Chronic Epilepsy Rat

Next, we also investigated whether the SNO-thiol-to-total thiol ratio on NMDAR is relevant to spontaneous seizure activity in chronic epileptic animals. In vehicle-infusion period, the mean seizure frequency was $\sim 5.6/2$ -h recording session, the total seizure duration was ~ 270 s, and behavioral seizure severity (Racine score) was ~ 3 (**Figures 8A,B**). NO level immediately rose after spontaneous seizure on-set, and gradually decreased to basal level after seizure cessation (**Figure 8A**). L-NAME could not affect seizure frequency, duration and score in chronic epilepsy rat, but effectively inhibited NO synthesis during seizures (**Figures 8A,B**).

In chronic epilepsy rats, the expression levels of GluN1 and GluN2A were reduced to 0.74- and 0.65-fold of control level, respectively ($p < 0.05$; **Figures 9A–C** and **Supplementary Figure 8**). However, the amounts of total and SNO-thiols on GluN1 were increased to 2.1- and 1.71-fold of control level, respectively ($p < 0.05$; **Figures 9A1,B**). Thus, the SNO-thiol-to-total thiol ratio on GluN1 was decreased to 0.85-fold of control level ($p < 0.05$; **Figure 9B**). In addition, the amounts of total and SNO-thiol on GluN2A were 2.01- and 1.62-fold of control level, respectively ($p < 0.05$; **Figures 9A2,C**). The SNO-thiol-to-total thiol ratio on GluN2A was 0.82-fold of control level

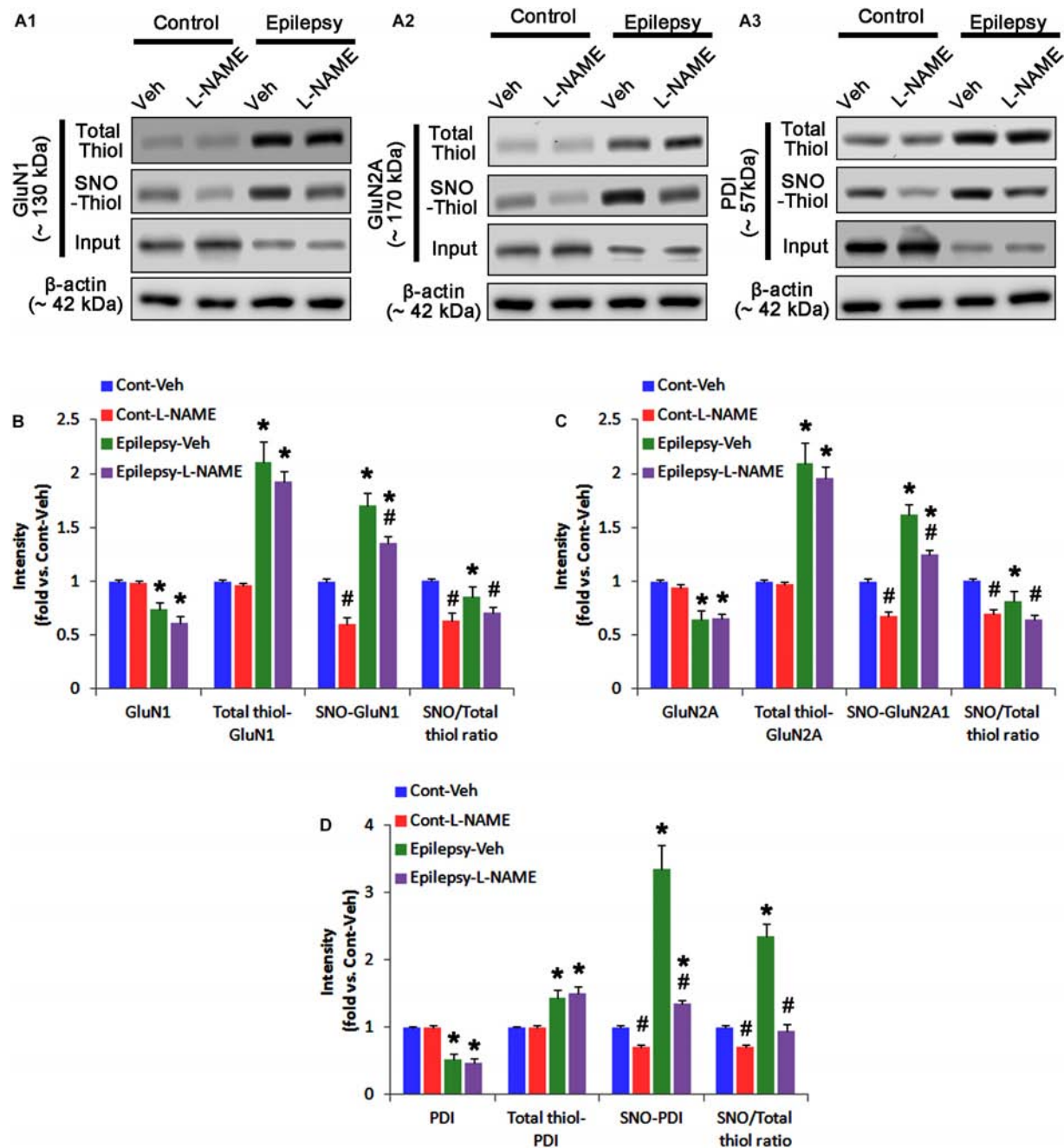


FIGURE 9 | The effect of L-NAME on SNO- and total thiol levels on NMDAR subunits and PDI in chronic epilepsy rats. **(A)** Representative western blot for expressions, and the amounts of total- and SNO-thiols on GluN1 **(A1)**, GluN2A **(A2)**, and PDI **(A3)**. In chronic epilepsy animals, the total- and SNO-thiol levels are increased on NMDAR, but the SNO-thiol-to-total thiol ratios are reduced. L-NAME reduces SNO-thiol level and the SNO-thiol-to-total thiol ratios on both NMDAR subunits and PDI without changing their total thiol levels. **(B–D)** Quantification of expressions (panel 1), the amounts of total thiols (panel 2), SNO-thiol (panel 3), and the SNO-thiol-to-total thiol ratio (SNO ratio; panel 4) on GluN1 **(B)**, GluN2A **(C)**, and PDI **(D)**. Error bars indicate SEM (*, # $p < 0.05$ vs. control and vehicle, respectively; $n = 7$, respectively).

($p < 0.05$; **Figure 9C**). Although PDI expression was 0.55-fold of control level ($p < 0.05$; **Figures 9A3,D**), the amounts of total and SNO-thiol on PDI were 1.44- and 3.36-fold of control level, respectively ($p < 0.05$; **Figures 9A3,D**). The SNO-thiol-to-total thiol ratio on PDI was 2.36-fold of control level ($p < 0.05$;

Figure 9D). In addition, the bindings of PDI to GluN1 and GluN2A were 1.67- and 1.66-fold of control level, respectively ($p < 0.05$; **Figures 10A–C** and **Supplementary Figure 9**). L-NAME abolished S-nitrosylation levels of GluN1, GluN2A and PDI to 1.35-, 1.25-, and 1.35-fold of vehicle level in control

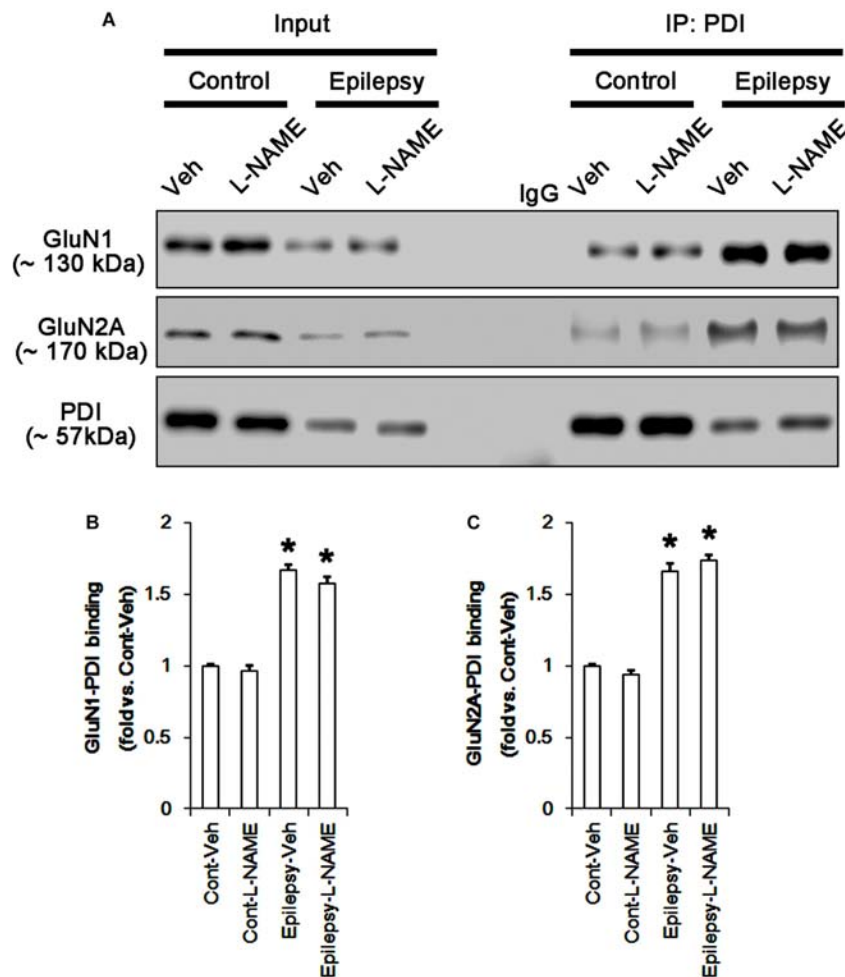


FIGURE 10 | The effect of L-NAME on the binding of PDI to NMDAR subunits in chronic epilepsy model. **(A)** Co-immunoprecipitation of PDI and NMDAR. Chronic epilepsy animals show the increase in PDI-NMDAR bindings. L-NAME cannot affect them. **(B,C)** Quantitative analyses of co-immunoprecipitation of PDI with GluN1 and GluN2A. Error bars indicate SEM (* $p < 0.05$ vs. control; $n = 7$, respectively).

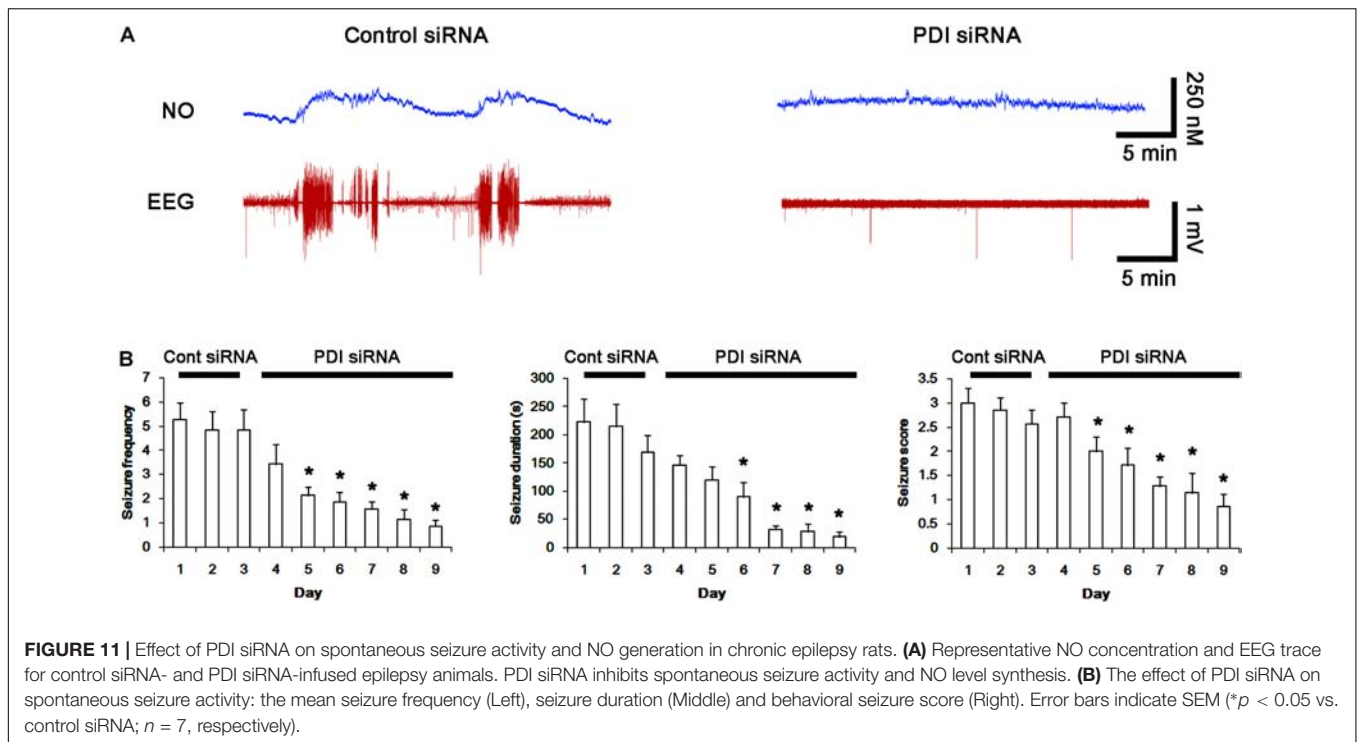
animals, respectively ($p < 0.05$ vs. vehicle; **Figures 9A–D**), but not expression levels and the amount of disulfide bonds on NMDAR subunits and PDI (**Figures 9A–D**). The SNO-thiol-to-total thiol ratios on GluN1, GluN2A and PDI were 0.71-, 0.65-, and 0.95-fold of vehicle level in control animals, respectively ($p < 0.05$; **Figures 9B–D**). L-NAME did not influence the bindings of PDI to GluN1 and GluN2A in control and epilepsy animals ($p < 0.05$ vs. vehicle; **Figures 10A–C**). These findings indicate that the decreased SNO-thiol-to-total thiol ratio on NMDAR may be involved in spontaneous seizure activity in chronic epilepsy rats, similar to acute seizures.

PDI Knockdown Inhibits Spontaneous Seizure Activity With the Increased SNO-Thiol-to-Total Thiol Ratio on NMDAR

Next, we investigated the effect of PDI knockdown on NMDAR redox as well as its S-nitrosylation in chronic epilepsy rats,

because PDI siRNA effectively inhibits the generation of spontaneous seizures in chronic epilepsy rats (Kim et al., 2017c). In control siRNA-infusion period, the mean seizure frequency was $\sim 5/2$ -h recording session, the total seizure duration was ~ 220 s, and behavioral seizure severity (Racine score) was ~ 3 (**Figures 11A,B**). On the final day in PDI siRNA infusion period (7 day-over PDI siRNA infusion), the mean seizure frequency and the total seizure duration were reduced to $\sim 0.85/\text{recording session}$ and 19 s, respectively. Behavioral seizure score was also decreased to 1.7 ($p < 0.05$ vs. control siRNA; **Figures 11A,B**).

As compared to control siRNA, PDI knockdown did not affect expression levels and S-nitrosylation of NMDAR subunits. However, it decreased the amount of total thiols on GluN1 and GluN2A in chronic epilepsy rats ($p < 0.05$ vs. control siRNA; **Figures 12A–C** and **Supplementary Figure 10**). Thus, PDI knockdown increased the SNO-thiol-to-total thiol ratio on GluN1 and GluN2A to 1.57- and 1.45-fold of control siRNA-infused control animals, respectively ($p < 0.05$;



Figures 12B,C). PDI siRNA reduced PDI expression without altering the amount of total thiol, S-nitrosylation and the SNO-thiol-to-total thiol ratio on PDI ($p < 0.05$ vs. control siRNA; **Figures 12A3,D**). PDI knockdown also alleviated the bindings of PDI to GluN1 and GluN2A ($p < 0.05$ vs. control siRNA; **Figures 13A–C** and **Supplementary Figure 11**). Taken together, our findings suggest that that PDI may not be a NO donor or a denitrosylase for NMDAR subunits, and that increase in total thiol levels on NMDAR by PDI siRNA may inhibit spontaneous seizure activity in epilepsy rats.

PDI Knockdown Reduces Neuronal Activity in Response to NMDA

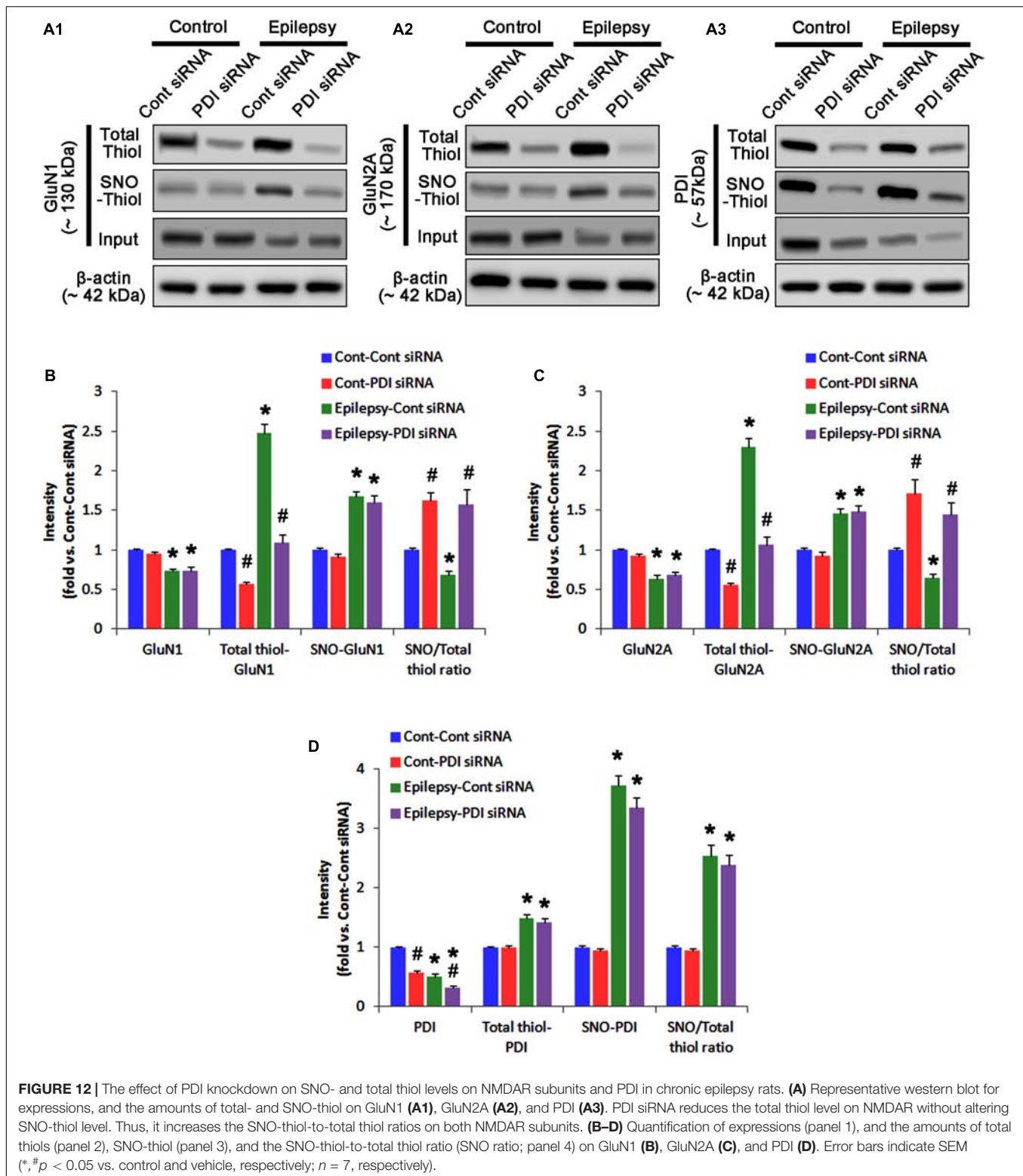
To directly confirm PDI-mediated regulation of NMDAR activity, we applied NMDA injection (20 μ M) into the ventricle. NMDA increased the amplitude, frequency of neuronal discharges and EEG total power in control siRNA-treated animals ($p < 0.05$ vs. basal level; $n = 7$; **Figures 14A–C**). However, NMDA did not affect them in PDI siRNA-treated rats, as compared the basal level ($p < 0.05$ vs. control siRNA; $n = 7$; **Figures 14A–C**). Similarly, the direct infusion of NMDA and AMPA into the hippocampus evoked epileptiform discharges in control siRNA-treated animals, while PDI knockdown inhibited field potentials in response to the direct NMDA or AMPA infusion ($p < 0.05$ vs. control siRNA; $n = 7$; **Figures 14D–G**). These findings indicate that PDI siRNA may reduce NMDAR functionality via regulating thiolation of NMDAR subunits.

DISCUSSION

The major findings in the present study are that PDI was not a NO donor or a denitrosylase for NMDAR, and that PDI knockdown inhibited seizure activity in acute seizure and spontaneous seizure activity in chronic epilepsy rats, independent of S-nitrosylation on NMDAR.

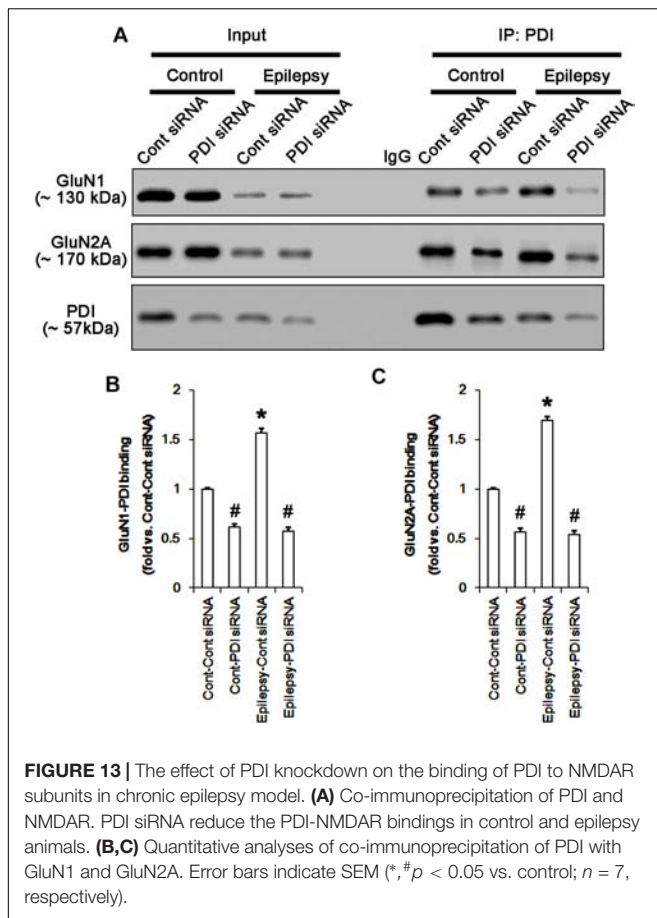
NMDAR over-activation results in neuronal death in a variety of acute and chronic neurological diseases including epilepsy (Lipton and Rosenberg, 1994). Thus, the maintenance of appropriate NMDAR activity is one of the potential antiepileptic and neuroprotective strategies. However, therapeutic doses of NMDAR antagonists result in the severe adverse effects including cognitive defects (Kornhuber and Weller, 1997; Chapman, 1998; Dannhardt and Kohl, 1998). The cysteine residues on NMDAR are involved in redox modulation and S-nitrosylation (Sucher and Lipton, 1991; Sucher et al., 1996; Lipton et al., 2002), which regulate NMDAR-mediate currents (Choi et al., 2000, 2001). Therefore, it is likely that the modulation of these post-translational modifications may be an interesting therapeutic target against epilepsy. Indeed, we have reported that PDI siRNA decreases seizure susceptibility by inhibiting the direct thiol reductase activity of PDI on NMDAR without glutathionylation of thiol modification in acute seizure- and chronic epilepsy model (Kim et al., 2017c). Since S-nitrosylation is a redox-based post-translational modification (Lei et al., 1992; Choi et al., 2000; Lipton et al., 2002), it is expected that PDI-mediated thiolation would affect the S-nitrosylation on NMDAR, but it has not been elucidated.

In the present study, acute seizure- and chronic epilepsy models showed the reductions in GluN1 and GluN2A expression



levels. These findings are consistent with previous studies demonstrating the reduced NMDAR expression in acute seizure- and epilepsy rats (Lasón et al., 1997; Suh et al., 2001; Khan et al., 2008). Since NMDAR is inactivated by intracellular

Ca^{2+} through the C-terminal splicing of the GluN1 subunit (Legendre et al., 1993; Okabe et al., 1999), it is likely that the reduced NMDAR expression may be a compensatory reaction to regulate the seizure activity by diminishing NMDA



receptor responsiveness. Adversely, it could not be excluded that the diminished NMDAR expression may be due to massive neuronal loss in these models. In the present study, both acute seizure- and chronic epilepsy models showed the elevations of SNO-thiol levels on NMDAR subunit and PDI-NMDAR subunit bindings. PDI is a modulator of S-nitrosylation, since it regulates the entry of SNO-thiols into cells (Ramachandran et al., 2001) and denitrosylates SNO-thiols (Root et al., 2004). PDI itself also acts as a NO carrier by the formation of SNO-PDI (Sliskovic et al., 2005; Kallakunta et al., 2013). Therefore, it is likely that PDI would also regulate NMDAR functionality via S-nitrosylation in both animal models. However, PDI siRNA effectively inhibited seizure activities in acute seizure- and epilepsy animals without changing S-nitrosylation levels of NMDAR. Furthermore, PDI siRNA reduced the amplitude and frequency of neuronal discharges induced by intracerebroventricular and intrahippocampal NMDA and AMPA injection in control animals. The present data also reveal that PDI siRNA increased the fraction of the amount of SNO-thiols in total thiols on NMDAR subunits due to diminishing total thiol levels. Unlike PDI knockdown, L-NAME could not influence seizure activities in both models, although it reduced SNO-thiol, not total thiol, level on NMDAR. Therefore, these findings indicate that PDI may not be a NO donor or a denitrosylase for NMDAR, and that PDI-mediated reduction

of disulfide bonds on NMDAR rather than S-nitrosylation on this receptor may relevant to seizure generations. Since NMDAR activation regulates conductance of the AMPA receptor (AMPA; Selvakumar et al., 2013), furthermore, our findings suggest that the PDI siRNA may affect AMPAR activity by inhibiting NMDAR functionality.

Protein disulfide isomerase is originally a chaperone in the ER (Edman et al., 1985; Koch, 1987; Yoshimori et al., 1990). Therefore, it is likely that PDI siRNA would lead to ER stress. Consistent with our previous study (Kim et al., 2017c), however, the present data reveal that PDI siRNA did not affect the phosphorylation or expression levels of PERK, IRE1 α , ATF6 and GRP78, which are indicatives of ER stress (Ko et al., 2015b; Kim et al., 2017c, 2018). Furthermore, SE induces ER stress in astrocytes rather than neurons, which provoke autophagic astroglial death (clasmotodendrosis; Ko et al., 2015b; Kim et al., 2017a, 2018). Therefore, our findings suggest that PDI knockdown may not induce ER stress in neurons under physiological condition.

On the other hand, S-nitrosylation of the active-site thiols of PDI inhibits its isomerase activity (Uehara et al., 2006). Therefore, it is plausible that the diminished PDI activity by S-nitrosylation would also affect its isomerase or reductase activity in both animal models. However, the present study shows that L-NAME could not affect the total thiol levels on NMDAR and PDI bindings to GluN1 and GluN2A in both models, although it reduced SNO-PDI level. Furthermore, PDI siRNA effectively decreased total thiol levels on NMDAR without changing the degree of S-nitrosylation of PDI. These findings indicate that S-nitrosylation of PDI may not influence its reductase activity and the PDI-NMDAR bindings at least in seizure or epilepsy models.

There are many debates concerning the role of NO in seizure activity. Some investigators claim that NO is one of the endogenous anti-convulsive factors, since L-NAME or other NOS inhibitors show proconvulsive effects against pilocarpine- and NMDA-induced seizure activity (Starr and Starr, 1993; Przeglasiński et al., 1996; Riazzi et al., 2006; Capannolo et al., 2014). However, others reported that NO has proconvulsive properties (Vasconcelos Rios et al., 2013; Payandemehr et al., 2015). Moreover, NO is neither proconvulsive nor anti-convulsive substance for chronic spontaneous seizures, pilocarpine-, petylenetetrazol- or electroshock-induced acute seizures (Przeglasiński et al., 1996; Noyan et al., 2007). In the present study, L-NAME could not abrogate seizure activities in both animal models. Therefore, our findings indicate that NO synthesis may be a consequent response to seizure activity, and that NO itself may not be directly involved in ictogenesis. The present study also reveals that seizure on-set increased NO generation, which maintained after seizure termination in the acute seizure model. In contrast, NO level immediately elevated after spontaneous seizure on-set, and recovered to basal level after seizure cessation in chronic epilepsy animals. We cannot explain these differences in NO synthesis between two animal models in the present study. However, PDI siRNA-treated animals showed the shorter seizure duration in response

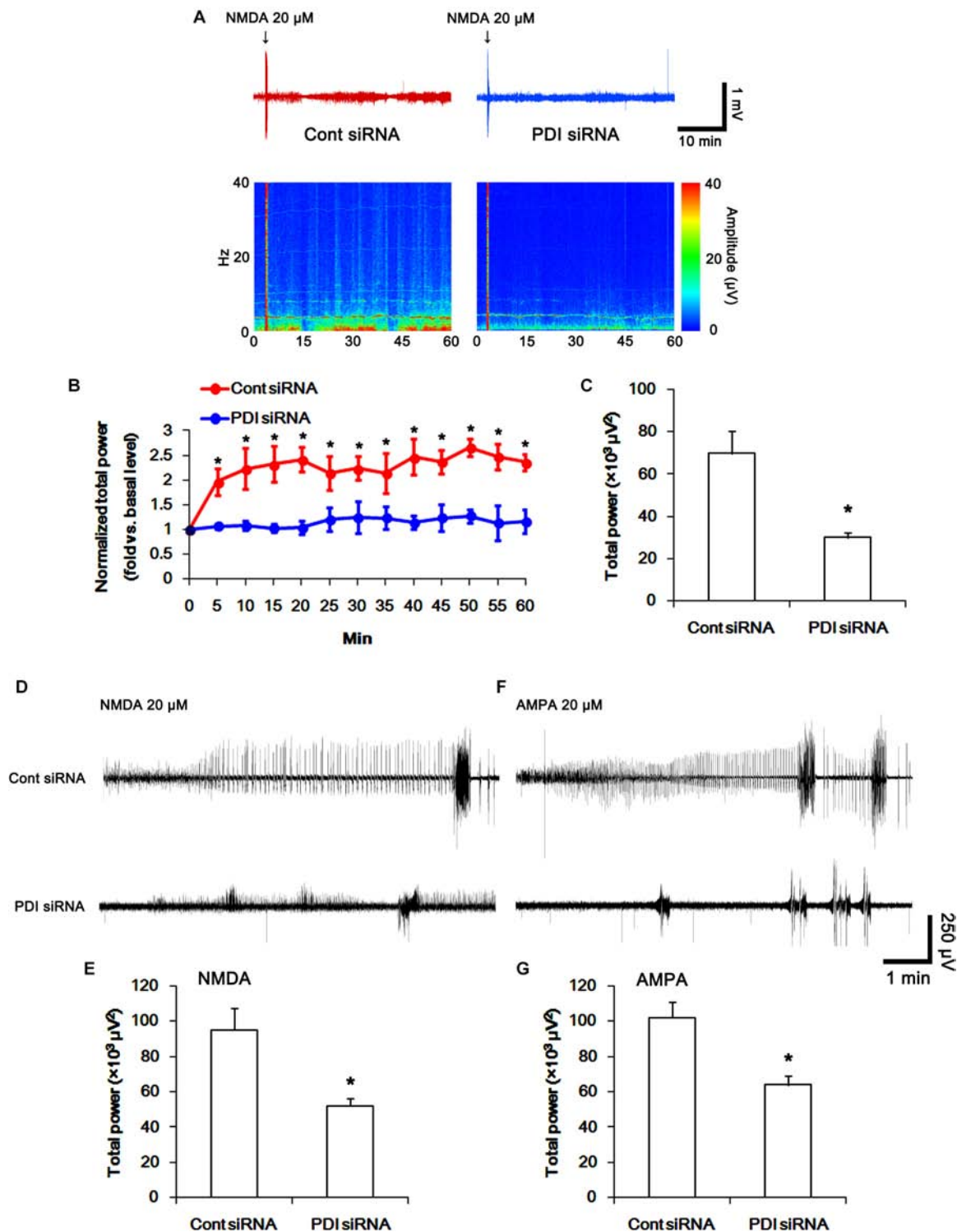


FIGURE 14 | The effect of PDI siRNA on neuronal activity in response to NMDA and AMPA in control animals. PDI knockdown effectively inhibits neuronal excitation in response to NMDA. **(A)** Representative EEG trace and frequency-power spectral temporal maps in response to intracerebroventricular NMDA injection. **(B)** Quantification of normalized total EEG power in response to NMDA (mean \pm S.E.M.; $*p < 0.05$ vs. basal level; $n = 7$, respectively). **(C)** Quantification of total EEG power in response to NMDA (mean \pm S.E.M.; $*p < 0.05$ vs. control siRNA; $n = 7$, respectively). **(D)** Representative EEG trace in response to focal NMDA injection into the hippocampus. **(E)** Quantification of total EEG power in response to focal NMDA injection into the hippocampus (mean \pm S.E.M.; $*p < 0.05$ vs. basal level; $n = 7$, respectively). **(F)** Representative EEG trace in response to focal AMPA injection into the hippocampus. **(G)** Quantification of total EEG power in response to focal AMPA injection into the hippocampus (mean \pm S.E.M.; $*p < 0.05$ vs. basal level; $n = 7$, respectively).

to pilocarpine and the reverse of NO signal to basal level following diazepam. Therefore, it is plausible that the different seizure duration in acute seizure model and chronic epilepsy model would result in these discrepancies of NO generation. Conversely, it is also possible that the basal level of NO synthesis in epilepsy rats would be higher than that in control animals that used as acute seizure models. Further studies are needed to elucidate the underlying mechanisms of these discrepancies.

CONCLUSION

In conclusion, our present data demonstrate that PDI was not a NO donor or a denitrosylase for NMDAR, and that PDI siRNA inhibited seizure activity by the S-nitrosylation-independent reduction of disulfide bonds on NMDAR. Therefore, our findings suggest that the modification of PDI reductase activity may be one of the important factors for the regulation of neuronal activity and the potential anti-epileptic therapeutic strategies.

REFERENCES

- Aizenman, E., Lipton, S. A., and Loring, R. H. (1989). Selective modulation of NMDA responses by reduction and oxidation. *Neuron* 2, 1257–1263. doi: 10.1016/0896-6273(89)90310-3
- Bi, S., Hong, P. W., Lee, B., and Baum, L. G. (2011). Galectin-9 binding to cell surface protein disulfide isomerase regulates the redox environment to enhance T-cell migration and HIV entry. *Proc. Natl. Acad. Sci. U.S.A.* 108, 10650–10655. doi: 10.1073/pnas.1017954108
- Capannolo, M., Ciccarelli, C., Molteni, R., Fumagalli, F., Rocchi, C., Romeo, S., et al. (2014). Nitric oxide synthase inhibition reverts muscarinic receptor down-regulation induced by pilocarpine- and kainic acid-evoked seizures in rat fronto-parietal cortex. *Epilepsy Res.* 108, 11–19. doi: 10.1016/j.eplepsyres.2013.10.011
- Chapman, A. G. (1998). Glutamate receptors in epilepsy. *Prog. Brain Res.* 116, 371–383. doi: 10.1016/S0079-6123(08)60449-5
- Choi, Y., Chen, H. V., and Lipton, S. A. (2001). Three pairs of cysteine residues mediate both redox and Zn²⁺ modulation of the NMDA receptor. *J. Neurosci.* 21, 392–400. doi: 10.1523/JNEUROSCI.21-02-00392.2001
- Choi, Y. B., Tanneti, L., Le, D. A., Ortiz, J., Bai, G., Chen, H. S., et al. (2000). Molecular basis of NMDA receptor-coupled ion channel modulation by S-nitrosylation. *Nat. Neurosci.* 3, 15–21. doi: 10.1038/71090
- Dannhardt, G., and Kohl, B. K. (1998). The glycine site on the NMDA receptor: structure-activity relationships and possible therapeutic applications. *Curr. Med. Chem.* 5, 253–263.
- Edman, J. C., Ellis, L., Blacher, R. W., Roth, R. A., and Rutter, W. J. (1985). Sequence of protein disulfide isomerase and implications of its relationship to thioredoxin. *Nature* 317, 267–270. doi: 10.1038/317267a0
- Jaffrey, S. R., Erdjument-Bromage, H., Ferris, C. D., Tempst, P., and Snyder, S. H. (2001). Protein S-nitrosylation: a physiological signal for neuronal nitric oxide. *Nat. Cell Biol.* 3, 193–197. doi: 10.1038/35055104
- Kallakunta, V. M., Slama-Schwok, A., and Mutus, B. (2013). Protein disulfide isomerase may facilitate the efflux of nitrite derived S-nitrosothiols from red blood cells. *Redox Biol.* 1, 373–380. doi: 10.1016/j.redox.2013.07.002
- Khan, R., Krishnakumar, A., and Paulose, C. S. (2008). Decreased glutamate receptor binding and NMDA R1 gene expression in hippocampus of pilocarpine-induced epileptic rats: neuroprotective role of *Bacopa monnieri* extract. *Epilepsy Behav.* 12, 54–60. doi: 10.1016/j.yebeh.2007.09.021
- Kim, J. E., Hyun, H. W., Min, S. J., and Kang, T. C. (2017a). Sustained HSP25 expression induces clasmotodendrosis via ER stress in the rat hippocampus. *Front. Cell. Neurosci.* 11:47. doi: 10.3389/fncel.2017.00047

AUTHOR CONTRIBUTIONS

J-EK designed and supervised the project. AJ designed and performed the experiments described in the manuscript with J-EK and analyzed the data. J-EK wrote the manuscript.

FUNDING

This study was supported by a grant of National Research Foundation of Korea (NRF) grant (Nos. 2013R1A6A3A04058272 and 2018R1C1B6005216). The funders had no role in study design, data collection and analysis, decision to publish, or preparation of the manuscript.

SUPPLEMENTARY MATERIAL

The Supplementary Material for this article can be found online at: <https://www.frontiersin.org/articles/10.3389/fncel.2018.00438/full#supplementary-material>

- Kim, J. E., Hyun, H. W., Min, S. J., Lee, D. S., Jeon, A. R., Kim, M. J., et al. (2017b). PLPP/CIN regulates seizure activity by the differential modulation of calenilin binding to GluN1 and Kv4.2 in Mice. *Front. Mol. Neurosci.* 10:303. doi: 10.3389/fnmol.2017.00303
- Kim, J. Y., Ko, A. R., Hyun, H. W., Min, S. J., and Kim, J. E. (2017c). PDI regulates seizure activity via NMDA receptor redox in rats. *Sci. Rep.* 7:42491. doi: 10.1038/srep42491
- Kim, J. E., and Kang, T. C. (2011). The P2X7 receptor-pannexin-1 complex decreases muscarinic acetylcholine receptor-mediated seizure susceptibility in mice. *J. Clin. Invest.* 121, 2037–2047. doi: 10.1172/JCI44818
- Kim, J. E., Kim, Y. J., Lee, D. S., Kim, J. Y., Ko, A. R., Hyun, H. W., et al. (2016). PLPP/CIN regulates bidirectional synaptic plasticity via GluN2A interaction with postsynaptic proteins. *Sci. Rep.* 6:26576. doi: 10.1038/srep26576
- Kim, J. E., Ko, A. R., Hyun, H. W., Min, S. J., and Kang, T. C. (2018). P2RX7-MAPK1/2-SP1 axis inhibits MTOR independent HSPB1-mediated astroglial autophagy. *Cell Death Dis.* 9:546. doi: 10.1038/s41419-018-0586-x
- Kim, J. E., Ryu, H. J., and Kang, T. C. (2013). Status epilepticus induces vasogenic edema via tumor necrosis factor- α / endothelin-1-mediated two different pathways. *PLoS One* 8:e74458. doi: 10.1371/journal.pone.0074458
- Ko, A. R., Hyun, H. W., Min, S. J., Kim, J. E., and Kang, T. C. (2015a). Endothelin-1 induces LIMK2-mediated programmed necrotic neuronal death independent of NOS activity. *Mol. Brain* 8, 58. doi: 10.1186/s13041-015-0149-3
- Ko, A. R., Kim, J. Y., Hyun, H. W., and Kim, J. E. (2015b). Endoplasmic reticulum (ER) stress protein responses in relation to spatio-temporal dynamics of astroglial responses to status epilepticus in rats. *Neuroscience* 307, 199–214. doi: 10.1016/j.neuroscience.2015.08.061
- Ko, A. R., and Kang, T. C. (2015). Blockade of endothelin B receptor improves the efficacy of levetiracetam in chronic epileptic rats. *Seizure* 31, 133–140. doi: 10.1016/j.seizure.2015.07.019
- Koch, G. L. (1987). Reticuloplasmins: a novel group of proteins in the endoplasmic reticulum. *J. Cell Sci.* 87, 491–492.
- Kornhuber, J., and Weller, M. (1997). Psychotogenicity and N-methyl-D-aspartate receptor antagonism: implications for neuroprotective pharmacotherapy. *Biol. Psychiatry* 41, 135–144. doi: 10.1016/S0006-3223(96)00047-9
- Lasón, W., Turchan, J., Przewłocki, R., Machelska, H., Labuz, D., and Przewłocka, B. (1997). Effects of pilocarpine and kainate-induced seizures on N-methyl-D-aspartate receptor gene expression in the rat hippocampus. *Neuroscience* 78, 997–1004. doi: 10.1016/S0306-4522(96)00635-5

- Lee, D. S., and Kim, J. E. (2018). PDI-mediated S-nitrosylation of DRP1 facilitates DRP1-S616 phosphorylation and mitochondrial fission in CA1 neurons. *Cell Death Dis.* 9:869. doi: 10.1038/s41419-018-0910-5
- Legendre, P., Rosenmund, C., and Westbrook, G. L. (1993). Inactivation of NMDA channels in cultured hippocampal neurons by intracellular calcium. *J. Neurosci.* 13, 674–684. doi: 10.1523/JNEUROSCI.13-02-00674.1993
- Lei, S. Z., Pan, Z. H., Aggarwal, S. K., Chen, H. S., Hartman, J., Sucher, N. J., et al. (1992). Effect of nitric oxide production on the redox modulatory site of the NMDA receptor-channel complex. *Neuron* 8, 1087–1099. doi: 10.1016/0896-6273(92)90130-6
- Lipton, S. A., Choi, Y. B., Takahashi, T., Zhang, D., Li, W., Godzik, A., et al. (2002). Cysteine regulation of protein function—as exemplified by NMDA-receptor modulation. *Trends Neurosci.* 25, 474–480. doi: 10.1016/S0166-2236(02)02245-2
- Lipton, S. A., and Rosenberg, P. A. (1994). Mechanisms of disease: excitatory amino acids as a final common pathway for neurologic disorders. *N. Engl. J. Med.* 330, 613–622. doi: 10.1056/NEJM199403033300907
- Noyan, B., Jensen, M. S., and Danscher, G. (2007). The lack of effects of zinc and nitric oxide in initial state of pilocarpine-induced seizures. *Seizure* 16, 410–416. doi: 10.1016/j.seizure.2007.02.012
- Okabe, S., Miwa, A., and Okado, H. (1999). Alternative splicing of the C-terminal domain regulates cell surface expression of the NMDA receptor NR1 subunit. *J. Neurosci.* 19, 7781–7792. doi: 10.1523/JNEUROSCI.19-18-07781.1999
- Payandemehr, B., Khoshneviszadeh, M., Varastehmoradi, B., Gholizadeh, R., Bahremand, T., Attar, H., et al. (2015). A COX/5-LOX inhibitor licofelone revealed anticonvulsant properties through iNOS diminution in mice. *Neurochem. Res.* 40, 1819–1828. doi: 10.1007/s11064-015-1669-z
- Popescu, N. I., Lupu, C., and Lupu, F. (2010). Extracellular protein disulfide isomerase regulates coagulation on endothelial cells through modulation of phosphatidylserine exposure. *Blood* 116, 993–1001. doi: 10.1182/blood-2009-10-249607
- Przegaliński, E., Baran, L., and Siwanowicz, J. (1996). The role of nitric oxide in chemically- and electrically-induced seizures in mice. *Neurosci. Lett.* 217, 145–148. doi: 10.1016/0304-3940(96)13085-8
- Ramachandran, N., Root, P., Jiang, X. M., Hogg, P. J., and Mutus, B. (2001). Mechanism of transfer of NO from extracellular S-nitrosothiols into the cytosol by cell-surface protein disulfide isomerase. *Proc. Natl. Acad. Sci. U.S.A.* 98, 9539–9544. doi: 10.1073/pnas.171180998
- Riazi, K., Roshanpour, M., Rafiei-Tabatabaei, N., Homayoun, H., Ebrahimi, F., and Dehpour, A. R. (2006). The proconvulsant effect of sildenafil in mice: role of nitric oxide–cGMP pathway. *Br. J. Pharmacol.* 147, 935–943. doi: 10.1038/sj.bjp.0706680
- Rigobello, M. P., Donella-Deana, A., Cesaro, L., and Bindoli, A. (2001). Distribution of protein disulphide isomerase in rat liver mitochondria. *Biochem. J.* 356, 567–570. doi: 10.1042/bj3560567
- Root, P., Sliskovic, I., and Mutus, B. (2004). Platelet cell-surface protein disulphide-isomerase mediated S-nitrosoglutathione consumption. *Biochem. J.* 382, 575–580. doi: 10.1042/BJ20040759
- Sanchez, R. M., Wang, C., Gardner, G., Orlando, L., Tauck, D. L., Rosenberg, P. A., et al. (2000). Novel role for the NMDA receptor redox modulatory site in the pathophysiology of seizures. *J. Neurosci.* 20, 2409–2417. doi: 10.1523/JNEUROSCI.20-06-02409.2000
- Sander, J. W. (2003). The epidemiology of epilepsy revisited. *Curr. Opin. Neurol.* 16, 165–170. doi: 10.1097/00019052-200304000-00008
- Selvakumar, B., Jenkins, M. A., Hussain, N. K., Haganir, R. L., Traynelis, S. F., and Snyder, S. H. (2013). S-nitrosylation of AMPA receptor GluA1 regulates phosphorylation, single-channel conductance, and endocytosis. *Proc. Natl. Acad. Sci. U. S. A.* 110, 1077–1082. doi: 10.1073/pnas.1221295110
- Sliskovic, I., Raturi, A., and Mutus, B. (2005). Characterization of the S-denitrosation activity of protein disulfide isomerase. *J. Biol. Chem.* 280, 8733–8741. doi: 10.1074/jbc.M408080200
- Starr, M. S., and Starr, B. S. (1993). Paradoxical facilitation of pilocarpine-induced seizures in the mouse by MK-801 and the nitric oxide synthesis inhibitor L-NAME. *Pharmacol. Biochem. Behav.* 45, 321–325. doi: 10.1016/0091-3057(93)90246-P
- Sucher, N. J., Awobuluyi, M., Choi, Y. B., and Lipton, S. A. (1996). NMDA receptors: from genes to channels. *Trends Pharmacol. Sci.* 17, 348–355. doi: 10.1016/S0165-6147(96)80008-3
- Sucher, N. J., and Lipton, S. A. (1991). Redox modulatory site of the NMDA receptor-channel complex: regulation by oxidized glutathione. *J. Neurosci. Res.* 30, 582–591. doi: 10.1002/jnr.490300316
- Suh, J. G., Ryoo, Z. W., Won, M. H., Oh, Y. S., and Kang, T. C. (2001). Differential alteration of NMDA receptor subunits in the gerbil dentate gyrus and subiculum following seizure. *Brain Res.* 904, 104–111. doi: 10.1016/S0006-8993(01)02490-8
- Sullivan, J. M., Traynelis, S. F., Chen, H. S., Escobar, W., Heinemann, S. F., and Lipton, S. A. (1994). Identification of two cysteine residues that are required for redox modulation of the NMDA subtype of glutamate receptor. *Neuron* 13, 929–936. doi: 10.1016/0896-6273(94)90258-5
- Tang, L. H., and Aizenman, E. (1993). The modulation of N-methyl-D-aspartate receptors by redox and alkylating reagents in rat cortical neurones in vitro. *J. Physiol.* 465, 303–323. doi: 10.1113/jphysiol.1993.sp019678
- Turano, C., Coppari, S., Altieri, F., and Ferraro, A. (2002). Proteins of the PDI family: unpredicted non-ER locations and functions. *J. Cell Physiol.* 193, 154–163. doi: 10.1002/jcp.10172
- Uehara, T., Nakamura, T., Yao, D., Shi, Z. Q., Gu, Z., Ma, Y., et al. (2006). S-nitrosylated protein-disulphide isomerase links protein misfolding to neurodegeneration. *Nature* 441, 513–517. doi: 10.1038/nature04782
- Vasconcelos Rios, E. R., Moura Rocha, N. F., Rodrigues Carvalho, A. M., Freire Vasconcelos, L., Leite Dias, M., de Carvalho Lima, C. N., et al. (2013). Involvement of the nitric oxide/cyclic guanylate monophosphate pathway in the pilocarpine-induced seizure model in mice. *Pharmacology* 91, 131–134. doi: 10.1159/000346268
- Yoshimori, T., Semba, T., Takemoto, H., Akagi, S., Yamamoto, A., and Tashiro, Y. (1990). Protein disulfide-isomerase in rat exocrine pancreatic cells is exported from the endoplasmic reticulum despite possessing the retention signal. *J. Biol. Chem.* 265, 15984–15990.

Conflict of Interest Statement: The authors declare that the research was conducted in the absence of any commercial or financial relationships that could be construed as a potential conflict of interest.

Copyright © 2018 Jeon and Kim. This is an open-access article distributed under the terms of the Creative Commons Attribution License (CC BY). The use, distribution or reproduction in other forums is permitted, provided the original author(s) and the copyright owner(s) are credited and that the original publication in this journal is cited, in accordance with accepted academic practice. No use, distribution or reproduction is permitted which does not comply with these terms.



Morphine Binds Creatine Kinase B and Inhibits Its Activity

Ivan Weinsanto^{1†}, Jinane Mouheiche^{1†}, Alexis Laux-Biehlmann^{1,2†}, François Delalande², Arnaud Marquette³, Virginie Chavant^{1,4}, Florian Gabel¹, Sarah Cianferani², Alexandre Charlet¹, Marie-Odile Parat⁵ and Yannick Goumon^{1,4*}

¹Institut des Neurosciences Cellulaires et Intégratives, CNRS UPR3212 and Université de Strasbourg, Strasbourg, France,

²Laboratoire de Spectrométrie de Masse BioOrganique, IPHC-DSA, CNRS UMR7178 and Université de Strasbourg, Strasbourg, France, ³CNRS UMR7177 and Université de Strasbourg, Strasbourg, France, ⁴Mass Spectrometry Facilities of the CNRS UPR3212, Strasbourg, France, ⁵School of Pharmacy, University of Queensland, PACE, Woolloongabba, QLD, Australia

OPEN ACCESS

Edited by:

Lisa Mapelli,
University of Pavia, Italy

Reviewed by:

Jolanta B. Zawilska,
Medical University of Lodz, Poland
Jean Albert Boutin,
Servier, France

*Correspondence:

Yannick Goumon
yannick.goumon@inserm.u-strasbg.fr

[†]These authors have contributed
equally to this work

*Present Address:

Alexis Laux-Biehlmann,
Bayer AG, Research & Development,
Pharmaceuticals, Berlin, Germany

Received: 10 August 2018

Accepted: 15 November 2018

Published: 03 December 2018

Citation:

Weinsanto I, Mouheiche J, Laux-Biehlmann A, Delalande F, Marquette A, Chavant V, Gabel F, Cianferani S, Charlet A, Parat M-O and Goumon Y (2018) Morphine Binds Creatine Kinase B and Inhibits Its Activity.
Front. Cell. Neurosci. 12:464.
doi: 10.3389/fncel.2018.00464

Morphine is an analgesic alkaloid used to relieve severe pain, and irreversible binding of morphine to specific unknown proteins has been previously observed. In the brain, changes in the expression of energy metabolism enzymes contribute to behavioral abnormalities during chronic morphine treatment. Creatine kinase B (CK-B) is a key enzyme involved in brain energy metabolism. CK-B also corresponds to the imidazoline-binding protein I₂ which binds dopamine (a precursor of morphine biosynthesis) irreversibly. Using biochemical approaches, we show that recombinant mouse CK-B possesses a μ M affinity for morphine and binds to morphine *in vitro*. The complex formed by CK-B and morphine is resistant to detergents, reducing agents, heat treatment and SDS-polyacrylamide gel electrophoresis (SDS-PAGE). CK-B-derived peptides CK-B₁₋₇₅ and CK-B₁₈₄₋₂₅₈ were identified as two specific morphine binding-peptides. *In vitro*, morphine (1–100 μ M) significantly reduces recombinant CK-B enzymatic activity. Accordingly, *in vivo* morphine administration (7.5 mg/kg, i.p.) to mice significantly decreased brain extract CK-B activity compared to saline-treated animals. Together, these results show that morphine strongly binds CK-B and inhibits its activity *in vitro* and *in vivo*.

Keywords: morphine, complex, ligand-binding protein, creatine kinase, high affinity

BACKGROUND

Morphine, an alkaloid from *Papaver somniferum*, is used to relieve pain in multiple clinical settings. In addition to its analgesic properties, morphine decreases intestinal motility, suppresses cough and has vasodilatory effects (Andersen et al., 2003). It influences many other physiological processes and notably decreases ATP availability in specific brain structures (Nasello et al., 1973). In addition, endogenous morphine has been characterized in numerous mammalian cells and tissues, and its structure is identical to that of morphine isolated from the poppy (for review Laux-Biehlmann et al., 2013).

Only a few unspecific morphine-binding proteins with low affinity have been identified so far and include serum albumin (Judis, 1977; Leow et al., 1993). In the past, our laboratory has

Abbreviations: ASB9, ankyrin repeat and SOCS box protein 9; CK-B, brain creatine kinase; CK-M, muscular creatine kinase; CNS, central nervous system; I₂B, I₂-binding; M3G, morphine-3-glucuronide; M6G, morphine-6-glucuronide; PEBP, phosphatidylethanolamine-binding protein; SEM, standard error of the mean.

demonstrated that the phosphatidylethanolamine-binding protein (PEBP; Goumon et al., 2004) binds to morphine-6-glucuronide (M6G) and morphine-3-glucuronide (M3G) with an affinity equal to that of its reference ligand, phosphatidylethanolamine, but has no affinity for morphine (Atmanene et al., 2009). In addition to these low affinity binding-proteins, covalent binding of morphine to proteins has been proposed to result in irreversible binding to insoluble tissue components after administration (Misra et al., 1971; Mullis et al., 1979; Nagamatsu et al., 1983).

The implication of the imidazoline system, and particularly the I₂-binding site (I2B; Li, 2017), in the modulation of morphine-induced analgesia and morphine analgesic tolerance has been documented (Gentili et al., 2006; Caprioli et al., 2015). Interestingly, creatine kinase B (CK-B) represents the main I2B site for imidazoline and its derivatives (clonidine, guanfacine; Kimura et al., 2009; Li, 2017). Molecular modeling using the crystal structure of chicken CK-B and the irreversible ligand BU990006-binding site has indicated the importance of Thr₇₁, Val₇₂, Val₇₅, Leu₂₀₁, Leu₂₀₂, Cys₂₈₃ and Ser₂₈₅ in this interaction (Kimura et al., 2009). Dopamine, a morphine precursor in plants and mammals (Laux-Biehlmann et al., 2013), has been shown to covalently bind to CK-B (Van Laar et al., 2009). CK-B also forms highly stable complexes with ankyrin repeat and SOCS box protein 9 (ASB9; Balasubramaniam et al., 2015).

CK-B is a 42 kDa protein expressed in neurons, oligodendrocytes and astrocytes of the central nervous system (CNS; Manos and Bryan, 1993). Different CK isoenzymes exist in the cytoplasm as dimers or multimers in specific cells: CK-BB in the brain, CK-MM in muscles and CK-MB in the heart (Wyss and Kaddurah-Daouk, 2000). CK catalyzes the reversible phosphorylation of creatine by ATP to produce phosphocreatine and ADP. Mitochondrial isoforms of CK form phosphocreatine from ATP, whereas cytoplasmic CK isoenzymes form ATP from phosphocreatine.

In the present study, we have investigated whether CK-B might represent a morphine-binding protein. Recombinant mouse CK-B (rCK-B) and mouse CK-B-derived synthetic peptides, together with biochemistry approaches, were used to characterize the affinity of potential morphine-binding sites. To assess the functional significance of CK-B/morphine interactions, the impact of morphine on rCK-B activity was studied *in vitro* and *in vivo*.

MATERIALS AND METHODS

Experimental Design

Our animal study is reported in accordance with the ARRIVE Guidelines for reporting experiments involving animals (McGrath et al., 2010). Experiments were carried out in a randomized and blind manner, and statistical analyses were done prior to revealing treatment groups. At least three technical replicates were used for *in vitro* experiments. Mice were assigned an identity number and assigned to groups randomly so that the experimenter was blind to treatment.

Drugs

Morphine base was purchased from Euromedex (Souffelweyersheim, France). A stock solution of 35 mM morphine was prepared by dissolving morphine in H₂O after adding an equimolar concentration of HCl. Codeine monohydrate, morphine-3-β-D-glucuronide and morphine-6-β-D-glucuronide dihydrate powders were purchased from Sigma-Aldrich (Lyon, France) and dissolved in H₂O to prepare stock solutions. Working concentrations for *in vitro* and *in vivo* experiments were prepared from the stock on the day of experiment. When necessary, the pH of the working solutions was adjusted to 7.4 with NaOH before use.

Animals

All procedures were performed in accordance with European directives (86/609/EEC) and were approved by the regional ethics committee and the French Ministry of Agriculture (license No. 00456.02 to YG). Experiments were performed with C57BL/6 mice (45 day-old adult male, 24 ± 3 g; Charles River, L'Arbresle, France). Animals were given food and water *ad libitum*, and maintained in a 12 h light–dark cycle at a room temperature of 22°C ± 2°C. Cage bedding was from Anibed (Pontvallain, France; reference AB3) and food from SAFE (Augy, France; reference A04). Mice were kept group-housed at five per cage (Type II cage, 370 cm², height 14 cm).

Drug Injections

Mice were weighed and then i.p. injected (light phase at 10 AM) with a single dose of 7.5 mg/kg morphine or an equivalent volume of saline (NaCl 0.9% in H₂O). The volume of injection was 240 ± 30 μL for mice weighing 24 ± 3 g. After 90 min, mice were anesthetized with a solution of ketamine and xylazine (17 mg/mL ketamine and 2.5 mg/mL xylazine, 4 mL/kg i.p.; Centravet, Taden, France). After 5 min, adequate anesthesia was ensured by pinching the hind paws and observing no reflex response. Animals were then euthanized by decapitation. Brains were then collected and frozen at −80°C.

Preparation of Brain Extracts From Morphine and Saline-Treated Mice

Brains from morphine- and saline-treated mice were homogenized with an Ultra Turrax instrument (Ika, Staufen, Germany) in 1 ml of H₂O containing protease inhibitors (cOmplete Mini, EDTA-free, Roche, Basel, Switzerland). The homogenates were then sonicated (two times 10 s, 90 W) with a Vibra Cell apparatus (Sonics, Newtown, CT, USA) and centrifuged (14,000× g, 30 min) at 4°C. Supernatants were recovered and protein concentration was determined using the Bradford method (Protein Assay, Bio-Rad, Marnes-la-Coquette, France). Samples were then frozen at −80°C until further use.

Production of the Mouse rCK-B

The N-terminal His-tagged cDNA coding region for the mouse Ckb (residues 1–318, accession number NM_021273; ref.

MR205953, Origene, Herford, Germany) was cloned into the vector pET15b (CIGEx, CEA, Fontenay aux Roses, France). The N-terminal hexahistidine-tagged fusion protein was expressed in *Escherichia coli* BL21 (DE3). Cells were grown in LB medium (Euromedex) at 37°C until an A_{600} of 0.4 and subsequently induced for 3 h at 37°C with 0.1 mM isopropyl 1-thio-D-galactopyranoside (Euromedex). Harvested bacterial pellets were resuspended in buffer containing isopropyl thio- β -D-galactoside (IPTG; Euromedex). The cell pellets were resuspended in binding buffer (10 mM Tris-HCl, 300 mM NaCl, 10% glycerol, 2 mM CHAPS and 10 mM imidazole, pH 8.0; Euromedex), lysed by sonication on ice (8 \times 30 s, 90 W) and then clarified by centrifugation (20,000 \times g, 50 min, 4°C). The cleared supernatant was loaded on a nickel-Hitrap column (GE Healthcare; Aulnay Sous Bois, France). The protein was eluted using 50 and 250 mM imidazole (10 mM Tris-HCl, 300 mM NaCl, pH 8.0; Euromedex). The protein was then dialyzed 12 h at 4°C against a buffer containing 10 mM Tris, and 150 mM NaCl (pH 8). The purity and homogeneity of the protein were assessed by SDS-polyacrylamide gel electrophoresis (SDS-PAGE; see below).

Enzyme-Linked ImmunoSorbent Assay (ELISA)

Enzyme-linked immunosorbent assays (ELISAs) were performed to determine the affinity and specificity of the binding of mouse rCK-B and its derived peptides to opiate alkaloids. 96-well plates (NUNC, Roskilde, Denmark) were coated for 1 h at 37°C with 100 μ l of a solution of CK-B-derived peptides or rCK-B (10 μ g/ml) in carbonate-bicarbonate buffer (15 mM Na₂CO₃, 35 mM NaHCO₃, pH 9.6). After three washes with 100 mM phosphate buffer pH 7.4 (PT buffer; 5 min), the wells were incubated for 30 min with 200 μ l of bovine serum albumin (BSA) diluted in PT buffer (5%, w/v; PT-BSA buffer) to saturate non-specific sites. After saturation, wells were incubated for 1 h with 100 μ l of morphine, M6G, M3G or codeine, diluted in H₂O at increasing concentrations. The plate was then washed three times with PT buffer, and 100 μ l of the mouse primary anti-morphine antibody (which detects morphine, codeine, M3G and M6G according to the manufacturer's antibody datasheet) diluted in PT-BSA buffer (1:2,000, v/v; 3A6, ref AMM00033; Aviva System Biology, San Diego, CA, USA) were added. After three more washes with PT buffer, 100 μ l of the secondary antibody in PT-BSA buffer (HRP-conjugated donkey anti-mouse IgG, P.A.R.I.S. CliniSciences, Nanterre, France; 1:500, v/v) were added and incubated for 30 min at room temperature. After two washes with PT buffer, followed by two washes with a pH 7.5 phosphate-citrate-0.05% Tween 20 buffer (10 min), revelation was performed with 200 μ l of a 1-Step Ultra TMB substrate solution (3,3',5,5' tetramethylbenzidine, Thermo Fischer Scientific). After 15 min of incubation at RT, the reaction was stopped by the addition of 50 μ l of 2N hydrochloric acid. Optical density was determined at 450 nm with a Multiskan EX plate reader (Thermo Life Sciences, Cergy Pontoise, France). Each ELISA points was tested in triplicate in three independent experiments. All samples with a triplicate CV > 10% were retested to obtain a CV below or equal to 10%.

Association Assays

Association assays were performed with 0.5 μ g of the mouse rCK-B in the presence of 1 or 5 μ g of morphine, in a final volume of 10 μ l incubated during 15 min at 37°C. Samples were diluted 1:2 with the gel-loading buffer (see below).

Gel Electrophoresis

Proteins were separated on SDS-PAGE gradient gels (4%–12% acrylamide; Novex, MES running buffer). Samples were suspended in 20 μ l of loading buffer containing 60 mM Tris HCl pH 6.8, 2% SDS (w/v), 4 M urea, 5% glycerol (v/v), 5 mM EDTA, 1% β -mercaptoethanol (v/v) and 0.05% bromophenol blue (w/v) and subjected to heat treatment (100°C, 5 min). Gels were run in duplicate. One gel was silver-stained, and the other one was used for Western Blot analysis (see below).

Silver Staining

Silver staining was done according to the manufacturer's (Proteabio Europe, Langlade, France) instructions. Silver-stained gels and Western Blot analysis with an anti-CK antibody were used to assess the stability of CK after heat treatment. No difference in silver-stained band intensity or immunoreactivity was noticed in any experiment.

Western Blot

After electrophoretic separation, the gel was electrotransferred onto a polyvinylidene difluorene (PVDF) membrane (Bio-Rad). PVDF membranes were treated for 30 min with a saturation solution containing PBS, 5% BSA (w/v) and 0.05% Tween 20 (v/v). Then, PVDF membranes were incubated with the 3A6 mouse monoclonal anti-morphine primary antibody for 1 h at room temperature (1:1,000). The mouse monoclonal 3A6 anti-morphine antibodies (ref AMM00033; Aviva System Biology) were raised against a ((5 alpha 6 alpha) 7 8 dihydro-4 5 epoxy-17methylmorphinan-3 5diol)-BSA conjugate. Binding of the primary antibody was detected using HRP-conjugated donkey anti-mouse antiserum (P.A.R.I.S.; 1:50,000 in PBS, 5% of BSA (w/v), 0.05% Tween 20 (v/v)). Luminata FORTE™ (Millipore, France) was used as the substrate. Non-specific binding of the secondary antibody was ruled out by omitting the primary antibody: non-specific labeling was absent with the secondary antibody alone (data not shown).

Peptide Synthesis

CK-B-derived peptides were synthesized by Proteogenix (Schiltigheim, France): CK-B_{1–75}, CK-B_{65–140}, CK-B_{127–199}, CK-B_{184–258}, CK-B_{248–343}, CK-B_{286–381}, CK-B_{184–258}, CK-B_{199–223}, CK-B_{214–238}, CK-B_{214–238}.

Circular Dichroism

Circular dichroism spectra were recorded from 260 nm to 190 nm using a J-810 spectropolarimeter (Jasco, Tokyo, Japan). Spectral resolution and data pitch were adjusted to 1 nm while the scanning speed was set up at 50 nm/min. Samples containing 0.2 mg/mL of CK-B_{1–75} in H₂O (pH 6) and CK-B_{184–258} (in 2.5 mM of NaOH, pH 7) were transferred into a quartz cuvette

of 1 mm path length and maintained at the temperature of 23°C. The absence of aggregates was confirmed by a Dynamic Light Scattering analysis (DLS, Zetasizer NanoS; Malvern Panalytical, Malvern, UK). The secondary structures of the peptides were calculated from the spectra using a least squares fit procedure implemented in the DicroProt analysis software (Deléage and Geourjon, 1993).

CK Activity Assay

We used a commercial creatine kinase activity assay kit (MAK116, Sigma-Aldrich) to measure the potential impact of morphine binding on CK-B enzymatic activity. The protocol followed the manufacturer's instructions at room temperature. Briefly, 1 µg of rCK-B or 75 µg of brain extract were added per well (96-well plates, NUNC) with increasing concentrations of morphine (0, 0.01, 0.1, 1, 10, 25, 50, 100 µM final). The reconstituted reagent (made of assay buffer, enzyme mix and substrate solution) was then added to start the reaction. Fluorescence was recorded using a Mithras LB940 fluorescence plate reader (Berthold, Bad Wildbad, Germany), with excitation and emission filters of 350 nm and 460 nm, respectively. Four replicates were used for each data point.

Statistics

Data were analyzed using Graphpad Prism Software 7.0. Non-parametric statistical tests were used due to low sample size and the non-Gaussian distribution of some groups. For *in vitro* rCK-B assays, data were expressed as percentage of the control (no morphine condition) to account for variability across replicates done on separate days. Statistical differences were tested with the Kruskal-Wallis test and Dunn's multiple comparisons as *post hoc*. Brain extract assays were analyzed using the Mann-Whitney U test. Differences between groups were considered statistically significant at $p < 0.05$.

RESULTS

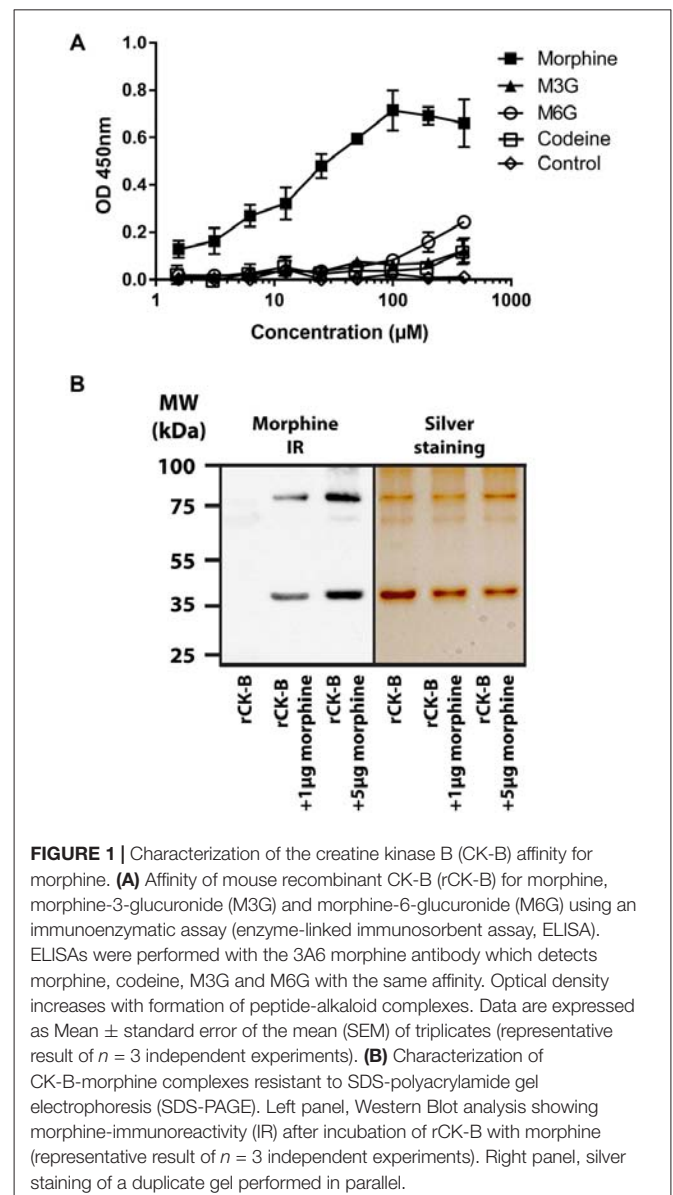
Characterization of the CK-B Affinity for Morphine

The binding of mouse rCK-B, produced in *E. coli* to increasing concentrations (1.56 µM to 400 µM) of morphine, codeine, M3G or M6G was tested by ELISA. The results show that mouse rCK-B binds morphine (Figure 1A) with a calculated K_d of 10.8 µM. Our results further revealed that M3G, M6G and codeine only weakly bind to rCK-B ($K_d > 100$ µM) compared to morphine. As a non-specific binding control, a series of wells were coated with BSA instead of rCK-B and incubated with increasing concentrations of morphine, M3G or M6G. No binding of morphine, M3G or M6G to BSA was observed (Figure 1A, control).

Together, these results indicate that rCK-B binds morphine with a micromolar range affinity.

Characterization of a Morphine-rCK-B Complex Resistant to SDS-PAGE

Mouse rCK-B (0.5 µg) was incubated 15 min in the presence of 1 or 5 µg of morphine. Samples were resuspended in loading



buffer containing both SDS and urea. A heating step (100°C; 5 min) was performed before polyacrylamide gel electrophoresis (PAGE).

Western Blot analysis using anti-morphine antibody showed that the mouse rCK-B alone is not labeled by the anti-morphine antibody (Figure 1B, left panel). Morphine immunolabeling was observed at 42 kDa (CK-B monomers) and 84 kDa (CK-B dimers) only when CK-B was incubated with 1 and 5 µg of morphine. As a control, an identical gel was run in parallel and silver-stained (Figure 1B, right panel). This control shows the presence of two bands at 42 kDa and 84 kDa in each condition. These two bands correspond to the monomers and dimers of mouse rCK-B, respectively.

These results indicate that morphine-mouse rCK-B complexes are resistant to SDS-PAGE.

Identification of the CK-B Fragments Displaying an Affinity for Morphine

To identify the morphine-binding motifs of CK, six overlapping peptides, namely CK-B₁₋₇₅, CK-B₆₅₋₁₄₀, CK-B₁₂₇₋₁₉₉, CK-B₁₈₄₋₂₅₈, CK-B₂₄₈₋₃₄₃ and CK-B₂₈₆₋₃₈₁ were tested for morphine, M3G, M6G and codeine binding *via* ELISA (Figure 2A). Increasing concentrations of opiates (0.1 μ M to 324 μ M) were added to wells pre-coated with the peptides (0.5 μ g). CK-B₁₋₇₅ and CK-B₁₈₄₋₂₅₈ were able to bind morphine (Figures 2B,C) with a calculated K_d of 12.5 μ M and 13.2 μ M, respectively. However, ELISA analysis revealed that the six CK-derived peptides have no affinity for M3G, M6G or codeine (Figures 2B,C). Circular dichroism analysis revealed that in H₂O, CK-B₁₋₇₅ adopts a structure consisting of 3% alpha helix, 15% beta sheets and 82% random coils. Similarly, the calculated secondary structure of CK-B₁₈₄₋₂₅₈ is 8% alpha helix, 19% beta sheets and 73% random coils. Focusing on the CK-B₁₈₄₋₂₅₈ peptide, we tested the affinity of four smaller overlapping peptides (CK-B₁₈₄₋₂₅₈, CK-B₁₉₉₋₂₂₃, CK-B₂₁₄₋₂₃₈, CK-B₂₁₄₋₂₃₈). None of these four peptides displayed an affinity for morphine using an ELISA approach (data not shown).

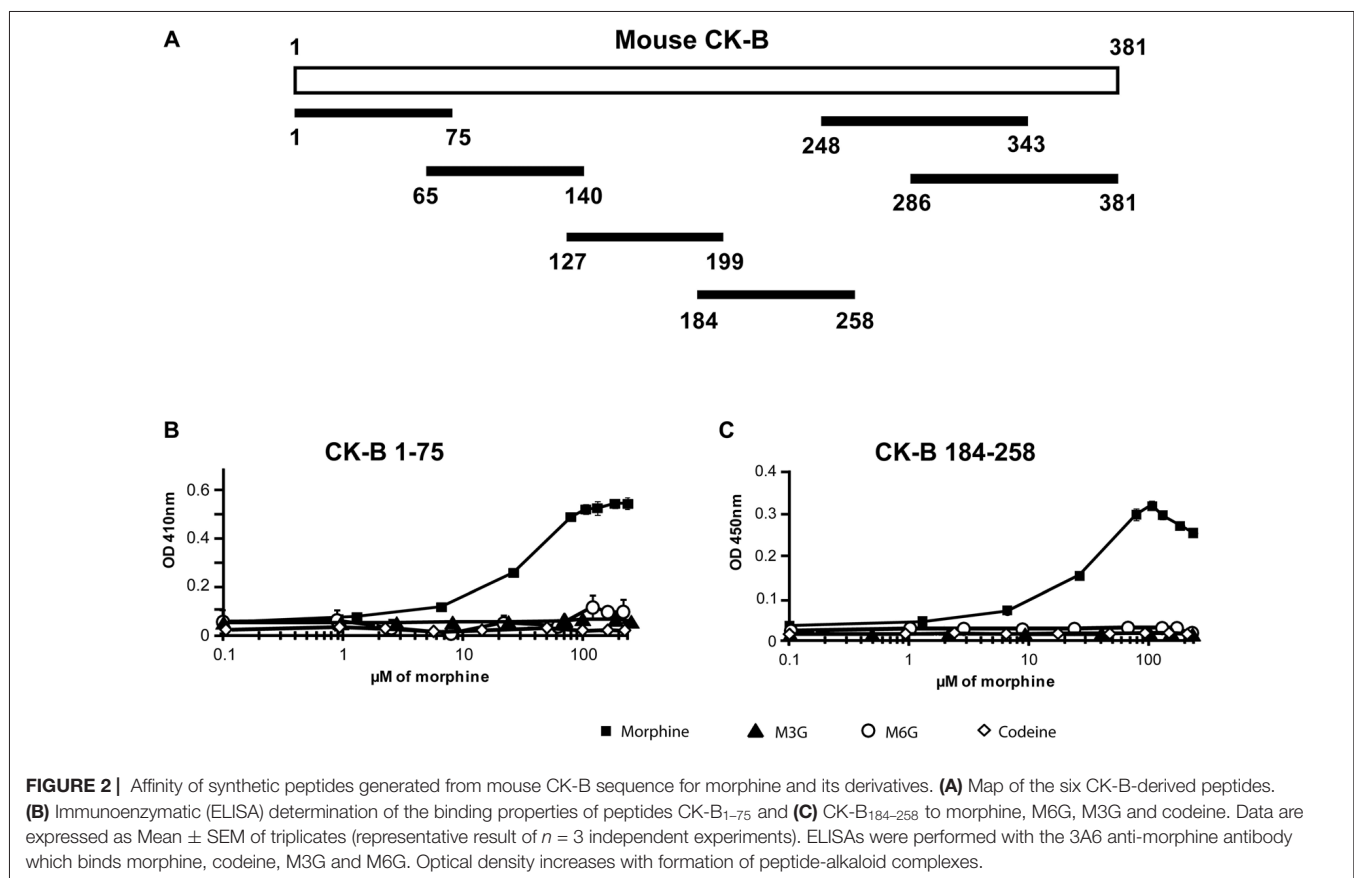
Taken together, these results indicate that mouse CK-B₁₋₇₅ and CK-B₁₈₄₋₂₅₈ have a micromolar range affinity restricted to morphine, as observed for the mouse rCK-B.

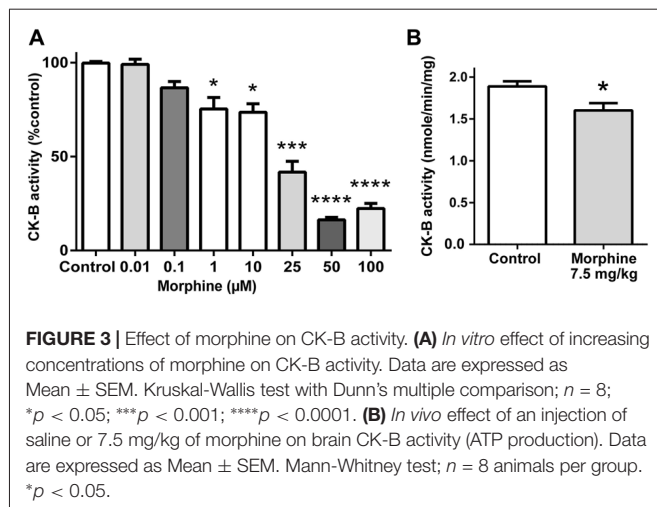
Characterization of the Effect of Morphine Binding on rCK-B Activity *in vitro*

Next, we measured the potential impact of morphine binding to CK-B on the formation of ATP from phosphocreatine. Mouse rCK-B (1 μ g) was incubated in the presence of increasing concentrations of morphine (0, 0.01, 0.1, 1, 10, 25, 50 and 100 μ M; Figure 3A). The activity of rCK-B was monitored by measuring the production of ATP during 20 min. Morphine (1 μ M) significantly decreased the formation of ATP by 27% (36.4 ± 1.8 nmol/min/mg) compared to the control condition (50 ± 1.4 nmol/min/mg). Further increasing morphine concentrations dose-dependently inhibited CK-B activity until a maximal level of inhibition was reached (80% decrease in activity for morphine >50 μ M). This experiment shows that 1 μ M morphine, corresponding to a concentration close to the K_d of CK-B for morphine, significantly decreases CK-B activity *in vitro*.

Characterization of the Effect of Morphine on CK-B Activity *in vivo*

In mice, the effect of morphine on CK-B activity *in vivo* was measured after a single injection of morphine (7.5 mg/kg, i.p.). Endogenous CK-B activity was tested on 75 μ g of brain extract, by monitoring ATP production over 10 min. Results indicate that acute morphine treatment induces a statistically significant decrease of CK-B activity by 15.3% (1.60 ± 0.09 μ mole/min/mg





of total brain protein) compared to saline-treated animals (1.89 ± 0.06 μ mole/min/mg of total brain protein; **Figure 3B**).

DISCUSSION

The present study reports that recombinant mouse rCK-B displays a micromolar affinity for morphine but not for M3G, M6G or codeine. Two morphine-binding sites were identified, namely peptides CK-B₁₋₇₅ and CK-B₁₈₄₋₂₅₈, which displayed a similar micromolar affinity for morphine. In addition, we show that CK-B-morphine complexes are resistant to detergents (SDS), chaotropic agents (urea), reducing agents and heat treatment. Finally, our results show that at a concentration that results in complex formation, morphine significantly decreases the activity of the mouse rCK-B *in vitro* and endogenous mouse brain CK-B *in vivo*.

The Morphine-CK-B Complexes

CK-B is the main I2B site for imidazoline and derivatives (such as clonidine, guanfacine...; Gentili et al., 2006; Kimura et al., 2009; Li, 2017). In addition, CK was described to covalently bind dopamine (Van Laar et al., 2009), which is a morphine precursor in plants and animals (Laux-Biehlmann et al., 2013), and to form highly stable complexes with ASB9 (Kwon et al., 2010; Balasubramaniam et al., 2015). However, the potential binding of CK-B to morphine, as well as a potential modulatory role of morphine on CK-B activity, have never been studied.

Covalent binding of morphine to proteins has been first proposed by Misra and Mitchell (1971) and Misra et al. (1971). This group was able to demonstrate that a single subcutaneous injection of 10 mg/kg of [¹⁴C]-morphine-N-methyl led to morphine-related radioactivity lasting in the rat CNS for at least 3 weeks. Later, [C¹-³H]-morphine and [N-¹⁴CH₃]-morphine were found to irreversibly bind insoluble tissue components after administration (Mullis et al., 1979; Nagamatsu et al., 1983). In addition, S-glutathionylmorphine complexes have been characterized (Correia et al., 1984; Kumagai et al., 1990) and are

likely formed first by the action of morphine-6-deshydrogenase (EC 1.1.1.218) leading to the formation of morphinone (Endo et al., 2013), followed by a spontaneous step allowing conjugation to glutathione (GSH) or proteins displaying cysteine residues. Besides, the binding of morphine to 35–50 kDa proteins in mice has also been reported (Nagamatsu et al., 1983; Nagamatsu and Hasegawa, 1992, 1993). Morphine binding to these unknown proteins was described as “covalent” because morphine-protein complexes were resistant to both methanol precipitation and SDS-PAGE denaturing conditions (Nagamatsu and Hasegawa, 1992).

In this article, we similarly unveil the formation of mouse rCK-B-morphine complexes that are resistant to SDS-PAGE treatment. Such a strong binding seems incompatible with the micromolar range affinity measured by ELISA. However, ELISA only reflects a biased affinity: (i) resulting from conditions that do not especially promote interactions of morphine with CK-B or its derived fragments; and (ii) dependent on the primary and secondary antibodies. This point is strengthened by the fact that both CK-B₁₋₇₅ and CK-B₁₈₄₋₂₅₈ display an affinity (μ M range) similar to that of the full-length mouse rCK-B. In addition, the control condition performed with a nonspecific morphine-binding protein (i.e., BSA) did not result in any binding and therefore highlights the stringency of our ELISA (Judis, 1977; Leow et al., 1993). It is likely that morphine-binding sites are present in a well-defined structure of the peptides rather than in unstructured parts. Smaller CK-B₁₈₄₋₂₅₈-derived peptides did not show any affinity for morphine, therefore we could not determine a specific morphine-binding site. This suggests that multiple structural parts all along the sequence of CK-B₁₈₄₋₂₅₈ are required for the binding of morphine. The formation of strong morphine-CK-B complexes can be explained by two hypotheses: (i) non-covalent interactions involving ionic, hydrophobic and/or van der Waals interactions lead to a highly stable complex or (ii) a covalent binding of morphine to cysteine residues present in the CK-B occurs. However, our *in vitro* experimental conditions rule out a possible cross-linking involving cysteine residues (experiments performed in reducing conditions) and the action of morphine-6-deshydrogenase (reaction media do not contain this enzyme). Thus, it is likely that non-covalent complexes are formed with morphine and involve specific interactions as shown for the CK-ASB9 complexes (Balasubramaniam et al., 2015).

CK-B Activity Modulation by Morphine

As CK-B represents a crucial enzyme that regulates ATP bioavailability in the brain, the ability of morphine to alter CK-B activity may dramatically affect CNS metabolism. Notably, the binding of the irreversible I2B ligand BU99006 (20 μ M) to CK-B was shown to decrease the apparent V_{max} of CK-B by up to 16% (Kimura et al., 2009). However, other I2B ligands (2-BFI, BU224, agmatine) did not affect CK-B activity. In addition, it was shown that a chronic administration of cannabidiol increases CK activity by up to 20% in the rat brain (Valvassori et al., 2013).

The implication of I2B sites in the modulation of morphine-induced analgesia has been well documented (Sanchez-Blázquez et al., 2000; Gentili et al., 2006; Ciubotariu and Nechifor, 2012; Caprioli et al., 2015) and the involvement of I2B sites in the modulation of morphine withdrawal and tolerance has been reported in rodents (Boronat et al., 1998; Ruiz-Durántez et al., 2003; Miralles et al., 2005). For example, the I2 ligand agmatine increases morphine-induced analgesia and inhibits tolerance and dependence to opioids (Dardonville et al., 2006).

In the brain, changes in the expression of energy metabolism enzymes contribute to behavioral abnormalities during chronic morphine treatment (Chen et al., 2007) but can also deeply impact gliotransmission through the modulation of ATP release (Harada et al., 2016). Accordingly, morphine-binding significantly decreases CK-B enzymatic activity by 27% when morphine is present at a concentration close to the K_d value. In addition, we have shown that *in vivo*, CK-B activity in brain tissue is decreased by 15 % after injection of an analgesic dose of morphine. Interestingly, our results are in agreement with the effect of morphine on ATP levels in the rat neocortex and thalamus, where respective decreases of 14% and 26% have been observed *in vivo* (Nasello et al., 1973).

Our results reveal two potential morphine-CK-B binding sites, namely CK-B_{1–75} and CK-B_{184–258}. The former is not involved in CK-B activity. Conversely, CK-B_{184–258} contains a conserved, negatively charged amino acid cluster, Glu₂₂₆, Glu₂₂₇, Asp₂₂₈ (EED) located in the active site of CK isoenzymes (Eder et al., 2000). This particular motif has been described as essential for CK enzymatic activity. Thus, we can hypothesize that morphine alters CK-B function through binding to the CK-B_{184–258} sequence. A limitation of our study is that we only evaluated a fixed time point after euthanizing the animals, and a different pattern of CK-B responses might occur at different time points. Further clarification of the impact of morphine on CK-B function *in vivo* is needed, e.g., through brain microdialysis and ATP quantification. Another open question is the impact of chronic morphine treatment in patients on CK-B activity, which is likely to differ from our acute morphine-exposure treatment. Indeed, a chronic morphine exposure might inhibit CK-B during a long period leading to important physiological changes and a measurable phenotype.

In vivo Complex Formation

After administration, morphine rapidly reaches the CNS where it binds to mu opioid receptors (MORs) to produce analgesia. Then, morphine is taken up by glial cells including microglial cells and astrocytes through the action of the organic cation transporter OCT1 (Tzvetkov et al., 2013). After conversion by UDP-glucuronosyl-transferase (UGT) enzymes (King et al., 2000; Weinsanto et al., 2018), glucuronides are released through the efflux MRP3 transporter (multidrug resistance protein 3; Zelcer et al., 2005). In this context, it is plausible that after administration and cellular uptake, morphine can form complexes with cytoplasmic CK-B and therefore negatively modulate its activity. Interestingly, injection (i.v., i.p. or s.c.) of an analgesic dose of morphine (10 to 20 mg/kg) to mice

results in serum concentrations ranging from 2 μ M to 35 μ M. Similarly, morphine content in the brain reaches nmol/g of tissue levels (corresponding to a μ M range), indicating that our findings are relevant *in vivo* (Patrick et al., 1975; Vekovischeva et al., 2001; Handal et al., 2002; Xie et al., 2017).

Endogenous morphine has been detected in numerous cerebral areas and brain cells of different species including the mouse (Laux et al., 2011, 2012; Laux-Biehlmann et al., 2013). Specifically, endogenous morphine is detected in GABA-basket cells, astrocytes and microglial cells (Muller et al., 2008; Laux et al., 2011, 2012; Togna et al., 2013). In addition, an increase of endogenous morphine and M6G blood levels has been linked to stress (Meijerink et al., 1999; Brix-Christensen et al., 2000; Goumon et al., 2000) and pathologies such as sepsis, with concentrations reaching up to 0.25 μ M (Glattard et al., 2010; Laux-Biehlmann et al., 2012). In contrast to opioidergic peptides (e.g., enkephalins), the functional role of endogenous morphine in the CNS remains to be elucidated. Endogenous morphine is found in the cytoplasm of astrocytes expressing both OCT1 (Schreiber et al., 1990) and CK-B (Tachikawa et al., 2004). Although endogenous morphine concentrations are unlikely to reach 1 μ M, uptake by astrocytic processes could theoretically bring endogenous morphine in contact with cytoplasmic CK-B. Whether endogenous morphine-CK-B complexes exist and might influence bioavailability of ATP in astrocytes and impact ATP-mediated gliotransmission through CK-B inhibition remains to be investigated in further studies.

Clinical Relevance of Morphine-CK-B Interactions

The *in vitro* and *in vivo* impact of morphine on CK-B activity in the mouse raises the question of a potential relevance of morphine-CK-B interactions in the case of clinical or recreational use of morphine or its derivatives in humans.

First, doses administered to morphine-naïve humans are usually two orders of magnitude lower than those needed to elicit analgesia in rodents. Thus, peak morphine blood concentrations (and presumably tissue concentrations) after oral therapeutic dosing typically only reach 100 nM (Klimas and Mikus, 2014), a concentration far below the 1 μ M of morphine needed for CK-B modulation.

However, it is possible that intracellular morphine could reach micromolar concentrations in chronically treated, tolerant patients. Indeed, dose escalation following long-term treatment can lead to patients receiving 500 mg of morphine or more per day. Thus, in the case of chronic use of morphine or codeine, whether in clinical (e.g., cancer patients) or drug abuse settings, morphine concentrations rise to low μ M levels in both plasma and brain (Säwe et al., 1983; Frost et al., 2016). In addition, morphine concentrations in the cerebrospinal fluid (CSF) and brain extracellular fluid (ECF) have been reported to reach nM to μ M values in different conditions, including epidural injection during chronic intractable pain due to cancer and codeine overdoses (Coombs et al., 1985; Bouw et al., 2001; Ederoth et al., 2004).

It is also important to mention the fact that M3G concentrations in these cases are far higher than those of morphine. CK-B is an intracellular protein highly expressed in astrocytes which are known to metabolize morphine into M3G (Suleman et al., 1998; Heurtaux et al., 2006; Sabolovic et al., 2007; Ouzzine et al., 2014). The active uptake of morphine by astrocytes might allow intracellular morphine to reach μM levels. Unfortunately, intracellular morphine concentrations have never been measured in the human brain, although it has been shown in rodents that morphine preferentially accumulates inside cells, especially astrocytes rather than in the ECF or CSF (Stain-Textier et al., 1999; Ouzzine et al., 2014).

In conclusion, CK-B/morphine interactions have the potential to be of clinical relevance and this warrants further investigation. While morphine concentrations may not reach sufficient levels to significantly impact CK-B activity in normal dosing regimens, chronic administration and high doses administered to tolerant patients might affect ATP bioavailability in humans.

CONCLUSION

Taken together, our results unveil a strong interaction between CK-B and morphine, occurring *in vitro* and *in vivo*. This interaction negatively impacts CK-B activity and thus has the potential to affect energy metabolism and glial transmission. Whether or not morphine is able to bind to and modulate CK-M or mitochondrial CK remains to be studied, but this seems likely given a high sequence homology between these enzymes and CK-B. Additional experiments will allow to further elucidate the binding site of morphine and study, in detail, the consequences of this interaction. The impact of CK-B and its

derived peptides on morphine analgesia and metabolism will be investigated in the future. Finally, a detailed study has to focus on endogenous morphine in order to determine its potential implication in energy bioavailability in both physiological and pathological processes.

AUTHOR CONTRIBUTIONS

YG, IW, AL-B, JM, M-OP, SC and AC: conceptualization. IW, AL-B, JM, VC, FD, FG, AM and YG: methodology. IW, AL-B, JM, VC, FD, AM and YG: investigation. YG, IW, FG, SC, M-OP, AM and AC: writing, review and editing. YG: funding acquisition, resources and supervision.

FUNDING

This work was funded by Inserm, CNRS (Postdoctoral fellowship to AL-B), University of Strasbourg, French Ministère Délégué à la Recherche et à l'Enseignement Supérieur (Ph.D. fellowship to AL-B, and IW), Alsace contre le Cancer, National Council for Scientific Research of Lebanon (CNRS-Lebanon to JM) and SATT-Conectus Alsace. We thank the following research programs of excellence for their support: FHU Neurogenycs, French National Research Agency (ANR) through the Programme d'Investissement d'Avenir (contract ANR-17-EURE-0022, EURIDOL graduate school of pain).

ACKNOWLEDGMENTS

We acknowledge Morgane Razafimahatratra for her technical help and Tando Maduna for her advice on the manuscript.

REFERENCES

- Andersen, G., Christrup, L., and Sjogren, P. (2003). Relationships among morphine metabolism, pain and side effects during long-term treatment: an update. *J. Pain Symptom. Manage.* 25, 74–91. doi: 10.1016/s0885-3924(02)00531-6
- Atmanene, C., Laux, A., Glattard, E., Muller, A., Schoentgen, F., Metz-Boutigue, M.-H., et al. (2009). Characterization of human and bovine phosphatidylethanolamine-binding protein (PEBP/RKIP) interactions with morphine and morphine-glucuronides determined by noncovalent mass spectrometry. *Med. Sci. Monit.* 15, BR178–BR187.
- Balasubramaniam, D., Schiffer, J., Parnell, J., Mir, S. P., Amaro, R. E., and Komives, E. A. (2015). How the ankyrin and SOCS box protein, ASB9, binds to creatine kinase. *Biochemistry* 54, 1673–1680. doi: 10.1021/bi501420n
- Boronat, M. A., Olmos, G., and García-Sevilla, J. A. (1998). Attenuation of tolerance to opioid-induced antinociception and protection against morphine-induced decrease of neurofilament proteins by idazoxan and other I2-imidazoline ligands. *Br. J. Pharmacol.* 125, 175–185. doi: 10.1038/sj.bjp.0720231
- Bouw, R., Ederoth, P., Lundberg, J., Ungerstedt, U., Nordström, C. H., and Hammarlund-Udenaes, M. (2001). Increased blood-brain barrier permeability of morphine in a patient with severe brain lesions as determined by microdialysis. *Acta Anaesthesiol. Scand.* 45, 390–392. doi: 10.1034/j.1399-6576.2001.045003390.x
- Brix-Christensen, V., Goumon, Y., Tønnesen, E., Chew, M., Bilfinger, T., and Stefano, G. B. (2000). Endogenous morphine is produced in response to cardiopulmonary bypass in neonatal pigs. *Acta Anaesthesiol. Scand.* 44, 1204–1208. doi: 10.1034/j.1399-6576.2000.441004.x
- Caprioli, G., Mammoli, V., Ricciutelli, M., Sagratini, G., Ubaldi, M., Domi, E., et al. (2015). Biological profile and bioavailability of imidazoline compounds on morphine tolerance modulation. *Eur. J. Pharmacol.* 769, 219–224. doi: 10.1016/j.ejphar.2015.11.021
- Chen, X.-L., Lu, G., Gong, Y.-X., Zhao, L.-C., Chen, J., Chi, Z.-Q., et al. (2007). Expression changes of hippocampal energy metabolism enzymes contribute to behavioural abnormalities during chronic morphine treatment. *Cell Res.* 17, 689–700. doi: 10.1038/cr.2007.63
- Ciubotariu, D., and Nechifor, M. (2012). Involvement of imidazoline system in drug addiction. *Rev. Med. Chir. Soc. Med. Nat. Iasi* 116, 1118–1122.
- Coombs, D. W., Frattin, J. D., Meier, F. A., Nierenberg, D. W., and Saunders, R. L. (1985). Neuropathologic lesions and CSF morphine concentrations during chronic continuous intraspinal morphine infusion. A clinical and post-mortem study. *Pain* 22, 337–351. doi: 10.1016/0304-3959(85)90040-5
- Correia, M. A., Krowech, G., Caldera-Munoz, P., Yee, S. L., Straub, K., and Castagnoli, N. Jr. (1984). Morphine metabolism revisited. II. Isolation and chemical characterization of a glutathionylmorphine adduct from rat liver microsomal preparations. *Chem. Biol. Interact.* 51, 13–24. doi: 10.1016/0009-2797(84)90016-4
- Dardonville, C., Fernandez-Fernandez, C., Gibbons, S. L., Ryan, G. J., Jagerovic, N., Gabilondo, A. M., et al. (2006). Synthesis and pharmacological studies of new hybrid derivatives of fentanyl active at the μ -opioid receptor and I2-imidazoline binding sites. *Bioorg. Med. Chem.* 14, 6570–6580. doi: 10.1016/j.bmc.2006.06.007
- Deléage, G., and Geourjon, C. (1993). An interactive graphic program for calculating the secondary structure content of proteins from circular dichroism spectrum. *Comput. Appl. Biosci.* 9, 197–199. doi: 10.1093/bioinformatics/9.2.197

- Eder, M., Stolz, M., Wallimann, T., and Schlattner, U. (2000). A conserved negatively charged cluster in the active site of creatine kinase is critical for enzymatic activity. *J. Biol. Chem.* 275, 27094–27099. doi: 10.1074/jbc.M004071200
- Ederoth, P., Tunblad, K., Bouw, R., Lundberg, C. J., Ungerstedt, U., Nordström, C. H., et al. (2004). Blood-brain barrier transport of morphine in patients with severe brain trauma. *Br. J. Clin. Pharmacol.* 57, 427–435. doi: 10.1046/j.1365-2125.2003.02032.x
- Endo, S., Matsunaga, T., Fujimoto, A., Kumada, S., Arai, Y., Miura, Y., et al. (2013). Characterization of rabbit morphine 6-dehydrogenase and two NAD⁺-dependent 3 α (17 β)-hydroxysteroid dehydrogenases. *Arch. Biochem. Biophys.* 529, 131–139. doi: 10.1016/j.abb.2012.11.013
- Frost, J., Løkken, T. N., Helland, A., Nordrum, I. S., and Slørdal, L. (2016). Post-mortem levels and tissue distribution of codeine, codeine-6-glucuronide, norcodeine, morphine and morphine glucuronides in a series of codeine-related deaths. *Forensic Sci. Int.* 262, 128–137. doi: 10.1016/j.forsciint.2016.02.051
- Gentili, F., Cardinaletti, C., Carrieri, A., Ghelfi, F., Mattioli, L., Perfumi, M., et al. (2006). Involvement of I2-imidazoline binding sites in positive and negative morphine analgesia modulatory effects. *Eur. J. Pharmacol.* 553, 73–81. doi: 10.1016/j.ejphar.2006.09.031
- Glattard, E., Welters, I. D., Lavaux, T., Muller, A. H., Laux, A., Zhang, D., et al. (2010). Endogenous morphine levels are increased in sepsis: a partial implication of neutrophils. *PLoS One* 5:e8791. doi: 10.1371/journal.pone.0008791
- Goumon, Y., Angelone, T., Schoentgen, F., Chasserot-Golaz, S., Almas, B., Fukami, M. M., et al. (2004). The hippocampal cholinergic neurostimulating peptide, the N-terminal fragment of the secreted phosphatidylethanolamine-binding protein, possesses a new biological activity on cardiac physiology. *J. Biol. Chem.* 279, 13054–13064. doi: 10.1074/jbc.M308533200
- Goumon, Y., Bouret, S., Casares, F., Zhu, W., Beauvillain, J. C., and Stefano, G. B. (2000). Lipopolysaccharide increases endogenous morphine levels in rat brain. *Neurosci. Lett.* 293, 135–138. doi: 10.1016/S0304-3940(00)01507-X
- Handal, M., Grung, M., Skurtveit, S., Ripel, A., and Mørland, J. (2002). Pharmacokinetic differences of morphine and morphine-glucuronides are reflected in locomotor activity. *Pharmacol. Biochem. Behav.* 73, 883–892. doi: 10.1016/S0091-3057(02)00925-5
- Harada, K., Kamiya, T., and Tsuboi, T. (2016). Gliotransmitter release from astrocytes: functional, developmental, and pathological implications in the brain. *Front. Neurosci.* 9:499. doi: 10.3389/fnins.2015.00499
- Heurtaux, T., Benani, A., Moulin, D., Muller, N., Netter, P., and Minn, A. (2006). Induction of UGT1A6 isoform by inflammatory conditions in rat astrocytes. *Neuropharmacology* 50, 317–328. doi: 10.1016/j.neuropharm.2005.09.007
- Judis, J. (1977). Binding of codeine, morphine, and methadone to human serum proteins. *J. Pharm. Sci.* 66, 802–806. doi: 10.1002/jps.2600660615
- Kimura, A., Tyacke, R. J., Robinson, J. J., Husbands, S. M., Minchin, M. C., Nutt, D. J., et al. (2009). Identification of an imidazoline binding protein: creatine kinase and an imidazoline-2 binding site. *Brain Res.* 1279, 21–28. doi: 10.1016/j.brainres.2009.04.044
- King, C. D., Rios, G. R., Green, M. D., and Tephly, T. R. (2000). UDP-glucuronosyltransferases. *Curr. Drug Metab.* 1, 143–161. doi: 10.2174/138920000339171
- Klimas, R., and Mikus, G. (2014). Morphine-6-glucuronide is responsible for the analgesic effect after morphine administration: a quantitative review of morphine, morphine-6-glucuronide and morphine-3-glucuronide. *Br. J. Anaesth.* 113, 935–944. doi: 10.1093/bja/aeu186
- Kumagai, Y., Todaka, T., and Toki, S. (1990). A new metabolic pathway of morphine: *in vivo* and *in vitro* formation of morphinone and morphine-glutathione adduct in guinea pig. *J. Pharmacol. Exp. Ther.* 255, 504–510.
- Kwon, S., Kim, D., Rhee, J. W., Park, J. A., Kim, D. W., Kim, D. S., et al. (2010). ASB9 interacts with ubiquitous mitochondrial creatine kinase and inhibits mitochondrial function. *BMC Biol.* 8:23. doi: 10.1186/1741-7007-8-23
- Laux, A., Delalande, F., Mouheiche, J., Stuber, D., Van Dorsselaer, A., Bianchi, E., et al. (2012). Localization of endogenous morphine-like compounds in the mouse spinal cord. *J. Comp. Neurol.* 520, 1547–1561. doi: 10.1002/cne.22811
- Laux, A., Muller, A. H., Miehe, M., Dirrig-Grosch, S., Deloulme, J. C., Delalande, F., et al. (2011). Mapping of endogenous morphine-like compounds in the adult mouse brain: evidence of their localization in astrocytes and GABAergic cells. *J. Comp. Neurol.* 519, 2390–2416. doi: 10.1002/cne.22633
- Laux-Biehlmann, A., Grafe, N., Mouheiche, J., Stuber, D., Welters, I. D., Delalande, F., et al. (2012). Comparison of serum and lithium-heparinate plasma for the accurate measurements of endogenous and exogenous morphine concentrations. *Br. J. Clin. Pharmacol.* 74, 381–383. doi: 10.1111/j.1365-2125.2012.04199.x
- Laux-Biehlmann, A., Mouheiche, J., Vérièpe, J., and Goumon, Y. (2013). Endogenous morphine and its metabolites in mammals: history, synthesis, localization and perspectives. *Neuroscience* 233, 95–117. doi: 10.1016/j.neuroscience.2012.12.013
- Leow, K. P., Wright, A. W., Cramond, T., and Smith, M. T. (1993). Determination of the serum protein binding of oxycodone and morphine using ultrafiltration. *Ther. Drug Monit.* 15, 440–447. doi: 10.1097/00007691-199310000-00014
- Li, J. X. (2017). Imidazoline I2 receptors: an update. *Pharmacol. Ther.* 178, 48–56. doi: 10.1016/j.pharmthera.2017.03.009
- Manos, P., and Bryan, G. K. (1993). Cellular and subcellular compartmentation of creatine-kinase in brain. *Dev. Neurosci.* 15, 271–279. doi: 10.1159/00011344
- McGrath, J. C., Drummond, G. B., McLachlan, E. M., Kilkeny, C., and Wainwright, C. L. (2010). Guidelines for reporting experiments involving animals: the ARRIVE guidelines. *Br. J. Pharmacol.* 160, 1573–1576. doi: 10.1111/j.1476-5381.2010.00873.x
- Meijerink, W. J., Molina, P. E., and Abumrad, N. N. (1999). Mammalian opiate alkaloid synthesis: lessons derived from plant biochemistry. *Shock* 12, 165–173. doi: 10.1097/00024382-199909000-00001
- Miralles, A., Esteban, S., Sastre-Coll, A., Moranta, D., Asensio, V. J., and Garcia-Sevilla, J. A. (2005). High-affinity binding of β -carbolines to imidazoline I_{2b} receptors and MAO-A in rat tissues: norharman blocks the effect of morphine withdrawal on DOPA/noradrenaline synthesis in the brain. *Eur. J. Pharmacol.* 518, 234–242. doi: 10.1016/j.ejphar.2005.06.023
- Misra, A. L., and Mitchell, C. L. (1971). Metal ion-catalysed interaction of peroxidase with morphine and protein. *Experientia* 27, 1442–1444. doi: 10.1007/bf02154278
- Misra, A. L., Mitchell, C. L., and Woods, L. A. (1971). Persistence of morphine in central nervous system of rats after a single injection and its bearing on tolerance. *Nature* 232, 48–50. doi: 10.1038/232048a0
- Muller, A., Glattard, E., Taleb, O., Kemmel, V., Laux, A., Miehe, M., et al. (2008). Endogenous morphine in SH-SY5Y cells and the mouse cerebellum. *PLoS One* 3:e1641. doi: 10.1371/journal.pone.0001641
- Mullis, K. B., Perry, D. C., Finn, A. M., Stafford, B., and Sadée, W. (1979). Morphine persistence in rat brain and serum after single doses. *J. Pharmacol. Exp. Ther.* 208, 228–231.
- Nagamatsu, K., and Hasegawa, A. (1992). Covalent binding of morphine to isolated rat hepatocytes. *Biochem. Pharmacol.* 43, 2631–2635. doi: 10.1016/0006-2952(92)90152-9
- Nagamatsu, K., and Hasegawa, A. (1993). Effect of sodium selenite on morphine-induced hepatotoxicity in mice. *Drug Chem. Toxicol.* 16, 241–253. doi: 10.3109/01480549309081818
- Nagamatsu, K., Kido, Y., Terao, T., Ishida, T., and Toki, S. (1983). Studies on the mechanism of covalent binding of morphine metabolites to proteins in mouse. *Drug Metab. Dispos.* 11, 190–194.
- Nasello, A. G., Depiante, R., Tannhauser, M., and Izquierdo, I. (1973). Effect of morphine on the RNA and ATP concentration of brain structures of the rat. *Pharmacology* 10, 56–59. doi: 10.1159/000136422
- Ouzzine, M., Gulberti, S., Ramalanjaona, N., Magdalou, J., and Fournel-Gigleux, S. (2014). The UDP-glucuronosyltransferases of the blood-brain barrier: their role in drug metabolism and detoxication. *Front. Cell. Neurosci.* 8:349. doi: 10.3389/fncel.2014.00349
- Patrick, G. A., Dewey, W. L., Spaulding, T. C., and Harris, L. S. (1975). Relationship of brain morphine levels to analgesic activity in acutely treated mice and rats and in pellet implanted mice. *J. Pharmacol. Exp. Ther.* 193, 876–883.
- Ruiz-Durántez, E., Torrecilla, M., Pineda, J., and Ugedo, L. (2003). Attenuation of acute and chronic effects of morphine by the imidazoline receptor ligand 2-(2-benzofuranyl)-2-imidazoline in rat locus coeruleus neurons. *Br. J. Pharmacol.* 138, 494–500. doi: 10.1038/sj.bjp.0705052

- Sabolovic, N., Heurtaux, T., Humbert, A. C., Krisa, S., and Magdalou, J. (2007). *cis*- and *trans*-Resveratrol are glucuronidated in rat brain, olfactory mucosa and cultured astrocytes. *Pharmacology* 80, 185–192. doi: 10.1159/000104149
- Sanchez-Blázquez, P., Boronat, M. A., Olmos, G., García-Sevilla, J. A., and Garzón, J. (2000). Activation of I₂-imidazoline receptors enhances supraspinal morphine analgesia in mice: a model to detect agonist and antagonist activities at these receptors. *Br. J. Pharmacol.* 130, 146–152. doi: 10.1038/sj.bjp.0703294
- Säwe, J., Svensson, J. O., and Rane, A. (1983). Morphine metabolism in cancer patients on increasing oral doses—no evidence for autoinduction or dose-dependence. *Br. J. Clin. Pharmacol.* 16, 85–93. doi: 10.1111/j.1365-2125.1983.tb02148.x
- Schreiber, E., Harshman, K., Kemler, I., Malipiero, U., Schaffner, W., and Fontana, A. (1990). Astrocytes and glioblastoma cells express novel octamer-DNA binding proteins distinct from the ubiquitous Oct-1 and B cell type Oct-2 proteins. *Nucleic Acids Res.* 18, 5495–5503. doi: 10.1093/nar/18.18.5495
- Stain-Textier, F., Boschi, G., Sandouk, P., and Scherrmann, J. M. (1999). Elevated concentrations of morphine 6- β -D-glucuronide in brain extracellular fluid despite low blood-brain barrier permeability. *Br. J. Pharmacol.* 128, 917–924. doi: 10.1038/sj.bjp.0702873
- Suleman, F. G., Abid, A., Gradinaru, D., Daval, J. L., Magdalou, J., and Minn, A. (1998). Identification of the uridine diphosphate glucuronosyltransferase isoform UGT1A6 in rat brain and in primary cultures of neurons and astrocytes. *Arch. Biochem. Biophys.* 358, 63–67. doi: 10.1006/abbi.1998.0842
- Tachikawa, M., Fukaya, M., Terasaki, T., Ohtsuki, S., and Watanabe, M. (2004). Distinct cellular expressions of creatine synthetic enzyme GAMT and creatine kinases uCK-Mi and CK-B suggest a novel neuron-glial relationship for brain energy homeostasis. *Eur. J. Neurosci.* 20, 144–160. doi: 10.1111/j.1460-9568.2004.03478.x
- Togna, A. R., Antonilli, L., Dovizio, M., Salemme, A., De Carolis, L., Togna, G. I., et al. (2013). *In vitro* morphine metabolism by rat microglia. *Neuropharmacology* 75C, 391–398. doi: 10.1016/j.neuropharm.2013.08.019
- Tzvetkov, M. V., dos Santos Pereira, J. N., Meineke, I., Saadatmand, A. R., Stingl, J. C., and Brockmoeller, J. (2013). Morphine is a substrate of the organic cation transporter OCT1 and polymorphisms in OCT1 gene affect morphine pharmacokinetics after codeine administration. *Biochem. Pharmacol.* 86, 666–678. doi: 10.1016/j.bcp.2013.06.019
- Valvassori, S. S., Bavaresco, D. V., Scaini, G., Varela, R. B., Streck, E. L., Chagas, M. H., et al. (2013). Acute and chronic administration of cannabidiol increases mitochondrial complex and creatine kinase activity in the rat brain. *Braz. J. Psychiatry* 35, 380–386. doi: 10.1590/1516-4446-2012-0886
- Van Laar, V. S., Mishizen, A. J., Cascio, M., and Hastings, T. G. (2009). Proteomic identification of dopamine-conjugated proteins from isolated rat brain mitochondria and SH-SY5Y cells. *Neurobiol. Dis.* 34, 487–500. doi: 10.1016/j.nbd.2009.03.004
- Vekovischeva, O. Y., Zamanillo, D., Echenko, O., Seppälä, T., Uusi-Oukari, M., Honkanen, A., et al. (2001). Morphine-induced dependence and sensitization are altered in mice deficient in AMPA-type glutamate receptor-A subunits. *J. Neurosci.* 21, 4451–4459. doi: 10.1523/JNEUROSCI.21-12-04451.2001
- Weinsanto, I., Laux-Biehlmann, A., Mouheiche, J., Maduna, T., Delalande, F., Chavant, V., et al. (2018). Stable isotope-labelled morphine to study *in vivo* central and peripheral morphine glucuronidation and brain transport in tolerant mice. *Br. J. Pharmacol.* 175, 3844–3856. doi: 10.1111/bph.14454
- Wyss, M., and Kaddurah-Daouk, R. (2000). Creatine and creatinine metabolism. *Physiol. Rev.* 80, 1107–1213. doi: 10.1152/physrev.2000.80.3.1107
- Xie, N., Gomes, F. P., Deora, V., Gregory, K., Vithanage, T., Nassar, Z. D., et al. (2017). Activation of mu-opioid receptor and Toll-like receptor 4 by plasma from morphine-treated mice. *Brain Behav. Immun.* 61, 244–258. doi: 10.1016/j.bbi.2016.12.002
- Zelcer, N., van de Wetering, K., Hillebrand, M., Sarton, E., Kuil, A., Wielinga, P. R., et al. (2005). Mice lacking multidrug resistance protein 3 show altered morphine pharmacokinetics and morphine-6-glucuronide antinociception. *Proc. Natl. Acad. Sci. U S A* 102, 7274–7279. doi: 10.1073/pnas.0502530102

Conflict of Interest Statement: The authors declare that the research was conducted in the absence of any commercial or financial relationships that could be construed as a potential conflict of interest.

Copyright © 2018 Weinsanto, Mouheiche, Laux-Biehlmann, Delalande, Marquette, Chavant, Gabel, Cianferani, Charlet, Parat and Goumon. This is an open-access article distributed under the terms of the Creative Commons Attribution License (CC BY). The use, distribution or reproduction in other forums is permitted, provided the original author(s) and the copyright owner(s) are credited and that the original publication in this journal is cited, in accordance with accepted academic practice. No use, distribution or reproduction is permitted which does not comply with these terms.



Corrigendum: Morphine Binds Creatine Kinase B and Inhibits Its Activity

OPEN ACCESS

Approved by:

Frontiers Editorial Office,
Frontiers Media SA, Switzerland

*Correspondence:

Yannick Goumon
yannick.goumon@inserm.u-strasbg.fr

[†]These authors have contributed
equally to this work

[‡]Present Address:

Alexis Laux-Biehlmann,
Bayer AG, Research & Development,
Pharmaceuticals, Berlin, Germany

Specialty section:

This article was submitted to
Cellular Neurophysiology,
a section of the journal
Frontiers in Cellular Neuroscience

Received: 13 June 2019

Accepted: 14 June 2019

Published: 02 July 2019

Citation:

Weinsanto I, Mouheiche J,
Laux-Biehlmann A, Delalande F,
Marquette A, Chavant V, Gabel F,
Cianferani S, Charlet A, Parat M-O
and Goumon Y (2019) Corrigendum:
Morphine Binds Creatine Kinase B
and Inhibits Its Activity.
Front. Cell. Neurosci. 13:292.
doi: 10.3389/fncel.2019.00292

Ivan Weinsanto^{1†}, Jinane Mouheiche^{1†}, Alexis Laux-Biehlmann^{1‡}, François Delalande²,
Arnaud Marquette³, Virginie Chavant^{1,4}, Florian Gabel¹, Sarah Cianferani²,
Alexandre Charlet¹, Marie-Odile Parat⁵ and Yannick Goumon^{1,4*}

¹ Institut des Neurosciences Cellulaires et Intégratives, CNRS UPR3212 and Université de Strasbourg, Strasbourg, France,

² Laboratoire de Spectrométrie de Masse BioOrganique, IPHC-DSA, CNRS UMR7178 and Université de Strasbourg, Strasbourg, France, ³ CNRS UMR7177 and Université de Strasbourg, Strasbourg, France, ⁴ Mass Spectrometry Facilities of the CNRS UPR3212, Strasbourg, France, ⁵ School of Pharmacy, University of Queensland, PACE, Woolloongabba, QLD, Australia

Keywords: morphine, complex, ligand-binding protein, creatine kinase, high affinity

A Corrigendum on

Morphine Binds Creatine Kinase B and Inhibits Its Activity

by Weinsanto, I., Mouheiche, J., Laux-Biehlmann, A., Delalande, F., Marquette, A., Chavant, V., et al. (2018). *Front. Cell. Neurosci.* 12:464. doi: 10.3389/fncel.2018.00464

In the published article, there was an error in affiliation “2.” Instead of “Global Drug Discovery, Global Therapeutic Research Groups, Gynecological Therapies, Bayer Healthcare, Berlin, Germany”, it should be “Laboratoire de Spectrométrie de Masse BioOrganique, IPHC-DSA, CNRS UMR7178 and Université de Strasbourg, Strasbourg, France.”

Additionally, the current address of one author has been added as a footnote and is denoted using “[‡].”

The authors apologize for this error and state that this does not change the scientific conclusions of the article in any way. The original article has been updated.

Copyright © 2019 Weinsanto, Mouheiche, Laux-Biehlmann, Delalande, Marquette, Chavant, Gabel, Cianferani, Charlet, Parat and Goumon. This is an open-access article distributed under the terms of the Creative Commons Attribution License (CC BY). The use, distribution or reproduction in other forums is permitted, provided the original author(s) and the copyright owner(s) are credited and that the original publication in this journal is cited, in accordance with accepted academic practice. No use, distribution or reproduction is permitted which does not comply with these terms.



Long-Lasting Response Changes in Deep Cerebellar Nuclei *in vivo* Correlate With Low-Frequency Oscillations

Letizia Moscato^{1†}, Ileana Montagna^{1†}, Licia De Propriis², Simona Tritto¹, Lisa Mapelli^{1*‡} and Egidio D'Angelo^{1,2*‡}

¹ Department of Brain and Behavioral Sciences, University of Pavia, Pavia, Italy, ² IRCCS Mondino Foundation, Pavia, Italy

OPEN ACCESS

Edited by:

Sergey M. Korogod,
Bogomoletz Institute of Physiology,
National Academy of Sciences
of Ukraine, Ukraine

Reviewed by:

Takashi Tominaga,
Tokushima Bunri University, Japan
Mario U. Manto,
University of Mons, Belgium

*Correspondence:

Lisa Mapelli
lisa.mapelli@unipv.it
Egidio D'Angelo
dangelo@unipv.it

[†]Co-first authors

[‡]Co-last authors

Received: 30 October 2018

Accepted: 19 February 2019

Published: 06 March 2019

Citation:

Moscato L, Montagna I,
De Propriis L, Tritto S, Mapelli L and
D'Angelo E (2019) Long-Lasting
Response Changes in Deep
Cerebellar Nuclei *in vivo* Correlate
With Low-Frequency Oscillations.
Front. Cell. Neurosci. 13:84.
doi: 10.3389/fncel.2019.00084

The deep cerebellar nuclei (DCN) have been suggested to play a critical role in sensorimotor learning and some forms of long-term synaptic plasticity observed *in vitro* have been proposed as a possible substrate. However, till now it was not clear whether and how DCN neuron responses manifest long-lasting changes *in vivo*. Here, we have characterized DCN unit responses to tactile stimulation of the facial area in anesthetized mice and evaluated the changes induced by theta-sensory stimulation (TSS), a 4 Hz stimulation pattern that is known to induce plasticity in the cerebellar cortex *in vivo*. DCN units responded to tactile stimulation generating bursts and pauses, which reflected combinations of excitatory inputs most likely relayed by mossy fiber collaterals, inhibitory inputs relayed by Purkinje cells, and intrinsic rebound firing. Interestingly, initial bursts and pauses were often followed by stimulus-induced oscillations in the peri-stimulus time histograms (PSTH). TSS induced long-lasting changes in DCN unit responses. Spike-related potentiation and suppression (SR-P and SR-S), either in units initiating the response with bursts or pauses, were correlated with stimulus-induced oscillations. Fitting with resonant functions suggested the existence of peaks in the theta-band (burst SR-P at 9 Hz, pause SR-S at 5 Hz). Optogenetic stimulation of the cerebellar cortex altered stimulus-induced oscillations suggesting that Purkinje cells play a critical role in the circuits controlling DCN oscillations and plasticity. This observation complements those reported before on the granular and molecular layers supporting the generation of multiple distributed plasticities in the cerebellum following naturally patterned sensory entrainment. The unique dependency of DCN plasticity on circuit oscillations discloses a potential relationship between cerebellar learning and activity patterns generated in the cerebellar network.

Keywords: deep cerebellar nuclei, cerebellum, plasticity, oscillations, *in vivo* electrophysiology

INTRODUCTION

Two functional aspects of the cerebellum, that have been emphasized in turn but proved hard to reconcile, are the pronounced oscillatory dynamics (Llinas, 1988) and the role in sensorimotor learning (Marr, 1969; Albus, 1971; Ito, 1972). Key nodes in the cerebellar circuitry are the deep cerebellar nuclei (DCN). DCN convey rhythmic outputs to the motor system (Jacobson et al., 2008)

and, at the same time, have been suggested to be the site of plasticity by studies using local lesions (Ohyama et al., 2003, 2006) or electrical stimulation of afferent fiber bundles (Racine et al., 1986). Multiple forms of plasticity have been reported in DCN synapses *in vitro* (Morishita and Sastry, 1996; Ouardouz and Sastry, 2000; Zhang et al., 2004; Zhang and Linden, 2006; Pugh and Raman, 2009) (reviewed in Hansel et al., 2001; Gao et al., 2012; D'Angelo, 2014; Mapelli et al., 2015; D'Angelo et al., 2016b) and have been proposed to play a critical role in animal associative behaviors by computational models (Medina and Mauk, 1999; Casellato et al., 2015; Antonietti et al., 2016; D'Angelo et al., 2016a). Despite this evidence, the demonstration that long-lasting changes can actually be measured in DCN *in vivo* and can be related to internal circuit oscillations and plasticity was still lacking.

Deep cerebellar nuclei neurons are autorhythmic (Jahnsen, 1986a,b) and receive both excitatory inputs from collaterals of mossy and climbing fibers and inhibitory inputs from Purkinje cells (PCs) (Llinas and Muhlethaler, 1988). DCN neurons respond to tactile stimulation generating discharge patterns, which reflect the combination of inhibitory and excitatory inputs (Rowland and Jaeger, 2005, 2008; Chen et al., 2010; Canto et al., 2016; Yarden-Rabinowitz and Yarom, 2017). DCN neurons send output fibers to thalamus and to various precerebellar nuclei, influencing neuronal activity both in descending systems and in the cerebral cortex (Watson et al., 2014; Gao et al., 2018). Specific pathways also connect DCN with the inferior olive (Jacobson et al., 2008) and cerebellar granular layer (Ankri et al., 2015; Gao et al., 2016). These connections form the basis for reverberating loops that have been predicted to sustain rebound excitation and oscillatory cycles (Llinas and Muhlethaler, 1988; Kistler and De Zeeuw, 2003; Marshall and Lang, 2004; Hoebeek et al., 2010; Witter et al., 2013).

In the DCN, long-term synaptic plasticity [long-term potentiation and depression (LTP and LTD)] has been identified both at excitatory and inhibitory connections *in vitro*. Interestingly, excitatory plasticity depended on post-inhibitory rebound bursts (Pugh and Raman, 2006) and inhibitory plasticity required co-activation of mossy fibers (Morishita and Sastry, 1996; Ouardouz and Sastry, 2000), so that plasticity at the two synapses appears to be correlated and to require precise activation sequences.

In this work, we asked whether long-lasting changes could be induced in DCN single unit responses in anesthetized mice *in vivo* using facial theta sensory stimulation (TSS), which proved able in previous works to induce long-lasting changes in responses recorded from the cerebellum granular layer and molecular layer (Roggeri et al., 2008; Ramakrishnan et al., 2016). TSS actually induced long-lasting changes in DCN unit responses. Interestingly, these changes were uniquely correlated with the frequency of stimulus-induced oscillations, suggesting a close relationship between oscillatory dynamics and plasticity (D'Angelo and De Zeeuw, 2009; Cheron et al., 2016) reminiscent of induction schemes identified in hippocampus and neocortex (Buzsaki, 2006; Roy et al., 2014).

MATERIALS AND METHODS

Multiple single-unit recordings were performed from the fastigial nucleus of C57BL/6 mice of either sex (40.2 ± 1.8 days old; $n = 51$) under urethane anesthesia. Urethane was used as its anesthetic action is exerted through multiple weak effects (including a 10% reduction of NMDA, 18% reduction of AMPA and 23% enhancement of GABA-A receptor-mediated currents) (Hara and Harris, 2002) compared to ketamine or isoflurane, which act by powerfully blocking NMDA receptors (up to 80 and 60%, respectively; Hara and Harris, 2002) and could therefore severely compromise the induction of plasticity (Godaux et al., 1990; Muller et al., 1993; Bengtsson and Jorntell, 2007; Marquez-Ruiz and Cheron, 2012; Mawhinney et al., 2012). Moreover, urethane was successfully used before in similar recording conditions to investigate plasticity in the granular layer (Roggeri et al., 2008) and molecular layer (Ramakrishnan et al., 2016) of cerebellum.

All experimental protocols were conducted in accordance with international guidelines from the European Union Directive 2010/63/EU on the ethical use of animals and were approved by the ethical committee of Italian Ministry of Health (638/2017-PR; 7/2018-PR).

Surgical Procedures

Mice were deeply anesthetized with intraperitoneal injections of urethane (Sigma-Aldrich). Induction (1.3 g/kg urethane dissolved in 0.9% NaCl) was followed by booster injections (10% of the induction dose) in order to stabilize anesthesia, starting 30 min after induction and repeating 3 – 4 times every 30 min. The level of anesthesia was monitored by evaluating the leg withdrawal after pinching and spontaneous whisking. The animal was then placed on a custom-built stereotaxic table covered with a heating plate (HP-1M: RTD/157, Physitemp Instruments, Inc., Clifton, NJ, United States). Body temperature was monitored with a rectal probe and maintained at 36°C through a feedback controller (TCAT-2LV controller, Physitemp Instruments, Inc., Clifton, NJ, United States). The mouse head was fixed over the Bregma to a metal bar connected to a pedestal anchored to the stereotaxic table. This arrangement allowed open access to the peri-oral area for air-puff stimulation. Surgery was performed to expose the cerebellar surface: local reflexes were reduced by subcutaneous application of lidocaine (0.2 ml; Astrazeneca), then the skin and muscles were removed. Craniotomy of the occipital bone (-7.8 mm AP, $+0.50$ mm ML from Bregma, in order to record from the fastigial nucleus) allowed to expose the cerebellar surface over the vermis. The *dura mater* was carefully removed and the surface was covered with saline (NaCl 0.9% ; Sigma) to prevent drying.

Single Unit Recordings *in vivo*

Quartz-coated platinum/tungsten fiber electrodes (1 – 5 M Ω) organized in a multi-electrode array (MEA) of 4×4 , with inter-electrode distance of 100 μm (Eckhorn matrix, Thomas Recording, GmBh, Germany) were used for neuronal recordings. Recording electrodes were positioned over the vermis, ipsilateral to the air puff stimulator, and lowered perpendicularly to the surface down to a depth of 2109.1 ± 65.5 μm ($n = 33$).

The electrophysiological signals were digitized at 25 kHz, using a 300–5000 Hz band-pass filter, amplified and stored using a RZ5D processor multi-channel workstation (Tucker-Davis Technologies, Alachua, FL, United States). DCN neurons were identified online by assessing recording depth, spontaneous activity, and stimulus-evoked responses. At the end of recordings, an electric lesion was made by injecting current through the recording electrode. The recording site was then confirmed by histological tissue processing (see below).

Sensory Stimulation

Tactile sensory stimulation was performed using air-puffs (30 ms pulses, 30–60 psi) delivered through a small tube ending with a nozzle (0.5 mm diameter) positioned 2–3 mm away from the snout area of the animal and connected to a MPPI-2 pressure injector (Applied Scientific Instrumentation, Eugene, OR, United States) (Roggeri et al., 2008; Ramakrishnan et al., 2016). While cerebellar cortical responses to skin receptive fields stimulation are organized in the so-called “fractured somatotopy” in the granular layer and in zonal or small regions in the molecular layer (Shambes et al., 1978; Kassel et al., 1984; Ekerot and Jorntell, 2001; Jorntell and Ekerot, 2002), DCN neurons have been described to respond to large portions of the body surface, both ipsi- and contra-lateral (Rowland and Jaeger, 2005). We nevertheless limited the sensory stimulation area to mouse upper lip, lower lip or whisker pad of the ipsilateral region. Following 5 min of spontaneous activity recording, low frequency stimuli (0.5 Hz) were delivered over the mouse upper lip, lower lip or whisker pad to activate the corresponding receptive fields and evoke the neuronal response (Bower and Woolston, 1983; Morissette and Bower, 1996; Vos et al., 1999; Roggeri et al., 2008; Ramakrishnan et al., 2016) (see **Figure 1A**). DCN single unit responses were monitored online by building peri-stimulus time histograms (PSTHs) triggered by the air-puffs. Once a responsive unit was detected, control stimuli were delivered for 20 min at 0.5 Hz, in order to characterize unit responses to tactile sensory stimulation. Then, the TSS pattern (a burst of 100 air-puffs at 4 Hz) was delivered, followed by post-induction recordings for at least 40 min at 0.5 Hz. Since the air puff has been reported to elicit a brief spike burst in the mossy fibers (Vos et al., 1999; Chadderton et al., 2004), the TSS is likely to determine short bursts repeated at 4 Hz. This pattern is known to induce plasticity in the cerebellar cortex (see Roggeri et al., 2008; Prestori et al., 2013; Ramakrishnan et al., 2016; Romano et al., 2018). In 12 recordings TSS was not delivered, monitoring the stability of responses for at least 60 min.

Pharmacology

In a subset of experiments, the AMPA and NMDA receptor antagonists, 100 μ M NBQX (Abcam) (Guo et al., 2016) and 250 μ M D-APV (Tocris Bioscience) (Zhang et al., 2017), were injected in the fastigial nucleus near the recording electrodes. APV and NBQX were added to a Krebs solution with the following composition (in mM): 120 NaCl, 2 KCl, 1.2 MgSO₄, 26 NaHCO₃, 1.2 KH₂PO₄, 2 CaCl₂, and 11 glucose, equilibrated with 95% O₂–5% CO₂ (pH 7.4). The solution containing the drugs was pre-loaded in a pneumatic picopump (PV820, World

Precision Instruments), operated through adjustable air pressure, terminating in a 35G needle, positioned using a Patch-Star micromanipulator (Scientifica, Ltd.). After 15 min of single-unit recording, the solution was injected at the rate of 1 μ l/5 min. It should be noted that the injection of GABAergic antagonists in the fastigial nucleus would not help discerning the origin of the pause, as it would affect the synapses coming from both local interneurons and PCs.

Optogenetics

Adeno Associated Virus Injection and Expression

The expression of ChR2 in the cerebellar vermis was obtained through local injection of the adeno associated viral construct pAAV-hSyn-hChR2-EYFP (AAV1 serotype; Penn Vector Core, University of Pennsylvania, United States). C57BL6 mice of either sex (30 days old, $n = 13$) were anesthetized with 1–2% isoflurane in oxygen 100% at 0.7 L/min delivered from a gas vaporizer (Ugo Basile S.R.L., Italy) and were placed in a stereotaxic apparatus (Leica vernier stereotaxic instrument), where they constantly received isoflurane from a nose cone and had their head fixed with ear bars. Mice body temperature was constantly monitored by a heating pad connected to a rectal thermal probe (TCAT-2LV controller, Physitemp Instruments, Inc., Clifton, NJ, United States) and maintained at 36°C. After testing the absence of withdrawal reflexes, a sagittal incision on the head was performed to expose the cranium, and a burr hole was drilled to target lobule VI of cerebellar vermis 3.5 mm posterior to Lambda. The virus was loaded into a 10 μ l NanoFil syringe (World Precision Instruments) that was connected to an automatic syringe pump (Ugo Basile S.R.L., Italy). The injection needle (NF35BV, 35G, World Precision Instruments) was positioned into the vermis at 300 μ m depth and 0.2 μ l of virus solution at a titer of 1.168^{13} genome copies/ml was injected at a flow rate of 0.05 μ l/min. This procedure ensured a localized expression of ChR2 at the level of cerebellar molecular and PC layers. A good incorporation of the virus in the tissue was assured by keeping the needle in place for 10 min after the end of perfusion. The head was sutured and mice were kept under observation until recovery from the anesthesia, before returning to the animal facility. In order to ensure a good expression of ChR2, electrophysiological experiments were performed 21–28 days after viral injection.

ChR2 Expression in Acute Cerebellar Slices

In five mice that were injected with the construct but were not used for *in vivo* recordings, after 30 days the cerebellum was removed and used to prepare acute slices (220 μ m thick) following standard procedures (Mapelli et al., 2017). The efficacy of ChR2 expression was tested by extracellular recordings from PCs. The PC soma was selectively illuminated with blue led light (Polygon400, Mightex Systems). The extracellular signals were recorded using a Multiclamp 700B amplifier (Molecular Devices) controlled by pClamp10 through a Digidata1440A (Molecular Devices). When illuminated, the PCs increased firing activity as expected from effective ChR2 expression causing membrane depolarization (**Supplementary Figure S1**).

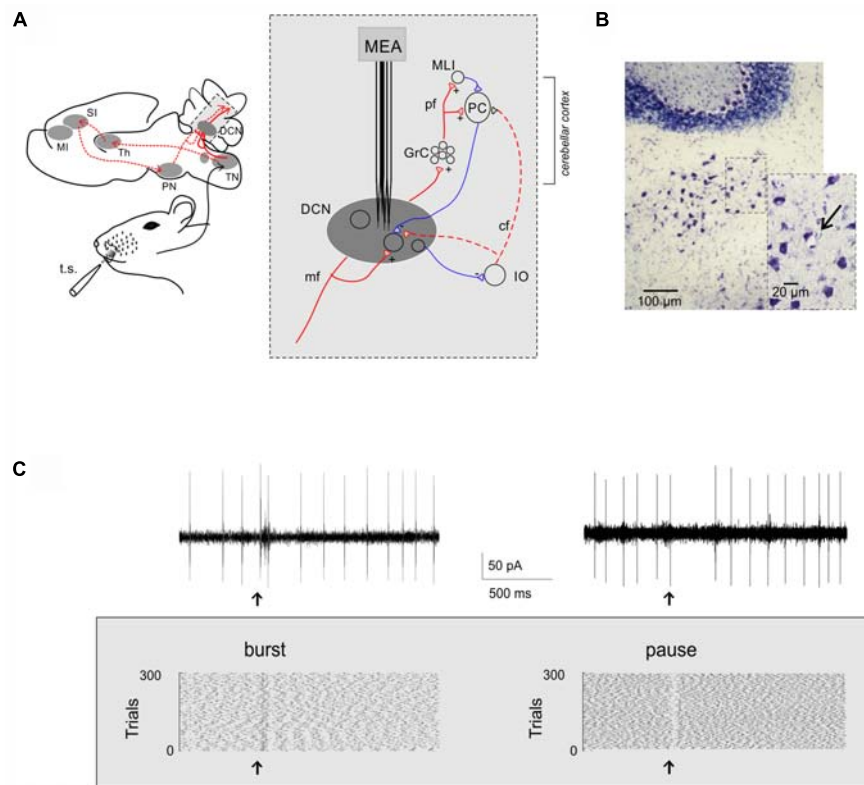


FIGURE 1 | Extracellular recordings from DCN units *in vivo*. **(A)** Schematic representation of the main pathways activated by air puff stimulation of the peri-oral region in mice: the trigemino-cerebellar (solid red line) and thalamo-cortical-pontine (dashed red line) pathways. The region in the gray box is expanded at the right to show the main circuit elements relevant to DCN neuron activity. MI, primary motor cortex; SI, primary sensory cortex; Th, thalamus; PN, pontine nuclei; TN, trigeminal nucleus; DCN, deep cerebellar nuclei; GrC, granule cells; MLIs, molecular layer interneurons; PC, Purkinje cell; IO, inferior olive; pf, parallel fibers; mf, mossy fibers; cf, climbing fiber; t.s., tactile stimulation. MEA, multi-electrode array (Eckhorn matrix, see section “Materials and Methods” for details). **(B)** Toluidine blue stained coronal cerebellar slice showing the electric lesion (arrow) made by the recording electrode in the fastigial nucleus. **(C)** Two single-unit recordings showing a burst and a pause in response to tactile stimulation (arrow). The raster plots show the spike discharge during ~2 s recordings and its change caused by tactile stimulation in 300 consecutive trials.

General Aspects of Optogenetics Experiments

Since our aim was to interfere with PC activity, the site of AAV1 injection was limited to restricted regions of the molecular layer (**Supplementary Figure S1A**). The Chr2 was expressed under a generic neuronal promoter in common to molecular layer interneurons, PCs and parallel fibers. Since local circuit wiring in the molecular layer is not homogeneous (Valera et al., 2016), optogenetic activation was not expected to sort out the same effect in all cases (cfr. **Figure 1A** for a scheme of the circuit). Indeed, depending on the individual experiment, optogenetic stimulation could either increase or decrease PC activity and the pause and, in 2 out of 8 cases, no response modification was detected.

Light Application During *in vivo* Recordings

A light-conducting glass fiber with 120 μm diameter cladding and numerical aperture NA = 0.22 (Thomas Recording GmbH, Germany) was mounted in the Eckhorn Matrix (Thomas Recording GmbH, Germany). Just as the recording electrodes, it was possible to drive the tip of the glass fiber down into the tissue with micrometric precision. The optic fiber was connected through a FC/PC patch cable (ThorLabs Ø105 μm, 0.22NA,

FC/PC-Fiber Patch Cable, 1 m) to a 473 nm MM laser (S1FC473MM fiber coupled laser, Thorlabs) with adjustable output power (50 mW maximum). The laser was gated by a (TTL) trigger signal generated by the RZ5D bioamp processor (Tucker Davis Technologies, Alachua, FL, United States) driven by the OpenEx software controlling data acquisition. YFP fluorescence allowed to determine the effectiveness of adenoviral expression *in vivo*. The tip of the fiber was placed at about 250 μm from the surface of the cerebellum, in order to obtain a localized optical stimulation of the molecular and PC layers. Laser light pulses (50 ms) were applied at 0.5 Hz paired to the air-puff (delay of 30 ms) with a power of 0.5–1 mW. The output power, measured with a power meter (PM100D, with s130c sensor; Thorlabs) at the tip of the glass fiber, was 0.03 mW (Kruse et al., 2014).

Histology

The location of recording electrodes in the DCN was confirmed histologically. Electrical lesions were obtained at the end of recordings by applying a 20 μA–20 s current pulse through the same recording electrode connected to a stimulus isolator and a stimulator unit. Then, the mouse was perfused

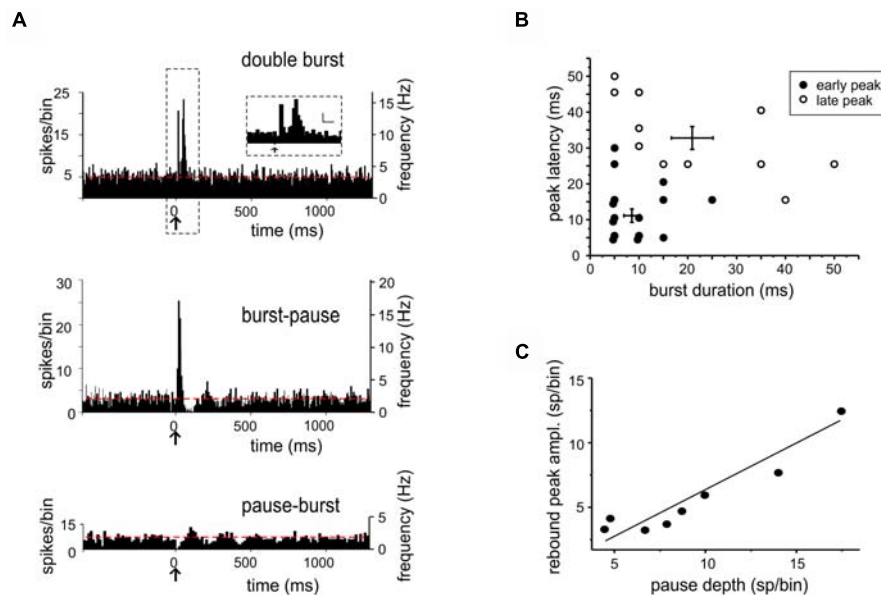


FIGURE 2 | Bursts and pauses in DCN unit responses to tactile stimulation. **(A)** Example of PSTHs obtained from DCN units showing different responses to tactile stimulation (arrows): double burst (5 ms-bin), burst-pause (5 ms-bin), and pause-burst (15 ms-bin). Red dashed lines show the basal discharge frequency. The scale bars in the inset on top are 5 sp/bin and 25 ms. **(B)** In the pool of responses starting with a burst, two groups were discriminated using cluster analysis (*k-means*) on peak latency and burst duration. This results in the identification of early and late peaks, whose latencies are compatible with inputs from the trigeminal and cortical pathways conveying sensory stimuli to the cerebellum (cfr. **Figure 1A**). **(C)** Characterization of pause-burst responses. A positive correlation was found between rebound-peak amplitude and pause depth [$R^2 = 0.87$, Fisher's *F*-test $p(F) = 0.001$, $n = 8$].

transcardially with phosphate-buffered saline (PBS) followed by 4% paraformaldehyde (Sigma-Aldrich) overnight at 4°C. The fixated brains were cryo-protected with 30% sucrose solution in PBS, embedded in OCT (Cryostat embedding medium, Killik, Bio-Optica), and stored at −80°C. 20-μm-thick histological sections were obtained and stained with toluidine blue. The histological confirmation of the recording sites was obtained by microscopic observation of the stained sections (see **Figure 1B**).

The identification of the viral expression was also analyzed histologically from the fixated brain of injected mice. Confocal images (see **Supplementary Figure S1**) were taken from 20-μm-thick sections washed with PBS (three times for 5 min), counterstained with Hoechst 33258 (Thermo Fisher Scientific; 2 μg/mL) for 15 min, washed again with PBS (three times for 5 min) and finally mounted with ProLongTM Gold Antifade Mountant (Thermo Fisher Scientific). Images were acquired with a TCS SP5 II (Leica Microsystems) equipped with a DM IRBE inverted microscope (Leica Microsystems) with 20, 40, or 63X objectives and visualized by LAS-AF Lite software (Leica Microsystems Application Suite Advanced Fluorescence Lite version 2.6.0) or with ImageJ (Fiji distribution, SciJava). Fluorescence microscopy showed that the site of injection was confined to limited regions of the molecular layer (see **Supplementary Figure S1**).

Data Analysis and Statistics

Electrophysiological signals were acquired using OpenEx software (Tucker-Davis Technologies) and analyzed offline using custom-written routines in MATLAB (Mathworks, Natick,

MA, United States) and Excel. Openscope (part of the OpenEx suite) was used to construct online PSTH triggered by air-puffs, in order to identify responding units. The raw traces were analyzed and sorted offline using SpikeTrain (Neurasmus BV, Rotterdam, Netherlands) running under MATLAB. The stability of recordings was carefully assessed ($< \pm 20\%$ amplitude fluctuation over the duration of the recording) and only units with stable spike size were considered for further analysis. PSTHs and raster plots were used for the analysis of responses to stimulation, normally consisting of peaks and pauses emerging from background discharge. To optimize PSTH resolution, a 5 ms bin width was used to analyze peaks and a 15 ms bin width was used to analyze pauses. The “burst” was defined as an increase in firing frequency generating a PSTH peak after the stimulus. The “pause” was defined as a decrease in firing frequency generating a PSTH pause after the stimulus. The threshold for peaks and pauses detection in PSTHs was set at twice the standard deviation of the basal frequency in the pre-stimulus period, calculated for each bin. No constraints on the number of bins showing significant changes compared to the pre-stimulus period were applied, since some response might show small duration (as the case of peaks, lasting 5–10 ms and therefore described by one or few bins). Statistical comparisons of peak and pause changes in optogenetic experiments was performed against changes in the stability controls at the same experimental times (histograms in **Figures 3B, 4F**).

The effect of TSS was evaluated by measuring the corresponding changes in PSTH peaks and pauses as the post-TSS responses (computed over the first 15 min after TSS)

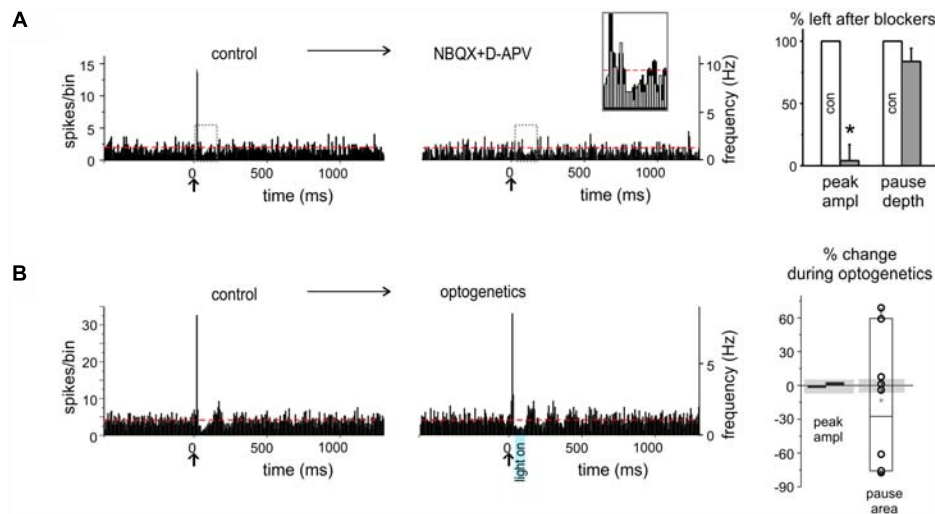


FIGURE 3 | Pharmacological and optogenetic manipulations of burst and pause responses. **(A)** Example of PSTHs from a DCN unit showing a burst as initial response (*left*), that was prevented (*right*) by excitatory transmission blockers (NBQX and D-APV) injection in the nucleus (*red dashed lines* show the basal discharge frequency). The gray dashed rectangles show the areas that are overlapped in the inset. The histogram shows the % of the response, whether PSTH peaks or pauses, left after blockers injection, compared to control ($n = 4$ for both; paired Student's t -test; $*p < 0.05$). **(B)** Example of PSTHs from a DCN unit showing burst-pause response before (*left*) and during (*right*) optogenetic stimulation of the molecular layer (the blue rectangle showing the time and duration of laser activation; *red dashed lines* show the basal discharge frequency). The histograms on the right show the percent change on the peak amplitude of the excitatory response and on the pause area (obtained by multiplying pause depth and duration) during optogenetic stimulation compared to control, in the single units recorded. The gray shadows show the average % change observed at the same time points in the stability controls (see section "Materials and Methods"). Note that peak amplitude is not affected, while the pause is significantly modified.

that exceeded twice the standard deviation of the pre-TSS response (computed over the last 15 min before TSS). Positive changes were considered as a potentiation and negative changes were considered as a suppression of basal firing (a minority of units did not show any significant changes with respect to this criterion).

Statistical comparisons were carried out using paired or unpaired Student's t -test or Fisher's F -test. The normality of the data was assessed using the Shapiro–Wilk test. In the few cases data were not distributed normally, the Brown-Forsythe test was applied to assess the homogeneity of variances. Data in the text are reported as mean \pm SEM. Clustering k -mean analysis and autocorrelation analysis on PSTHs were performed using MATLAB routines. Autocorrelations were performed using a function (*xcorr*) yielding oscillation frequency and magnitude (with magnitudes normalized to 1). The statistical significance of the changes in oscillation frequency in pharmacological and optogenetic experiments was evaluated with respect to stability controls at the same experimental times.

Data fitting was performed using routines written in OriginPro8 (OriginLab, Co., Northampton, MA, United States). A Lorentzian function was used to fit the frequency-dependence of plasticity changes:

$$y = y_0 + \frac{2A}{\pi} \cdot \frac{w}{4(x - fc)^2 + w^2}$$

where y_0 and A are curve baseline and amplitude, w is curve width, fc is the resonance frequency.

RESULTS

Single-unit recordings were performed from the cerebellar fastigial nucleus in urethane anesthetized mice (**Figure 1A**). All units were spontaneously active and showed a basal frequency of 8.19 ± 0.99 Hz (range: 2–27 Hz; $n = 51$), in agreement with previous reports of spontaneous activity under urethane anesthesia (Sweeney et al., 1992; LeDoux et al., 1998; Raman et al., 2000). The recording site was confirmed by electric lesions made through the recording electrode and identified histologically (**Figure 1B**). Single-unit responses to low frequency tactile stimulation (0.5 Hz) generated spike *bursts* and *pauses* modifying the basal discharge (**Figure 1C**) that were likely to reflect the neuronal response to excitatory and inhibitory synaptic inputs impinging onto DCN neurons (Rowland and Jaeger, 2005, 2008).

Bursts and Pauses in DCN Unit Responses

Single-unit responses to low frequency tactile stimulation generated combinations of peaks and pauses in PSTHs and, in some cases, the response continued with an oscillation (see below). Over a total of 51 units, we identified 2 fundamental categories of patterns, with either the burst or the pause as the initial response (**Figure 2A**).

When the *burst* initiated the response ("burst-first" category, $n = 26$), some units ($n = 18$) showed a single PSTH peak with latency of 14.27 ± 4.07 ms (duration 11.80 ± 2.51 ms), while others ($n = 8$) showed two PSTH peaks with latencies of 9.87 ± 1.99 and 33 ± 3.7 ms (duration of 8.12 ± 1.31

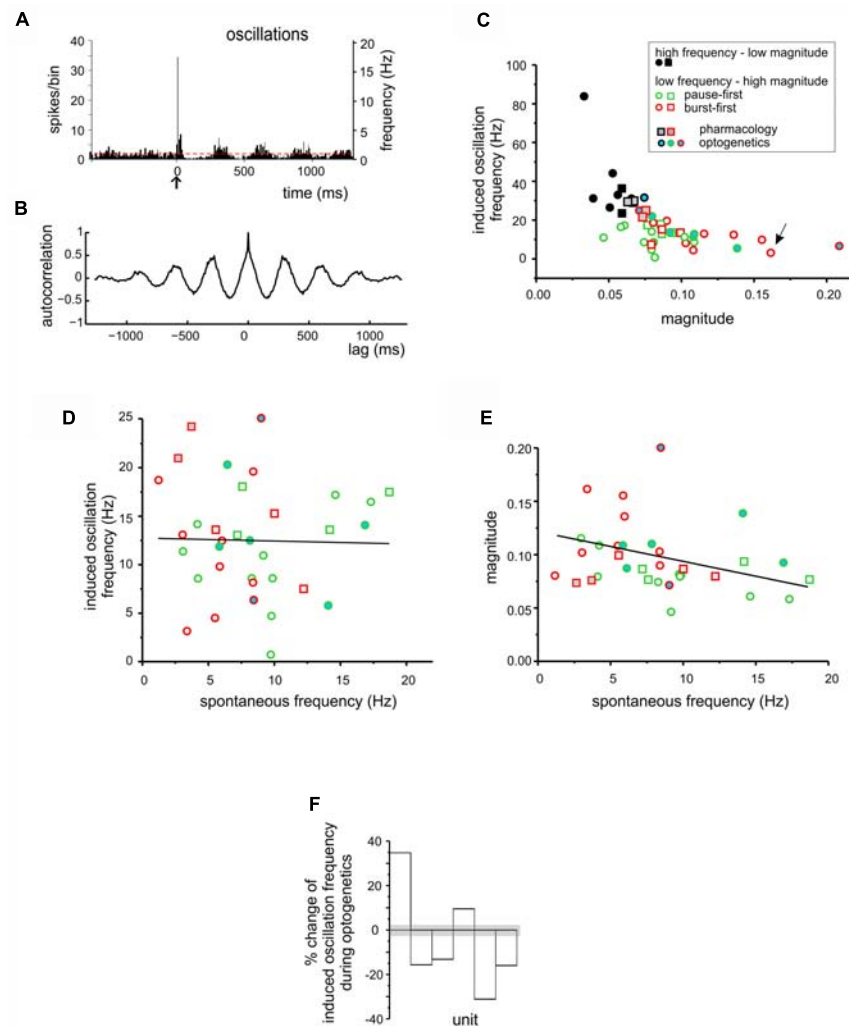


FIGURE 4 | Stimulus-induced oscillations in DCN units. **(A)** PSTH obtained from a DCN unit showing low frequency oscillation following a burst-pause response. **(B)** Autocorrelogram obtained from the unit shown in **(A)** (oscillation frequency 3.15 Hz; magnitude 0.16). **(C)** The magnitude and frequency of oscillations deriving from the autocorrelation analysis shown in **(B)** were plotted for each unit. The k-means clustering revealed two groups of data, characterized by high frequency – low magnitude oscillations (black symbols) and low frequency – high magnitude oscillations (green and red symbols, for pause-first and burst-first responses respectively). The units in which the TSS was delivered are represented as circles, while those in which the TSS was not delivered are represented as squares. Gray filled symbols are used for the units in which pharmacology was applied, while blue-filled circles are used for the units in the optogenetics experiments. The arrow indicates the unit shown in **(A,B)**. **(D)** Relationship between stimulus-induced oscillation frequency and spontaneous firing frequency for the low frequency – high magnitude oscillation units in **(C)**. The linear fitting shows no evident trend [$R^2 = 0.03$, Fisher's F -test $p(F) = 0.89$]. **(E)** Relationship between magnitude of stimulus-induced oscillations and spontaneous firing frequency for the low frequency – high magnitude oscillation units in **(C)**. The linear fitting suggests a positive trend [$R^2 = 0.25$, Fisher's F -test $p(F) < 0.08$]. In **(C–E)**, the data points are divided into burst-first and pause-first units, and circles represent the units that were further used for plasticity induction (see **Figures 5, 6**). **(F)** The histogram shows the percent change in stimulus-induced oscillation frequency during optogenetics in the same units reported in **(C–E)**. The gray shadow shows the average percent change observed at the same time points in the stability controls (see section “Materials and Methods”).

and 15 ± 3.27 ms). These peak latencies corresponded to those reported for trigeminal and cortical responses of granular layer neurons (Vos et al., 1999; Roggeri et al., 2008), suggesting that the initial bursts most likely corresponded to synaptic excitation of DCN neurons through trigeminal and cortical mossy fibers (**Figure 2B**; see section “Materials and Methods” for details).

In a subset of experiments, selective AMPA and NMDA receptor antagonists ($100 \mu\text{M}$ NBQX + $250 \mu\text{M}$ D-APV,

respectively) were injected in the fastigial nucleus close to the recording site. In 4 (out of 4) neurons that initiated the response with a burst, the burst was abolished (peak change $-95.9 \pm 12.8\%$, $n = 4$; paired Student's t -test; $p = 0.026$), while pauses remained unaltered (pause depth change $-16.2 \pm 10.2\%$; $n = 4$, paired Student's t -test; $p = 0.14$; see below) (**Figure 3A**).

When the *pause* initiated the response (“pause-first” category, $n = 25$), it occurred with a latency of 28.8 ± 5.2 ms (duration 25.0 ± 3.8 ms). This delay was compatible with

signal transmission along the mossy fiber – granule cell – PC – DCN neuronal pathway (Ramakrishnan et al., 2016), rather than resulting from local interneurons, suggesting that the initial pause most likely corresponded to DCN neuron inhibition by PCs. In a subset of experiments ($n = 8$), optogenetic stimulation of the molecular layer was applied to disrupt the cortical output, by delivering a light impulse 30 ms after the air-puff, i.e., in coincidence with the pause. In six of these recordings optogenetic stimulation caused a change in pause depth and duration exceeding three times the standard deviation of time-matched controls (see section “Materials and Methods” and histograms in **Figure 3B**). It should be noted that the pause in three cases increased and in three cases decreased, possibly reflecting the balance between optogenetic activation of PCs and molecular layer interneurons (see section “Materials and Methods” and **Figure 1A** and **Supplementary Figure S1** for details). In the remaining 2 units, no evident effect of optogenetics was observed.

Several units initiating the response with a burst (21 out of 26) showed a pause following peak(s), and some units initiating the response with a pause (8 out of 24) showed a burst following the pause (**Figure 2A**). The nature of these *burst-pause* and *pause-burst* patterns showed peculiar properties.

In *burst-pause* responses, the pause was significantly delayed (58.17 ± 5.52 ms, $n = 21$, unpaired Student's *t*-test; $p = 0.00039$) compared to that measured when it initiated the response. This longer delay suggests the intervention of additional mechanisms, like signal reentry through the recently discovered DCN – granule cells connections (Gao et al., 2016) or through precerebellar nuclei (Kistler and De Zeeuw, 2003), capable of protracting and enhancing PCs activation through cerebello-cortical loops. Phase reset, an intrinsic electroresponsive phenomenon observed in neurons (e.g., see Solinas et al., 2007), was unlikely to be responsible for this effect, as explained below (see **Figure 4D**).

In *pause-burst* responses, the bursts followed with a latency of 90.61 ± 20.63 ms (duration 12.14 ± 3.54 ms, unpaired Student's *t*-test; $p = 0.01$), that was significantly longer compared to that measured when it initiated the response. A positive correlation was found between pause depth and the subsequent peak amplitude [$R^2 = 0.89$, Fisher's *F*-test $p(F) < 0.001$, $n = 8$] (**Figure 2C**). A plausible explanation is that these bursts are non-synaptic and reflect post-inhibitory rebound discharge in DCN neurons (Alviña et al., 2008; Witter et al., 2013; Canto et al., 2016), which is the stronger the deeper the pause. This is supported by a recording in which the AMPA and NMDA receptor antagonists were injected in the fastigial nucleus while recording a pause-burst unit. In this case, the burst following the pause was unaffected (single observation, not shown).

Spontaneous Activity and Stimulus-Induced Oscillations in DCN Units

The PSTH elicited by tactile stimulation in several cases showed an *oscillation* following the initial peaks and pauses (**Figure 4A**). This oscillatory pattern was apparent in autocorrelation analysis (**Figure 4B**). The frequency/magnitude plot revealed a negative

trend, with slower oscillations showing larger magnitude and *vice versa* (**Figure 4C**). K-means analysis identified two significantly different clusters of points (unpaired Student's *t*-test; $p = 0.00175$), one at higher and the other at lower frequency. Low-frequency oscillations averaged 12.7 ± 1.0 Hz, $n = 34$.

The relationship between low-frequency stimulus-induced oscillations and spontaneous activity is shown in **Figures 4D,E**. No significant correlation was found either for frequency [$R^2 = 0.03$, Fisher's *F*-test $p(F) = 0.89$, $n = 34$] or magnitude [$R^2 = 0.25$, Fisher's *F*-test $p(F) < 0.08$, $n = 34$]. It should be noted that, out of 34 units, 15 were of the burst-first and 19 of the pause-first category. At a closer analysis, the burst-first units showed a significantly higher magnitude (0.11 ± 0.01 vs. 0.08 ± 0.01 ; unpaired Student's *t*-test; $p = 0.037$) and lower spontaneous frequency (6.2 ± 0.8 vs. 10.0 ± 1.1 Hz, unpaired Student's *t*-test; $p = 0.01$) than the pause-first units (**Figures 4C–E**) suggesting the existence of two distinct functional classes of DCN neurons (see below).

The injection of AMPA and NMDA receptor antagonists in the fastigial nucleus did not modify the stimulus induced oscillation frequency of the units (average absolute variation from control of $5.1 \pm 0.6\%$, not different from that of stability controls of $5.1 \pm 0.5\%$, $n = 4$ and $n = 10$ respectively; unpaired Student's *t*-test; $p = 0.99$). Conversely, optogenetic stimulation of the molecular layer caused a change in the stimulus induced oscillation frequency of the recorded units exceeding three times the standard deviation of time-matched controls (see section “Materials and Methods” and **Figure 4F**). It should be noted that the induced-oscillation frequency in two cases increased and in four cases decreased, possibly reflecting the balance between optogenetic activation of PCs and molecular layer interneurons.

Long-Lasting Changes Induced by TSS in DCN Unit Responses

The cerebellar cortex in rodents is known to respond to TSS of the whisker pad with long-lasting changes in the granular and molecular layers (Roggeri et al., 2008; Diwakar et al., 2011; Prestori et al., 2013; Ramakrishnan et al., 2016). We therefore investigated whether the delivery of the same TSS pattern was able to affect DCN neuron responsiveness. We defined Spike-Related Potentiation (SR-P) and Spike-Related Suppression (SR-S) as the increase or decrease in spike response probability with respect to baseline (cf. Ramakrishnan et al., 2016), both in bursts and pauses. For simplicity, we considered only the initial bursts and pauses, since their amplitude is not influenced by preceding electrical events. The values of changes were measured for each unit in the first 15 min following TSS with respect to the last 15 min before TSS.

TSS-Induced Changes in Initial Bursts

Theta-sensory stimulation was delivered in 13 recordings showing an initial excitatory burst (burst-first, **Figure 5A**). A significant SR-P of the first PSTH peak was observed in four units ($45.27 \pm 10.73\%$, $n = 4$, paired Student's *t*-test; $p = 0.01$; **Figure 5A**), while a significant SR-S was observed in another 8 units ($-27.16 \pm 5.34\%$, paired Student's *t*-test;

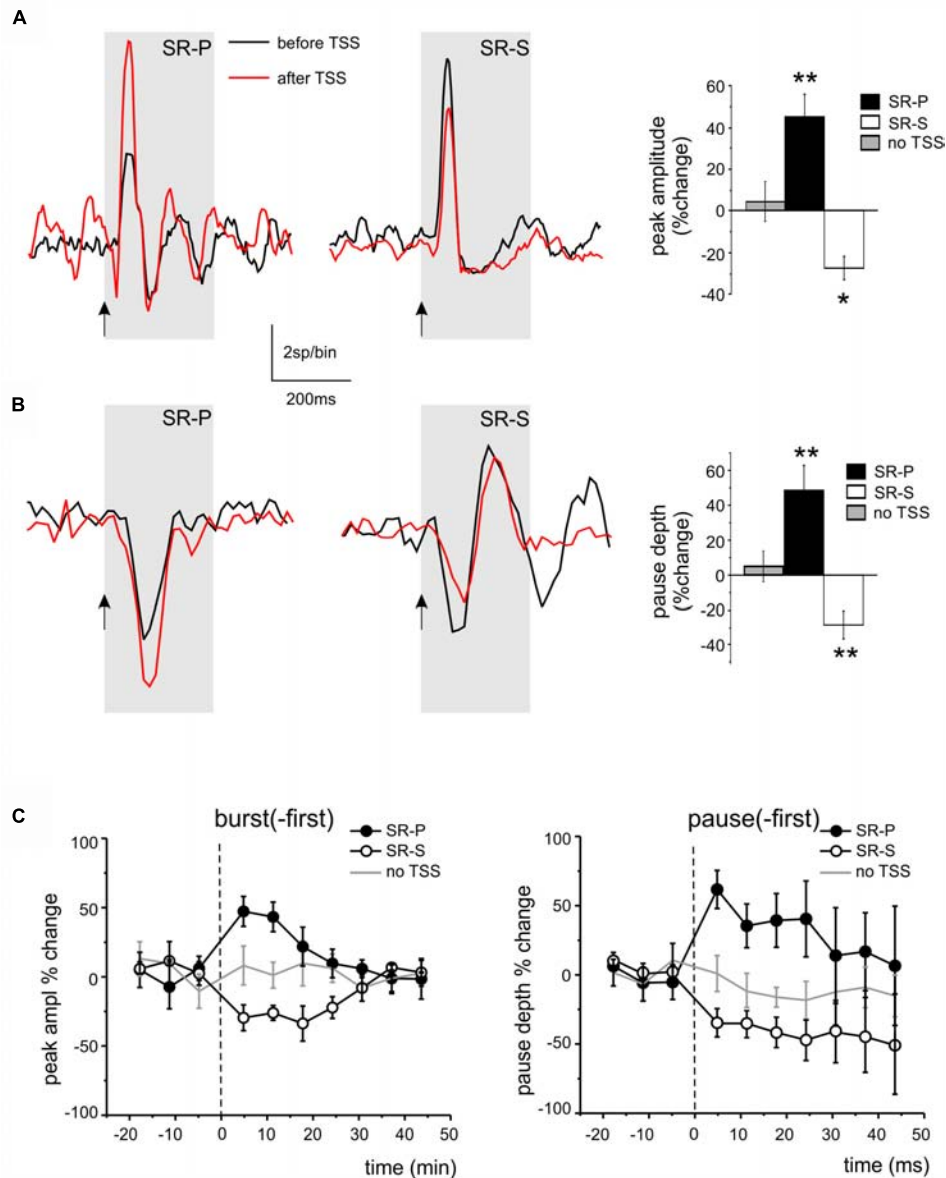


FIGURE 5 | Long-lasting changes induced by TSS in DCN unit responses. **(A)** Example of PSTHs illustrating the *peak* changes (SR-P or SR-S) induced by TSS in DCN units of the burst-first category. The histogram shows the average percent changes in PSTH peak amplitude for all the units showing SR-P, SR-S, or stability controls (no TSS; paired Student's *t*-test; * $p < 0.05$, ** $p < 0.01$). **(B)** Example of PSTHs illustrating the *pause* changes (SR-P or SR-S) induced by TSS in DCN units of the pause-first category. The histogram shows the average percent changes in PSTH peak amplitude for all the units showing SR-P, SR-S, or stability controls (no TSS; paired Student's *t*-test; ** $p < 0.01$). **(C)** Average time-course of peak (in burst-first units, *left*) and pause (in pause-first units, *right*) amplitude percent changes normalized to the control period before TSS (*dashed line*) in the units showing SR-P, SR-S and in the stability group (TSS not delivered). Note that the response changes for peaks and pauses differed significantly from the stability controls in the first 15 min after the TSS.

$p = 0.01$). Only in 1 out of these 13 units, no significant changes were observed.

TSS-Induced Changes in Initial Pauses

Theta-sensory stimulation was delivered in 13 recordings showing an initial pause in the response (pause-first, **Figure 5B**). A significant SR-P of the pause was observed in 4 units ($48.43 \pm 14.77\%$, $n = 4$, paired Student's *t*-test; $p = 0.004$), while a significant SR-S of the pause depth was observed in another 7

units ($-27.19 \pm 7.65\%$, $n = 7$, paired Student's *t*-test; $p = 0.007$; **Figure 5B**). In 2 units, no pause depth changes were found.

Stability Controls

In 7 units showing an initial excitatory burst and in 5 units showing an initial pause, TSS was not delivered. In these units, the bursts and pauses remained stable for a duration similar to that of experiments in which the TSS was delivered (bursts: $4.7 \pm 11.7\%$ change, paired Student's *t*-test, $n = 7$, $p = 0.9$; pauses: $5.6 \pm 10.0\%$

change, $n = 5$, paired Student's t -test; $p = 0.1$). These controls ruled out possible spurious changes due to intrinsic response amplitude fluctuations with time.

Average Time Course

The average time course for burst and pause changes was constructed by grouping all the units in each given category. The SR-P and SR-S of peaks and pauses reported above, which were statistically significant for the first 15 min after TSS, returned back to baseline within 30 min (Figure 5C).

Correlation Between Long-Lasting Changes and Stimulus-Induced Oscillations

In Figure 4, two functional classes of units have been identified based on their response pattern and low frequency oscillatory properties, summing up to a total of 15 burst-first units and 17 pause-first units. Here we have considered the relationship between long-lasting changes and stimulus-induced oscillation frequency in the 8 burst-first and 10 pause-first units that received TSS in control condition (without pharmacological manipulation or optogenetics). The changes were weakly correlated to frequency, with larger changes occurring at lower frequencies [linear correlation: $R^2 = -0.07$ and $p(F) < 0.05$ for *burst-first* units; $R^2 = 0.32$ $p(F) < 0.03$ for *pause-first* units]. The hypothesis that changes were centered on the theta-band was assessed by fitting the data using resonant functions. In particular, the Lorentzian distribution fitted the data better than linear, suggesting that peak and pause changes after TSS might be correlated with the frequency of stimulus-induced oscillations. By using a Lorentzian distribution, peak changes in the *burst-first* units (Figure 6A) peaked at 9.2 Hz with 53% SR-P and settled down to -17.2% SR-S at lower and higher frequencies [$R^2 = 0.83$; Fisher's F -test $p(F) < 0.01$]. Pause changes in the *pause-first* units (Figure 6B) peaked at 5.5 Hz with -42% SR-S and settled to 26.2% SR-P at higher frequencies [$R^2 = 0.78$; Fisher's F -test $p(F) < 0.02$]. Thus, Lorentzian fitting of SR-P and SR-S distributions showed opposite changes in burst-first and pause-first units with peaks in the low frequency range of stimulus-induced oscillations.

We then asked whether and how these long-lasting changes were influenced by cerebellar cortical activity. To this end, we used optogenetic stimulation of the cerebellar molecular layer, which allows a broader activation than electrical stimulation and is therefore more likely to capture neuronal chains involved in controlling the recorded DCN units. We have shown above that optogenetic stimulation of the molecular layer could indeed modify DCN responsiveness (see Figures 3B, 4F), disrupting the cortical output by modifying PC firing. It should be noted that, as explained in Section "Materials and Methods," this test was not expected to yield a deterministic increase or decrease in PC firing, but rather to impact on DCN units and change their ability to generate long-term response changes after TSS. We thus compared DCN units response changes with or without the use of optogenetics assuming the Lorentzian distribution as the best fit to our data. Optogenetic stimulation of the molecular

layer during TSS altered the long-lasting changes compared to those expected from controls, in such a way that these always fell beyond the confidence limits predicted from control data, both for peaks in burst-first units (Figure 7A) and for pauses in pause-first units (Figure 7B). The distance from the control curves in Figures 6A,B, estimated at the frequency of stimulus-induced oscillation recorded during optogenetic stimulation, was $45.1 \pm 7.0\%$ ($n = 6$, unpaired Student's t -test; $p = 0.03$; significantly different from the distance from the same curve calculated from control data: 9.1 ± 2.1 , $n = 20$, unpaired Student's t -test; $p = 0.0028$; Figure 7C). Therefore, optogenetics did not seem to primarily address the same mechanism of frequency-dependent induction of long-lasting changes occurring in DCN units but rather to affect different mechanisms, presumably located in the molecular layer (see section "Discussion").

DISCUSSION

Deep cerebellar nuclei units were spontaneously active and responded to tactile sensory stimulation with different combinations of bursts, pauses and oscillations. Following theta-frequency stimulation (TSS), DCN units showed spike-related potentiation or suppression, SR-P or SR-S, both in bursts and pauses. To our knowledge, SR-P and SR-S are the first electrophysiological evidence that long-lasting changes can be observed following naturally patterned sensory entrainment in DCN neurons *in vivo*. Unique in the cerebellum among the other long-lasting changes observed *in vivo* (Roggeri et al., 2008; Gao et al., 2012; D'Angelo, 2014; D'Angelo et al., 2016a; Ramakrishnan et al., 2016), the DCN SR-P/SR-S distributions were correlated to the stimulus-induced oscillation frequency of DCN units through Lorentzian functions peaking in the theta-frequency range, disclosing the complex nature of the underlying plasticity mechanisms.

The Nature of DCN Unit Responses

All DCN units responded to tactile stimulation with short delays typical of the fast cerebellar reaction to sensory inputs. In some units (53%), bursts were the first DCN response and occurred either as a single peak at 10–14 ms or a double peak (in a third of cases) about 10 ms later. This pattern closely matches that observed in the granular layer (Morissette and Bower, 1996; Vos et al., 1999; Roggeri et al., 2008), suggesting that DCN neurons can receive double mossy fiber activation through the trigeminal pathway and the somato-sensory cortex [the trigeminal connection might not be direct for the fastigial nucleus though (Morcuende et al., 2002; Rowland and Jaeger, 2005, 2008)]. The excitatory nature of these bursts was confirmed by their extinction after injection of AMPA and NMDA receptors blockers into the DCN. In the remaining units (47%), pauses were the first DCN response with delays of 25–29 ms, most likely reflecting signal transfer through the cerebellar cortex down to PCs and DCN. This delay can be accounted for by considering that PC excitation through mossy fibers and granule cells takes about 15 ms (Ramakrishnan et al., 2016) and an additional time is required to inhibit DCN cells. Indeed, optogenetic

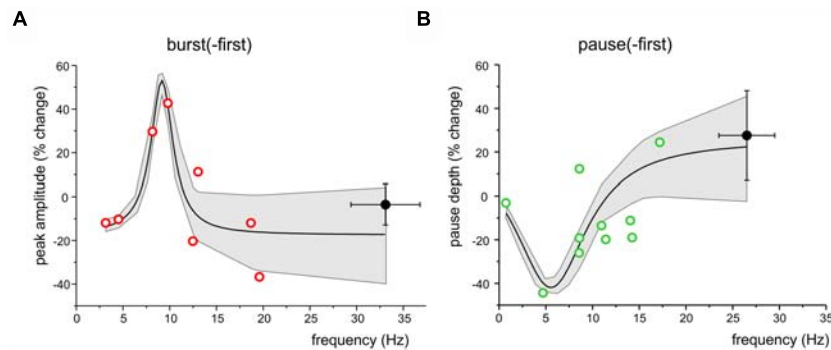


FIGURE 6 | Frequency-dependence of long-lasting changes after TSS. **(A)** The plot shows the distribution of peak amplitude changes after TSS in burst-first units with respect to stimulus induced oscillation frequency. The Lorentzian fitting [$R^2 = 0.83$; Fisher's F -test $p(F) = 0.01$] shows a peak at 9.2 Hz. **(B)** The plot shows the distribution of pause amplitude changes after TSS in pause-first units with respect to stimulus induced oscillation frequency. The Lorentzian fitting [$R^2 = 0.78$; Fisher's F -test $p(F) = 0.02$] shows a peak at 5.5 Hz. Both in **(A,B)**, open symbols identify the same low-frequency units reported in **Figure 4** and filled symbols are the average values (\pm SEM) of high frequency oscillation units. Both in **(A,B)**, the gray area shows the 95% confidence interval of the fitting.

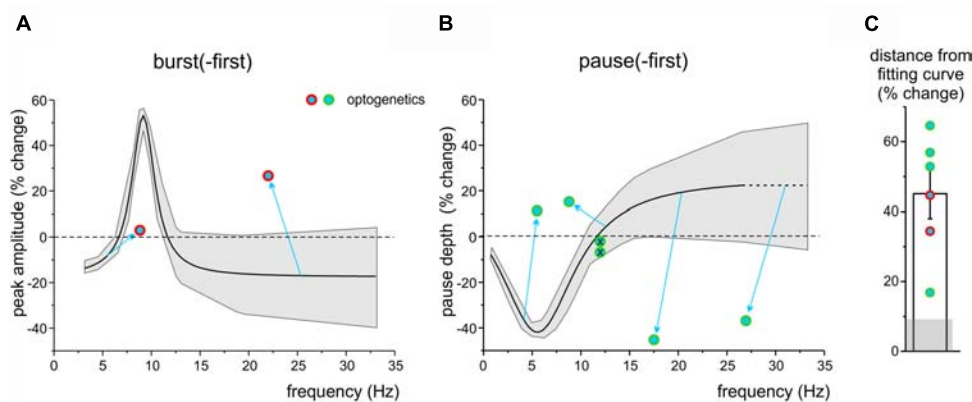


FIGURE 7 | The impact of optogenetic stimulation on long-lasting response changes. **(A)** The plot shows the Lorentzian fitting as **Figure 6A**, with the gray area showing the 95% confidence interval. Note that the data-points representing burst-first units in which the TSS was paired with optogenetics fall far outside the confidence interval. **(B)** The plot shows the Lorentzian fitting as in **Figure 6B**, with the gray area showing the 95% confidence interval, extrapolated beyond the last point of control to compare new data. Note that the data-points representing pause-first units in which the TSS was paired with optogenetics fall far outside the confidence interval (except for the two points representing the units in which optogenetics did not show any effect; crossed circles). **(C)** The histogram shows the average distance of the optogenetics data points from the fitting curves in **(A,B)**. The gray shadow shows the average distance of control data in **Figure 6** from the same fitting curves.

stimulation of the molecular layer was able to modulate pause duration and depth.

It should be noted that, in principle, climbing fibers could also contribute to DCN excitation through axonal collaterals. However, in comparable recording conditions (Ramakrishnan et al., 2016), PC complex spikes that reflect climbing fiber activation were only sporadically observed and had a latency of 40–50 ms, which is too long to explain the latency of the DCN unit responses. Although climbing fibers could contribute to DCN activation, when actively stimulated (Mogensen et al., 2017), it seems very unlikely that they took part to generate the PSTH peaks analyzed here.

The pauses occurring after initial bursts were also modified by optogenetic stimulation of the molecular layer and reflected therefore DCN inhibition by PCs. These pauses, which were evident about 50 ms after the stimulus, could have been

protracted by signal reentry into the cerebellar cortex through intracerebellar (Ankri et al., 2015; Gao et al., 2016) or extracerebellar loops (Kistler and De Zeeuw, 2003). The bursts following the pauses correlated with the depth of the preceding pause and were therefore probably rebound activities due to intrinsic electroresponsiveness (Alviña et al., 2008; Hoebeek et al., 2010; Witter et al., 2013) (this conclusion was supported by rebound burst persistence after injection of AMPA and NMDA receptors blockers into the DCN in a single experiment).

Some units continued their response with an oscillatory cycle independent on whether the responses started with a burst or a pause. The frequency and magnitude of oscillations induced by stimulation were not significantly correlated with spontaneous discharge in the same units. Therefore, oscillations could not be explained by phase reset, since in that case the two frequencies should coincide (Solinas et al., 2007). The origin

of these oscillations should then reflect circuit mechanisms (see **Figure 1A**). A first mechanism was hypothesized by Yarom (Jacobson et al., 2008; Chen et al., 2010) and involves DCN control of inferior olive (IO) oscillations that reverberate through climbing fibers into the DCN-PC-IO loop. Stimulus-induced oscillations similar to ours are indeed evident in the PSTH of DCN neurons following direct climbing fiber activation (Cheron and Cheron, 2018). A second mechanism hypothesized by De Zeeuw could involve signal reentry through extra-cerebellar circuits (Kistler and De Zeeuw, 2003; Gao et al., 2016) or through the more recently identified connections between DCN and granular layer (Ankri et al., 2015; Gao et al., 2016), therefore passing again through PCs. That PCs could actually be a node in the loops controlling the stimulus-induced oscillations was supported by their perturbation by optogenetic stimulation of the molecular layer.

There were two groups of units showing stimulus-induced oscillations, *burst-first* and *pause-first* units, which turned out to show opposite frequency-dependent changes following TSS. The potential relationship between these functional groups and the DCN neuron subpopulations reported *in vitro* (Bagnall et al., 2009; Uusisaari and Knopfel, 2012) remains to be determined.

Long-Lasting Changes in DCN Unit Responses and Their Relationship With Plastic Mechanisms

By being connected to the sensory input through multi-synaptic chains, the long-lasting changes in DCN unit responses could either be generated locally or occur upstream in the cerebellar cortex.

On one hand, according to fittings using Lorentzian functions, SR-P peaked at 9.2 Hz in *burst-first* units and SR-S at 5.5 Hz in *pause-first* units. This property favors the engagement of local mechanisms, since no similar frequency-dependent changes have ever been observed either in the granular or molecular layer *in vivo* (Roggeri et al., 2008; Ramakrishnan et al., 2016) or *in vitro* (for review see Hansel et al., 2001; Gao et al., 2012; D'Angelo, 2014; D'Angelo et al., 2016b). Moreover, LTP and LTD reported in DCN neurons *in vitro* are based on specific sequences of excitation, inhibition and rebounds (Morishita and Sastry, 1996; Ouardouz and Sastry, 2000; Pugh and Raman, 2006; Zhang and Linden, 2006). Therefore, the different synapses impinging on DCN neurons could reciprocally influence one each other, providing a plausible mechanism for SR-P and SR-S induction during stimulus-induced oscillations. The robust potentiation in PC responses observed *in vivo* following TSS (Ramakrishnan et al., 2016) is likely to contribute to DCN plasticity in *pause-first* units, independently of the frequency of stimulus-induced oscillations.

On the other hand, SR-P and SR-S of the initial burst and pause were remarkably altered by optogenetic stimulation of the molecular layer. Optogenetic stimulation caused long-lasting changes in DCN unit responses that went much beyond those expected from the alteration of stimulus-dependent oscillation frequency. This suggests the engagement of additional mechanisms. For example, similar to electrical stimulation,

optogenetic stimulation might cause a broad set of long-lasting changes in the molecular layer (for details see, Ramakrishnan et al., 2016) modifying the PC output, which would eventually perturb the long-lasting changes observed in DCN unit responses. Further insights on the role of cortical input on DCN responses to TSS might derive from the use of genetically modified models with known alterations in the cerebellar cortex (e.g., mice lacking the phosphatase PP2B in PCs, that show selective loss of PC potentiation, as in Schonewille et al., 2010; Romano et al., 2018).

A further issue is about the time course of SR-P and SR-S, which decayed over 30 min. Both in rodents and humans, cerebellar learning has been predicted to occur in two steps, a faster one in the cerebellar cortex and a slower one in DCN (Medina and Mauk, 2000; Attwell et al., 2001; Smith et al., 2006; Monaco et al., 2014). Mathematical modeling further predicts that fast plasticity at the parallel fiber-PC synapse would be able to tune slow and more stable plasticity in DCN (Medina et al., 2001; Garrido et al., 2013; Casellato et al., 2014). So why *in vivo* recordings have shown more persistent changes in the granular layer (Roggeri et al., 2008) and molecular layer (Ramakrishnan et al., 2016) than in DCN? There are three key issues to consider. First, more intense or repeated stimulation may be needed to promote plasticity consolidation in DCN. Secondly, here DCN was not entrained in active sensorimotor feedback that can enhance cerebellar oscillations (Marshall and Lang, 2004). Thirdly, there was no attentional or motivational state, as the animal was anesthetized. Indeed, neuromodulation by noradrenaline, acetylcholine or serotonin is thought to be critical to drive oscillations and plasticity and promote learning (Sugihara et al., 1995; Schweighofer et al., 2004). It should also be noted that a similar trend, with a stimulus inducing long-term plasticity in the cerebellar cortex but having less effects on the cerebellar nuclei, has been recently described for the anterior interposed nucleus in cats (Mogenssen et al., 2017).

It cannot be excluded that stimulus-induced oscillations and the induction or expression of long-lasting changes in DCN neuron responses might have been influenced by anesthesia. We notice, however, that urethane is very conservative on the NMDA and GABA-A receptor-dependent mechanisms of neurotransmission and has been successfully used to demonstrate long-lasting changes at other cerebellar synapses *in vivo* (Roggeri et al., 2008; Ramakrishnan et al., 2016). Moreover, stimulus-induced oscillations in DCN neurons have been recently shown using ketamine-xylidodihydrothiazin anesthesia (Cheron and Cheron, 2018).

CONCLUSION

The identification of a possible relationship between DCN long-lasting changes and oscillatory dynamics engaged by tactile stimuli suggests that two key cerebellar functions can be reconciled: oscillatory activity in DCN may not just be needed to gate motor activity (Llinas, 1988; Marshall and Lang, 2004) but also to control plasticity and acquisition of sensorimotor engrams (D'Angelo and De Zeeuw, 2009; Cheron et al., 2016).

Interestingly, the preferential frequency of long-lasting DCN response changes identified by Lorentzian fittings was in the theta-band, i.e., the characteristic oscillatory frequency of the IO-PC-DCN circuit (Jacobson et al., 2008) and of the cerebello-extracerebellar loops (Kistler and De Zeeuw, 2003) following mossy fiber inputs. It is tempting to speculate that the cerebellum uses oscillating and resonant mechanisms similar to those that are known to favor the induction of plasticity in hippocampal and cortical synapses (Buzsaki, 2006; Roy et al., 2014) and that the frequency of oscillations provides a signal binding DCN plasticity to specific neuronal ensembles and brain states (Buzsaki, 2005; Buzsaki, 2006; Timofeev, 2011). This would be eventually reflected into neuro-muscular coherence on the systemic scale (Gruart et al., 2000; Koekkoek et al., 2002; Sánchez-Campusano et al., 2007, 2009; Wang et al., 2018). The frequency dependence of burst and pause changes in DCN units *in vivo* prompts for a further characterization of LTP and LTD mechanisms in DCN neurons *in vitro*, also considering the existence of functionally distinct DCN neuronal populations. New experiments may also be conducted in awake animals and combined with computational modeling (Medina and Mauk, 2000; Casellato et al., 2014; Luque et al., 2014; D'Angelo et al., 2016a) to address the impact of frequency-dependent forms of plasticity during cerebellar adaptation and learning.

DATA AVAILABILITY

The datasets generated for this study are available on request to the corresponding author.

AUTHOR CONTRIBUTIONS

LeM performed *in vivo* recordings, data analysis, and wrote the first draft of the manuscript. IM performed the sets of *in vivo* recordings with pharmacology and optogenetics, and

data analysis. LDP performed the initial *in vivo* recordings. ST performed histology and image analysis. LiM and ED coordinated the work and wrote the manuscript. All authors approved the final version of the manuscript.

FUNDING

This project/research received funding from the European Union's Horizon 2020 Framework Program for Research and Innovation under the Framework Partnership Agreement No. 650003 (HBP FPA); the European Union's Horizon 2020 Framework Program for Research and Innovation under the Specific Grant Agreement No. 720270 (Human Brain Project SGA1), and under the Specific Grant Agreement No. 785907 (Human Brain Project SGA2). This work was supported by grant [7(17)] of Centro Fermi to ED, Blue-Sky Research grant of the University of Pavia (BSR77992) to LiM.

SUPPLEMENTARY MATERIAL

The Supplementary Material for this article can be found online at: <https://www.frontiersin.org/articles/10.3389/fncel.2019.00084/full#supplementary-material>

FIGURE S1 | ChR2 expression in the cerebellar cortex of mice used for optogenetics. **(A)** Confocal image of green fluorescence (YFP) in the cerebellar cortex of a mouse sacrificed after *in vivo* recordings. Since YFP is expressed under the same promoter, YFP fluorescence reports the place of ChR2 expression. Note that fluorescence is mostly confined to the molecular and Purkinje cell layers. GL, granular layer; ML, molecular layer; PC, Purkinje cell. **(B)** Acute brain slice in bright field, with the recording electrode placed near a Purkinje cell (PC). The blue circle indicates that illuminated region is confined to PC soma and the trace shows the corresponding response in the stimulated PC (single trace, scale bars: 10 pA/200 ms). Note the increase in PC firing frequency during optical stimulation, followed by a pause configuring a typical burst-pause PC response (Cao et al., 2012; Herzfeld et al., 2015; Masoli and D'Angelo, 2017). GL, granular layer; ML, molecular layer.

REFERENCES

- Albus, J. (1971). The theory of cerebellar function. *Math. Biosci.* 10, 25–61. doi: 10.1016/0025-5564(71)90051-4
- Alviña, K., Walter, J., Kohn, A., Ellis-Davies, G., and Khodakhah, K. (2008). Questioning the role of rebound firing in the cerebellum. *Nat. Neurosci.* 11, 1256–1258. doi: 10.1038/nn.2195
- Ankri, L., Husson, Z., Pietrajtis, K., Proville, R., Lena, C., Yarom, Y., et al. (2015). A novel inhibitory nucleo-cortical circuit controls cerebellar Golgi cell activity. *Elife* 4:e06262. doi: 10.7554/eLife.06262
- Antonietti, A., Casellato, C., Garrido, J. A., Luque, N. R., Naveros, F., Ros, E. E. D. A., et al. (2016). Spiking neural network with distributed plasticity reproduces cerebellar learning in eye blink conditioning paradigms. *IEEE Trans. Biomed. Eng.* 63, 210–219. doi: 10.1109/TBME.2015.2485301
- Attwell, P. J. E., Rahman, S., and Yeo, C. H. (2001). Acquisition of eyeblink conditioning is critically dependent on normal function in cerebellar cortical lobule HVI. *J. Neurosci.* 21, 5715–5722. doi: 10.1523/JNEUROSCI.21-15-05715.2001
- Bagnall, M. W., Zingg, B., Sakatos, A., Moghadam, S. H., Zeilhofer, H. U., and du Lac, S. (2009). Glycinergic projection neurons of the cerebellum. *J. Neurosci.* 29, 10104–10110. doi: 10.1523/JNEUROSCI.2087-09.2009
- Bengtsson, F., and Jorntell, H. (2007). Ketamine and xylazine depress sensory-evoked parallel fiber and climbing fiber responses. *J. Neurophysiol.* 98, 1697–1705. doi: 10.1152/jn.00057.2007
- Bower, J. M., and Woolston, D. C. (1983). Congruence of spatial organization of tactile projections to granule cell and Purkinje cell layers of cerebellar hemispheres of the albino rat: vertical organization of cerebellar cortex. *J. Neurophysiol.* 49, 745–766. doi: 10.1152/jn.1983.49.3.745
- Buzsaki, G. (2005). Theta rhythm of navigation: link between path integration and landmark navigation, episodic and semantic memory. *Hippocampus* 15, 827–840. doi: 10.1002/hipo.20113
- Buzsaki, G. (2006). *Rhythms of the Brain*. New York, NY: Oxford University Press US. doi: 10.1093/acprof:oso/9780195301069.001.0001
- Canto, C. B., Witter, L., and De Zeeuw, C. I. (2016). Whole-cell properties of cerebellar nuclei neurons *in vivo*. *PLoS One* 11:e0165887. doi: 10.1371/journal.pone.0165887
- Cao, Y., Maran, S. K., Dhamala, M., Jaeger, D., and Heck, D. H. (2012). Behavior-related pauses in simple-spike activity of mouse Purkinje cells are linked to spike rate modulation. *J. Neurosci.* 32, 8678–8685. doi: 10.1523/JNEUROSCI.4969-11.2012
- Casellato, C., Antonietti, A., Garrido, J. A., Carrillo, R. R., Luque, N. R., Ros, E., et al. (2014). Adaptive robotic control driven by a versatile spiking cerebellar network. *PLoS One* 9:e112265. doi: 10.1371/journal.pone.0112265

- Casellato, C., Antonietti, A., Garrido, J. A., Carrillo, R. R., Luque, N. R., Ros, E., et al. (2015). Distributed cerebellar plasticity implements generalized multiple-scale memory components in real-robot sensorimotor tasks. *Front. Comput. Neurosci.* 9:24. doi: 10.3389/fncom.2015.00024
- Chadderton, P., Margrie, T. W., and Häusser, M. (2004). Integration of quanta in cerebellar granule cells during sensory processing. *Nature* 428, 856–860. doi: 10.1038/nature02442
- Chen, X., Kovalchuk, Y., Adelsberger, H., Henning, H. A., Sausbier, M., Wietzorrek, G., et al. (2010). Disruption of the olivo-cerebellar circuit by Purkinje neuron-specific ablation of BK channels. *Proc. Natl. Acad. Sci. U.S.A.* 107, 12323–12328. doi: 10.1073/pnas.1001745107
- Cheron, G., Marquez-Ruiz, J., and Dan, B. (2016). Oscillations, timing, plasticity, and learning in the cerebellum. *Cerebellum* 15, 122–138. doi: 10.1007/s12311-015-0665-9
- Cheron, J., and Cheron, G. (2018). Beta-gamma burst stimulations of the inferior olive induce high-frequency oscillations in the deep cerebellar nuclei. *Eur. J. Neurosci.* 48, 2879–2889. doi: 10.1111/ejn.13873
- D'Angelo, E. (2014). The organization of plasticity in the cerebellar cortex: from synapses to control. *Prog. Brain Res.* 210, 31–58. doi: 10.1016/B978-0-444-63356-9.00002-9
- D'Angelo, E., and De Zeeuw, C. I. (2009). Timing and plasticity in the cerebellum: focus on the granular layer. *Trends Neurosci.* 32, 30–40. doi: 10.1016/j.tins.2008.09.007
- D'Angelo, E., Antonietti, A., Casali, S., Casellato, C., Garrido, J. A., Luque, N. R., et al. (2016a). Modeling the cerebellar microcircuit: new strategies for a long-standing issue. *Front. Cell Neurosci.* 10:176. doi: 10.3389/fncel.2016.00176
- D'Angelo, E., Mapelli, L., Casellato, C., Garrido, J. A., Luque, N., Monaco, J., et al. (2016b). Distributed circuit plasticity: new clues for the cerebellar mechanisms of learning. *Cerebellum* 15, 139–151. doi: 10.1007/s12311-015-0711-7
- Diwakar, S., Lombardo, P., Solinas, S., Naldi, G., and D'Angelo, E. (2011). Local field potential modeling predicts dense activation in cerebellar granule cells clusters under LTP and LTD control. *PLoS One* 6:e21928. doi: 10.1371/journal.pone.0021928
- Ekerot, C. F., and Jörntell, H. (2001). Parallel fibre receptive fields of Purkinje cells and interneurons are climbing fibre-specific. *Eur. J. Neurosci.* 13, 1303–1310. doi: 10.1046/j.0953-816x.2001.01499.x
- Gao, Z., Proietti-Onori, M., Lin, Z., Ten Brinke, M. M., Boele, H. J., Potters, J. W., et al. (2016). Excitatory cerebellar nucleocortical circuit provides internal amplification during associative conditioning. *Neuron* 89, 645–657. doi: 10.1016/j.neuron.2016.01.008
- Gao, Z., van Beugen, B. J., and De Zeeuw, C. I. (2012). Distributed synergistic plasticity and cerebellar learning. *Nat. Rev. Neurosci.* 13, 619–635. doi: 10.1038/nrn3312
- Gao, Z., Davis, C., Thomas, A. M., Economo, M. N., Abrego, A. M., Svoboda, K., et al. (2018). A cortico-cerebellar loop for motor planning. *Nature* 563, 113–116. doi: 10.1038/s41586-018-0633-x
- Garrido, J. A., Luque, N. R., D'Angelo, E., and Ros, E. (2013). Distributed cerebellar plasticity implements adaptable gain control in a manipulation task: a closed-loop robotic simulation. *Front. Neural Circuits* 7:159. doi: 10.3389/fncir.2013.00159
- Godaux, E., Cheron, G., and Mettens, P. (1990). Ketamine induces failure of the oculomotor neural integrator in the cat. *Neurosci. Lett.* 116, 162–167. doi: 10.1016/0304-3940(90)90403-V
- Gruart, A., Guillazo-Blanch, G., Fernandez-Mas, R., Jimenez-Diaz, L., and Delgado-García, J. M. (2000). Cerebellar posterior interpositus nucleus as an enhancer of classically conditioned eyelid responses in alert cats. *J. Neurophysiol.* 84, 2680–2690. doi: 10.1152/jn.2000.84.5.2680
- Guo, A., Feng, J. Y., Li, J., Ding, N., Li, Y. J., Qiu, D. L., et al. (2016). Effects of norepinephrine on spontaneous firing activity of cerebellar Purkinje cells in vivo in mice. *Neurosci. Lett.* 629, 262–266. doi: 10.1016/j.neulet.2016.06.058
- Hansel, C., Linden, D. J., and D'Angelo, E. (2001). Beyond parallel fiber LTD: the diversity of synaptic and non-synaptic plasticity in the cerebellum. *Nat. Neurosci.* 4, 467–475. doi: 10.1038/87419
- Hara, K., and Harris, R. A. (2002). The anesthetic mechanism of urethane: the effects on neurotransmitter-gated ion channels. *Anesth. Analg.* 94, 313–318; Table of contents.
- Herzfeld, D. J., Kojima, Y., Soetedjo, R., and Shadmehr, R. (2015). Encoding of action by the Purkinje cells of the cerebellum. *Nature* 526, 439–442. doi: 10.1038/nature15693
- Hoebbeck, F. E., Witter, L., Ruigrok, T. J., and De Zeeuw, C. I. (2010). Differential olivo-cerebellar cortical control of rebound activity in the cerebellar nuclei. *Proc. Natl. Acad. Sci. U.S.A.* 107, 8410–8415. doi: 10.1073/pnas.0907118107
- Ito, M. (1972). Neural design of the cerebellar motor control system. *Brain Res.* 40, 81–84. doi: 10.1016/0006-8993(72)90110-2
- Jacobson, G. A., Rokni, D., and Yarom, Y. (2008). A model of the olivo-cerebellar system as a temporal pattern generator. *Trends Neurosci.* 31, 617–625. doi: 10.1016/j.tins.2008.09.005
- Jahnsen, H. (1986a). Electrophysiological characteristics of neurones in the guinea-pig deep cerebellar nuclei in vitro. *J. Physiol.* 372, 129–147. doi: 10.1113/jphysiol.1986.sp016001
- Jahnsen, H. (1986b). Extracellular activation and membrane conductances of neurones in the guinea-pig deep cerebellar nuclei in vitro. *J. Physiol.* 372, 149–168. doi: 10.1113/jphysiol.1986.sp016002
- Jörntell, H., and Ekerot, C. F. (2002). Reciprocal bidirectional plasticity of parallel fiber receptive fields in cerebellar Purkinje cells and their afferent interneurons. *Neuron* 34, 797–806. doi: 10.1016/S0896-6273(02)00713-4
- Kassel, J., Shambes, G. M., and Welker, W. (1984). Fractured cutaneous projections to the granule cell layer of the posterior cerebellar hemisphere of the domestic cat. *J. Comp. Neurol.* 225, 458–468. doi: 10.1002/cne.902250311
- Kistler, W. M., and De Zeeuw, C. I. (2003). Time windows and reverberating loops: a reverse-engineering approach to cerebellar function. *Cerebellum* 2, 44–54. doi: 10.1080/14734220309426
- Koekkoek, S. K., Den Ouden, W. L., Perry, G., Highstein, S. M., and De Zeeuw, C. I. (2002). Monitoring kinetic and frequency-domain properties of eyelid responses in mice with magnetic distance measurement technique. *J. Neurophysiol.* 88, 2124–2133. doi: 10.1152/jn.2002.88.4.2124
- Kruse, W., Krause, M., Aarse, J., Mark, M. D., Manahan-Vaughan, D., and Herlitze, S. (2014). Optogenetic modulation and multi-electrode analysis of cerebellar networks in vivo. *PLoS One* 9:e105589. doi: 10.1371/journal.pone.0105589
- LeDoux, M. S., Hurst, D. C., and Lorden, J. F. (1998). Single-unit activity of cerebellar nuclear cells in the awake genetically dystonic rat. *Neuroscience* 86, 533–545. doi: 10.1016/S0306-4522(98)00007-4
- Llinas, R., and Muhlethaler, M. (1988). An electrophysiological study of the in vitro, perfused brain stem-cerebellum of adult guinea-pig. *J. Physiol.* 404, 215–240. doi: 10.1113/jphysiol.1988.sp017287
- Llinas, R. R. (1988). The intrinsic electrophysiological properties of mammalian neurons: insights into central nervous system function. *Science* 242, 1654–1664. doi: 10.1126/science.3059497
- Luque, N. R., Garrido, J. A., Carrillo, R. R., D'Angelo, E., and Ros, E. (2014). Fast convergence of learning requires plasticity between inferior olive and deep cerebellar nuclei in a manipulation task: a closed-loop robotic simulation. *Front. Comput. Neurosci.* 8:97. doi: 10.3389/fncom.2014.00097
- Mapelli, L., Gagliano, G., Soda, T., Laforenza, U., Moccia, F., and D'Angelo, E. U. (2017). Granular layer neurons control cerebellar neurovascular coupling through an NMDA receptor/NO-dependent system. *J. Neurosci.* 37, 1340–1351. doi: 10.1523/JNEUROSCI.2025-16.2016
- Mapelli, L., Pagani, M., Garrido, J. A., and D'Angelo, E. (2015). Integrated plasticity at inhibitory and excitatory synapses in the cerebellar circuit. *Front. Cell Neurosci.* 9:169. doi: 10.3389/fncel.2015.00169
- Marquez-Ruiz, J., and Cheron, G. (2012). Sensory stimulation-dependent plasticity in the cerebellar cortex of alert mice. *PLoS One* 7:e36184. doi: 10.1371/journal.pone.0036184
- Marr, D. (1969). A theory of cerebellar cortex. *J. Physiol.* 202, 437–470. doi: 10.1113/jphysiol.1969.sp008820
- Marshall, S. P., and Lang, E. J. (2004). Inferior olive oscillations gate transmission of motor cortical activity to the cerebellum. *J. Neurosci.* 24, 11356–11367. doi: 10.1523/JNEUROSCI.3907-04.2004
- Masoli, S., and D'Angelo, E. (2017). Synaptic activation of a detailed purkinje cell model predicts voltage-dependent control of burst-pause responses in active dendrites. *Front. Cell. Neurosci.* 11:278. doi: 10.3389/fncel.2017.00278
- Mawhinney, L. J., de Rivero Vaccari, J. P., Alonso, O. F., Jimenez, C. A., Furones, C., Moreno, W. J., et al. (2012). Isoflurane/nitrous oxide anesthesia induces

- increases in NMDA receptor subunit NR2B protein expression in the aged rat brain. *Brain Res.* 1431, 23–34. doi: 10.1016/j.brainres.2011.11.004
- Medina, J. F., Garcia, K. S., and Mauk, M. D. (2001). A mechanism for savings in the cerebellum. *J. Neurosci.* 21, 4081–4089. doi: 10.1523/JNEUROSCI.21-11-04081.2001
- Medina, J. F., and Mauk, M. D. (1999). Simulations of cerebellar motor learning: computational analysis of plasticity at the mossy fiber to deep nucleus synapse. *J. Neurosci.* 19, 7140–7151. doi: 10.1523/JNEUROSCI.19-16-07140.1999
- Medina, J. F., and Mauk, M. D. (2000). Computer simulation of cerebellar information processing. *Nat. Neurosci.* 3(Suppl.), 1205–1211. doi: 10.1038/81486
- Mogensen, H., Bengtsson, F., and Jorntell, H. (2017). No medium-term spinocerebellar input plasticity in deep cerebellar nuclear neurons *in vivo*? *Cerebellum* 16, 638–647. doi: 10.1007/s12311-016-0839-0
- Monaco, J., Casellato, C., Koch, G., and D'Angelo, E. (2014). Cerebellar theta burst stimulation dissociates memory components in eyeblink classical conditioning. *Eur. J. Neurosci.* 40, 3363–3370. doi: 10.1111/ejn.12700
- Morcuende, S., Delgado-García, J. M., and Ugolini, G. (2002). Neuronal premotor networks involved in eyelid responses: retrograde transneuronal tracing with rabies virus from the orbicularis oculi muscle in the rat. *J. Neurosci.* 22, 8808–8818. doi: 10.1523/JNEUROSCI.22-20-08808.2002
- Morishita, W., and Sastry, B. R. (1996). Postsynaptic mechanisms underlying long-term depression of GABAergic transmission in neurons of the deep cerebellar nuclei. *J. Neurophysiol.* 76, 59–68. doi: 10.1152/jn.1996.76.1.59
- Morisette, J., and Bower, J. M. (1996). Contribution of somatosensory cortex to responses in the rat cerebellar granule cell layer following peripheral tactile stimulation. *Exp. Brain Res.* 109, 240–250. doi: 10.1007/BF00231784
- Muller, T., Grosche, J., Ohlemeyer, C., and Kettenmann, H. (1993). NMDA-activated currents in Bergmann glial cells. *Neuroreport* 4, 671–674. doi: 10.1097/00001756-199306000-00017
- Ohshima, T., Nores, W. L., and Mauk, M. D. (2003). Stimulus generalization of conditioned eyelid responses produced without cerebellar cortex: implications for plasticity in the cerebellar nuclei. *Learn. Mem.* 10, 346–354. doi: 10.1101/lm.67103
- Ohshima, T., Nores, W. L., Medina, J. F., Riusech, F. A., and Mauk, M. D. (2006). Learning-induced plasticity in deep cerebellar nucleus. *J. Neurosci.* 26, 12656–12663. doi: 10.1523/JNEUROSCI.4023-06.2006
- Ouardouz, M., and Sastry, B. R. (2000). Mechanisms underlying LTP of inhibitory synaptic transmission in the deep cerebellar nuclei. *J. Neurophysiol.* 84, 1414–1421. doi: 10.1152/jn.2000.84.3.1414
- Prestori, F., Bonardi, C., Mapelli, L., Lombardo, P., Goselink, R., De Stefano, M. E., et al. (2013). Gating of long-term potentiation by nicotinic acetylcholine receptors at the cerebellum input stage. *PLoS One* 8:e64828. doi: 10.1371/journal.pone.0064828
- Pugh, J. R., and Raman, I. M. (2006). Potentiation of mossy fiber EPSCs in the cerebellar nuclei by NMDA receptor activation followed by postinhibitory rebound current. *Neuron* 51, 113–123. doi: 10.1016/j.neuron.2006.05.021
- Pugh, J. R., and Raman, I. M. (2009). Nothing can be coincidence: synaptic inhibition and plasticity in the cerebellar nuclei. *Trends Neurosci.* 32, 170–177. doi: 10.1016/j.tins.2008.12.001
- Racine, R. J., Wilson, D. A., Gingell, R., and Sunderland, D. (1986). Long-term potentiation in the interpositus and vestibular nuclei in the rat. *Exp. Brain Res.* 63, 158–162. doi: 10.1007/BF00235658
- Ramakrishnan, K. B., Voges, K., De Propriis, L., De Zeeuw, C. I., and D'Angelo, E. (2016). Tactile stimulation evokes long-lasting potentiation of purkinje cell discharge *in vivo*. *Front. Cell. Neurosci.* 10:36. doi: 10.3389/fncel.2016.00036
- Raman, I. M., Gustafson, A. E., and Padgett, D. (2000). Ionic currents and spontaneous firing in neurons isolated from the cerebellar nuclei. *J. Neurosci.* 20, 9004–9016. doi: 10.1523/JNEUROSCI.20-24-09004.2000
- Roggeri, L., Rivieccio, B., Rossi, P., and D'Angelo, E. (2008). Tactile stimulation evokes long-term synaptic plasticity in the granular layer of cerebellum. *J. Neurosci.* 28, 6354–6359. doi: 10.1523/JNEUROSCI.5709-07.2008
- Romano, V., De Propriis, L., Bosman, L. W., Wernaar, P., Ten Brinke, M. M., Lindeman, S., et al. (2018). Potentiation of cerebellar Purkinje cells facilitates whisker reflex adaptation through increased simple spike activity. *Elife* 7:e38852. doi: 10.7554/eLife.38852
- Rowland, N. C., and Jaeger, D. (2005). Coding of tactile response properties in the rat deep cerebellar nuclei. *J. Neurophysiol.* 94, 1236–1251. doi: 10.1152/jn.00285.2005
- Rowland, N. C., and Jaeger, D. (2008). Responses to tactile stimulation in deep cerebellar nucleus neurons result from recurrent activation in multiple pathways. *J. Neurophysiol.* 99, 704–717. doi: 10.1152/jn.01100.2007
- Roy, D., Sigala, R., Breakspear, M., McIntosh, A. R., Jirsa, V. K., Deco, G., et al. (2014). Using the virtual brain to reveal the role of oscillations and plasticity in shaping brain's dynamical landscape. *Brain Connect.* 4, 791–811. doi: 10.1089/brain.2014.0252
- Sánchez-Campusano, R., Gruart, A., and Delgado-García, J. M. (2007). The cerebellar interpositus nucleus and the dynamic control of learned motor responses. *J. Neurosci.* 27, 6620–6632. doi: 10.1523/JNEUROSCI.0488-07.2007
- Sánchez-Campusano, R., Gruart, A., and Delgado-García, J. M. (2009). Dynamic associations in the cerebellar-motoneuron network during motor learning. *J. Neurosci.* 29, 10750–10763. doi: 10.1523/JNEUROSCI.2178-09.2009
- Schoneville, M., Belmeguenai, A., Koekkoek, S. K., Houtman, S. H., Boele, H. J., et al. (2010). Purkinje cell-specific knockout of the protein phosphatase PP2B impairs potentiation and cerebellar motor learning. *Neuron* 67, 618–628. doi: 10.1016/j.neuron.2010.07.009
- Schweighofer, N., Doya, K., and Kuroda, S. (2004). Cerebellar aminergic neuromodulation: towards a functional understanding. *Brain Res. Brain Res. Rev.* 44, 103–116. doi: 10.1016/j.brainresrev.2003.10.004
- Shambes, G. M., Gibson, J. M., and Welker, W. (1978). Fractured somatotopy in granule cell tactile areas of rat cerebellar hemispheres revealed by micromapping. *Brain Behav. Evol.* 15, 94–140. doi: 10.1159/000123774
- Smith, M. A., Ghazizadeh, A., and Shadmehr, R. (2006). Interacting adaptive processes with different timescales underlie short-term motor learning. *PLoS Biol.* 4:e179. doi: 10.1371/journal.pbio.0040179
- Solinas, S., Forti, L., Cesana, E., Mapelli, J., Schutter, E. D., and Angelo, E. D. (2007). Fast-reset of pacemaking and theta-frequency resonance patterns in cerebellar Golgi cells: simulations of their impact *in vivo*. *Front. Cell. Neurosci.* 1:4. doi: 10.3389/neuro.03.004.2007
- Sugihara, I., Lang, E. J., and Llinas, R. (1995). Serotonin modulation of inferior olivary oscillations and synchronicity: a multiple-electrode study in the rat cerebellum. *Eur. J. Neurosci.* 7, 521–534. doi: 10.1111/j.1460-9568.1995.tb00657.x
- Sweeney, J. E., Lamour, Y., and Bassant, M. H. (1992). Arousal-dependent properties of medial septal neurons in the unanesthetized rat. *Neuroscience* 48, 353–362. doi: 10.1016/0306-4522(92)90495-N
- Timofeev, I. (2011). Neuronal plasticity and thalamocortical sleep and waking oscillations. *Prog. Brain Res.* 193, 121–144. doi: 10.1016/B978-0-444-53839-0.00009-0
- Uusisaari, M. Y., and Knopfel, T. (2012). Diversity of neuronal elements and circuitry in the cerebellar nuclei. *Cerebellum* 11, 420–421. doi: 10.1007/s12311-011-0350-6
- Valera, A. M., Binda, F., Pawlowski, S. A., Dupont, J. L., Casella, J. F., Rothstein, J. D., et al. (2016). Stereotyped spatial patterns of functional synaptic connectivity in the cerebellar cortex. *Elife* 5:e09862. doi: 10.7554/eLife.09862
- Vos, B. P., Volny-Luraghi, A., and De Schutter, E. (1999). Cerebellar Golgi cells in the rat: receptive fields and timing of responses to facial stimulation. *Eur. J. Neurosci.* 11, 2621–2634. doi: 10.1046/j.1460-9568.1999.00678.x
- Wang, D., Smith-Bell, C. A., Burhans, L. B., O'Dell, D. E., Bell, R. W., and Schreurs, B. G. (2018). Changes in membrane properties of rat deep cerebellar nuclear projection neurons during acquisition of eyeblink conditioning. *Proc. Natl. Acad. Sci. U.S.A.* 115, E9419–E9428. doi: 10.1073/pnas.1808539115
- Watson, T. C., Becker, N., Apps, R., and Jones, M. W. (2014). Back to front: cerebellar connections and interactions with the prefrontal cortex. *Front. Syst. Neurosci.* 8:4. doi: 10.3389/fnsys.2014.00004
- Witter, L., Canto, C. B., Hoogland, T. M., de Gruij, J. R., and De Zeeuw, C. I. (2013). Strength and timing of motor responses mediated by rebound firing in the cerebellar nuclei after Purkinje cell activation. *Front. Neural Circuits* 7:133. doi: 10.3389/fncir.2013.00133
- Yarden-Rabinowitz, Y., and Yarom, Y. (2017). *In vivo* analysis of synaptic activity in cerebellar nuclei neurons unravels the efficacy of excitatory inputs. *J. Physiol.* 595, 5945–5963. doi: 10.1111/JP274115

- Zhang, G. J., Wu, M. C., Shi, J. D., Xu, Y. H., Chu, C. P., Cui, S. B., et al. (2017). Ethanol modulates the spontaneous complex spike waveform of cerebellar Purkinje Cells Recorded *in vivo* in Mice. *Front. Cell. Neurosci.* 11:43. doi: 10.3389/fncel.2017.00043
- Zhang, W., and Linden, D. J. (2006). Long-term depression at the mossy fiber-deep cerebellar nucleus synapse. *J. Neurosci.* 26, 6935–6944. doi: 10.1523/JNEUROSCI.0784-06.2006
- Zhang, W., Shin, J. H., and Linden, D. J. (2004). Persistent changes in the intrinsic excitability of rat deep cerebellar nuclear neurones induced by EPSP or IPSP bursts. *J. Physiol.* 561, 703–719. doi: 10.1113/jphysiol.2004.071696

Conflict of Interest Statement: The authors declare that the research was conducted in the absence of any commercial or financial relationships that could be construed as a potential conflict of interest.

Copyright © 2019 Moscato, Montagna, De Propriis, Tritto, Mapelli and D'Angelo. This is an open-access article distributed under the terms of the Creative Commons Attribution License (CC BY). The use, distribution or reproduction in other forums is permitted, provided the original author(s) and the copyright owner(s) are credited and that the original publication in this journal is cited, in accordance with accepted academic practice. No use, distribution or reproduction is permitted which does not comply with these terms.



OPEN ACCESS

Approved by:
Frontiers Editorial Office,
Frontiers Media SA, Switzerland

***Correspondence:**
Lisa Mapelli
lisa.mapelli@unipv.it
Egidio D'Angelo
dangelo@unipv.it

† Co-first authors

‡ Co-last authors

Specialty section:
This article was submitted to
Cellular Neurophysiology,
a section of the journal
Frontiers in Cellular Neuroscience

Received: 20 June 2019

Accepted: 26 June 2019

Published: 10 July 2019

Citation:
Moscato L, Montagna I, De Propris L,
Tritto S, Mapelli L and D'Angelo E
(2019) Corrigendum: Long-Lasting
Response Changes in Deep
Cerebellar Nuclei *in vivo* Correlate
With Low-Frequency Oscillations.
Front. Cell. Neurosci. 13:313.
doi: 10.3389/fncel.2019.00313

Corrigendum: Long-Lasting Response Changes in Deep Cerebellar Nuclei *in vivo* Correlate With Low-Frequency Oscillations

Letizia Moscato^{1†}, Ileana Montagna^{1†}, Licia De Propris², Simona Tritto¹, Lisa Mapelli^{1*‡} and Egidio D'Angelo^{1,2*‡}

¹ Department of Brain and Behavioral Sciences, University of Pavia, Pavia, Italy, ² IRCCS Mondino Foundation, Pavia, Italy

Keywords: deep cerebellar nuclei, cerebellum, plasticity, oscillations, *in vivo* electrophysiology

A Corrigendum on

Long-Lasting Response Changes in Deep Cerebellar Nuclei *in vivo* Correlate With Low-Frequency Oscillations

by Moscato, L., Montagna, I., De Propris, L., Tritto, S., Mapelli, L., and D'Angelo, E. (2019). *Front. Cell. Neurosci.* 13:84. doi: 10.3389/fncel.2019.00084

In the published article, there was an error in affiliation 2. Instead of “Brain Connectivity Center, C. Mondino National Neurological Institute, Pavia, Italy,” it should be “IRCCS Mondino Foundation, Pavia, Italy.” The authors apologize for this error and state that this does not change the scientific conclusions of the article in any way. The original article has been updated.

Copyright © 2019 Moscato, Montagna, De Propris, Tritto, Mapelli and D'Angelo. This is an open-access article distributed under the terms of the Creative Commons Attribution License (CC BY). The use, distribution or reproduction in other forums is permitted, provided the original author(s) and the copyright owner(s) are credited and that the original publication in this journal is cited, in accordance with accepted academic practice. No use, distribution or reproduction is permitted which does not comply with these terms.



S1 Employs Feature-Dependent Differential Selectivity of Single Cells and Distributed Patterns of Populations to Encode Mechanosensations

Yoo Rim Kim^{1,2†}, Chang-Eop Kim^{1,3†}, Heera Yoon⁴, Sun Kwang Kim^{4,5*} and Sang Jeong Kim^{1,2,6*}

¹Department of Physiology, Seoul National University College of Medicine, Seoul, South Korea, ²Department of Biomedical Sciences, Seoul National University College of Medicine, Seoul, South Korea, ³Department of Physiology, College of Korean Medicine, Gachon University, Gyeonggi-do, South Korea, ⁴Department of Science in Korean Medicine, Graduate School, Kyung Hee University, Seoul, South Korea, ⁵Department of Physiology, College of Korean Medicine, Kyung Hee University, Seoul, South Korea, ⁶Neuroscience Research Institute, Seoul National University College of Medicine, Seoul, South Korea

OPEN ACCESS

Edited by:

Lisa Mapelli,
University of Pavia, Italy

Reviewed by:

Jamie Lynn Reed,
Vanderbilt University, United States
Matilde Cordero-Erausquin,
Centre National de la Recherche
Scientifique (CNRS), France

*Correspondence:

Sun Kwang Kim
skkim77@khu.ac.kr
Sang Jeong Kim
sangjkim@snu.ac.kr

[†]These authors have contributed
equally to this work

Received: 14 December 2018

Accepted: 18 March 2019

Published: 05 April 2019

Citation:

Kim YR, Kim C-E, Yoon H, Kim SK
and Kim SJ (2019) S1 Employs
Feature-Dependent Differential
Selectivity of Single Cells and
Distributed Patterns of Populations to
Encode Mechanosensations.
Front. Cell. Neurosci. 13:132.
doi: 10.3389/fncel.2019.00132

The primary somatosensory (S1) cortex plays an important role in the perception and discrimination of touch and pain mechanosensations. Conventionally, neurons in the somatosensory system including S1 cortex have been classified into low/high threshold (HT; non-nociceptive/nociceptive) or wide dynamic range (WDR; convergent) neurons by their electrophysiological responses to innocuous brush-stroke and noxious forceps-pinch stimuli. Besides this “noxiousness” (innocuous/noxious) feature, each stimulus also includes other stimulus features: “texture” (brush hairs/forceps-steel arm), “dynamics” (dynamic stroke/static press) and “intensity” (weak/strong). However, it remains unknown how S1 neurons inclusively process such diverse features of brushing and pinch at the single-cell and population levels. Using *in vivo* two-photon Ca^{2+} imaging in the layer 2/3 neurons of the mouse S1 cortex, we identified clearly separated response patterns of the S1 neural population with distinct tuning properties of individual cells to texture, dynamics and noxiousness features of cutaneous mechanical stimuli. Among cells other than broadly tuned neurons, the majority of the cells showed a highly selective response to the difference in texture, but low selectivity to the difference in dynamics or noxiousness. Between the two low selectivity features, the difference in dynamics was slightly more specific, yet both could be decoded using the response patterns of neural populations. In addition, more neurons are recruited and stronger Ca^{2+} responses are evoked as the intensity of forceps-pinch is gradually increased. Our results suggest that S1 neurons encode various features of mechanosensations with feature-dependent differential selectivity of single cells and distributed response patterns of populations. Moreover, we raise a caution about describing neurons by a single stimulus feature ignoring other aspects of the sensory stimuli.

Keywords: brushing, pinch, stimulus feature, primary somatosensory cortex, two-photon Ca^{2+} imaging

INTRODUCTION

It is well known that the primary somatosensory (S1) cortex plays an important role in the perception and discrimination of the mechanosensations. The S1 cortex receives innocuous and noxious somatosensory inputs from the thalamus, and is involved in sensory-discriminative aspects of pain including location, duration, and intensity (Bushnell et al., 1999; Apkarian et al., 2005; Basbaum et al., 2009). So far, electrophysiological studies investigating the role of S1 cortex for touch and pain have often focused on the responses of single neurons (Matsumoto et al., 1987; Quiton et al., 2010; Whitsel et al., 2010), or the population response for stimuli with a single feature (Reed et al., 2008; Lefort et al., 2009), limiting the opportunity of understanding the population-level encoding strategy of S1 cortex for multiple features. Hence, the unexplored question is how multiple S1 neurons simultaneously encode diverse features of touch and pain sensation, such as noxiousness, texture, or dynamics.

Traditionally, the somatosensory neurons in the central nervous system (CNS) have been classified as low threshold (LT), high threshold (HT) or wide dynamic range (WDR) neurons according to their electrophysiological responses to innocuous and noxious stimuli. For instance, neurons that respond best to brush-stroke are classified as LT; neurons only responsive to pinching with forceps are classified as HT; those responding to both brush and pinch but more intensely to pinch stimulus are classified as WDR (Lamour et al., 1983; Chung et al., 1986; Senapati et al., 2005). Despite the widespread adoption of this approach to identify the characteristics of the neurons in terms of the noxiousness (innocuous/noxious) or intensity (weak/strong) feature, however, it should be recognized that those stimuli can be qualitatively different (Chung et al., 1986). They are not only characterized by features such as noxiousness and intensity, but also by texture (brush hairs/forceps steel arm) and dynamics (dynamic stroke/static press), even though simple interpretations such as LT or HT have been made in many previous studies. In particular, this consideration will be more important if the neurons of interest can process multiple features of information. S1 neurons seem to be able to encode diverse features of sensory information compared to neurons in the spinal cord (Carter et al., 2014; Saal and Bensmaia, 2014), where the concept of LT/HT/WDR was originally proposed.

Here, we used *in vivo* two-photon Ca^{2+} imaging to simultaneously record the activity of layer 2/3 neurons in the S1 cortex in lightly anesthetized mice in response to cutaneous stimuli using brush and forceps with diverse features such as noxiousness (innocuous/noxious), intensity (weak/strong), texture (brush hair/forceps steel arm), and dynamics (dynamic stroke/static press). We identified individual neurons with distinct tuning properties to texture, dynamics and noxiousness features of the cutaneous stimuli, as well as many broadly tuned neurons. Overall, the majority of the tuned neurons showed a highly selective response to the difference in texture, but low selectivity to the difference in dynamics or noxiousness. Both dynamics and noxiousness features could be decoded using

the response patterns of neural populations, implying all the relevant information of these features is being processed in a distributed manner in the S1 cortex. Our findings show how the neural population in S1 encode sensory information with multiple features and also suggest that the tuning property of S1 neurons does not match with the previous concept of LT/HT/WDR.

MATERIALS AND METHODS

Animal Preparation and Virus Injection

All experimental procedures were approved by the Seoul National University Institutional Animal Care and Use Committee and performed in accordance with the guidelines of the National Institutes of Health. We used C57BL/6 male mice (5–6 weeks old at the surgery). All surgeries were conducted under isoflurane anesthesia (1%–1.5%). A cranial window was made over the left S1 cortex hind paw area (size, 2×2 mm; center relative to Bregma: lateral, 1.5; posterior, 0.5 mm; Eto et al., 2011; Kim and Nabekura, 2011). The animal skull was opened above the S1 cortex and a small craniotomy was carefully performed using a #11 surgical blade (Jin et al., 2016). The dura was left intact. This exposed cortex was superfused with ACSF. And we injected adeno-associated virus expressing GCaMP6s (AV-1-PV2824; produced by University of Pennsylvania Gene Therapy Program Vector Core) into the S1 cortex at 2–4 sites (30–50 nl per site; 200–300 μm from the surface) using a broken glass electrode (20–40 μm tip diameter). Finally, the exposed cortex was covered with a thin cover glass (Matsunami, Japan) and the margin between the skull and the cover glass was tightly sealed with Vetbond (3M). Mouse body temperature was maintained between 36 and 38°C using a heating pad (IL-H-80, Live Cell Instrument) during animal surgery and imaging experiments. Dexamethasone (0.2 mg/kg) and meloxicam (20 mg/kg) were administered by subcutaneous injection prior to surgery to minimize the potential edema and inflammation (Otazu et al., 2015; Jin et al., 2016). Imaging sessions started 2 weeks after the surgery. Only two mice were housed in each cage in the vivarium to minimize stress on each other. The vivarium was controlled with 12 h light/dark cycle and all experiments were performed during the daylight hours.

Peripheral Stimulation During Imaging Experiments

All stimuli were delivered to the right hind paw using brush or stainless forceps. For texture and dynamics features experiment ($N = 4$ mice, **Figure 2**), brush and forceps stimuli were subdivided into Brush-stroke (B-stroke, 1-Hz stroke by brush), Brush-press (B-press, light press by brush), Forceps-stroke (F-stroke, stroke by forceps) and Forceps-press (F-press, <2 g light press by forceps) according to their texture and dynamics (**Tables 1, 2**). Stimuli were applied for 5 s per stimulus and inter-stimulus intervals were 15–20 s to avoid sensitization. For aversive noxiousness and intensity experiment ($N = 6$ mice, **Figure 3**), pinch stimuli were delivered by the experimenter using a rodent pincher

meter [Rodent pincher, BIOSEB] for 3 s per stimulus to minimize sensitization (F-pinch; Poisbeau et al., 2005). Inter-stimulus intervals were 20 s and stimulation intensities were $P_0 < 2$ g, $P_1 = 100$ g, $P_2 = 200$ g and $P_3 = 300$ g. The intensities were manually controlled by the experimenter (Kim Y. S. et al., 2016).

In vivo Two-Photon Calcium Imaging of Layer 2/3 Neurons

Calcium imaging was performed with a two-photon microscope (Zeiss LSM 7 MP, Carl Zeiss, Jena, Germany) equipped with a water immersion objective (Apochromat 20×, NA = 1.0, Carl Zeiss). Two-photon excitation for GCaMP6s imaging (900 nm) was provided by a mode-locked Ti: sapphire laser system (Chameleon, Coherent). Imaging was acquired using ZEN software (Zeiss Efficient Navigation, Carl Zeiss). All the experiments were conducted under anesthesia with isoflurane (1%) and the body temperatures of mice were maintained between 36 and 38°C using a heating pad (IL-H-80, Live Cell Instrument). For layer 2/3 neurons calcium imaging, time-lapse imaging (512×300 pixels, $0.4 \mu\text{m}/\text{pixel}$, two line steps, 0.229 s per frame) was performed with imaging depth of 180–220 μm from the surface.

Data Analysis

We manually selected regions of interests (ROIs) corresponding to individual neurons by circling each fluorescence, using time-lapse movie program. Customized scripts in MATLAB were used to analyze the calcium transient signals. Calcium signal amplitudes were calculated as $\Delta F/F_0$ ($\Delta F = F - F_0$) for each cell. F_0 means the baseline fluorescence signal calculated by averaging lowest 30% of all fluorescence signals from individual traces. Responding neurons were defined as neurons with fluorescence change $>30\%$ of F_0 , and we further analyzed only responding neurons. To determine the tuning properties of each cell for each stimulus, we defined and computed preference index (PI) that ranges from 0 to 1. Preference index of cell i for stimulus j (PI_{ij}) was defined as:

$$PI_{ij} = \frac{\overline{P_{ij}}}{\text{Max}_i}$$

where $\overline{P_{ij}}$ is the mean of the peak values of cell i for stimulus j across repeated trials (P_{ijk}) and P_{ijk} was determined as the highest value of amplitude during each trial k for stimulus j in cell i . Max_i is the highest value that cell i showed during the experiments. We defined cell i to be “preferentially responsive” or “tuned” to stimulus j when PI_{ij} is larger than $0.8 * \overline{PI_i}$, where $\overline{PI_i}$ is the average of PI_{ij} for all the given stimulus. Response index (RI) was defined the same as PI except that RI is computed for one kind of stimulus (noxious) with different intensities rather than different kind of stimuli. To represent population activity patterns of S1 neurons to different stimuli in the low dimensional space, principal component analysis (PCA), a dimensionality reduction method, was used. N-dimensional activity patterns (n , number of cells) over time were projected onto their two or three principal

component axes (each axis being a linear combination of n neural activities). In order to understand the encoding strategy of S1 neurons for each stimulus, we constructed scatter-plots of PI values (PI scatter plots) between each pair of two stimuli. Then, the Euclidean distances were computed and averaged between each scatter-plotted point and “equally tuned” line which passes through points of “stimulus 1 = stimulus 2.” To standardize the average distance for each pair of stimuli, 100,000,000 reshuffled pairs of PIs were constructed for each pair of stimuli. The reshuffled pairs of PIs conserve the original PI values for each cell, but no associations between two PIs remain. Means and standard deviations of distances were computed from these permutation data and z-distances were calculated using the means and standard deviations. To test the significance of z-distances (i.e., whether there is any association between each pair of PIs in cells), empirical p -values were directly computed from the permutation sets and Bonferroni corrections were conducted. To investigate whether the sensory information of the stimulus with each feature is encoded in S1 as a pattern of the population activity, we applied the supervised machine learning algorithm, k -nearest neighbor classifier ($k = 5$, and Euclidian metric). Vectors P_{ijk} containing ($i = 1, \dots, n$; $n = 101$ cells from six mice) were used as training and test samples for stimulus j . Ten-fold cross-validation was used to evaluate the decoding performance. This validation procedure ensures trained classifiers to be tested using data unseen during training phases. Empirical p -values were computed with 100,000,000 random permutations of the label (features to predict).

Statistics

Data were processed, analyzed and plotted using custom-written MATLAB scripts (MathWorks, Natick, MA, USA) or Prism software (Graph Pad Software, San Diego, CA, USA). All data are represented as mean \pm s.e.m. Two-tailed unpaired t -test (Figures 2C,G), Wilcoxon signed-rank test (Supplementary Figure S1C), two-tailed paired t -test (Supplementary Figure S1D), one-way ANOVA with Tukey’s *post hoc* test (Figures 1F, 3C–E), and permutation tests with Bonferroni-corrections (Figures 4B,C) were used to determine the significance in statistical comparisons. The differences were considered significant if a p value is below 0.05. NS indicates $p > 0.05$, * indicates $p < 0.05$, ** indicates $p < 0.01$, *** and ### indicates $p < 0.001$.

RESULTS

Neural Response Patterns to Innocuous and Noxious Stimuli in the S1 Cortex of Mouse

Using two-photon Ca^{2+} imaging in lightly anesthetized mice expressing GCaMP6s in the layer 2/3 neurons of the left S1 cortex, we first tried to determine the response of S1 neurons by applying innocuous brushing and noxious pinch stimuli to the right hind paw as conventionally done in pain studies. However, since these two stimuli with the different noxiousness

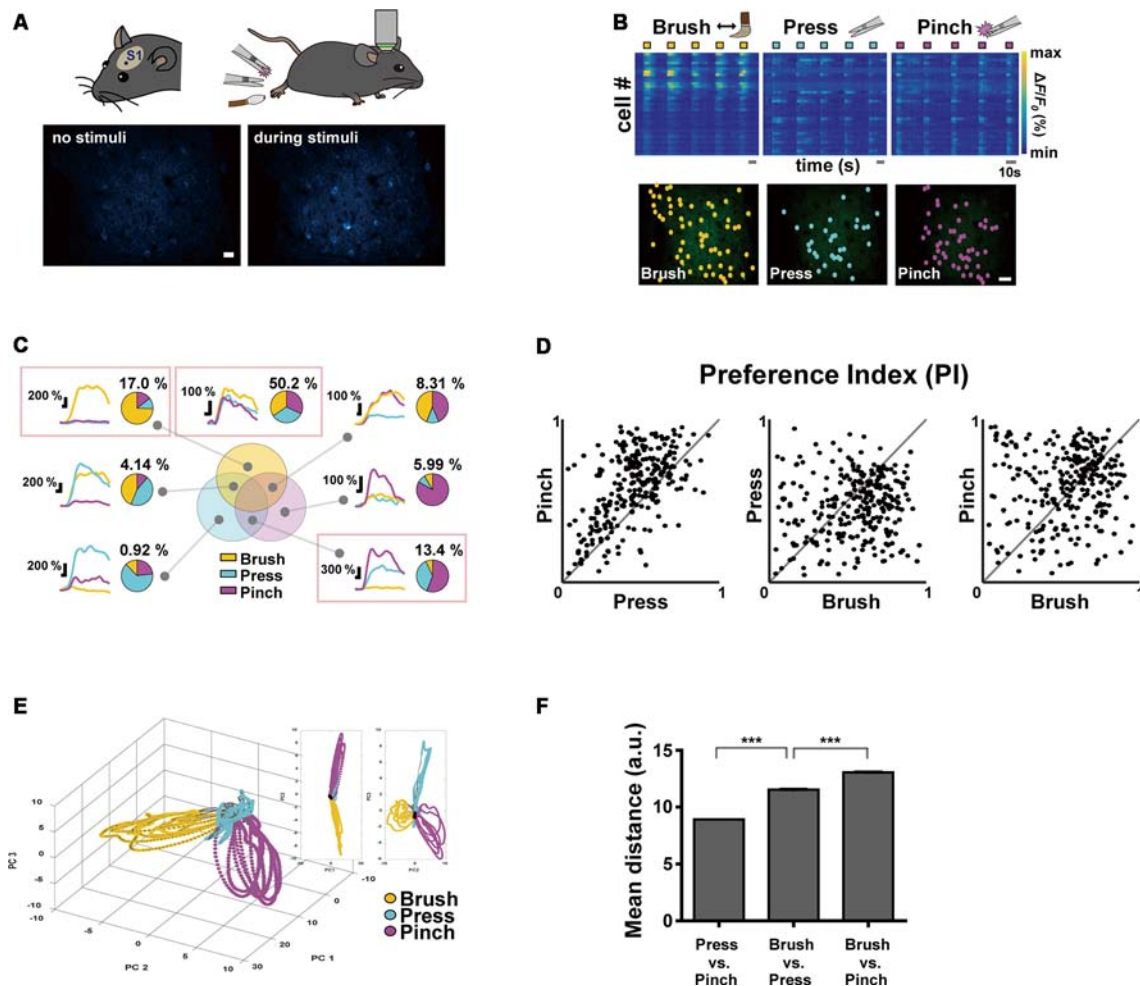


FIGURE 1 | Neural response properties evoked by innocuous and noxious stimuli in the mouse primary somatosensory (S1) cortex. **(A:)** Top) Schematic diagrams of experimental approach: a craniotomy was made over the S1 cortex corresponding to the hind limb in the left hemisphere and three types of sensory stimuli were delivered to the right hind paw of anesthetized head-fixed mice using brush and forceps. (Bottom) Representative *in vivo* two-photon Ca^{2+} fluorescence images of layer 2/3 S1 neurons during rest and pinch stimulation with forceps. Scale bar, 20 μm . **(B:)** Top) Color-coded raster plots of representative Ca^{2+} transients in S1 neurons in response to Brush, Press and Pinch. Each stimulus was applied in five trials for 5 s. Color-coded $\Delta F/F_0$ (%) ranges from 0 to 1,000. Scale bar, 10 s. (Bottom) Spatial distribution of responsive neurons to Brush (yellow), Press (cyan) or Pinch (purple) for an example mouse. Scale bar, 50 μm . **(C:)** Seven types of Ca^{2+} responses of the neurons responding to three different stimuli: on the right side of each response type, a representative pie chart shows proportions of the neurons responding to Brush (yellow), Press (cyan) and Pinch (purple), and their percentage to the total. Each portion of the Venn diagram corresponds to a type of neuron. Three red-boxed figures point the proportions of Brush specific (17.0%), Press/Pinch preferred (13.4%) and broadly tuned (50.2%) neurons ($n = 217$ cells from four mice). **(D:)** Scatter plots of the preference indexes (PIs) of individual neurons for two different stimuli: (Left) Press vs. Pinch; (Middle) Brush vs. Press; (Right) Brush vs. Pinch ($n = 217$ cells from four mice). **(E:)** An example of state-space representation of population activity patterns in response to the three stimuli from an example mouse. N-dimensional activity patterns (N, number of cells) over time were projected onto their two or three principal components via dimensionality reduction method. Each color (yellow, cyan, and purple) corresponds to each type of the stimuli. Black dots indicate states before stimuli onset and gray dots indicate states of inter-stimuli time. **(F:)** Mean Euclidean distances between states in the state-space represented in (E). Distances were calculated between states in Press vs. Pinch (8.92 ± 0.01 , 46,872 pairs from four mice), Brush vs. Press (11.54 ± 0.02 , 47,524 pairs from four mice) and Brush vs. Pinch (13.05 ± 0.03 , 47,304 pairs from four mice). Data are represented as mean \pm s.e.m. Statistics was performed with one-way ANOVA with Tukey's *post hoc* test, $F = 6,577$, $***p < 0.001$.

feature also have distinct texture and dynamics features, we added another innocuous stimulation, Press, in this first experiment session (Figure 1A, Table 1). Our idea is that if the neural response patterns to Press are similar to those to Brush, but not to Pinch, it indicates a fine-tuning of S1 neurons to the noxiousness feature; in the opposite case, it means that S1 neurons are highly tuned to the texture or dynamics feature.

To analyze neuronal response patterns to different stimuli, we calculated the preference index (PI) of individual cells to each stimulus based upon their response amplitude and fidelity (see “Materials and Methods” section). About a half of the responding neurons (fluorescence change $>30\%$ of F_0) were tuned to all the three stimuli (50.2%) and the majority of the other preferentially responded to either of Brush (17.0%) or Press-Pinch (13.4%). Interestingly, Press-

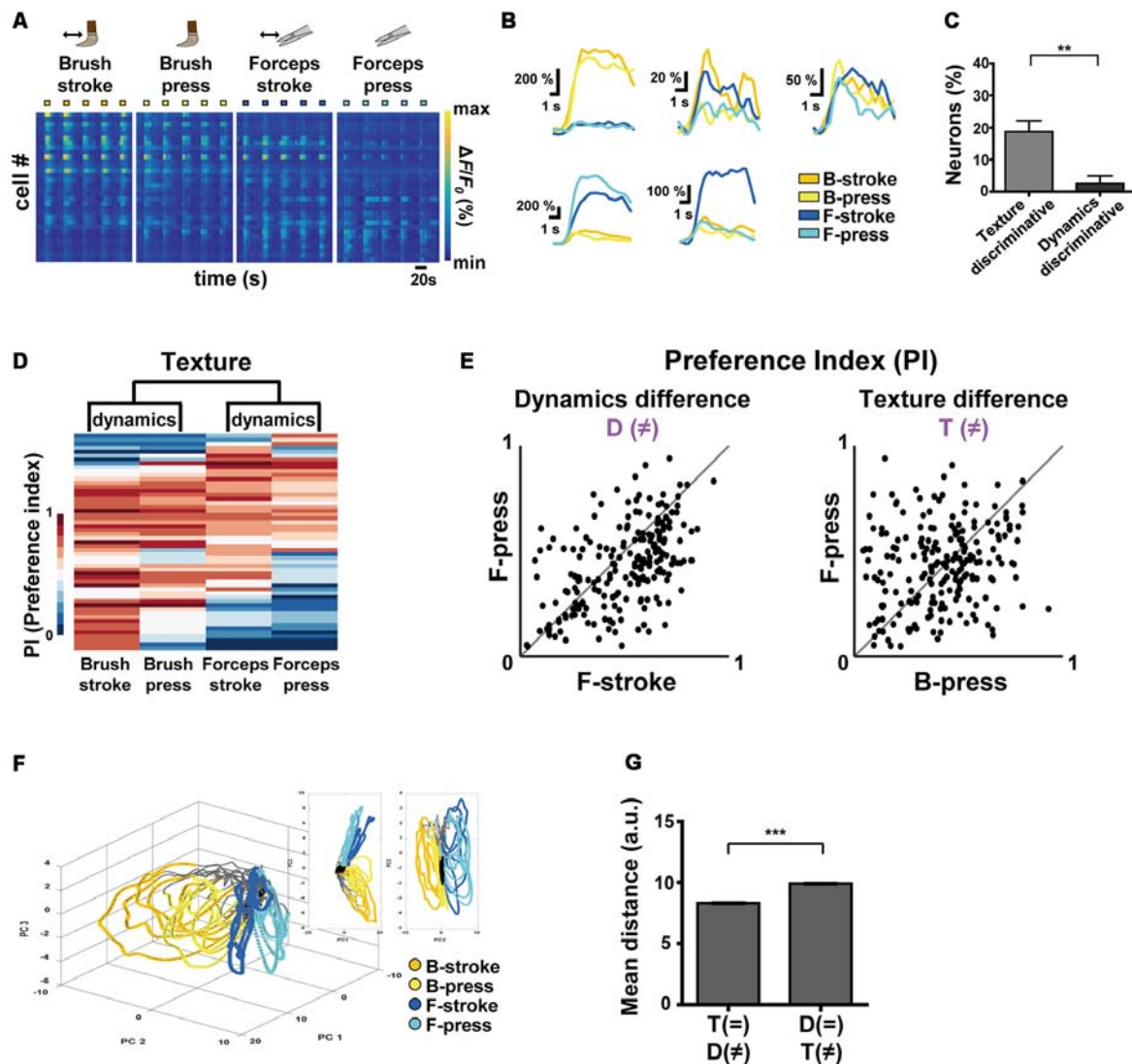


FIGURE 2 | Differential encoding of texture and dynamics features of innocuous stimuli by S1 neurons. **(A)** Color-coded raster plots of representative Ca^{2+} transients in S1 neurons in response to Brush-stroke (B-stroke), Brush-press (B-press), Forceps-stroke (F-stroke) and Forceps-press (F-press). Each stimulus was applied in five trials for 5 s. Color-coded $\Delta F/F_0$ (%) ranges from 0 to 800. Time scale, 20 s. **(B)** Examples of various Ca^{2+} responses from five neurons to B-stroke (yellow), B-press (light-yellow), F-stroke (blue) and F-press (cyan) stimuli. **(C)** The percentage of texture-discriminative neurons (preferentially responsive to B-stroke/B-press or F-stroke/F-press, $18.75\% \pm 3.43\%$) and that of dynamics-discriminative (preferentially responsive to B-stroke/F-stroke or B-press/F-press, $2.67\% \pm 2.21\%$) neurons. Data are represented as mean \pm s.e.m. Statistics was performed with a two-tailed unpaired *t*-test ($n = 208$ cells from four mice; $t = 3.94$; $**p = 0.0015$). **(D)** Hierarchical clustering analysis based on Ca^{2+} responses of S1 neurons to the different textures or dynamics. Ca^{2+} responses of each cell were normalized to a single PI per each stimulus and four types of stimuli were clustered according to the PIs of cells. **(E)** Scatter plots of PIs of individual neurons for two different stimuli: (Left) Dynamic difference, F-stroke vs. F-press; (Right) Texture difference, B-press vs. F-press ($n = 208$ cells from four mice). **(F)** An example of State-space representation of population activity patterns in response to the four stimuli. N-dimensional activity patterns (N, number of cells) over time were projected onto their two or three principal components via dimensionality reduction method. Each color (yellow, light-yellow, blue and cyan) corresponds to each type of the stimuli. Black dots indicate states before stimuli onset and gray dots indicate states of inter-stimuli time. **(G)** Mean Euclidean distances between states in the state-space represented in (F). Distances were calculated between states that differ in dynamics (F-stroke vs. F-press and B-stroke vs. B-press, 8.308 ± 0.014), and texture (B-stroke vs. F-stroke and B-press vs. F-press, 9.910 ± 0.014). Data are represented as mean \pm s.e.m (97,886 pairs from four mice). Statistics was performed with a two-tailed unpaired *t*-test ($t = 81.71$; $**p < 0.01$, $***p < 0.0001$).

responsive neurons also exhibited Ca^{2+} responses to Pinch with higher amplitude, rather than to Brush (Figures 1B,C). PI scatter plots between two stimuli indicated that S1 neurons have low selectivity to Press vs. Pinch, but high selectivity to Press (or Pinch) vs. Brush ($n = 217$ cells from four mice,

Figure 1D). PCA, which represents population activity patterns, also showed that Press and Pinch evoke distinct, but very close neural population responses from each other, which were clearly separated from those of Brush ($N = 4$ mice, Figures 1E,F). Taken together, these results

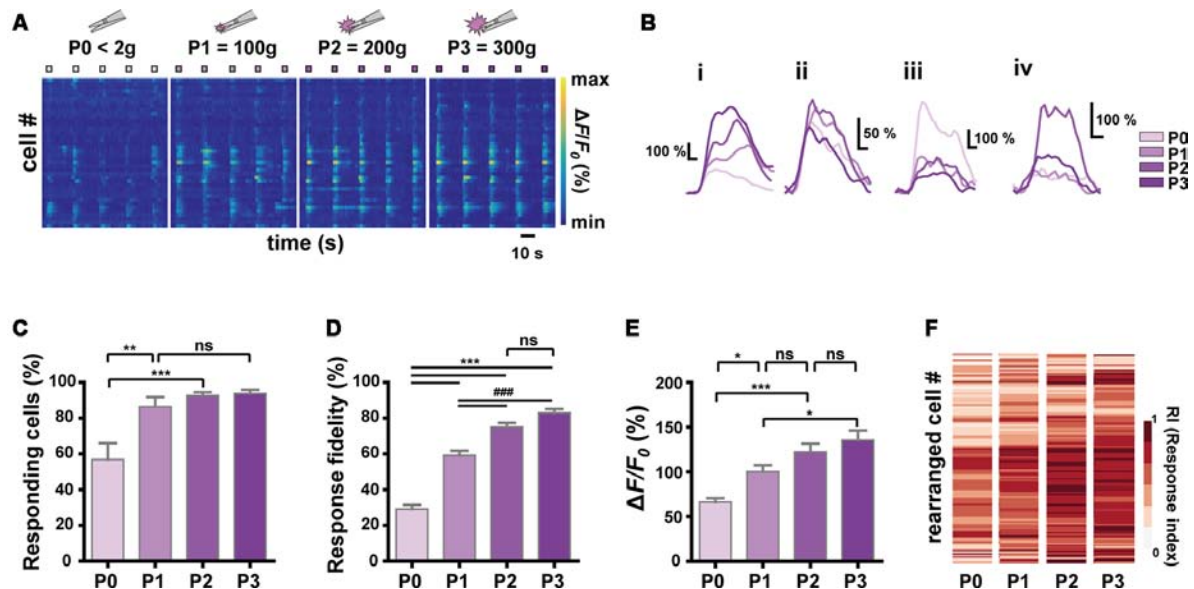


FIGURE 3 | Relationship between stimulus intensity and Ca^{2+} responses of S1 neurons. **(A)** Color-coded raster plots of representative Ca^{2+} transients in S1 neurons in response to the four different intensities ($P0 < 2\text{ g}$, $P1 = 100 \pm 30\text{ g}$, $P2 = 200 \pm 30\text{ g}$ and $P3 = 300 \pm 30\text{ g}$ pressure). Each type of stimuli was applied in five trials for 3 s. Color-coded $\Delta F/F_0$ (%) ranges from 0 to 1,000. Time scale, 10 s. **(B)** Examples of various Ca^{2+} responses from four neurons to the graded pinch stimuli. Time scale, 1 s. **(C)** The relationship between the number of responding cells and the stimulus intensity ($N = 6$ mice; one-way ANOVA, $F = 10.16$; $p = 0.0003$). **(D)** The relationship between the response fidelity of neurons and the stimulus intensity ($n = 197$ cells from six mice; one-way ANOVA, $F = 104$; $p < 0.0001$). **(E)** The relationship between Ca^{2+} transients amplitude and the stimulus intensity ($n = 197$ cells from six mice; one-way ANOVA, $F = 13.54$; $p < 0.0001$). Data are represented as mean \pm s.e.m. One-way ANOVA test was performed with Tukey's *post hoc* for multiple comparisons. ns $p > 0.05$, * $p < 0.05$, ** $p < 0.01$, *** and ### $p < 0.001$. **(F)** Heat maps from the response indexes (RIs) of cells to the stimuli with different intensities ($P0$, $P1$, $P2$, and $P3$). Cells (rows) are rearranged for the purpose of visualization ($n = 197$ cells from $N = 6$ mice).




suggest that S1 neurons are more finely tuned to the texture or dynamics feature compared to the noxiousness/intensity feature.

Encoding Texture and Dynamics Features of Innocuous Stimuli by S1 Neurons

To comprehensively investigate how S1 neurons differentially encode the texture and the dynamics of mechanical stimuli, we recorded neuronal Ca^{2+} activity in the S1 cortex evoked by Brush-stroke (B-stroke), Brush-press (B-press), Forceps-stroke (F-stroke) and Forceps-press (F-press) hind paw stimuli

(Figure 2A, Tables 1, 2). B-stroke and F-press are relabeled terms of Brush and Press stimulus in Figure 1, respectively, and in addition, B-press and F-stroke were added for more comprehensive investigation. From a variety of response patterns of individual neurons (Figures 2A,B), we found that B-stroke (F-stroke) responsive neurons also showed Ca^{2+} activities in response to B-press (F-press), rather than to F-stroke/press (B-stroke/press, respectively). The proportion of texture-discriminative neurons, preferentially responding to B-stroke and B-press (F-stroke and F-press) regardless of the dynamics feature, was much higher than that of dynamics-

TABLE 1 | Explanatory table for the different types of stimuli applied to the experiment in each figure using a brush or forceps.

| | Figure 1 | Figure 2 | Figure 3 |
|---|----------|---------------------------------|----------------------|
|  | Brush | B-stroke B-press F-stroke | |
|  | Press | F-press | |
|  | Pinch | | F-pinch |
| | | | P0 P1 P2 P3 |

Innocuous Brush, Innocuous Press and noxious Pinch stimulus are applied in Figure 1. B-stroke and F-press are relabeled terms of Brush and Press stimulus in Figure 1, respectively, and in addition, B-press and F-stroke are added in Figure 2. The Pinch stimulus in Figure 1 is applied in four different intensities in Figure 3.

TABLE 2 | Explanatory table for the different types of stimuli applied to the experiment in Figure 2 and Figure 3.

| | | Texture | Noxiousness | Dynamics |
|----------|----------|---------|-------------|-----------|
| Figure 2 | B-stroke | Brush | Innocuous | Dynamic |
| | B-press | | Innocuous | Static |
| | F-stroke | Forceps | Innocuous | Dynamic |
| | F-press | | Innocuous | Static |
| Figure 3 | F-pinch | P0 | Forceps | Innocuous |
| | | P1 | | Static |
| | | P2 | Noxious | |
| | | P3 | | |

Each stimulus was classified by texture, noxiousness and dynamics using a brush or forceps. F-pinch stimulus was subdivided into four intensities. $P0 < 2\text{ g}$, $P1 = 100\text{ g}$, $P2 = 200\text{ g}$ and $P3 = 300\text{ g}$.

discriminative neurons, preferentially responding to B-stroke and F-stroke (B-press and F-press) stimulus regardless of the texture ($n = 208$ cells from four mice, **Figure 2C**). Hierarchical clustering analysis suggests that S1 neurons are primarily categorized by their Ca^{2+} responses to the different textures, and secondarily by those to the different dynamics (**Figure 2D**). PI scatter plots also indicate that S1 neurons have relatively low selectivity to the dynamics (i.e., F-press vs. F-stroke), but show high selectivity to the texture (i.e., F-press vs. B-press; $n = 208$ cells from four mice, **Figure 2E**). PCA also showed that neural population response patterns to four different stimuli can be separated, but B-stroke evokes similar response patterns to those by B-press, while relatively distinct from those by F-stroke/press (**Figures 2F,G**). Taken together, these results suggest that S1 neurons are more selective to the texture than dynamics at individual cell level.

Encoding Noxiousness/Intensity Features of Stimuli by S1 Neurons

Next, we sought to identify the encoding strategy of S1 neurons for the noxiousness/intensity feature of mechanical stimuli, to which S1 neurons appear to be widely tuned (to Press and Pinch; **Figure 1**, Press-specific, 0.92%; Pinch-specific, 5.99%; Both, 13.4%). We applied graded Forceps-pinch (F-pinch) stimuli ($P0 < 2$ g: noxiousness = innocuous; $P1 = 100$ g, $P2 = 200$ g and $P3 = 300$ g pressure: noxiousness = noxious) to the hind paw, all of which have the same texture/dynamics feature (**Tables 1, 2**, **Figures 3A,B**). We found various response patterns of individual neurons. Interestingly, we identified “intensity coding neurons” in a certain amount of the imaged cells (**Figure 3B_i**, 21.93%), which show a positive correlation of Ca^{2+} amplitude with the stimulus intensity. Some other neurons (**Figure 3B_{ii}**, 15.30%) exhibited similar amplitudes of Ca^{2+} responses to the stimuli with four different intensities, but the neurons showing $P0$ (innocuous)-preference or inverse correlation of their Ca^{2+} amplitude with the stimulus intensity were rarely detected (**Figure 3B_{iii}**, 1.53%). The remaining neurons (61.24%) showed irregular patterns of Ca^{2+} responses to the stimuli with different intensities (**Figure 3B_{iv}**). The positive relationship between the stimulus intensity and the proportion of responding cells was observed in a non-linear fashion with steep and gentle slopes ($N = 6$ mice, **Figure 3C**). We also found such a non-linear positive relationship between the stimulus intensity and the average response fidelity (**Figure 3D**) or amplitude (**Figure 3E**) of S1 neurons, which are reflected in the RIs (see “Materials and Methods” section) of individual cells in response to the graded F-pinch stimuli ($n = 197$ cells from six mice, **Figure 3F**). These results suggest that the stronger the stimuli, the more S1 neurons are recruited, evoking stronger Ca^{2+} responses represented by higher amplitude and fidelity.

Differential Selectivity of S1 Neurons to Multiple Stimulus Features of Brushing and Pinch

The results so far indicated that S1 neurons have different levels of selectivity for the given stimuli with different features. To more clearly determine selectivity properties of S1 neurons for

multiple stimulus features of the stimuli, we reanalyzed the obtained data in **Figures 1, 2** using only non-broadly tuned neurons (i.e., neurons with selectivity to specific features), except for neurons that were tuned to all types of stimuli. PI scatter plots of non-broadly tuned neurons were generated between two stimuli with only a single difference of features: noxiousness, dynamics, or texture ($n = 101$ cells from six mice, **Figure 4A**). It turned out that a certain amount of individual S1 neurons show a highly specific response to the difference in texture, but low specificity to the difference in dynamics or noxiousness. Between the latter two features, neurons were slightly more specific to dynamics than noxiousness. Indeed, the average z-distance between PIs and “equally tuned” lines (gray line) for pairs of stimuli were significantly positive only in the discrimination of texture, meaning the non-broadly tuned neurons tend to be exclusive in texture coding compared to corresponding null model (**Figure 4B**, see “Materials and Methods” section).

Decoding Features Using the Response Patterns of the Population Activity

Finally, we tried to decode the difference between the stimuli of noxiousness, dynamics, and texture using the response patterns of the population activity, rather than individual cells. K-nearest neighbor classifier achieved perfect performance in 10-fold cross validation in all the discrimination task-difference in noxiousness, dynamics, and texture (**Figure 4C**, see “Materials and Methods” section). This result suggests that the information of sensory stimuli can be efficiently represented in S1 as patterns of the population, particularly in the case of low specificity to the stimuli features, such as noxiousness and dynamics.

DISCUSSION

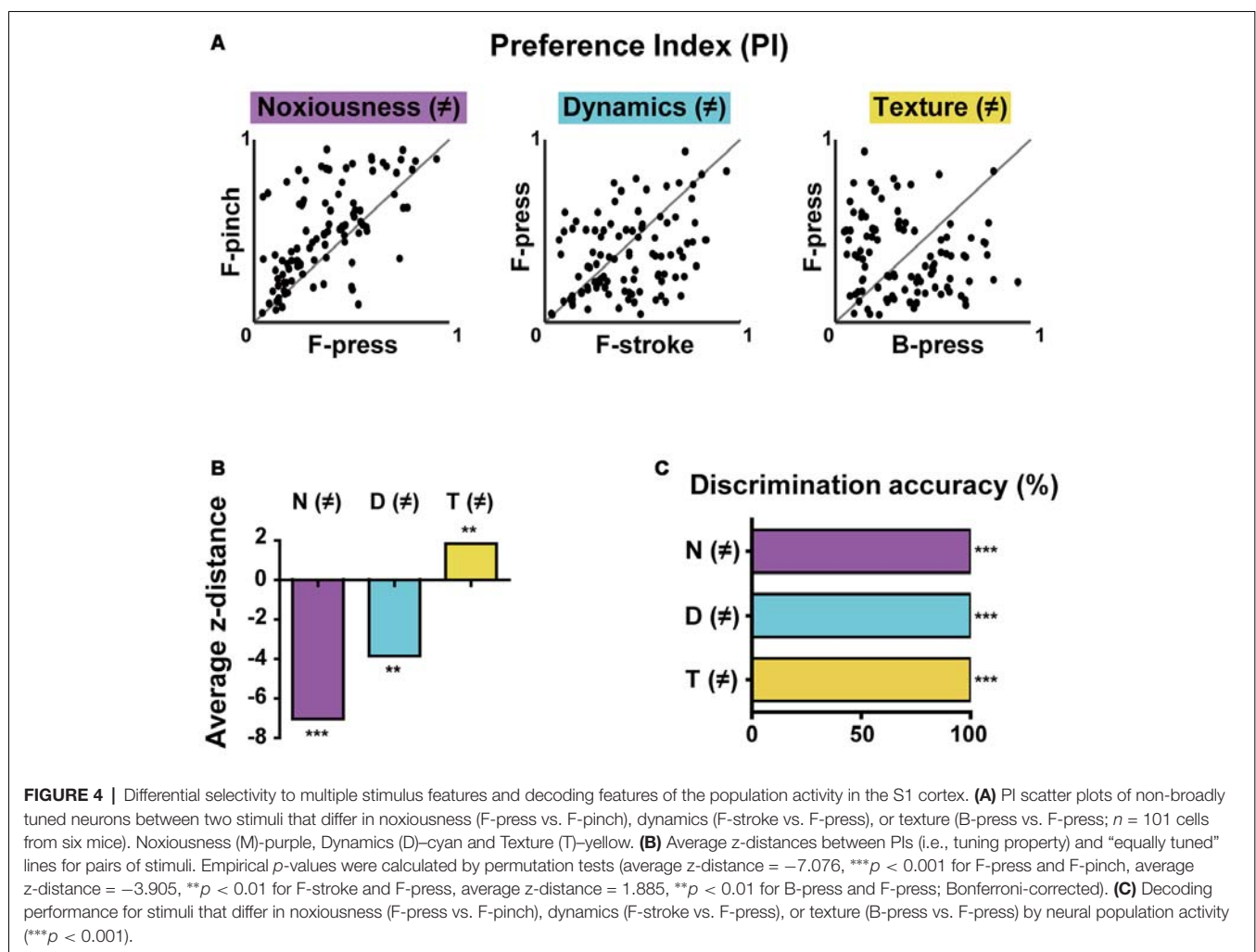
S1 cortex integrates sensory information from diverse afferent sources, leading to perception of the location, intensity, quality of touch, and pain (Vierck et al., 2013). However, it remains largely unknown how the neural circuits in S1 inclusively process such various features at the single-cell and population levels. In this study, we determined how diverse features of cutaneous inputs are encoded in layer 2/3 S1 cortex of the mouse. We found that different aspects of the stimuli are encoded with different levels of selectivity at the individual neuron level. Under the stimuli conditions given here, texture was the most dominant feature that was selectively encoded at the single-cell level, followed by dynamics, and noxiousness. However, it turned out that the stimulus features with low neuronal selectivity can be successfully decoded by the supervised machine learning technique, implying the distributed information encoding of such features. Our findings suggest that S1 neurons encode multiple stimulus features of touch and pain at the individual cell and population levels in a feature-dependent manner.

Previous electrophysiological studies characterizing S1 neurons for noxiousness in animals demonstrated that the proportion of nociceptive specific HT neurons is much smaller than that of non-nociceptive LT and convergent WDR neurons (Lamour et al., 1983; Kenshalo et al., 2000). Our results also showed that a majority of S1 neurons responded

to non-nociceptive brushing/press stimuli and exhibited highly selective responses toward non-nociceptive texture features derived from a brush or a forceps steel arm. Previous *in vivo* studies of S1 barrel cortex have reported that layer 2/3 neurons show preferred response patterns to specific texture coarsenesses, while a minority of neurons respond monotonically to the graded texture coarsenesses (Garion et al., 2014; Bourgeon et al., 2016). Taken together, these results imply that texture features of tactile information are well discriminated at the individual cell level in S1.

Traditionally, cutaneous sensory information is thought to be conveyed from peripheries to the cortex *via* independent neural pathways according to their submodality, which is characterized by response properties of afferent classes: rapidly adapting (RA), slowly adapting type 1 (SA1), slowly adapting type 2 (SA2), and pacinian (PC) afferents. These led to the notion that neurons in relatively high levels of the sensory system such as the thalamus and S1 are highly selective to specific submodality as in the periphery. Recent evidence, however, shows that individual neurons in S1 receive inputs from multiple afferent classes, and therefore should not be

defined based on submodality, but on their function (Saal and Bensmaia, 2014). Our results are consistent with this emerging evidence; about half of the analyzed neurons responded to both static and dynamic stimuli, with the former indicating SA 1 input, the latter RA or PC input. These results evidently indicate the submodality convergence rather than its segregation in the S1 cortex during touch sensation. More importantly, we revealed that S1 neurons are primarily tuned to texture features, rather than the noxiousness or intensity feature. This raises concerns about using the conventional concept of LT/HT/WDR in classifying cortical or thalamic neurons in pain studies. Indeed, it was already reported that thalamic neurons are not adequately classified by this classification scheme. Clustering results of thalamic neurons based on the response properties to several tested stimuli were different from that of spinal cord neurons (Chung et al., 1986). Using classification scheme of LT/HT/WDR in the brain is based on the assumption that relatively well-defined concept in the spinal cord will be preserved at a higher level by segregated channels, however, our data and the previous evidence suggest that the modality of noxiousness is intermixed in S1, as well



as submodalities of touch sensation. Therefore, it is necessary to develop an objective method to describe S1 neurons by their function (response properties) based on quantitative data rather than predefined modality such as LT, HT or “nociceptive-specific.”

Our study also examined how different pain intensities are represented in the S1 neurons. We observed response of S1 neurons to the noxiousness/intensity feature by applying graded F-pinch stimuli with the same Texture/Dynamics feature but only with different intensities. Most of the neurons exhibited irregular or broadly tuned responses to the graded F-pinch stimuli. At the population level, however, we found that more S1 neurons are recruited and stronger Ca^{2+} responses are evoked as the stimulus intensity is increased in a nonlinear manner. This result agrees with the previous studies showing that the stimulation intensity is positively correlated with S1 neuronal responses in a nonlinear fashion (Timmermann et al., 2001; Bornhövd et al., 2002; Eto et al., 2011). It also should be noted that a subset of S1 neurons show gradually increased amplitude of Ca^{2+} transients with increasing stimulus intensity and exhibit a linear relationship for stimulus intensity. It would be challenging, but of high interest, to further clarify the distinct functional and genetic properties of these “intensity coding neurons” in the future study. Nevertheless, these neurons could be potentially used for the objective measurement of the degree of pain or the efficacy of analgesics.

In our study, a majority of S1 neurons responded to more than two types of stimuli, rather than selectively responding to each texture, dynamics or noxiousness, indicating that individual S1 neurons encode multiple features of sensory information. Given the multifaceted nature of the sensory information in real life setting, this is a reasonable and efficient strategy to process numerous types of distinct stimuli within a limited sensory system resource (Chu et al., 2016). Indeed, similar phenomena have been reported in complex cognitive tasks of the prefrontal cortex, known as “mixed selectivity” (Rigotti et al., 2013; Ramirez-Cardenas and Viswanathan, 2016; Parthasarathy et al., 2017). Thus, our findings extend this “mixed selectivity” concept to the somatosensory cortex, suggesting that it is a more general mechanism in the cortex than previously thought.

All the data in this study were obtained from layer 2/3. Neurons in layer 2/3 receive inputs mainly from layer 4, which is a target layer for thalamic projections to S1, and predominantly project to layer 5. There are also abundant local connections within layer 2/3 (Lefort et al., 2009). Previous *in vivo* electrophysiological studies in barrel cortex have demonstrated that whisker stimulation evokes subthreshold depolarization of layer 2/3 neurons with much broader receptive fields than in layer 4 (Brecht and Sakmann, 2002; Brecht et al., 2003; Kim T. et al., 2016). These results suggest that somatotopically organized input from the thalamus along layer 4 becomes intermingled in layer 2/3. Related to these results, our findings of differential selectivity for different aspects of the sensory information in layer 2/3 might provide a cross-sectional view of the complex sensory information processing for multiple features beyond receptive fields. It will be interesting to compare the selectivity of the neurons for features we

analyzed in this study in upstream areas such as layer 4 and the thalamus.

It is known that about 80% of the neocortical neurons are excitatory pyramidal neurons and the remaining 20% are GABAergic inhibitory neurons (Markram et al., 2004). Recorded neurons in our study may be comprised of the same proportion of excitatory and inhibitory neurons if the sampling was not systematically biased. However, we do not perfectly rule out the possibility of sampling bias in our study. For example, neurons with low burst activity in the anesthetized state could have less chance of the selection for analysis, and this might introduce some difference in the proportion of excitatory and inhibitory neurons in our data. There is evidence that most excitatory and inhibitory neurons in layer 2/3 of S1 cortex in awake mice increase their action potentials during passive and active whisker deflection except for somatostatin-expressing neurons, which reduce the tonic firing rates in response to whisker sensing (Gentet et al., 2012). However, there were no neurons showing decreased calcium response to stimuli in our experiments, and this is presumably because such neurons could not be selected for analysis due to their low calcium activity under anesthesia. Future experiments investigating cell type-specific recordings in awake mice are needed to gain a more detailed understanding of the encoding mechanism of S1 circuits for diverse features of sensory information.

Some limitations of our study are worth mentioning: (1) all the experiments in this study were performed under isoflurane anesthesia. The anesthesia was inevitable since it is extremely difficult to repeatedly stimulate the same regions in awake animals and to control other sensory inputs from movements. It has been shown that the anesthesia reduces the tuning properties of neurons to stimuli in the V1 and A1 cortex of rodents (Gaese and Ostwald, 2001; Goltstein et al., 2015). Thus, we cannot completely rule out the possibility that the evoked responses of the neurons are influenced by the isoflurane anesthesia, although it is unlikely that such changes will appear in a feature-dependent manner; (2) there exist the ambiguity in the comparison design of multiple stimulus features in our study. For example, the difference of the qualitative texture between brush and forceps steel arm cannot be directly comparable to the intensity difference of quantitative pinch stimuli, such as 100 g and 300 g. Furthermore, there might be confounding features that could bias our interpretation of the selective response of neurons, such as temperature or indentation depth of the stimuli. In other words, selective responses of neurons for the different texture stimuli might be caused by the subtle difference in surface temperature or intensity of pressures between the brush and the forceps steel arm. To rule out this possibility, first, we measured the surface temperature of brush and forceps using an infrared thermometer (**Supplementary Figure S1A**). The temperature difference between the two stimulation tools was only 0.5°C. This tiny difference does not cause selective responses of S1 neurons (Milenkovic et al., 2014). We then applied two pressures with different intensity (20 g and 50 g) to the hind paw in a random order, assuming that the difference in indentation depth induced by the two stimulation tools is not

as large as those by these two pressure stimuli ($N = 3$ mice, **Supplementary Figures S1B–D**). PI scatter plots showed that the neurons have similar response patterns to the pressure stimuli with different indentation depth in terms of the fidelity and response amplitude. Calcium response amplitude of cells differed between the two pressures, but the proportion of the responding cells was not significantly different. Although there are several neurons with a difference in response amplitudes between the pressures, it is difficult to say that the small difference in force has contributed to the selective response in S1 individual neurons (Ferrington et al., 1988; Moehring et al., 2018). Therefore, it is unlikely that subtle differences in temperature or indentation depth caused by the stimuli with the brush and forceps affect the observed results in this study; (3) it is worthy to note that there are differences of the organization, gene expression patterns, and the response characteristics of cortical neurons between species (Kenshalo et al., 2000; Hutsler et al., 2005; Zeng et al., 2012). For example, there have been some discussions about the distinct response properties to sensory stimuli of the different cytoarchitectural areas of S1 (such as 3b, 3a, 1, and 2; Vierck et al., 2013), yet our results cannot suggest valuable insights with regard to these issues since these cytoarchitectonic distinction does not exist in mice. The fact that layers 2 and 3 are greatly expanded layers in the cortex of primates compared to rodents might cause bias in translating our results to humans. It would be a valuable work to verify our results in primates by applying the experimental design and analytical approaches employed in this study.

In conclusion, we demonstrated the differential selectivity of S1 neurons for multiple stimulus features of brushing and pinch. The majority of tuned neurons selectively responded to texture features rather than noxiousness features, implying that conventional classification of neurons (LT, HT, and WDR) in pain studies cannot be simply employed in the S1 cortex. Sensory stimuli could be decoded *via* patterns of neural population activity, even for the features with low specificity at the individual cell level. We also showed a group of neurons in the S1 cortex encodes pain intensity by amplitude and fidelity. Our results

provide an important insight into the encoding strategy of S1 neural circuits for multiple stimulus features of touch and pain.

ETHICS STATEMENT

All experimental procedures were approved by the Seoul National University Institutional Animal Care and Use Committee and performed in accordance with the guidelines of the National Institutes of Health.

AUTHOR CONTRIBUTIONS

YK, SKK and SJK conceived and designed the study. YK and HY performed the experiments. C-EK developed analytic tools and MATLAB codes. YK and C-EK analyzed the data. SKK and SJK supervised the experiments and analyses. YK, C-EK, SKK and SJK wrote the manuscript. All of the authors read and discussed the manuscript.

FUNDING

This study was supported by National Research Foundation of Korea grants funded by the Korea government to SJK (NRF-2018R1A5A2025964 and NRF-2017M3C7A1029609) and to SKK (NRF-2017M3C7A1025604), and by the Gachon University research fund of 2016 to C-EK (GCU-2016-0493).

ACKNOWLEDGMENTS

We thank Jae Yoon Hwang and Gaeun Park for proofreading the manuscript.

SUPPLEMENTARY MATERIAL

The Supplementary Material for this article can be found online at: <https://www.frontiersin.org/articles/10.3389/fncel.2019.00132/full#supplementary-material>

REFERENCES

- Apkarian, A. V., Bushnell, M. C., Treede, R. D., and Zubieta, J. K. (2005). Human brain mechanisms of pain perception and regulation in health and disease. *Eur. J. Pain* 9, 463–484. doi: 10.1016/j.ejpain.2004.11.001
- Basbaum, A. I., Bautista, D. M., Scherrer, G., and Julius, D. (2009). Cellular and molecular mechanisms of pain. *Cell* 139, 267–284. doi: 10.1016/j.cell.2009.09.028
- Bornhövd, K., Quante, M., Glauche, V., Bromm, B., Weiller, C., and Buchel, C. (2002). Painful stimuli evoke different stimulus-response functions in the amygdala, prefrontal, insula and somatosensory cortex: a single-trial fMRI study. *Brain* 125, 1326–1336. doi: 10.1093/brain/awf137
- Bourgeon, S., Dépeault, A., Meftah el, M., and Chapman, C. E. (2016). Tactile texture signals in primate primary somatosensory cortex and their relation to subjective roughness intensity. *J. Neurophysiol.* 115, 1767–1785. doi: 10.1152/jn.00303.2015
- Brecht, M., Roth, A., and Sakmann, B. (2003). Dynamic receptive fields of reconstructed pyramidal cells in layers 3 and 2 of rat somatosensory barrel cortex. *J. Physiol.* 553, 243–265. doi: 10.1113/jphysiol.2003.044222
- Brecht, M., and Sakmann, B. (2002). Dynamic representation of whisker deflection by synaptic potentials in spiny stellate and pyramidal cells in the barrels and septa of layer 4 rat somatosensory cortex. *J. Physiol.* 543, 49–70. doi: 10.1113/jphysiol.2002.018465
- Bushnell, M. C., Duncan, G. H., Hofbauer, R. K., Ha, B., Chen, J. I., and Carrier, B. (1999). Pain perception: is there a role for primary somatosensory cortex? *Proc. Natl. Acad. Sci. U S A* 96, 7705–7709.
- Carter, A. W., Chen, S. C., Lovell, N. H., Vickery, R. M., and Morley, J. W. (2014). Convergence across tactile afferent types in primary and secondary somatosensory cortices. *PLoS One* 9:e107617. doi: 10.1371/journal.pone.0107617
- Chu, M. W., Li, W. L., and Komiyama, T. (2016). Balancing the robustness and efficiency of odor representations during learning. *Neuron* 92, 174–186. doi: 10.1016/j.neuron.2016.09.004
- Chung, J. M., Surmeier, D. J., Lee, K. H., Sorkin, L. S., Honda, C. N., Tsong, Y., et al. (1986). Classification of primate spinothalamic and somatosensory thalamic

- neurons based on cluster analysis. *J. Neurophysiol.* 56, 308–327. doi: 10.1152/jn.1986.56.2.308
- Eto, K., Wake, H., Watanabe, M., Ishibashi, H., Noda, M., Yanagawa, Y., et al. (2011). Inter-regional contribution of enhanced activity of the primary somatosensory cortex to the anterior cingulate cortex accelerates chronic pain behavior. *J. Neurosci.* 31, 7631–7636. doi: 10.1523/JNEUROSCI.0946-11.2011
- Ferrington, D. G., Downie, J. W., and Willis, W. D. Jr. (1988). Primate nucleus gracilis neurons: responses to innocuous and noxious stimuli. *J. Neurophysiol.* 59, 886–907. doi: 10.1152/jn.1988.59.3.886
- Gaese, B. H., and Ostwald, J. (2001). Anesthesia changes frequency tuning of neurons in the rat primary auditory cortex. *J. Neurophysiol.* 86, 1062–1066. doi: 10.1152/jn.2001.86.2.1062
- Garion, L., Dubin, U., Rubin, Y., Khateb, M., Schiller, Y., Azouz, R., et al. (2014). Texture coarseness responsive neurons and their mapping in layer 2-3 of the rat barrel cortex *in vivo*. *Elife* 3:e03405. doi: 10.7554/eLife.03405
- Gentet, L. J., Kremer, Y., Taniguchi, H., Huang, Z. J., Staiger, J. F., and Petersen, C. C. (2012). Unique functional properties of somatostatin-expressing GABAergic neurons in mouse barrel cortex. *Nat. Neurosci.* 15, 607–612. doi: 10.1038/nn.3051
- Goltstein, P. M., Montijn, J. S., and Pennartz, C. M. (2015). Effects of isoflurane anesthesia on ensemble patterns of Ca^{2+} activity in mouse v1: reduced direction selectivity independent of increased correlations in cellular activity. *PLoS One* 10:e0118277. doi: 10.1371/journal.pone.0118277
- Hutsler, J. J., Lee, D. G., and Porter, K. K. (2005). Comparative analysis of cortical layering and supragranular layer enlargement in rodent carnivore and primate species. *Brain Res.* 1052, 71–81. doi: 10.1016/j.brainres.2005.06.015
- Jin, Y., Dougherty, S. E., Wood, K., Sun, L., Cudmore, R. H., Abdalla, A., et al. (2016). Regrowth of serotonin axons in the adult mouse brain following injury. *Neuron* 91, 748–762. doi: 10.1016/j.neuron.2016.07.024
- Kenshalo, D. R., Iwata, K., Sholas, M., and Thomas, D. A. (2000). Response properties and organization of nociceptive neurons in area 1 of monkey primary somatosensory cortex. *J. Neurophysiol.* 84, 719–729. doi: 10.1152/jn.2000.84.2.719
- Kim, Y. S., Anderson, M., Park, K., Zheng, Q., Agarwal, A., Gong, C., et al. (2016). Coupled activation of primary sensory neurons contributes to chronic pain. *Neuron* 91, 1085–1096. doi: 10.1016/j.neuron.2016.07.044
- Kim, S. K., and Nabekura, J. (2011). Rapid synaptic remodeling in the adult somatosensory cortex following peripheral nerve injury and its association with neuropathic pain. *J. Neurosci.* 31, 5477–5482. doi: 10.1523/JNEUROSCI.0328-11.2011
- Kim, T., Oh, W. C., Choi, J. H., and Kwon, H. B. (2016). Emergence of functional subnetworks in layer 2/3 cortex induced by sequential spikes *in vivo*. *Proc. Natl. Acad. Sci. U S A* 113, E1372–E1381. doi: 10.1073/pnas.1513410113
- Lamour, Y., Willer, J. C., and Guilbaud, G. (1983). Rat somatosensory (SmI) cortex: I. Characteristics of neuronal responses to noxious stimulation and comparison with responses to non-noxious stimulation. *Exp. Brain Res.* 49, 35–45. doi: 10.1007/bf00235539
- Lefort, S., Tómm, C., Floyd Sarria, J. C., and Petersen, C. C. (2009). The excitatory neuronal network of the C2 barrel column in mouse primary somatosensory cortex. *Neuron* 61, 301–316. doi: 10.1016/j.neuron.2008.12.020
- Markram, H., Toledo-Rodriguez, M., Wang, Y., Gupta, A., Silberberg, G., and Wu, C. (2004). Interneurons of the neocortical inhibitory system. *Nat. Rev. Neurosci.* 5, 793–807. doi: 10.1038/nrn1519
- Matsumoto, N., Sato, T., Yahata, F., and Suzuki, T. A. (1987). Physiological properties of tooth pulp-driven neurons in the first somatosensory cortex (SI) of the cat. *Pain* 31, 249–262. doi: 10.1016/0304-3959(87)90040-6
- Milenkovic, N., Zhao, W. J., Walcher, J., Albert, T., Siemens, J., Lewin, G. R., et al. (2014). A somatosensory circuit for cooling perception in mice. *Nat. Neurosci.* 17, 1560–1566. doi: 10.1038/nn.3828
- Moehring, F., Cowie, A. M., Menzel, A. D., Weyer, A. D., Grzybowski, M., Arzua, T., et al. (2018). Keratinocytes mediate innocuous and noxious touch via ATP-P2X4 signaling. *Elife* 7:e31684. doi: 10.7554/eLife.31684
- Otazu, G. H., Chae, H., Davis, M. B., and Albeanu, D. F. (2015). Cortical feedback decorrelates olfactory bulb output in awake mice. *Neuron* 86, 1461–1477. doi: 10.1016/j.neuron.2015.05.023
- Parthasarathy, A., Herikstad, R., Bong, J. H., Medina, F. S., Libedinsky, C., and Yen, S. C. (2017). Mixed selectivity morphs population codes in prefrontal cortex. *Nat. Neurosci.* 20, 1770–1779. doi: 10.1038/s41593-017-0003-2
- Poisbeau, P., Patte-Mensah, C., Keller, A. F., Barrot, M., Breton, J. D., Luis-Delgado, O. E., et al. (2005). Inflammatory pain upregulates spinal inhibition via endogenous neurosteroid production. *J. Neurosci.* 25, 11768–11776. doi: 10.1523/JNEUROSCI.3841-05.2005
- Quiton, R. L., Masri, R., Thompson, S. M., and Keller, A. (2010). Abnormal activity of primary somatosensory cortex in central pain syndrome. *J. Neurophysiol.* 104, 1717–1725. doi: 10.1152/jn.00161.2010
- Ramirez-Cardenas, A., and Viswanathan, P. (2016). The role of prefrontal mixed selectivity in cognitive control. *J. Neurosci.* 36, 9013–9015. doi: 10.1523/JNEUROSCI.1816-16.2016
- Reed, J. L., Pouget, P., Qi, H. X., Zhou, Z., Bernard, M. R., Burish, M. J., et al. (2008). Widespread spatial integration in primary somatosensory cortex. *Proc. Natl. Acad. Sci. U S A* 105, 10233–10237. doi: 10.1073/pnas.0803800105
- Rigotti, M., Barak, O., Warden, M. R., Wang, X. J., Daw, N. D., Miller, E. K., et al. (2013). The importance of mixed selectivity in complex cognitive tasks. *Nature* 497, 585–590. doi: 10.1038/nature12160
- Saal, H. P., and Bensmaia, S. J. (2014). Touch is a team effort: interplay of submodalities in cutaneous sensibility. *Trends Neurosci.* 37, 689–697. doi: 10.1016/j.tins.2014.08.012
- Senapati, A. K., Huntington, P. J., LaGraize, S. C., Wilson, H. D., Fuchs, P. N., and Peng, Y. B. (2005). Electrical stimulation of the primary somatosensory cortex inhibits spinal dorsal horn neuron activity. *Brain Res.* 1057, 134–140. doi: 10.1016/j.brainres.2005.07.044
- Timmermann, L., Ploner, M., Haucke, K., Schmitz, F., Baltissen, R., and Schnitzler, A. (2001). Differential coding of pain intensity in the human primary and secondary somatosensory cortex. *J. Neurophysiol.* 86, 1499–1503. doi: 10.1152/jn.2001.86.3.1499
- Vierck, C. J., Whitsel, B. L., Favorov, O. V., Brown, A. W., and Tommerdahl, M. (2013). Role of primary somatosensory cortex in the coding of pain. *Pain* 154, 334–344. doi: 10.1016/j.pain.2012.10.021
- Whitsel, B. L., Favorov, O. V., Li, Y., Lee, J., Quibrera, P. M., and Tommerdahl, M. (2010). Nociceptive afferent activity alters the SI RA neuron response to mechanical skin stimulation. *Cereb. Cortex* 20, 2900–2915. doi: 10.1093/cercor/bhq039
- Zeng, H., Shen, E. H., Hohmann, J. G., Oh, S. W., Bernard, A., Royall, J. J., et al. (2012). Large-scale cellular-resolution gene profiling in human neocortex reveals species-specific molecular signatures. *Cell* 149, 483–496. doi: 10.1016/j.cell.2012.02.052

Conflict of Interest Statement: The authors declare that the research was conducted in the absence of any commercial or financial relationships that could be construed as a potential conflict of interest.

Copyright © 2019 Kim, Kim, Yoon, Kim and Kim. This is an open-access article distributed under the terms of the Creative Commons Attribution License (CC BY). The use, distribution or reproduction in other forums is permitted, provided the original author(s) and the copyright owner(s) are credited and that the original publication in this journal is cited, in accordance with accepted academic practice. No use, distribution or reproduction is permitted which does not comply with these terms.



Circuit Investigations With Open-Source Miniaturized Microscopes: Past, Present and Future

Daniel Aharoni^{1*} and Tycho M. Hoogland^{2,3*}

¹Department of Neurology, David Geffen School of Medicine, University of California, Los Angeles, Los Angeles, CA, United States, ²Department of Neuroscience, Erasmus Medical Center, Rotterdam, Netherlands, ³Netherlands Institute for Neuroscience, Royal Netherlands Academy of Arts and Sciences, Amsterdam, Netherlands

OPEN ACCESS

Edited by:

Philippe Isope,
Centre National de la Recherche
Scientifique (CNRS), France

Reviewed by:

Leonardo Sacconi,
University of Florence, Italy
Takashi Tominaga,
Tokushima Bunri University, Japan
Romain Goutagny,
UMR7364 Laboratoire de
Neurosciences Cognitives et
Adaptatives (LNCA), France

*Correspondence:

Daniel Aharoni
dbaharoni@gmail.com
Tycho M. Hoogland
tmhoogland@gmail.com

Received: 23 January 2019

Accepted: 20 March 2019

Published: 05 April 2019

Citation:

Aharoni D and Hoogland TM
(2019) Circuit Investigations With
Open-Source Miniaturized
Microscopes: Past, Present
and Future.
Front. Cell. Neurosci. 13:141.
doi: 10.3389/fncel.2019.00141

The ability to simultaneously image the spatiotemporal activity signatures from many neurons during unrestrained vertebrate behaviors has become possible through the development of miniaturized fluorescence microscopes, or miniscopes, sufficiently light to be carried by small animals such as bats, birds and rodents. Miniscopes have permitted the study of circuits underlying song vocalization, action sequencing, head-direction tuning, spatial memory encoding and sleep to name a few. The foundation for these microscopes has been laid over the last two decades through academic research with some of this work resulting in commercialization. More recently, open-source initiatives have led to an even broader adoption of miniscopes in the neuroscience community. Open-source designs allow for rapid modification and extension of their function, which has resulted in a new generation of miniscopes that now permit wire-free or wireless recording, concurrent electrophysiology and imaging, two-color fluorescence detection, simultaneous optical actuation and read-out as well as wide-field and volumetric light-field imaging. These novel miniscopes will further expand the toolset of those seeking affordable methods to probe neural circuit function during naturalistic behaviors. Here, we will discuss the early development, present use and future potential of miniscopes.

Keywords: miniscope, behavior, freely moving animals, open-source, miniaturization, 3D printing, systems neurobiology

INTRODUCTION

The past 5 years have seen a flurry of open-source development with respect to miniaturized fluorescence microscopes (miniscopes) for neuroscience applications, further advancing already existing technology and extending access to a much broader scientific user base (Cai et al., 2016; Liberti et al., 2016, 2017; Jacob et al., 2018b; Juneau et al., 2018; Liang et al., 2018; Scott et al., 2018; Skocek et al., 2018; Zhang et al., 2018). The open-source nature of ongoing miniscope projects allows for the rapid sharing of designs, modifications and ideas within the neuroscience community. This has led to a dramatic acceleration of innovation resulting in miniscopes

capable of controlling the activity of cell populations while imaging neural activity in freely moving vertebrates, distinguishing distinct cell populations using two-color capable versions (Jacob et al., 2018b; Leman et al., 2018), mapping out larger fields-of-view (Leman et al., 2018), imaging volumes at video frame rates (Skocek et al., 2018) and simultaneously recording animal vocalization (Liberti et al., 2017) or head acceleration (De Groot et al., 2018). In this review article, we summarize and compare the different ongoing open-source developments and their potential for neuroscientific inquiries. The main driving force behind the development of miniaturized microscopes is first and foremost their ability to record activity from many neurons with a defined topology in an animal that is unrestrained and can display its natural innate behavior. Factors affecting behavior such as elevated stress levels in head-fixed animals and the lack of vestibular input are likely to affect recorded neural activity patterns and thus the insights that can be inferred about brain function in more natural states (Thurley and Ayaz, 2017). In addition, miniscopes provide a window into neural activity underlying behavior across the large array of behavioral assays developed over the past decades (Morris, 1984; Graeff et al., 1998; Nadler et al., 2004; Gomez-Marin et al., 2014). As a result, accurate behavioral tracking and quantification (Matsumoto et al., 2013; Wiltschko et al., 2015; Mathis et al., 2018; Mimica et al., 2018; Pereira et al., 2019) become essential in understanding how activity recorded from targeted regions can be correlated with behavior. Furthermore, the ability to record from more than one region either by sampling from larger imaging areas or by using multiple imaging devices with a reduced footprint and weight (De Groot et al., 2018) should uncover how inter-regional signaling plays out during more natural behaviors.

MINIATURIZED ONE-PHOTON EXCITATION MICROSCOPES

A wide variety of approaches have been tried and tested to image neural activity in freely behaving animals. Many of the initial systems developed were optical fiber-based (Helmchen et al., 2001; Helmchen, 2002; Göbel et al., 2004; Flusberg et al., 2005, 2008)—with excitation light coupled in and fluorescence light collected away from the microscope housing—preceding the development of a head-mounted miniaturized microscope where fluorescence excitation and detection were combined onboard the microscope housing (Ghosh et al., 2011). The components of such a miniature microscope overcame cost limitations of table-top lasers and expensive detectors and instead made use of relatively accessible technologies such as CMOS imaging sensors, LEDs—as light source—, off-the-shelf optical components and Gradient Refractive Index (or GRIN) lenses. A typical design for such a miniaturized microscope is shown in **Figure 1**. The optical path is very similar to that of a conventional, wide-field fluorescence microscope with the notable difference being the use of a single or set of GRIN lenses. GRIN lenses provide an optical interface to the brain benefiting from their short working distance, flat bottom and range of lengths and diameters. For superficial brain imaging, a single objective GRIN lens is placed directly on the brain surface. For access to deeper areas, an objective GRIN lens is combined with a smaller diameter relay GRIN lens, implanted above the neurons of interest, typically at the expense of a more limited field-of-view. In comparison to two-photon excitation, one-photon excitation is particularly susceptible to out-of-focus fluorescence and poor optical sectioning. Despite this apparent drawback, it

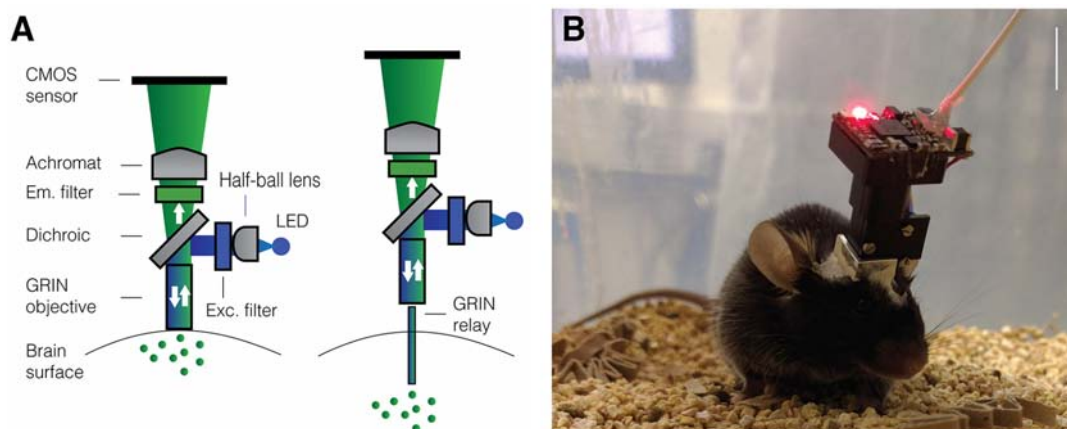
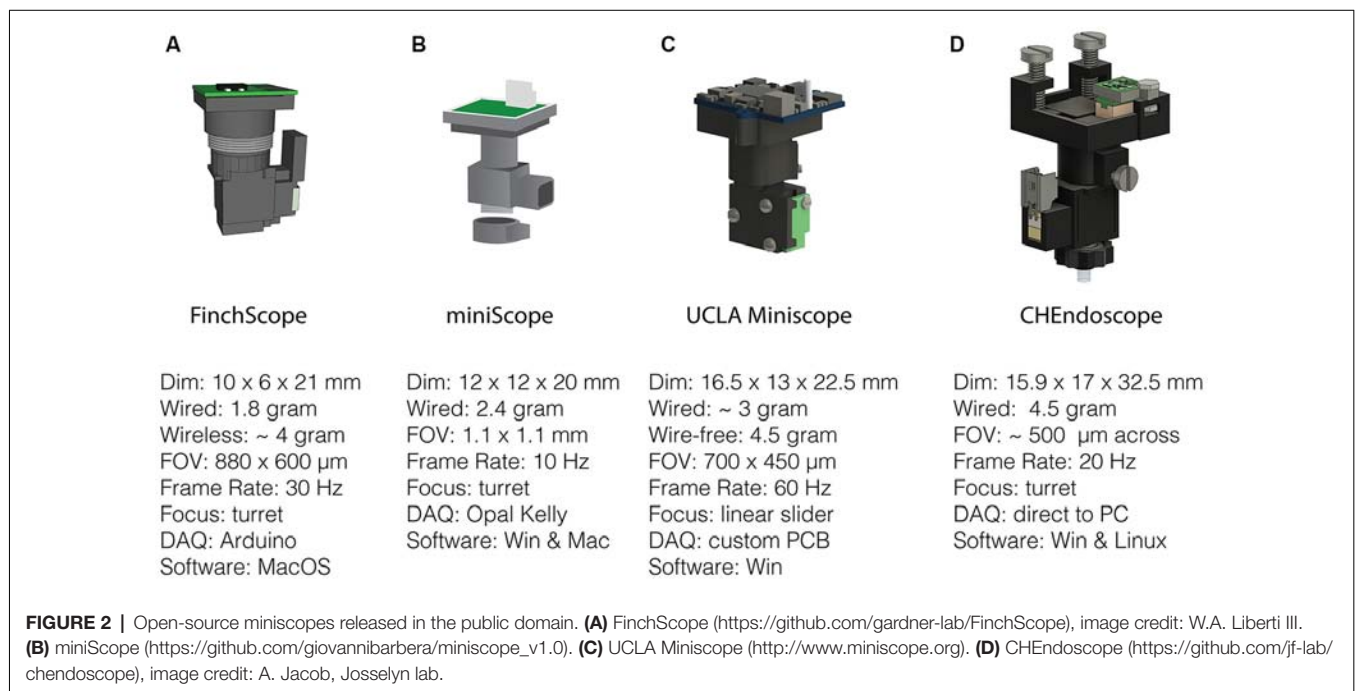


FIGURE 1 | Miniaturized one-photon excitation microscope design. **(A)** A typical design for a miniaturized one-photon excitation microscope used in combination with gradient refractive index (GRIN) lenses. It is comprised of an excitation LED light source, half-ball lens light collimator, excitation filter (Exc. filter) and dichroic mirror for reflecting excitation light down toward the specimen and transmitting emitted fluorescence up to the imaging detector. Emitted light is focused onto a CMOS imaging sensor using an achromatic lens after passing through an emission filter (Em. filter). The use of GRIN lenses permits imaging from both superficial (left) or deep-lying (right) brain structures. Adjustment of the focal plane in the specimen is achieved by moving the image sensor towards or away from the achromatic lens. For superficial imaging, the objective GRIN lens is placed directly on the brain surface, for deep brain imaging the objective GRIN lens is mounted inside the scope and combined with a thinner relay GRIN lens that is implanted into the brain to image from cells transduced with a fluorescent activity reporter (green dots). **(B)** An open-source first-generation UCLA Miniscope, which is mounted, via a baseplate, on a mouse for the duration of the recording session. Mice carry these 3-g miniscopes without any overt effects on overall behavior, although cabled versions may affect social interactions with other mice. Scale bar ~10 mm.

has proven possible to extract signals from individual neurons using analytical techniques, including a combination of principal and independent component analysis (PCA/ICA) and more recently constrained non-negative matrix factorization (CNMF) with an added term to model a time-varying fluorescence background signal (Mukamel et al., 2009; Lu et al., 2018; Zhou et al., 2018). Thus, miniaturized head-mounted fluorescence microscopes leverage the use of cheap components while still enabling cellular-resolution imaging in awake behaving animals. The availability of such miniscopes through commercial vendors has already led to a multitude of studies that have provided better insights into neural circuit activity underlying action sequencing, anxiety, vocalization—in birds—, social memories and sleep (Markowitz et al., 2015; Okuyama et al., 2016; Klaus et al., 2017; Chen et al., 2018; Jimenez et al., 2018). The release of open-source building plans for miniscopes has led to an even broader application of this technology in the past few years and will likely provide a consolidated platform for future iterations of tools to understand how topologically defined activity patterns in the brain contribute to behavior (Aharoni et al., 2019). The increased application of miniscopes to image neural activity in awake behaving animals would not have been possible without advances in the development of fluorescent activity reporters. For example, derivatives of the genetically encoded calcium indicator (GECI) protein GCaMP (Chen et al., 2013) have permitted cell-specific targeting of activity sensors in combination with improved detection of neural activity and subcellular targeting of such sensors (Dana et al., 2016). Moreover, strides are being made to develop more sensitive voltage sensors that can be targeted with cellular specificity *in vivo* (Bando et al., 2019; Quicke et al., 2019). Fluorescent sensors for glutamate and dopamine transients have also become available enabling imaging neurotransmitter

release in awake behaving animals (Marvin et al., 2018; Patriarchi et al., 2018). Thus, various aspects of circuit level function can now be investigated using miniscopes during unrestrained behavior. There are caveats associated with using miniaturized fluorescence microscopes. The use of GRIN lenses to access deeper-lying structures requires insertion of lenses into the brain, which is associated with tissue damage, despite some indications that careful surgical procedures may limit effects on behavior—at least in mice (Lee et al., 2016). In any case, care should be taken to ensure that inflammatory responses have abated after a craniotomy is made for access to the brain and GRIN lenses have been inserted (Bocarsly et al., 2015). Moreover, out of cost considerations as well as ease of use, most miniaturized fluorescence microscopes use single photon excitation, which limits optical sectioning and makes it harder to extract signals from a single source. The latter necessitates *post hoc* algorithmic extraction of signals that incorporate models of out-of-focus fluorescence, which themselves are based on assumptions. Despite these clear shortcomings, miniscopes and their open-source versions have opened up the study of large ensembles of neurons during naturalistic behavior. Since cost is no longer a limitation to perform such experiments, it is a good time to provide an overview of the accessibility and applicability of the open-source projects that have made this technology accessible. The requirement for behavioral mapping, direct control over circuit level activity as well as more fine-grained read-out of sub-populations of neurons within a circuit has led several labs to develop new iterations of miniscopes to meet these needs. We will therefore not only discuss currently existing open-source designs but elaborate on future iterations and technologies that are aimed at improving and expanding overall functionality of miniscopes.



OPEN-SOURCE MINISCOPE PROJECTS

UCLA Miniscope

With several labs having pursued unique versions of miniaturized microscopes (**Figure 2**) that were subsequently released into the public domain, the UCLA Miniscope project has probably been the most impactful in terms of its reach, with over 400 labs around the world building and applying these imaging devices in their research over the past 3 years. This broad dissemination was achieved through online documentation and tutorials on part procurement, assembly and experimental application as well as through numerous in person workshops (for details, please visit: <http://miniscope.org>). The first generation of UCLA Miniscopes, which were first used to show that memories formed close in time show a greater overlap of CA1 neural ensembles (Cai et al., 2016), can be built at a fraction of the cost of their commercial counterparts, weighs about 3 g, has a field-of-view of 700 by 450 μm (752 by 480 pixels, 6 μm pixel size), permits single channel fluorescence imaging up to a maximum rate of 60 Hz and concurrent monitoring of behavior with an additional USB camera. The optical design includes an achromat lens (Edmund Optics 49-923) which focuses nearly collimated light from an objective GRIN lens onto a CMOS sensor and a set of custom-diced optical filters (Chroma ET470/40x, T495lpxr, ET525/50 m). The housing is CNC machined out of black Delrin and custom electronics are used to control and read-out the excitation LED light source (Luxeon LXML-PB01-0030) and CMOS imaging sensor (On Semiconductor MT9V032C12STM, dynamic range > 55 dB). This CMOS imaging sensor was chosen due to its relatively small size at the time of design, low cost, large pixel size and availability at low order quantities. In addition, a similar CMOS imaging sensor had been previously shown to be able to resolve the fluorescent dynamics of GECIs (Ghosh et al., 2011). For superficial imaging, the objective GRIN lens is implanted on top of the brain surface. A metal base plate attached to the skull with dental cement allows mounting of the miniscope. For imaging deeper brain regions, a second thinner relay GRIN lens may be implanted. In this case the objective GRIN lens is mounted inside the miniscope and positioned above the relay lens to bring cells into focus (**Figure 1**). Focusing occurs through a linear slider that is manually adjusted in height, preserving the orientation of neurons between imaging sessions. Unique to the UCLA Miniscope project is the cabling connecting the head-mounted scope and the off-board DAQ hardware. Power, communication, and data transmission are achieved through a single, flexible coaxial cable in conjunction with supporting hardware (TI DS90UB913A/DS90UB914A and Power-Over-Coax filters). With a total cable diameter down to 0.3 mm (Molex 100065-0023) and compatibility with passive, low torque commutators, this design minimizes the impact of cabling on animal behavior.

A wire-free version of the UCLA Miniscope (4.5 g) has also been developed and used to record CA1 place cells during maze navigation in epileptic mice (Shuman et al., 2018). This

system incorporates a lithium-polymer battery (~ 1 g) for power, a MicroSD card for local data storage (~ 0.5 g) and a power efficient imaging sensor (E2V JADE EV76C454). In order to keep power consumption low, data is recorded at a resolution of 320 by 320 pixels using two times pixel sub-sampling. Although heavier than its wired counterpart, the use of a wire-free design resulted in social behavior comparable to that of mice without a Miniscope, whereas the lighter wired version in fact, showed reduced social exploration (Supplemental Data in Shuman et al., 2018).

FinchScope

The FinchScope project initiated at Boston University (Liberti et al., 2017) resulted in an open-source microscope around the same time as the UCLA Miniscope. This project uses high-resolution 3D printed parts (low-fluorescent resins FGPBLK01 and FGPBLK02 on a benchtop Form 2 printer) and cheap, off-the-shelf hardware components such as an integrated camera system with CMOS sensor with microphone (MC900, third eye electronics, dynamic range: 48 dB) and an Arduino Mega board for hardware control. It has a field-of-view of 800 by 600 μm (640 by 480 pixels) using an optical design similar to that of the first-generation UCLA Miniscope with a GRIN lens as an objective and an achromatic lens to focus an image on the CMOS imaging sensor. The camera sensor permits acquisitions at 30 Hz and the use of 3D printed components allows for rapid prototyping and lighter designs at a reduced cost relative to machined parts. This FinchScope incorporates a threaded turret for focusing, weighs approximately 1.8 g when used in a wired configuration and can be combined with a specially designed active commutator that allows for longitudinal observations of bird song in zebra finches. The software permits low-latency feedback to trigger recording during bird vocalization and was crucial in the discovery of neural dynamics underlying stable motor patterns (Liberti et al., 2016). With an added 2 g wireless transmitter and lithium-polymer battery, the FinchScope is capable of fully wireless recording and data transmission. The extra weight favors its application in larger animals capable of carrying the additional weight and the developers have claimed success using the wireless version in mice.

miniScope

The miniScope project developed at the National Institute on Drug Abuse (NIDA) is a 2.4 g miniscope that has been used to study direct and indirect pathway of the striatum, investigating how activity correlates with ongoing locomotory behavior (Barbera et al., 2016) as well as how activity patterns in medial prefrontal cortex associate with social salience and novelty during behavior (Liang et al., 2018; Zhang et al., 2018). The miniScope housing was 3D printed externally using SLArmor with nickel plating, a strong, light and light-tight material (Protolabs). Like the FinchScope, the miniScope has a threaded turret for focusing. It uses an achromatic doublet lens for focusing onto a CMOS imaging sensor and an aspheric lens in combination with a relay GRIN lens to reach deep targets. The field-of-view is large at 1.1 by 1.1 mm

and projected on a 400 by 400 pixel surface of a standard CMOS sensor (MT9V022IA7ATM, On Semiconductor, dynamic range > 55 dB) with a frame rate set to 10 Hz. Data acquisition occurs through an Opal Kelly field programmable gate array (FPGA) board which provides fast control over read-out of video data and control of the excitation LED light source.

CHEndoscope

At the University of Toronto, a miniscope design named the CHEndoscope has been developed. This miniscope has a housing that can be 3D printed (Jacob et al., 2018b) and is used with a 1.5 g 5 Megapixel integrated camera module (MU9PC-MBRD, Ximea, dynamic range: 38 dB) bringing the total weight of the scope to 4.5 g. To achieve 20 Hz sampling pixel binning is used to reach an effective imaging area of 648 by 486 pixels, corresponding to a field-of-view of approximately 500 μm across. Focusing is achieved through a threaded turret as in the FinchScope and miniScope. The power source to the miniscope has to be adjusted manually while video data is acquired through a Python software interface installed on a standard PC. The simplicity of the design, which uses commercially available imaging hardware like that of the FinchScope, makes it an attractive option for researchers that prefer to use off-the-shelf components rather than custom printed circuit boards (PCBs).

The miniscopes discussed above have variable ease of assembly, form factor and functionality, catering to specific needs of the researchers involved. Due to the open-source nature of these projects and their relatively simple components, this is not a major issue since modifications can be easily implemented making the development cycle short. Below we will focus on some of the ways in which miniscope functionality can be further improved.

IMPROVING FUNCTIONALITY OF OPEN-SOURCE MINISCOPES

Electrowetting Lenses

Electrowetting lenses (EWLs, a.k.a. Liquid lenses) consist of an interface of two immiscible liquids (typically water and oil) which, under voltage, deform and act as a lens allowing for electronic focusing without the need for manual adjustment (Figure 3). This is especially important for longitudinal studies where an experimenter needs to recover the previously used focal plane and the same miniscope is either used across multiple animals or different regions in the same animal. Moreover, the reduced need for mechanical handling of sensitive components of the miniscope ensures a longer shelf life. An additional benefit is the optical power of EWLs can be adjusted rapidly, within the typical frame rate used with miniscopes (30 Hz), which can be leveraged if one wants to perform interleaved recording from different focal planes. Commercial vendors have begun to implement electronic focusing in their miniscopes and the miniaturization and availability of these lenses (e.g., Varioptic Arctic 16F0) has allowed their incorporation in open-source miniscopes. For example, a head-mounted two-photon excitation fiber-coupled microscope has incorporated an EWL to allow multi-plane recordings in unrestrained mice (Ozbay et al., 2018) and one-photon excitation based miniscopes will follow suit.

Two-Color Fluorescence

With the availability of genetically encoded activity reporters that fluoresce at spectrally separable wavelengths (Chen et al., 2013; Dana et al., 2016), it becomes possible to target distinct cell populations for imaging, providing insight into how the dynamics of two neuronal populations are correlated to specific

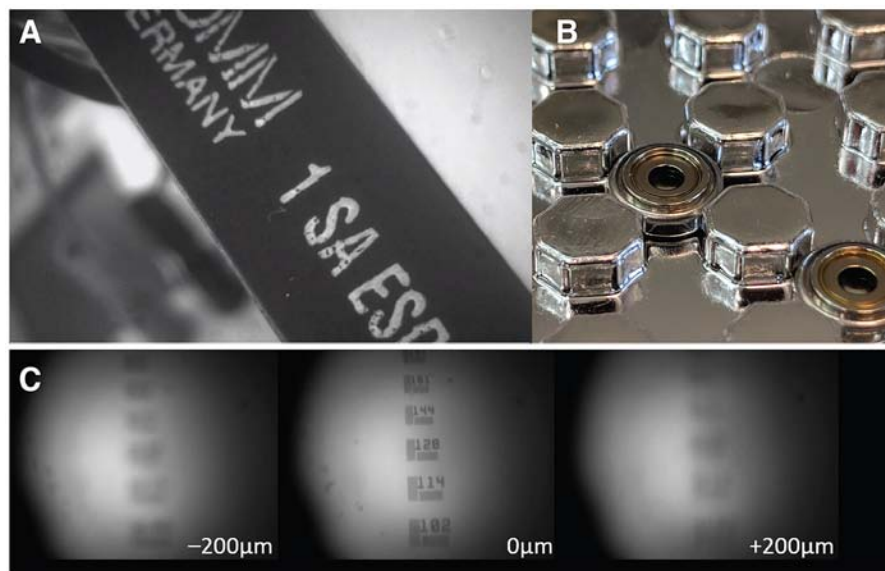


FIGURE 3 | Electrowetting Lenses (EWLs). **(A)** Image of an object brought into focus with an EWL. **(B)** Commercially available miniature EWLs weigh as little as 0.2 g with an outer diameter of ~6 mm. **(C)** Example use of an EWL (Varioptic Arctic 25H0) to focus onto a 1951 USAF test target with a $\pm 200 \mu\text{m}$ focal length shift.

behaviors (Jennings et al., 2019). One way to implement two-color imaging in a miniscope is to add an additional dichroic mirror in the emission path to split fluorescent light from two fluorophores onto two detectors which can independently be positioned. This solution, which has been implemented by a commercial vendor of miniaturized microscopes, bypasses the problem of chromatic aberration that is inherent in GRIN lenses. Such aberrations introduce a focal shift (up to $\sim 100\ \mu\text{m}$ for larger diameter GRIN lenses and depending on the optical configuration) that cause fluorescence of distinct wavelengths to be sampled from separate focal planes (**Figure 4**). Alternatively, optical elements can be used to correct for aberrations, either by positioning a plano-convex lens directly behind a shortened GRIN lens (Leiner and Prescott, 1983), by entirely replacing the objective GRIN lens with an achromatic stack of lenses, or by using diffractive optical elements (requiring custom optics). Simultaneous two-color imaging can also be achieved using a single imaging sensor with a modified miniscope optical path. Two alternating light sources combined with two band pass filters and a dichroic are used to generate and combine spectrally separated excitation. A dual-band pass dichroic and emission filter are used in the emission path to transmit emitted fluorescence. Detection of the distinct fluorescent wavelengths is achieved through interleaved read-out from a single sensor synchronized with the alternating light sources. Color imaging sensors, which use an RGB Bayer filter, can also be used for imaging two fluorophores but with the tradeoff of image resolution for spectral information and often require additional offline processing to isolate the distinct wavelengths from the spectrally overlapping RGB recording. The first forays into the development of open-source dual color

miniscopes have already begun and led to open-source two-color miniscopes with some correcting for chromatic aberrations (Jacob et al., 2018a; Leman et al., 2018). While chromatic aberration correction can be implemented by replacing the objective GRIN lens with achromatic optics, accessing deeper-lying structures may still require a relay GRIN lens which introduces its own aberrations.

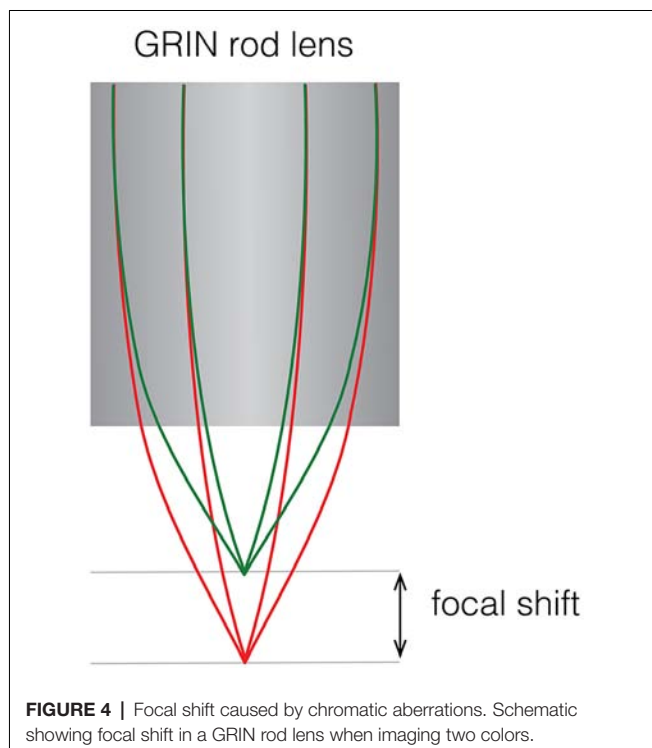
Optogenetics

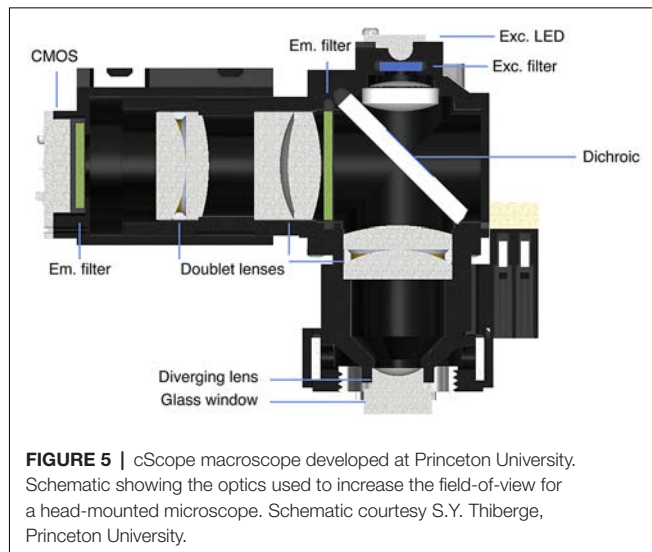
By using light-driven channels that have minimally overlapping spectra with a fluorescent activity reporter, it is possible to build a miniscope with concurrent neural imaging and manipulation capabilities in the field-of-view (Stamatakis et al., 2018). This can be achieved using a dual excitation path similar to the one described in the previous section. Depending on the opsin and fluorescent activity reporter chosen, these optogenetic capable miniscopes can have reduced, but not fully removed, cross-talk of between channels. For example, Stamatakis et al. showed in their commercial implementation of a miniaturized optogenetic microscope that the imaging light source attenuates the optogenetic response that could be evoked in a slice test preparation. This demonstrated that one should proceed cautiously when adjusting the excitation light source for imaging to provide a good trade-off between signal-to-noise and minimal signal crossover. An alternative approach is to stimulate away from the imaging field-of-view which is possible by implanting optical fibers or wireless implantable μLEDs (Shin et al., 2017). However, this requires a distinct LED driver that is synchronized with the miniscope. An alternative implementation could use an additional LED driver on the miniscope itself in combination with an implant for optogenetic stimulation (De Groot et al., 2018).

Wide-Field Imaging

Until recently, the fields-of-view of existing open-source miniscopes with single cell resolution extended up to a maximum reported field-of-view of ~ 1 by 1 mm using an achromatic objective (Zhang et al., 2018). In the realm of relatively small footprint microscopes that can be carried by mice, larger imaging sensors could be combined with a set of plano-convex lenses and double concave lens to achieve a larger (3 by $4\ \text{mm}^2$) field-of-view (Leman et al., 2018). For imaging applications in vertebrates larger than mice, the cScope (33 g) developed at Princeton University¹ provides the option to significantly expand the field-of-view (to $7.8\ \text{mm} \times 4\ \text{mm}$) and investigate intra-cortical activity patterns during free-roaming behavior at less than single cell resolution (Scott et al., 2018). Making use of the UCLA Miniscope imaging and data acquisition electronics, the cScope's large field-of-view was achieved through optimized macroscope optics and collating images taken at different angular positions of the imaging sensor (**Figure 5**). In general, by replacing the objective GRIN lens and a selection of aberration-corrected lens elements, a wider field of view can be obtained: a trend that we will see implemented in future open-source miniscopes.

¹<https://github.com/PrincetonUniversity/cScope>





Neurovascular Coupling

Hemodynamic signals contaminate fluorescence signals imaged with an epifluorescence microscope. In addition to a 480 nm LED light source for fluorescence imaging, the cScope microscope design integrates LED illumination (530 nm) to measure the intrinsic optical signal (OIS). The latter provides a measure of blood oxygenation that can be used to correct the fluorescence signal originating from neural activity. The cScope can thus be used not only to monitor neuronal activity in large areas of the brain and subtract the hemodynamic signal, but also provide insights into neurovascular coupling. To study this in mice, a 9-g miniscope—with a weight-relief system limiting the head-borne weight to 3 g—has recently been developed (Senarathna et al., 2019). This microscope uses a 452 nm LED for fluorescence excitation, a 570 nm LED light for OIS imaging and a 680 nm laser diode for deoxyhemoglobin absorption measurements. A set of orange LEDs is used for signal synchronization of the scope with peripheral hardware.

Volumetric Imaging

The principle underlying light-field microscopy is to collect angular information along with positional information of light rays emitting from a volume (e.g., their intensity, direction, wavelength, or polarization) and use computational methods to reconstruct volumetric information *post hoc* from information contained in a 2D image (Cohen et al., 2014; Prevedel et al., 2016). One common implementation of light-field microscopy uses a micro lens array (MLA) to focus light coming from different angles onto different pixels of the imaging sensor. An MLA was implemented in a reconfigured UCLA Miniscope (MiniFLM) to achieve a 700 by 600 by 360 μm^3 volume that could be acquired at 16 Hz (Skocek et al., 2018). An iterative source extraction procedure (Seed-Iterative Demixing, SID) was developed specifically for use with light-field imaging in scattering tissue (Nöbauer et al., 2017) and could be used in combination with the MiniFLM microscope to reliably extract signals from neurons separated by 15 μm or more. Some complexities arise

using MiniFLM given that it is harder to correct for motion artifacts and some spatial information is traded for angular information but the overall increase in the amount of data that can be collected when imaging volumes at video frame rates (e.g., in combination with cell-specific targeting of activity reporters) can be significant compared to wide-field imaging.

Wireless and Wire-Free Recordings

Wireless (Liberti et al., 2017) and wire-free (Shuman et al., 2018) open-source miniscopes have been developed. Both are powered by onboard lithium polymer batteries which add considerable weight to the microscope design. Power consumption scales with data bandwidth and is one of the limiting factors in designing a miniaturized wireless microscope due to battery size and weight requirements. Power efficient CMOS imaging sensors can be used along with pixel binning or pixel subsampling to minimize power consumption while maintaining a comparable field of view to wired miniscopes. Most imaging sensors used in miniaturized microscopes have a higher pixel density than required when compared with the calculated point spread function for their optical path and a reduced spatial resolution from scattering in tissue. Thus, lower or downsampled sensor resolution is chosen to extend recording time while maintaining acceptable weight requirements. In addition, wireless powering of a miniaturized design with low power consumption is feasible with near-field wireless power transfer similar to those that have already been implemented for wireless optogenetic stimulation (Montgomery et al., 2015; Park et al., 2015; Shin et al., 2017).

Electrophysiology

As part of the UCLA Miniscope project various miniscope implementations are under development that support simultaneous extracellular recordings and imaging. This can be achieved through a standalone ephys recording system synchronized to a miniscope or by fully incorporating ephys recording hardware into the Miniscope system using digital electrophysiology interface chips (e.g., Intan's RHD2132/64). For rats, an assembly for microdrive recordings of up to 18 channels (OvalDrive 18-ES) has been developed at UCLA², which allows for simultaneous electrophysiological recordings or voltammetry and imaging in rats. Moreover, fluid injection cannulae and optical fibers can also be inserted enabling manipulation of activity during miniscope imaging in freely-moving rats.

Behavioral Read-Out

Miniscope recordings can be combined with cameras that record animal behavior, but storing, processing and annotating such behavioral datasets is often nontrivial and time-consuming. A framework to process data streams named Bonsai (Lopes et al., 2015) aids in automating parts of such analysis and a module has been developed to support the UCLA Miniscope³. An alternate way to log the behavioral state of the animal is to integrate an inertial measurement unit (IMU) in a miniscope to

²<https://goo.gl/aJxJQy>

³<https://github.com/jonnew/Bonsai.Miniscope>

measure 3D head acceleration and orientation (De Groot et al., 2018). Grooming, eating and rearing behaviors are associated with distinct patterns of acceleration that can be leveraged to classify behavior (Venkatraman et al., 2010; Pasquet et al., 2016; Wilson et al., 2018). For more sophisticated behavioral tracking multi-camera systems have been used to e.g., track 3D posture (Mimica et al., 2018) but require significant resources that may not be accessible to all labs. Another tracking framework (3D Tracker)⁴ makes use of four RealSense™ depth sensing cameras and is relatively low-cost and effective for tracking posture and social interactions in rats but requires significant post-processing (Matsumoto et al., 2013; Nakamura et al., 2016). Advances in machine learning will lead to an automated analysis of behavioral motifs captured in camera data such as in the extraction of the temporal structure of animal pose (Wiltschko et al., 2015; Pereira et al., 2019) or to markerless animal tracking (Mathis et al., 2018). Open Ephys, which develops open-source tools for neuroscience⁵, has stepped forward with a solution for behavioral tracking using tracking systems originally developed for consumer gaming: Valve's SteamVR™ tracking. It makes use of orthogonal laser emitters in a base station that sweep space (two sweeps 2pi/360°) along with photodiodes and an IMU on the tracked object (e.g., miniscope) to derive information about a tracked objects orientation, velocity and angular velocity in real-time. This system is advantageous in that it does not require the same amount of post-processing as in the aforementioned systems, is affordable and can be integrated with other Open Ephys peripherals.

Two-Photon Excitation

Two-photon excitation offers well-known benefits over one-photon excitation, including a small excitation volume, increased tissue-penetration and reduced phototoxicity due to the use of longer excitation wavelengths. The small femtoliter excitation volume drastically improves the optical sectioning of the sample and thereby ensures that the light collected is only from the cellular and subcellular structures that lie along the focal plane. The first documented attempt to build a fiber-based miniaturized two-photon excitation microscope (Helmchen et al., 2001) demonstrated its overall feasibility, even though no functional imaging of neurons was achieved during behavior, in part due to strong motion artifacts. The microscope was also comparatively heavy and large (25 g, 70 mm high) limiting applications involving natural behavior in small animals. Initially, a piezoelectric element was used to drive vibrations in a stiffened fiber to generate a Lissajous scan pattern (Helmchen, 2002; Flusberg et al., 2005, 2008). Further improvements based on a similar design led to significantly lighter portable two-photon excitation microscopes (Göbel et al., 2004; Flusberg et al., 2008; Sawinski et al., 2009) used to image in freely moving mice and rats (see also Ozbay et al., 2018). Alternative scan designs based on micro-electro-mechanical systems (MEMS) mirrors have also been developed (Piyawattanametha et al.,

2006; Zong et al., 2017). Amongst those, a portable two-photon excitation scanning microscope weighing near 2 g has been used to study the entorhinal cortex in freely behaving mice (Zong et al., 2017; Obenaus et al., 2018). Expensive table-top lasers are used to achieve two-photon excitation and are coupled into one optical fiber while fluorescence is collected through an optical fiber for detection. The cost of a high-frequency pulsed laser and other peripherals (e.g., photomultiplier tubes, custom-made optical fibers for increased collection efficiency and flexibility) may limit the ubiquitous use of two-photon relative to one-photon excitation miniaturized microscopes. Furthermore, a recent comprehensive study pitching two-photon against one-photon excitation calcium imaging using respectively a benchtop two-photon and a miniaturized one photon excitation microscope revealed that orientation tuning of the same identified neurons was comparable irrespective of the type of fluorescence excitation used (Glas et al., 2018). Thus, despite the key advantages of two-photon excitation microscopy, miniaturized one-photon excitation fluorescence microscopes remain useful, affordable tools for cellular resolution imaging during unrestrained behavior. This holds even more so for highly mobile animals such as birds and bats, where fiber coupling of the excitation and emission light is impractical.

Data Analysis

The brains of animals move during free-roaming behavior, which means that motion-correction is required prior to signal extraction. Although different types of motion correction algorithms have been implemented (Dombeck et al., 2007; Greenberg and Kerr, 2009; Dubbs et al., 2016; Mitani and Komiyama, 2018), a piecewise rigid implementation⁶ adapted for fluorescence endoscopic data has proven particularly effective in correcting non-rigid deformations (Pnevmatikakis and Giovannucci, 2017). A more recent approach applying a hierarchical video registration framework to distinguish stable frames from those with large inter-frame shifts could provide even more robust image registration (Lu et al., 2018). Once frames are registered, signals need to be extracted and demixed from detected cells. Initially a PCA/ICA approach was used for data obtained with miniaturized fluorescence microscopes (Mukamel et al., 2009) but this approach has been mostly replaced by more accurate methods based on CNMF with an added model to estimate and account for time-varying background fluctuations in fluorescence entitled CNMF-E (Zhou et al., 2018). It has been proposed that, although accurate in finding cells, the CNMF-E algorithm⁷ may have a higher false positive rate than the MIN1PIPE approach⁸ developed by Lu et al. (2018) which uses an alternate method to remove background fluctuations in fluorescence and enhance neural signals. The signal output is typically a scaled version of the fractional change in fluorescence, which can be normalized by dividing by the standard deviation or a baseline noise estimate.

⁴<http://www.3dtracker.org>

⁵<http://www.open-ephys.org/>

⁶<https://github.com/flatironinstitute/NoRMCorre>

⁷https://github.com/zhoup/CNMF_E

⁸<https://github.com/JinghaoLu/MIN1PIPE>

Deconvolution on the raw signal is often performed to denoise the signal and allow estimation of event times, which reflect underlying neural spiking activity.

FUTURE DEVELOPMENTS

The open-source miniscope community is at the verge of releasing a wide variety of second-generation miniscopes that incorporate ETLs for focusing, two-color fluorescence detection, larger field-of-views, smaller footprints and optogenetic and behavioral read-out capabilities. What sort of developments lie ahead?

Closed-Loop Experiments

The availability of FPGA boards (Ciliberti and Kloosterman, 2017; Siegle et al., 2017; Buccino et al., 2018) enables fast closed-loop experiments (Ahrens et al., 2012; Clancy et al., 2014; Packer et al., 2014; Prsa et al., 2017) providing insights into e.g., sensorimotor and prosthetic learning in neural circuits, which are relevant for the development of brain-machine interfaces. Real-time detection of a specific type of behavior or activity pattern can be used to directly manipulate input pathways or targeted cell assemblies. The cellular substrates underlying the expression of behavior or the interactions between brain, body and environment could then be investigated (Buckley and Toyozumi, 2018). Closed-loop systems could also be utilized to detect and suppress the development of epileptiform activity (Sorokin et al., 2017) and delineate the cellular mechanisms underlying effective deep-brain stimulation (Parastarfeizabadi and Kouzani, 2017; Ghasemi et al., 2018). Open-source frameworks like Open Ephys have already developed hardware integrating FPGAs for low latency closed-loop experiments (Siegle et al., 2017) and such closed-loop capabilities could be ported to open-source miniscopes. Given the expansion of miniscope functionality and the concomitant increase in data channels that need to be processed, the use of FPGAs would streamline data processing and control. With miniscopes permitting volume imaging and the need for signal demultiplexing such technology could also aid efficient data extraction.

Custom Optics

The use of a set of achromatic lenses rather than an objective GRIN lens helps to reduce, but not fully remove, chromatic aberrations in most two-color miniscope configurations. One solution is the use of a diffractive element or axicon that corrects the chromatic aberration in the optical path. Nanolithography allows for the 3D printing of custom optical elements including ones that correct chromatic aberrations (Schmid et al., 2018), collimate light (Thiele et al., 2016) and act as high-resolution imaging lenses (Gissibl et al., 2016). The miniaturization of these optical components, when combined with a small footprint CMOS sensor, could lead to significantly lighter and smaller miniscopes enabling recording from multiple regions concurrently using more than one head-mounted miniscope. Moreover, resonant plasmonic metasurfaces in combination with phase-change materials can be used to create miniaturized

nano-optical elements than act as bifocal zoom lenses and can steer light (Yin et al., 2017). Three dimensional printing of optics still relies on expensive two-photon lasers that build-up components layer by layer in a time-consuming process, limiting their present widespread use in open-source miniscopes. However, a number of academic institutions have begun to provide a fee-for-service nanolithography infrastructure that could make this technology sufficiently mainstream to commence integration of 3D printed optical elements in miniscopes. Moreover, once a final 3D printed optical design has been tested, custom-machined optics inspired by these designs can be ordered through specialized contractors for micro-optics.

Lens-Free Imaging

Important strides towards further miniaturization of imaging devices for fluorescence microscopy are being made by replacing focusing elements in miniscopes with a diffuser or mask in the fluorescence emission path (Adams et al., 2017; Antipa et al., 2017). A diffusive element with an optimized amplitude mask in combination with computational signal unmixing permits reconstruction of signals from a volume based on information contained in 2D images (similar to what has been used for light-field imaging incorporating MLAs). Lensless miniscopes have the potential to significantly reduce the weight and footprint of head-mounted imaging systems while also increasing their field-of-view. One of the caveats at present is that light sources need to be integrated in the system to allow for fluorescence excitation. This could be done in principle by positioning μ LEDs around the imaging sensor or by implanting optical waveguides which can produce steerable light beams and sheets. Another caveat is that, as in the case of the MiniLFM microscope, motion correction can be hard to implement. However, the idea of a lensless miniscope holds a lot of promise and could lead to much lighter, large-field portable fluorescence microscopes.

High Frame-Rate Acquisition

Most miniscopes at present are used in combination with GECIs, which have—in addition to Ca^{2+} providing an indirect measure of ongoing activity—relatively slow kinetics. Thus, here typical frame rates of 30 Hz are generally sufficient. With the rapid improvement of genetically encoded voltage indicators and their potential for cell-specific targeting *in vivo* (Flytzanis et al., 2014; Marshall et al., 2016; Piatkevich et al., 2018; Bando et al., 2019; Quicke et al., 2019) it becomes relevant to achieve higher frame rates with high sensitivity imaging sensors. Currently available CMOS image sensors sufficiently small to integrate in miniscopes can oftentimes reach frame rates of several 100 Hz, sufficient to look at population level voltage oscillations (Marshall et al., 2016), through a combination of pixel subsampling, pixel binning, and reducing the number of active pixel rows. To achieve single cell and single action potential resolution, likely both brighter voltage indicators and smaller back illuminated scientific CMOS sensors will need to be developed. Given further electronics miniaturization, heating is an issue that needs to be resolved. Heat can be dissipated by providing sufficient air convection or through metal heat sinks, both of which could add significant weight to a miniscope design.

Operating at higher sampling frequencies will consume more power and generally require additional heat dissipation, setting a limit on using these high frame rates particularly in wire-free or wireless configurations.

CONCLUDING REMARKS

The development of open-source miniscopes has given a big boost to neuroscientists that want accessible, affordable and understandable tools to image the vertebrate brain during naturalistic behavior. Open-source designs typically have relatively simple design plans with modular components that are readily available or can be custom-fabricated using 3D printers. The low cost of these components and the comparative ease with which such scopes can be assembled have led to their widespread adaptation. While many of these systems are straightforward enough to be disseminated and implemented rather easily, it remains a challenge to integrate more complex, less mainstream technologies into open-source miniscopes at scale. Luckily, access to affordable, high quality, low quantity production lines for custom PCBs, optics, CNC machining and injection molded parts has seen significant growth in recent years and is likely to continue. Components that were bulky and expensive only a few years ago have now been miniaturized and are affordable such as EWLs for rapid electrical focusing, higher speed back-illuminated CMOS sensors and low-power IMUs that can be integrated on miniscopes to

read-out head acceleration and orientation. Following this trend, even technologies such as nanolithography that seem somewhat exotic at present for an open-source development project may be more a commonplace in a few years. The ability to build lightweight small footprint miniscopes will contribute to animal well-being and improve the read-out of neural activity under natural conditions. The open-source community has strength in numbers and the continued open exchange of new ideas will lead to improved miniscopes (e.g., sensitivity, field-of-view, and closed-loop experimental control), broader dissemination and a better understanding of the brain as it interacts with the environment.

AUTHOR CONTRIBUTIONS

DA and TH prepared the figures and wrote the manuscript.

FUNDING

This work was supported by Health~Holland (LSHM18001-H001; TH) and NSF Neurotech Hub (1700408; DA).

ACKNOWLEDGMENTS

We thank Will Liberti III, A. Jacob and S.Y. Thiberge for providing schematics of respectively the FinchScope, CHEndoscope and cScope.

REFERENCES

- Adams, J. K., Boominathan, V., Avants, B. W., Vercosa, D. G., Ye, F., Baraniuk, R. G., et al. (2017). Single-frame 3D fluorescence microscopy with ultraminiature lensless FlatScope. *Sci. Adv.* 3:e1701548. doi: 10.1126/sciadv.1701548
- Aharoni, D., Khakh, B. S., Silva, A. J., and Golshani, P. (2019). All the light that we can see: a new era in miniaturized microscopy. *Nat. Methods* 16, 11–13. doi: 10.1038/s41592-018-0266-x
- Ahrens, M. B., Li, J. M., Orger, M. B., Robson, D. N., Schier, A. F., Engert, F., et al. (2012). Brain-wide neuronal dynamics during motor adaptation in zebrafish. *Nature* 485, 471–477. doi: 10.1038/nature11057
- Antipa, N., Kuo, G., Heckel, R., Mildenhall, B., Bostan, E., Ng, R., et al. (2017). DiffuserCam: lensless single-exposure 3D imaging. *arXiv [Preprint]* 1710.02134 [cs.CV]. Available online at: <http://arxiv.org/abs/1710.02134>
- Bando, Y., Sakamoto, M., Kim, S., Ayzenshtat, I., and Yuste, R. (2019). Comparative evaluation of genetically encoded voltage indicators. *Cell Rep.* 26, 802.e4–813.e4. doi: 10.1016/j.celrep.2018.12.088
- Barbera, G., Liang, B., Zhang, L., Gerfen, C. R., Culurciello, E., Chen, R., et al. (2016). Spatially compact neural clusters in the dorsal striatum encode locomotion relevant information. *Neuron* 92, 202–213. doi: 10.1016/j.neuron.2016.08.037
- Bocarsly, M. E., Jiang, W.-C., Wang, C., Dudman, J. T., Ji, N., and Aponte, Y. (2015). Minimally invasive microendoscopy system for *in vivo* functional imaging of deep nuclei in the mouse brain. *Biomed. Opt. Express* 6, 4546–4556. doi: 10.1364/boe.6.004546
- Buccino, A. P., Lepperød, M. E., Dragly, S.-A., Häfliger, P., Fyhn, M., and Hafting, T. (2018). Open source modules for tracking animal behavior and closed-loop stimulation based on Open Ephys and Bonsai. *J. Neural Eng.* 15:055002. doi: 10.1088/1741-2552/aacf45
- Buckley, C. L., and Toyozumi, T. (2018). A theory of how active behavior stabilises neural activity: neural gain modulation by closed-loop environmental feedback. *PLoS Comput. Biol.* 14:e1005926. doi: 10.1371/journal.pcbi.1005926
- Cai, D. J., Aharoni, D., Shuman, T., Shobe, J., Biane, J., Song, W., et al. (2016). A shared neural ensemble links distinct contextual memories encoded close in time. *Nature* 534, 115–118. doi: 10.1038/nature17955
- Chen, T.-W., Wardill, T. J., Sun, Y., Pulver, S. R., Renninger, S. L., Baohan, A., et al. (2013). Ultrasensitive fluorescent proteins for imaging neuronal activity. *Nature* 499, 295–300. doi: 10.1038/nature12354
- Chen, K.-S., Xu, M., Zhang, Z., Chang, W.-C., Gaj, T., Schaffer, D. V., et al. (2018). A hypothalamic switch for REM and non-REM sleep. *Neuron* 97, 1168.e4–1176.e4. doi: 10.1016/j.neuron.2018.02.005
- Ciliberti, D., and Kloosterman, F. (2017). Falcon: a highly flexible open-source software for closed-loop neuroscience. *J. Neural Eng.* 14:045004. doi: 10.1088/1741-2552/aa7526
- Clancy, K. B., Koralek, A. C., Costa, R. M., Feldman, D. E., and Carmena, J. M. (2014). Volitional modulation of optically recorded calcium signals during neuroprosthetic learning. *Nat. Neurosci.* 17, 807–809. doi: 10.1038/nn.3712
- Cohen, N., Yang, S., Andalman, A., Broxton, M., Grosenick, L., Deisseroth, K., et al. (2014). Enhancing the performance of the light field microscope using wavefront coding. *Opt. Express* 22, 24817–24839. doi: 10.1364/OE.22.024817
- Dana, H., Mohar, B., Sun, Y., Narayan, S., Gordus, A., Hasseman, J. P., et al. (2016). Sensitive red protein calcium indicators for imaging neural activity. *Elife* 5:e12727. doi: 10.7554/eLife.12727
- De Groot, A., Bos, J., Van Veldhuijzen, J., Coppens, J., Hoedemaker, H., De Zeeuw, C. I., et al. (2018). “Reduced size miniscopes for multi-region brain imaging during natural behavior,” in *Abstract Number: F18–1717. Fens Forum 2018* Berlin, Germany.
- Dombeck, D. A., Khabbazi, A. N., Collman, F., Adelman, T. L., and Tank, D. W. (2007). Imaging large-scale neural activity with cellular resolution in awake, mobile mice. *Neuron* 56, 43–57. doi: 10.1016/j.neuron.2007.08.003
- Dubbs, A., Guevara, J., and Yuste, R. (2016). moco: fast motion correction for calcium imaging. *Front. Neuroinform.* 10:6. doi: 10.3389/fninf.2016.00006
- Flusberg, B. A., Jung, J. C., Cocker, E. D., Anderson, E. P., and Schnitzer, M. J. (2005). *In vivo* brain imaging using a portable 3.9 gram two-photon

- fluorescence microendoscope. *Opt. Lett.* 30, 2272–2274. doi: 10.1364/ol.30.002272
- Flusberg, B. A., Nimmerjahn, A., Cocker, E. D., Mukamel, E. A., Barretto, R. P. J., Ko, T. H., et al. (2008). High-speed, miniaturized fluorescence microscopy in freely moving mice. *Nat. Methods* 5, 935–938. doi: 10.1038/nmeth.1256
- Flytzanis, N. C., Bedbrook, C. N., Chiu, H., Engqvist, M. K. M., Xiao, C., Chan, K. Y., et al. (2014). Archaelhodopsin variants with enhanced voltage-sensitive fluorescence in mammalian and *Caenorhabditis elegans* neurons. *Nat. Commun.* 5:4894. doi: 10.1038/ncomms5894
- Ghasemi, P., Sahraee, T., and Mohammadi, A. (2018). Closed- and open-loop deep brain stimulation: methods, challenges, current and future aspects. *J. Biomed. Phys. Eng.* 8, 209–216. doi: 10.31661/jbpe.v8i2.898
- Ghosh, K. K., Burns, L. D., Cocker, E. D., Nimmerjahn, A., Ziv, Y., Gamal, A. E., et al. (2011). Miniaturized integration of a fluorescence microscope. *Nat. Methods* 8, 871–878. doi: 10.1038/nmeth.1694
- Gissibl, T., Thiele, S., Herkommer, A., and Giessen, H. (2016). Two-photon direct laser writing of ultracompact multi-lens objectives. *Nat. Photonics* 10, 554–560. doi: 10.1038/nphoton.2016.121
- Glas, A., Huebener, M., Bonhoeffer, T., and Goltstein, P. M. (2018). Benchmarking miniaturized microscopy against two-photon calcium imaging using single-cell orientation tuning in mouse visual cortex. *bioRxiv* [Preprint] 494641. doi: 10.1101/494641
- Göbel, W., Kerr, J. N. D., Nimmerjahn, A., and Helmchen, F. (2004). Miniaturized two-photon microscope based on a flexible coherent fiber bundle and a gradient-index lens objective. *Opt. Lett.* 29, 2521–2523. doi: 10.1364/ol.29.002521
- Gomez-Marin, A., Paton, J. J., Kampff, A. R., Costa, R. M., and Mainen, Z. F. (2014). Big behavioral data: psychology, ethology and the foundations of neuroscience. *Nat. Neurosci.* 17, 1455–1462. doi: 10.1038/nn.3812
- Graeff, F. G., Netto, C. F., and Zangrossi, H. Jr. (1998). The elevated T-maze as an experimental model of anxiety. *Neurosci. Biobehav. Rev.* 23, 237–246. doi: 10.1016/s0149-7634(98)00024-4
- Greenberg, D. S., and Kerr, J. N. D. (2009). Automated correction of fast motion artifacts for two-photon imaging of awake animals. *J. Neurosci. Methods* 176, 1–15. doi: 10.1016/j.jneumeth.2008.08.020
- Helmchen, F. (2002). Miniaturization of fluorescence microscopes using fibre optics. *Exp. Physiol.* 87, 737–745. doi: 10.1113/eph8702478
- Helmchen, F., Fee, M. S., Tank, D. W., and Denk, W. (2001). A miniature head-mounted two-photon microscope-high-resolution brain imaging in freely moving animals. *Neuron* 31, 903–912. doi: 10.1016/S0896-6273(01)00421-4
- Jacob, A. D., Ramsaran, A. I., Mocle, A. J., Tran, L. M., Yan, C., Frankland, P. W., et al. (2018a). A Two Colour System for in vivo Calcium Imaging of Engram Populations. Program No. 511.05. 2018 Neuroscience Meeting Planner San Diego, CA: Society for Neuroscience.
- Jacob, A. D., Ramsaran, A. I., Mocle, A. J., Tran, L. M., Yan, C., Frankland, P. W., et al. (2018b). A compact head-mounted endoscope for in vivo calcium imaging in freely behaving mice. *Curr. Protoc. Neurosci.* 84:e51. doi: 10.1002/cpns.51
- Jennings, J. H., Kim, C. K., Marshel, J. H., Raffiee, M., Ye, L., Quirin, S., et al. (2019). Interacting neural ensembles in orbitofrontal cortex for social and feeding behaviour. *Nature* 565, 645–649. doi: 10.1038/s41586-018-0866-8
- Jimenez, J. C., Su, K., Goldberg, A. R., Luna, V. M., Biane, J. S., Ordek, G., et al. (2018). Anxiety cells in a hippocampal-hypothalamic circuit. *Neuron* 97, 670.e6–683.e6. doi: 10.1016/j.neuron.2018.01.016
- Juneau, J., Duret, G., Robinson, J., and Kemere, C. (2018). “Enhanced image sensor module for head-mounted microscopes,” in *Proceedings of the 40th Annual International Conference of the IEEE Engineering in Medicine and Biology Society (EMBC)* (IEEE: Honolulu, HI), 826–829.
- Klaus, A., Martins, G. J., Paixao, V. B., Zhou, P., Paninski, L., and Costa, R. M. (2017). The spatiotemporal organization of the striatum encodes action space. *Neuron* 95, 1171.e7–1180.e7. doi: 10.1016/j.neuron.2017.08.015
- Lee, S. A., Holly, K. S., Voznyanov, V., Villaba, S. L., Tong, R., Grigsby, H. E., et al. (2016). Gradient index microlens implanted in prefrontal cortex of mouse does not affect behavioral test performance over time. *PLoS ONE* 11: e0146533. doi: 10.1371/journal.pone.0146533
- Leiner, D. C., and Prescott, R. (1983). Correction of chromatic aberrations in GRIN endoscopes. *Appl. Opt.* 22, 383–386. doi: 10.1364/ao.22.000383
- Leman, D. P., Chen, I. A., Yen, W. W., Markowitz, J. E., Perkins, L. N., Liberti, W. A., et al. (2018). An Expanded Open-Source Toolbox for Widefield Calcium Imaging in Freely Behaving Animals. Program No. 338.20. 2018 Neuroscience Meeting Planner. San Diego, CA: Society for Neuroscience.
- Liang, B., Zhang, L., Barbera, G., Fang, W., Zhang, J., Chen, X., et al. (2018). Distinct and dynamic ON and OFF neural ensembles in the prefrontal cortex code social exploration. *Neuron* 100, 700.e9–714.e9. doi: 10.1016/j.neuron.2018.08.043
- Liberti, W. A. III., Markowitz, J. E., Perkins, L. N., Liberti, D. C., Leman, D. P., Guitchounts, G., et al. (2016). Unstable neurons underlie a stable learned behavior. *Nat. Neurosci.* 19, 1665–1671. doi: 10.1038/nn.4405
- Liberti, W. A., Perkins, L. N., Leman, D. P., and Gardner, T. J. (2017). An open source, wireless capable miniature microscope system. *J. Neural Eng.* 14:045001. doi: 10.1088/1741-2552/aa6806
- Lopes, G., Bonacchi, N., Frazão, J., Neto, J. P., Atallah, B. V., Soares, S., et al. (2015). Bonsai: an event-based framework for processing and controlling data streams. *Front. Neuroinform.* 9:7. doi: 10.3389/fninf.2015.00007
- Lu, J., Li, C., Singh-Alvarado, J., Zhou, Z. C., Fröhlich, F., Mooney, R., et al. (2018). MIN1PIPE: a miniscope 1-photon-based calcium imaging signal extraction pipeline. *Cell Rep.* 23, 3673–3684. doi: 10.1016/j.celrep.2018.05.062
- Markowitz, J. E., Liberti, W. A. III., Guitchounts, G., Velho, T., Lois, C., and Gardner, T. J. (2015). Mesoscopic patterns of neural activity support songbird cortical sequences. *PLoS Biol.* 13:e1002158. doi: 10.1371/journal.pbio.1002158
- Marshall, J. D., Li, J. Z., Zhang, Y., Gong, Y., St-Pierre, F., Lin, M. Z., et al. (2016). Cell-type-specific optical recording of membrane voltage dynamics in freely moving mice. *Cell* 167, 1650.e15–1662.e15. doi: 10.1016/j.cell.2016.11.021
- Marvin, J. S., Scholl, B., Wilson, D. E., Podgorski, K., Kazemipour, A., Müller, J. A., et al. (2018). Stability, affinity, and chromatic variants of the glutamate sensor iGluSnFR. *Nat. Methods* 15, 936–939. doi: 10.1038/s41592-018-0171-3
- Mathis, A., Mamidanna, P., Cury, K. M., Abe, T., Murthy, V. N., Mathis, M. W., et al. (2018). DeepLabCut: markerless pose estimation of user-defined body parts with deep learning. *Nat. Neurosci.* 21, 1281–1289. doi: 10.1038/s41593-018-0209-y
- Matsumoto, J., Urakawa, S., Takamura, Y., Malcher-Lopes, R., Hori, E., Tomaz, C., et al. (2013). A 3D-video-based computerized analysis of social and sexual interactions in rats. *PLoS One* 8:e78460. doi: 10.1371/journal.pone.0078460
- Mimica, B., Dunn, B. A., Tombaz, T., Bojja, V. P. T. N. C. S., and Whitlock, J. R. (2018). Efficient cortical coding of 3D posture in freely behaving rats. *Science* 362, 584–589. doi: 10.1126/science.aau2013
- Mitani, A., and Komiyama, T. (2018). Real-time processing of two-photon calcium imaging data including lateral motion artifact correction. *Front. Neuroinform.* 12:98. doi: 10.3389/fninf.2018.00098
- Montgomery, K. L., Yeh, A. J., Ho, J. S., Tsao, V., Mohan Iyer, S., Grosenick, L., et al. (2015). Wirelessly powered, fully internal optogenetics for brain, spinal and peripheral circuits in mice. *Nat. Methods* 12, 969–974. doi: 10.1038/nmeth.3536
- Morris, R. (1984). Developments of a water-maze procedure for studying spatial learning in the rat. *J. Neurosci. Methods* 11, 47–60. doi: 10.1016/0165-0270(84)90007-4
- Mukamel, E. A., Nimmerjahn, A., and Schnitzer, M. J. (2009). Automated analysis of cellular signals from large-scale calcium imaging data. *Neuron* 63, 747–760. doi: 10.1016/j.neuron.2009.08.009
- Nadler, J. J., Moy, S. S., Dold, G., Trang, D., Simmons, N., Perez, A., et al. (2004). Automated apparatus for quantitation of social approach behaviors in mice. *Genes Brain Behav.* 3, 303–314. doi: 10.1111/j.1601-183x.2004.00071.x
- Nakamura, T., Matsumoto, J., Nishimaru, H., Bretas, R. V., Takamura, Y., Hori, E., et al. (2016). A markerless 3D computerized motion capture system incorporating a skeleton model for monkeys. *PLoS One* 11:e0166154. doi: 10.1371/journal.pone.0166154
- Nöbauer, T., Skocek, O., Pernia-Andrade, A. J., Weilguny, L., Traub, F. M., Molodtsov, M. I., et al. (2017). Video rate volumetric Ca^{2+} imaging across cortex using seeded iterative demixing (SID) microscopy. *Nat. Methods* 14, 811–818. doi: 10.1038/nmeth.4341
- Obenhaus, H. A., Rose, T., Zong, W., Tsao, A., Donato, F., Høydal, A., et al. (2018). Miniaturized two-photon microscopy enables the study of functional network topography in the medial entorhinal cortex. Program No. 689.06. 2018 Neuroscience Meeting Planner (San Diego, CA: Society

- for Neuroscience), Available online at: <https://www.abstractsonline.com/pp8/#!/4649/presentation/9606>
- Okuyama, T., Kitamura, T., Roy, D. S., Itohara, S., and Tonegawa, S. (2016). Ventral CA1 neurons store social memory. *Science* 353, 1536–1541. doi: 10.1126/science.aaf7003
- Ozbay, B. N., Futia, G. L., Ma, M., Bright, V. M., Gopinath, J. T., Hughes, E. G., et al. (2018). Three dimensional two-photon brain imaging in freely moving mice using a miniature fiber coupled microscope with active axial-scanning. *Sci. Rep.* 8:8108. doi: 10.1038/s41598-018-26326-3
- Packer, A. M., Russell, L. E., Dalglish, H. W. P., and Häusser, M. (2014). Simultaneous all-optical manipulation and recording of neural circuit activity with cellular resolution *in vivo*. *Nat. Methods* 12, 140–146. doi: 10.1038/nmeth.3217
- Parastarfeizabadi, M., and Kouzani, A. Z. (2017). Advances in closed-loop deep brain stimulation devices. *J. Neuroeng. Rehabil.* 14:79. doi: 10.1186/s12984-017-0295-1
- Park, S. I., Brenner, D. S., Shin, G., Morgan, C. D., Copits, B. A., Chung, H. U., et al. (2015). Soft, stretchable, fully implantable miniaturized optoelectronic systems for wireless optogenetics. *Nat. Biotechnol.* 33, 1280–1286. doi: 10.1038/nbt.3415
- Pasquet, M. O., Tihy, M., Gourgeon, A., Pompili, M. N., Godsil, B. P., Léna, C., et al. (2016). Wireless inertial measurement of head kinematics in freely-moving rats. *Sci. Rep.* 6:35689. doi: 10.1038/srep35689
- Patriarchi, T., Cho, J. R., Merten, K., Howe, M. W., Marley, A., Xiong, W.-H., et al. (2018). Ultrafast neuronal imaging of dopamine dynamics with designed genetically encoded sensors. *Science* 360: eaat4422. doi: 10.1126/science.aat4422
- Pereira, T. D., Aldarondo, D. E., Willmore, L., Kislin, M., Wang, S. S.-H., Murthy, M., et al. (2019). Fast animal pose estimation using deep neural networks. *Nat. Methods* 16, 117–125. doi: 10.1038/s41592-018-0234-5
- Piatkevich, K. D., Jung, E. E., Straub, C., Linghu, C., Park, D., Suk, H.-J., et al. (2018). A robotic multidimensional directed evolution approach applied to fluorescent voltage reporters. *Nat. Chem. Biol.* 14, 352–360. doi: 10.1038/s41589-018-0004-9
- Piyawattanametha, W., Barretto, R. P. J., Ko, T. H., Flusberg, B. A., Cocker, E. D., Ra, H., et al. (2006). Fast-scanning two-photon fluorescence imaging based on a microelectromechanical systems two-dimensional scanning mirror. *Opt. Lett.* 31, 2018–2020. doi: 10.1364/ol.31.002018
- Pnevmatikakis, E. A., and Giovannucci, A. (2017). NoRMCorre: an online algorithm for piecewise rigid motion correction of calcium imaging data. *J. Neurosci. Methods* 291, 83–94. doi: 10.1016/j.jneumeth.2017.07.031
- Prevedel, R., Verhoef, A. J., Pernía-Andrade, A. J., Weisenburger, S., Huang, B. S., Nöbauer, T., et al. (2016). Fast volumetric calcium imaging across multiple cortical layers using sculpted light. *Nat. Methods* 13, 1021–1028. doi: 10.1038/nmeth.4040
- Prsa, M., Galíñanes, G. L., and Huber, D. (2017). Rapid integration of artificial sensory feedback during operant conditioning of motor cortex neurons. *Neuron* 93, 929.e6–939.e6. doi: 10.1016/j.neuron.2017.01.023
- Quicke, P., Song, C., McKimm, E. J., Milosevic, M. M., Howe, C. L., Neil, M., et al. (2019). Single-Neuron level one-photon voltage imaging with sparsely targeted genetically encoded voltage indicators. *Front. Cell. Neurosci.* 13:39. doi: 10.3389/fncel.2019.00039
- Sawinski, J., Wallace, D. J., Greenberg, D. S., Grossmann, S., Denk, W., and Kerr, J. N. D. (2009). Visually evoked activity in cortical cells imaged in freely moving animals. *Proc. Natl. Acad. Sci. U S A* 106, 19557–19562. doi: 10.1073/pnas.0903680106
- Schmid, M., Thiele, S., Herkommer, A., and Giessen, H. (2018). Three-dimensional direct laser written achromatic axicons and multi-component microlenses. *Opt. Lett.* 43, 5837–5840. doi: 10.1364/ol.43.005837
- Scott, B. B., Thiberge, S. Y., Guo, C., Tervo, D. G. R., Brody, C. D., Karpova, A. Y., et al. (2018). Imaging cortical dynamics in GCaMP transgenic rats with a head-mounted widefield macroscope. *Neuron* 100, 1045.e5–1058.e5. doi: 10.1016/j.neuron.2018.09.050
- Senarathna, J., Yu, H., Deng, C., Zou, A. L., Issa, J. B., Hadjiabadi, D. H., et al. (2019). A miniature multi-contrast microscope for functional imaging in freely behaving animals. *Nat. Commun.* 10:99. doi: 10.1038/s41467-018-07926-z
- Shin, G., Gomez, A. M., Al-Hasani, R., Jeong, Y. R., Kim, J., Xie, Z., et al. (2017). Flexible near-field wireless optoelectronics as subdermal implants for broad applications in optogenetics. *Neuron* 93, 509.e3–521.e3. doi: 10.1016/j.neuron.2016.12.031
- Shuman, T., Aharoni, D., Cai, D. J., Lee, C. R., Chavlis, S., Taxis, J., et al. (2018). Breakdown of spatial coding and neural synchronization in epilepsy. *bioRxiv [Preprint]*. 358580. doi: 10.1101/358580
- Siegle, J. H., López, A. C., Patel, Y. A., Abramov, K., Ohayon, S., and Voigts, J. (2017). Open Ephys: an open-source, plugin-based platform for multichannel electrophysiology. *J. Neural Eng.* 14:045003. doi: 10.1088/1741-2552/aa5eea
- Skocek, O., Nöbauer, T., Weiglun, L., Martinez Traub, F., Xia, C. N., Molodtsov, M. I., et al. (2018). High-speed volumetric imaging of neuronal activity in freely moving rodents. *Nat. Methods* 15, 429–432. doi: 10.1038/s41592-018-0008-0
- Sorokin, J. M., Davidson, T. J., Frechette, E., Abramian, A. M., Deisseroth, K., Huguenard, J. R., et al. (2017). Bidirectional control of generalized epilepsy networks via rapid real-time switching of firing mode. *Neuron* 93, 194–210. doi: 10.1016/j.neuron.2016.11.026
- Stamatakis, A. M., Schachter, M. J., Gulati, S., Zitelli, K. T., Malanowski, S., Tajik, A., et al. (2018). Simultaneous optogenetics and cellular resolution calcium imaging during active behavior using a miniaturized microscope. *Front. Neurosci.* 12:496. doi: 10.3389/fnins.2018.00496
- Thiele, S., Gissibl, T., Giessen, H., and Herkommer, A. M. (2016). Ultra-compact on-chip LED collimation optics by 3D femtosecond direct laser writing. *Opt. Lett.* 41, 3029–3032. doi: 10.1364/ol.41.003029
- Thurley, K., and Ayaz, A. (2017). Virtual reality systems for rodents. *Curr. Zool.* 63, 109–119. doi: 10.1093/cz/zow070
- Venkatraman, S., Jin, X., Costa, R. M., and Carmenta, J. M. (2010). Investigating neural correlates of behavior in freely behaving rodents using inertial sensors. *J. Neurophysiol.* 104, 569–575. doi: 10.1152/jn.00121.2010
- Wilson, J. J., Alexandre, N., Trentin, C., and Tripodi, M. (2018). Three-dimensional representation of motor space in the mouse superior colliculus. *Curr. Biol.* 28, 1744.e12–1755.e12. doi: 10.1016/j.cub.2018.04.021
- Wiltschko, A. B., Johnson, M. J., Iurilli, G., Peterson, R. E., Katon, J. M., Pashkovski, S. L., et al. (2015). Mapping sub-second structure in mouse behavior. *Neuron* 88, 1121–1135. doi: 10.1016/j.neuron.2015.11.031
- Yin, X., Steinle, T., Huang, L., Taubner, T., Wuttig, M., Zentgraf, T., et al. (2017). Beam switching and bifocal zoom lensing using active plasmonic metasurfaces. *Light Sci. Appl.* 6:e17016. doi: 10.1038/lsa.2017.16
- Zhang, L., Liang, B., Barbera, G., Hawes, S., Zhang, Y., Stump, K., et al. (2018). Miniscope GRIN lens system for calcium imaging of neuronal activity from deep brain structures in behaving animals. *Curr. Protoc. Neurosci.* 86:e56. doi: 10.1002/cpns.56
- Zhou, P., Resendez, S. L., Rodriguez-Romaguera, J., Jimenez, J. C., Neufeld, S. Q., Giovannucci, A., et al. (2018). Efficient and accurate extraction of *in vivo* calcium signals from microendoscopic video data. *Elife* 7:e28728. doi: 10.7554/elife.28728
- Zong, W., Wu, R., Li, M., Hu, Y., Li, Y., Li, J., et al. (2017). Fast high-resolution miniature two-photon microscopy for brain imaging in freely behaving mice. *Nat. Methods* 14, 713–719. doi: 10.1038/nmeth.4305

Conflict of Interest Statement: The authors declare that the research was conducted in the absence of any commercial or financial relationships that could be construed as a potential conflict of interest.

Copyright © 2019 Aharoni and Hoogland. This is an open-access article distributed under the terms of the Creative Commons Attribution License (CC BY). The use, distribution or reproduction in other forums is permitted, provided the original author(s) and the copyright owner(s) are credited and that the original publication in this journal is cited, in accordance with accepted academic practice. No use, distribution or reproduction is permitted which does not comply with these terms.



Spontaneous and Acetylcholine Evoked Calcium Transients in the Developing Mouse Utricle

Holly A. Holman^{1*}, Lauren A. Poppi^{1,2}, Micah Frerck¹ and Richard D. Rabbitt^{1,3,4}

¹ Department of Biomedical Engineering, University of Utah, Salt Lake City, UT, United States, ² School of Biomedical Science and Pharmacy, Hunter Medical Research Institute, University of Newcastle, Newcastle, NSW, Australia, ³ Neuroscience Program, University of Utah, Salt Lake City, UT, United States, ⁴ Otolaryngology-Head and Neck Surgery, University of Utah, Salt Lake City, UT, United States

OPEN ACCESS

Edited by:

Philippe Isope,
Centre National de la Recherche
Scientifique (CNRS), France

Reviewed by:

Régis Nouvian,
INSERM U1051 Institut des
Neurosciences de Montpellier, France
Adrian Rodriguez-Contreras,
City College of New York (CUNY),
United States

*Correspondence:

Holly A. Holman
holly.holman@utah.edu

Specialty section:

This article was submitted to
Cellular Neurophysiology,
a section of the journal
Frontiers in Cellular Neuroscience

Received: 03 December 2018

Accepted: 12 April 2019

Published: 07 May 2019

Citation:

Holman HA, Poppi LA, Frerck M and
Rabbitt RD (2019) Spontaneous and
Acetylcholine Evoked Calcium
Transients in the Developing Mouse
Utricle. *Front. Cell. Neurosci.* 13:186.
doi: 10.3389/fncel.2019.00186

Spontaneous calcium transients are present during early postnatal development in the mouse retina and cochlea, and play an important role in maturation of the sensory organs and neural circuits in the central nervous system (CNS). It is not known whether similar calcium transients occur during postnatal development in the vestibular sensory organs. Here we demonstrate spontaneous intracellular calcium transients in sensory hair cells (HCs) and supporting cells (SCs) in the murine utricular macula during the first two postnatal weeks. Calcium transients were monitored using a genetically encoded calcium indicator, GCaMP5G (G5), at 100 ms-frame⁻¹ in excised utricle sensory epithelia, including HCs, SCs, and neurons. The reporter line expressed G5 and tdTomato (tdT) in a Gad2-Cre dependent manner within a subset of utricular HCs, SCs and neurons. Kinetics of the G5 reporter limited temporal resolution to calcium events lasting longer than 200 ms. Spontaneous calcium transients lasting 1-2 s were observed in the expressing population of HCs at birth and slower spontaneous transients lasting 10-30 s appeared in SCs by P3. Beginning at P5, calcium transients could be modulated by application of the efferent neurotransmitter acetylcholine (ACh). In mature mice, calcium transients in the utricular macula occurred spontaneously, had a duration 1-2 s, and could be modulated by the exogenous application of acetylcholine (ACh) or muscarine. Long-lasting calcium transients evoked by ACh in mature mice were blocked by atropine, consistent with previous reports describing the role of muscarinic receptors expressed in calyx bearing afferents in efferent control of vestibular sensation. Large spontaneous and ACh evoked transients were reversibly blocked by the inositol trisphosphate receptor (IP₃R) antagonist aminoethoxydiphenyl borate (2-APB). Results demonstrate long-lasting calcium transients are present in the utricular macula during the first postnatal week, and that responses to ACh mature over this same time period.

Keywords: utricle, calcium, hair cell, supporting cell, neuron, GCaMP5G

SIGNIFICANCE STATEMENT

Here, we demonstrate the presence of spontaneous calcium transients in sensory hair cells and supporting cells of the developing mouse utricle, prior to the onset of sensing linear gravito-inertial acceleration. Based on these observations, spontaneous calcium activity in the utricle during development is hypothesized to play a role in maturation of vestibular circuits, similar to the role of spontaneous calcium activity in other sensory organs including the retina and cochlea. We further demonstrate that calcium transients can be modulated by the neurotransmitter acetylcholine by postnatal day 5, thus demonstrating a mechanism hypothesized to close the loop between the sensory organ and the central nervous system during maturation of vestibular pathways.

INTRODUCTION

During development, immature vestibular sensory epithelia include hair cells (HCs), supporting cells (SCs), and undifferentiated precursor cells. In mice, this active developmental period continues during the first two postnatal weeks (Dechesne, 1986; Desmadryl et al., 1986; Burns et al., 2012; Gao et al., 2016). Unique afferent synaptic contacts distinguishing type I vs. type II hair cells (Lysakowski et al., 2011; Warchol et al., 2019) are established during this period. Immature afferent nerve endings either extend to form calyx nerve terminals enveloping the basolateral surfaces of flask-shaped type I hair cells or extend to form bouton terminals on cylindrically-shaped type II hair cells. Evidence suggests that postnatal differentiation of supporting cells adds significant numbers of hair cells to the utricular macula during this period, primarily type II (Warchol, 2007; Kim et al., 2011; Burns and Stone, 2017; Warchol et al., 2019). Gross morphological development of synapses and hair cells precedes mature physiological function as demonstrated by the appearance of hair bundles before mechanoelectrical transduction (MET), and the appearance of afferent calyces surrounding type I hair cells before mature ionic currents (Rüsch et al., 1998; Géléoc and Holt, 2003). The maturation of action potential discharge rate, regularity of discharge inter-spike intervals, and sensitivity to physiological stimulation follows a similar time course as hair cells and synapses reaching mature properties near postnatal day 10 (Curthoys, 1983; Desmadryl and Sans, 1990). During this period, spontaneous bursts of action potentials occur in vestibular ganglion neurons in the absence of gravito-inertial stimulation, thereby providing inputs to vestibular pathways in the central nervous system (CNS). At the same time, efferent synaptic contacts on HCs and afferent nerves are maturing in the vestibular sensory epithelium providing a route for the CNS to modulate excitability and action potentials (Favre and Sans, 1977, 1978; Desmadryl and Sans, 1990; Sans and Scarfone, 1996; Lysakowski, 1999; Kharkovets et al., 2000; Demêmes et al., 2001; Hurley et al., 2006; Sienknecht et al., 2014). How spontaneous vestibular afferent nerve activity is generated, if it is modulated during postnatal development by efferent action, and what role it might play in establishing functional vestibular physiology are as yet unknown.

Like vestibular ganglion neurons, cochlear spiral ganglion neurons in mice exhibit spontaneous action potentials at birth. Spiral ganglion activity occurs before the onset of hearing, and is important to establish tonotopy in the CNS and functional hearing (Lippe, 1994; Kotak and Sanes, 1995; Kros et al., 1998; Glowatzki and Fuchs, 2000; Beutner and Moser, 2001; Tritsch et al., 2007; Sendin et al., 2014). In early postnatal mouse development, spontaneous firing in spiral ganglion neurons is driven by calcium action potentials in auditory inner hair cells (IHCs) (Lippe, 1994; Beutner and Moser, 2001; Glowatzki and Fuchs, 2002; Marcotti et al., 2003; Tritsch et al., 2010; Johnson et al., 2011; Jones and Jones, 2011). Hair cell activity is spontaneous, but modulated by purinergic signaling from supporting cells in Kölliker's organ and by cholinergic signaling from olivocochlear efferent neurons (Zhao et al., 2005; Roux et al., 2011; Zhu and Zhao, 2012; Johnson et al., 2013). Blocking this activity disrupts the fine synaptic organization at all levels in the auditory pathway (Hashisaki and Rubel, 1989; Sanes and Siverls, 1991; Kotak and Sanes, 1995; Rubel and Fritzsche, 2002; Cao et al., 2008; Seal et al., 2008). In the auditory system, calcium currents and intracellular signaling established developmentally are essential substrates of this crucial process (Chabbert, 1997; Kros et al., 1998; Glowatzki and Fuchs, 2000; Marcotti et al., 2003; Katz et al., 2004). Like cochlear IHCs, cells in immature vestibular epithelia express the machinery required to generate spontaneous calcium-dependent activity (Marcotti et al., 2003; Levic et al., 2007), but it is not known if spontaneous activity occurs in vestibular HCs or neighboring SCs during postnatal development, or if calcium transients might play a role in maturation of vestibular sensitivity or neural circuits.

Here, we present direct evidence that spontaneous intracellular calcium transients $[Ca^{2+}]_i$ are present in vestibular HCs, SCs, and neuronal terminals in the first postnatal week of the developing mouse utricle. The genetically encoded reporter GCaMP5G was used to monitor calcium activity, and hence results reflect events detectable by this calcium indicator. Spontaneous calcium transients were present at birth in HCs, followed by spontaneous calcium transients in SCs and subsequently neuronal terminals. We further demonstrate that $[Ca^{2+}]_i$ transients in the utricular macula could be modulated by the efferent neurotransmitter ACh, as soon as postnatal day 3.

MATERIALS AND METHODS

Animals and Strains

All animal experiments were approved by the Institutional Animal Care and Use Committee (IACUC) and conducted at the University of Utah in accordance with NIH guidelines. In the present work we used the wild-type strain C57BL/6J and two transgenic mouse lines: a dual Cre-dependent reporter Polr2a-based GCaMP5G-IRES-tdTomato, referred to as PC::G5-tdT (Gee et al., 2014) and a Gad2-IRES-Cre knock-in mouse driver line referred to as Gad2::Cre (Taniguchi et al., 2011). Both breeding pairs were obtained from The Jackson Laboratory [Polr2a^{tm1(CAG-GCaMP5g-tdTomato)}Tvrd <http://jaxmice.jax.org/strain/024477>; Gad2^{tm2(cre)Zjh} <http://jaxmice.jax.org/strain/010802>]. First generation heterozygous offspring were used

in these studies and hereafter referred to as Gad2-G5-tdT. Pups were genotyped using real time PCR (probes: “Polr2a-3”, “GCamp3-1 Tg”, and “tdRFP”; Transnetyx, Inc., Cordova, TN).

Histological Preparation and Fixed Tissue Imaging

Mice of either sex at early postnatal ages (P1-P15) and adult controls (P73-P533) were used in this study. For immunohistological preparations, membranous labyrinths were harvested and immersion fixed in 4% paraformaldehyde overnight at 4°C. Whole mount utricle neuroepithelia were micro dissected, including the removal of otoconia, using fine forceps in 0.1 M phosphate-buffered saline (PBS) (Dumont #5, #55; Leica, M165 FC).

Whole Mount Preparation

Membranous labyrinths were incubated transiently three times in 0.1M PBS to remove residual aldehydes, followed by incubating in a blocking/permeabilization buffer [10% normal serum specific to the antisera (i.e., donkey or goat), 1% BSA, 0.5% Triton X-100 in 0.1M PBS] for 1-2h on a nutating rocker platform at room temperature (RT). Tissues were subsequently incubated overnight at 4°C with a combination of the following primary antisera: anti-Atoh1 (SAB2100177, Sigma); anti-SOX2 (sc-365823, Santa Cruz); anti-Myosin-VIIa (25-6790, Proteus Biosciences). A monoclonal mouse anti-Tubulin β 3 antibody conjugated with AlexaFluor® 647 was used at a dilution of 1:500 and included during primary antisera incubation (BioLegend cat# 801209). Tissues were subsequently rinsed three times for 15 min in 0.1M PBS, then placed in fresh blocking buffer and incubated for another 1 h at RT with secondary antisera conjugated to either AlexaFluor® [donkey anti-rabbit IgG H&L 405 nm (ab175651), DyLight™ [405 nm (cat# 35550), or 488 nm (cat# 35552)], Thermo Scientific, Inc.]. After incubations with secondary antisera, tissues were gently rinsed three times in PBS, placed onto glass bottom dishes (MatTek) submerged in PBS for confocal imaging (Olympus, FV1000). Z-stacks were acquired using a 5X air (N.A. 0.1), 40X water (N.A. 0.8), or 60X water (N.A. 1.0) objective with a digital zoom up to 3, and aspect ratio of 620 x 620 pixels.

Cryostat Sectioned Preparation

Intact bony labyrinths from P15 mice were harvested, and immersion fixed in 4% paraformaldehyde overnight at 4°C. Fixed intact labyrinths were placed in 5% EDTA in 0.1M PBS at RT and checked daily for decalcification and softening (up to 5 days). Once the bony labyrinths were pliable they were removed from EDTA, rinsed in fresh 0.1M PBS, and placed in a solution of 30% sucrose in 0.1M PBS to cryo-protect tissue. When tissues were no longer buoyant in the sucrose solution they were placed in a 1:1 solution of 30% sucrose: OCT for infiltration for ~1 h. Each labyrinth was placed in a mold containing OCT and oriented so that the oval window was facing up and basilar membrane was perpendicular to the bottom surface of the mold. Molds were frozen on dry ice and wrapped in parafilm to prevent evaporation until sectioning (Leica CM3050s; Prof Altschuler's laboratory, University of Michigan). Sections

of 10–15 μ m were collected on electrostatically charged slides (Superfrost™ Plus Slides, Fisher). Slides were kept at –20°C until processed for immunohistochemistry. Regions of tissues were optically examined and areas of interest were circled using a hydrophobic pen (Z377821, Sigma) and allowed to dry. Tissues were rehydrated in 0.1M PBS for 20 min and permeabilized in 0.1% Triton-X (PBS) for 20 min at RT. Permeabilization buffer was carefully removed and primary antisera (as described in the whole mount preparation section above) were added in fresh permeabilization buffer and incubated for 2 h at 37°C. Slides were rinsed in 0.1M PBS three times for 10 min with gentle rocking. Secondary antisera dilutions were added to tissues and incubated for 1 h at RT and subsequently rinsed in PBS as described for primary antisera. Finally mounting media was added and coverslips placed over tissues and allowed to dry at RT overnight. Images were obtained on Olympus FV1000 using a 60X oil immersion confocal microscope, images were post processed in FluoRender, and formatted for publication in Adobe Illustrator.

Live Tissue Imaging and ACh Stimulation

Membranous labyrinths were micro-dissected from Gad2-G5-tdT temporal bones (P1-P15; and adults up to age P533), in cold glycerol-modified Ringer's (in mM: 26 NaHCO₃, 11 glucose, 250 glycerol, 2.5 KCl, 1.2 NaH₂PO₄, 1.2 MgCl₂ and 2.4 CaCl₂; pH 7.4) (Rabbitt et al., 2016). The utricle, horizontal and anterior cristae were further dissected to expose the apical surfaces of sensory neuroepithelia (Lim et al., 2011). Tissues were transferred to an imaging chamber (Warner Instruments; RC-22C) and continuously perfused with buffer (5.8 KCl, 144 NaCl, 0.9 MgCl₂, 1.3 CaCl₂, 0.7 NaH₂PO₄, 5.6 glucose, 10 HEPES, 300 mOsm, pH 7.4) at 21°C (Sadeghi et al., 2014). The recording chamber was placed under an upright swept field confocal microscope (Bruker; Prairie SFC), and imaged with a water immersion 60x objective (Olympus, LUMPLFN60XW). Confocal images were collected using a 35 μ m slit aperture in linear galvanometer mode, and a 512 × 512 detector (Photometrics, Rolera MGi Plus EMCCD) providing in-plane single pixel size of 0.27 × 0.27 μ m. For G5 detection and tdT expression imaging, 488 and 561 nm lasers, respectively, were interleaved for excitation, and a blocking filter (Semrock, R405/488/561/635-25) was used for detection. For G5 fluorescence calcium imaging, excitation was limited to 488 nm and the detection filter was replaced with a band pass filter (Semrock 525/50-25) to block any residual tdT emission at the 488 nm excitation wavelength. A pressure driven perfusion system configured with a micro-manifold (ALA Scientific Instruments, VC3-4PP, uflow-4) was used to continuously perfuse the tissue with control media, or 100 μ M–1 mM ACh, 100 μ M muscarine, 50 μ M of the membrane permeable D-myo-inositol trisphosphate receptor (IP₃R) antagonist 2-aminoethoxydiphenyl diphenylborinate (2-APB, Sigma), or 5 μ M muscarinic cholinergic receptor antagonist atropine (ATR). A computer controlled micro-manifold system was used to rapidly switch between media, ACh, 2-APB or ATR. The SFC confocal, stage position (Scientifica), and perfusion system (ALA, VM4) were controlled and monitored at 10 kHz by custom software (WaveMetrics, Igor) via AD hardware (Heka, ITC-18), IEEE-488 instrumentation interface (National

Instruments, GPIB-USB; Sony/Tektronix, AFG-320) and serial interface (USB).

Experimental Design and Statistical Analysis

G5 fluorescence was imaged at each “z” focal depth in a time sequence with images collected before, during, and after each ACh puff. Unless otherwise noted, image sequences consisted of 600–1,000 frames collected at 10 frames per second. The puff of each drug was delivered 10 s after initiating the sequence for a duration of 500 ms, unless otherwise noted. The image acquisition time sequence and ACh stimulus was repeated for each z focal depth (x,y,z) to generate 4D XYZT image stacks. Each xy image was smoothed in (x,y) space with a 3 pixel Gaussian filter (WaveMetrics, Igor Pro). To correct motion artifact, time-sequences at each focal plane were registered prior to analysis for full image rotation and translation (Thévenaz et al., 1998). G5 fluorescence modulation was determined pixel-by-pixel using $\Delta F/F_{\min}$, where $\Delta F = F(t) - F_{\min}$, and F_{\min} was the minimum fluorescence intensity pixel-by-pixel over the entire time sequence of images. Image processing and pseudo-color images were generated in Igor Pro (WaveMetrics). Statistical significance of differences in the mean between groups was determined using Student's *t*-test with $p = 0.05$. All population data were presented as a mean \pm standard error of the mean (SEM).

RESULTS

Characterization of the Gad2-G5-tdT Transgenic Mouse Vestibular System

At the earliest age examined in this study, postnatal day 1 (P1), a unique population of developing HCs and SCs express the transgene tdTomato (tdT) (Figure 1). These tdT expressing cells map to the extrastricular regions of the otolithic organs in all first generation heterozygous animals. A maximum intensity projection (MIP) from confocal images taken through seventy-microns of the utricle and saccule (1 μ m per slice) shows tdT expressing cells primarily in the extrastricular region of the utricle and saccule in Gad2-G5-tdT mice at P1 (Figure 1A; Olympus FV100, 40XW obj). Immunolabeling was performed with the SC marker, SOX2, and the developmental HC differentiation marker, ATOH1, to further identify the tdT expressing cell types at P1 in the utricle (Figure 1B). One of the distinguishing morphological features of HCs and SCs during early postnatal developmental stages are their mosaics, which coincide with the Delta-Notch signaling (Figures 1B,C). Immunolabeling with SOX2 antibody revealed a mosaic pattern with six SCs surrounding a single HC (white arrows) by age P1 in the utricle (Figure 1B, green). During this early postnatal age, the tdT expressing cells immunolabeled with ATOH1 (Figure 1B, blue), but not SOX2, suggesting that at P1 these cells constitute a more sensory hair cell function (Figure 1B, blue). By postnatal day 15 (P15), tdT expressing cells (Figure 1C, red) remained predominantly sensory HCs (Figure 1C, myosin VIIa blue). SCs immunolabeled with SOX2 also showed tdT fluorescence, but at a low level relative to HCs

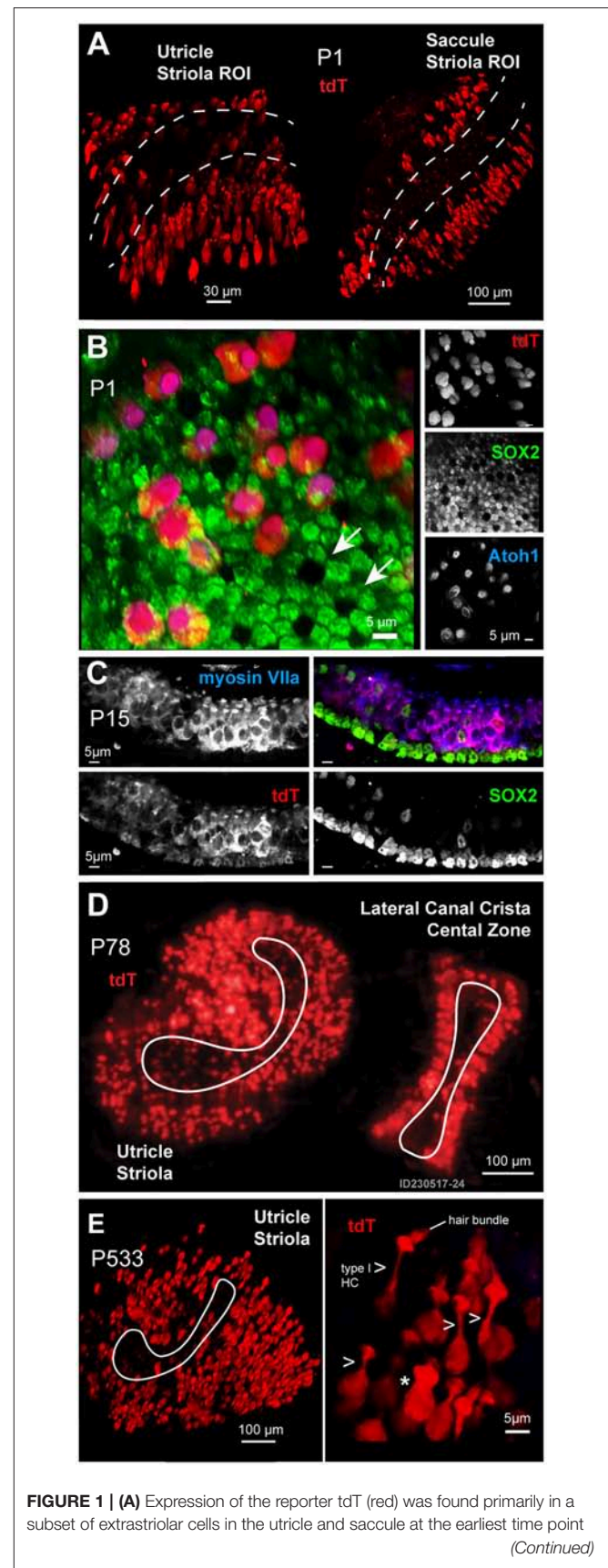


FIGURE 1 | (A) Expression of the reporter tdT (red) was found primarily in a subset of extrastricular cells in the utricle and saccule at the earliest time point (Continued)

FIGURE 1 | examined, postnatal day 1 (P1). Images are maximum intensity projections (MIPs) from 70 μm z-stacks through excised tissues. The striola in both the utricle and saccule are outlined with dotted lines. **(B)** Cells expressing tdT (red) at P1 immunolabeled with an antibody against ATOH1 (blue) and were identified as immature hair cells (HCs), while supporting cells (SCs) immunolabeled with an antibody against SOX2 (green). **(C)** By age P15, tdT (red) expressing cells immunolabeled with myosin VIIa (blue), with a few tdT negative hair cells immunolabeled with the SOX2 antibody (green). **(D,E)** Cells expressing tdT (red) had a flask-shaped morphology (arrows) and maintained their extrastricular location within the utricle in adults **(D: P78)** and geriatric ages **(E: P533)**.

(**Figure 1C**). The extrastricular HCs and SCs expressing tdT by the end of the first two postnatal weeks persisted throughout adulthood. This extrastricular tdT cell population is illustrated in a low magnification (SFC, 10X air obj) image of live tissue excised from an adult mouse (**Figure 1D**, P78) (**Figure 1D**). At the oldest age examined in the present study, postnatal day 533 (P533), tdT expressing cells maintained their extrastricular location in the utricle. A representative image fixed whole mount utricle is shown from 110 μm confocal z-stack MIP where an ROI is centered on the utricle striola (white outline; **Figure 1E** Olympus FV1000, 40XW obj). Cells with prevalent tdT expression have hair bundles, although not all hair bundles are visible in the surface preparation shown. Two main cell morphologies among these tdT expressing cells were observed in mature tissue; cells with a long neck and hair bundles typical of type extrastricular I HCs (arrows; 7 cells in ROI shown; **Figure 1E**, right panel); and a small number of cells lacking the characteristic long neck. This small subset of cells was not positively identified in the present study, and could be atypical shaped type I HCs, type II HCs, or other cell types.

Spontaneous Calcium Transients in Hair Cells at Birth

Spontaneous G5 $\Delta F/F_0$ transients ($[\text{Ca}^{2+}]_i$ transients) were observed in tdT expressing HCs at P1 ($n = 166$ cells analyzed; $k = 3$ P1 mice; see **Supplement Video 1**). G5 transients were imaged in excised utricles, with the confocal focal plane imaging transversely through the epithelium (**Figures 2A–D**). The minimum G5 fluorescence over all images in the time sequence was used to define the pixel-by-pixel resting G5 fluorescence, shown within one imaging plane (F_0 ; **Figure 2A**; blue). After recording time sequences of G5 fluorescence modulation, tdT was imaged with 60 confocal planes to reconstruct reporter-expressing cells in **Figure 3D**. Cells expressing tdT in **Figure 2A** were identified as immature HCs based upon their morphology and immunolabeling (**Figure 1**). HCs are rendered as orthographic projections (**Figure 2A** i, ii) viewed perpendicular to the G5 confocal slice. HCs with high resting G5 fluorescence (**Figure 2A**, blue) also had abundant tdT expression (**Figure 2A**, red & white), indicating that resting G5 fluorescence in HCs primarily reflects expression of the reporter rather than high resting $[\text{Ca}^{2+}]_i$ in these cells. Three example HCs (1–3) exhibiting the largest spontaneous $[\text{Ca}^{2+}]_i$ transients in this tissue are rendered white to highlight their morphology and location (**Figure 2A**; i,ii). These same three HCs (**Figure 2A**; G5

F_0 , blue) are outlined in the orthogonal cross-section (**Figure 2A** i,ii) with solid white outlines (**Figure 2F**; 1–3) to define regions of interest (ROIs) for fluorescence modulation analysis. Two additional modulating HCs are outlined with white dashed outlines in one optical focal plane (**Figure 2A**; 4–5), but not rendered white in the 3D stacks.

$[\text{Ca}^{2+}]_i$ transients were tracked in time by computing $\Delta F/F_0$ pixel-by-pixel within outlined ROIs for each frame (1000 frames at 100 ms frame⁻¹). **Figure 2B**, shows the maximum $\Delta F/F_0$ the over an example 100 s imaging sequence in this tissue. Of 35 HCs exhibiting resting G5 fluorescence in **Figure 2** (F_0 blue), an average of $5.4 (\pm 1.46)$ cells per $138 \times 138 \mu\text{m}^2$ focal plane exhibited spontaneous $[\text{Ca}^{2+}]_i$ transients ($\Delta F/F_0 > 0.5$) within each 100 s image acquisition sequence. In the present report, we use the term “spontaneous” in reference to events in the baseline control condition, distinct from stimulus evoked modulation relative to the baseline condition. It is important to acknowledge that baseline spontaneous events observed in excised tissue depend on history and condition of the preparation, which differ from physiological conditions the cell may experience *in vivo*. Spontaneous $[\text{Ca}^{2+}]_i$ transients in utricular HCs excised from P1 mice were not synchronized with each other, and occurred in different cells at different times (see **Supplement Video 1**). G5 $\Delta F/F_0$ transients were largest in magnitude near the plasma membrane, leading to a ring of increased $\Delta F/F_0$ near the membrane when imaged in cross section (**Figure 2B**; 1,2,4,5 examples). Although only 16% of 166 P1 HCs examined with prominent tdT expression exhibited spontaneous transients with $\Delta F/F_0 > 0.5$, 87% percent exhibited spontaneous transients at P1 with $\Delta F/F_0 > 0.2$ in at least one image during the sequence, indicating relatively rapid but small $[\text{Ca}^{2+}]_i$ fluctuations were likely present in the majority of utricular HCs expressing G5 at birth. $[\text{Ca}^{2+}]_i$ transients lasting only one frame were likely due to events shorter than the 100 ms exposure time and too fast to be resolved by the kinetics of the G5 fluorescent signal used in the present study (Podor et al., 2015). Temporal events with a half width < 1 s (10 frames) were not analyzed in the present report.

Spontaneous calcium transients are shown in **Figure 2C** for the 5 specific HCs highlighted in **Figures 2A,B**. Waveforms provide the peak $\Delta F/F_0$ within each outlined cell. Transients at birth consisted of small calcium increases, which we refer to as short “S” transients with characteristic waveforms (**Figures 2C–F**: 1S, 2S, 5S), large events with complex temporal waveforms (**Figure 2C**: 1L, 2L, 3L), and multiple medium size events falling between the two extremes. Other time sequences in this same tissue, and sequences from utricles excised from other P1 mice, also revealed 0–7 HCs with large and small spontaneous $[\text{Ca}^{2+}]_i$ transients within each $138 \times 138 \mu\text{m}^2$ image plane. Additional spontaneous transients are shown in **Figure 2E**, arranged front to back by maximum $\Delta F/F_0$, with cells from panel C shown in the same colors. Spontaneous HC $[\text{Ca}^{2+}]_i$ transients rising above the background fluorescence fluctuation occurred with an average rate of $0.035 \text{ s}^{-1} (\pm 0.026)$ in P1 mice. Small events had a rise time to peak of $0.659 \text{ s} (\pm 0.062)$, a half width of $1.26 \text{ s} (\pm 0.075)$, and a decay time of $3.80 \text{ s} (\pm 0.297)$. Large transients “L” emerged from the background with a steep slope, consistent with the rise of S events, and had multiple peaks and jagged

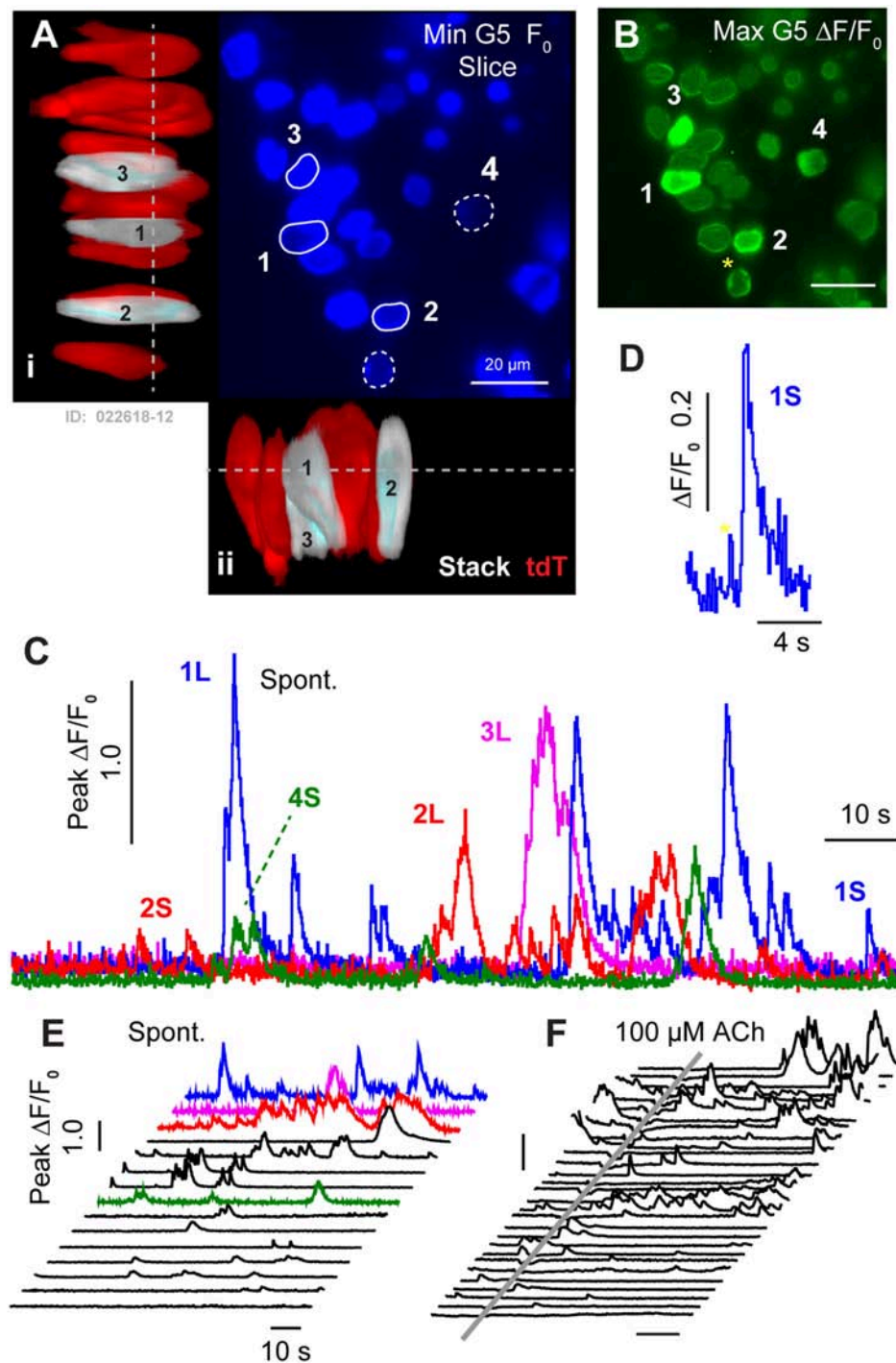


FIGURE 2 | Spontaneous $[Ca^{2+}]_i$ transients in utricular HCs at P1. **(A)** Resting G5 fluorescence in HCs (F_0 , blue) in a plan view optical slice, and orthographic projections through the thickness of the epithelium showing expression of tdT (red & white) in HCs. Nominal Z-focus of the plan view is indicated with dashed lines. Three highlighted HCs exhibiting $\Delta F/F_0$ transients are pseudo-colored white (1–3). ROIs surrounding 5 cells are shown (white curves, 1–5). **(B)** Spontaneous $[Ca^{2+}]_i$ transients (peak G5 $\Delta F/F_0$ over 100 s, green) in tdT-expressing HCs, sampled at ten frames per second. SCs lacking resting G5 fluorescence did not exhibit detectable spontaneous transients at P1. The largest $[Ca^{2+}]_i$ transients in HCs were located near the plasma membrane (e.g., 4*). **(C)** $\Delta F/F_0$ transients were complex in temporal waveform, as if consisting of the superposition of **(D)** small "S" events and large "L" calcium transients. **(E)** Spontaneous $\Delta F/F_0$ transients in HCs arranged by increasing magnitude, with colors corresponding to cells in **(A–C)**. **(F)** Application of ACh did not increase the rate or size of $\Delta F/F_0$ transients (arranged by increasing of $\Delta F/F_0$). Time near ACh application was blocked by optical interference from the wash. See **Supplement Video 1**.

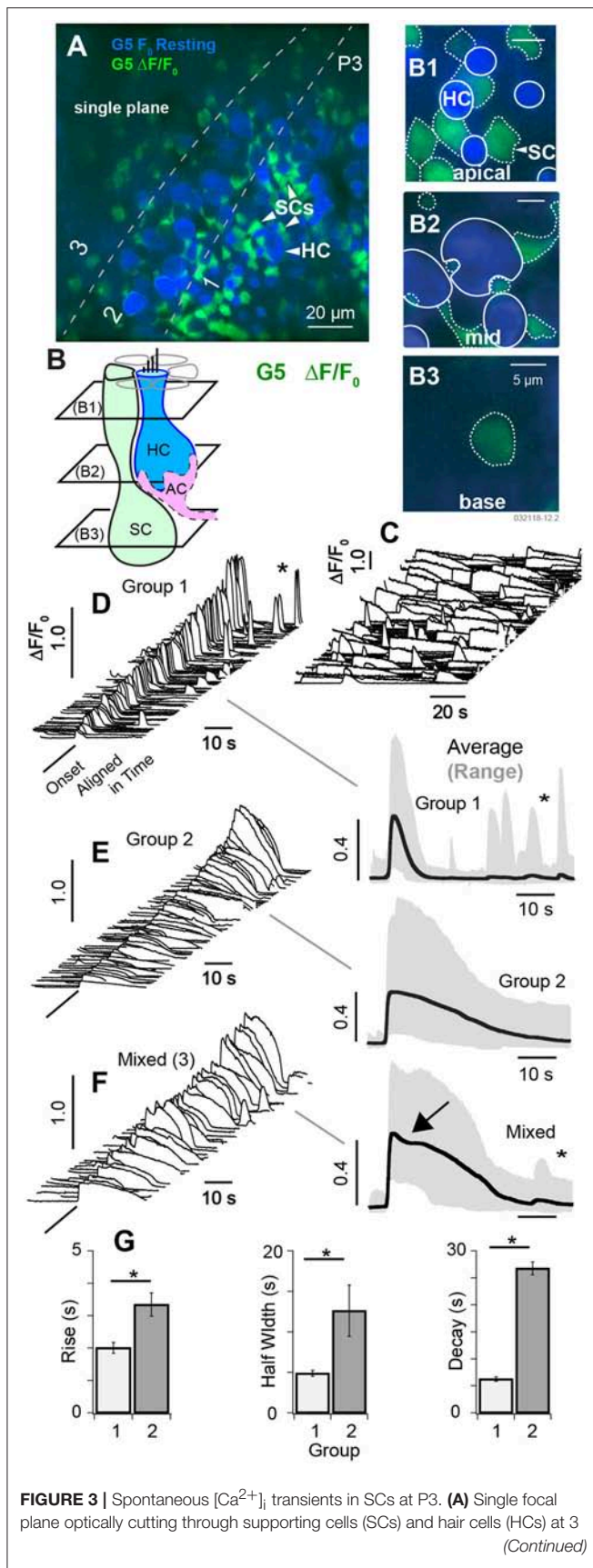


FIGURE 3 | depths in the tissue (1: apical region, 2: central region, 3: below HCs). Resting, G5 fluorescence (F_0 blue) and G5 $\Delta F/F_0$ transients (green) are superimposed. **(B)** Cartoon depicting 3 optical slices through SCs (**B1–B3**) and two through HCs (**B1,B2**). The apical region of SCs and HCs (**B1**), the middle region of SCs and HCs (**B2**), and the base of SCs (**B3**). Large spontaneous $\Delta F/F_0$ $[Ca^{2+}]_i$ transients were present in SCs, most easily identified by their hexagonal patterning around the apical necks of HCs (**A,B1**). Solid white outlines show HC ROIs with large resting fluorescence, and dotted white lines show ROIs with large $\Delta F/F_0$ transients. **(C)** Example spontaneous $\Delta F/F_0$ transients sampled at 10 frames per second unaligned in time. **(D–F)** Spontaneous $\Delta F/F_0$ transients aligned in time and sorted by duration, magnitude, and waveform. $\Delta F/F_0$ transient waveforms show the average within $5\mu m$ ROIs centered on individual cells. **(D)** Group 1 short $[Ca^{2+}]_i$ transients with duration $<10s$. Traces on the right show population averages (black) and range (gray). **(E)** Group 2 transients with durations $>10s$. **(F)** Mixed transients with some events showing an inflection point just after the peak $\Delta F/F_0$ (arrow). **(G)** Population statistics over all $\Delta F/F_0$ transients from P3 aged mice showing the rise time, half width, and decay time by group. See **Supplement Videos 2–4**. $*p = 0.05$.

waveforms consistent with the hypothesis that large events might have resulted from the summation of multiple small S events occurring at different times within each HC. If large transients indeed occurred due to a superposition or burst of S events (**Figures 2E,F, 3G**), the rate of spontaneous Q events would be predicted to have occurred at an average rate of $2.19 s^{-1}$ (± 2.74 ; range 0–4.6). $[Ca^{2+}]_i$ transients recorded in P1 HCs appeared to be “spontaneous”, and did not synchronize with each other in time. We were also unable to detect synchronization or modulation of HC $[Ca^{2+}]_i$ transients at P1 by ACh. This is illustrated by comparison of spontaneous transients (**Figures 2E,F**; independent experiments) to transients in after a 500 ms puff application of $100\mu M$ ACh (**Figure 2F**) in the same tissue, where the time average $\Delta F/F_0$ was not changed by ACh. Data during ACh application was blocked due to image distortion caused by the fluid motion. Although, previous reports suggest METs can be functional as early as embryonic development (Géléoc and Holt, 2003), we did not detect fluid jet evoked G5 fluorescence modulation at P1, suggesting HC MET currents in this preparation were either not functional or insufficient to evoke $[Ca^{2+}]_i$ transients detectable by the G5 indicator at P1.

Spontaneous Calcium Transients at P3

At postnatal day P3, spontaneous $[Ca^{2+}]_i$ transients observed in HCs were largely superseded by a period of spontaneous $[Ca^{2+}]_i$ activity in cells with low resting G5 fluorescence consisting primarily of SCs (see **Supplement Videos 2, 3**). **Figure 3A** shows a single confocal slice cutting through HCs, SCs, and immature afferent calyces (AC). Using the same color format as **Figure 2**, the minimum fluorescence over the 100 s time sequence of images was used to define the resting fluorescence (**Figures 3A,B**, min F_0 ; blue), and the change in fluorescence ($\Delta F/F_0$, green) was used to track changes in $[Ca^{2+}]_i$, with **Figures 3A,B** showing the superposition of the two. The confocal optical slice was tilted relative to the epithelium in this tissue, cutting through the apical necks of hair cells in zone 1 (**Figures 3A,B1**), basolateral region in zone 2 (**Figures 3A,B2**), and below hair cells in

zone 3 (**Figures 3A,B3**). Over 160 cells exhibited detectable G5 fluorescence in each $138 \times 138 \mu\text{m}^2$ image and, of these, 97 (± 19.6) cells per focal plane exhibited G5 spontaneous calcium transients (874 events per experiment). SCs were easily identified in apical regions of live tissue based on their hexagonal spatial patterning around HCs (**Figure 3B**, also see **Figure 1**). Solid white lines in **Figure 3B1** show HC ROIs with high resting G5 fluorescence (blue) while dotted white lines show SC ROIs with relatively low resting G5 fluorescence, but high $\Delta F/F_0$ transients (green). Type I HCs were identified based on their relatively high G5 resting fluorescence (blue) and tdT expression (e.g., **Figure 1**), as well as their characteristic morphology. Although $\Delta F/F_0$ transients were observed near the plasma membrane of some HCs, these events did not extend into HC somata. The spatial resolution was insufficient in the present imaging paradigm to determine if these localized events were in HCs or adjacent cells. Spontaneous G5 $\Delta F/F_0$ transients were present at all focal depths, including below HCs. Although spontaneous G5 transients in the apical zone (A1,B1) were clearly localized in SCs at P3, SCs could not be positively distinguished from other key cell types at deeper focal planes, leaving open the possibility that some spontaneous transients might also be present in afferent neurons or calyces (ACs) at P3 as well.

In utricles excised from P3 mice, spontaneous transients were not synchronized with each other and occurred in different cells at different times (**Figure 3C**, **Supplement Videos 2, 3**). Transients were divided into 2 groups for statistical analysis based on kinetics of the G5 $\Delta F/F_0$ temporal waveforms. Group 1 transients were distinguished by their relatively short duration (<10 s) relative to Group 2. A third set of ROIs (3) had mixed $[\text{Ca}^{2+}]_i$ transients characterized by an inflection point (**Figure 3E**, arrow), and possibly arising from fluorescence events from $\Delta F/F_0$ reporting a combination of two events with different waveforms occurring within the same ROI or from distinct calcium kinetics (Taheri et al., 2017). Example events are shown in **Figures 3D–F** (left), aligned in time and arranged in increasing $\Delta F/F_0$ magnitude. Population averages are shown on the right, and population statistics are summarized in **Figure 3G**. Short duration Group 1 transients (**Figure 3C**) had an average rise time of 1.96 s, half width of 4.31 s, decay of 6.00 s and peak $\Delta F/F_0$ of 0.44 (data not shown). Long duration Group 2 transients had an average rise time of 2.76 s, half width of 11.7 s, decay of 25.3 s and peak $\Delta F/F_0$ of 0.40 (**Figure 3G**). Mixed (3) transients had an average rise time of 2.98 s, half width of 18.8 s, decay of 27.2 s (**Figure 3G**); and peak $\Delta F/F_0$ of 0.42 consistent with a superposition of events from groups 1 and 2 (data not shown). Transients in each group occurred with similar $\Delta F/F_0$ magnitude and could not be distinguished from each other based on $\Delta F/F_0$ magnitude alone. Occurrence of long transients (56%) modestly outnumbered short transients (44%). There was no detectable correlation between any group and focal depth in tissue at P3 (B1–B3 depths). Group 1 events were more likely to reoccur during the imaging, sequence leading to a second peak in time-domain traces (**Figure 3C**, *). The average rate of spontaneous short events (Group 1) occurring within a single cell was 0.044 s^{-1} (± 0.043) and long events within a single cell was

0.016 s^{-1} (± 0.0035). Since $\Delta F/F_0$ transients at the apical surface were clearly identified as SCs, the lack of correlation with focal depth suggests $\Delta F/F_0$ transients might have been dominated by SCs at all focal depths through the epithelium in P3 aged mice (see **Supplement Video 2**). However, there were numerous exceptions at P3, based primarily on morphology, where spontaneous $[\text{Ca}^{2+}]_i$ transients likely occurred in other cell types including HCs, ACs, or other terminals at the base of HCs (see **Supplement Videos 3,4**).

We applied $50 \mu\text{M}$ 2-APB to block spontaneous $[\text{Ca}^{2+}]_i$ transients in SCs of P3–5 aged mice B ($k = 3$ mice). Example G5 F_0 and $\Delta F/F_0$ are provided in **Figure 4** in the control condition (A: resting F_0 , gray and B: $\Delta F/F_0$, green), blocked condition (C: $\Delta F/F_0$, red), and after wash (D: $\Delta F/F_0$, blue). G5 $\Delta F/F_0$ transients were reduced more than 5 fold after application of the IP₃R antagonist 2-APB. G5 $\Delta F/F_0$ images were merged (**Figure 4E**) to reveal specific cells that lost spontaneous $[\text{Ca}^{2+}]_i$ modulation after application of 2-APB. A vast majority of SCs had a complete cessation of $\Delta F/F_0$ transients in the presence of the antagonist as evidenced by the near absence of overlap between the red and green fluorescent channels (**Figure 4E**, overlap = yellow). Although washout was incomplete, a subset of SCs clearly recovered spontaneous $\Delta F/F_0$ transients (**Figure 4E**, recovery=blue-green, e.g., insets i & ii). SCs are arranged in canonical patterns of 6 around the necks of HCs, corresponding to the locations of SC $\Delta F/F_0$ transients (**Figure 4E**, i). A subset of cells continued to show low-intensity spontaneous $\Delta F/F_0$ transients in the presence of $50 \mu\text{M}$ 2-APB (**Figures 4C,E**, red). Although the precise identity of these cells is uncertain due to their developmental age and the likelihood that they are actively undergoing differentiation, modulating $\Delta F/F_0$ domains often localized with tdT positive HCs at their base (e.g., **Figure 4E** i & ii R), suggesting potential origins in other cell types, possibly HCs or developing ACs at this age. On average, the few $[\text{Ca}^{2+}]_i$ transients that remained in the presence of $50 \mu\text{M}$ 2-APB were relatively small and slow compared with pre-treatment control conditions. Specific examples are shown in **Figure 4F**, with average transients for all cells in the control condition compared with 2-APB treated cells in **Figure 4G**. Averages in the control condition are shown for $[\text{Ca}^{2+}]_i$ transients lasting <10 s (Group 1) and for transients lasting >10 s (Group 2). Population statistics comparing responses in the control condition vs. in the presence of 2-APB are provided in **Figure 4H**. Group 1 events in the control condition for mice tested with 2-APB (**Figure 4**, P3–P5) were slightly faster than Group 1 events at P3 (**Figure 3**), but this study did not determine if this was due differences in maturation or some other unidentified factor. Compared to Group 1 events in the control condition, $[\text{Ca}^{2+}]_i$ transients in the presence of 2-APB had a reduced peak $\Delta F/F_0$ (0.44 ± 0.21 vs. 0.11 ± 0.023), increased decay time (5.99 ± 0.45 vs. 26.26 ± 2.84 s), with no statistically significant difference in rise time. Compared to Group 2 events in the control condition, $[\text{Ca}^{2+}]_i$ transients in the presence of 2-APB had a reduced peak of $\Delta F/F_0$ (0.41 ± 0.24 vs. 0.11 ± 0.023), a reduced rise time (3.14 ± 0.43 vs. 1.56 ± 0.26 s), with no significant difference in half width or decay time. These results demonstrate that 2-APB interferes with spontaneous $[\text{Ca}^{2+}]_i$ transients, significantly reducing the

magnitude of all events and reducing the number and kinetics of short duration $[Ca^{2+}]_i$ transients in multiple developing cell types. Antagonist action of 2-APB on IP_3R is sufficient to explain these results through disruption of CICR. However, the present experiments did not completely rule out other hypothetical $[Ca^{2+}]_i$ mechanisms, which is the focus of future studies.

At postnatal day P5, $\Delta F/F_0$ $[Ca^{2+}]_i$ transients were similar to those observed in P3 mice (Figure 3), but significantly fewer in number, occurring in only $4.7 (\pm 1.8)$ cells per $138 \times 138 \mu m^2$ focal plane. Figure 5 provides example data recorded at a single focal plane (Figures 5A–J), and with population statistics across animals (F–H: $n = 75$ cells; $k = 3$ mice). Using the same approach as earlier ages, spontaneous $[Ca^{2+}]_i$ $\Delta F/F_0$ transients at P5 were grouped based on duration, with cells having $\Delta F/F_0$ duration <10 s placed in Group 1 and others placed in Group 2 (Figures 5E–H). Similar to P3 aged mice, these two groups at P5 had similar $\Delta F/F_0$ peak magnitudes (Group 1 0.19 ± 0.04 vs. Group 2 0.20 ± 0.03 ; Figure 5F), but statistically significant differences in kinetics (Figures 5G–H). Compared to events in Group 1 transients in Group 2 had a slower rise time (1.32 ± 0.17 vs. 3.56 ± 0.49 s; Figure 5G), increased half width (4.59 ± 0.68 vs. 17.7 ± 1.75 s; data not shown), and longer decay times (8.88 ± 2.22 vs. 19.9 ± 1.79 s; Figure 5H). Smaller $\Delta F/F_0$ events approaching the kinetics of G5 resolution occurred in some cells from both groups (C1, D2, arrows). Although the small events sometimes appeared before the large $[Ca^{2+}]_i$ transients, most large transients were not preceded by detectable small events suggesting the small $[Ca^{2+}]_i$ transients are not likely to be required precursors. Both types of $[Ca^{2+}]_i$ transients occurred spontaneously in the control condition, at random times in the imaging sequence. This is illustrated in Figure 5E where individual traces recorded in one focal plane show $\Delta F/F_0$ transients from individual cells. Domains exhibiting spontaneous transients in utricles from P5 mice were often complex in morphology and contacted the basolateral membranes of HCs, similar to domains showing spontaneous transients near the base of HCs at earlier ages.

Development of ACh Evoked $[Ca^{2+}]_i$ Transients

Although ACh application did not evoke G5 detectable $[Ca^{2+}]_i$ ($\Delta F/F_0$) transients in utricles from P1–P3 aged mice, we hypothesized that ACh would begin to evoke G5 detectable $[Ca^{2+}]_i$ transients as calyces developed due to the presence of muscarinic AChRs (Holt et al., 2017). In utricular maculae excised from P5 aged mice, puff application of $100 \mu M$ ACh indeed synchronized the timing of $\Delta F/F_0$ transients. Figure 5 compares spontaneous $\Delta F/F_0$ $[Ca^{2+}]_i$ transients (Figure 5E) to ACh synchronized transients (Figure 5I) in the same cells for repeated application of ACh. Traces were collected in time sequences, repeated following a 5 s delay at 4 sequential focal planes. Cells became refractory immediately following a calcium transient, requiring a period of time to recover before a subsequent transient could be evoked by ACh or occurred spontaneously. This is consistent with similar calcium transients

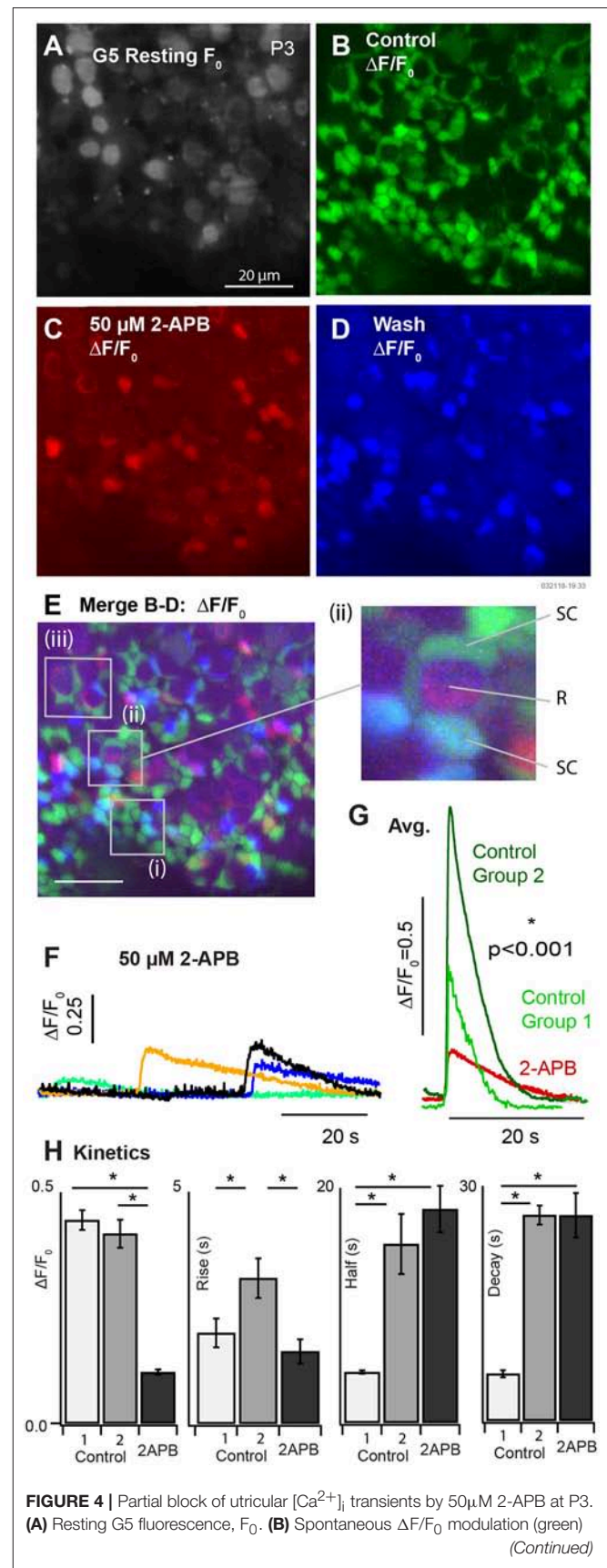


FIGURE 4 | in the control condition. **(C)** $\Delta F/F_0$ modulation (red) after bath application of 50 μM 2-APB. **(D)** Spontaneous $\Delta F/F_0$ modulation (blue) after washout of 2-APB. **(E)** Merge **(B–D)** showing modulation in the control condition (green), in the presence of 2-APB (red), and after washout (blue). The red channel was amplified to allow visualization of small $\Delta F/F_0$ in the presence of 2-APB. 50 μM 2-APB reversibly blocked spontaneous activity in SCs. Cells that continued to respond in the presence of 2-APB were located near the base of HCs at P3. **(F)** Example transients in the presence of 2-APB, and **(G)** average waveforms in the control condition and in the presence of 2-APB. **(H)** Population statistics summarizing the action of 2-APB on the exponential rise time, half width, and decay time of $\Delta F/F_0$ transients. Spontaneous transients in the control condition are shown as fast events (Group 1) and slow events (Group 2) as in **Figure 3**. All events in the presence of 2-APB were slow and indistinguishable on the basis of kinetics.

observed in astrocytes (Taheri et al., 2017), and is likely due to the long time course of CICR dynamics and signaling. The refractory time during repeated stimuli accounts for the lack of “spontaneous” activity prior to ACh application in **Figure 5I** (ACh stimuli were repeated in 45s intervals). Synchronization by ACh is illustrated in the form of average response histograms (**Figure 5J**) where spontaneous transients occurred at random times relative to the onset of the imaging sequence (dotted gray), but became synchronized by application of ACh resulting in a peak probability of a $\Delta F/F_0$ transient occurring at latency of 9.7 s (± 7.1) after the ACh puff (**Figure 5J**, black).

ACh evoked transients became more pronounced in P10–14 mice. **Figure 6** shows resting G5 fluorescence (A, blue), superimposed on peak G5 ($\Delta F/F_0$) (C, green) recorded over an 80 s imaging sequence (100 ms frame⁻¹). For quantification, $\Delta F/F_0$ [Ca^{2+}]_i transients were recorded in 5 μm diameter ROIs in cells with complex morphological shapes (**Figure 6A**: “a” closed arrows. **Figures 6B,C**: 1-red, 2-green, 3-blue) and in simple morphological shapes (**Figure 6A**: “s” open arrows, **Figure 6B**: black). Spontaneous transients exhibited similar kinetics in all ROIs and, on average, had a rise time 1.28 s (± 0.045), decay time of 1.98 s (± 0.083), and half width 1.59 s (± 0.075) (**Figures 6B,H**). A puff application of 100 μM ACh for 1s evoked distinctly longer lasting $\Delta F/F_0$ transients in a subset of ROIs (**Figure 6A**: “a”. **Figures 6C,D**: 1-red, 2-green, 3-blue) which, on average, had a rise time 2.80 s (± 1.45), decay time of 3.97 s (± 1.60), and half width 3.37 s (± 0.44). Population kinetics of $\Delta F/F_0$ [Ca^{2+}]_i transients in ATR insensitive cells (“s”) vs. ATR-sensitive cells are summarized in **Figures 6H,I**. The long lasting ACh-evoked transients were blocked by the muscarinic ACh receptor (mAChR) antagonist ATR (5 μM , **Figures 6E,F**), with residual small transients persisting in some ACh sensitive ROIs (**Figure 6F**, 1-3). Cells responding to ACh with long lasting calcium transients had morphological shapes consistent with calyceal afferent endings contacting type I hair cells. This is illustrated by comparing the morphology of tubulin labeled afferent endings (cyan) contacting tdT hair cells (red) from the same P14 tissue after fixation (**Figure 6G**, maximum intensity projection from a 62 μm z-stack). Present data suggest ACh activation of mAChRs on calyceal endings triggers large and long lasting CICR by P14 (**Figure 6**) that likely plays an important role in responses of mature calyces to ACh and efferent activation (Holt et al., 2017).

Intracellular calcium transients were also observed using G5 in utricles excised from adult mice (**Figure 7**). [Ca^{2+}]_i transients recorded from a mature P533 aged mouse shows persistence of spontaneous $\Delta F/F_0$ transients in control conditions recorded in 18 distinct cells in this tissue at a sampling rate of 100 ms-frame⁻¹. The average of these traces is shown as the solid black curve above the waterfall, and example cells are shown in inset images 1–3 ($\Delta F/F_0$: green, F_0 blue). Based strictly on morphology and contacts on HCs (blue) these modulating domains are likely to include calyceal endings near the base of HCs (1–2) and bouton terminals (3). The 18 cells in this tissue exhibited spontaneous transients at a rate of 0.37 s⁻¹ (± 0.033). When the same cells were exposed to 100 μM ACh for 1s the rate of transients increased to 0.83 s⁻¹ (± 0.091), (**Figures 7B–D**). ACh also evoked a slow increase in [Ca^{2+}]_i evidenced by the slow increase of $\Delta F/F_0$ not present in the control condition (**Figure 7B**: large gray arrows, black trace). In some cells ACh extended the spatial extent of the intracellular [Ca^{2+}]_i transient relative to spontaneous events in the same cell in the control condition (**Figure 7**: A-3 vs. B-3), possibly due to the activation of CICR these cells. Population statistics in this aged utricle confirms that ACh evokes a significant increase in the rate of fast transients in addition to a slow increase in [Ca^{2+}]_i (**Figure 7C**), but there was no detectable influence on kinetics of the fast [Ca^{2+}]_i transients as measured by the rise time, half width, or $\Delta F/F_0$ relative to controls (**Figure 7D**).

DISCUSSION

Intracellular calcium transients during the first week of postnatal development in mouse utricular macula are summarized schematically in **Figure 8**. Spontaneous whole-cell [Ca^{2+}]_i transients were present in HCs with tdT expression at birth (**Figure 7B**; also see **Supplement Video 1**) and were largely reduced in HCs at P3 (**Figure 7C**; **Supplement Video 2**). In mature mice from this transgenic cross, HCs with strong tdT expression are primarily extrastrisolar type 1, which are known to be contacted by calyx endings of dimorphic afferent neurons (Eatock et al., 1998; Goldberg, 2012). If the tdT expression is maintained through postnatal development, HCs expressing tdT at P1 would be expected to have extrastrisolar type I fate. Because of this, spontaneous HC transients reported here at P1 would be expected to drive action potentials in dimorphic afferents prior to the onset of mature vestibular function. Vestibular afferent neurons have irregularly spaced inter-spike-intervals at P1 (Desmadryl et al., 1986), consistent with the firing pattern expected in neurons that contact type I HCs (Rüsch et al., 1998; Goldberg, 2012), and consistent with spontaneous [Ca^{2+}]_i transients observed in putative type I HCs examined here at P1 (**Figures 1, 2**). Present results support the hypothesis that extrastrisolar type I hair cells generate spontaneous calcium activity at P1, which is likely to drive spontaneous action potential modulation in immature afferents with dimorphic fate. Since the G5 reporter was preferentially expressed in these specific HCs, present results cannot address possible spontaneous activity in other hair cell types or partner afferent neurons. Based on the

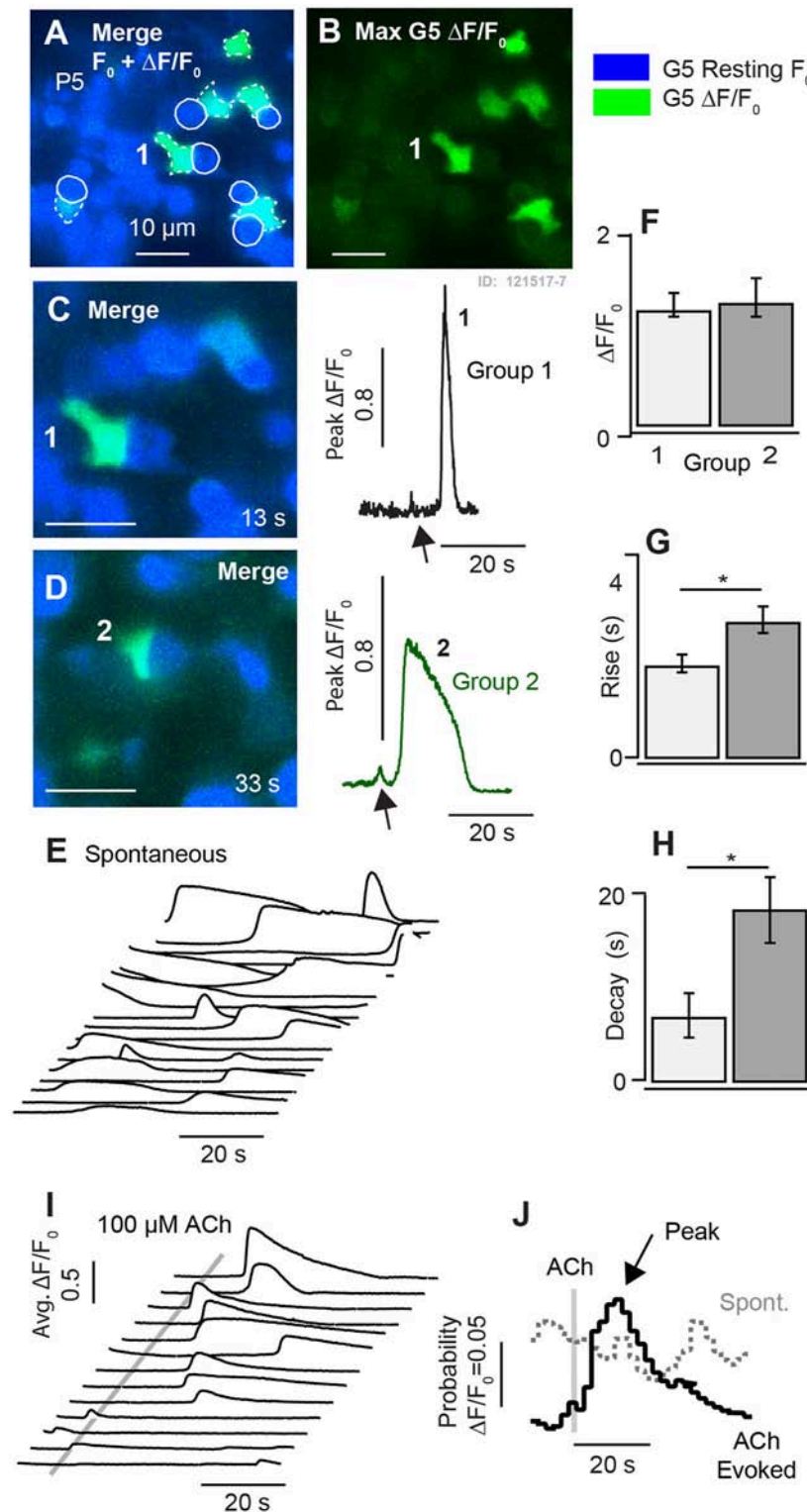


FIGURE 5 | Synchronization of $[\text{Ca}^{2+}]_i$ transients by 100 μM ACh at P5. **(A,B)** Resting G5 fluorescence (blue) and spontaneous $[\text{Ca}^{2+}]_i$ transients based on the maximum G5 $\Delta F/F_0$ (green) over a 100s time sequence imaged at 10 frames per second. **(C,D)** Two example instants in time showing spontaneous transients in example cells (1–2). **(E)** Time sequence of spontaneous $\Delta F/F_0$ transients in individual cells. **(F–H)** Population statistics at P5 showing the size, rise time, and decay time of fast (Group 1) and slow (Group 2) transients. **(I)** Time sequence showing synchronization of $\Delta F/F_0$ transients by puff application of 100 μM ACh. **(J)** Stimulus averaged $\Delta F/F_0$ transients illustrating synchronization by ACh. * $p = 0.05$.

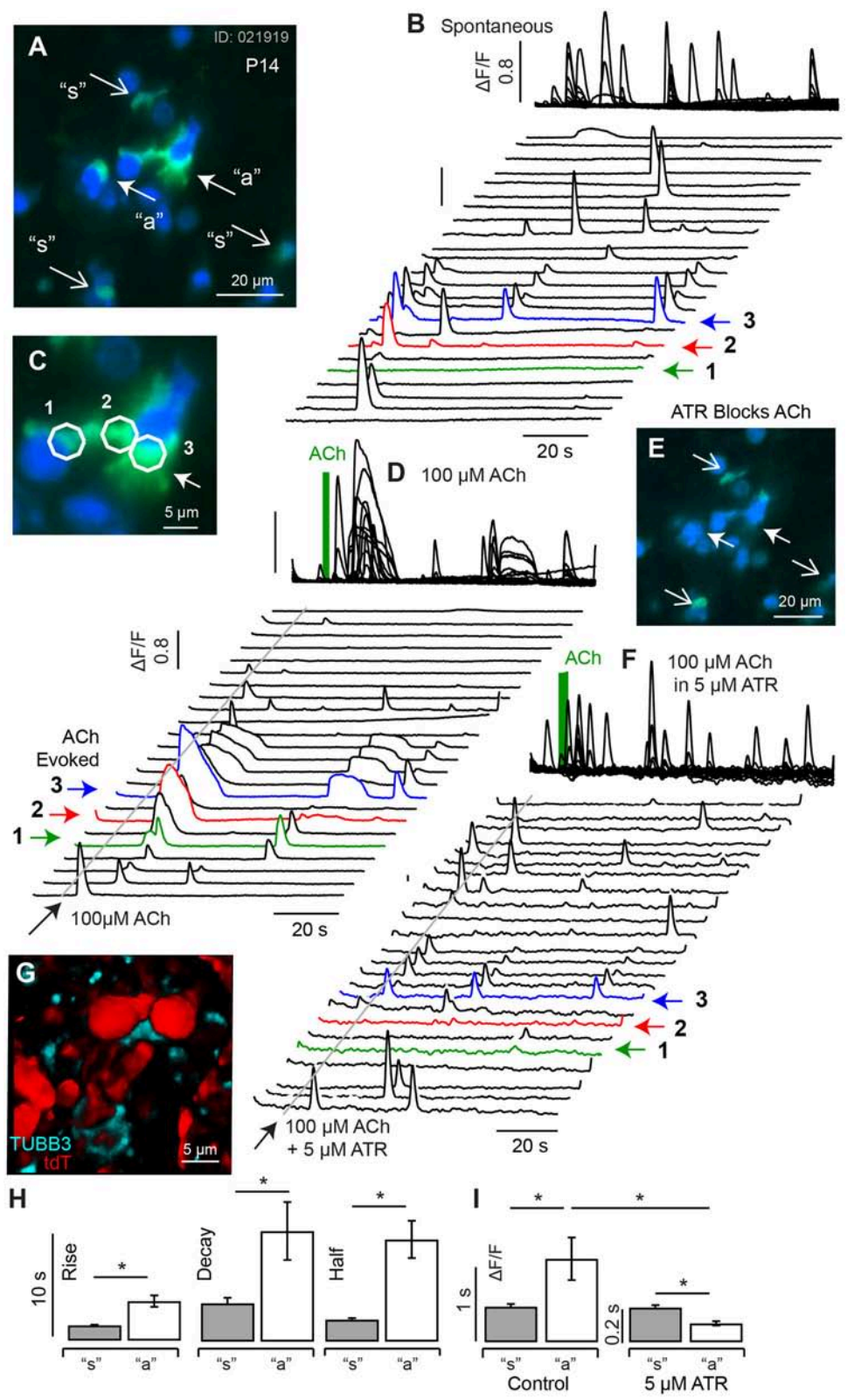


FIGURE 6 | Spontaneous and ACh evoked $[Ca^{2+}]_i$ transients at P14. **(A)** Resting G5 fluorescence (blue) and peak G5 $\Delta F/F_0$ (green) showing superposition of spontaneous ("s") and ACh evoked events ("a"). **(B)** Spontaneous transients in 23 example 5 μ m diameter ROIs, with transients in 3 ACh sensitive ROIs highlighted (Continued)

FIGURE 6 | (1,2,3), at higher magnification of in (C). (D) ACh evoked transients were observed in a subset of cells (e.g., 1,2,3), with morphology consistent with calyx terminals contacting hair cells. (E) G5 $\Delta F/F_0$ was blocked by 50 μ M ATR in a subset of cells (closed arrows) but persisted in other cells (open arrows). (F) ATR blocked long-lasting responses in ACh sensitive cells but not in other cells. (G) Confocal image of P14 fixed tissue showing the morphology of tdT positive hair cells (red) and synaptic contacts (anti-Tubulin) in an imaging slice similar to (A), suggesting ATR-sensitive cells are calyx endings. (H) ACh evoked transients could be distinguished from spontaneous transients by their kinetics, with ACh evoked events rising more slowly and lasting longer. (I) ACh evoked transients were largely blocked by ATR, while short-duration transients were not. * $p = 0.05$.

developmental time course in humans, this same process might be expected to occur at 10–15 weeks gestation (Lim et al., 2014; Lim and Brichta, 2016).

Whole-cell spontaneous $[Ca^{2+}]_i$ transients in HCs became rare by P3, demonstrating a change in operation of these HCs (Figure 7C). The activity of utricular ganglion neurons also changes by P3, with some neurons beginning to discharge with regularly spaced inter-spike intervals, supplementing neurons discharging with irregularly spaced intervals (Desmadryl et al., 1986). The appearance of units with regular discharge statistics suggests HCs with type II fate are likely releasing neurotransmitter at P3 in addition to HCs with type I fate, although not examined directly in the present study. Spontaneous action potentials in vestibular ganglion neurons reported previously combined with the near absence of whole-cell $\Delta F/F_0$ transients in HCs reported here in P3 mice, suggests spontaneous neurotransmitter release from HCs at P3 does not require large whole cell $[Ca^{2+}]_i$ transients, but instead likely relies on smaller localized $[Ca^{2+}]_i$ transients similar to mature HCs, unlikely to be detectable by the present G5 indicator.

The pattern of spontaneous $[Ca^{2+}]_i$ activity changed dramatically by P3 when ubiquitous $\Delta F/F_0$ $[Ca^{2+}]_i$ transients appeared in utricular SCs (Figures 3, 4; Supplement Videos 2, 3). SC $[Ca^{2+}]_i$ transients occurred in scattered patterns across the epithelium (Figure 3; Supplement Video 2) and did not exhibit detectable intercellular calcium wave propagation from one cell to adjacent cells as might be expected from gap-junction communication. This appears to differ from the developing cochlea, where spontaneous calcium activity in Köllikers organ is propagated between adjacent cells and likely coordinates local purinergic signaling to inner HCs during early postnatal development (Tritsch et al., 2010; Zhu and Zhao, 2012; Dayaratne et al., 2014, 2015). Intracellular calcium transients in utricular SCs were likely IP_3 dependent (Figure 4), but we did not observe $[Ca^{2+}]_i$ propagation that would be expected if connexin-dependent intercellular signaling between adjacent SCs was present at levels similar to the cochlea (Beltramello et al., 2005; Zhang et al., 2005). Although sequence variants in *connexin* genes are responsible for the most common forms of hereditary deafness (Cohen-Salmon et al., 2002, 2004; Chang et al., 2003; Teubner et al., 2003; Leibovici et al., 2008; Wan et al., 2013), vestibular function is not as profoundly impaired with these genetic mutations (Todd et al., 2005; Eppsteiner and Smith, 2011). Results of the present study suggest this relative *connexin* insensitivity in vestibular organs compared to the cochlea could be due to differences in the role of intercellular calcium signaling during development.

Intracellular calcium transients occurred in different SCs at sequential times, however these cells were rarely adjacent to each other (Figure 3 and Supplement Videos). If temporal

correlations between transients occurring in SCs were causally related it would require signaling between distant SCs. One hypothesis is that utricular SC calcium transients could be modulated by efferent neural activity acting primarily on HCs and afferent terminals (Holt et al., 2015, 2017) and subsequently signaling SCs. Synaptic inputs from efferent neurons are active in the cochlea during this developmental period and are likely critical for maturation of synaptic function, tonotopy and hearing (Katz et al., 2004; Johnson et al., 2013). Extension of this concept to the utricle is supported by the present data showing that exogenous application of the efferent transmitter ACh synchronized SC calcium transients beginning in aged P3–P5 mice (Figure 5). The dendritic fields of vestibular efferent neurons in the utricle are morphologically complex, making synaptic contacts with HCs and afferent terminals across broad regions. Hence, activation of a single efferent neuron could potentially synchronize SC activity and HCs across diverse spatial locations in the epithelium. This mechanism hypothetically has potential to close the loop between afferent inputs to the CNS and efferent feedback to the sensory organ—closed loop feedback that might be a general developmental principle organizing the auditory and vestibular systems from the sensory organs to the CNS and back again.

Mice aged P8 and older (Figure 7D) continued to show “spontaneous” $\Delta F/F_0$ $[Ca^{2+}]_i$ transients in SCs. Spontaneous $[Ca^{2+}]_i$ activity suggests SCs in adult utricles exhibit whole cell transients as part of their mature physiological function, perhaps serving roles similar to astrocytes in the CNS (Dani et al., 1992; Agulhon et al., 2008; Bazargani and Attwell, 2016; Shigetomi et al., 2016). Adult vestibular organs express both nicotinic nAChRs and muscarinic mAChRs that together underlie both inhibitory and excitatory responses to activation of the efferent vestibular nucleus or to the application of ACh (Guth et al., 1994, 1998; Elgoyhen et al., 2001; Holt et al., 2003, 2017; Boyle et al., 2009; Goldberg, 2012; Lee et al., 2017; Parks et al., 2017). nAChRs are calcium permeable and their activation leads to short local calcium increases, while mAChRs are metabotropic and can evoke long lasting responses. The G5 indicator used in the present study is has kinetics likely unable to track localized $[Ca^{2+}]_i$ events associated with nAChR activation, but is well suited to examine long lasting G protein coupled $[Ca^{2+}]_i$ transients associated with mAChR activation. Some of the most striking $[Ca^{2+}]_i$ transients observed in the present report were ACh evoked, with increases in $[Ca^{2+}]_i$ largely blocked by 50 μ M 2-APB and/or ATR (Figures 6, 7; Supplement Video 7). ACh sensitive cells in mature utricles contacted type I hair cells and had morphologies consistent with calyx afferent endings. The long-lasting ACh-evoked $[Ca^{2+}]_i$ transients in mature utricles in the present report had durations similar to mAChR dependent electrophysiological responses reported previously in

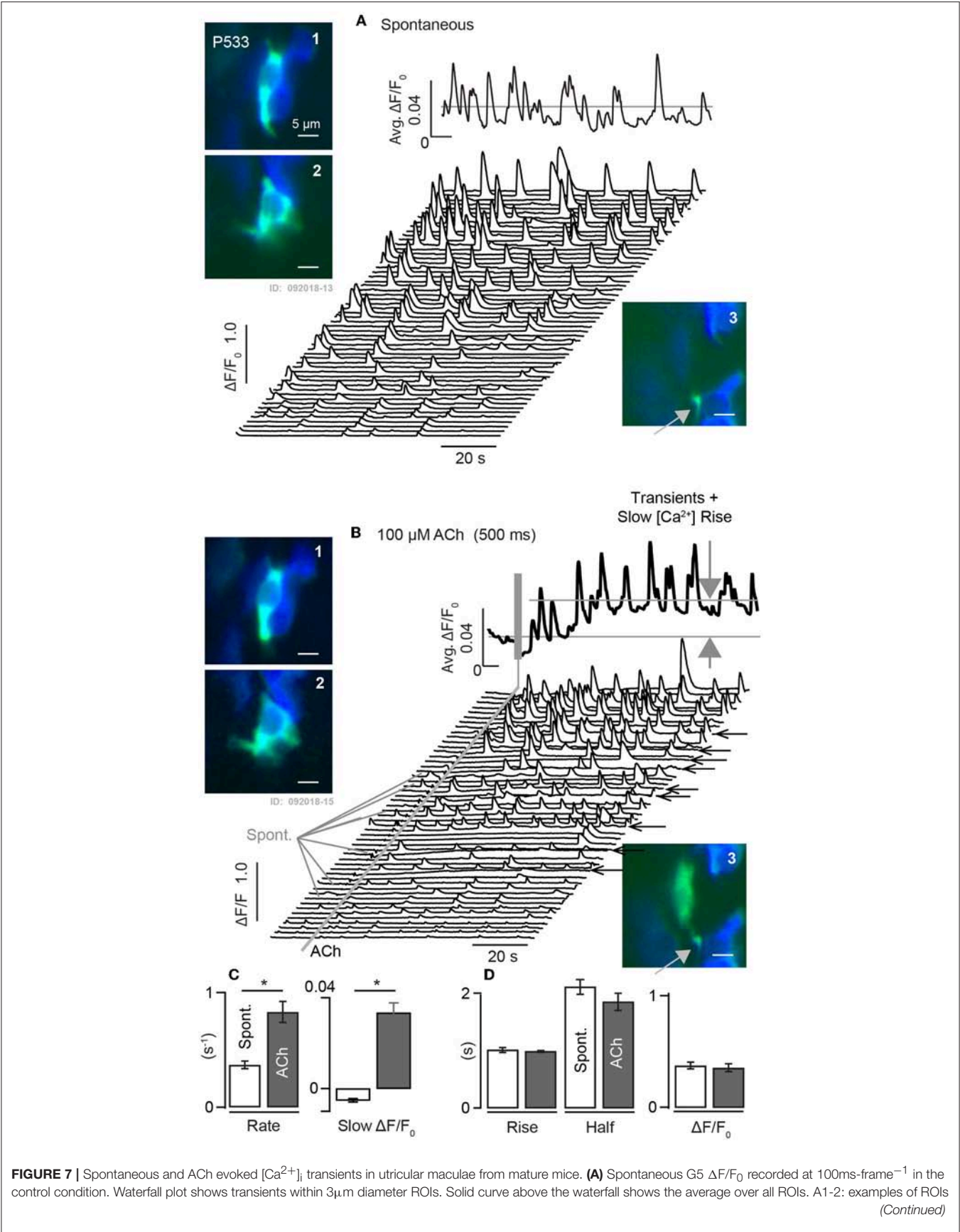


FIGURE 7 | within cells of calyceal morphology near the base of HCs, and A3: example with bouton morphology. **(B)** Same ROIs modulating in response to 1s puff application of 100 μ M ACh. ACh increased the rate of transient events and evoked a slow rise in $[Ca^{2+}]_i$ (large gray arrows). B1-3: same ROIs as **(A)**, but with transients evoked by ACh. B3: ACh extended the spatial extent of the transient relative to spontaneous events. Solid curve above the waterfall shows the average over all ROIs. **(C,D)** Population statistics demonstrating that ACh evoked a significant increase in the rate of fast transients as well as a slow increase in $[Ca^{2+}]_i$. No change was detectable in kinetics, duration, or magnitude of fast transients in the ACh condition relative to controls. * $p = 0.05$.

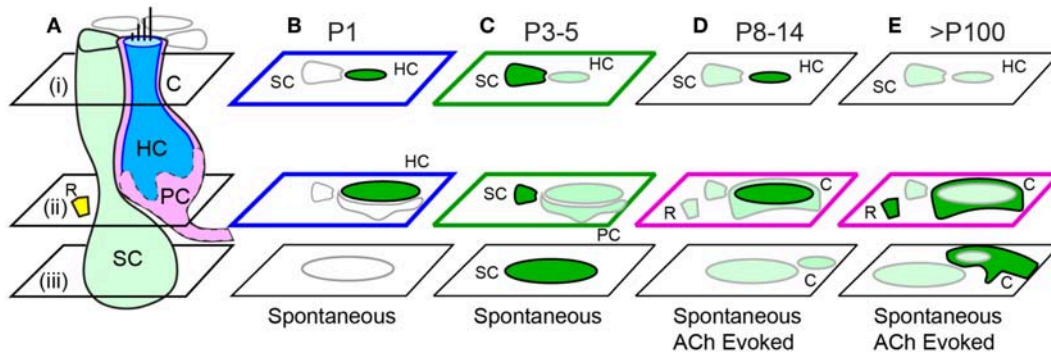


FIGURE 8 | Summary of spontaneous and ACh evoked $[Ca^{2+}]_i$ transients with age. **(A)** Cartoon depicting a supporting cell (SC), extrastricular type I tdt positive hair cell (HC), calyx ending (C), immature proto-calyx ending (PC), and small ACh activated domains (R) near the base of HCs. Focal planes are denoted i-iii. **(B)** Intense spontaneous $\Delta F/F_0$ transients in immature HCs at P1. **(C)** Intense spontaneous $\Delta F/F_0$ transients in SCs and additional transients in HCs and PCs at P3-5. ACh synchronized of transients at P5. **(D)** Sparse spontaneous transients in SCs, intense ACh evoked transients in some HCs, and additional transients in Cs and Rs in P8 and older mice. **(E)** Spontaneous transients in SCs and intense ACh-evoked transients C endings.

calyx bearing afferents (Holt et al., 2017), suggesting a potential role for CICR in modulating KCNQ channels during activation of the efferent system in calyces.

The fact that the Gad2-IRES-Cre used in the present study drove expression preferentially in a distinct subset of type I hair cells could have important implications, but was not addressed in the present study. Although there is evidence of glutamate decarboxylase isoform GAD67 expression in vestibular SCs (Tavazzani et al., 2014), the pattern of tdt-G5 expression observed in the present study suggests embryonic transcriptional regulation of Gad2 in a subset of type I hair cells. Previous studies indicate that GAD65 has multiple transcription start sites (Skak and Michelsen, 1999), and that GABA might act as a morphogen during development (Owens and Kriegstein, 2002). It is therefore difficult to draw direct conclusions of the Gad2 related transcriptome from the complex expression pattern in the present transgenic mouse. Nevertheless, the pattern observed at birth and into adulthood suggests the role of Gad2 in extrastricular type I HCs likely differs significantly from type II HCs and from striolar type I HCs. While the primary vesicular transmitter in HCs is glutamate, the expression pattern provides further evidence that the GAD65-dependent molecular machinery responsible for synthesizing GABA is present (Usami et al., 2001; Moser et al., 2006; Meza, 2008). Furthermore, there is evidence that GABA may be utilized as a secondary intercellular transmitter in a subset of vestibular HCs in toadfish (Holstein et al., 2004), but evidence of similar mechanisms have not been reported in mammals to date. Although present results are suggestive, examination of the role of GAD65 in vestibular organs remains an important subject for future research. Irrespective of the involvement of Gad2,

using its transcriptional machinery to drive expression of the genetically encoded calcium indicator G5 enabled examination of $[Ca^{2+}]_i$ transients in early postnatal developmental stages in the present study.

The $[Ca^{2+}]_i$ transients in the present report are limited by the speed and dynamic range of the G5 transgenic reporter. The dissociation constant, K_d , of G5 is approximately 460 nM, similar to Fluo-4 (350 nM) and useful for $[Ca^{2+}]_i$ imaging in SCs, HCs, and neurons but not always ideal (Oliver et al., 2003; Akerboom et al., 2012; Spinelli and Gillespie, 2012). Cell dependent differences in resting $[Ca^{2+}]_i$ influence optimum K_d , and differences in level of expression contribute to gain, both influencing the quantitative relationship between $\Delta F/F_0$ and changes in $[Ca^{2+}]_i$. Because of this, G5 $\Delta F/F_0$ in the present study reports the spatial extent and kinetics of $[Ca^{2+}]_i$ modulation without addressing quantitative magnitude. The sampling rate used in experiments described here was 100 ms per frame, nearly equivalent to the rise time and faster than the decay time of the G5 indicator (Akerboom et al., 2012; Chen et al., 2013). Although present results demonstrate postnatal maturation of spontaneous calcium transients and development of ACh sensitivity, expanding these studies with additional techniques *in vivo* will be important to fully elucidate $[Ca^{2+}]_i$ activity during development.

It's important to emphasize that spontaneous activity comprised of coordinated $[Ca^{2+}]_i$ transients is essential to the developing vestibular nervous system, shown previously to extend through the CNS as well as in the developing retina and cochlea (Wong et al., 1995; O'Donovan, 1999; Brandt et al., 2003; Tritsch et al., 2007; Ackman et al., 2012). Data in the

present report demonstrate spontaneous activity is present in mouse utricular sensory HCs and that these cells are likely undergoing differentiation at birth, before the onset of mature vestibular function. Spontaneous activity in HCs subsides by P2, while spontaneous activity in SCs develops during the first two weeks and is maintained into old age. Present results further demonstrate the development of long-lasting, ATR sensitive, ACh-evoked transients during this same time period putatively associated with maturation of mAChR-dependent vestibular action on calyx-bearing afferent responses.

ETHICS STATEMENT

This study was carried out in accordance with the recommendations of the University of Utah Institutional Animal Care and Use Committee (IACUC). The protocol was approved by the University of Utah IACUC.

AUTHOR CONTRIBUTIONS

HH and RR designed experiments. HH, LP, and RR performed experiments. MF designed and built components of the swept field confocal microscope. HH and RR analyzed and processed the data. HH and RR wrote the manuscript. LP, MF, HH, and RR proofread and edited the manuscript.

FUNDING

The research described in this manuscript was solely supported by the National Institutes of Health (NIDCD) from grant R01 DC006685 awarded to Professor RR.

ACKNOWLEDGMENTS

We thank Richard Altschuler and Ariane Kanicki for reagents, equipment and expertise to generate **Figure 1B**. We thank our colleagues Matt Wachowiak, Robert Baker and Marta Iversen for

their assistance. We also thank the animal husbandry oversight by Lauren Lentsch and Mary Dickerson.

SUPPLEMENTARY MATERIAL

The Supplementary Material for this article can be found online at: <https://www.frontiersin.org/articles/10.3389/fncel.2019.00186/full#supplementary-material>

Supplement Video 1 | Supplement to **Figure 2** in the parent paper. Time sequence of images showing spontaneous $[Ca^{2+}]_i$ transients in extrastricular type I utricular hair cells (HCs) at P1. Resting G5 fluorescence (blue) is merged with G5 $\Delta F/F$ fluorescence modulation (green) reporting changes in $[Ca^{2+}]_i$ (green).

Supplement Video 2 | Supplement to **Figure 3** in the parent paper. Time sequence of images showing spontaneous $[Ca^{2+}]_i$ transients in utricular supporting cells (SCs) at P3. Resting G5 fluorescence (blue) is merged with G5 $\Delta F/F$ fluorescence modulation (green) reporting changes in $[Ca^{2+}]_i$ (green). Image plane cut through the epithelium at a shallow angle to image deep in the tissue through the based of supporting cells (upper left) and near the apical surface (lower right). Note high levels of resting G5 fluorescence in type I HCs and large numbers of spontaneous transients in SCs.

Supplement Video 3 | Supplement to **Figure 3** in the parent paper. Same format as **Supplement Video 2**, but from a different animal.

Supplement Video 4 | Supplement to **Figure 3** in the parent paper. Same format as **Supplement Video 2** in alternative tissue with $\Delta F/F$ in multiple cell types and regions.

Supplement Video 5 | Supplement to **Figure 6** in the parent paper. Time sequence of images showing spontaneous $[Ca^{2+}]_i$ transients in utricular SCs at P8. G5 $\Delta F/F$ fluorescence modulation reporting changes in $[Ca^{2+}]_i$ (green) and resting G5 fluorescence (blue) are merged.

Supplement Video 6 | Supplement to **Figure 6** in the parent paper. Time sequence of images showing 100 μM ACh evoked $[Ca^{2+}]_i$ transients in utricular HCs, calyces (C), and unidentified small domains (R) at P8. G5 $\Delta F/F$ fluorescence modulation reporting changes in $[Ca^{2+}]_i$ (green) and resting G5 fluorescence (blue) are merged. Image blurring following ACh application is an artifact caused by motion as the ACh solution washed over the epithelium.

Supplement Video 7 | Supplement to **Figure 7** in the parent paper. Time sequence of images showing spontaneous and 100 μM ACh evoked $[Ca^{2+}]_i$ transients at P533. G5 $\Delta F/F$ fluorescence modulation reporting changes in $[Ca^{2+}]_i$ (green) and resting G5 fluorescence (blue) are merged.

REFERENCES

- Ackman, J. B., Burbidge, T. J., and Crair, M. C. (2012). Retinal waves coordinate patterned activity throughout the developing visual system. *Nature* 490, 219–225. doi: 10.1038/nature11529
- Agulhon, C., Petravic, J., McMullen, A. B., Sweager, E. J., Minton, S. K., Taves, S. R., et al. (2008). What is the role of astrocyte calcium in neurophysiology? *Neuron* 59, 932–946. doi: 10.1016/j.neuron.2008.09.004
- Akerboom, J., Chen, T. W., Wardill, T. J., Tian, L., Marvin, J. S., Mutlu, S., et al. (2012). Optimization of a GCaMP calcium indicator for neural activity imaging. *J. Neurosci.* 32, 13819–13840. doi: 10.1523/JNEUROSCI.2601-12.2012
- Bazargani, N., and Attwell, D. (2016). Astrocyte calcium signaling: the third wave. *Nat. Neurosci.* 19, 182–189. doi: 10.1038/nn.4201
- Beltramello, M., Piazza, V., Bukauskas, F. F., Pozzan, T., and Mammano, F. (2005). Impaired permeability to Ins(1,4,5)P₃ in a mutant connexin underlies recessive hereditary deafness. *Nat. Cell Biol.* 7, 63–69. doi: 10.1038/ncb1205
- Beutner, D., and Moser, T. (2001). The presynaptic function of mouse cochlear inner hair cells during development of hearing. *J. Neurosci.* 21, 4593–4599. doi: 10.1523/JNEUROSCI.21-13-04593.2001
- Boyle, R., Rabbitt, R. D., and Highstein, S. M. (2009). Efferent control of hair cell and afferent responses in the semicircular canals. *J. Neurophysiol.* 102, 1513–1525. doi: 10.1152/jn.91367.2008
- Brandt, A., Striessnig, J., and Moser, T. (2003). CaV1.3 channels are essential for development and presynaptic activity of cochlear inner hair cells. *J. Neurosci.* 23, 10832–10840.
- Burns, J. C., On, D., Baker, W., Collado, M. S., and Corwin, J. T. (2012). Over half the hair cells in the mouse utricle first appear after birth, with significant numbers originating from early postnatal mitotic production in peripheral and striolar growth zones. *J. Assoc. Res. Otolaryngol.* 13, 609–627. doi: 10.1007/s10162-012-0337-0
- Burns, J. C., and Stone, J. S. (2017). Development and regeneration of vestibular hair cells in mammals. *Semin. Cell Dev. Biol.* 65, 96–105. doi: 10.1016/j.semcdb.2016.11.001
- Cao, X. J., McGinley, M. J., and Oertel, D. (2008). Connections and synaptic function in the posteroventral cochlear nucleus of deaf jerker mice. *J. Comp. Neurol.* 510, 297–308. doi: 10.1002/cne.21788
- Chabbert, C. H. (1997). Heterogeneity of hair cells in the bullfrog sacculus. *Pflugers Arch.* 435, 82–90. doi: 10.1007/s004240050486
- Chang, E. H., Van Camp, G., and Smith, R. J. (2003). The role of connexins in human disease. *Ear Hear.* 24, 314–323. doi: 10.1097/01.AUD.0000079801.55588.13
- Chen, T. W., Wardill, T. J., Sun, Y., Pulver, S. R., Renninger, S. L., Baohan, A., et al. (2013). Ultrasensitive fluorescent proteins for imaging neuronal activity. *Nature* 499, 295–300. doi: 10.1038/nature12354

- Cohen-Salmon, M., Maxeiner, S., Krüger, O., Theis, M., Willecke, K., and Petit, C. (2004). Expression of the connexin43- and connexin45-encoding genes in the developing and mature mouse inner ear. *Cell Tissue Res.* 316, 15–22. doi: 10.1007/s00441-004-0861-2
- Cohen-Salmon, M., Ott, T., Michel, V., Hardelin, J. P., Perfettini, I., Eybalin, M., et al. (2002). Targeted ablation of connexin26 in the inner ear epithelial gap junction network causes hearing impairment and cell death. *Curr. Biol.* 12, 1106–1111. doi: 10.1016/S0960-9822(02)00904-1
- Curthoys (1983). “The development of function of primary vestibular neurons,” in *Development of Auditory and Vestibular Function*, ed. R. Romand (New York, NY: Academic Press), 425–461.
- Dani, J. W., Chernjavsky, A., and Smith, S. J. (1992). Neuronal activity triggers calcium waves in hippocampal astrocyte networks. *Neuron* 8, 429–440.
- Dayaratne, M. W., Vlajkovic, S. M., Lipski, J., and Thorne, P. R. (2014). Kolliker's organ and the development of spontaneous activity in the auditory system: implications for hearing dysfunction. *Biomed. Res. Int.* 2014:367939. doi: 10.1155/2014/367939
- Dayaratne, M. W., Vlajkovic, S. M., Lipski, J., and Thorne, P. R. (2015). Putative role of border cells in generating spontaneous morphological activity within Kolliker's organ. *Hear Res.* 330(Pt A), 90–97. doi: 10.1016/j.heares.2015.06.017
- Dechesne, C. (1986). Postnatal development of vestibular receptor surfaces in the rat. *Acta Otolaryngol* 101, 11–18.
- Demêmes, D., Dechesne, C. J., Venteo, S., Gaven, F., and Raymond, J. (2001). Development of the rat efferent vestibular system on the ground and in microgravity. *Brain Res. Dev. Brain Res.* 128, 35–44. doi: 10.1016/S0165-3806(01)00146-8
- Desmadryl, G., Raymond, J., and Sans, A. (1986). *In vitro* electrophysiological study of spontaneous activity in neonatal mouse vestibular ganglion neurons during development. *Brain Res.* 390, 133–136.
- Desmadryl, G., and Sans, A. (1990). Afferent innervation patterns in crista ampullaris of the mouse during ontogenesis. *Brain Res. Dev. Brain Res.* 52, 183–189.
- Eatock, R. A., Rüsch, A., Lysakowski, A., and Saeki, M. (1998). Hair cells in mammalian utricles. *Otolaryngol. Head Neck Surg.* 119, 172–181. doi: 10.1016/S0194-5998(98)70052-X
- Elgoyhen, A. B., Vetter, D. E., Katz, E., Rothlin, C. V., Heinemann, S. F., and Boulter, J. (2001). $\alpha 10$: a determinant of nicotinic cholinergic receptor function in mammalian vestibular and cochlear mechanosensory hair cells. *Proc. Natl. Acad. Sci. U.S.A.* 98, 3501–3506. doi: 10.1073/pnas.051622798
- Eppsteiner, R. W., and Smith, R. J. (2011). Genetic disorders of the vestibular system. *Curr. Opin. Otolaryngol. Head Neck Surg.* 19, 397–402. doi: 10.1097/MOO.0b013e32834a9852
- Favre, D., and Sans, A. (1977). Synaptogenesis of the efferent vestibular nerve endings of the cat: ultrastructural study. *Arch. Otorhinolaryngol.* 215, 183–186.
- Favre, D., and Sans, A. (1978). The development of vestibular efferent nerve endings during cat maturation: ultrastructural study. *Brain Res.* 142, 333–337.
- Gao, Z., Kelly, M. C., Yu, D., Wu, H., Lin, X., Chi, F. L., et al. (2016). Spatial and age-dependent hair cell generation in the postnatal mammalian utricle. *Mol. Neurobiol.* 53, 1601–1612. doi: 10.1007/s12035-015-9119-0
- Gee, J. M., Smith, N. A., Fernandez, F. R., Economo, M. N., Brunert, D., Rothermel, M., et al. (2014). Imaging activity in neurons and glia with a Polr2a-based and cre-dependent GCaMP5G-IRES-tdTomato reporter mouse. *Neuron* 83, 1058–1072. doi: 10.1016/j.neuron.2014.07.024
- Géléoc, G. S., and Holt, J. R. (2003). Developmental acquisition of sensory transduction in hair cells of the mouse inner ear. *Nat. Neurosci.* 6, 1019–1020. doi: 10.1038/nn1120
- Glowatzki, E., and Fuchs, P. A. (2000). Cholinergic synaptic inhibition of inner hair cells in the neonatal mammalian cochlea. *Science* 288, 2366–2368. doi: 10.1126/science.288.5475.2366
- Glowatzki, E., and Fuchs, P. A. (2002). Transmitter release at the hair cell ribbon synapse. *Nat. Neurosci.* 5, 147–154. doi: 10.1038/nn796
- Goldberg, J. M. (2012). *The Vestibular System: A Sixth Sense*. Oxford / NY: Oxford University Press.
- Guth, P. S., Dunn, A., Kronomer, K., and Norris, C. H. (1994). The cholinergic pharmacology of the frog saccule. *Hear Res.* 75, 225–232.
- Guth, P. S., Holt, J. C., Perin, P., Athas, G., Garcia, M., Puri, A., et al. (1998). The metabotropic glutamate receptors of the vestibular organs. *Hear Res.* 125, 154–162.
- Hashisaki, G. T., and Rubel, E. W. (1989). Effects of unilateral cochlea removal on anteroventral cochlear nucleus neurons in developing gerbils. *J. Comp. Neurol.* 283, 5–73.
- Holstein, G. R., Rabbitt, R. D., Martinelli, G. P., Friedrich, V. L. Jr., Boyle, R. D., and Highstein, S. M. (2004). Convergence of excitatory and inhibitory hair cell transmitters shapes vestibular afferent responses. *Proc. Natl. Acad. Sci. U.S.A.* 101, 15766–15771. doi: 10.1073/pnas.0402824101
- Holt, J. C., Jordan, P. M., Lysakowski, A., Shah, A., Barsz, K., and Contini, D. (2017). Muscarinic acetylcholine receptors and M-currents underlie efferent-mediated slow excitation in calyx-bearing vestibular afferents. *J. Neurosci.* 37, 1873–1887. doi: 10.1523/JNEUROSCI.2322-16.2017
- Holt, J. C., Kewin, K., Jordan, P. M., Cameron, P., Klapczynski, M., McIntosh, J. M., et al. (2015). Pharmacologically distinct nicotinic acetylcholine receptors drive efferent-mediated excitation in calyx-bearing vestibular afferents. *J. Neurosci.* 35, 3625–3643. doi: 10.1523/JNEUROSCI.3388-14.2015
- Holt, J. C., Lioudyno, M., and Guth, P. S. (2003). A pharmacologically distinct nicotinic ACh receptor is found in a subset of frog semicircular canal hair cells. *J. Neurophysiol.* 90, 1526–1536. doi: 10.1152/jn.00273.2002
- Hurley, K. M., Gaboyard, S., Zhong, M., Price, S. D., Woollorton, J. R., Lysakowski, A., et al. (2006). M-like K⁺ currents in type I hair cells and calyx afferent endings of the developing rat utricle. *J. Neurosci.* 26, 10253–10269. doi: 10.1523/JNEUROSCI.2596-06.2006
- Johnson, C. E., Newman, C. W., Danhauer, J. L., and Williams, V. A. (2011). Problem with baby's hearing? an intervention checklist. *J. Fam. Pract.* 60, E1–7.
- Johnson, S. L., Wedemeyer, C., Vetter, D. E., Adachi, R., Holley, M. C., Elgoyhen, A. B., et al. (2013). Cholinergic efferent synaptic transmission regulates the maturation of auditory hair cell ribbon synapses. *Open. Biol.* 3:130163. doi: 10.1098/rsob.130163
- Jones, S. M., and Jones, T. A. (2011). *Genetics, Embryology, and Development of Auditory and Vestibular Systems*. San Diego: Plural Pub.
- Katz, E., Elgoyhen, A. B., Gómez-Casati, M. E., Knipper, M., Vetter, D. E., Fuchs, P. A., et al. (2004). Developmental regulation of nicotinic synapses on cochlear inner hair cells. *J. Neurosci.* 24, 7814–7820. doi: 10.1523/JNEUROSCI.2102-04.2004
- Kharkovets, T., Hardelin, J. P., Safieddine, S., Schweizer, M., El-Amraoui, A., Petit, C., et al. (2000). KCNQ4, a K⁺ channel mutated in a form of dominant deafness, is expressed in the inner ear and the central auditory pathway. *Proc. Natl. Acad. Sci. U.S.A.* 97, 4333–4338. doi: 10.1073/pnas.97.8.4333
- Kim, E., Hyrc, K. L., Speck, J., Salles, F. T., Lundberg, Y. W., Goldberg, M. P., et al. (2011). Missense mutations in Otopetrin 1 affect subcellular localization and inhibition of purinergic signaling in vestibular supporting cells. *Mol. Cell Neurosci.* 46, 655–661. doi: 10.1016/j.mcn.2011.01.005
- Kotak, V. C., and Sanes, D. H. (1995). Synaptically evoked prolonged depolarizations in the developing auditory system. *J. Neurophysiol.* 74, 1611–1620.
- Kros, C. J., Ruppersberg, J. P., and Rüsch, A. (1998). Expression of a potassium current in inner hair cells during development of hearing in mice. *Nature* 394, 281–284. doi: 10.1038/28401
- Lee, C., Holt, J. C., and Jones, T. A. (2017). The effect of M-current modulation on mammalian vestibular responses to transient head motion. *J. Neurophysiol.* 118, 2991–3006. doi: 10.1152/jn.00384.2017
- Leibovici, M., Safieddine, S., and Petit, C. (2008). Mouse models for human hereditary deafness. *Curr. Top. Dev. Biol.* 84, 385–429. doi: 10.1016/S0070-2153(08)00608-X
- Levic, S., Nie, L., Tuteja, D., Harvey, M., Sokolowski, B. H., and Yamoah, E. N. (2007). Development and regeneration of hair cells share common functional features. *Proc. Natl. Acad. Sci. U.S.A.* 104, 19108–19113. doi: 10.1073/pnas.0705927104
- Lim, R., and Brichta, A. M. (2016). Anatomical and physiological development of the human inner ear. *Hear Res.* 338, 9–21. doi: 10.1016/j.heares.2016.02.004
- Lim, R., Drury, H. R., Camp, A. J., Tadros, M. A., Callister, R. J., and Brichta, A. M. (2014). Preliminary characterization of voltage-activated whole-cell currents in developing human vestibular hair cells and calyx afferent terminals. *J. Assoc. Res. Otolaryngol.* 15, 755–766. doi: 10.1007/s10162-014-0471-y
- Lim, R., Kindig, A. E., Donne, S. W., Callister, R. J., and Brichta, A. M. (2011). Potassium accumulation between type I hair cells and calyx terminals in mouse crista. *Exp. Brain Res.* 210, 607–621. doi: 10.1007/s00221-011-2592-4

- Lippe, W. R. (1994). Rhythmic spontaneous activity in the developing avian auditory system. *J. Neurosci.* 14(3 Pt 2), 1486–1495.
- Lysakowski, A. (1999). Development of synaptic innervation in the rodent utricle. *Ann. NY. Acad. Sci.* 871, 422–425.
- Lysakowski, A., Gaboyard-Niay, S., Calin-Jageman, I., Chatlani, S., Price, S. D., and Eatock, R. A. (2011). Molecular microdomains in a sensory terminal, the vestibular calyx ending. *J. Neurosci.* 31, 10101–10114. doi: 10.1523/JNEUROSCI.0521-11.2011
- Marcotti, W., Johnson, S. L., Rusch, A., and Kros, C. J. (2003). Sodium and calcium currents shape action potentials in immature mouse inner hair cells. *J. Physiol.* 552(Pt 3), 743–761. doi: 10.1113/jphysiol.2003.043612
- Meza, G. (2008). Modalities of GABA and glutamate neurotransmission in the vertebrate inner ear vestibule. *Neurochem. Res.* 33, 1634–1642. doi: 10.1007/s11064-008-9734-5
- Moser, T., Brandt, A., and Lysakowski, A. (2006). Hair cell ribbon synapses. *Cell Tissue Res.* 326, 347–359. doi: 10.1007/s00441-006-0276-3
- O'Donovan, M. J. (1999). The origin of spontaneous activity in developing networks of the vertebrate nervous system. *Curr. Opin. Neurobiol.* 9, 94–104. doi: 10.1016/S0959-4388(99)80012-9
- Oliver, D., Knipper, M., Derst, C., and Fakler, B. (2003). Resting potential and submembrane calcium concentration of inner hair cells in the isolated mouse cochlea are set by KCNQ-type potassium channels. *J. Neurosci.* 23, 2141–2149. doi: 10.1523/JNEUROSCI.23-06-02141.2003
- Owens, D. F., and Kriegstein, A. R. (2002). Is there more to GABA than synaptic inhibition? *Nat. Rev. Neurosci.* 3, 715–727. doi: 10.1038/nrn919
- Parks, X. X., Contini, D., Jordan, P. M., and Holt, J. C. (2017). Confirming a role for $\alpha 9$ nAChRs and SK potassium channels in Type II hair cells of the turtle posterior crista. *Front. Cell Neurosci.* 11:356. doi: 10.3389/fncel.2017.00356
- Podor, B., Hu, Y. L., Ohkura, M., Nakai, J., Croll, R., and Fine, A. (2015). Comparison of genetically encoded calcium indicators for monitoring action potentials in mammalian brain by two-photon excitation fluorescence microscopy. *Neurophotonics* 2:021014. doi: 10.1117/1.NPH.2.2.021014
- Rabbitt, R. D., Brichta, A. M., Tabatabaee, H., Boutros, P. J., Ahn, J., Della Santina, C. C., et al. (2016). Heat pulse excitability of vestibular hair cells and afferent neurons. *J. Neurophysiol.* 116, 825–843. doi: 10.1152/jn.00110.2016
- Roux, I., Wersinger, E., McIntosh, J. M., Fuchs, P. A., and Glowatzki, E. (2011). Onset of cholinergic efferent synaptic function in sensory hair cells of the rat cochlea. *J. Neurosci.* 31, 15092–15101. doi: 10.1523/JNEUROSCI.2743-11.2011
- Rubel, E. W., and Fritzsch, B. (2002). Auditory system development: primary auditory neurons and their targets. *Annu. Rev. Neurosci.* 25, 51–101. doi: 10.1146/annurev.neuro.25.112701.142849
- Rüsch, A., Lysakowski, A., and Eatock, R. A. (1998). Postnatal development of type I and type II hair cells in the mouse utricle: acquisition of voltage-gated conductances and differentiated morphology. *J. Neurosci.* 18, 7487–7501. doi: 10.1523/JNEUROSCI.18-18-07487.1998
- Sadeghi, S. G., Pyott, S. J., Yu, Z., and Glowatzki, E. (2014). Glutamatergic signaling at the vestibular hair cell calyx synapse. *J. Neurosci.* 34, 14536–14550. doi: 10.1523/JNEUROSCI.0369-13.2014
- Sanes, D. H., and Siverls, V. (1991). Development and specificity of inhibitory terminal arborizations in the central nervous system. *J. Neurobiol.* 22, 837–854. doi: 10.1002/neu.480220805
- Sans, A., and Scarfone, E. (1996). Afferent calyces and type I hair cells during development. A new morphofunctional hypothesis. *Ann. NY. Acad. Sci.* 781, 1–12.
- Seal, R. P., Akil, O., Yi, E., Weber, C. M., Grant, L., Yoo, J., et al. (2008). Sensorineural deafness and seizures in mice lacking vesicular glutamate transporter 3. *Neuron* 57, 263–275. doi: 10.1016/j.neuron.2007.11.032
- Sendin, G., Bourien, J., Rassendren, F., Puel, J. L., and Nouvian, R. (2014). Spatiotemporal pattern of action potential firing in developing inner hair cells of the mouse cochlea. *Proc. Natl. Acad. Sci. U.S.A.* 111, 1999–2004. doi: 10.1073/pnas.1319615111
- Shigetomi, E., Patel, S., and Khakh, B. S. (2016). Probing the complexities of astrocyte calcium signaling. *Trends Cell Biol.* 26, 300–312. doi: 10.1016/j.tcb.2016.01.003
- Sienknecht, U. J., Köppl, C., and Fritzsch, B. (2014). Evolution and development of hair cell polarity and efferent function in the inner ear. *Brain Behav. Evol.* 83, 150–161. doi: 10.1159/000357752
- Skak, K., and Michelsen, B. K. (1999). The TATA-less rat GAD65 promoter can be activated by Sp1 through non-consensus elements. *Gene* 236, 231–241.
- Spinelli, K. J., and Gillespie, P. G. (2012). Monitoring intracellular calcium ion dynamics in hair cell populations with Fluo-4 AM. *PLoS ONE* 7:e51874. doi: 10.1371/journal.pone.0051874
- Taheri, M., Handy, G., Borisjuk, A., and White, J. A. (2017). Diversity of evoked astrocyte Ca^{2+} dynamics quantified through experimental measurements and mathematical modeling. *Front. Syst. Neurosci.* 11:79. doi: 10.3389/fnsys.2017.00079
- Taniguchi, H., He, M., Wu, P., Kim, S., Paik, R., Sugino, K., et al. (2011). A resource of Cre driver lines for genetic targeting of GABAergic neurons in cerebral cortex. *Neuron* 71, 995–1013. doi: 10.1016/j.neuron.2011.07.026
- Tavazzani, E., Tritto, S., Spaiardi, P., Botta, L., Manca, M., Prigioni, I., et al. (2014). Glutamic acid decarboxylase 67 expression by a distinct population of mouse vestibular supporting cells. *Front. Cell Neurosci.* 8:428. doi: 10.3389/fncel.2014.00428
- Teubner, B., Michel, V., Pesch, J., Lautermann, J., Cohen-Salmon, M., Söhl, G., et al. (2003). Connexin30 (Gjb6)-deficiency causes severe hearing impairment and lack of endocochlear potential. *Hum. Mol. Genet.* 12, 13–21. doi: 10.1093/hmg/ddg001
- Thévenaz, P., Ruttimann, U., and Unser, M. (1998). A pyramid approach to subpixel registration based on intensity. *IEEE Trans. Image Process.* 7, 27–41.
- Todt, I., Hennies, H. C., Basta, D., and Ernst, A. (2005). Vestibular dysfunction of patients with mutations of Connexin 26. *Neuroreport* 16, 1179–1181. doi: 10.1097/00001756-200508010-00009
- Tritsch, N. X., Yi, E., Gale, J. E., Glowatzki, E., and Bergles, D. E. (2007). The origin of spontaneous activity in the developing auditory system. *Nature* 450, 50–55. doi: 10.1038/nature06233
- Tritsch, N. X., Zhang, Y. X., Ellis-Davies, G., and Bergles, D. E. (2010). ATP-induced morphological changes in supporting cells of the developing cochlea. *Purinergic Signal* 6, 155–166. doi: 10.1007/s11302-010-9189-4
- Usami, S. I., Takumi, Y., Matsubara, A., Fujita, S., and Ottersen, O. P. (2001). Neurotransmission in the vestibular endorgans—glutamatergic transmission in the afferent synapses of hair cells. *Biol. Sci. Space* 15, 367–370. doi: 10.2187/bss.15.367
- Wan, G., Corfas, G., and Stone, J. S. (2013). Inner ear supporting cells: rethinking the silent majority. *Semin. Cell Dev. Biol.* 24, 448–459. doi: 10.1016/j.semcdb.2013.03.009
- Warchol, M. E. (2007). Characterization of supporting cell phenotype in the avian inner ear: implications for sensory regeneration. *Hear Res.* 227, 11–18. doi: 10.1016/j.heares.2006.08.014
- Warchol, M. E., Massoodnia, R., Pujol, R., Cox, B. C., and Stone, J. S. (2019). Development of hair cell phenotype and calyx nerve terminals in the neonatal mouse utricle. *J. Comp. Neurol.* 1–16. doi: 10.1002/cne.24658
- Wong, R. O., Chernjavsky, A., Smith, S. J., and Shatz, C. J. (1995). Early functional neural networks in the developing retina. *Nature* 374, 716–718. doi: 10.1038/374716a0
- Zhang, Y., Tang, W., Ahmad, S., Sipp, J. A., Chen, P., and Lin, X. (2005). Gap junction-mediated intercellular biochemical coupling in cochlear supporting cells is required for normal cochlear functions. *Proc. Natl. Acad. Sci. U.S.A.* 102, 15201–15206. doi: 10.1073/pnas.0501859102
- Zhao, H. B., Yu, N., and Fleming, C. R. (2005). Gap junctional hemichannel-mediated ATP release and hearing controls in the inner ear. *Proc. Natl. Acad. Sci. U.S.A.* 102, 18724–18729. doi: 10.1073/pnas.0506481102
- Zhu, Y., and Zhao, H. B. (2012). ATP activates P2X receptors to mediate gap junctional coupling in the cochlea. *Biochem. Biophys. Res. Commun.* 426, 528–532. doi: 10.1016/j.bbrc.2012.08.119

Conflict of Interest Statement: The authors declare that the research was conducted in the absence of any commercial or financial relationships that could be construed as a potential conflict of interest.

Copyright © 2019 Holman, Poppi, Frerck and Rabbitt. This is an open-access article distributed under the terms of the Creative Commons Attribution License (CC BY). The use, distribution or reproduction in other forums is permitted, provided the original author(s) and the copyright owner(s) are credited and that the original publication in this journal is cited, in accordance with accepted academic practice. No use, distribution or reproduction is permitted which does not comply with these terms.



Enriched Environment Shortens the Duration of Action Potentials in Cerebellar Granule Cells

Abdelmoneim Eshra¹, Petra Hirrlinger² and Stefan Hallermann^{1*}

¹ Medical Faculty, Carl-Ludwig-Institute for Physiology, Leipzig University, Leipzig, Germany, ² Medical Faculty, Medizinisch-Experimentelles Zentrum, Leipzig University, Leipzig, Germany

OPEN ACCESS

Edited by:

Philippe Isope,
Centre National de la Recherche
Scientifique, France

Reviewed by:

Alanna Watt,
McGill University, Canada
Roy Vincent Sillitoe,
Baylor College of Medicine,
United States

*Correspondence:

Stefan Hallermann
hallermann@medizin.uni-leipzig.de

Specialty section:

This article was submitted to
Cellular Neurophysiology,
a section of the journal
Frontiers in Cellular Neuroscience

Received: 02 February 2019

Accepted: 14 June 2019

Published: 16 July 2019

Citation:

Eshra A, Hirrlinger P and
Hallermann S (2019) Enriched
Environment Shortens the Duration
of Action Potentials in Cerebellar
Granule Cells.
Front. Cell. Neurosci. 13:289.
doi: 10.3389/fncel.2019.00289

Environmental enrichment for rodents is known to enhance motor performance. Structural and molecular changes have been reported to be coupled with an enriched environment, but functional alterations of single neurons remain elusive. Here, we compared mice raised under control conditions and an enriched environment. We tested the motor performance on a rotarod and subsequently performed whole-cell patch-clamp recordings in cerebellar slices focusing on granule cells of lobule IX, which is known to receive vestibular input. Mice raised in an enriched environment were able to remain on an accelerating rotarod for a longer period of time. Electrophysiological analyses revealed normal passive properties of granule cells and a functional adaptation to the enriched environment, manifested in faster action potentials (APs) with a higher depolarized voltage threshold and larger AP overshoot. Furthermore, the maximal firing frequency of APs was higher in mice raised in an enriched environment. These data show that enriched environment causes specific alterations in the biophysical properties of neurons. Furthermore, we speculate that the ability of cerebellar granule cells to generate higher firing frequencies improves motor performance.

Keywords: enriched environment, action potential, granule cell, cerebellum, electrophysiology

INTRODUCTION

Environmental enrichment (EE) refers to refined conditions for housing animals, which result in enhanced motor, social, sensory and cognitive performances (Nithianantharajah and Hannan, 2006). In the 1940s, Donald Hebb used EE and showed that rats, which were raised in his home, had superior problem solving abilities compared to laboratory-raised rats (Hebb, 1947, 1949). In addition, EE has been reported to improve motor performance when checked with assays such as rotarod, eyeblink conditioning, grid walking, rope suspension, footfault, and walk initiation tests (Madroñal et al., 2010; Horvath et al., 2013; Lee et al., 2013).

On the anatomical level, EE leads to thicker regions in the cerebellar cortex (Diamond et al., 1966) and altered dendritic and spine morphology (Volkmar and Greenough, 1972; Restivo et al., 2005). EE robustly induces neurogenesis in the hippocampus (Kempermann et al., 1997) and cell proliferation in the amygdala (Okuda et al., 2009) as well as gliogenesis, manifested in an increase in the number of new astrocytes in the visual cortex (Sirevaag and Greenough, 1987), the motor cortex (Ehninger and Kempermann, 2003) and the hippocampus (Kronenberg et al., 2007). Furthermore, EE increases the number of myelin-forming oligodendrocytes (Szeligo and Leblond, 1977; Sirevaag and Greenough, 1987) and the number of myelinated fibers in the cerebral white matter (Yang et al., 2013).

On the molecular level, EE has been extensively studied. A change in the expression level of many genes involved in neuronal structure, synaptic plasticity, and neurotransmission have been reported (Rampon et al., 2000; Barak et al., 2013). Moreover, the expression levels of brain-derived neurotrophic factor (BDNF) and nerve growth factor (NGF) were found to be increased in association with EE (Torasdotter et al., 1998; Rossi et al., 2006).

Granule cells are the most abundant neurons in the brain (Williams and Herrup, 1988), representing the input layer, which translates mossy fiber signals into parallel fiber signals that project to Purkinje cells (Eccles et al., 1967). Granule cells seem to have various functional roles for sensory processing (Chadderton et al., 2004), locomotion (Powell et al., 2015), and reward predictions (Wagner et al., 2017). To gain a better understanding of the improvement of motor performance induced by EE on a cellular level, we here focused on the biophysical properties of granule cells in a specific region of the cerebellum, lobule IX, which receives vestibular sensory signals (Barmack, 2003) and is involved in motor tasks such as the rotarod test (Ruediger et al., 2011). We found that EE changed fundamental biophysical parameters of granule cells, such as the duration of action potentials.

MATERIALS AND METHODS

Animals and Housing

Mice were bred and treated in accordance with the German Protection of Animals Act and with the guidelines for the welfare of experimental animals issued by the European Communities Council Directive. Mice were housed in either EE or control conditions from birth (pre-weaning) until the age of P70–80 before testing. The EE cages were designed to be bigger (height: 140 and 150 mm, for control and EE, respectively; bottom: 252×167 and 427×267 mm, for control and EE, respectively) and contained climbing ladders, plastic tubes, tunnels and small boxes as well as a variety of other toys like igloos and saucer wheels (Figure 1A). Groups of mice designated to the EE cohort were housed in larger groups (~5 and ~9, for control and EE, respectively) to allow more social interactions. The configuration of the EE was changed approximately twice per week by rearranging the position of the toys and by adding and removing toys to provide novelty, complexity, and different opportunities for learning. Both mice groups, EE and controls, were housed under an appropriate temperature (21–23°C) and humidity (40–60%) in a controlled atmosphere with a 12 h/12 h light/dark cycle, and had free access to both water and food.

Preparation and Electrophysiology

Acute cerebellar slices were prepared from mature (P70–80) C57BL/6 mice of either sex. Mice were lightly anesthetized with isoflurane and killed rapidly by decapitation. The cerebellar vermis was removed quickly and then placed in a chamber filled with ice-cold extracellular solution. Parasagittal slices of 300 μ m were cut using a Leica VT1200 microtome (Leica Microsystems, Wetzlar, Germany), transferred to an incubation chamber at ~35°C for 30 min, and subsequently stored at room temperature.

The extracellular solution for slice preparation, storage, and electrophysiological recordings contained (in mM) the following: NaCl 125, NaHCO₃ 25, glucose 20, KCl 2.5, CaCl₂ 2, NaH₂PO₄ 1.25 and MgCl₂ 1 [310 mOsm, pH 7.3 when bubbled with Carbogen (5% (vol/vol) O₂ and 95% (vol/vol) CO₂)].

Cerebellar granule cells were visualized after mounting a slice into a recording chamber placed on the stage of a Nikon upright microscope equipped with infrared differential interference contrast. Slices were continuously superfused with extracellular solution and the temperature in the center of the recording chamber was set to 36°C using a TC-324B perfusion heat controller (Warner Instruments, Hamden, CT, United States). Patch pipettes were pulled from borosilicate glass (Science Products, Hofheim, Germany) using a DMZ Puller (Zeitz-Instruments, Munich, Germany). Patch pipettes had open-tip resistances of 6–8 M Ω (when filled with intracellular solution). The intracellular solution contained the following (in mM): K-gluconate 150, NaCl 10, K-HEPES 10, MgATP 3 and Na-GTP 0.3 (300–305 mOsm, pH adjusted to 7.3 with KOH). Whole-cell patch-clamp recordings from granule cells were made using a HEKA EPC10/2 amplifier (HEKA Elektronik, Lambrecht, Germany) operated by the corresponding software PatchMaster (HEKA Elektronik), running on a personal computer. Recordings were performed in the middle region of the granule cell layer of lobule IX of the cerebellar vermis. Measurements were corrected for a liquid junction potential of +13 mV. Series resistance was typically <40 M Ω . Experiments with series resistance >40 M Ω were excluded. Action potentials were evoked in current-clamp mode by injecting brief current pulses (amplitude 10–500 pA; duration 300 ms). Recordings from neurons of mice raised in an enriched environment and the corresponding control, of the same gender, were done in the same day in an interleaved manner.

Rotarod Test

Before testing began, mice were given a trial in order to familiarize them with the procedure. Mice were placed on the rotarod (Panlab, Harvard apparatus) at a constant acceleration from 4 to 40 rounds per minute for a total of 120 s so that the longer the mouse remained on the rod, the faster it had to move to maintain balance. Each time the mouse fell, it was immediately returned to the rod and the process was restarted for ~10 trials per mouse. EE and control mice were compared on an animal-to-animal basis by averaging the latencies per mouse (Figure 1B) and on a trial-to-trial basis by averaging the latencies per trial number (Figure 1C). Motor assessment of each EE mouse and the corresponding control, having the same gender, was done on the same day, and both were later sacrificed to be used for electrophysiological recordings.

Analysis of Action Potential Parameters

Data were analyzed using custom-made procedures in Igor Pro software (WaveMetrics, Tigard, OR, United States). The parameters of the action potentials (APs) were determined in the trace at current threshold, the trace with 60-pA-current injection, and the trace with most APs elicited. In each of these three traces the analysis was restricted to the first AP, average of the first five

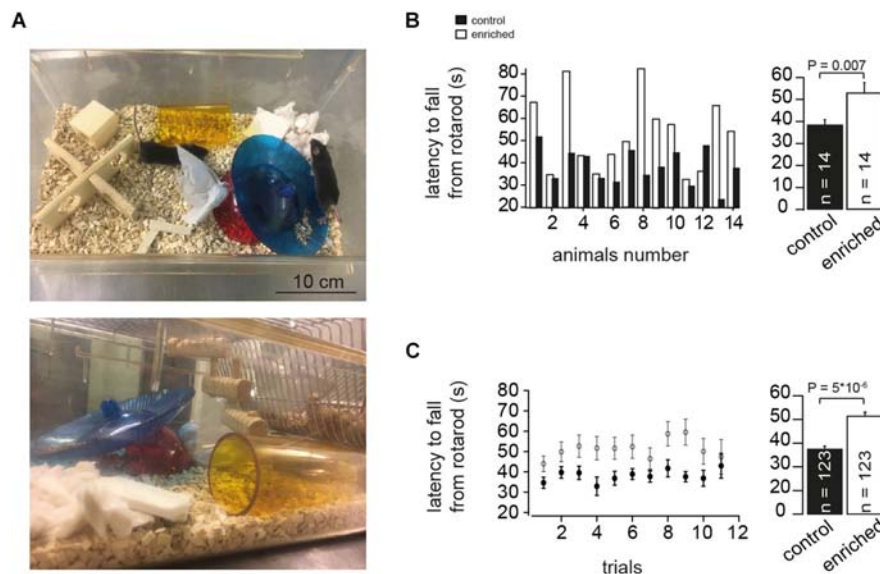


FIGURE 1 | Enriched environment improves motor performance. **(A)** Example photographs of EE cage showing different items placed during the housing of the mice. **(B)** Left: Bar graphs showing comparison of the absolute latency on the rotarod per animal (animal-to-animal basis). Right: Bar graph of the average latency on the rotarod assessment test for EE and control mice, $n = 14$ and 14 mice, respectively; Student's t -test was used to measure statistical significance, $P_{t-test} = 0.007$. **(C)** Left: Bar graphs showing comparison of the absolute latency on the rotarod per trial number (trial-to-trial basis). Right: Bar graph of the grand average of the latency on the rotarod, $n = 123$ and 123 trials, for control and EE mice, respectively; $P_{t-test} = 5 \times 10^{-6}$.

APs at the beginning of the current injection, and average of all APs. In traces with less than five APs, the value for the first five APs was the average of those up to four APs. In four and one out of 299 cells in control and EE mice, respectively, the current threshold was above 60 pA, and accordingly the numbers of cells for the 60-pA-current trace were 295 and 298 for control and EE mice, respectively. The half duration of AP was measured at half maximum amplitude. The amplitude was measured from threshold to peak. The threshold was defined as the membrane voltage at which the first derivative exceeded 100 V/s. Action potentials with a peak smaller than -20 mV, an amplitude smaller than 20 mV, and a half duration smaller than 50 μ s or larger than 500 μ s were excluded. These exclusion criteria were chosen to ensure that only proper APs are analyzed. For example, the distribution of AP duration is well within the 50 and 500 μ s borders (**Supplementary Figure S2B**).

Statistics

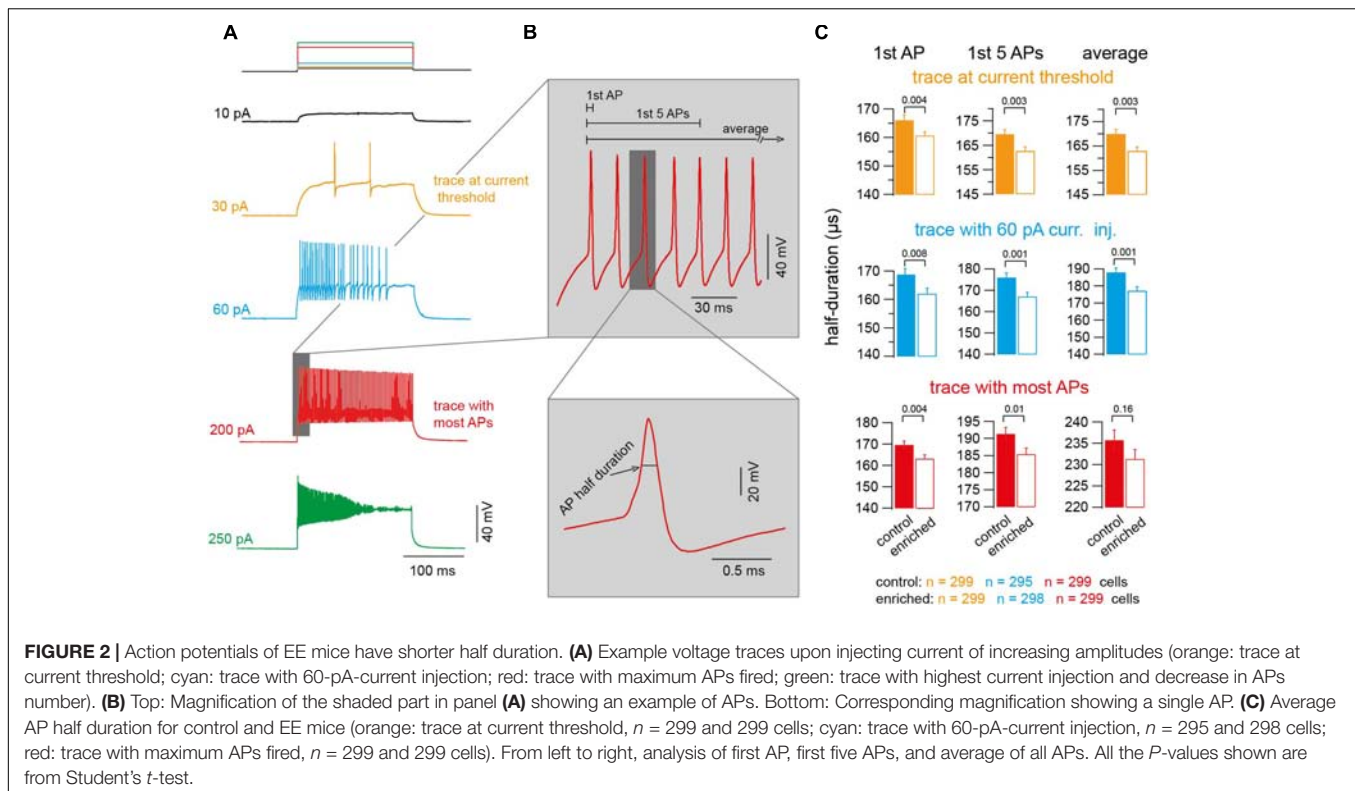
Data are presented as mean \pm SEM. To provide a simple measure of the statistical difference of the shown comparisons, the P -value of the Student's t -test is provided for each bar graph (using Microsoft Excel or Igor Pro software). In addition, a four-way ANOVA test with the following four factors was used: (1) AP parameters (half-duration, amplitude, overshoot and threshold), (2) trace per cell (trace at current threshold, trace with 60 pA, and trace with maximal number of APs), (3) APs per trace (first AP, first five APs, and average of all APs), and (4) animal group (control and EE). For the comparison of control vs. EE mice (4th factor), the P -value was 0.0002. However, the significance level of the four-way ANOVA is most likely

an overestimation, because the investigated parameters are not completely independent. We therefore focused on the P -values of the t -test (P_{t-test}). For each of the four AP parameters, there was the same trend between control and enriched conditions in the various analyzed APs. In addition, we addressed the statistical significance of the difference of the AP half duration not only on a neuron-to-neuron but also on a mouse-to-mouse basis (i.e., the average value for each mouse). To address the significance of the correlations (**Figure 4D** and **Supplementary Figures S3A,B**), we provided the Pearson correlation coefficient ($R_{Pearson}$) and the corresponding P -value ($P_{Pearson}$) as well as the P -value of the Spearman rank correlation coefficient ($P_{Spearman Rank}$). T -tests were calculated with Microsoft Excel and the other statistical tests with built-in functions of Mathematica 10 (Wolfram Research, Champaign, IL, United States).

RESULTS

Enriched Environment Improves Motor Performance

To investigate the effect of continuous long-term EE (**Figure 1A**) on the motor performance of mice, we used the rotarod test. The performance of mice raised in an EE (referred to as EE mice in the following) was significantly better on the rotating rod than the corresponding control mice. This was manifested in a significantly longer latency to fall from the rotarod in the case of EE mice than for the corresponding controls, both for animal-to-animal overall performance (38.7 ± 2.1 and 53.2 ± 4.5 s for control and EE mice, $n = 14$ and 14 mice, respectively;



$P_{t-test} = 0.007$; **Figure 1B**) and for trial-to-trial basis (38.1 ± 0.9 and 51.3 ± 1.4 s for control and enriched animals, $n = 123$ and 123 trials, respectively; $P_{t-test} = 5 \times 10^{-6}$; **Figure 1C**). This is consistent with previous findings where EE was reported to have a direct effect on motor functions when assessed with different motor coordination assays (Madroñal et al., 2010; Horvath et al., 2013; Lee et al., 2013). These data indicate that EE mice have improved motor capabilities as evaluated by the rotarod test.

Action Potentials of EE Mice Have Shorter Half Duration

To test if and how these improvements in motor skills go along with alterations of the biophysical parameters of single neurons, we performed whole-cell current-clamp recordings from granule cells and measured the excitability of the neurons and the properties of the APs. We analyzed 90,750 APs, in 600 neurons in 30 mice, elicited by injection of depolarizing current of different amplitudes (10–500 pA; **Figure 2A**). Due to several reasons (like AP broadening and amplitude reduction), which can change the AP shape over the duration of injected current, and in order to properly compare the APs in both conditions, we focused on three traces to be representative for all the APs fired per neuron: (1) the trace with lowest current injection and at least one AP (current threshold), (2) the trace where APs were elicited upon 60 pA current injection, and (3) the trace where the highest number of APs appeared. Within each of these three traces, we analyzed the first AP, the average of the first five APs, and the average of all APs (**Figure 2B**). The half duration of the AP of neurons of EE mice

was found to be significantly shorter than the half duration of APs of neurons of control mice (e.g., first AP in the traces at a current threshold: 166.1 ± 1.6 and $159.7 \pm 1.5 \mu s$ for control and EE mice, $n = 299$ and 299 , respectively; $P_{t-test} = 0.002$; **Figure 2C**). The analysis of other APs in other traces revealed similar results (**Figure 2C**). To further test the observed effect of EE on AP half duration, we compared the AP half duration on a mouse-to-mouse basis (i.e., the average value for each mouse). We found a tendency toward faster APs in EE compared to control mice ($P_{t-test} \approx 0.1$; **Supplementary Figure S1**), indicating that a trend with a significance level of 10% exists even on a mouse-to-mouse basis. In order to test the robustness of our measurements, we compared the AP half duration of control mice of different ages from P20 to 1 year, and found that the AP half duration did not change significantly between different age groups (**Supplementary Figure S2A**), indicating that our technique allows precise and reliable determination of AP parameters. The AP seems to be a constant parameter throughout development between the age of P20 and 1 year. Despite this developmental constancy, our data demonstrate that the AP half duration of cerebellar granule cells of mice raised in an EE environment is shorter compared to the corresponding control mice.

Alteration in Threshold, Overshoot, and Amplitude of Action Potentials Upon Enrichment

To gain insight into the different biophysical properties of APs of EE mice, we first compared the input resistance by injecting

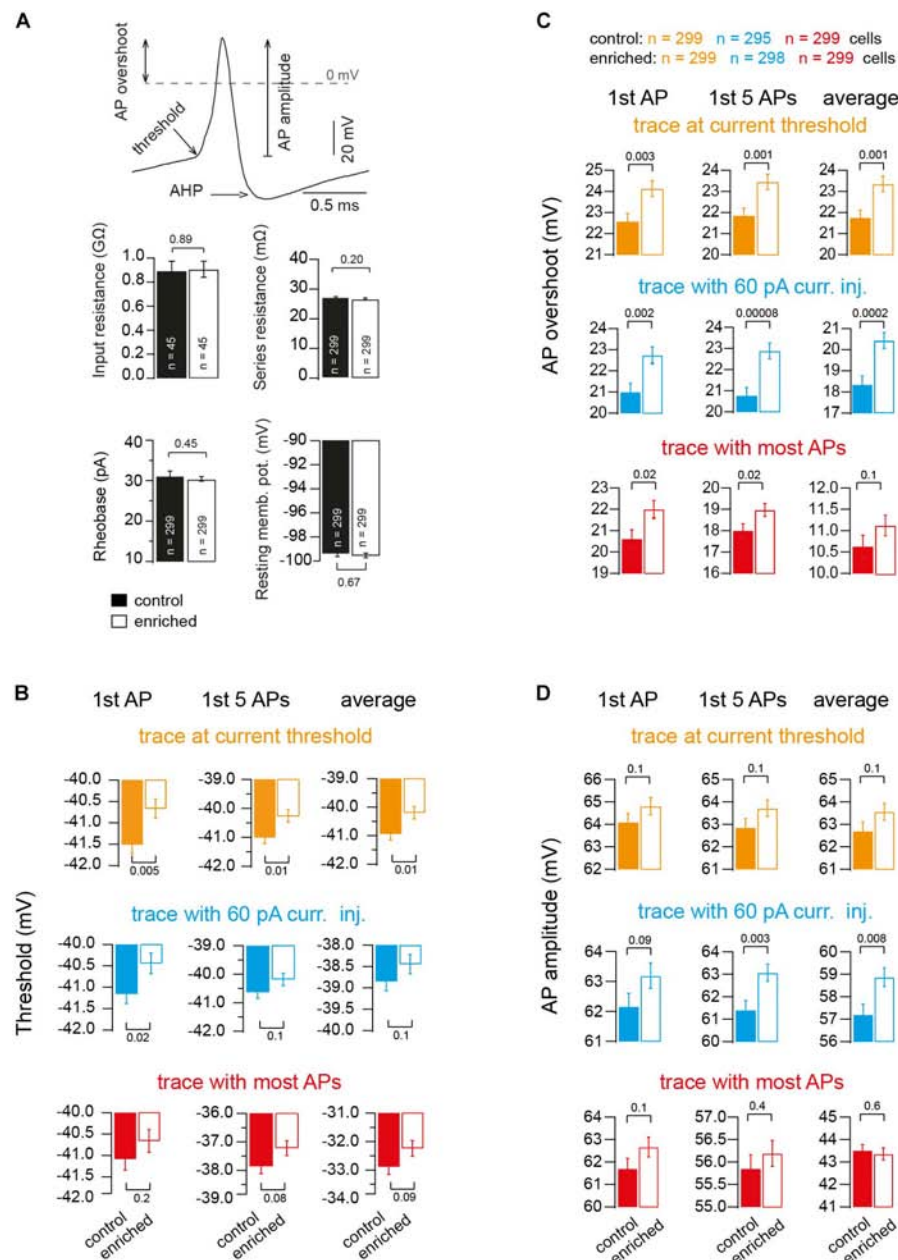


FIGURE 3 | Alteration in threshold, overshoot and amplitude of action potentials upon enrichment. **(A)** Example of an AP illustrating the criteria of measuring AP threshold, AP overshoot and AP amplitude. Bar graphs showing the average of resting membrane potential, $n = 299$ and 299 cells; input resistance, $n = 45$ and 45 cells; rheobase, $n = 299$ and 299 cells; and series resistance, $n = 299$ and 299 cells, of neurons of control and EE mice, respectively. **(B)** Average voltage threshold of APs of neurons of control and EE mice (orange: trace at current threshold, $n = 299$ and 299 cells; cyan: trace with 60 -pA-current injection, $n = 295$ and 298 cells; red: trace with maximum APs fired, $n = 299$ and 299 cells). From left to right, analysis of first AP, first five APs and average of all APs, respectively. **(C)** Corresponding average AP overshoot. **(D)** Corresponding average AP amplitude. All the P -values shown are from Student's t -test.

current of low amplitude into a subset of granule cells (~ 3) from each animal of either the EE or control groups, and observed no significant change (0.88 ± 0.08 and 0.90 ± 0.07 G Ω , for control and EE mice, $n = 45$ and 45 , respectively; $P_{t-test} = 0.89$; **Figure 3A**). Other passive parameters of neurons were similar, too (series resistance: 27.4 ± 0.4 and 26.7 ± 0.4 M Ω , for control and EE mice, $n = 299$ and 299 , respectively; $P_{t-test} = 0.2$;

rheobase: 31.3 ± 1.1 and 30.4 ± 0.5 pA; $P_{t-test} = 0.45$; and resting membrane potential: -99.4 ± 0.3 and -99.5 ± 0.2 mV; $P_{t-test} = 0.67$; **Figure 3A**).

In order to gain more mechanistic insights, we focused on additional parameters of the APs and found that the threshold potential of the APs of EE mice had a more depolarized voltage than the APs of control mice (e.g., first AP in the traces at current

threshold: -41.5 ± 0.21 and -40.67 ± 0.22 mV for control and EE mice, $n = 299$ and 299 , respectively; $P_{t\text{-test}} = 0.005$). The analysis of other APs in other traces revealed similar results (**Figure 3B**). The maximum peak of the voltage overshoot reached during the AP was higher in EE compared to control mice (e.g., first AP in the traces at current threshold 22.58 ± 0.36 and 24.13 ± 0.37 mV, for control and EE mice, $n = 299$ and 299 , respectively, $P_{t\text{-test}} = 0.003$). The analysis of other APs in other traces revealed similar results (**Figure 3C**). Furthermore, there was also a tendency for the absolute amplitude of APs to be higher in the case of EE mice compared to control mice (e.g., first AP in the traces at current threshold 64.09 ± 0.38 and 64.8 ± 0.38 mV, for control and EE mice, $n = 299$ and 299 , respectively; $P_{t\text{-test}} = 0.1$). The analysis of other APs in other traces revealed similar results (**Figure 3D**).

Interestingly, when analyzing the after-hyperpolarizing (AHP) component of the APs, there was no significant difference between EE and control mice. For the trace at current threshold, the delay between the peak (maximum) of the AP and the peak (minimum) of the AHP was not different between EE and control mice groups (402.6 ± 3.3 and 401.9 ± 3.4 μ s for control and EE mice, $n = 299$ and 299 , respectively; $P_{t\text{-test}} = 0.89$), and the AHP voltage did not change either (e.g., first AP in the traces at current threshold: -64.9 ± 0.2 and -64.8 ± 0.2 mV for control and EE mice, $n = 299$ and 299 , respectively; $P_{t\text{-test}} = 0.85$). The analysis of other APs in other traces revealed similar results, indicating that channels responsible for the after-hyperpolarization of APs were not altered. Thus, these data indicate that several fundamental parameters of APs are altered in EE mice compared to control mice.

Enriched Environment Tunes Neurons for Firing at Higher Frequencies

The shortening of the AP half duration suggests that neurons are able to fire at higher frequencies after EE. We analyzed the maximum firing frequency of the first two APs (instantaneous frequency), the average of the first five APs, and average of all APs of the trace where most APs occurred (**Figure 4A**), and found that neurons of EE mice were able to reach higher firing frequencies than neurons of control mice (e.g., instantaneous frequency of 495.5 ± 9.8 and 521.6 ± 9.4 Hz, for control and EE mice, $n = 299$ and 299 , respectively; $P_{t\text{-test}} = 0.05$; **Figure 4B**). We also analyzed the maximum firing frequency on a mouse-to-mouse basis corresponding to the analysis of the AP half duration in **Supplementary Figure S1**. Again, the maximum firing frequency showed a tendency to be larger in EE compared to control mice ($P_{t\text{-test}} \approx 0.1$; **Figure 4C**). Finally, we observed a correlation between the maximum firing frequency per animal (i.e., the average from ~ 20 granule cells) and the motor performance of the same animal measured on the same day (i.e., average latency of ~ 10 trials on the rotarod; **Figure 4D**). In addition, there was an inverse correlation between maximum firing frequency and AP half duration (**Supplementary Figure S3A**). As a result, there was also a tendency of an inverse correlation between the latency on the rotarod and the AP half duration (**Supplementary Figure S3B**; see last paragraph of the discussion for a cautious

interpretation of the correlations described here). These data indicate that the maximal firing frequency of granule cells is higher in EE compared to control mice.

DISCUSSION

Our data show that, upon EE, cerebellar granule cells of lobule IX of the cerebellum have altered AP parameters and can fire APs at higher frequencies. Thus, fundamental biophysical parameters of the neurons are influenced by the environment. Furthermore, the maximal firing frequency of granule cells correlated with the motor performance of the mice. This correlation does not provide a causal relationship between firing rate and behavior, but it is tempting to speculate that higher firing frequencies of cerebellar granule cells are beneficial for rapid sensory-motor integration.

EE-Induced Changes in Action Potentials

We found that EE shortened the half-duration, increased the overshoot, and increased the threshold of APs. The observed effect is likely due to an alteration induced by EE on ion channels, so that voltage-gated potassium channels (K_v) and sodium channels (Na_v) have different densities and/or different properties (Keyvani et al., 2004). The observed shortening in the AP half duration could be explained by faster activating K_v channels. In fact, a regulatory effect of EE on potassium channels and particularly the regulatory subunit $K_v\beta 1$ has been reported (Need et al., 2003). The observed increase in the amplitude and the threshold of APs could be linked to a change in the density or properties of Na_v channels. Interestingly, an effect of EE on sodium channel $Na_v 1.6$ has been reported, in which EE decreased the amplitude of the ramp-induced persistent sodium current of the medium spiny neurons in the nucleus accumbens (Scala et al., 2018). Our data showing that the input resistance and the resting membrane potential were not altered upon EE is consistent with other work showing constant passive cell parameters during intrinsic homeostatic plasticity of cortical pyramidal neurons (Desai et al., 1999). Thus, the changes in ion channel properties and/or density upon EE are specific to channels shaping the AP and do not extend to channels setting the passive neuronal properties.

Our finding that EE alters AP properties adds to the emerging idea that AP properties are dynamically regulated. For example, it was recently shown that a direct modulation of presynaptic K_v channels in hippocampal mossy fiber boutons mediates a form of synaptic plasticity by activity-dependent release of arachidonic acid from the postsynaptic CA3 neurons (Carta et al., 2014). In addition, prominent alterations of AP half duration were observed during homeostatic plasticity induced in fast spiking interneurons (Miller et al., 2011). Furthermore, the AP half-duration of specific neurons in the amygdala and the cochlear nucleus was changed by fear extinction and noise exposure, respectively (Senn et al., 2014; Ngodup et al., 2015). Finally, altered neuronal activity in avian brainstem auditory neurons (Kuba et al., 2010) or hippocampal neurons (Grubb and Burrone, 2010) causes a rearrangement of the Na_v channels in the axon initial segment, contributing to the excitability and firing patterns

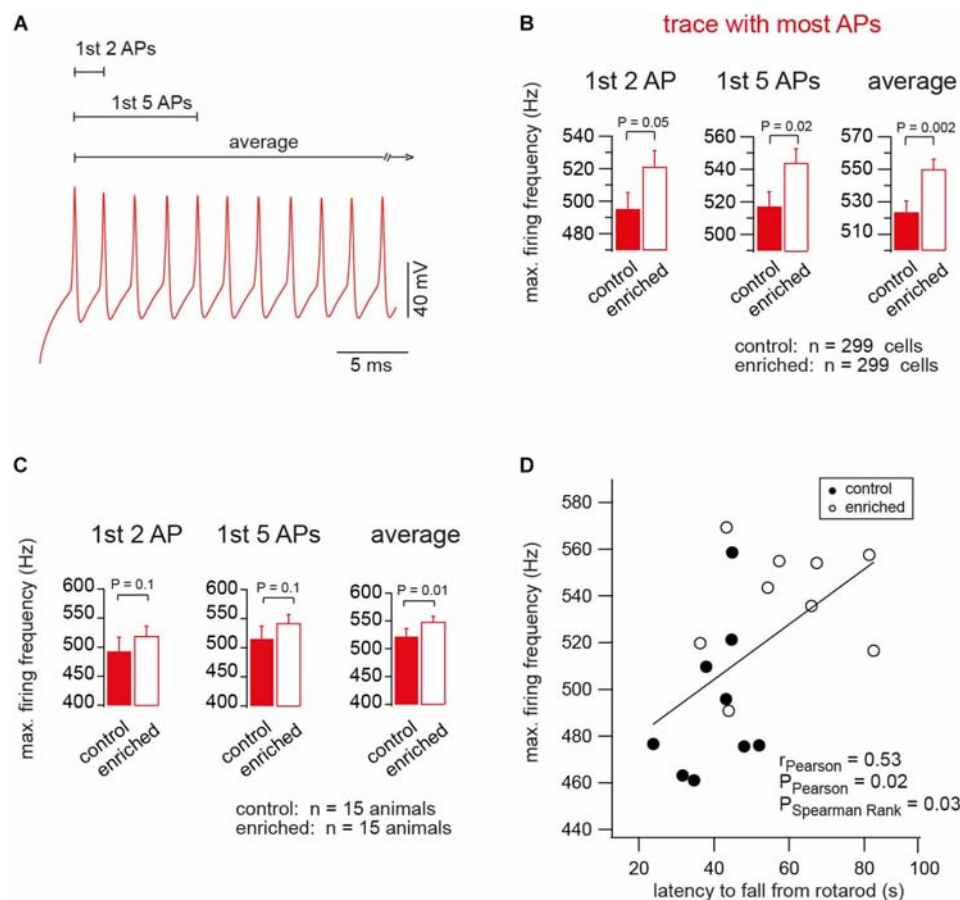


FIGURE 4 | Enriched environment tunes neurons for firing at higher frequencies. **(A)** An example of the APs of the trace of maximum firing frequency (color-code as in **Figure 2**). **(B)** Average maximum firing frequency of neurons of EE and control mice, $n = 299$, 299 cells, based on the first two, first five APs, and average of all APs in the trace, in which most APs were fired, $P_{t\text{-test}} = 0.05$, 0.02, 0.002, respectively. **(C)** Average maximum firing frequency of neurons of EE and the corresponding control mice, $n = 15$, 15 mice. For the first two, first five APs and average of all APs in the trace, in which most APs were fired, $P_{t\text{-test}} = 0.1$, 0.1 and 0.01, respectively. **(D)** Correlation between the maximum firing frequency and the latency of the mouse to fall from rotarod, for control and EE mice, $n = 9$ and 9 mice, $r_{\text{Pearson}} = 0.53$, $P_{\text{Pearson}} = 0.02$, and $P_{\text{Spearman Rank}} = 0.03$.

of neurons (Evans et al., 2015; Kole and Brette, 2018). Our results are thus consistent with a scenario, in which EE alters neuronal activity, which in turn induces plastic alterations in ion channels responsible for shaping the AP waveform.

Relation of Motor Performance and Firing Rate

Information can be coded as the average firing rate or as the temporal correlation of the exact time of the APs (Rieke et al., 1997). For example, vestibular, proprioceptive, and somatosensory information (Van Kan et al., 1993; Jörntell and Ekerot, 2006; Arenz et al., 2008) as well as the control of muscles (Adrian and Bronk, 1929) relies on rate coding. Our finding that improved motor performance correlates with AP frequency is therefore consistent with the idea that an increased bandwidth of firing accelerates information processing (reviewed in Delvendahl and Hallermann, 2016). Particularly, the increase in firing frequency of granule cells guarantees the precision of

information transfer from the granule cell level to the Purkinje cell level, assuring a more precise pace-making role for Purkinje cells, which is critical in motor coordination (Walter et al., 2006).

We observed both a shortening of the AP half duration and an increase in the maximal firing frequency upon EE. There was an inverse correlation between maximum firing frequency and AP half duration (**Supplementary Figure S3A**). Such inverse correlation has also been observed within vestibular nucleus neurons (Gittis et al., 2010), across cell types (Carter and Bean, 2009), and across different species (Wang et al., 2016). As expected from the correlation between the latency on the rotarod and the maximal firing frequency (**Figure 4D**), we therefore also observed a tendency for an inverse correlation between the latency on the rotarod and the AP half duration (**Supplementary Figure S3B**).

Thus, our data provide support to the idea that the duration of the AP and the maximum frequency of firing are related to the speed of sensory-motor information processing. Interestingly, action potential kinetics were recently shown to correlate with

another behavioral parameter (the intelligence quotient; IQ) in humans (Goriounova et al., 2018). However, several caveats should be considered regarding the relation between behavior and biophysical properties of neurons. (1) The correlations, which we observed here between performance on the rotarod and AP firing in granule cells, is statistically significant but not very strong. (2) The correlations do not imply causal relationships. (3) Our results were obtained in acute brain slices and future studies in freely behaving animals need to confirm the correlation between behavior and neuronal firing patterns *in vivo*. (4) Several other neuronal factors changing upon EE could contribute to the improved motor performance, such as myelination (Szeligo and Leblond, 1977; McKenzie et al., 2014), neuronal density (Kempermann et al., 1997), and dendritic and spine morphology (Volkmar and Greenough, 1972; Restivo et al., 2005). (5) Other parts of the nervous system (e.g., other types of neurons, other cerebellar lobules, the motor cortex, and the vestibular and proprioceptive systems) could change and cause the improved motor performance. (6) Factors independent of the nervous system (e.g., muscle strength and body weight) could underlie the improved rotarod performance. Yet, independent of the difficult question of the relation between behavior and neuronal biophysical properties, our data convincingly demonstrate that fundamental parameters such as AP duration and maximum firing frequency are influenced by the environment.

ETHICS STATEMENT

All experiments were approved in advance by the Institutional Ethics Committees and animals were treated in accordance with

the European (EU Directive 2010/63/EU, Annex IV for animal experiments), national, and Leipzig University guidelines.

AUTHOR CONTRIBUTIONS

AE and SH designed the study, analyzed the data, and wrote the manuscript. AE performed the experiments. All authors approved the final version of the manuscript.

SUPPLEMENTARY MATERIAL

The Supplementary Material for this article can be found online at: <https://www.frontiersin.org/articles/10.3389/fncel.2019.00289/full#supplementary-material>

FIGURE S1 | Statistical analysis of AP half duration considering the average value for each mouse instead of the average value for each cell. The average AP half duration of 15 EE and 15 control mice is shown; (orange: trace at current threshold; cyan: trace with 60-pA-current injection; red: trace with maximum APs fired). From left to right, analysis of first AP, first five APs, and average of all APs, respectively. All the *P*-values shown are from Student's *t*-test.

FIGURE S2 | Constancy of action potential half duration between different age groups. **(A)** Average AP half duration of control mice of different age groups (*n* refers to the number of cells). **(B)** Histogram showing the distribution of the half duration of all APs recorded.

FIGURE S3 | Correlation between behavior and electrophysiology. **(A)** Correlation between maximum firing frequency and AP half duration, for control and EE mice, *n* = 9, 9 mice, $r_{\text{Pearson}} = 0.70$, $P_{\text{Pearson}} = 0.0007$, $P_{\text{Spearman Rank}} = 0.0002$. **(B)** Correlation between AP half duration and latency to fall from rotarod, for control and EE mice, *n* = 9, 9 mice, $r_{\text{Pearson}} = 0.43$, $P_{\text{Pearson}} = 0.07$, $P_{\text{Spearman Rank}} = 0.04$.

REFERENCES

- Adrian, E. D., and Bronk, D. W. (1929). The discharge of impulses in motor nerve fibres: part II. The frequency of discharge in reflex and voluntary contractions. *J. Physiol.* 67, 119–151. doi: 10.1113/jphysiol.1929.sp002557
- Arenz, A., Silver, R. A., Schaefer, A. T., and Margrie, T. W. (2008). The contribution of single synapses to sensory representation *in vivo*. *Science* 321, 977–980. doi: 10.1126/science.1158391
- Barak, B., Shvarts-Serebro, I., Modai, S., Gilam, A., Okun, E., Michaelson, D. M., et al. (2013). Opposing actions of environmental enrichment and Alzheimer's disease on the expression of hippocampal microRNAs in mouse models. *Transl. Psychiatry* 3:e304. doi: 10.1038/tp.2013.77
- Barmack, N. H. (2003). Central vestibular system: vestibular nuclei and posterior cerebellum. *Brain Res. Bull.* 60, 511–541. doi: 10.1016/S0361-9230(03)00055-8
- Carta, M., Lanore, F., Rebola, N., Szabo, Z., Da Silva, S. V., Lourenço, J., et al. (2014). Membrane lipids tune synaptic transmission by direct modulation of presynaptic potassium channels. *Neuron* 81, 787–799. doi: 10.1016/j.neuron.2013.12.028
- Carter, B. C., and Bean, B. P. (2009). Sodium entry during action potentials of mammalian neurons: incomplete inactivation and reduced metabolic efficiency in fast-spiking neurons. *Neuron* 64, 898–909. doi: 10.1016/j.neuron.2009.12.011
- Chadderton, P., Margrie, T. W., and Häusser, M. (2004). Integration of quanta in cerebellar granule cells during sensory processing. *Nature* 428, 856–860. doi: 10.1038/nature02442
- Delvendahl, I., and Hallermann, S. (2016). The cerebellar mossy fiber synapse as a model for high-frequency transmission in the mammalian CNS. *Trends Neurosci.* 39, 722–737. doi: 10.1016/j.tins.2016.09.006
- Desai, N. S., Rutherford, L. C., and Turrigiano, G. G. (1999). Plasticity in the intrinsic excitability of cortical pyramidal neurons. *Nat. Neurosci.* 2, 515–520. doi: 10.1038/9165
- Diamond, M. C., Law, F., Rhodes, H., Lindner, B., Rosenzweig, M. R., Krech, D., et al. (1966). Increases in cortical depth and glia numbers in rats subjected to enriched environment. *J. Comp. Neurol.* 128, 117–125. doi: 10.1002/cne.901280110
- Eccles, J. C., Ito, M., and Szentagothai, J. (1967). *The Cerebellum as a Neuronal Machine*. Berlin: Springer.
- Ehninger, D., and Kempermann, G. (2003). Regional effects of wheel running and environmental enrichment on cell genesis and microglia proliferation in the adult murine neocortex. *Cereb. Cortex* 13, 845–851. doi: 10.1093/cercor/13.8.845
- Evans, M. D., Dumitrescu, A. S., Kruijssen, D. L. H., Taylor, S. E., and Grubb, M. S. (2015). Rapid modulation of axon initial segment length influences repetitive spike firing. *Cell Rep.* 13, 1233–1245. doi: 10.1016/j.celrep.2015.09.066
- Gittis, A. H., Moghadam, S. H., and du Lac, S. (2010). Mechanisms of sustained high firing rates in two classes of vestibular nucleus neurons: differential contributions of resurgent Na, Kv3, and BK currents. *J. Neurophysiol.* 104, 1625–1634. doi: 10.1152/jn.00378.2010
- Goriounova, N. A., Heyer, D. B., Wilbers, R., Verhoog, M. B., Giugliano, M., Verbist, C., et al. (2018). Large and fast human pyramidal neurons associate with intelligence. *eLife* 7:e41714. doi: 10.7554/eLife.41714
- Grubb, M. S., and Burrone, J. (2010). Activity-dependent relocation of the axon initial segment fine-tunes neuronal excitability. *Nature* 465, 1070–1074. doi: 10.1038/nature09160
- Hebb, D. (1947). The effects of early experience on problem solving at maturity. *Am. Psychol.* 2, 306–307.
- Hebb, D. (1949). *The Organization of Behavior*. New York, NY: John Wiley & Sons.

- Horvath, G., Reglodi, D., Vadasz, G., Farkas, J., and Kiss, P. (2013). Exposure to enriched environment decreases neurobehavioral deficits induced by neonatal glutamate toxicity. *Int. J. Mol. Sci.* 14, 19054–19066. doi: 10.3390/ijms140919054
- Jörntell, H., and Ekerot, C.-F. (2006). Properties of somatosensory synaptic integration in cerebellar granule cells *in vivo*. *J. Neurosci.* 26, 11786–11797. doi: 10.1523/JNEUROSCI.2939-06.2006
- Kempermann, G., Kuhn, H. G., and Gage, F. H. (1997). More hippocampal neurons in adult mice living in an enriched environment. *Nature* 386, 493–495. doi: 10.1038/386493a0
- Keyvani, K., Sachser, N., Witte, O. W., and Paulus, W. (2004). Gene expression profiling in the intact and injured brain following environmental enrichment. *J. Neuropathol. Exp. Neurol.* 63, 598–609. doi: 10.1093/jnen/63.6.598
- Kole, M. H., and Brette, R. (2018). The electrical significance of axon location diversity. *Curr. Opin. Neurobiol.* 51, 52–59. doi: 10.1016/j.conb.2018.02.016
- Kronenberg, G., Wang, L. P., Geraerts, M., Babu, H., Synowitz, M., Vicens, P., et al. (2007). Local origin and activity-dependent generation of nestin-expressing protoplasmic astrocytes in CA1. *Brain Struct. Funct.* 212, 19–35. doi: 10.1007/s00429-007-0141-5
- Kuba, H., Oichi, Y., and Ohmori, H. (2010). Presynaptic activity regulates Na⁺ channel distribution at the axon initial segment. *Nature* 465, 1075–1078. doi: 10.1038/nature09087
- Lee, M. Y., Yu, J. H., Kim, J. Y., Seo, J. H., Park, E. S., Kim, C. H., et al. (2013). Alteration of synaptic activity-regulating genes underlying functional improvement by long-term exposure to an enriched environment in the adult brain. *Neurorehabil. Neural Repair* 27, 561–574. doi: 10.1177/1545968313481277
- Madroñal, N., López-Aracil, C., Rangel, A., del Río, J. A., Delgado-García, J. M., and Gruart, A. (2010). Effects of enriched physical and social environments on motor performance, associative learning, and hippocampal neurogenesis in mice. *PLoS One* 5:e11130. doi: 10.1371/journal.pone.0011130
- McKenzie, I. A., Ohayon, D., Li, H., De Faria, J. P., Emery, B., Tohyama, K., et al. (2014). Motor skill learning requires active central myelination. *Science* 346, 318–322. doi: 10.1126/science.1254960
- Miller, M. N., Okaty, B. W., Kato, S., and Nelson, S. B. (2011). Activity-dependent changes in the firing properties of neocortical fast-spiking interneurons in the absence of large changes in gene expression. *Dev. Neurobiol.* 71, 62–70. doi: 10.1002/dneu.20811
- Need, A. C., Irvine, E. E., and Giese, K. P. (2003). Learning and memory impairments in Kvβ1.1-null mutants are rescued by environmental enrichment or ageing. *Eur. J. Neurosci.* 18, 1640–1644. doi: 10.1046/j.1460-9568.2003.02889.x
- Ngodup, T., Goetz, J. A., McGuire, B. C., Sun, W., Lauer, A. M., and Xu-Friedman, M. A. (2015). Activity-dependent, homeostatic regulation of neurotransmitter release from auditory nerve fibers. *Proc. Natl. Acad. Sci. U.S.A.* 112, 6479–6484. doi: 10.1073/pnas.1420885112
- Nithianantharajah, J., and Hannan, A. J. (2006). Enriched environments, experience-dependent plasticity and disorders of the nervous system. *Nat. Rev. Neurosci.* 7, 697–709. doi: 10.1038/nrn1970
- Okuda, H., Tatsumi, K., Makinodan, M., Yamauchi, T., Kishimoto, T., and Wanaka, A. (2009). Environmental enrichment stimulates progenitor cell proliferation in the amygdala. *J. Neurosci. Res.* 87, 3546–3553. doi: 10.1002/jnr.22160
- Powell, K., Mathy, A., Duguid, I., and Häusser, M. (2015). Synaptic representation of locomotion in single cerebellar granule cells. *eLife* 4:e07290. doi: 10.7554/eLife.07290
- Rampon, C., Jiang, C. H., Dong, H., Tang, Y.-P., Lockhart, D. J., Schultz, P. G., et al. (2000). Effects of environmental enrichment on gene expression in the brain. *Proc. Natl. Acad. Sci. U.S.A.* 97, 12880–12884. doi: 10.1073/pnas.97.23.12880
- Restivo, L., Ferrari, F., Passino, E., Sgobio, C., Bock, J., Oostra, B. A., et al. (2005). Enriched environment promotes behavioral and morphological recovery in a mouse model for the fragile X syndrome. *Proc. Natl. Acad. Sci. U.S.A.* 102, 11557–11562. doi: 10.1073/pnas.0504984102
- Rieke, F., Warland, D., de Ruyter Van Steveninck, R. R., and Bialek, W. (1997). “Spikes: exploring the neural code,” in *Computational Neuroscience*, ed. K. Robertson (Cambridge, MA: MIT Press).
- Rossi, C., Angelucci, A., Costantin, L., Braschi, C., Mazzantini, M., Babbini, F., et al. (2006). Brain-derived neurotrophic factor (BDNF) is required for the enhancement of hippocampal neurogenesis following environmental enrichment. *Eur. J. Neurosci.* 24, 1850–1856. doi: 10.1111/j.1460-9568.2006.05059.x
- Ruediger, S., Vittori, C., Bednarek, E., Genoud, C., Strata, P., Sacchetti, B., et al. (2011). Learning-related feedforward inhibitory connectivity growth required for memory precision. *Nature* 473, 514–518. doi: 10.1038/nature09946
- Scala, F., Nenov, M. N., Crofton, E. J., Singh, A. K., Folorunso, O., Zhang, Y., et al. (2018). Environmental enrichment and social isolation mediate neuroplasticity of medium spiny neurons through the GSK3 pathway. *Cell Rep.* 23, 555–567. doi: 10.1016/j.celrep.2018.03.062
- Senn, V., Wolff, S. B. E., Herry, C., Grenier, F., Ehrlich, I., Gründemann, J., et al. (2014). Long-range connectivity defines behavioral specificity of amygdala neurons. *Neuron* 81, 428–437. doi: 10.1016/j.neuron.2013.11.006
- Sirevaag, A. M., and Greenough, W. T. (1987). Differential rearing effects on rat visual cortex synapses. III. neuronal and glial nuclei, boutons, dendrites, and capillaries. *Brain Res.* 424, 320–332. doi: 10.1016/0006-8993(87)91477-6
- Szeligo, F., and Leblond, C. P. (1977). Response of the three main types of glial cells of cortex and corpus callosum in rats handled during suckling or exposed to enriched, control and impoverished environments following weaning. *J. Comp. Neurol.* 172, 247–263. doi: 10.1002/cne.901720205
- Torassdotter, M., Metsis, M., Henriksson, B. G., Bengt, W., and Mohammed, A. H. (1998). Environmental enrichment results in higher levels of nerve growth factor mRNA in the rat visual cortex and hippocampus. *Behav. Brain Res.* 93, 83–90. doi: 10.1016/S0166-4328(97)00142-3
- Van Kan, P. L., Gibson, A. R., and Houk, J. C. (1993). Movement-related inputs to intermediate cerebellum of the monkey. *J. Neurophysiol.* 69, 74–94. doi: 10.1152/jn.1993.69.1.74
- Volkmar, F. R., and Greenough, W. T. (1972). Rearing complexity affects branching of dendrites in the visual cortex of the rat. *Science* 176, 1445–1447. doi: 10.1126/science.176.4042.1445
- Wagner, M. J., Kim, T. H., Savall, J., Schnitzer, M. J., and Luo, L. (2017). Cerebellar granule cells encode the expectation of reward. *Nature* 544, 96–100. doi: 10.1038/nature21726
- Walter, J. T., Alviña, K., Womack, M. D., Chevez, C., and Khodakhah, K. (2006). Decreases in the precision of purkinje cell pacemaking cause cerebellar dysfunction and ataxia. *Nat. Neurosci.* 9, 389–397. doi: 10.1038/nn1648
- Wang, B., Ke, W., Guang, J., Chen, G., Yin, L., Deng, S., et al. (2016). Firing frequency maxima of fast-spiking neurons in human, monkey, and mouse neocortex. *Front. Cell. Neurosci.* 10:239. doi: 10.3389/fncel.2016.00239
- Williams, R. W., and Herrup, K. (1988). The control of neuron number. *Annu. Rev. Neurosci.* 11, 423–453. doi: 10.1146/annurev.neuro.11.1.423
- Yang, S., Li, C., Qiu, X., Zhang, L., Lu, W., Chen, L., et al. (2013). Effects of an enriched environment on myelin sheaths in the white matter of rats during normal aging: a stereological study. *Neuroscience* 234, 13–21. doi: 10.1016/j.neuroscience.2013.01.003

Conflict of Interest Statement: The authors declare that the research was conducted in the absence of any commercial or financial relationships that could be construed as a potential conflict of interest.

Copyright © 2019 Eshra, Hirrlinger and Hallermann. This is an open-access article distributed under the terms of the Creative Commons Attribution License (CC BY). The use, distribution or reproduction in other forums is permitted, provided the original author(s) and the copyright owner(s) are credited and that the original publication in this journal is cited, in accordance with accepted academic practice. No use, distribution or reproduction is permitted which does not comply with these terms.

Advantages of publishing in Frontiers



OPEN ACCESS

Articles are free to read
for greatest visibility
and readership



FAST PUBLICATION

Around 90 days
from submission
to decision



HIGH QUALITY PEER-REVIEW

Rigorous, collaborative,
and constructive
peer-review



TRANSPARENT PEER-REVIEW

Editors and reviewers
acknowledged by name
on published articles

Frontiers

Avenue du Tribunal-Fédéral 34
1005 Lausanne | Switzerland

Visit us: www.frontiersin.org

Contact us: info@frontiersin.org | +41 21 510 17 00



REPRODUCIBILITY OF RESEARCH

Support open data
and methods to enhance
research reproducibility



DIGITAL PUBLISHING

Articles designed
for optimal readership
across devices



FOLLOW US

@frontiersin



IMPACT METRICS

Advanced article metrics
track visibility across
digital media



EXTENSIVE PROMOTION

Marketing
and promotion
of impactful research



LOOP RESEARCH NETWORK

Our network
increases your
article's readership